International
Progress Report

IPR-04-06

Äspö Hard Rock Laboratory

Analysis of overcoring stress data at the Äspö HRL, Sweden

Analysis of overcoring rock stress measurements preformed using the CSIRO HI

Daniel Ask, KTH/LTU, Sweden

August 2003

Svensk Kärnbränslehantering AB
Swedish Nuclear Fuel
and Waste Management Co
Box 5864
SE-102 40 Stockholm Sweden
Tel 08-459 84 00
+46 8 459 84 00
Fax 08-661 57 19
+46 8 661 57 19

Äspö Hard Rock
Laboratory

Report no.
IPR-04-06
No.
F86K
Author
Daniel Ask
Date
August 2003
Checked by
Rolf Christiansson
Date
Approved
Christer Svemar
Date
2004-06-09

Äspö Hard Rock Laboratory

Analysis of overcoring stress data at the Äspö HRL, Sweden

Analysis of overcoring rock stress measurements preformed using the CSIRO HI

Daniel Ask, KTH/LTU, Sweden

August 2003

Keywords: Rock stress, overcoring, CSIRO HI, Äspö HRL

This report concerns a study which was conducted for SKB. The conclusions and viewpoints presented in the report are those of the author(s) and do not necessarily coincide with those of the client.

Abstract

This report describes a detailed analysis of existing overcoring rock stress data from the CSIRO HI cells obtained at the Äspö HRL and central Oskarshamn, Sweden. The aim of the study is to create a new overcoring strain database on which future work and stress determinations will be based. For this purpose, a new analysis method for overcoring strain data has been developed. In principle, the method involves detailed analysis of the strain versus time curves recorded including all data before and after the overcoring phase. The uncertainty of each strain gauge is considered and based on: (1) the stability of the strain gauges before the overcoring phase; and (2) the difference between the calculated and observed strain.

The biaxial tests for determination of the elastic parameters E and ν have also been analyzed in detail. These parameters have been determined using the secant modulus and unloading curves and at pressures as close to the measured *in situ* stress values as possible. The biaxial testing were conducted using too high loads (up to 20 MPa) leading to radial fractures in the core. These fractures mostly affect the axial gauges, and therefore the determination of Poisson's ratio. However, the re-analysis of the data show that very few gauges are unaffected by the core fracturing. Unaffected or less affected gauges were identified using detailed analysis of the biaxial plots and used to calculate the elastic parameters. The result indicates that Young's modulus end Poisson's ratio are 61.6±5.2 GPa and 0.26±0.02, respectively. This result is different to the original interpretation giving E=65.0±7.1 and υ=0.36±0.07. The original interpretation was made as loading secant modulus at pressures up to 20 MPa. Re-interpreted elastic parameters agree well with results from Borre Probe cores with E=62.2±8.2 GPa and υ=0.26±0.05, and when using data unaffected by the tunnel excavation of E=60.9±6.9 GPa and υ=0.25±0.03. Although more reliable values of the elastic parameters have been derived, the elastic parameters are associated with uncertainties, especially the Poisson's ratio, because many gauges that are less affected by the fracturing had to be used in this study.

The analysis of CSIRO HI overcoring data presented in this report revealed that 57 strain gauges out of 567 are erroneous. Furthermore, 32 strain gauges are of doubtful quality, 1 measurement points requires temperature correction (14.87 m in KA2870A) and another 46 measurement points indicate a high temperature in the test section (most pronounced in boreholes KA1899A, KA2198A, and KA2870A). The re-analysis indicates that a majority of the measurements suffer from boundary yield but the longitudinal expansion has been accounted for (Ask, 2003).

After re-analysis, a standard least squares program was used to determine the stresses at three scales: (1) single tests; (2) borehole averages; and (3) site averages. The results indicate that the stress magnitudes are lower or much lower than the original interpretation, whereas the stress orientations are little affected by the re-analysis. The applied corrections for boundary yield and the updated elastic parameters proved to have about equal effect on the average stress ($(\sigma_H+\sigma_h+\sigma_v)/3$) with an average lowering of about 3.5 MPa. Both corrections had strongest influence on σ_H and the correction ratio between σ_H, σ_h, and σ_v is 2.8:1.8:1.

The NE-2 fracture zone proved to have a major impact on the stresses at Äspö, dividing the rock stress data into two groups: (i) West of the NE-2 the orientation of σ_H is 124±14°N; and (ii) East of the NE-2 the orientation of σ_H is 139±16°N. The latter disregards data from boreholes KA1192A and KA3068A, which are likely to be influenced by ESE-WNW striking minor fracture zones.

To avoid measurement-related uncertainties in future testing with the CSIRO HI cell following recommendations are made: (1) the overcoring strains and temperature readings should be sampled with a frequency that facilitates verification of the strain response and enabling control of drilling-induced heat (at least one recording per minute); (2) the recording of overcoring strains should include about 30 minutes prior to overcoring enabling verification of glue hardening and the post overcoring strains should be sampled until the temperature at the strain gauge position is equal to the initial temperature; (3) the axial strains versus rotation of σ_H towards the borehole direction should be studied in cases where boundary yield is suspected; (4) the load increment during biaxial testing should not exceed 1 MPa and the maximum load must not exceed 10 MPa (with the current core dimensions); and finally (5) all field and laboratory work such as daily logs, drilling protocols, core mapping with respect to grain size, fractures, glue bonding should be carefully documented.

Sammanfattning

Denna rapport innehåller en detaljerad analys av existerande överborrningdata vid Äspö HRL, Sverige. Målet med studien är att etablera en ny töjningsdatabas på vilken framtida arbete och spänningsbestämningar kommer att vara baserade. För detta ändamål har en ny analysmetod utvecklats. Metoden består i princip av att detaljanalysera töjningsdata inklusive data före och efter överborrningsfasen. Kvalitén för varje töjningsgivare bestäms av två delar: (1) stabiliteten av givare före överborrningsfasen samt (2) skillnaden mellan beräknad och uppmätt töjning.

Biaxialtesterna som används för bestämning av de elastiska parametrarna E och ν har också detaljstuderats. Dessa parametrar har bestämts med sekantmetoden från avlastningskurvorna och med laster som ligger så nära spänningsnivån *in situ* som möjligt. Biaxialtesterna utfördes med för höga laster (upp till 20 MPa), vilket resulterat i radiella sprickor i kärnorna. Dessa sprickor påverkar främst de axiella givarna och därmed bestämningen av Poisson's tal. Omtolkningen av data visar dock att få givare är opåverkade av dessa sprickorna. De opåverkade eller mindre påverkade givarna identifierades genom en noggrann analys av biaxialdiagrammen och användes för att bestämma de elastiska parametrarna. Resultaten ger att elasticitetsmodulen och Poisson's tal är 61.6±5.2 GPa och 0.26±0.02. Detta resultat skiljer sig från den ursprungliga tolkningen som gav E=65.0±7.1 GPa och υ=0.36±0.07. Detta kan till viss del förklaras av att den ursprungliga tolkningen gjordes som sekantmodul under pålastning vid tryck upp till 20 MPa. Det omtolkade resultatet stämmer väl överens med resultat erhållna från biaxialprover på kärnor från Borre Probe, E=62.2±8.2 Gpa och υ=0.26±0.05. Om enbart data används som ej störts av tunnelutsprängningen används fås E=60.9±6.9 GPa och υ=0.25±0.03 (Ask, 2003). Trots att mer realistiska värden på de elastiska parametrarna erhållits, är resultaten osäkra, speciellt för Poisson's tal. Anledningen till detta är att även givare som är mindre påverkade av de radiella sprickorna har använts för att överhuvudtaget kunna erhålla ett resultat.

Analysen av CSIRO HI överborrningsdata har visat att 57 givare av 567 inte fungerat samt 32 givare är förknippade med osäkerheter. Vidare kräver 1 mätpunkt temperaturkorrektion (14.87 m i KA2870A) och ytterligare 46 punkter indikerar en hög temperatur i testsektionen (tydligast i borrhål KA1899A, KA2198A och KA2870A). Omtolkningen visar att majoriteten av CSIRO HI data är påverkade av boundary yield men att effekten av detta kan kompenseras i analysarbetet (den longitudinella delen; Ask, 2003).

Efter omtolkning av data användes ett standard minsta-kvadrat program för att bestämma spänningarna i enskilda mätpunkter, borrhål samt för ett område genom analys av data från flera borrhål. Resultaten indikerar betydligt lägre spänningsmagnituder jämfört med publicerade resultat medan spänningsorienteringarna i princip är opåverkade av omtolkningen. Korrektionen för boundary yield och effekten av uppgraderade elastiska parametrar sänkte medelspänningen ($(\sigma_H+\sigma_h+\sigma_v)/3$) ungefär lika mycket. I medel sänktes medelspänningen med 3.5 MPa med den största förändringen för σ_H enligt förhållandet 2.8:1.8:1 (σ_H, σ_h och σ_v).

Zonen NE-2 delar upp bergspänningsdata i ett östligt och ett västligt block baserat på orientering av σ_H. Orienteringen av σ_H öster och väster är 139±16°N respektive 124±14°N. Resultaten från borrhål KA1192A och KA3068A indikerar en öst-västlig orientering av σ_H som troligtvis föranleds av två mindre vattenförande sprickzoner orienterade ESE-WNW.

För att undvika mätrelaterade osäkerheter i framtida överborrningsmätningar med CSIRO HI cellen rekommenderas följande: (1) töjningar under överborrningsfasen liksom avläsning av temperaturer bör ske med en frekvens som möjliggör bedömning av kvalitén på töjningadata samtidigt som borrinducerad värme kan kontrolleras; (2) töjningsdata bör täcka ca 30 minuter fore överborrning så att härdningen av limmet kan verifieras. Dessutom bör data efter överborrningen insamlas till dess att temperaturen vid läget av töjningsgivarna motsvarar temperaturen innan överborrning; (3) de axiella töjningarna som funktion av σ_H-rotation mot borrhålsriktningen bör kontrolleras; (4) belastningssteget under biaxialtester bör ej överstiga 1 MPa och den maximala lasten bör ej överstiga 10 MPa för att undvika sprickor i kärnan; och (5) allt arbete i fält och i lab bör noggrant dokumenteras i dagrapporter, borrprotokoll, kärnkartering mm för att underlätta senare analys.

Table of contents

1 Introduction

1.1 General

The Äspö Hard Rock Laboratory (HRL) of the Swedish Nuclear Fuel and Waste Management Co. (SKB) has been a geoscientific research area since 1986 (Fig. 1-1). The underground laboratory provides an implementation and operation test site for a future deep repository for radioactive waste in Sweden. The vast number of research projects conducted has enabled valuable development and verification of site characterization methods from ground surface, boreholes and underground excavations, among them *in situ* rock stress measurements.

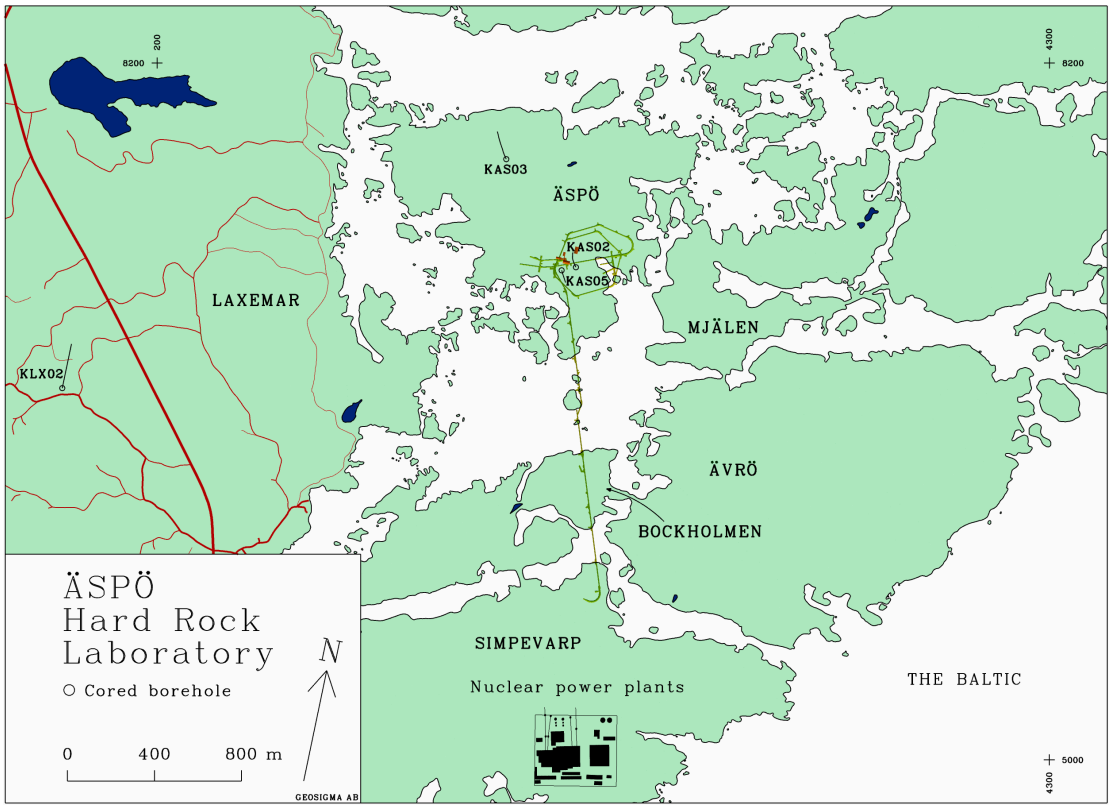

Figure 1-1. *Surface borehole locations in the Äspö region where rock stress measurements have been conducted (Modified after Ekman (2001)).*

A detailed knowledge of the *in situ* stress field is important for several rock-engineering aspects, including investigation, design, construction, and performance of engineered structures built on, in or of rock. Storage facilities for hazardous waste, e.g. spent nuclear fuel are suggested to be located in rock at great depth. A full understanding of the stresses is essential in order to provide (i) boundary conditions for the storage facility; (ii) means to make a proper design and to analyze the mechanical response and possible failure of the rock mass; and (iii) insight on how fluids flow underground (Stephansson, 1997).

Generally, in-situ stress measuring techniques consist of perturbing the rock. The response associated with the perturbance, and often also the process of the disturbance itself, is measured (strain, displacement or hydraulic pressure record) and analyzed by making several assumptions about the rock's constitutive behavior. Over the past 30 years, numerous techniques have been developed and improved. These may be divided into six main groups: hydraulic methods, relief methods, jacking methods, strain recovery methods, borehole breakout methods, and others (Amadei and Stephansson, 1997).

Hydraulic stress measurements record the state of stress in boreholes using fluid pressure to open, generate, propagate and reopen fractures in rock. The directions of the in-situ stresses using hydraulic methods are inferred by inversion techniques or by observing or measuring the orientation of hydraulically induced fractures. The hydraulic methods may be divided into three subgroups: hydraulic fracturing measurements (HF), sleeve fracturing, and hydraulic test in pre-existing fractures (HTPF).

The general idea behind overcoring, or relief, methods are to isolate a rock sample, partially or wholly, from the stress field in the surrounding rock volume and to measure its response (Merrill, 1964; Amadei and Stephansson, 1997). The stresses are inferred from strain or displacement measurements created by the stress relief. A number of assumptions have to be made in order to determine the stress field: (1) the rock behaves as an ideally, linear elastic material; (2) the rock is isotropic (anisotropic solution exists for some cells); (3) the material is continuous and subjected to a homogeneous stress field in the volume of interest. The assumption regarding an elastic and isotropic rock material implies that theory of elasticity applies, hence the deformation of the core sample during overcoring is assumed identical in magnitude to that by the *in situ* stress field but of opposite sign. Application of elastic theory also requires knowledge of the elastic parameters of the rock, Young's modulus, E, and Poisson's ratio, ν.

1.2 Background

The results of the *in situ* hydraulic stress measurements at Äspö indicate a non-linear stress distribution versus depth and the magnitudes seems influenced by discontinuities (Bjarnason et al., 1989; Leijon, 1995; Hansson et al., 1995; Ljunggren and Klasson, 1997; Ekman, 1997; Ekman et al., 1997; Lundholm, 2000a and 2000b; Ask, 2001; Ask et al., 2001a and 2001b; Christiansson and Jansson, 2002; Hudson, 2002; Hakami et al., 2002; Ask et al, 2003; Ask, 2003), see also Figs. 1-3 to 1-9.

When comparing the hydraulic and overcoring stress measurement results, there is a considerable difference in the stress magnitudes. Generally, the overcoring stress measurements (all cells) indicate larger or even much larger magnitudes compared to the hydraulic stress measurements. The orientation of the maximum horizontal stress is though rather consistent for both methods, NW-SE.

The discrepancies between the hydraulic and overcoring measurements at Äspö have been investigated by Ljunggren et al. (1998), based on statistical analyses of the Äspö stress data (Andersson, 1996 and 1997), and a comparison of the Äspö stress data with the data in the Fennoscandian Rock Stress Data Base (FRSDB) (Ljunggren and Persson, 1995). The results also indicate that the variance of the stresses at Äspö differs significantly between the methods. To some extent, this could be explained by depth-

dependency, but the remaining variance is large for the two methods and presumably Gaussian distributed. However, in average, the difference is quite small (Ljunggren et al., 1998).

The variability from the different measuring methods and campaigns has called for re-analysis of existing stress data. Lundholm (2000a and 2000b) used existing hydraulic and overcoring stress data and correlated these to existing geological structures using numerical modeling tools (FLAC, UDEC, and 3DEC). Later, Ask (2001), Ask et al. (2001a and 2001b), Ask et al. (2002), Ask (2003) and Ask et al. (2003) have re-analyzed the hydraulic and overcoring rock stress data, partly using the Integrated Stress Determination Method (ISDM; Cornet, 1993).

This report is the second in a series in which attempts to seek explanations to the observed variability in stress magnitudes are made, see Ch. 1.4.

1.3 Existing rock stress data at the ÄSPÖ HRL

At Äspö HRL the in-situ rock stress measurements consists of hydraulic fracturing stress measurements (HF), hydraulic tests in pre-existing fractures (HTPF) and overcoring stress measurements. Totally, the in-situ rock stress data consist of about 110 HF, 5 HTPF and 140 overcoring stress measurement points (including data in borehole KOV01 in central Oskarshamn), Table 1-1 and Appendix 1.

The overcoring rock stress data have been collected in 21 boreholes. KAS05 and KOV01 (in central Oskarshamn) are the only surface drilled boreholes and the remaining 19 boreholes were drilled from the underground laboratory below the island of Äspö, Fig. 1-2. Four different cells for overcoring rock stress measurements have been used: (1) The Swedish State Power Boards (SSPB) Borre Probe; (2) Three different CSIRO (Commonwealth Scientific and Industrial Research Organization) Hollow Inclusion cells (9 and 12 strain gauges respectively, the latter with thick and thin hollow inclusions); and (3) The Atomic Energy of Canada (AECL) Doorstopper. Of the total 140 measurement points, about 50 are influenced by the underground excavation (Table 1-1). Note that the measurements conducted in the pillar between the TBM and drill&blast tunnels at the Zedex Test Site indicate a stress field similar to the overall stress field at the HRL (Ask et al., 2003; Ask 2003).

The applied data analysis in this study is based on existing overcoring rock stress data from the CSIRO HI cells, which have been extracted and re-evaluated from raw data and from reports (Lee et al., 1993; Lee et al., 1994; Litterbach et al., 1994; Nilsson et al., 1997). Complementary material has also been received from Australian Mining Consultants. A number of studies papers relating to the rock stress data have also been reviewed (Leijon, 1995; Ekman, 1997; Ekman et al., 1997; Myrvang, 1997; Lundholm, 2000a and 2000b; Christiansson, 2000; Ask, 2001; Ask et al., 2001a and 2001b; Ask et al., 2002; Christiansson and Jansson, 2002; Hudson, 2002; Hakami et al., 2002; Ask et al., 2003; Ask, 2003). Figures 1-3 and 1-9 present the reported results from the Äspö region. The results from the above references will be used for comparison with the results obtained in the present study.

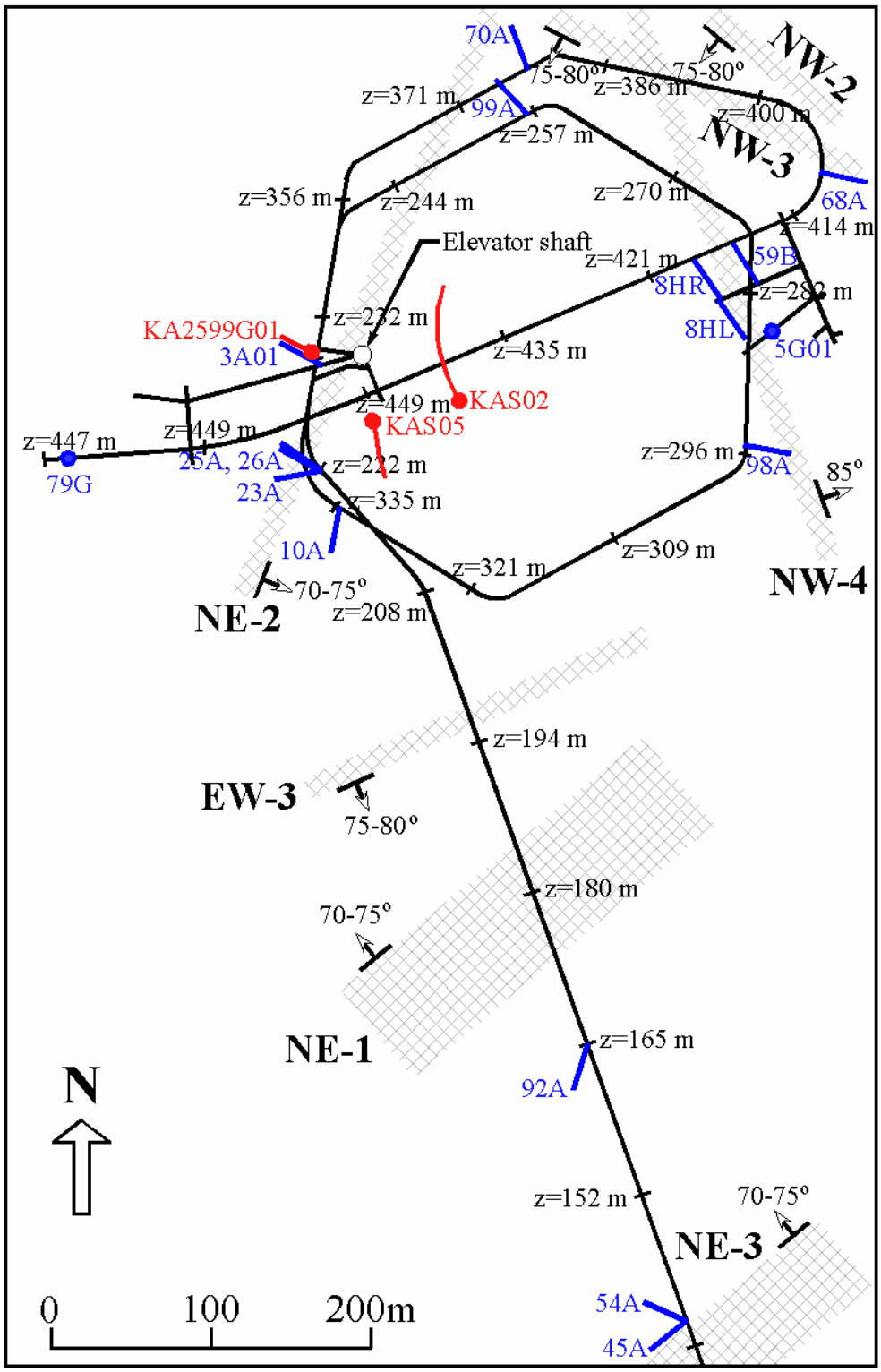

Figure 1-2. *Detailed map of the Äspö HRL showing stress measurement boreholes and major fracture zones at tunnel intersection depth (with abbreviated overcoring borehole names). Overcoring and hydraulic fracturing boreholes are represented by solid blue and red lines, respectively. Note that the blue-marked borehole 3A01 also includes hydraulic fracturing stress data. Vertical boreholes are marked with circles and sub-vertical boreholes with circles and solid line in the borehole direction (Modified after Rhén et al, 1997).*

Table 1-1. Stress measurements performed in the Äspö region (Bjarnason et al., 1989; Lee et al., 1993; Lee et al., 1994; Litterbach et al., 1994; Ljunggren and Klasson, 1996; Ljunggren and Klasson, 1997; Ekman, 1997; Ekman et al., 1997; Nilsson et al., 1997; Ljunggren and Bergsten, 1998; Klasson et al., 2001; Klasson and Andersson, 2001; Klasson et al., 2002; Klee and Rummel, 2002; Rummel et al., 2002). Number in brackets indicate the number of measurement points strongly influenced by the tunnel excavation.

Borehole	Hydraulic data		Overcoring data			
	HF (number)	HTPF (number)	BP (number)	CHI_9 (number)	CHI_12 (number)	AECL (number)
KAS02	22	-	-	-	-	-
KAS03	21	-	-	-	-	-
KAS05	-	-	7	-	-	-
KLX02	37	5	-	-	-	-
KOV01	19	-	9	-	-	-
KA1045A	-	-	-	4	-	-
KA1054A	-	-	-	3	-	-
KA1192A	-	-	-	-	3	-
KA1623A	-	-	-	-	3	-
KA1625A	-	-	-	-	4	-
KA1626A	-	-	-	-	3	-
KA1899A	-	-	-	-	5	-
KA2198A	-	-	-	-	4	-
KA2510A	-	-	-	-	6	-
KA2870A	-	-	-	-	5	-
KA3068A	-	-	-	-	4	-
KZ0059B	-	-	-	-	6 (6)	-
KXZSD8HR	-	-	23 (23)	-	-	-
KXZSD81HR	-	-	4 (4)	-	-	-
KXZSD8HL	-	-	4	-	-	-
KK0045G01	-	-	19 (11)	-	-	-
KA2599G01	6	-	-	-	-	4
KF0093A01	6	-	4	-	-	3
KA3579G	-	-	11 (7)	-	-	-
SUM	111	5	81 (45)	7 (0)	43 (6)	7 (0)
	116		138 (51)			

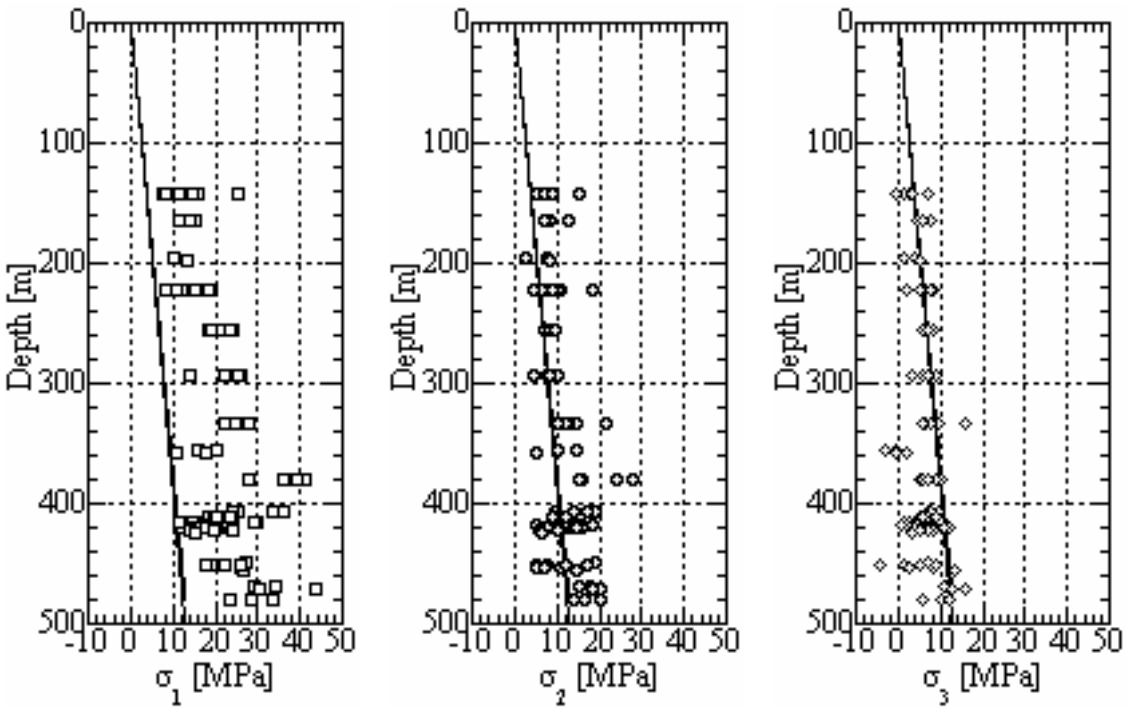

Figure 1-3. *Compilation of principal stress magnitudes versus depth from overcoring rock stress data at the Äspö HRL. Solid line is vertical stress from weight of overburden.*

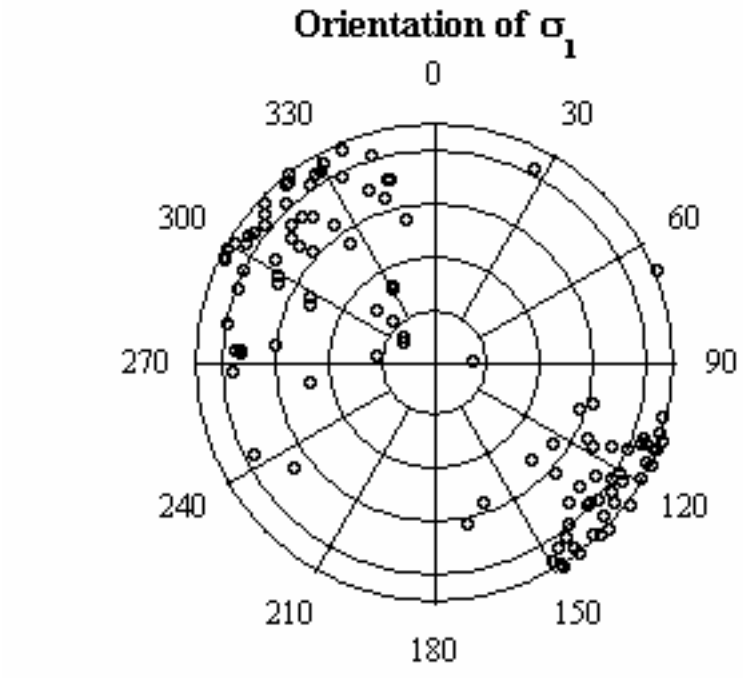

Figure 1-4. *Compilation of orientation of major principal stress σ_1 between 140 to 480 m depth from overcoring rock stress measurements at the Äspö HRL.*

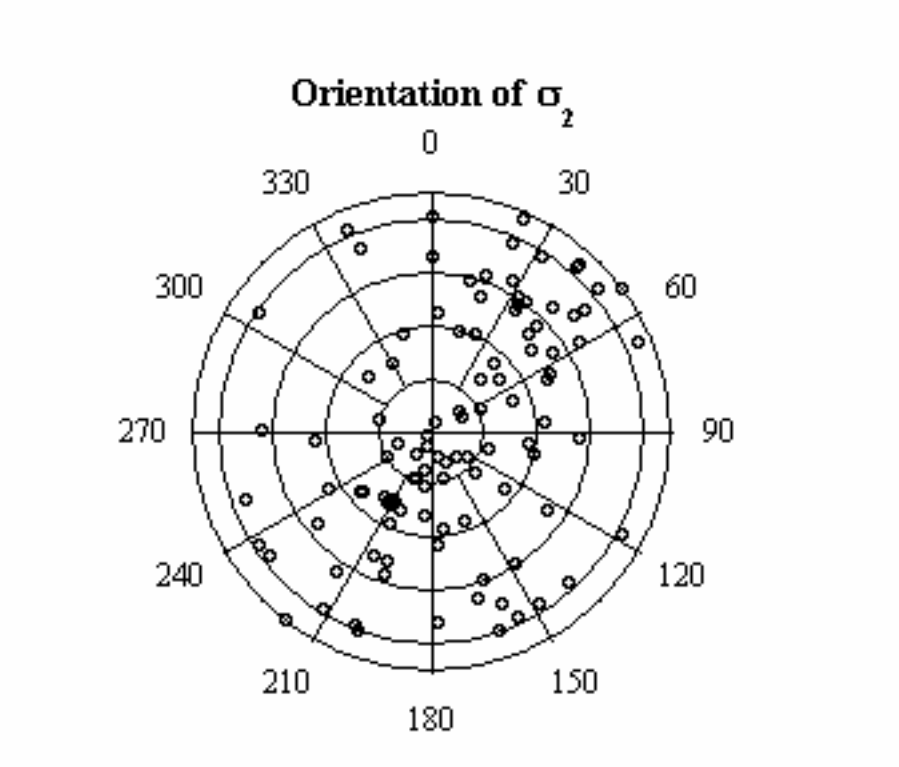

Figure 1-5. *Compilation of orientation of intermediate principal σ_2 between 140 to 480 m depth from overcoring rock stress measurements at the Äspö HRL.*

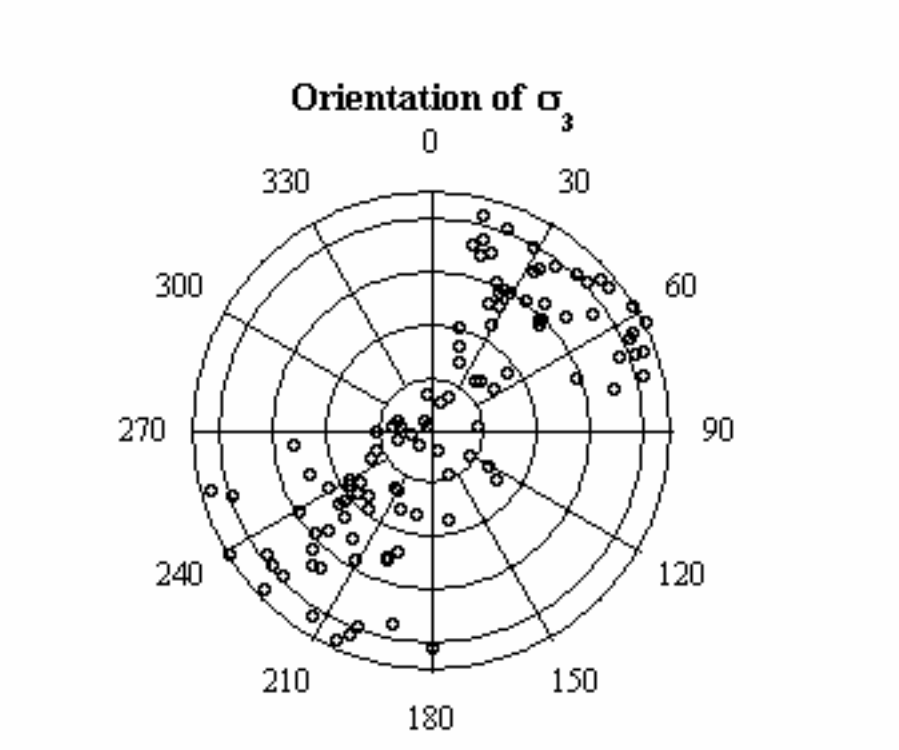

Figure 1-6. *Compilation of orientation of minor principal stress σ_3 between 140 to 480 m depth from overcoring rock stress measurements at the Äspö HRL.*

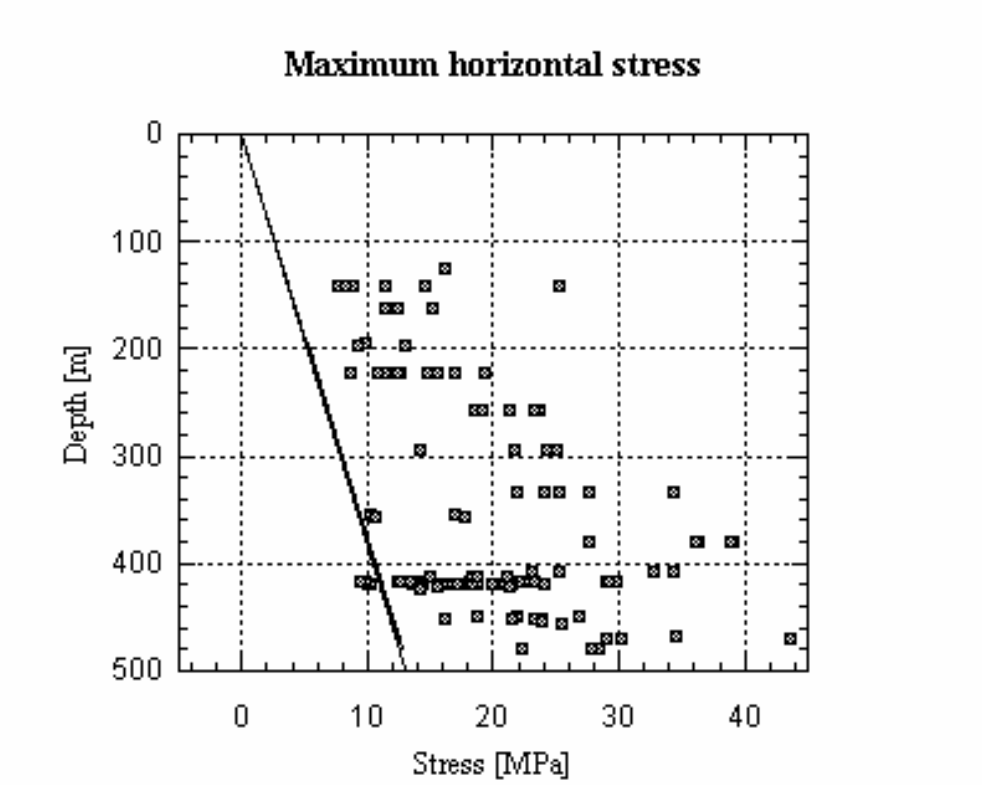

Figure 1-7. *Compilation of maximum horizontal stress σ_H versus depth from overcoring rock stress measurements at the Äspö HRL. Solid line is vertical stress from weight of overburden.*

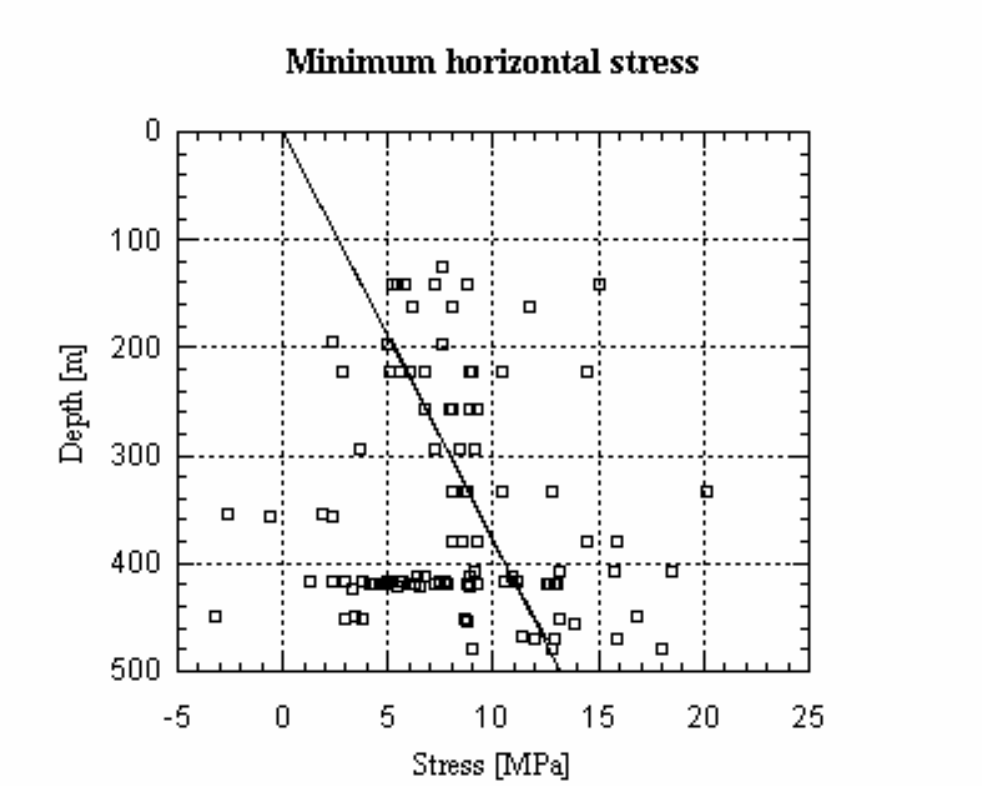

Figure 1-8. *Compilation of minimum horizontal stress σ_h versus depth from overcoring rock stress measurements at the Äspö HRL. Solid line is vertical stress from weight of overburden.*

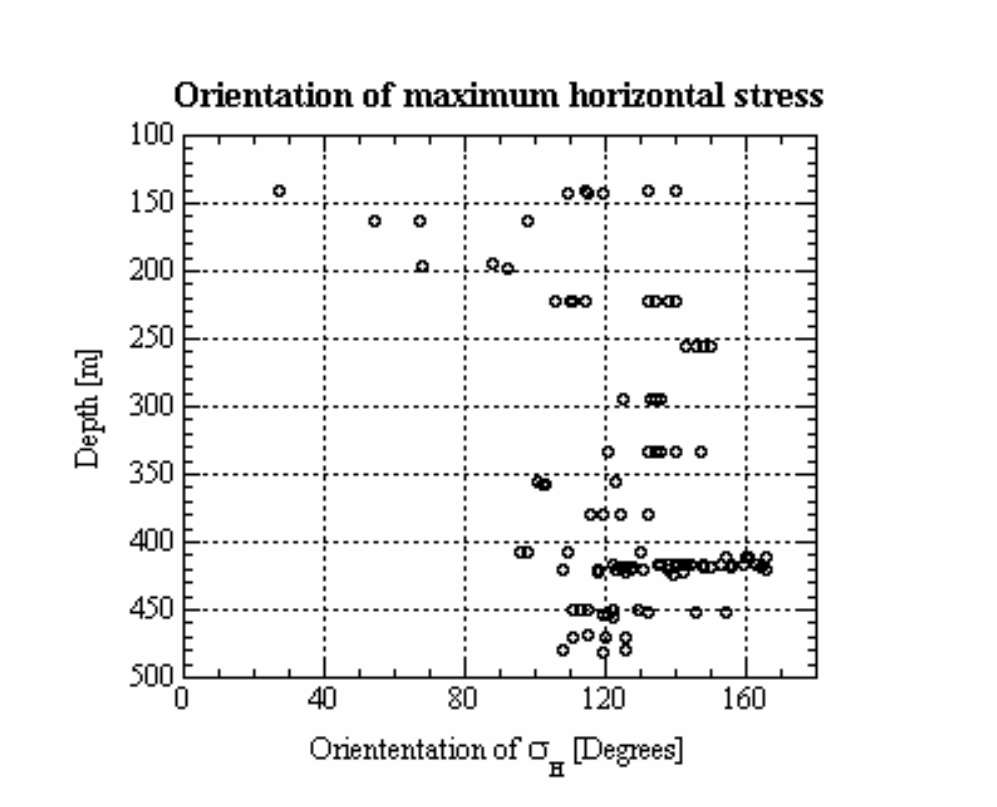

Figure 1-9. *Compilation of orientation of maximum horizontal stress versus depth from overcoring rock stress measurements at the Äspö HRL.*

1.4 Aim of study

The present study aims at improving the quality of the existing overcoring rock stress database in the Äspö region. The detailed analysis of overcoring rock stress data aim at eliminating information from doubtful strain gauges and thereby improve and receive a more reliable overcoring strain database. The re-analyzed strain database will be used for stress calculations at different scales and to evaluate the observed variability between different measuring techniques at Äspö HRL and improve the consistency in results obtained from different methods.

In this report, the overcoring strain data from the CSIRO HI cells will be analyzed. The stress data may be grouped according to three different scales: (1) The single test scale; (2) The measuring location scale, which includes results from one or more boreholes; and (3) The application scale, representing results from a larger rock volume for a particular rock engineering problem, i.e. following the strategy suggested by Gray and Toews (1974) and Leijon (1989).

This report is the third of a series in which the inversion method developed by Cornet and Valette (1984); Cornet (1993) is applied. The first and second reports dealt with the hydraulic stress data (boreholes KAS02, KAS03 and KLX02; Ask et al., 2001b) and overcoring data using the Borre Probe (Ask et al., 2002), respectively.

2 The overcoring cells used in the ÄSPÖ region

2.1 General

The measurements performed at the Äspö HRL are so called borehole relief methods (Amadei and Stephansson, 1997). The relief process is in this case accomplished by drilling a large borehole concentric with an existing borehole (pilot hole), in which the measurement cell is located (see Fig. 2-1).

2.2 The Swedish state power Board's Borre Probe

The Borre Probe is described in detail in a separate SKB-report (Ask et al., 2002) and the details of this device are not described here.

2.3 The CSIRO HI cells

2.3.1 General

The CSIRO Hollow Inclusion cells (HI) were developed in Australia in the beginning of the 1970s (Worotnicki and Walton, 1976). The CSIRO-types are so-called soft inclusion cells implying that they are compliant and deform simultaneously with the rock during overcoring. The methodology prevents the strain gauges from being affected by water and dust. The CSIRO HI cells exist with 9 and 12 strain gauges as well as in thin and thick wall versions. The thinner version was developed especially for weak rock (Walton and Worotnicki, 1986) but both types have been used at the Äspö HRL. A detailed description of the methodology is found in Worotnicki (1993).

2.3.2 Techniques, equipment and procedures

The cell is composed of Araldite (epoxy) thin-walled pipe with an inner diameter of 32 mm and outer diameter of 36 mm. The cell is glued to the wall of the pilot hole (38 mm) using a 1 mm thick layer of epoxy cement, Fig. 2-1. The thinner version, developed for weak rocks, has a thickness of one-third of the regular cell.

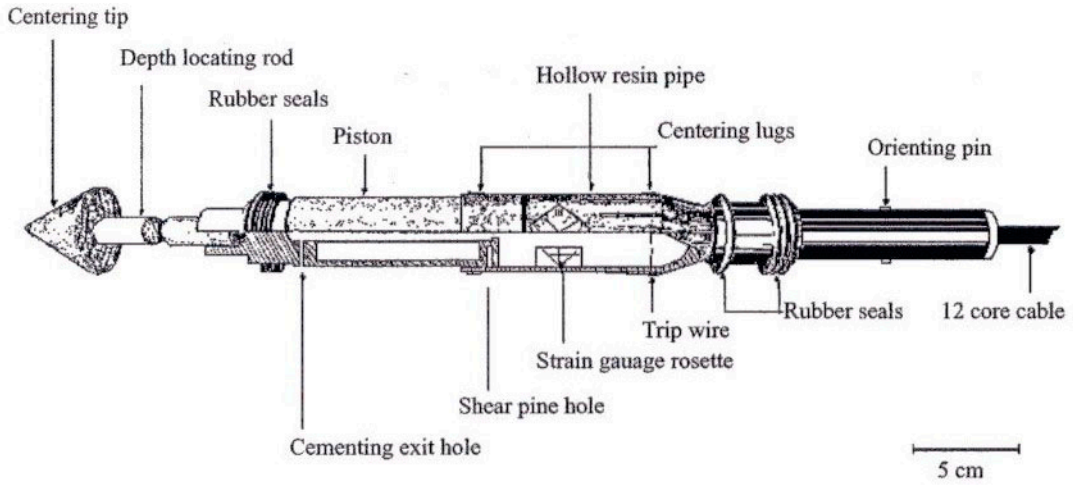

Figure 2-1. *Detailed description of the CSIRO HI cell (Worotnicki, 1993)*

The cell contains three strain rosettes 120° apart. The gauge configuration is as follows: 2 axial; 3 tangential and 4 gauges inclined ±45° for the 9-gauge cell. The 12-gauge cell has one additional 45° and two additional tangential gauges (Fig. 2-2). The gauges are 10 mm long and are located 0.5 mm below the cell outer surface.

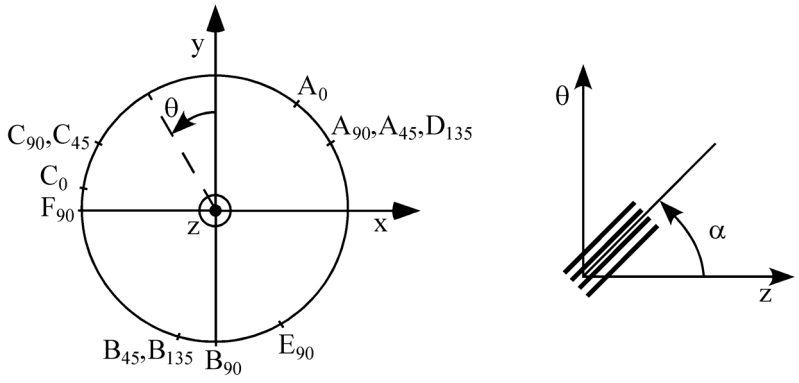

Gauge	θ [°]	α [°]
A_0	322.9	0
A_{90}	300.0	90
A_{45}	300.0	45
B_{45}	163.6	45
B_{135}	163.6	135
B_{90}	180.0	90
C_0	82.9	0
C_{90}	60.0	90
C_{45}	60.0	45
D_{135}	300.0	135
E_{90}	210.0	90
F_{90}	90.0	90

Figure 2-2. *Strain gauge configuration for the 9- and 12-gauge CSIRO HI cells (After Stillborg and Leijon (1982) and Worotnicki (1993)). The 9 gauge version lacks gauges D_{135}, E_{90}, and F_{90}.*

Grouting of the cell is achieved by filling the epoxy tube with epoxy cement. The cement is thereafter extruded by displacement with a piston. The piston activation is done either by forcing a protruding rod against the end of the borehole or by manually pulling the piston into the epoxy shell. Seals are used to confine the grout around the cell.

At present, three types of epoxy cement are available depending on the ambient rock temperature (Worotnicki, 1993). The bond strength is approximately 4 and 8 MPa, for the regular and thin versions respectively.

Overcoring of the cell is usually done with a 150 mm diameter drill bit. Satisfactory results are usually achieved with 200 to 400 mm long overcores.

The HI cells measure the strain and temperature continuously during the overcoring phase. The CSIRO HI cells require 10-20 hours for the epoxy adhesive to cure.

2.3.3 Remarks

The CSIRO HI cells are capable of measuring the complete stress tensor in one single borehole. Reliable results have been achieved in isotropic, homogeneous materials and acceptable results in moderately non-homogeneous and medium-grained rock. Unlike the Borre Probe, the CSIRO HI is little influenced by rock inhomogeneities and grain size (good results up to 4-5 mm grain size).

If the rock has a high porosity or if intensive water flow from joints occurs, it may be difficult/impossible to achieve a satisfactory bonding between the cell and the rock.

The epoxy adhesive may yield (especially in low temperature rock) as a consequence of the increased temperature during overcoring (Irvin et al., 1987). This result in a relative increase in the strain measured in the axial and ±45° directions, thus indicating a principal stress in the direction of the borehole, Fig. 2-3.

During biaxial testing, the rock core are usually loaded up to 20 MPa, which in several cases has lead to initiation of axial fractures resulting in unrealistic Poisson's ratios.

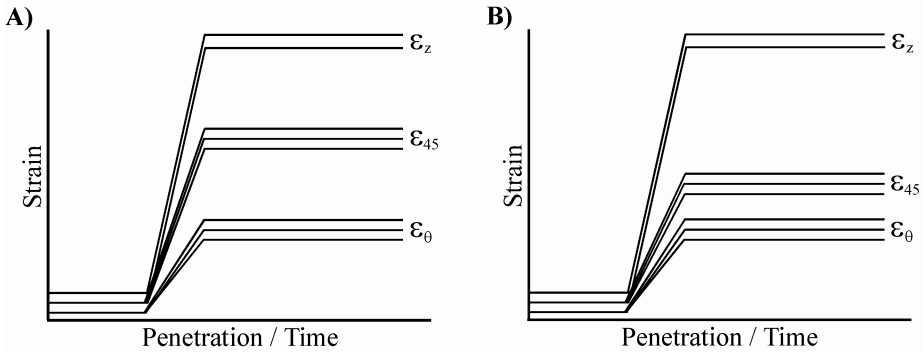

Figure 2-3. *Effect of epoxy yield on overcoring strains (After Irvin et al. (1987)). A) Normal overcoring results and B) result when boundary yield has taken giving large axial strains relative to the other strains.*

3 Analysis of existing overcoring rock stress data

3.1 General

The general idea behind overcoring, or relief, methods are to isolate a rock sample, partially or wholly, from the stress field in the surrounding rock volume and to measure its response (Merrill, 1964; Amadei and Stephansson, 1997). The stresses are inferred from strain or displacement measurements created by the stress relief. A number of assumptions have to be made in order to determine the stress field: (1) the rock behaves as an ideally linear elastic material; (2) the rock is isotropic (anisotropic solution exists for some cells); (3) the material is continuous and subjected to a homogeneous stress field in the volume of interest.

The assumption regarding an elastic and isotropic rock material implies that elastic theory applies, hence the deformation of the core sample during overcore is assumed identical in magnitude to that by the *in situ* stress field, but of opposite sign. Application of elastic theory also requires knowledge of the elastic parameters of the rock, Young's modulus, E, and Poisson's ratio, ν.

The measurements performed at the Äspö HRL are so called borehole relief methods (Amadei and Stephansson, 1997). The relief process is in this case accomplished by drilling a large borehole concentric with an existing borehole (pilot hole), in which the measurement cell is located (see Fig. 2-1).

The Borre Probe has been used in 7 different boreholes in the Äspö HRL. In total, 72 measurement points are available (see Table 1.1). Of these, only 57 are reported successful due to a variety of reasons. The Borre Probe data are dealt with in an individual study (Ask et al., 2002) and is not commented further in this report.

The 9 gauge CSIRO Hollow Inclusion cell were used in the early stage of the construction of the Äspö HRL. They are therefore located at rather shallow depth (boreholes KA1045A and KA1054A at approx. 140 m). The 9-gauge was exchanged with the 12-gauge CSIRO HI cell and were primarily used for measurements in the ramp of the HRL, except for the measurements conducted at the Zedex area. In total, 7 measurement points are available with the 9-gauge cell and 43 points with the 12-gauge version. During the entire measurement campaign, both the thick and thin versions of the 12-gauge cell have been used.

3.2 Methodology

The overcoring strain data is analyzed at three different scales: (1) the single test scale; (2) the measuring location scale, which includes results from one or more boreholes; and (3) the application scale, representing results from a larger rock volume for a particular rock engineering problem or site, i.e. following the work by Gray and Toews (1974) and Leijon (1989).

3.3 Brief theory of overcoring rock stress measurements

3.3.1 General

The theory of relief methods are generally based on elastic theory and it is normally assumed that the rock behaves in a isotropical, linear elastic manner. Hence, the deformation of the core sample during stress relief is assumed identical in magnitude to that produced by the *in situ* stress field but opposite in sign. It is assumed that the rock mass is both continuous and homogeneous. Furthermore, it is assumed that the measuring probe is mounted far enough from the end of the probe, to ensure that no stress/strain variations exist along the axis of the probe (Amadei and Stephansson, 1997).

Consider a hole in a plate composed of an ideally elastic and isotropic material. If the material is subjected to a homogeneous stress field, stress will concentrate around the hole. The corresponding displacements around the borehole are given by (Hiramatsu and Koga, 1968):

$$u_r = \frac{1+\nu}{2E} r \left[\begin{array}{l} \dfrac{R^2}{r^2}\left(\sigma_x + \sigma_y\right) + \left\{1 + 4(1-\nu)\dfrac{R^2}{r^2} - \dfrac{R^4}{r^4}\right\}\left\{\left(\sigma_x - \sigma_y\right)\cos 2\theta + 2\tau_{xy}\sin 2\theta\right\} \\ + \left\{\dfrac{1-\nu}{1+\nu}\left(\sigma_x + \sigma_y\right) - 2\dfrac{\nu}{1+\nu}\sigma_z\right\} \end{array} \right] \quad (3\text{-}1)$$

$$u_\theta = \frac{1+\nu}{2E} r \left[\left\{1 + 2(1-2\nu)\frac{R^2}{r^2} + \frac{R^4}{r^4}\right\}\left\{\left(\sigma_x - \sigma_y\right)\sin 2\theta - 2\tau_{xy}\cos 2\theta\right\} \right] \quad (3\text{-}2)$$

$$u_z = \frac{1+\nu}{2E} \left[2r\left\{1 + \frac{R^2}{r^2}\right\}\left(\tau_{yz}\sin\theta + \tau_{zx}\cos\theta\right) + \frac{z}{1+\nu}\left\{\sigma_z - \nu\left(\sigma_x + \sigma_y\right)\right\} \right] \quad (3\text{-}3)$$

where E is Young's modulus, ν is Poisson's ratio, R is the borehole radius, r is the radial distance to the measurement point, σ_i and τ_i are components of the in-situ stress field, and θ is the orientation of the strain gauges (see Fig. 2-2).

3.3.2 The CSIRO HI cells

The CSIRO HI data includes nine or 12 strain gauges which are related to the *in situ* stress field according to (Timoshenko and Goodier, 1934):

$$\varepsilon_\theta = \frac{1}{R}\left\{(u_r)_{r=R} + \left(\frac{\partial u_\theta}{\partial \theta}\right)_{r=R}\right\} \tag{3-4}$$

$$\varepsilon_z = \left(\frac{\partial u_z}{\partial z}\right)_{r=R} \tag{3-5}$$

$$\gamma_{\theta z} = \frac{1}{R}\left(\frac{\partial u_z}{\partial \theta}\right)_{r=R} \tag{3-6}$$

$$\varepsilon_{45^\circ} = \frac{1}{2}(\varepsilon_z + \varepsilon_\theta + \gamma_{\theta z}) \tag{3-7}$$

where

$$\left(\frac{\partial u_\theta}{\partial \theta}\right)_{r=R} = -\frac{4(1-\nu^2)}{E} R\left[(\sigma_x - \sigma_y)\cos 2\theta + 2\tau_{xy}\sin 2\theta\right] \tag{3-8}$$

$$\left(\frac{\partial u_z}{\partial z}\right)_{r=R} = \frac{1}{E}\left[\sigma_z - \nu(\sigma_x + \sigma_y)\right] \tag{3-9}$$

$$\left(\frac{\partial u_z}{\partial \theta}\right)_{r=R} = \frac{R}{E}\left[4(1+\nu)(\tau_{yz}\cos\theta - \tau_{zx}\sin\theta)\right] \tag{3-10}$$

Combining these equations and using r = R, gives the final solution (this time including K-factors for the CSIRO HI cell)

$$\varepsilon_\theta = \left[(\sigma_X^\infty + \sigma_Y^\infty)K_1 - 2(1-\nu^2)\{(\sigma_X^\infty - \sigma_Y^\infty)\cos 2\theta + 2\tau_{XY}\sin 2\theta\}K_2 - \nu\sigma_Z^\infty K_4\right]/E \tag{3-11}$$

$$\varepsilon_z = \left[\sigma_Z^\infty - \nu(\sigma_X^\infty + \sigma_Y^\infty)\right]/E \tag{3-12}$$

$$\gamma_{\theta z} = \left[4(1+\nu)(\tau_{YZ}^\infty\cos\theta - \tau_{ZX}^\infty\sin\theta)\right]K_3/E \tag{3-13}$$

$$\varepsilon_{45^\circ} = \frac{1}{2}(\varepsilon_z + \varepsilon_\theta + \gamma_{\theta z}) \tag{3-14}$$

The K-factors involve the effect of locating the strain gauges at some distance from the rock surface and the resistance of the HI cell to deformation. Thus, each K-factor represents the ratio between a particular strain at the location of a strain gauge in the HI pipe caused on overcoring by a particular component on the *in situ* stress field and the strain which would have been caused by the stress component at the opposite point on the surface of the pilot hole if there was no HI cell installed (Worotnicki, 1993; Appendix 3).

3.4 Analysis of recorded strains

3.4.1 Determination of strains

Generally, when determining the observed strains from overcoring, a stable value is preferential before overcoring starts and after overcoring stops. The difference between these values is assumed to correspond to the strain relief involved in the overcoring process. Further, the value after overcoring stop is chosen in such a manner that temperature effect is minimized. In practice, this means that flushing is continued until the temperature in the test section is close to the *in situ* rock mass temperature.

However, in some cases, this is not possible and temperature corrections are necessary (if more than 1°C), see Chap. 3.4.3.

The CSIRO HI measurements were conducted with a poor sampling frequency which made the analysis of overcoring data from the CSIRO HI cells difficult, especially regarding identification of malfunctioning strain gauges, Fig. 3-1. This also prevented application of the same analysis technique of strain data to both the Borre Probe (Ask et al., 2002) and the CSIRO HI cells.

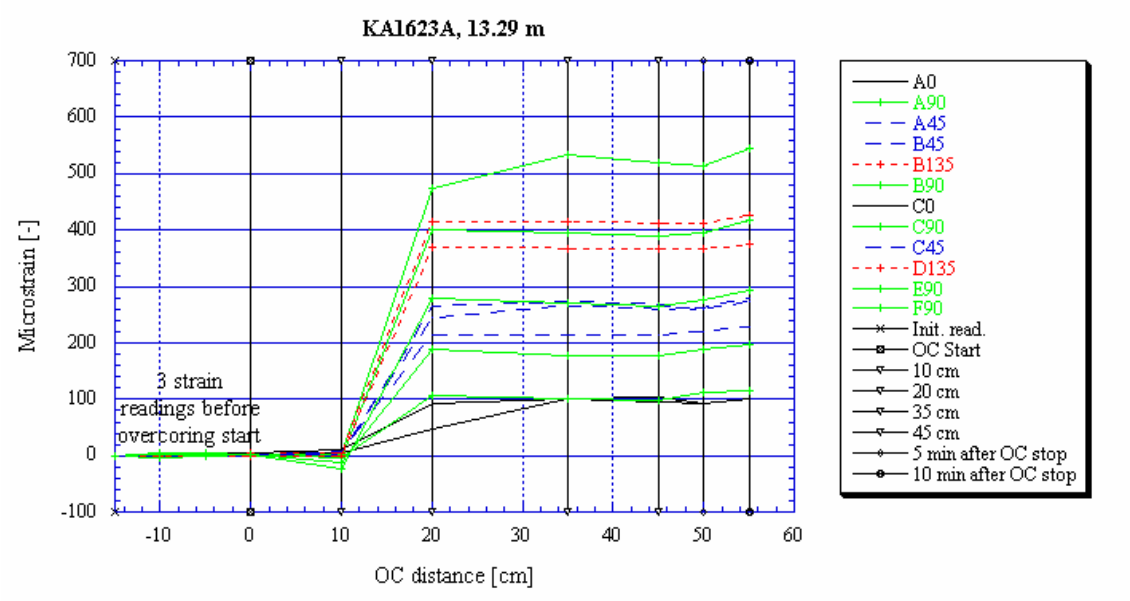

Figure 3-1. *Typical strain gauge response during overcoring. In this measurement point at 13.29 m in KA1623A, 10 strain readings are made during the overcoring test of which 3 and 2 readings are made before respectively after the overcoring process. Thus, only 5 readings cover the strain response during the relaxation process (including the overcoring start reading).*

The analysis of strain data from the CSIRO HI cells was therefore extended to include the strain versus time response during overcoring, as well as a careful examination of the recorded strains in each borehole. The CSIRO HI data have an advantage compared to the Borre Probe data because the cell is installed with the same orientation in each measurement point along a borehole (Fig. 3-2). This facilitates direct comparison for each group of recorded strains (e.g. Myrvang, 1997).

For example, tangential strains from borehole KA1623A (Table 3-1) reveals maximum tangential strains for gauge B90, implying roughly a horizontal-vertical strain distribution. Strain gauges A90 and E90 have intermediate strain levels and symmetry implies that strain gauges C90 and F90 should have the smallest recorded strains. Following this reasoning, the recorded strains for gauge A90 and possibly also for F90 in the first measurement point are identified as too high, leading to the conclusion that these two strain gauges are regarded as uncertain in the subsequent stress calculation. These strains are thus removed if they have a strong impact on the stress tensor.

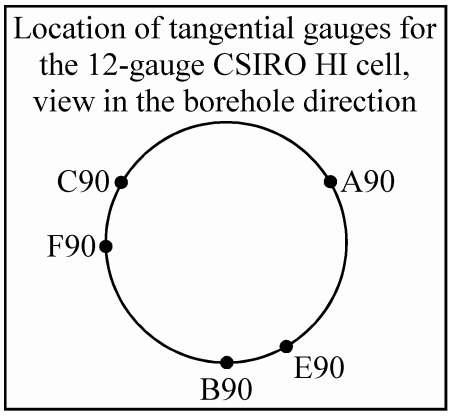

Figure 3-2. *Location of tangential gauges for the 12-gauge CSIRO HI cell, view in the borehole direction (After Ask, 2003).*

Table 3-1. Analysis of tangential strains from CSIRO HI measurements in borehole 1623A (After Ask, 2003).

Depth [m]	A90 [-]	B90 [-]	C90 [-]	E90 [-]	F90 [-]
222.62	544	418	116	197	292
222.60	267	423	104	298	120
222.58	200	310	116	232	108

In general, the overcoring data before overcoring start include three strain readings: (1) before initiation of drilling water; (2) 5 minutes with drilling water; and (3) 10 minutes with drilling water. After completed overcoring, two readings are generally made, i.e. 5 and 10 minutes after overcoring. Verification of the gluing of strain gauges in connection to initiation/termination of flushing with drilling water is difficult as the sampling frequency is poor (see Ask et al., 2002). Moreover, because the temperature is not recorded continuously, possible strain jumps could be due to increasing/decreasing rock temperatures from the drilling fluid used. Thus, poor gluing of strain gauges can only be suspected when there is a strong strain reaction displayed between the readings with respectively without drilling water (e.g. measurement point 17.15 m in borehole KA1054A; Fig. 3-3). The overcoring graphs are presented in Appendix 4 and the results of the strain analysis are presented in Appendix 6.

3.4.2 Determination of standard deviation for strains

The analysis of the strain data is based on the assumption that all errors obey Gaussian distribution. The analysis may be divided in two steps: (1) The stability of the strain gauge readings; and (2) The difference between calculated and observed strain.

The strain gauge readings should be stable, if the gauges are properly attached to the rock, and if there are small or no fluctuations of the temperature of the drilling water. Only the strain variations before overcoring start were used because of high transient temperatures after completed overcoring (the analysis of Borre Probe data included strain variation before and after the overcoring phase (Fig. 3-4)). The resulting interval is assumed to be equal to a 99 % confidence interval, and is used to determine the first part of the standard deviation for the strain gauge, denominated SD^{gauge}.

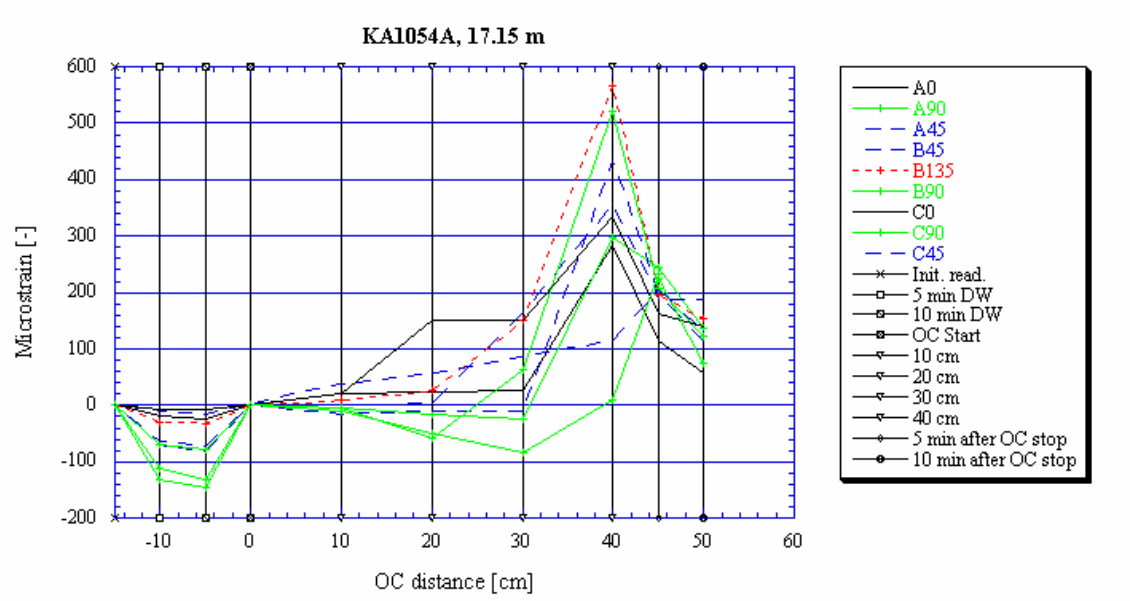

Figure 3-3. *Strain gauge response during overcoring in measurement point 17.15 m in borehole KA1054A. A strong strain gauge reaction is found when drill water is turned on. The core fractures between 30 and 40 cm of drilling giving abnormal values at the 40 cm reading. However, reasonable strain values are still recorded after completed overcoring.*

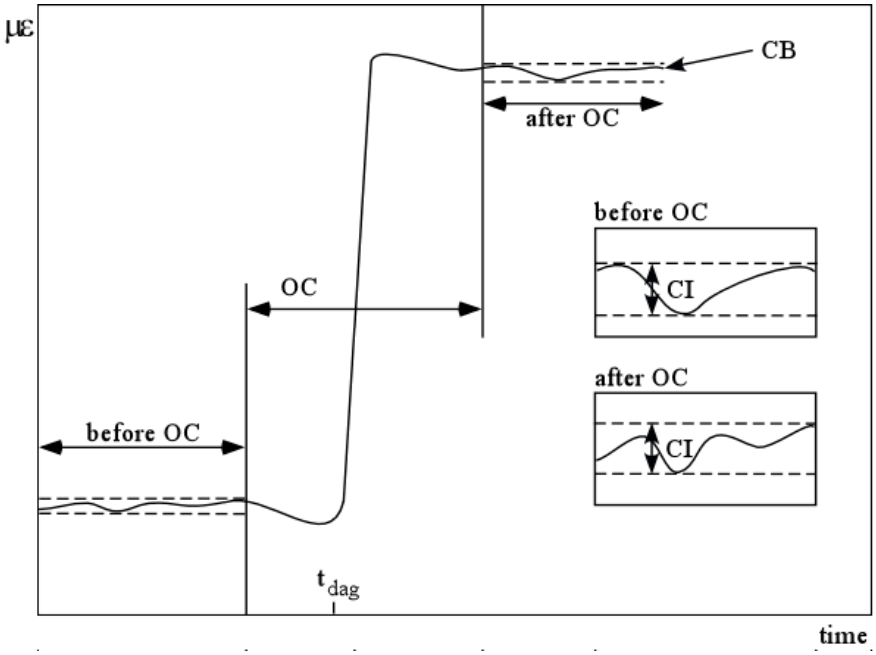

Figure 3-4. *Schematic response of a tangential strain gauge during overcoring. The strongest strain gauge response occurs at t_{dag}, i.e. when the **d**rill bit is **a**t the **g**auge position. The dotted lines show the 99 % confidence intervals (CI) before and after overcoring (OC). CB denotes core break. For the CSIRO HI measurements, only the strain variation before overcoring is used.*

The difference between the calculated and observed strain values may be used to determine the standard deviation for each strain gauge (Fig. 3-5). For calculation of the strains, a standard least-squares program was developed. The calculation is based on following data, of which only the first is presented in this report: (1) individual measurement points; (2) average values for a number of measurement points in one borehole that has been judged to represent the same *in-situ* stress field; and (3) average values for a number of measurement points in multiple boreholes that has been judged to represent the same *in-situ* stress field.

The resulting interval is assumed to be equal to a 99 % confidence interval and is used to determine the second part of the standard deviation for the strain gauge, denominated $SD^{diff, ind}$, $SD^{diff, avsb}$ and $SD^{diff, avmb}$ for the **ind**ividual; **av**erage for **s**ingle **b**orehole; and **av**erage for **m**ultiple **b**oreholes, respectively.

The final standard deviation for the gauge is the sum of these sources, $SD = SD^{gauge} + SD^{diff}$, i.e. giving maximum three values according to the classification above. The reason for this choice of standard deviation is that the least squares solution may give zero standard deviation when based solely on the difference between measured and calculated strain, i.e. $SD^{diff}=0$, although one strain rosette is malfunctioning.

If a strain gauge is judged unreliable (malfunctioning or removed based Chauvenet's criteria for outlyers) and, hence, excluded during the later stress calculation, the strain gauge is removed and a new set of standard deviations is calculated (only SD^{diff} and SD will change). Note that only one measurement at the time is removed (the most erroneous). Thus, a stepwise procedure will be conducted during stress determinations.

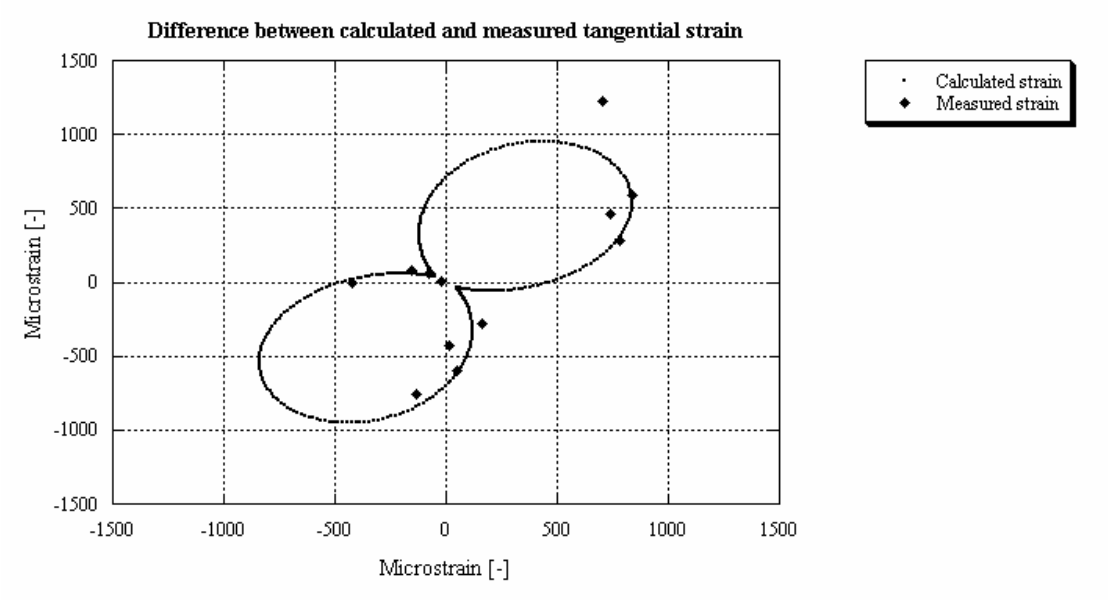

Figure 3-5. *Difference between calculated and measured tangential strain for the deeper measurement points in the Borre Probe borehole KA3579G, Prototype Repository. This difference is assumed equal to a 99% confidence interval, giving SD^{Diff} for each strain gauge (After Ask et al., 2002).*

The methodology for the determination of strains and their standard deviation to be included in the stress analysis is presented in Fig. 3-6. Strain gauges are discarded when obvious problems have occurred (e.g. unglued rosettes) or when the differences between calculated and measured strains exceed the empirical Chauvenet's criteria (Holman, 1994) for outlyers.

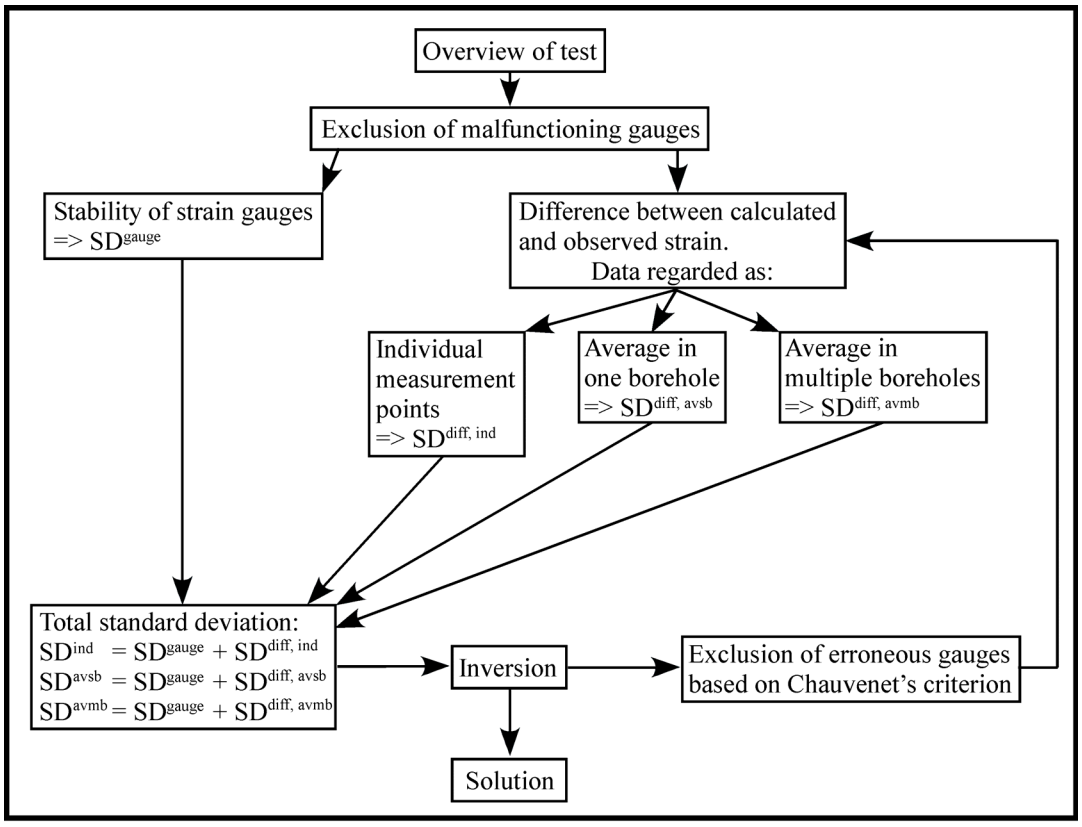

Figure 3-6. *Flow chart showing the steps included in the determination of strains.*

3.4.3 Temperature effects

The CSIRO HI data include strain records up to 10 minutes after the end of drilling. The average temperature difference between post- and pre-readings of strains is small (commonly less than 1 °C), implying that the temperature effects are small and corrections not necessary. However, in a few cases, the temperature difference has not been recorded (all tests in boreholes KA1045A, KA1054A, and KA1626A and a few tests in boreholes KA1625A, KA1899A and KA2510A) leading to uncertainties in the stress magnitudes in these boreholes. In the original interpretations, corrections of about 1°C were applied to three measurement points and 4.3°C in one measurement point (borehole KA2870A). In the analysis of the Borre Probe data (Ask et al., 2002), temperature effects below 1°C have been neglected and corrections only applied to the results from borehole KA2870A (4.3°C).

The temperature correction may be determined using following equation (Leijon, 1988):

$$\alpha_M^{Theoretical} = \alpha_A + \alpha_s \qquad (3\text{-}15)$$

where $\alpha_M^{Theoretical}$ is the recorded heating response of strain per unit temperature ($\mu\varepsilon$/°C); α_A is the thermal expansion coefficient for the rock; α_S is the inherent thermal expansion compensation factor of the strain gauges. The inherent thermal expansion compensation factor is by the manufacturer specified to –10.8 $\mu\varepsilon$/°C for the CSIRO HI cells.

The thermal expansion coefficient for two Äspö rocks, diorite and granite, have been determined by Larsson (2001) for a temperature interval between 20° and 70°C. The average thermal expansion coefficient, α_A, for diorite and granite within this interval was found to be $4.5 \cdot 10^{-6}$/°C. Larsson used both loaded and unloaded samples and found that the axial thermal expansion coefficient was independent of loading condition. Thus, both these data types may be combined, see Fig. 3-7.

The temperature interval is considerably larger than the temperature experienced during overcoring, but may be used for extrapolation to the temperature interval of interest (10°-20°C). Extrapolation, using both loaded and unloaded samples, gives an average thermal expansion (diorite and granite) between 2.9 to 3.2 $\mu\varepsilon$/°C (Fig. 3-7) between 10° and 20°C.

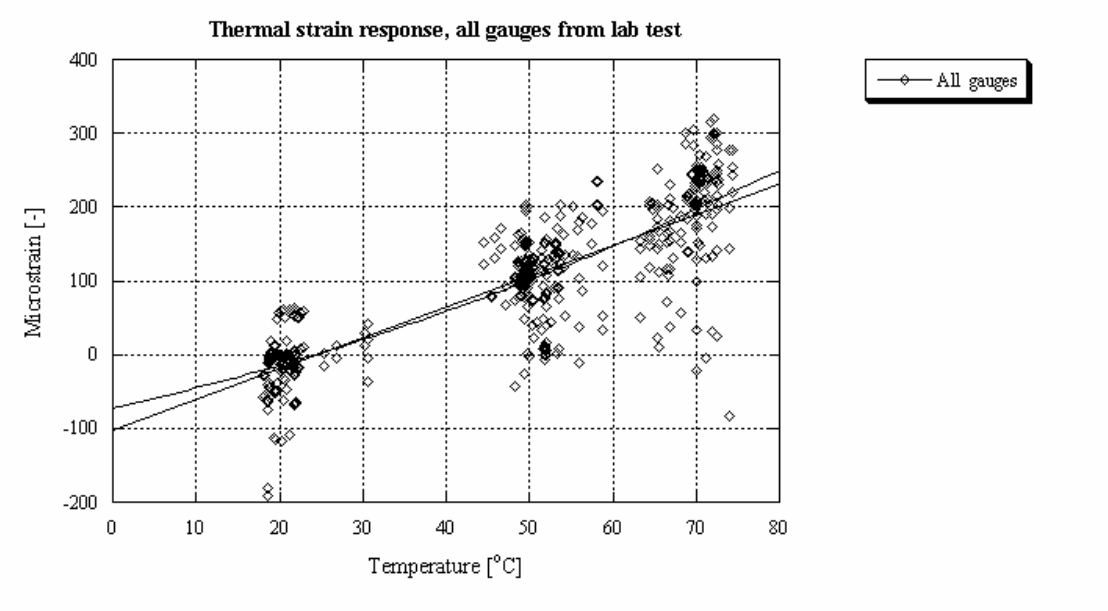

Figure 3-7. *Average thermal response (diorite and granite) using laboratory data (Larsson, 2001). The lines are linear and 2nd degree polynomial fitted curves, respectively.*

Using a thermal expansion coefficient between 10°-20°C equal to α_A = 3.0 $\mu\varepsilon$/°C gives the temperature correction factor for the CSIRO HI overcoring strain gauges according to

$$\alpha_M^{Theoretical,CSIROHI} = 3 - 10.8 \approx -8 \mu\varepsilon / °C \qquad (3\text{-}16)$$

i.e. if the temperature is 1°C higher during the strain reading after overcoring compared to the temperature during the reading before overcoring, 8 με should be added to all strain gauges. A temperature difference between 2.5-3.0°C corresponds to a stress magnitude increase of about 1.0 MPa (Ask, 2003).

The elastic parameters are also influenced by temperature (e.g. Lama and Vutukuri (1978); Heuze (1983)). However, the effect on the elastic parameters for the small temperature variations applicable in this study is assumed to be negligible.

3.4.4 Boundary yield

General

Boundary yield occurs when friction generated by the drilling heats up both the overcoring annulus and the cell, which leads to softening of the adhesive grout. If yield occurs at the boundary between the cell and the rock in the adhesive grout, and /or if it occurs in the rock substrate, the cell will be exposed to longitudinal and radial expansion. The radial expansion is limited by a proportion of the relaxation related to overcoring relief, the thermal expansion of the rock annulus, and the volume of softened grout extruded from annulus (Irvin et al., 1987), whereas the longitudinal expansion is unrestricted and therefore dominating. The yield results in anomalous high values for the axial and 45°-/135°-inclined strain gauges, giving a large stress component parallel to the borehole axis and an overestimation of the stresses in the plane perpendicular to the borehole axis (Irvin et al., 1987). Irvin et al. (1987) concludes that doubts should be raised if results indicate a high principal stress parallel to the borehole axis and higher stresses than anticipated in the plane perpendicular to the borehole axis. All CSIRO HI data at Äspö HRL indicate significantly higher stress magnitudes compared to Borre Probe data and hydraulic fracturing stress data. Furthermore, maximum horizontal stress is, in 32 out of 49 CSIRO HI measurements, oriented close to the borehole direction. This can, to a large extent, be explained by the fact that 8 of the 12 boreholes are oriented with its axis close to the average σ_H-orientation using all available data at Äspö (130°N). As a consequence, the influence of boundary yield must be considered using three indicators: (1) rotation of σ_H towards the borehole direction ($\sigma_H \approx \sigma_1$ at Äspö HRL); (2) distribution of axial strains versus depth; and (3) temperatures during the overcoring phase. These indicators are discussed below.

Rotation of σ_H towards the borehole direction

The majority (11 of 12) of boreholes indicates that increasing axial strain leads to a rotation of σ_H towards the borehole direction, i.e. according to the definition of the boundary yield effect. Figure 3-8 displays the effect of a strong yield for one measurement point in borehole KA1045A, which have resulted in abnormal high axial strains and stresses, and with σ_H oriented in the borehole direction. A gradual rotation of σ_H is found in 10 out of 12 boreholes and by comparing minimum and maximum recorded average strains in each borehole, Figs. 3-9 to 3-19 and with rotations schematically indicated with arrows. For boreholes KA1054A, the observed rotations are based on comparison of results from adjacent boreholes (borehole KA1045A; see Fig. 1-2).

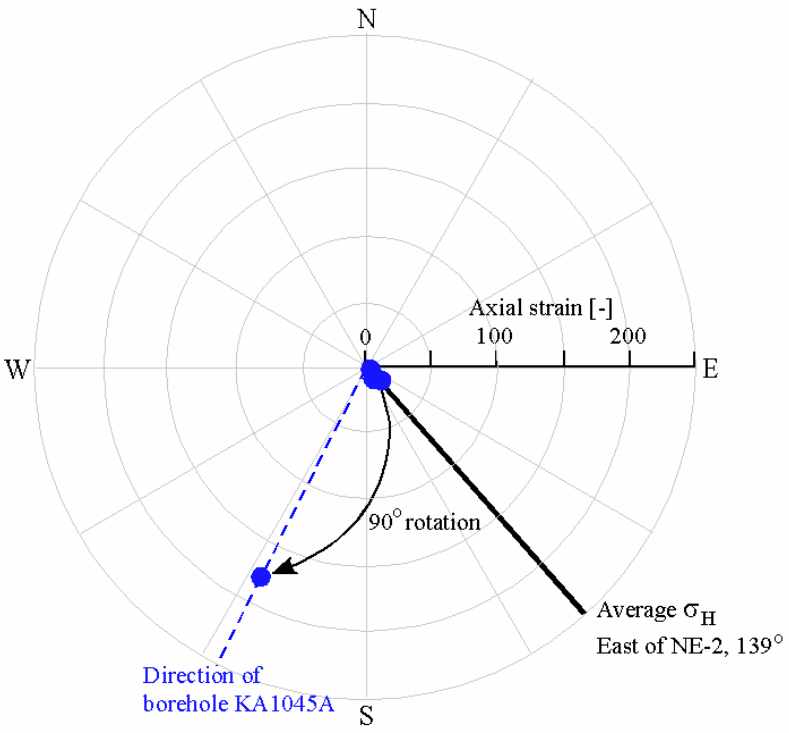

Figure 3-8. *Average axial strains versus orientation of σ_H for borehole KA1045A. Solid and dotted lines represent the average orientation of σ_H East of the NE-2 zone (139±16°N) and the borehole directions, respectively.*

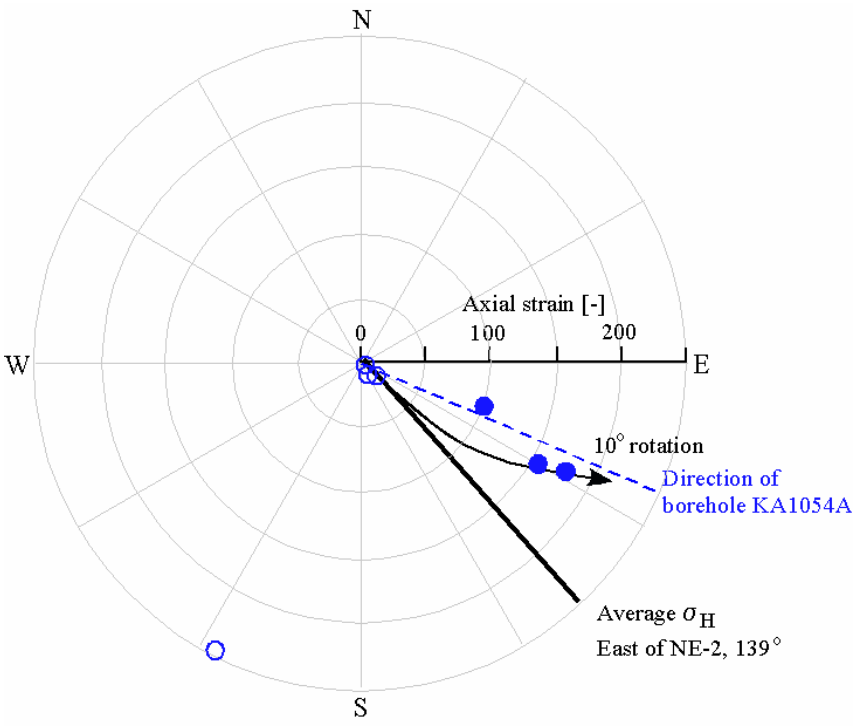

Figure 3-9. *Average axial strains versus orientation of σ_H for borehole KA1054A. Solid and dotted lines represent the average orientation of σ_H East of the NE-2 zone (139±16°N) and the borehole directions, respectively.*

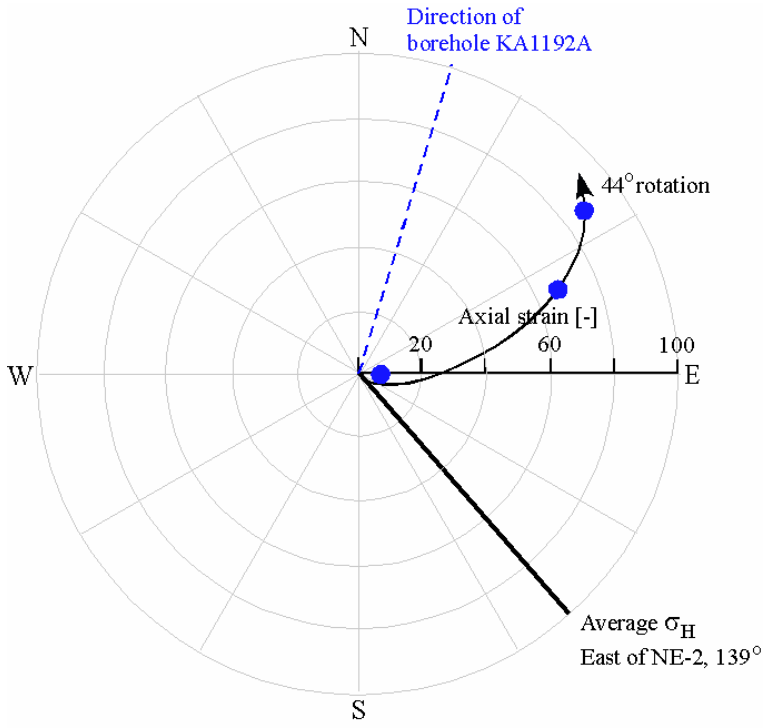

Figure 3-10. *Average axial strains versus orientation of σ_H for borehole KA1192A. Solid and dotted lines represent the average orientation of σ_H East of the NE-2 zone (139±16°N) and the borehole directions, respectively.*

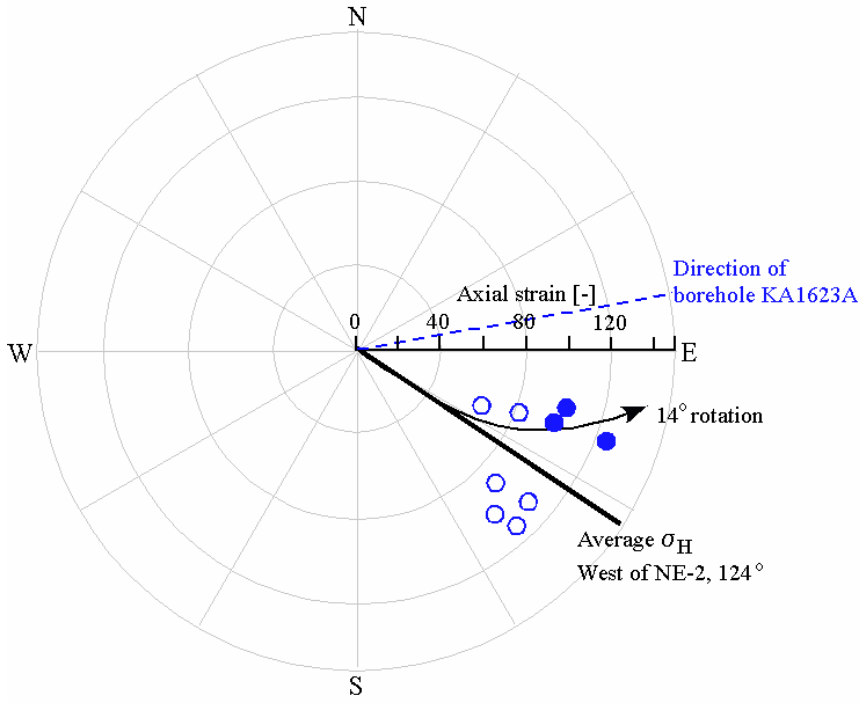

Figure 3-11. *Average axial strains versus orientation of σ_H for borehole KA1623A (filled symbols). Solid and dotted lines represent the average orientation of σ_H West of the NE-2 zone (124±14°N) and the borehole directions, respectively.*

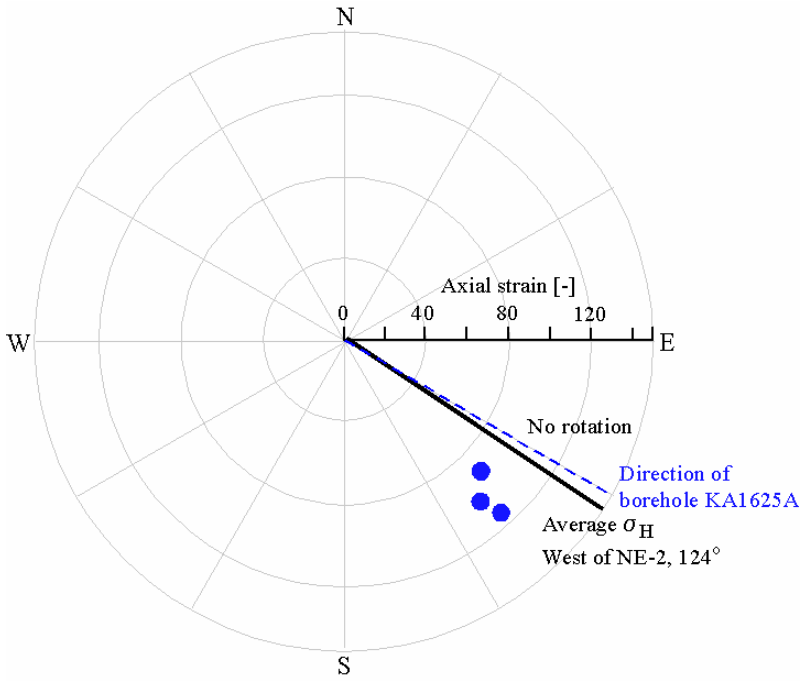

Figure 3-12. *Average axial strains versus orientation of σ_H for borehole KA1625A. Solid and dotted lines represent the average orientation of σ_H West of the NE-2 zone (124±14°N) and the borehole directions, respectively.*

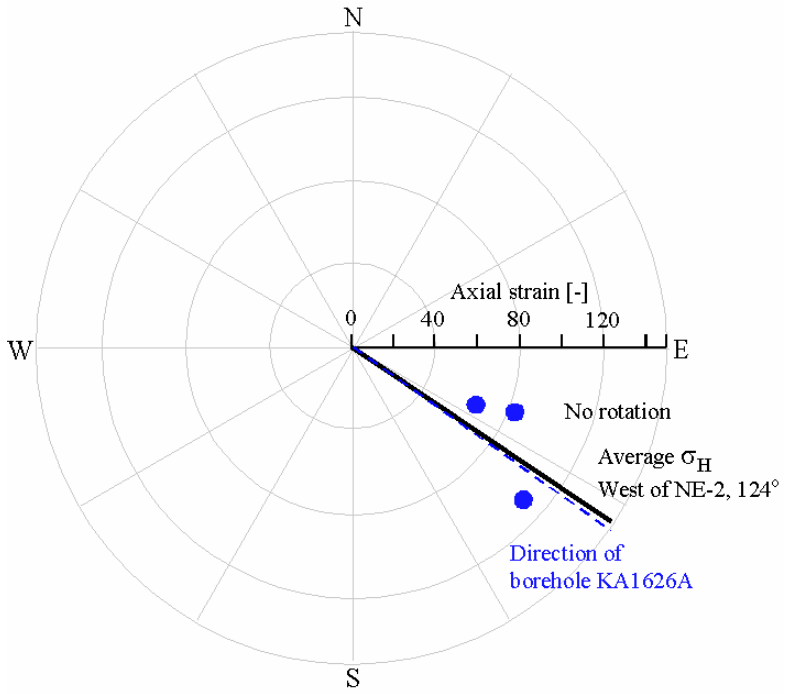

Figure 3-13. *Average axial strains versus orientation of σ_H for borehole KA1626A. Solid and dotted lines represent the average orientation of σ_H West of the NE-2 zone (124±14°N) and the borehole directions, respectively.*

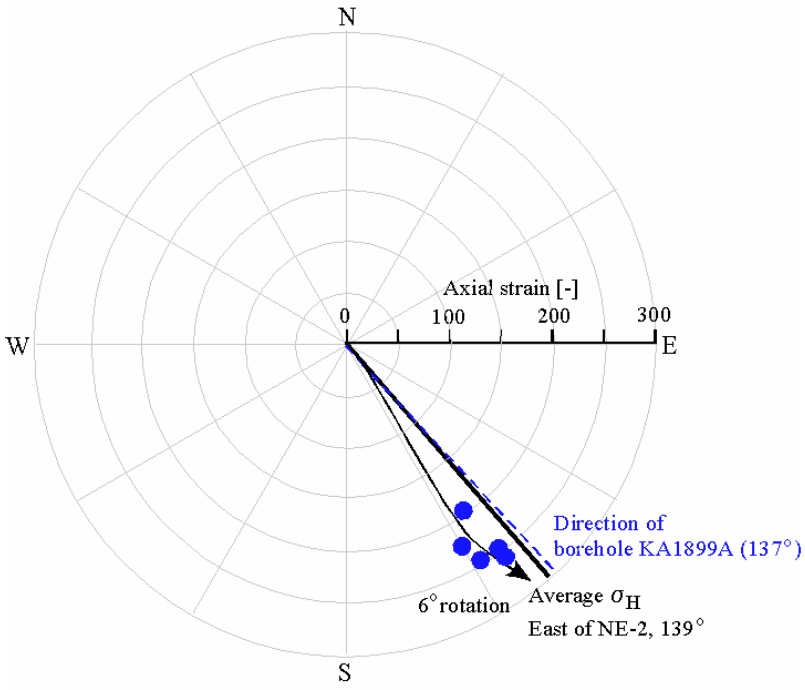

Figure 3-14. *Average axial strains versus orientation of σ_H for borehole KA1899A. Solid and dotted lines represent the average orientation of σ_H East of the NE-2 zone (139±16°N) and the borehole directions, respectively.*

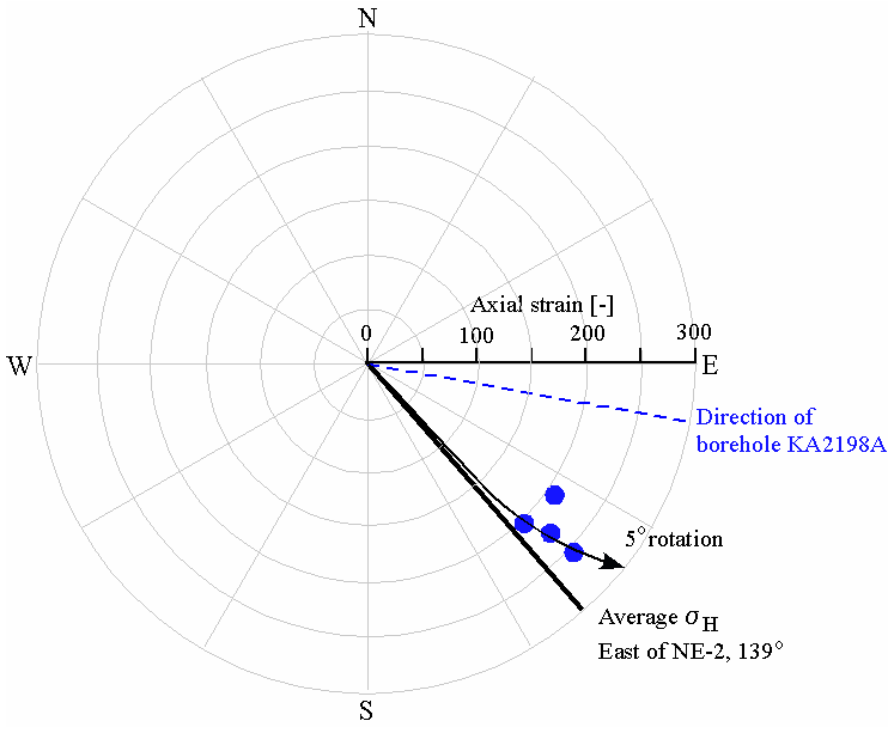

Figure 3-15. *Average axial strains versus orientation of σ_H for borehole KA2198. Solid and dotted lines represent the average orientation of σ_H East of the NE-2 zone (139±16°N) and the borehole directions, respectively.*

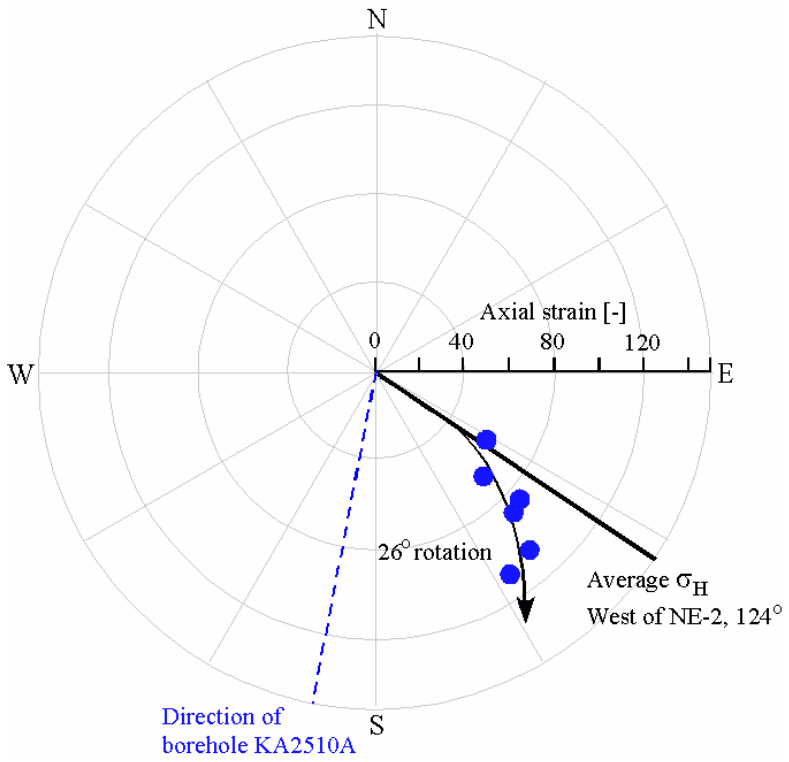

Figure 3-16. *Average axial strains versus orientation of σ_H for borehole KA2510A. Solid and dotted lines represent the average orientation of σ_H West of the NE-2 zone (124±14°N) and the borehole directions, respectively.*

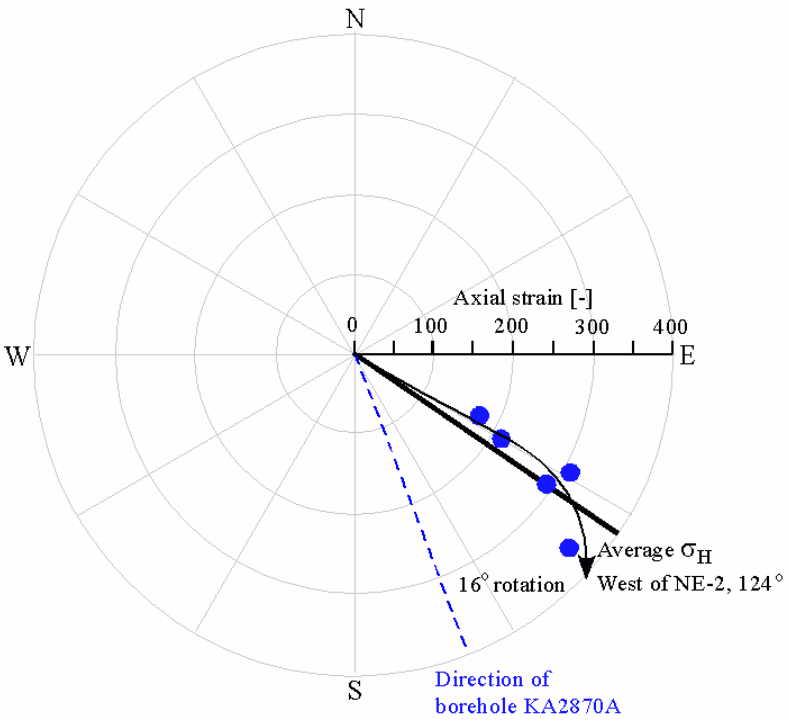

Figure 3-17. *Average axial strains versus orientation of σ_H for borehole KA2870A. Solid and dotted lines represent the average orientation of σ_H West of the NE-2 zone (124±14°N) and the borehole directions, respectively.*

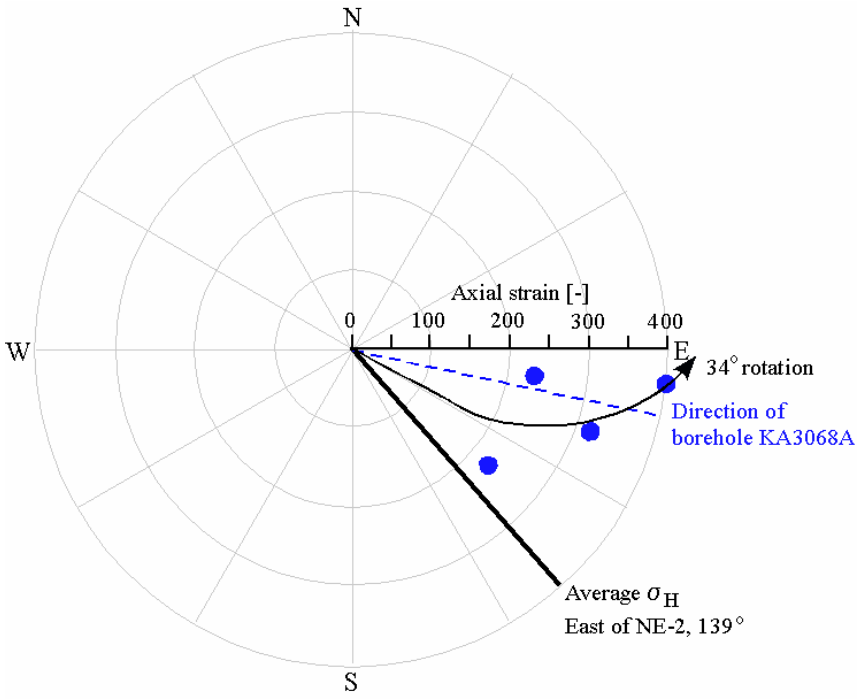

Figure 3-18. *Average axial strains versus orientation of σ_H for borehole KA3068A. Solid and dotted lines represent the average orientation of σ_H East of the NE-2 zone (139±16°N) and the borehole directions, respectively. This borehole indicates a strongly non-linear stress field versus borehole length and the rotation caused by boundary yield is therefore more uncertain.*

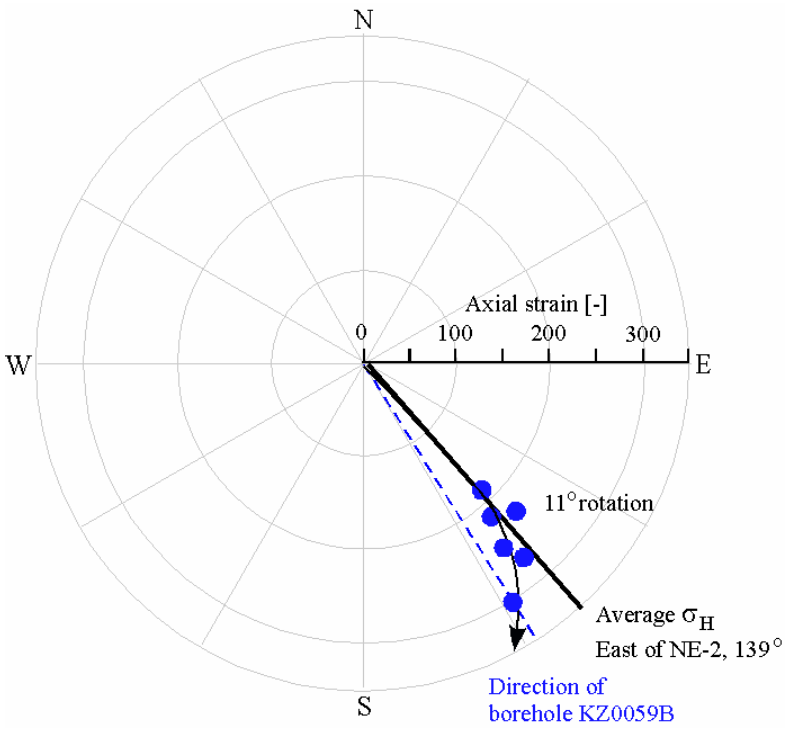

Figure 3-19. *Average axial strains versus orientation of σ_H for borehole KZ0059B. Solid and dotted lines represent the average orientation of σ_H East of the NE-2 zone (139±16°N) and the borehole directions, respectively.*

Distribution of axial strains versus depth

Because the borehole direction influences the axial strain magnitude, the data have been divided into two groups with respect to the average orientation of σ_H (130°N): sub-parallel boreholes (126±21°N); and sub-perpendicular boreholes (198±8°N). Borehole KA1623A, oriented 80°N, was included in the group with sub-perpendicular boreholes. The axial strain magnitudes of the CSIRO HI data collected in sub-parallel boreholes may be compared with results from the Borre Probe (Fig. 3-20). Both cells have a strain gauge length of 10 mm which allows direct comparison and the measurements have been collected by both cells in boreholes with similar orientations (126±21°N and 124±16°N for the CSIRO HI and Borre Probe, respectively). Because the Borre Probe data are considered not to have yielded, these data give the upper and lower boundaries for the axial strain with depth (dotted lines in Fig. 3-20). This comparison indicates that the axial strain data from the CSIRO HI cells are significantly higher than those from the Borre Probe.

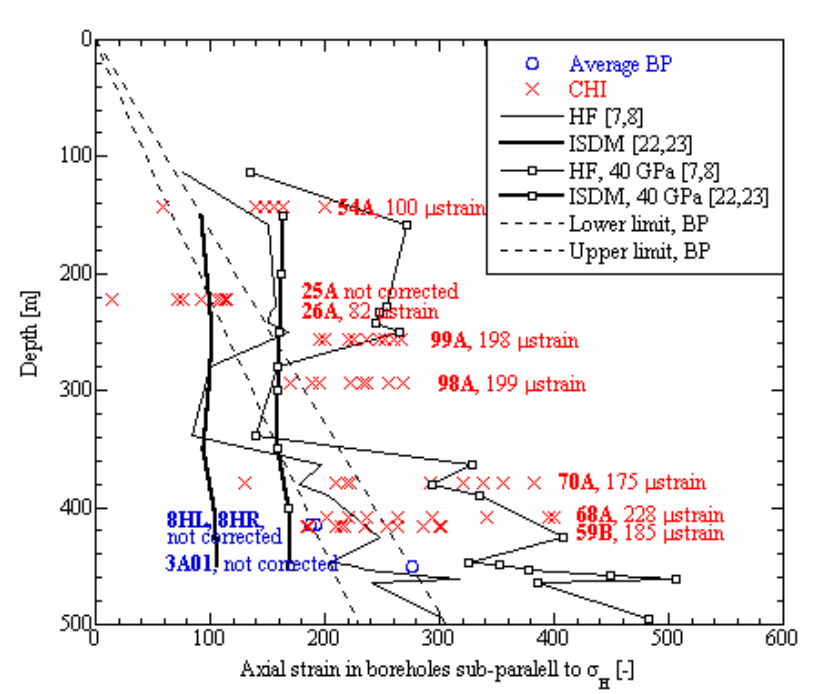

Figure 3-20. *Recorded axial strains versus depth for CSIRO HI (CHI; crosses) and Borre Probe (BP; circles) in boreholes sub-parallel to σ_H. Dotted lines represent the approximate boundary for the axial strain versus depth for the Borre Probe data. Thin solid line with empty squares represent calculated axial strains using hydraulic fracturing data and with elastic parameters from the biaxial tests, whereas the thick solid line with unfilled squares are based on a rock mass modulus of 40 GPa. The axial strains used in stress calculations for each CSIRO HI borehole are given next to borehole (Modified after Ask, 2003).*

An independent estimate of the distribution of axial strains with depth can be obtained from hydraulic fracturing stress data (Bjarnasson et al., 1989; Klee and Rummel, 2001) and ISDM-analysis (Integrated Stress Determination Method; Cornet, 1993a) of hydraulic fracturing data (Ask, 2001; Ask et al., 2001b) using the relationships (Price and Cosgrove, 1990):

$$\varepsilon_{ax}^{//\sigma_H} = \frac{[\sigma_H - \upsilon(\sigma_h + \sigma_v)]}{E} \quad (3\text{-}17)$$

$$\varepsilon_{ax}^{\perp\sigma_H} = \frac{[\sigma_h - \upsilon(\sigma_H + \sigma_v)]}{E} \quad (3\text{-}18)$$

for axial strains sub-parallel ($\varepsilon_{ax}^{//\sigma H}$) and perpendicular ($\varepsilon_{ax}^{\perp\sigma H}$) to σ_H, respectively, and using elastic parameters from overcoring biaxial tests.

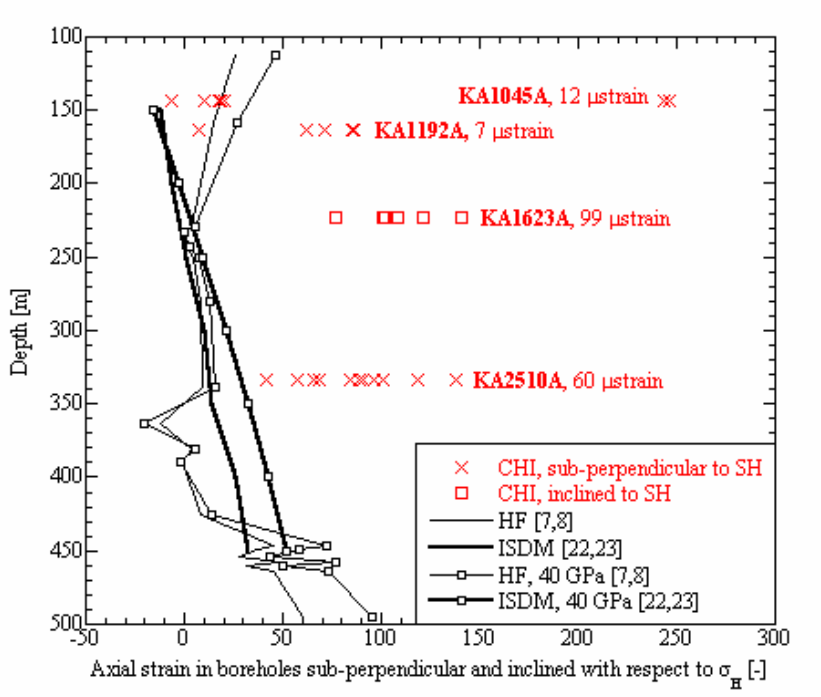

Figure 3-21. *Recorded axial strains versus depth for CSIRO HI (CHI; crosses) in boreholes sub-perpendicular and inclined with respect to σ_H. Thin solid line with empty squares represent calculated axial strains using hydraulic fracturing data and with elastic parameters from the biaxial tests, whereas the thick solid line with empty squares are based on a rock mass modulus of 40 GPa. The axial strains used in stress calculations for each CSIRO HI borehole are given next to borehole (After Ask, 2003).*

Because the hydraulic stress data involve a much larger scale compared to the overcoring data (0.5-50 m^3 and 10^{-3}-10^{-2} m^3, respectively; Amadei and Stephansson, 1997), the axial strain versus depth was also determined using a rock mass modulus of 40 GPa (involving very large rock volumes; Hudson, 2002). This implies that the hydraulic data give upper and lower boundaries for the axial strains versus depth. A disadvantage of using hydraulic fracturing data is that the method has known uncertainties regarding the magnitude of σ_H (e.g. Ito et al., 1999; Rutqvist et al., 2000).

For boreholes oriented sub-parallel to σ_H (Fig. 3-20), the hydraulic fracturing data generally indicate a good fit with the trend given by the Borre Probe data, whereas the ISDM-solution seem to underestimate the axial strains compared to both CSIRO HI and Borre Probe data. For boreholes sub-perpendicular to σ_H (Fig. 3-21), the solutions obtained by hydraulic fracturing and ISDM-analyzed hydraulic fracturing data indicate smaller axial strains magnitudes compared to the CSIRO HI data.

Temperatures during the overcoring phase

The CSIRO HI data commonly display high temperatures immediately after the end of drilling (e.g. Lee et al., 1994; Litterbach et al., 1994), which is especially pronounced in borehole KA1899A, KA2198A, and KA2870A (Fig. 3-22). This implies that high temperatures have been present in the rock. Laboratory studies showed that a temperature increase of only 2°C, from 10 to 12°C, resulted in softening of the studied grout (Irvin et al., 1987). Continuous temperature readings are not available for the measurements at Äspö HRL, but based on the strain readings between 5 and 10 minutes after overcoring, the total average temperature decrease after overcoring is in the order of 4-6°C. This is well beyond the limit of 2°C found by Irvin et al (1987) but because the characteristics of the glue used in the Äspö measurements are unknown, firm conclusions cannot be made.

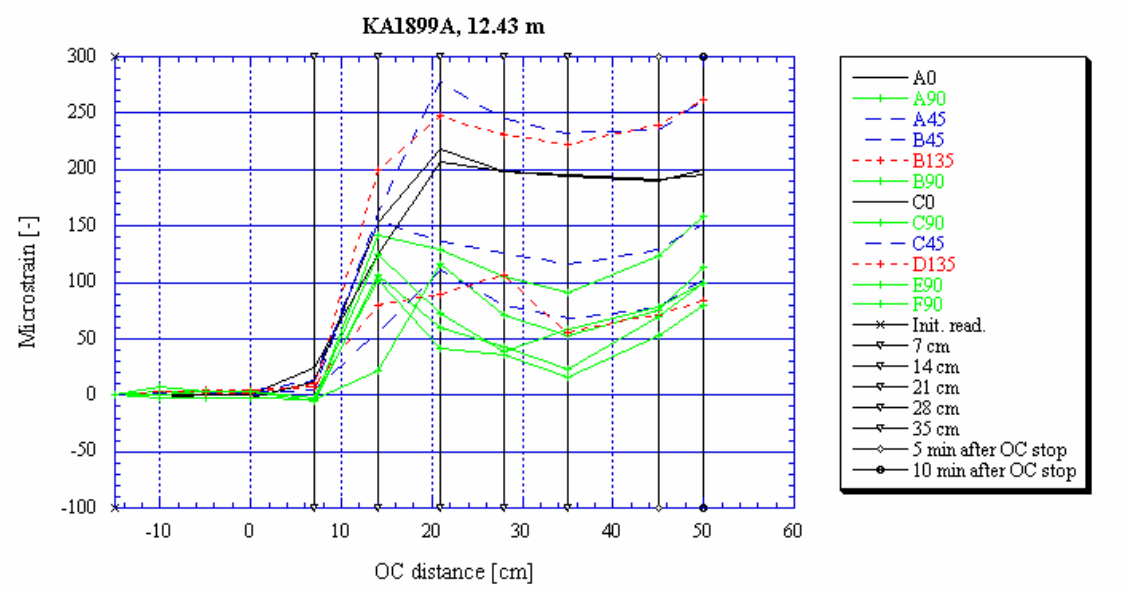

Figure 3-22. *Strain gauge response during overcoring in measurement point 12.43 m in KA1899A displaying high temperatures in the end of overcoring.*

Applied corrections for boundary yield

Based on the identification of boundary yield according to the three indicators above, corrections were applied to data in boreholes KA1045A, KA1054A, KA1192A, KA1623A, KA1626A, KA1899A, KA2198A, KA2510A, KA2870A, KA3068A, and KZ0059B. The corrections applied here are the same as in Ask (2003) except for boreholes KA1626A and KA2198A, where Ask (2003) did not correct for boundary yield. The total effect of boundary yield concerns longitudinal and radial expansion of

the cell. If not corrected, the longitudinal expansion will result in overestimation of stress in the borehole direction and in the plane perpendicular to the borehole axis, whereas the radial expansion overestimates of the stresses in the plane perpendicular to the borehole axis. Because the longitudinal expansion of the cell can be visualized by the axial strain magnitudes versus rotation of σ_H towards the borehole direction, one would expect to find the effect of the radial expansion when comparing the axial and tangential strain magnitudes or when comparing tangential strain magnitudes versus rotation of σ_H towards the borehole direction. However, correlations cannot be found except for borehole KA1045A (Fig. 3-23) and possibly also in borehole KZ0059B. This implies that the effect of radial expansion on strains and stresses is small, and it is therefore neglected in the further analysis.

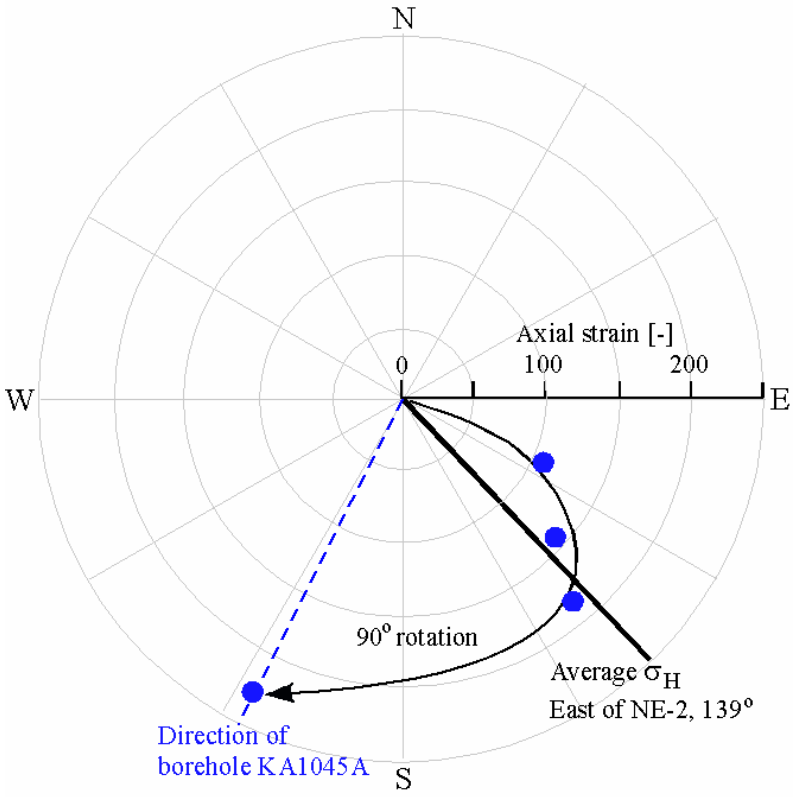

Figure 3-23. *Average tangential strains versus orientation of σ_H for borehole KA1045A. Solid and dotted lines represent the average orientation of σ_H East of the NE-2 zone (139±16°N) and the borehole directions, respectively. Arrow schematically indicates rotation of σ_H towards the borehole direction as a function of increasing tangential strain.*

Thus, the boundary yield correction applied in this study only involves the longitudinal expansion. This correction is based on the measurement point with the minimum average axial strain, which is assumed not to have yielded. The average axial magnitudes for the remaining measurements in that borehole were reduced to that minimum strain value. The applied correction also involves the 45°-/135°-inclined strain gauges, which are corrected with a factor of 0.5 times the axial strain reduction (see eq. 3-14).

3.5 Analysis of elastic parameters

3.5.1 General

Application of elastic theory also requires knowledge of the elastic parameters of the rock material, i.e. Young's modulus, E, and Poisson's ratio, υ. The elastic parameters are determined using biaxial tests. During testing the induced strains in the sample are monitored. The test sequence includes both loading and unloading, which allows examination of possible inelastic behavior of the rock sample. The elastic parameters are determined from the unloading parts of the load cycles, as it reflects the overcoring test. Preferably, the maximum applied load should correspond to the measured stress magnitudes. However, to avoid cracking of the thin-walled hollow cylinder sample, the maximum applied load should be restricted (e.g. 10 MPa for the Borre Probe; see calculation example in Appendix 2). The load/unload increment for the CSIRO HI data is 5 MPa. The results are plotted as strains versus applied pressure (Fig. 3-24).

Theoretically, the strain gauges within each group (i.e. axial, tangential, and 45° inclined) should respond identically to loading/unloading. The elastic properties are derived using the theory for an infinitely long, thick-walled hollow cylinder subject to uniform external pressure, and the assumption that plane stress applies:

$$E = K_1 \frac{p}{\varepsilon_\theta} \frac{2}{1-\left(\frac{D_i}{D_o}\right)^2} \tag{3-19}$$

and

$$\nu = -K_1 \frac{\varepsilon_z}{\varepsilon_\theta} \tag{3-20}$$

where E is Young's modulus; p is applied load, ε_θ and ε_z are tangential and axial strain, respectively (on inner surface); D_i and D_o are inner and outer diameter, respectively, of the cylinder; and K_1 is a correction factor. Note that the K_1-factor is a function of the elastic parameters and is therefore determined iteratively (normally only one iteration is required).

3.5.2 Determination of elastic parameters

The values of E and υ are determined as secant values, derived from the strain data during the unloading of the core sample. The calculation is based on: (1) individual measurement points; (2) average values for a single borehole; and (3) average values for several boreholes. The majority of tested cores fractured during the biaxial tests, usually between 10 and 15 MPa, and secant modulus above 10 MPa cannot be calculated. Thus, the secant values from zero loads to pressures 5 and 10 MPa are chosen which is reasonably representative for the stress magnitudes *in situ*.

The CSIRO HI cores fractured because the tests were made at too high loads (in general 15-20 MPa) resulting in large axial strains. The calculation example in Appendix 2 shows that critical tensional strains will indeed result at pressures above about 10 MPa.

When the tangential strain exceeds the tangential strength of the core, radial fractures are initiated. This implies, that primarily the axial gauges are affected, which is clearly seen as abnormal values for Poisson's ratio in the original interpretations (Lee et al., 1993; Lee et al., 1994; Litterbach et al., 1994; Nilsson et al., 1997), Fig. 3-25.

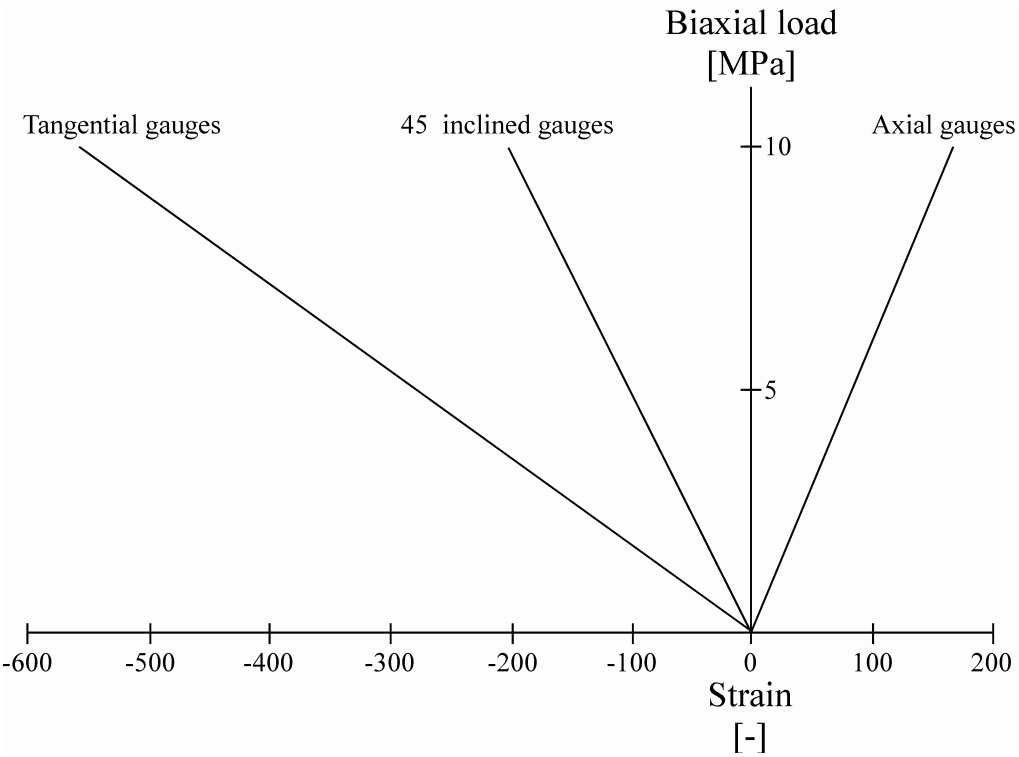

Figure 3-24. *Hypothetical result from biaxial testing of an ideal material (After Ljunggren and Bergsten, 1998).*

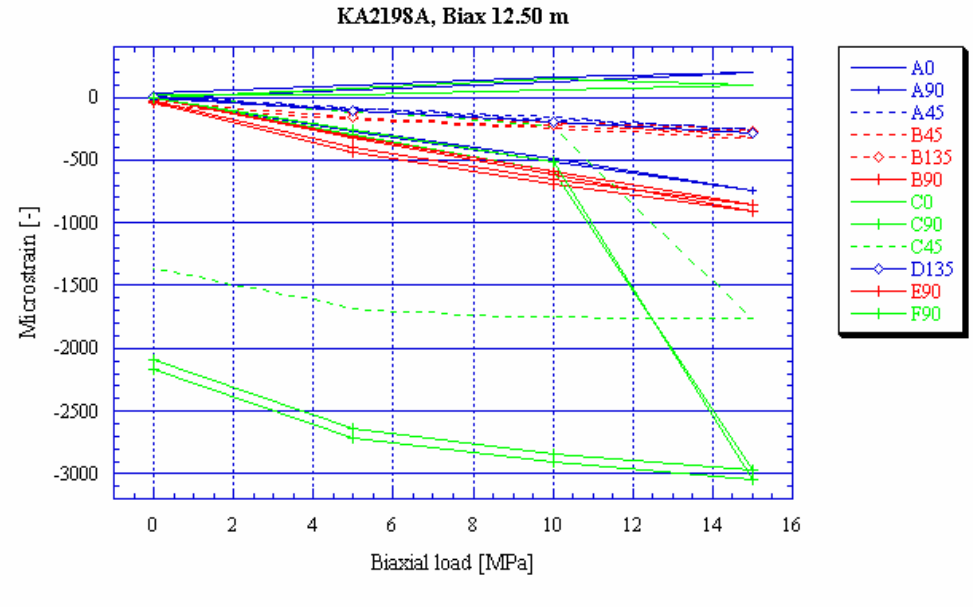

Figure 3-25. *Typical example of core fracturing during biaxial testing. Data from 12.50 m borehole length in borehole KA2198A.*

Although the axial gauges are the most sensitive to core extension and fracturing, erroneous strain responses are also observed on the remaining strain gauges. The strain gauges that were strongly affected by core fracturing were excluded in the analysis of this study. This implies that, in many cases, very few strain gauges are available for determination of elastic parameters from unloading curves and more importantly, many of them are associated with uncertainties. To overcome this deficit, the analysis was extended to include following steps:

1. Identification of strain gauges unaffected or less affected by core fracturing.
2. Determination of elastic parameters using tangential and axial strain gauges according to equations 3-19 and 3-20 above.
3. Determination of elastic parameters using 45- and 135°-inclined gauges (equations 3-21 and 3-22 below).
4. The analysis of Poisson's ratio was made using both loading and unloading curves of the axial gauges at two levels:
   A: Limiting the values of Poisson's ratio within 0.10 to 0.35

   B: Limiting the values of Poisson's ratio within 0.15 to 0.30
5. Determination of ratio between unloading and loading elastic parameters and comparison with data from biaxial tests from measurements on Borre Probe cores.
6. Calculation of unloading elastic parameters from loading parameters using the ratios mentioned above.

The biaxial plots are presented in Appendix 5 and the evaluated elastic parameters in Chapter 5 and Appendix 7.

Strain gauges used for determination of elastic parameters

The standard analysis of CSIRO HI data includes 3 and 5 values of Young's modulus and 6 to 10 values of Poisson's ratio, for the 9- and 12-gauge cells, respectively. Using the 45°- and 135°-inclined gauges implies that the axial gauges must be utilized for the calculation of Young's modulus (eq. 3-21). The calculation of Poisson's ratio requires both axial and tangential strain gauges in combination with the 45°- and 135°-inclined gauges (eq. 3-22).

$$E = K_1 \frac{p}{\varepsilon_\theta} \frac{2}{1-\left(\frac{D_i}{D_o}\right)^2} = K_1 \frac{p}{\left(2\varepsilon_{45/135} - \varepsilon_z\right)} \frac{2}{1-\left(\frac{D_i}{D_o}\right)^2} \tag{3-21}$$

and

$$\nu = -K_1 \frac{\left(2\varepsilon_{45/135} - \varepsilon_\theta\right)}{\left(2\varepsilon_{45/135} - \varepsilon_z\right)} \tag{3-22}$$

This approach may, when combining all available strain gauges, give 10 and 25 values of Young's modulus and Poisson's ratio, respectively (for the 12-gauge cell). Thus in total, 15 and 35 values of Young's modulus and Poisson's ratio may be used for determination of the elastic parameters for the 12-gauge cell (11 and 18, respectively, for the 9-gauge cell). The results are ranked based on the number of gauges or gauge combinations used to calculate the elastic parameters:

A: 100-80 % of gauge combinations; very good result
B: 79-60 % of gauge combinations; good result
C: 59-40 % of gauge combinations; fair result
D: 39-20 % of gauge combinations; poor result
E: 19-0 % of gauge combinations; very poor result

Analysis of Poisson's ratio

Because the Poisson's ratio is sensitive to the observed core fracturing, the analysis was made at two levels: (1) using data within the limits 0.10 to 0.35; and (2) using data within the limits 0.15 to 0.30. These limits are motivated by the results achieved from biaxial tests on Borre Probe cores (which are in the range 0.15 to 0.30; Ask et al. (2002)) and results from uniaxial compression tests on four typical Äspö rocks (Stille and Olsson, 1989; Nordlund et al., 1999; Staub et al., 2002) giving an average Poisson's ratio of 0.24.

Because most cores have fractured during biaxial testing and because the least affected gauges must be used to be able to determine the elastic parameters, the results are somewhat uncertain. The fracturing of the core leads in general to higher axial strain than expected and the calculated value of Poisson's ratio will therefore tend to overestimate the Poisson's ratio. For comparison, the Poisson's ratio was also calculated using the loading values of the axial gauges. This determination, should in unfractured cores, give the lower limit of the Poisson's ratio. However, because also the tangential gauges are affected by the fracturing, also these values are associated with uncertainties.

Anisotropy

The results from the biaxial tests may be used to estimate effects of rock anisotropy. However, because most cores fractured during loading effects of potential anisotropy could not be analyzed.

3.6 Uncertainties in existing overcoring data

3.6.1 General

A number of factors limit the applicability of the overcoring method, particularly its small measuring scale and the requirements of delicate handling during measurements. This commonly results in a considerable scatter in both magnitudes and orientations of the calculated stresses (Amadei and Stephansson, 1997; Cornet, 1993b). For example, Leijon (1989) showed that the random error in overcoring data in hard rock is ±2 MPa, implying that when stress magnitudes are low (i.e. shallow depths), the overcoring results are more uncertain. The uncertainties in the analysis of overcoring strain data involve: (1) natural (intrinsic, inherent) uncertainty; (2) measurement related uncertainties; and (3) uncertainties associated with the analysis of the stress measurement data (Amadei and Stephansson, 1997).

The natural uncertainties mainly involve the variation of the rock material (grain size, fabric, geological structures etc), which may result in varying stresses even at small distances or volumes. The variation of the rock material also affects the elastic parameters. The calculated *in situ* rock stresses are directly related to the Young's modulus while the effect of varying Poisson's ratio is more complex but usually of less importance compared to Young's modulus.

Measurement related uncertainties are errors or mistakes due to the construction of the instrument used to measure the stresses. These involve poor installation of cell, malfunctioning of strain gauges, creep of glue, temperature effects (environment, drilling water, and heat generated during overcoring drilling), electrical problems, borehole eccentricity, borehole oversize etc.

Data analysis related uncertainties involve the assumption of a linearly elastic, isotropic and homogeneous continuum material (neglecting effects of grain size, anisotropy, nonlinear or inelastic response, time-dependent response, yielding of rock after drilling, inhomogeneities at the scale of the overcore sample). It is further assumed that the diameter of overcoring does not influence the results, that the relieved stresses during overcoring are equal to the stresses in its precoring condition, and that the rock deforms in plane strain or plane stress. The latter implies that the measurement points must be in a plane distant from the overcore ends by three to four times the borehole diameter (i.e. for a 38 mm borehole a minimum total overcore length of 300 mm).

The determination of the elastic parameters is also subject to some errors. The biaxial test loading cycle should preferably reach the stress magnitudes measured *in situ* but at the same time not be too high which may lead to radial fracturing of the core.

A comparative study of overcore samples using both biaxial and triaxial tests revealed 20% lower Young's modulus, more scattered, and on average twice as large Poisson's ratio for the biaxial tests compared to the triaxial tests (Leijon and Stillborg, 1986). Because Leijon and Stillborg (1986) did not observe such a difference between the biaxial and triaxial tests on aluminum cylinders, they attributed the discrepancy in the elastic parameters to the rock material. Possibly, the results achieved by Leijon and Stillborg (1986) could be related to the fact that biaxial test does not fully mimic the situation in-situ. The overcore sample expands in all directions as the stresses are removed during the overcoring and relief process, whereas it is forced to contract in the radial direction and to expand in the axial direction in the biaxial testing (e.g. Sandström, 1999; Fig. 3-26).

The results from Leijon and Stillborg (1986) were based on rock samples from the Luossavaara Mine, of the Kiruna iron ore fields in Northern Sweden, and were constituted of quartz and syenite porphyry, and magnetite. The rock samples proved to have non-ideal mechanical characteristics and with Poisson's ratios from the biaxial tests ranging between about 0.27 to 0.66. The non-ideal rock properties and odd values of Poisson's ratio from the biaxial tests, thus, reduce the confidence of the results presented by Leijon and Stillborg (1986).

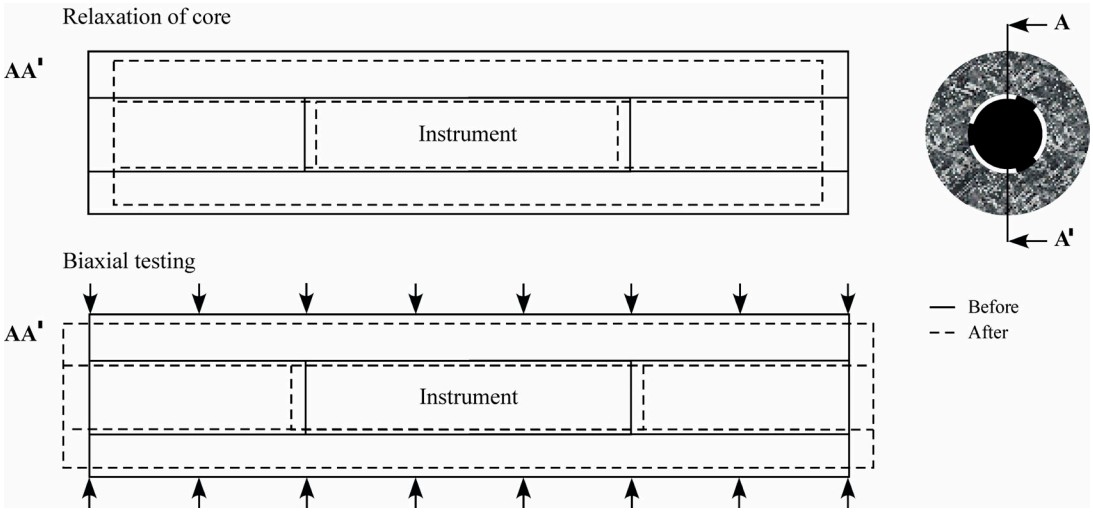

Figure 3-26. *Effect of core relaxation and reloading during biaxial testing (After Sandström, 1999).*

3.6.2 Uncertainties of strains and calculated elastic parameters in this study

In this report, the recorded strains and calculated elastic parameters are assumed to follow Gaussian distribution. The preliminary data analysis in this study is based on the following assumptions: (1) the strain gauge response immediately before and after overcoring; and (2) the difference between calculated and measured strains. It is assumed that other sources of uncertainty are incorporated using this approach.

The assumption that the strain data follows Gaussian distribution can be roughly estimated by plotting histograms and cumulative frequency plots of the strain deviation, i.e. difference between observed and calculated strain (Worotnicki, 1993). The results for the raw data and re-analyzed CSIRO HI data indicate that the strain data are reasonably consistent with the assumed Gaussian distribution (Figs. 3-27 to 3-28 and using about 560 values) for both re-analyzed and raw data. As would be expected, the average deviation for both the raw data and the re-analyzed data is close to zero ($7.6 \cdot 10^{-3}$ and $1.3 \cdot 10^{-1}$, respectively).

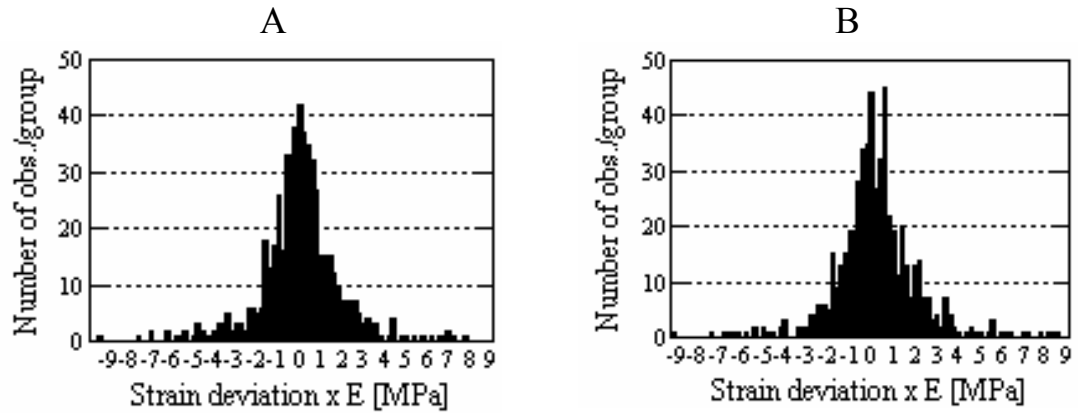

Figure 3-27. *Histogram of the strain deviation times E using strains and Young's modulus measured with the CSIRO HI cells; A and B are re-analyzed and raw data, respectively.*

The results for the re-analyzed CSIRO HI and Borre Probe data are shown in Fig. 3-29 (using 1100 values) and confirm that the overcoring data at the Äspö HRL can be assumed to follow Gaussian distribution.

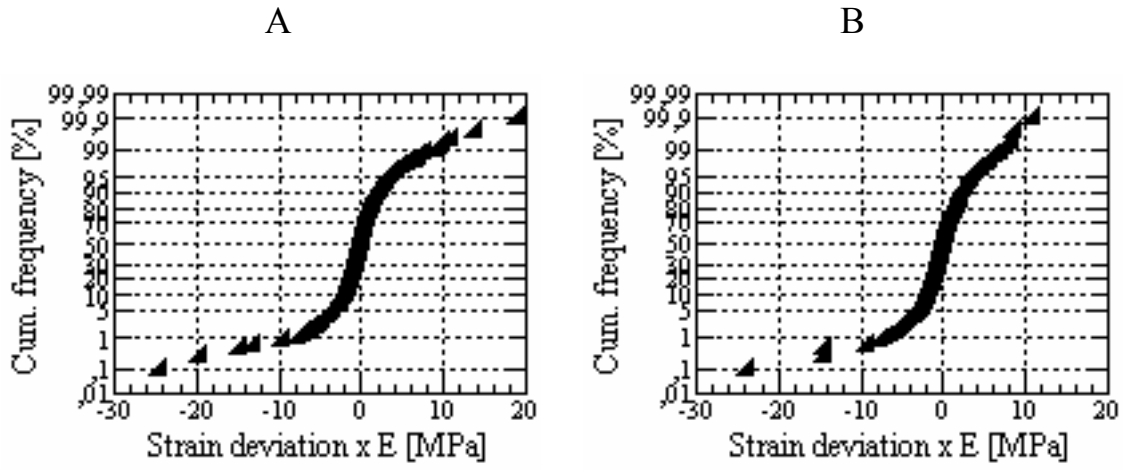

Figure 3-28. *Cumulative frequency distribution using strains and Young's modulus measured with the CSIRO HI cells; A and B are re-analyzed and raw data, respectively.*

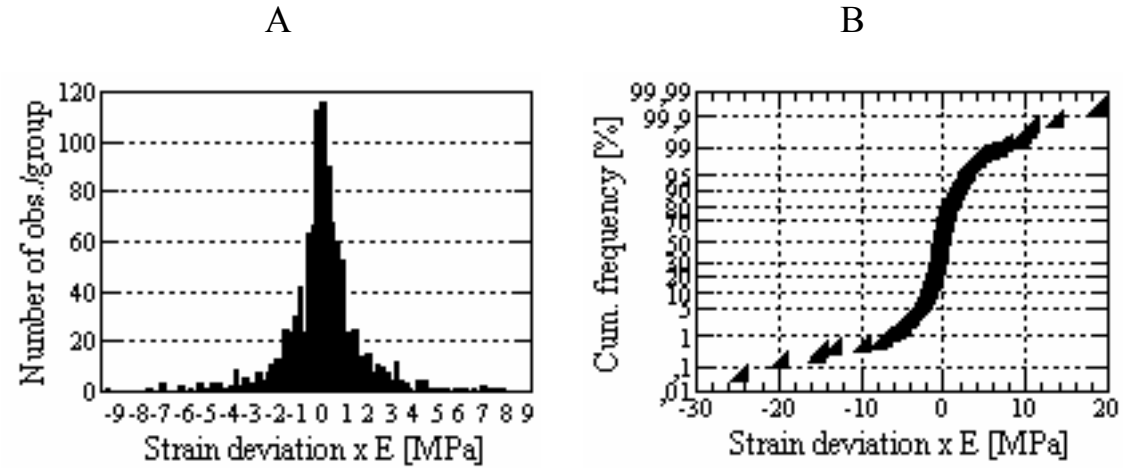

Figure 3-29. *Histogram of the strain deviation times E using re-analyzed strains and Young's modulus measured with both CSIRO HI cells and Borre Probe (A) and cumulative frequency distribution using re-analyzed strains measured with both CSIRO HI cells and Borre Probe (B).*

4 Example of strain analysis

4.1 General

In this chapter, an analysis example is presented from 14.20 m borehole length (12-gauge CSIRO HI cell) in borehole KZ0059B in the Zedex area. The results from the other boreholes are presented in Appendices 4 to 7.

4.2 Analysis of test at 14.20 m depth in borehole KZ0059B

The overcoring and evaluated strains and their standard deviation are presented in Fig. 4-1 and Table 4-1 and the corresponding elastic parameters in Table 4-2. The results from the biaxial tests are typical for the majority of tests, i.e. with radial fracturing of the core, (Fig. 4-2). Only 2 of 15 gauge combinations for determination of Young's modulus (C90 and C45-C0) and only one combination for determination of Poisson's ratio (C0-C45-C90) were used, i.e. giving rank E for both parameters (very poor).

For all E-rank elastic parameters, the final results were complemented with the results from the relationship received between unloading and loading parameters. The Young's modulus is chosen as the average of the results from biaxial analysis and the relationship unloading/loading parameters from the CSIRO HI cells. For the Poisson's ratio, the value used for stress calculation is the average of the result from biaxial analysis (made at to levels 0.10-0.35 and 0.15-0.30) and the relationship unloading/loading parameters from the Borre Probe.

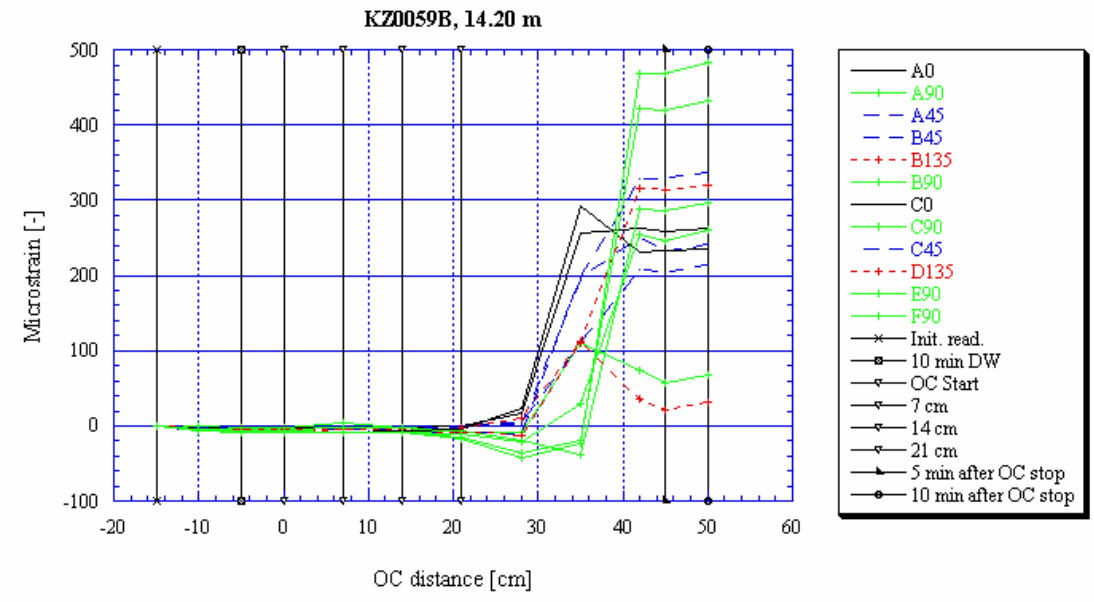

Figure 4-1. *Overcoring result at 14.20 m borehole length in borehole KZ0059B.*

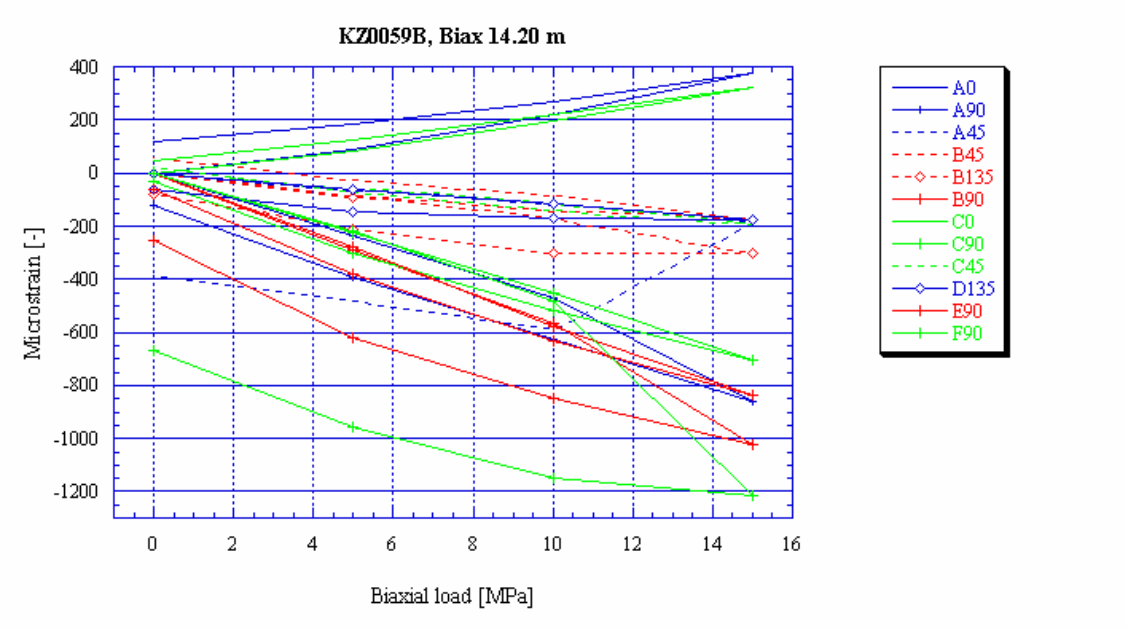

Figure 4-2. *Result from biaxial testing at 14.20 m borehole length in borehole KZ0059B. The core breaks between 10 and 15 MPa pressure, resulting in erroneous determination of the elastic parameters.*

Table 4-1. Strains and associated standard deviation for the measurement at 14.20 m borehole length in borehole KZ0059B. The original interpretation is found below the re-analyzed result.

Depth [m]	Microstrains [-]											
	A0	A90	A45	B45	B135	B90	C0	C90	C45	D135	E90	F90
14.20	195 265	297 300	181 218	210 246	-1 36	68 71	174 243	433 438	306 346	288 324	261 268	483 489
SD^{gauge} [-]												
	1	1	1	1	1	1	2	1	2	1	1	1
$SD^{diff, ind}$ [-]												
	4	2	3	0	7	1	3	8	5	5	4	2
SD^{ind} [-]												
	5	3	4	1	8	2	5	9	7	6	5	3

Table 4-2. Elastic parameters and their standard deviation for the measurement at 14.20 m depth in borehole KZ0059B. Note that these values correspond to the loading part of the biaxial test.

Depth [m]	Elastic parameters			
	E_{secant}	$E_{rel.ship}$	E_{used}	$E_{original}$
14.20	61.1	55.5	58.3	61.3
	υ_{secant}	$\upsilon_{rel.ship}$	υ_{used}	$\upsilon_{original}$
14.20	0.24	0.26	0.25	0.48

5 Results from data analysis

5.1 General

In this chapter, a summary of the analysis results is presented. The results are presented in tables indicating erroneous or questionable strain gauges for each measurement point. Erroneous strain data will be excluded in the stress determination. Questionable strain data will be included in this study and future stress determination, keeping the uncertainty in mind. The detailed results of the data analysis are presented in Appendices 4 to 7.

The analysis of the elastic parameters are made in three steps: 1) using standard biaxial evaluation methods (including the 45°- and 135°-inclined gauges; Chapter 5.3.1); 2) determination using the relationship between elastic parameters for unloading and loading (Chapters 5.3.2 and 5.3.3); 3) combination of step 1 and 2 and determination of final elastic parameters to be used in stress calculations (Chapter 5.3.3).

5.2 General results from overcoring data analysis

The general results of the analysis of the overcoring and biaxial data for the CSIRO HI cells are presented in Tables 5-1 and 5-2.

5.3 Results from analysis of biaxial tests

5.3.1 Elastic parameters determined using all strain gauges

The re-interpreted elastic parameters are presented in Tables 5-3 and 5-4. The results indicate the average Young's modulus and Poisson's ratio equals 62.9±7.1 and 0.26±0.06 (unloading parameters at 10 MPa biaxial load; see also Table 5-6). The Poisson's ratio was chosen as the average of the two evaluated levels 0.10-0.35 and 0.15-0.30. For comparison, values for Poisson's ratio using the loading values for the axial gauges are included in Table 5-4. In unfractured cores, these give a lower value of the Poisson's ratio.

The re-analyzed elastic parameters from the CSIRO HI cores are very similar to the results from re-interpretation of Borre Probe cores giving E=62.2±8.2 GPa and υ=0.26±0.05 (Ask et al., 2002). When using only in-situ gauges, the Borre Probe data gives E=60.9±6.9 GPa and υ=0.25±0.03 (Ask et al., 2002; Ask, 2003). Although more realistic values of the elastic parameters have been found when comparing with Borre Probe data and uniaxial compression tests, still the results are associated with uncertainties, especially for the Poisson's ratio.

Table 5-1. Results from analysis of strain data during the overcoring test using the CSIRO HI cells. Temperature corrections and probable temperature induced strains indicated by T.

Borehole	Borehole depth [m]	Excluded	Questionable data	Temp effects
KA1045A	16.09	A45, B135	B90	
	16.60			
	17.00	A90, C0		
	17.47	A90		
KA1054A	16.19			
	17.15	B45, C90	A90, C45	
	18.46	A90		
KA1192A	14.43	C90, F90		
	15.62			
	16.19	A0, A90, A45, D135		
KA1623A	13.29	A90, D135, F90		
	13.84			
	14.27			
KA1625A	14.07	A45, C90, C45		
	14.57			
	15.07	C0, F90		
KA1626A	12.17	A90, B45		
	12.67	A90, A45		
	13.23		B135, B90, C0, C90, C45, E90	
KA1899A	12.09	B45		
	12.43			
	12.89			
	13.38			
	13.81			

Borehole	Borehole depth [m]	Excluded	Questionable data	Temp effects
KA2198A	12.50		C45	
	13.55			
	14.11			
	14.68			
KA2510A	12.04	B135, B90, E90	B45, D135	
	12.36	A90, A45, E90	B45, B90, D135	
	12.87			
	13.36	D135	C45	
	13.75	C90, F90	B45, B135, B90, C45, D135	
	14.20	A90, B135, F90		
KA2870A	12.73	D135	A45, F90	
	13.23	A90	A45, D135	
	13.64	C90		
	14.25			
	14.87[1]	B135, B90, C90	E90	
KA3068A	14.73	B45	A90, C45, D135	
	16.18	C90		
	16.50	A90		
	16.85		A90	
KZ0059B	7.77	C45	D135	
	8.33	B45, B135, B90, F90		
	9.05	C90	F90	
	12.22		A45, C90	
	14.20			
	14.72			

Table 5-2. Results from analysis of strain data during the biaxial test using the CSIRO HI cells.

Borehole	Borehole depth [m]	Excluded	Questionable data	Borehole	Borehole depth [m]	Excluded	Questionable data
KA1045A	16.09	A45, B45, B135, C45	All gauges	**KA2198A**	12.50	A45, C0, C90, C45, F90	All gauges
	16.60	A90, B135, C0, C90	All gauges		13.55	B45, B135, B90, E90	Most gauges
	17.00	A90, B135, B90, C45, D135	All gauges		14.11	A90, A45, C0, C90, C45, D135	Most gauges
	17.47	B135, C0	Most gauges		14.68	A45, B45, B135, B90, E90, F90	Most gauges
KA1054A	16.19	A90, B135, C90	All gauges	**KA2510A**	12.04	B135, C0, C90, C45	Most gauges
	17.15	All gauges			12.36	A90, A45, C0	Most gauges
	18.46	A0, B135, B90, C90, F90	All gauges		12.87	E90	
KA1192A	14.43	A0, A90, A45, B135, B90, D135, E90	Most gauges		13.36	B90, D135	
	15.62	B45, B135, B90, C0	All gauges		13.75		
	16.19	A90, A45, D135			14.20	A0, B135	
KA1623A	13.29	A0, A90, A45, B90, D135	All gauges	**KA2870A**	12.73	A90, A45, C0, D135	Most gauges
	13.84	A90, A45, B45, B135, B90, E90	All gauges		13.23	A0, B90, E90	Most gauges
	14.27	All gauges			13.64	B45, B135, B90, C0	Most gauges
KA1625A	13.6	All gauges			14.25	All but A0, C45, F90	All gauges
	14.07	B45, B90, E90	All gauges		14.87	Not tested in biax	
	14.57	B45, B135, B90, C0, C90, C45, F90	Most gauges	**KA3068A**	14.73	C45, F90	Most gauges
	15.07	A90, B90	All gauges		16.18	A0, A45, B90, C45	Most gauges
KA1626A	12.17	A90, B135, B90, C0, C90, C45, F90	All gauges		16.50	B45, C0	Most gauges
	12.67	A90, A45, D135	Most gauges		16.85	B90, C0, D135	Most gauges
	13.23	A0, B90, C90, C45	Most gauges	**KZ0059B**	7.77	Not tested in biax	
KA1899A	12.09	B90, D135, E90	All gauges		8.33	A0, A45, B45, B135, B90, C90, C45, E90, F90	All gauges
	12.43	A45, B45, B90, C0, C90	Most gauges		9.05	Only loading data available	
	12.89	All gauges			12.22	A0, A90, B45, B135, B90, C45, D135	Most gauges
	13.38	All gauges			14.20	A0, A90, A45, B45, B90, E90, F90	All gauges
	13.81		All gauges		14.72	All gauges	

Table 5-3a. Results from analysis of Young's modulus using CSIRO HI cores, single test scale.

			Re-analysis		Orig. interpretation					Re-analysis		Orig. interpretation	
Borehole	**Borehole depth [m]**	**Unload pressure [MPa]**	**Secant modulus [GPa]**	**Number**	**Load pressure [MPa]**	**Secant modulus [GPa]**	**Borehole**	**Borehole depth [m]**	**Unload pressure [MPa]**	**Secant modulus [GPa]**	**Number**	**Load pressure [MPa]**	**Secant modulus [GPa]**
KA1045A	16.09	10	67.0	3 of 11	20	72.3	**KA2198A**	12.50	10	53.5	7 of 15	15	56.5
	16.60	10	60.9	4 of 11	20	65.8		13.55	10	62.2	9 of 15	15	36.5
	17.00	10	63.8	8 of 11	20	69.5		14.11	10	56.4	3 of 15	15	51.7
	17.47	10	63.1	7 of 11	20	68.7		14.68	10	52.5	6 of 15	15	53.1
KA1054A	16.19	10	67.1	7 of 11	20	70.1	**KA2510A**	12.04	10	62.0	6 of 15	15	71.8
	17.15	10	63.2	2 of 11	15	72.7		12.36	10	60.9	10 of 15	15	66.7
	18.46	10	59.6	4 of 11	20	74.7		12.87	10	62.3	15 of 15	15	66.1
KA1192A	14.43	10	69.7	8 of 15	20	75.3		13.36	10	69.1	15 of 15	15	72.1
	15.62	10	67.5	7 of 15	20	72.3		13.75	10	63.2	15 of 15	15	68.8
	16.19	10	74.5	10 of 15	15	74.8		14.20	10	65.3	10 of 15	15	68.9
KA1623A	13.29	10	58.1	5 of 15	15	63.8	**KA2870A**	12.73	10	57.8	7 of 15	10	64.7
	13.84[1]	10	57.7	0 of 15	10	53.3		13.23	10	65.2	15 of 15	15	68.2
	14.27[1]	10	57.7	0 of 15	10	61.9		13.64	10	64.1	7 of 15	15	63.9
KA1625A	14.07	10	67.3	12 of 15	15	71.7		14.25[3]	5	63.1	0 of 15	5	62.5
	14.57	10	53.7	4 of 15	15	58.7		14.87[3]	-	63.1	-	-	64.8
	15.07	10	53.6	11 of 15	15	59.5	**KA3068A**	14.73	10	63.2	12 of 15	15	63.9
KA1626A	12.17	10	47.7	5 of 15	15	58.8		16.18	10	69.1	10 of 15	15	72.1
	12.67	10	57.3	10 of 15	20	66.0		16.50	10	68.3	13 of 15	15	71.6
	13.23[1]	5	57.7	0 of 15	10	58.6		16.85[4]	5	66.8	0 of 15	10	70.6
KA1899A	12.09	10	59.5	13 of 15	15	63.8	**KZ0059B**	7.77[5]	-	63.1	-	-	64.2
	12.43	10	60.6	6 of 15	10	65.0		8.33	10	63.3	2 of 15	5	65.3
	12.89[2]	10	59.0	0 of 15	10	62.0		9.05[5]	10	63.1	0 of 15	10	67.4
	13.38[2]	10	59.0	0 of 15	10	59.7		12.22	10	63.2	12 of 15	15	62.1
	13.81	10	58.0	15 of 15	15	64.3		14.20	10	61.1	2 of 15	10	61.3
								14.72	10	64.4	2 of 15	10	64.9

Keys: 1) Average of tests at 1620 m level; 2) Average of tests in KA1899A; 3) Average of tests in KA2870A; 4) Average of tests in KA3068A; and 5) Average of tests in KZ0059B.

Table 5-3b. Results from analysis of Young's modulus using CSIRO HI cores, average borehole and site scale.

			Re-analysis		Orig. interpretation					Re-analysis		Orig. interpretation	
Borehole	**Borehole depth [m]**	**Unload pressure [MPa]**	**Secant modulus [GPa]**	**Number**	**Load pressure [MPa]**	**Secant modulus [GPa]**	**Borehole**	**Borehole depth [m]**	**Unload pressure [MPa]**	**Secant modulus [GPa]**	**Number**	**Load pressure [MPa]**	**Secant modulus [GPa]**
Average KA1045A	16.79	-	63.5	22 of 44		69.2	**Average 1620-level**	-	-	57.7	44 of 135	-	61.6
Average KA1054A	17.27	-	64.2	13 of 33	-	72.7	**Average KA1899A**	12.92	-	59.0	34 of 75	-	63.0
Average 1050-level	-	-	63.8	35 of 77	-	70.3	**Average KA2198A**	13.71	-	56.7	25 of 60	-	49.5
Average KA1192A	15.41	-	71.0	25 of 45	-	74.6	**Average KA2510A**	13.10	-	64.1	71 of 90	-	68.9
Average KA1623A	13.80	-	58.1	5 of 45	-	61.8	**Average KA2870A**	13.74	-	63.1	29 of 60	-	64.8
Average KA1625A	14.57	-	59.7	27 of 45	-	63.4	**Average KA3068A**	16.07	-	66.8	35 of 60	-	69.5
Average KA1626A	12.69	-	54.1	15 of 45	-	61.6	**Average KZ0059B**	11.05	-	63.1	18 of 75	-	64.2 64.3

Table 5-4a. Results from analysis of Poisson's ratio using CSIRO HI cores, single test scale.

Borehole	Depth [m]	υ unloading		υ with loading axial gauges		Number of gauge combinations used				υ orig int. pre.	Borehole	Depth [m]	υ unloading		υ with loading axial gauges		Number of gauge combinations used				υ orig int. pre.
		A 0.10-0.35	B 0.15-0.30	C 0.10-0.35	D 0.15-0.30	A	B	C	D				A 0.10-0.35	B 0.15-0.30	C 0.10-0.35	D 0.15-0.30	A	B	C	D	
KA1045A	16.09	0.28	0.27	0.26	0.26	6	5	6	6	0.32	**KA2198A**	12.50	0.26	0.26	0.25	0.29	7	4	10	7	0.30
	16.60[1]	0.18	0.18	0.26	0.22	2	2	4	3	0.44		13.55	0.28	0.25	0.28	0.26	8	3	10	4	0.29
	17.00[1]	-	-	0.28	0.28	0	0	8	7	0.38		14.11[4]	0.30	0.26	0.27	0.21	2	1	4	2	0.42
	17.47[1]	-	-	0.34	-	0	0	9	0	0.46		14.68	0.25	0.27	0.27	0.26	7	2	9	5	0.33
KA1054A	16.19	0.25	0.26	0.25	0.24	6	4	11	8	0.25	**KA2510A**	12.04	0.26	0.21	0.27	0.23	5	3	7	4	0.39
	17.15[1]	-	-	-	-	0	0	0	0	0.27		12.36[5]	0.32	-	0.31	0.28	1	0	9	4	0.40
	18.46	0.27	0.24	0.25	0.24	3	2	10	9	0.28		12.87	0.29	0.27	0.28	0.26	24	16	24	19	0.30
KA1192A	14.43	0.29	0.27	0.27	0.26	6	4	12	10	0.30		13.36	0.25	0.24	0.23	0.23	23	17	22	18	0.27
	15.62	0.30	0.26	0.31	0.28	6	3	10	4	0.38		13.75	0.26	0.25	0.26	0.26	27	13	27	15	0.30
	16.19	0.24	0.24	0.24	0.24	16	14	16	14	0.27		14.20	0.27	0.22	0.28	0.26	11	5	18	12	0.34
KA1623A	13.29[2]	0.22	0.18	0.26	0.25	5	1	8	2	0.40	**KA2870A**	12.73	0.28	0.26	0.25	0.24	11	5	9	8	0.33
	13.84[2]	0.25	0.25	0.25	0.22	8	8	8	6	0.40		13.23	0.25	0.23	0.25	0.23	15	10	19	14	0.30
	14.27[2]	-	-	0.28	0.28	0	0	1	1	0.44		13.64	0.25	0.26	0.26	0.26	11	6	15	8	0.27
KA1625A	14.07[2]	0.24	0.19	0.27	0.19	7	3	10	3	0.38		14.25[6]	0.25	0.25	0.25	0.25	2	2	3	3	0.21
	14.57[2]	0.30	0.28	0.27	0.25	4	2	6	4	0.35		14.87[6]	-	-	-	-	-	-	-	-	0.28
	15.07[2]	0.20	0.23	0.25	0.26	4	3	10	8	0.33	**KA3068A**	14.73	0.31	0.24	0.29	0.27	7	2	11	7	0.37
KA1626A	12.17[2]	0.18	0.24	0.26	0.26	2	1	4	1	0.43		16.18	0.27	0.23	0.26	0.25	11	7	11	9	0.34
	12.67[2]	0.22	0.23	0.22	0.22	14	9	15	9	0.32		16.50	0.25	0.22	0.27	0.22	10	7	16	8	0.31
	13.23[2]	0.26	0.21	0.27	0.23	9	5	13	7	0.36		16.85	0.24	0.22	0.27	0.25	11	3	18	8	0.34
KA1899A	12.09	0.27	0.22	0.27	0.22	8	3	8	4	0.41	**KZ0059B**	7.77[7]	-	-	-	-	-	-	-	-	0.43
	12.43[3]	0.30	0.30	0.35	-	1	1	1	0	0.38		8.33[7]	-	-	-	-	0	0	0	0	0.49
	12.89[3]	-	-	-	-	0	0	0	0	0.42		9.05[7]	-	-	-	-	0	0	0	0	0.32
	13.38[3]	-	-	-	-	0	0	0	0	0.40		12.22[7]	0.28	0.20	0.33	0.22	3	1	10	1	0.43
	13.81[3]	0.34	-	0.33	-	2	0	10	0	0.40		14.20[7]	0.12	-	0.12	-	1	0	1	0	0.48
												14.72[7]	-	-	-	-	0	0	0	0	0.44

Table 5-4b. Results from analysis of Poisson's ratio using CSIRO HI cores, average borehole and site scale.

Borehole	Depth [m]	υ unloading		υ with loading axial gauges		Number of gauge combinations used				υ orig int. pre.	Borehole	Depth [m]	υ unloading		υ with loading axial gauges		Number of gauge combinations used				υ orig int-pre.
		A 0.10-0.35	B 0.15-0.30	C 0.10-0.35	D 0.15-0.30	A	B	C	D				A 0.10-0.35	B 0.15-0.30	C 0.10-0.35	D 0.15-0.30	A	B	C	D	
Average KA1045A	16.79	0.26	0.24	0.29	0.26	8	7	27	16	0.41	**Average 1620-level**	-	0.24	0.23	0.25	0.25	53	32	75	39	0.38
Average KA1054A	17.27	0.26	0.25	0.25	0.24	9	6	21	16	0.27	**Average KA1899A**	12.92	0.29	0.24	0.31	0.22	11	4	19	4	0.38
Average 1050-level	-	0.26	0.25	0.27	0.26	17	13	48	32	0.36	**Average KA2198A**	13.71	0.27	0.26	0.27	0.27	24	10	33	18	0.34
Average KA1192A	15.41	0.26	0.25	0.27	0.25	28	21	38	28	0.32	**Average KA2510A**	13.10	0.27	0.25	0.27	0.25	91	54	107	72	0.33
Average KA1623A	13.80	0.24	0.24	0.26	0.23	13	9	17	9	0.41	**Average KA2870A**	13.74	0.26	0.25	0.25	0.24	39	23	46	33	0.28
Average KA1625A	14.57	0.25	0.23	0.26	0.24	15	8	26	15	0.35	**Average KA3068A**	16.07	0.26	0.23	0.27	0.25	39	19	56	32	0.34
Average KA1626A	12.69	0.23	0.22	0.25	0.23	25	15	32	17	0.37	**Average KZ0059B**	11.05[7]	0.27	0.20	0.31	0.22	4	1	11	1	0.43

Keys Tables 5.4a and b: 1) Average of tests 16.09 m in KA1045A and 16.19 and 18.46 m in KA1054A; 2) Average of all tests at the 1620 m level, i.e. 0.24; 3) Data from 12.09 m; 4) Average of all tests in KA2198A, i.e. 0.26; 5) Average of all tests in KA2510A, i.e. 0.26; 6) Average of all tests in KA2870A, i.e. 0.25; and 7) Average of all tests in the adjacent Borre Probe borehole KXZSD8HR (Average of CSIRO HI data gives υ=0.23).

Table 5-5. Quality ranking of elastic parameters.

Borehole	Borehole depth [m]	Quality of E	Quality of υ	Borehole	Borehole depth [m]	Quality of E	Quality of υ
KA1045A	16.09	D	D	**KA2198A**	12.50	C	E
	16.60	D	E		13.55	B	E
	17.00	B	E		14.11	D	E
	17.47	B	E		14.68	C	E
Average	16.79	C	D	**Average**	13.71	C	E
KA1054A	16.19	B	D	**KA2510A**	12.04	C	E
	17.15	E	E		12.36	B	E
	18.46	D	E		12.87	A	C
Average	17.27	D	E		13.36	A	C
KA1192A	14.43	C	E		13.75	A	C
	15.62	C	E		14.20	B	D
	16.19	B	C	**Average**	13.10	B	B
Average	15.41	C	D	**KA2870A**	12.73	C	D
KA1623A	13.29	D	E		13.23	A	D
	13.84	E	D		13.64	C	D
	14.27	E	E		14.25	E	E
Average	13.80	E	E		14.87	E	E
KA1625A	14.07	A	E	**Average**	13.74	C	D
	14.57	D	E	**KA3068A**	14.73	A	E
	15.07	B	E		16.18	B	D
Average	14.57	B	E		16.50	A	D
KA1626A	12.17	D	E		16.85	E	D
	12.67	B	D	**Average**	16.07	C	C
	13.23	E	D	**KZ0059B**	7.77	E	E
Average	12.69	D	D		8.33	E	E
KA1899A	12.09	A	E		9.05	E	E
	12.43	C	E		12.22	A	E
	12.89	E	E		14.20	E	E
	13.38	E	E		14.72	E	E
	13.81	A	E	**Average**	11.05	D	E
Average	12.92	C	E				

Therefore, the elastic parameters have been quality ranked based on the relationship between the number of gauge combinations used to calculate the parameters and the maximum number of gauge combinations (Table 5-5). The ranking is performed according to: A) very good result (100-80 % of gauge combinations); B) good result (79-60 % of gauge combinations); C) fair result (59-40 % of gauge combinations); D) poor result (39-20 % of gauge combinations); and E) very poor result (19-0 % of gauge combinations).

5.3.2 Relationship between Young's modulus and Poisson's ratio for biaxial tests at Äspö HRL

The relationship between Young's modulus and Poisson's ratio is well defined for the CSIRO HI cell and the Borre Probe (Figs. 5-1 to 5-4, Table 5-6). The linear fitted curve for the Borre Probe and the CSIRO HI cell indicate that, for most data, the Poisson's ratio is below 0.30 for Young's modulus below 75 GPa. The latter correspond to the upper limit of Young's modulus of the re-analyzed CSIRO HI data. Exception is the

loading parameters for the CSIRO HI cell, which indicate a Poisson's ratio of 0.32 at 75 GPa (Fig. 5-3). However, for the average Young's modulus of the CSIRO HI data (62.9 GPa), all plots indicate a Poisson's ratio well below 0.30. The Borre Probe data includes pressures between 3 and 10 MPa, whereas the CSIRO HI data includes only the pressures 5 and 10 MPa. However, when using only 5 and 10 MPa for the Borre Probe data, very similar results are obtained as of the evaluation of the larger pressure range.

Table 5-6. Summary of results from analysis of biaxial tests of CSIRO HI cores and comparison with results from the Borre Probe.

	Loading parameters				**Unloading parameters**			
Pressure	**5**		**10**		**5**		**10**	
Cell	**E**	**std E**	**E**	**std E**	**E**	**std E**	**E**	**std E**
CSIRO HI	66.0	8.4	66.2	7.5	57.1	9.7	62.9	7.1
Borre Probe	59.7	8.9	62.2	8.2	57.0	10.1	62.2	8.2
Cell	**υ**	**std υ**	**υ**	**std υ**	**υ**	**std υ**	**υ**	**std υ**
CSIRO HI	0.27	0.10	0.27	0.08	0.25	0.09	0.26[1]	0.06[1]
Borre Probe	0.25	0.05	0.26	0.05	0.25	0.07	0.26	0.05

Keys: All available Borre Probe data are used, i.e. also data affected by the tunnel excavation. Only in-situ data gives unloading E=60.9±6.9 GPa and υ=0.25±0.03 at 10 MPa (Ask, 2003). 1) Average of the two levels A and B in Table 5-4; and 2) Range of the two levels A and B in Table 5-4.

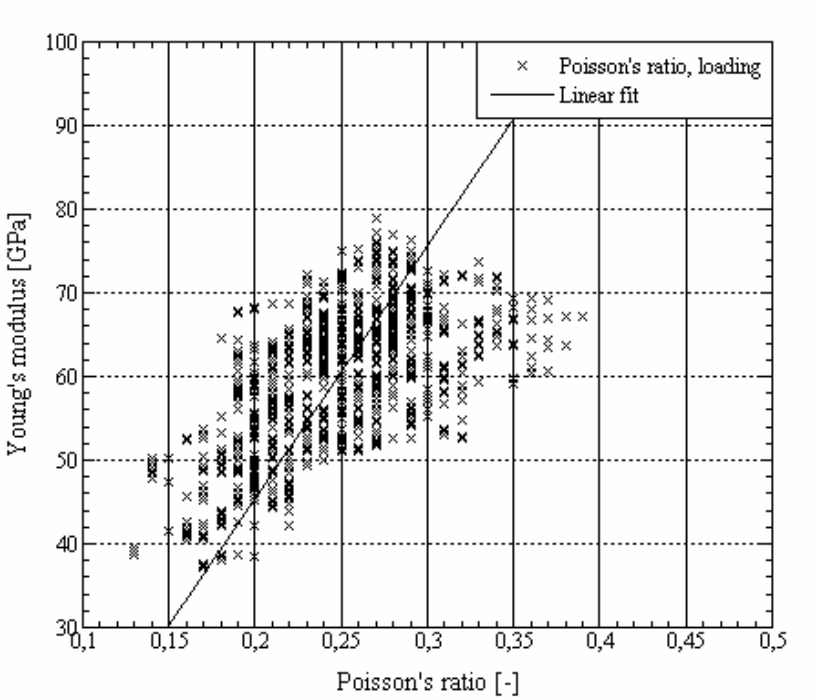

Figure 5-1. *Young's modulus versus Poisson's ratio for the Borre Probe. Loading parameters between 3 and 10 MPa biaxial pressure.*

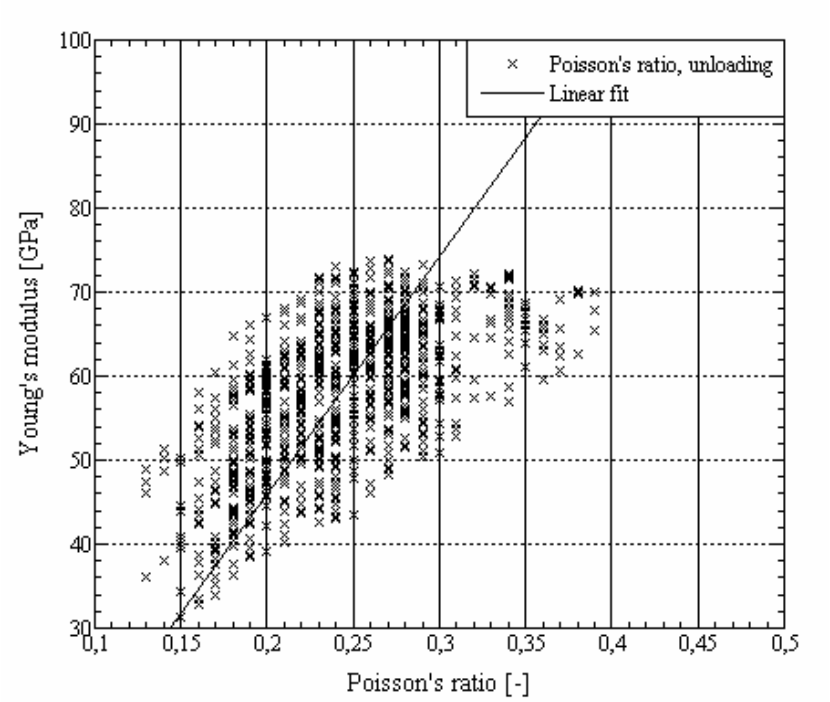

Figure 5-2. *Young's modulus versus Poisson's ratio for the Borre Probe. Unloading parameters between 3 and 10 MPa biaxial pressure.*

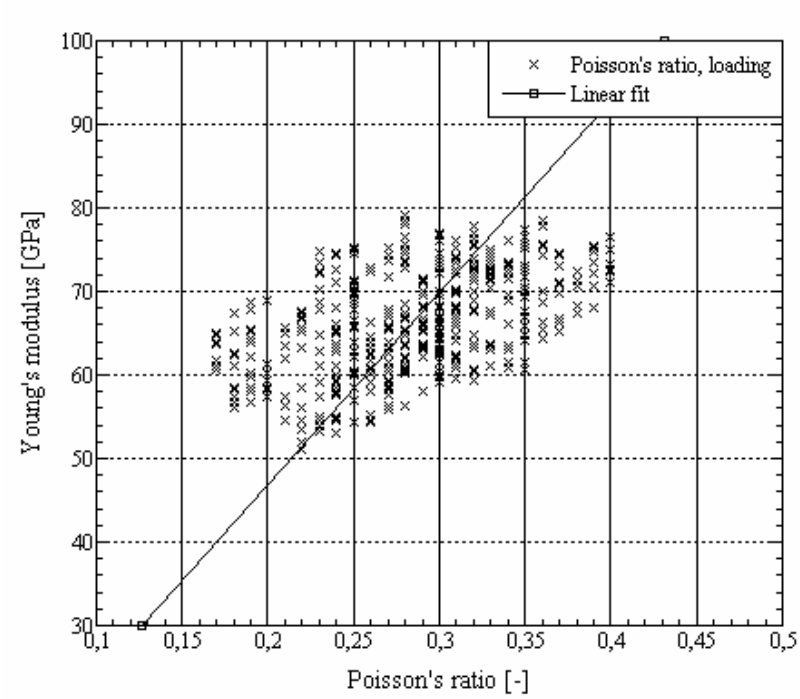

Figure 5-3. *Young's modulus versus Poisson's ratio for the CSIRO HI cell. Loading parameters at 5 and 10 MPa biaxial pressure.*

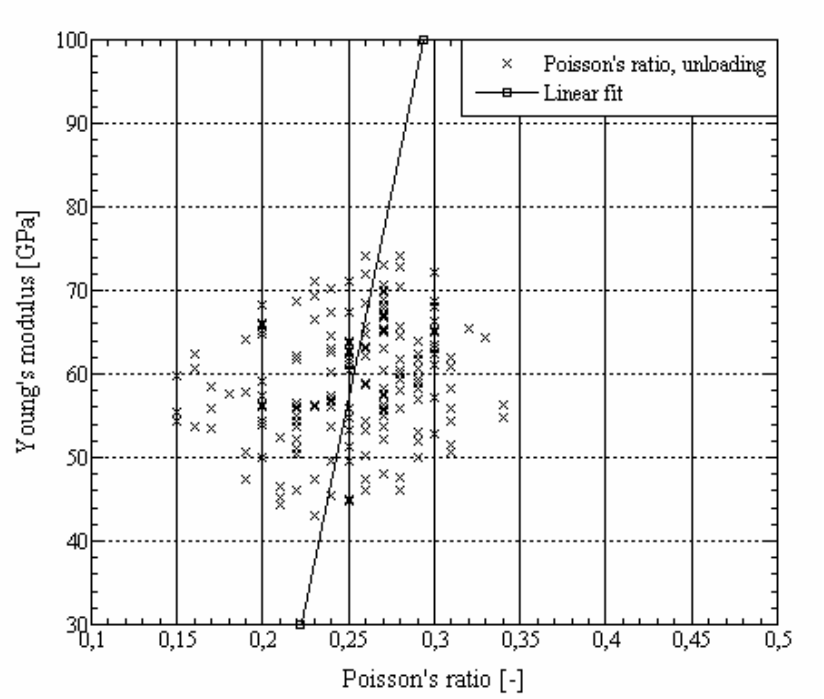

Figure 5-4. *Young's modulus versus Poisson's ratio for the CSIRO HI cell. Unloading parameters at 5 and 10 MPa biaxial pressure.*

5.3.3 Estimating the relationship unloading versus loading modulus

The ratios unloading/loading elastic parameters (eq. 5-1 and 5-2) were determined with the aim at using the loading curves to calculate the elastic parameters. The results from biaxial testing from the Borre Probe cores are presented in Figs. 5-5 to 5-9 and Table 5-7. The ratio unloading/loading for both elastic parameters are close to 1. Corresponding values for the CSIRO HI data are given in Table 5-7.

$$R_{E,\upsilon} = \frac{E,\upsilon_{unloading}}{E,\upsilon_{loading}} \tag{5-1}$$

The relationship in eq. 5-1 does not consider the effect of the different core properties for the determination of Young's modulus (the Poisson's ratio is independent of core properties). The CSIRO HI core is a few millimeters thicker and has a slightly larger inner and outer diameter compared to the Borre Probe. The Borre Probe relationship for Young's modulus is therefore corrected according to:

$$R_{BP,corr} = R_{BP} \frac{2/\left(1-\left(\frac{D_i}{D_o}\right)^2\right)_{CHI}}{2/\left(1-\left(\frac{D_i}{D_o}\right)^2\right)_{BP}} \tag{5-2}$$

The average inner and outer diameter for the Borre Probe and the CSIRO HI cores were used and the results are displayed in Table 5-7.

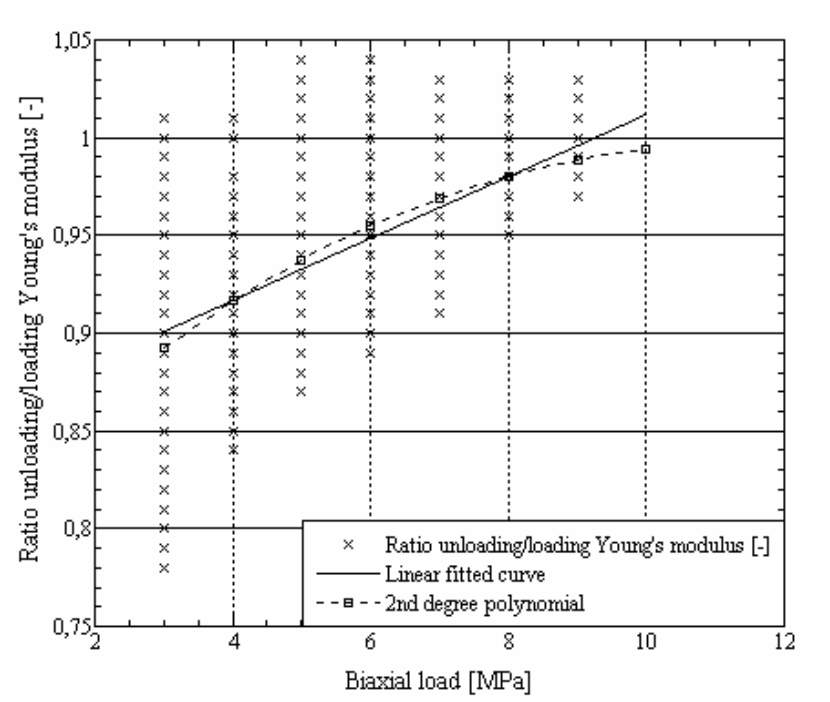

Figure 5-5. *Relationship unloading and loading Young's modulus from biaxial testing on Borre Probe cores using 3 to 10 MPa biaxial load. About 120 values are available at each biaxial load level. The average of the linear and 2nd degree polynomial curves give 0.93 and 1.00 at 5 and 10 MPa, respectively.*

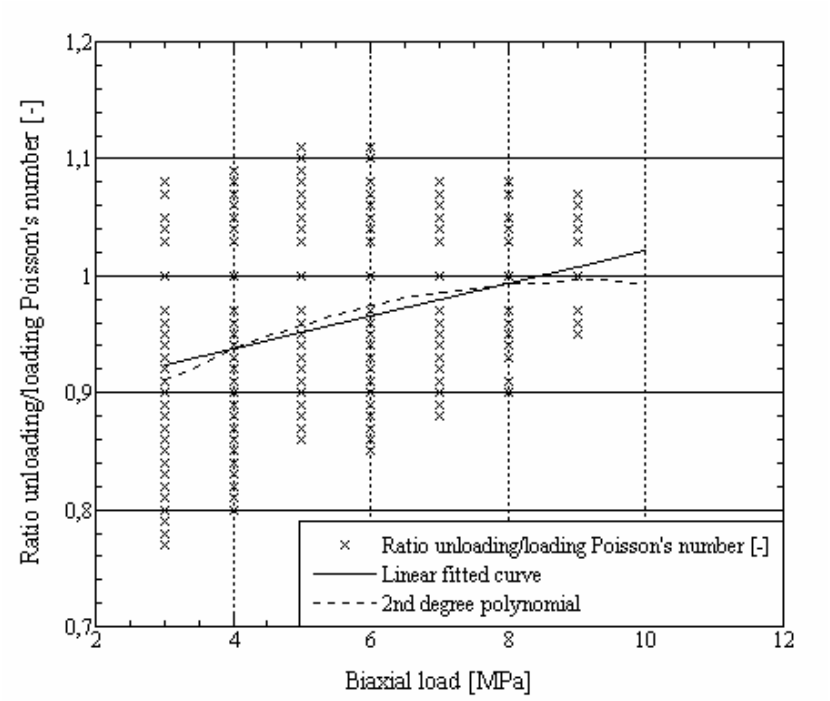

Figure 5-6. *Relationship unloading and loading Poisson's ratio from biaxial testing on Borre Probe cores using 3 to 10 MPa biaxial load. About 120 values are available at each biaxial load level. The average of the linear and 2nd degree polynomial curves give 0.95 and 1.00 at 5 and 10 MPa, respectively.*

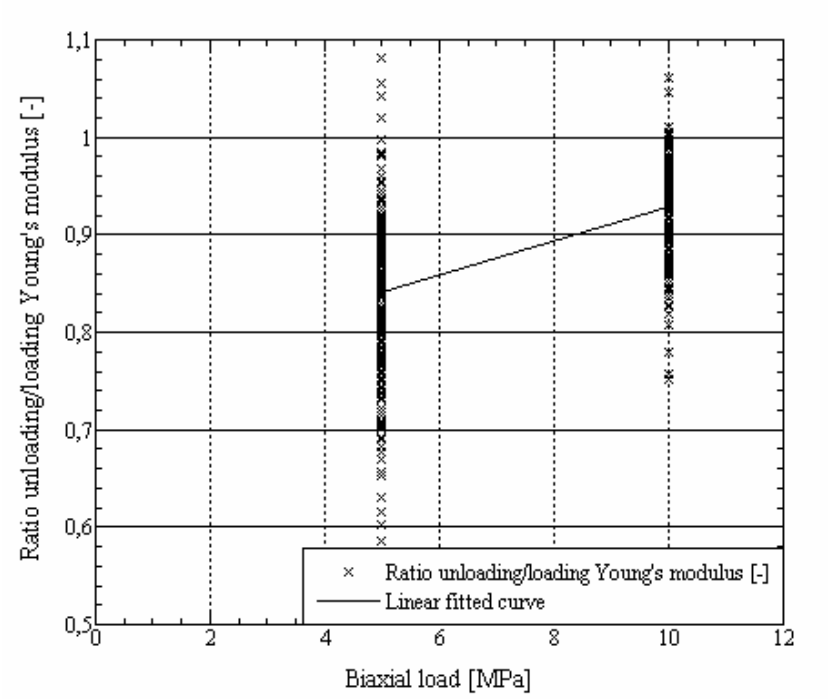

Figure 5-7. *Relationship unloading and loading Young's modulus from biaxial testing on CSIRO HI cores. About 250 values are available at each biaxial load level. The linear fitted curve gives 0.84 and 0.93 at 5 and 10 MPa, respectively.*

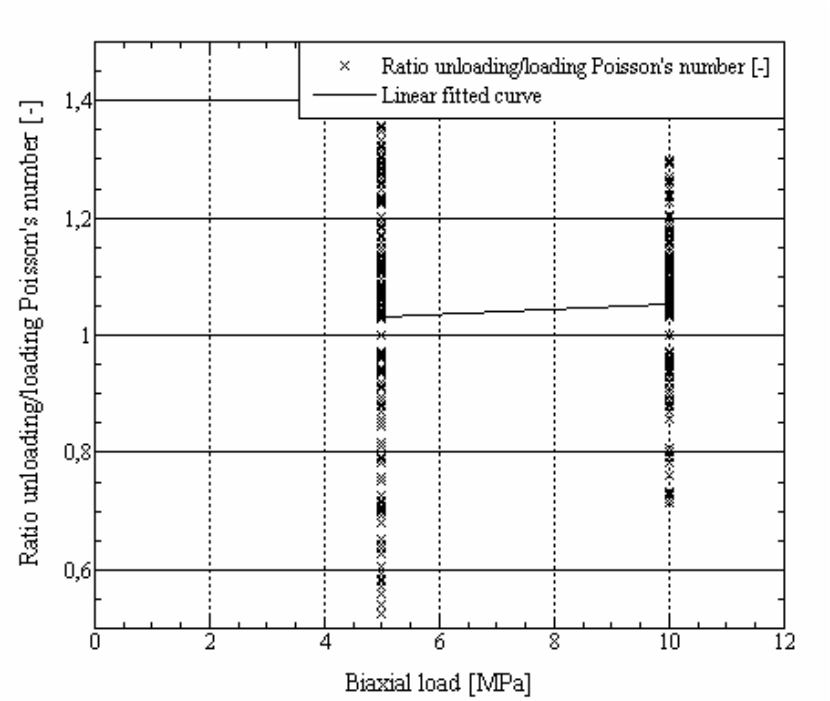

Figure 5-8. *Relationship unloading and loading Poisson's ratio from biaxial testing on CSIRO HI cores at the level 0.10-0.35. About 280 and 210 values are available at 5 and 10 MPa biaxial load, respectively. The linear fitted curve gives 1.03 and 1.05 at 5 and 10 MPa, respectively.*

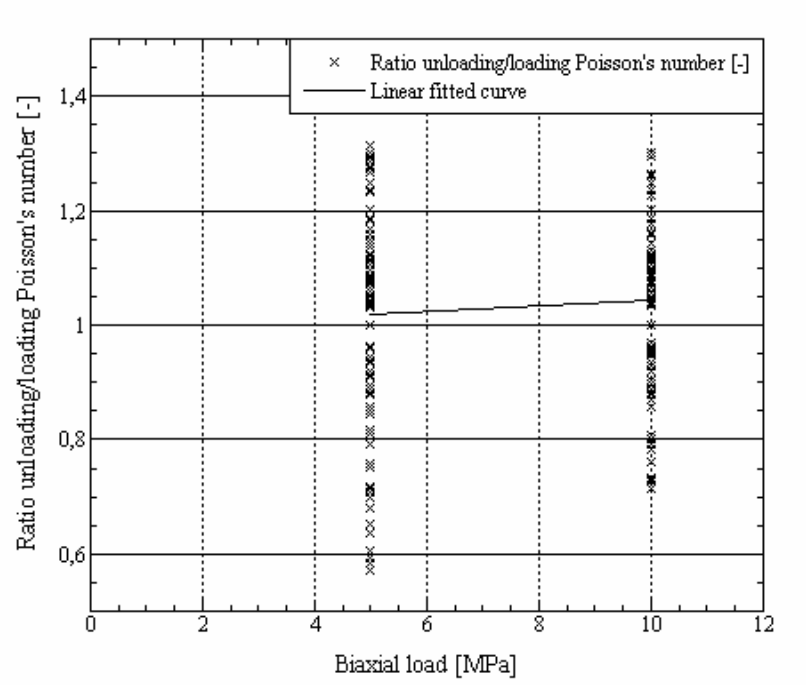

Figure 5-9. *Relationship unloading and loading Poisson's ratio from biaxial testing on CSIRO HI cores at the level 0.15-0.30. About 160 and 130 values are available at 5 and 10 MPa biaxial load, respectively. The linear fitted curve gives 1.02 and 1.04 at 5 and 10 MPa, respectively.*

Table 5-7. Relationship between unloading and loading elastic parameters.

	Young's modulus		**Poisson's ratio**					
					0.10-0.35		**0.15-0.30**	
Biaxial load	**5**	**10**	**5**	**10**	**5**	**10**	**5**	**10**
Borre Probe	0.93	1.00	0.95	1.00	-	-	-	-
Borre Probe, corrected	0.89	0.96			-	-	-	-
CSIRO HI	0.84	0.93	-	-	1.03	1.05	1.02	1.04

The relationships for the Borre Probe cores are generally slightly lower than corresponding ratios of the CSIRO HI cores. The relationship between unloading and loading elastic parameters were used in the measurement points with E-ranking, i.e. very poor quality data (marked with * in Tables 5-8 and 5-9). The Young's modulus was chosen as the average of the secant unloading values and the relationship unloading/loading of 0.93, i.e. according to the CSIRO HI data. For the Poisson's ratio, the Borre Probe relationship of 1.00 was used because the unloading ratios of Poisson's ratio include many gauges affected by the fracturing, i.e. giving too high unloading values. The final result for the elastic parameters thus become E=61.6±5.2 and υ=0.26±0.02.

Corresponding K-factors (eqs. 3-19 to 3-22) for the re-analyzed elastic parameters of the CSIRO HI cores are found in Table 5-10, which are used in the stress calculation. Worotnicki (1993) concluded that the K-factors strongly influence the elastic parameters, and hence, the calculated stresses, in soft rocks with low Young's modulus. Thus, the contribution of the updated K-factors on the calculated stresses is likely less than one percent.

Table 5-8a. Young's modulus used for stress calculation (10 MPa biaxial load), single test scale.

				Unloading/loading relationship							Unloading/loading relationship		
Borehole	**Depth [m]**	**Secant load std**	**Secant unload std**	**CHI rel.ship 0.93**	**BP rel.ship 0.96**	**E stress calc.**	**Borehole**	**Depth [m]**	**Secant load std**	**Secant unload std**	**CHI rel.ship 0.93**	**BP rel.ship 0.96**	**E stress calc.**
KA1045A	16.09	71.8	67.0	66.8	68.9	**67.0**	**KA2198A**	12.50	58.4	53.5	54.3	56.1	**53.5**
	16.60	64.7	60.9	60.2	62.1	**60.9**		13.55	61.8	62.2	57.5	59.3	**62.2**
	17.00	72.3	63.8	67.2	69.4	**63.8**		14.11	54.0	56.4	50.2	51.8	**56.4**
	17.47	70.2	63.1	65.3	67.4	**63.1**		14.68	59.2	52.5	55.1	56.8	**52.5**
KA1054A	16.19	68.3	67.1	63.5	65.6	**67.1**	**KA2510A**	12.04	66.2	62.0	61.6	63.6	**62.0**
	17.15	65.9	63.2	61.2	63.3	**62.2***		12.36	66.1	60.9	61.5	63.5	**60.9**
	18.46	61.8	59.6	57.5	59.3	**59.6**		12.87	65.5	62.3	60.9	62.9	**62.3**
KA1192A	14.43	77.9	69.7	72.4	74.8	**69.7**		13.36	72.1	69.1	67.1	69.2	**69.1**
	15.62	77.1	67.5	71.7	74.0	**67.5**		13.75	66.8	63.2	62.1	64.1	**63.2**
	16.19	76.1	74.5	70.8	73.1	**74.5**		14.20	67.5	65.3	62.8	64.8	**65.3**
KA1623A	13.29	66.7	58.1	62.0	64.0	**58.1**	**KA2870A**	12.73	65.8	57.8	61.2	63.2	**57.8**
	13.84	56.5	57.7	52.5	54.2	**52.5***		13.23	70.1	65.2	65.2	67.3	**65.2**
	14.27	64.7	57.7	60.2	62.1	**60.2***		13.64	68.7	64.1	63.9	66.0	**64.1**
KA1625A	14.07	71.1	67.3	66.1	68.3	**67.3**		14.25	71.7	63.1	66.7	68.8	**66.7***
	14.57	62.6	53.7	58.2	60.1	**53.7**		14.87	-	63.1	-	-	**63.1***
	15.07	60.5	53.6	56.3	58.1	**53.6**	**KA3068A**	14.73	66.7	63.2	62.0	64.0	**63.2**
KA1626A	12.17	58.6	47.7	54.5	56.3	**47.7**		16.18	76.1	69.1	70.8	73.1	**69.1**
	12.67	64.6	57.3	60.1	62.0	**57.3**		16.50	72.4	68.3	67.3	69.5	**68.3**
	13.23	64.2	57.7	59.7	61.6	**59.7***		16.85	69.3	66.8	64.4	66.5	**64.4***
KA1899A	12.09	65.5	59.5	60.9	62.9	**59.5**	**KZ0059B**	7.77	-	63.1	-	-	**63.1***
	12.43	66.8	60.6	62.1	64.1	**60.6**		8.33	64.1	63.3	59.6	61.5	**63.3***
	12.89	62.1	59.0	57.8	59.6	**57.8***		9.05	68.3	63.1	63.5	65.6	**63.5***
	13.38	60.7	59.0	56.5	58.3	**56.5***		12.22	63.9	63.2	59.4	61.3	**63.2**
	13.81	64.4	58.0	59.9	61.8	**58.0**		14.20	59.7	61.1	55.5	57.3	**58.3***
								14.72	62.7	64.4	58.3	60.2	**61.4***

Keys: Values marked with * have quality rank E

Table 5-8b. Young's modulus used for stress calculation (10 MPa biaxial load), average borehole and site scale.

				Unloading/loading relationship							Unloading/loading relationship		
Borehole	**Depth [m]**	**Secant load std**	**Secant unload std**	**CHI rel.ship 0.93**	**BP rel.ship 0.96**	**E stress calc.**	**Borehole**	**Depth [m]**	**Secant load std**	**Secant unload std**	**CHI rel.ship 0.93**	**BP rel.ship 0.96**	**E stress calc.**
Average KA1045A	16.79	69.6	63.5	64.7	66.8	**63.5**	**Average 1620-level**	-	62.9	57.7	58.5	60.4	**57.7**
Average KA1054A	17.27	65.0	64.2	60.5	62.4	**64.2**	**Average KA1899A**	12.92	63.7	59.0	59.2	61.1	**59.0**
Average 1050-level	-	67.7	63.8	63.0	65.0	**63.8**	**Average KA2198A**	13.71	58.6	56.7	54.5	56.3	**56.7**
Average KA1192A	15.41	77.1	71.0	71.7	74.0	**71.0**	**Average KA2510A**	13.10	67.5	64.1	62.8	64.8	**64.1**
Average KA1623A	13.80	62.3	58.1	57.9	59.8	**58.0***	**Average KA2870A**	13.74	68.7	63.1	63.9	66.0	**63.1**
Average KA1625A	14.57	64.4	59.7	59.9	61.8	**59.7**	**Average KA3068A**	16.07	71.2	66.8	66.2	68.4	**66.8**
Average KA1626A	12.69	62.1	54.1	57.8	59.6	**54.1**	**Average KZ0059B**	11.05	64.1	63.1	59.6	61.5	**63.1**

Keys: Values marked with * have quality rank E

Table 5-9a. Poisson's ratio used for stress calculation (10 MPa biaxial load), single test scale.

				Unloading/loading relationships							Unloading/loading relationships		
Borehole	**Depth [m]**	**Secant load std**	**Secant unload std**	**CHI rel.ship 1.04**	**BP rel.ship 1.00**	**υ stress calc.**	**Borehole**	**Depth [m]**	**Secant load std**	**Secant unload std**	**CHI rel.ship 1.04**	**BP rel.ship 1.00**	**υ stress calc.**
KA1045A	16.09	0.27	0.28	0.28	0.27	**0.28**	**KA2198A**	12.50	0.25	0.26	0.26	0.25	**0.255***
	16.60	0.26	0.26	0.27	0.26	**0.26***		13.55	0.27	0.27	0.28	0.27	**0.27***
	17.00	0.31	0.26	0.32	0.31	**0.285***		14.11	0.24	0.26	0.25	0.24	**0.25***
	17.47	-	0.26	-	-	**0.26***		14.68	0.28	0.25	0.29	0.28	**0.265***
KA1054A	16.19	0.26	0.25	0.27	0.26	**0.25**	**KA2510A**	12.04	0.24	0.24	0.25	0.24	**0.24***
	17.15	-	0.26	-	-	**0.26***		12.36	0.28	0.26	0.29	0.28	**0.27***
	18.46	0.25	0.26	0.26	0.25	**0.255***		12.87	0.27	0.28	0.28	0.27	**0.28**
KA1192A	14.43	0.29	0.28	0.30	0.29	**0.285***		13.36	0.25	0.25	0.26	0.25	**0.25**
	15.62	0.29	0.29	0.30	0.29	**0.29***		13.75	0.24	0.26	0.25	0.24	**0.26**
	16.19	0.24	0.24	0.25	0.24	**0.24**		14.20	0.28	0.25	0.29	0.28	**0.25**
KA1623A	13.29	0.27	0.24	0.28	0.27	**0.255***	**KA2870A**	12.73	0.26	0.27	0.27	0.26	**0.27**
	13.84	0.29	0.24	0.30	0.29	**0.24**		13.23	0.29	0.24	0.30	0.29	**0.24**
	14.27	0.28	0.24	0.29	0.28	**0.26***		13.64	0.28	0.25	0.29	0.28	**0.25**
KA1625A	14.07	0.32	0.24	0.33	0.32	**0.28***		14.25	0.26	0.25	0.27	0.26	**0.255***
	14.57	0.24	0.24	0.25	0.24	**0.24***		14.87	-	0.25	-	-	**0.25***
	15.07	0.23	0.24	0.24	0.23	**0.235***	**KA3068A**	14.73	0.28	0.29	0.29	0.28	**0.285***
KA1626A	12.17	0.28	0.24	0.29	0.28	**0.26***		16.18	0.26	0.25	0.27	0.26	**0.25**
	12.67	0.30	0.24	0.31	0.30	**0.24**		16.50	0.28	0.24	0.29	0.28	**0.24**
	13.23	0.27	0.24	0.28	0.27	**0.24**		16.85	0.27	0.24	0.28	0.27	**0.24**
KA1899A	12.09	0.27	0.26	0.28	0.27	**0.265***	**KZ0059B**	7.77	-	0.24	-	-	**0.24***
	12.43	0.30	0.26	0.31	0.30	**0.28***		8.33	-	0.24	-	-	**0.24***
	12.89	0.27	0.26	0.28	0.27	**0.265***		9.05	0.25	0.24	0.26	0.25	**0.245***
	13.38	0.29	0.26	0.30	0.29	**0.275***		12.22	0.23	0.24	0.24	0.23	**0.235***
	13.81	-	0.26	-	-	**0.26***		14.20	0.26	0.24	0.27	0.26	**0.25***
								14.72	0.28	0.24	0.29	0.28	**0.26***

Keys: Values marked with * have quality rank E

Table 5-9b. Poisson's ratio used for stress calculation (10 MPa biaxial load), average borehole and site scale.

				Unloading/loading relationships							Unloading/loading relationships		
Borehole	**Depth [m]**	**Secant load std**	**Secant unload std**	**CHI rel.ship 1.04**	**BP rel.ship 1.00**	**υ stress calc.**	**Borehole**	**Depth [m]**	**Secant load std**	**Secant unload std**	**CHI rel.ship 1.04**	**BP rel.ship 1.00**	**υ stress calc.**
Average KA1045A	16.79	0.30	0.26	0.31	0.30	**0.26**	**Average 1620-level**		0.28	0.24	0.29	0.28	**0.26***
Average KA1054A	17.27	0.25	0.26	0.26	0.25	**0.255***	**Average KA1899A**	12.92	0.29	0.26	0.30	0.29	**0.275***
Average 1050-level		0.28	0.26	0.29	0.28	**0.27***	**Average KA2198A**	13.71	0.26	0.26	0.27	0.26	**0.26***
Average KA1192A	15.41	0.28	0.26	0.29	0.28	**0.26**	**Average KA2510A**	13.10	0.26	0.26	0.27	0.26	**0.26**
Average KA1623A	13.80	0.29	0.24	0.30	0.29	**0.265***	**Average KA2870A**	13.74	0.27	0.25	0.28	0.27	**0.25**
Average KA1625A	14.57	0.27	0.24	0.28	0.27	**0.255***	**Average KA3068A**	16.07	0.27	0.25	0.28	0.27	**0.25**
Average KA1626A	12.69	0.28	0.24	0.29	0.28	**0.24**	**Average KZ0059B**	11.05	0.27	0.24	0.28	0.27	**0.25***

Keys: Values marked with * have quality rank E

Table 5-10a. Results from analysis of K-factors using biaxial tests on CSIRO HI cores, single test scale.

Borehole	Depth [m]	K_1	K_2	K_3	K_4	Borehole	Depth [m]	K_1	K_2	K_3	K_4
KA1045A	16.09	1.112	1.119	1.068	0.946	**KA2198A**	12.50	1.123	1.242	1.078	0.922
	16.60	1.112	1.117	1.067	0.933		13.55	1.123	1.244	1.079	0.933
	17.00	1.111	1.118	1.067	0.949		14.11	1.124	1.243	1.078	0.917
	17.47	1.113	1.118	1.067	0.932		14.68	1.123	1.241	1.078	0.930
KA1054A	16.19	1.114	1.119	1.068	0.924	**KA2510A**	12.04	1.114	1.117	1.067	0.916
	17.15	1.113	1.117	1.067	0.932		12.36	1.112	1.117	1.067	0.940
	18.46	1.112	1.116	1.067	0.929		12.87	1.111	1.117	1.067	0.946
KA1192A	14.43	1.112	1.120	1.068	0.949		13.36	1.114	1.120	1.068	0.924
	15.62	1.112	1.120	1.068	0.952		13.75	1.124	1.244	1.079	0.925
	16.19	1.116	1.122	1.068	0.915		14.20	1.125	1.245	1.079	0.915
KA1623A	13.29	1.112	1.115	1.067	0.929	**KA2870A**	12.73	1.123	1.243	1.078	0.934
	13.84	1.112	1.112	1.066	0.918		13.23	1.125	1.245	1.079	0.908
	14.27	1.112	1.116	1.067	0.933		13.64	1.125	1.245	1.079	0.917
KA1625A	14.07	1.112	1.120	1.068	0.946		14.25	1.125	1.245	1.079	0.921
	14.57	1.112	1.113	1.066	0.918		14.87	1.125	1.244	1.079	0.917
	15.07	1.112	1.113	1.066	0.913	**KA3068A**	14.73	1.123	1.244	1.079	0.944
KA1626A	12.17	1.109	1.109	1.065	0.935		16.18	1.125	1.246	1.079	0.917
	12.67	1.113	1.115	1.067	0.917		16.50	1.126	1.245	1.079	0.907
	13.23	1.113	1.116	1.067	0.916		16.85	1.125	1.245	1.079	0.908
KA1899A	12.09	1.112	1.116	1.067	0.936	**KZ0059B**	7.77	1.125	1.245	1.079	0.908
	12.43	1.111	1.117	1.067	0.946		8.33	1.125	1.245	1.079	0.908
	12.89	1.123	1.243	1.078	0.930		9.05	1.125	1.245	1.079	0.912
	13.38	1.122	1.243	1.078	0.937		12.22	1.126	1.245	1.079	0.903
	13.81	1.124	1.243	1.078	0.926		14.20	1.124	1.243	1.079	0.917
							14.72	1.124	1.244	1.079	0.925

Table 5-10b. Results from analysis of K-factors using biaxial tests on CSIRO HI cores, borehole average and site scale.

Borehole	Depth [m]	K_1	K_2	K_3	K_4	Borehole	Depth [m]	K_1	K_2	K_3	K_4
Average KA1045A	16.79	1.112	1.118	1.067	0.940	**Average 1620-level**	-	1.112	1.114	1.067	0.925
Average KA1054A	17.27	1.113	1.117	1.067	0.928	**Average KA1899A**	12.92	1.118	1.192	1.074	0.935
Average 1050-level	-	1.112	1.118	1.067	0.935	**Average KA2198A**	13.71	1.123	1.243	1.078	0.926
Average KA1192A	15.41	1.113	1.121	1.068	0.939	**Average KA2510A**	13.10	1.117	1.160	1.071	0.928
Average KA1623A	13.80	1.112	1.114	1.067	0.927	**Average KA2870A**	13.74	1.125	1.244	1.079	0.919
Average KA1625A	14.57	1.112	1.115	1.067	0.926	**Average KA3068A**	16.07	1.125	1.245	1.079	0.919
Average KA1626A	12.69	1.112	1.113	1.066	0.923	**Average KZ0059B**	11.05	1.125	1.245	1.079	0.912

5.4 Comments on results from data analysis

5.4.1 Effect of applied corrections

The temperature corrections have only been applied to one measurement point, 14.87 m in borehole KA2870A (4.3°C). The correction increased the stress magnitudes with 2.5-3.0 MPa.

The identification of measurements that suffer from boundary yield has been entirely based on the correlation between increasing axial strains versus rotation of σ_H towards the borehole direction. The distribution of axial strain with depth has merely been used to verify that large axial strains for the CSIRO HI measurements indeed are found in boreholes with evident rotation of σ_H towards the borehole direction and as a function of increasing axial strain. The minimum recorded axial strains for the corrected boreholes and uncorrected axial strain data in boreholes KA1625A, fit well with the results from the Borre Probe and the hydraulic fracturing stress data. This indicates that the applied correction is reliable.

The applied correction for boundary yield was only applied to axial and inclined strain gauges based on longitudinal expansion of the cell, because this expansion was much more pronounced than the radial expansion. Considering all data, this correction lowered the average stress ($(\sigma_H+\sigma_h+\sigma_v)/3$) with 1.9 MPa. The correction ratio for σ_H, σ_h and σ_v is 5.8:2.7:1, i.e. with the strongest correction of boundary yield for σ_H. Corresponding correction for the elastic parameters lowered the average stress magnitude with 2.3 MPa (ratio 1.9:1.4:1). The combined effect gives a reduction of the average stress magnitude equal to 3.4 MPa (ratios 2.8:1.8:1). The strongest correction for boundary yield was applied to one measurement point in borehole KA1045A, which lowered the average stress by 8.3 MPa, and rotated σ_H by about 90°. The correction of the elastic parameters lowered the average stress 2.2 MPa compared with the original interpretation, resulting in a total reduction of the average stress for this test equal to 9.1 MPa. The effect of the correction for boundary yield and updated elastic parameters for the horizontal and the vertical stresses are given in Tables 5-11 to 5-13.

The difference in elastic parameters between the two data sets from Borre Probe and the CSIRO HI cells is mainly caused by the different biaxial pressures and loading/unloading modulus used for interpretation of the secant modulus. The re-analyzed data uses the unloading curves as close to the virgin raw stress as possible, i.e. 10 MPa. For the original interpretation, loading curves and pressures up to 20 MPa were used. The elastic parameters for the re-analyzed and original data are displayed in Fig. 5.10 and a summary of all biaxial tests using the CSIRO HI cells and the Borre Probe at Äspö in Fig. 5-11.

5.4.2 Complementary explanations for scattered overcoring stress data

The results from re-analyzed CSIRO HI data call for clarifying information for boreholes KA2510A, KA2870A, and KA3068A. The recorded strains in boreholes KA2510A and KA2870A are strongly scattered and it is difficult to identify suspect or malfunctioning gauges in an objective manner based on comparison of the strains in the same borehole (Table 3-1). The strain response during overcoring were poorly sampled and offered little help in the analysis. The same is valid for data recoded in borehole KA3068A, where a strongly non-linear stress field versus borehole length was obtained.

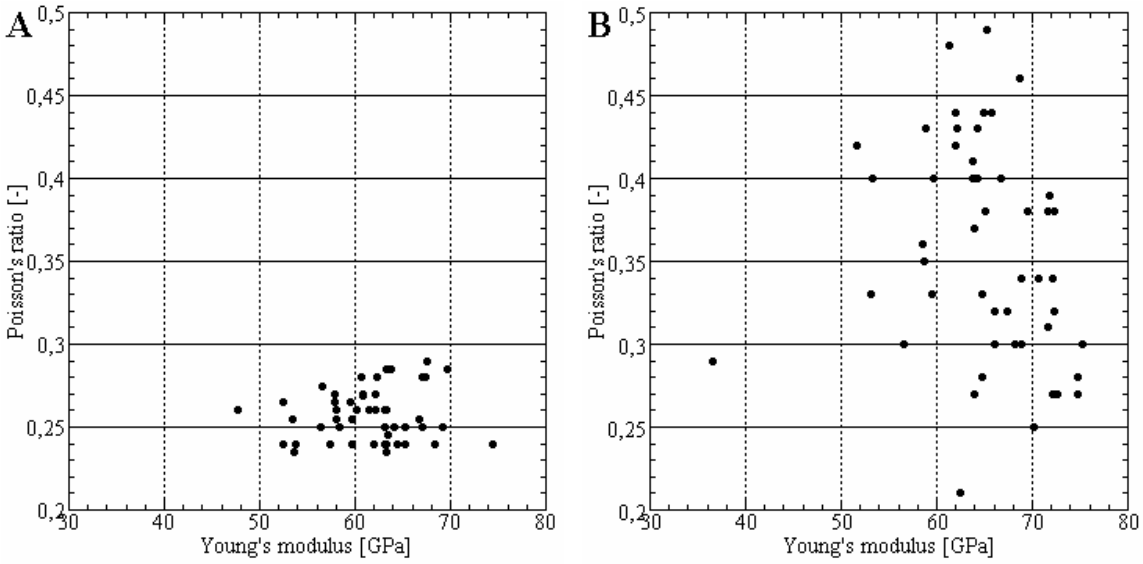

Figure 5-10. *Young's modulus versus Poisson's ratio for re-analyzed (A) and original (B) CSIRO HI overcoring stress data.*

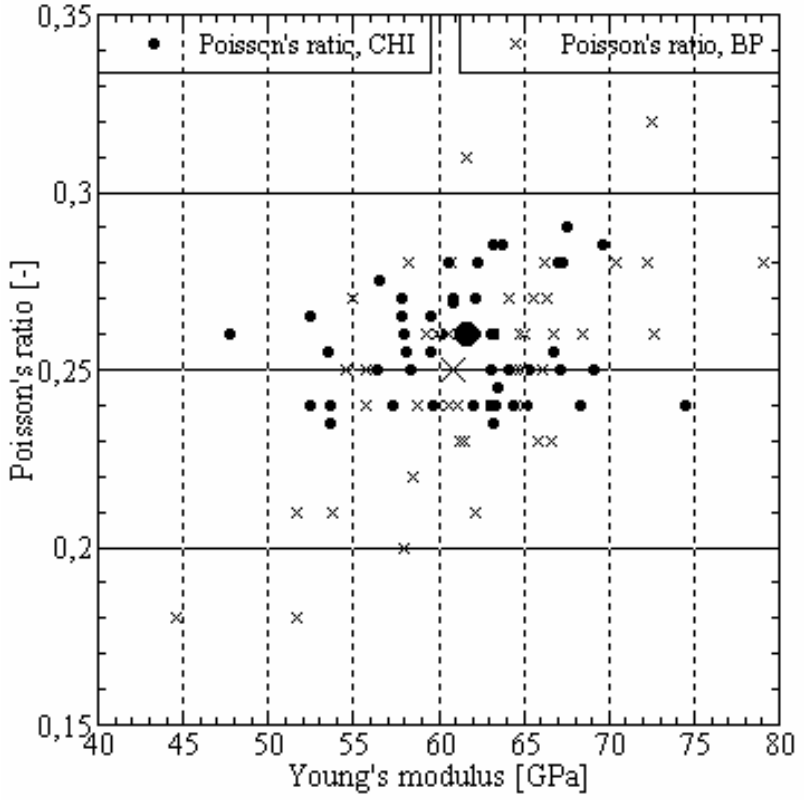

Figure 5-11. *Young's modulus versus Poisson's ratio for both the CSIRO HI cells and the Borre Probe after re-analysis. The CSIRO HI and Borre Probe averages are given as a larger circle and cross, respectively.*

Borehole KA2510A and also borehole KA1192A are oriented perpendicular to σ_H, i.e. giving maximum bond stress (Duncan Fama and Pender, 1980). A plausible explanation to the scattered strains in borehole KA2510A and the deviating orientation of σ_H stress in borehole KA1192A could be the effect of bond failure between the cell and the rock, especially when considering that the bonding between the cell and the rock is of questionable quality for many CSIRO HI measurements. In borehole KA2510A, several tests indicate bond failure (or possibly core fracturing).

Table 5-11. Effect of corrections for boundary yield and elastic parameters on maximum horizontal stress, σ_H, at the single test scale.

		Correction					Correction					Correction		
Borehole	Initial	B.Y.	E. par.	Final	Borehole	Initial	B.Y.	E. par.	Final	Borehole	Initial	B.Y.	E. par.	Final
KA1045A	24.9	11.7	21.4	10.7	KA1626A	12.3	-	7.5	7.5	KA2510A	21.8	20.3	19.8	18.2
KA1045A	7.5	-	5.7	5.7	KA1626A	10.8	9.4	8.6	7.1	KA2870A	39.1	34.7	33.7	29.4
KA1045A	8.7	-	7.2	7.2	KA1626A	8.6	6.5	7.5	5.7	KA2870A	38.8	37.5	35.4	34.1
KA1045A	8.1	-	5.8	5.8	KA1899A	21.2	17.9	17.1	14.1	KA2870A	27.6	-	28.1	28.1
KA1054A	15.2	9.1	14.1	8.7	KA1899A	18.5	-	15.5	15.5	KA2870A	36.3	30.3	38.2	33.0
KA1054A	11.5	-	8.5	8.5	KA1899A	23.6	20.0	18.7	15.3	KA2870A	36.1	25.0	33.5	23.9
KA1054A	14.5	10.1	11.2	7.8	KA1899A	19.1	18.0	16.0	14.6	KA3068A	25.1	-	23.0	23.0
KA1192A	11.5	9.9	10.5	9.1	KA1899A	23.3	20.5	18.4	15.7	KA3068A	32.7	26.0	28.2	21.9
KA1192A	15.1	12.7	12.7	11.0	KA2198A	25.0	22.9	23.1	21.0	KA3068A	34.3	22.7	31.5	19.7
KA1192A	12.4	-	11.9	11.9	KA2198A	14.2	-	24.0	24.0	KA3068A	23.1	23.0	18.6	18.3
KA1623A	19.3	18.7	13.8	13.7	KA2198A	21.7	21.3	19.4	19.2	KZ0059B	22.9	20.6	18.1	15.7
KA1623A	15.5	14.1	12.4	11.6	KA2198A	24.3	23.0	22.5	21.6	KZ0059B	29.8	24.7	23.4	15.7
KA1623A	14.8	-	11.7	11.7	KA2510A	34.4	-	25.4	25.4	KZ0059B	18.2	-	15.9	15.9
KA1625A	16.9	-	12.8	12.8	KA2510A	27.7	28.5	23.6	23.4	KZ0059B	22.0	19.6	17.2	15.4
KA1625A	11.4	-	9.2	9.2	KA2510A	24.0	22.7	22.4	21.1	KZ0059B	29.0	23.5	19.2	15.3
KA1625A	12.5	-	8.9	8.9	KA2510A	25.3	24.2	21.8	23.0	KZ0059B	29.2	22.8	21.5	16.2
					KA2510A	24.1	23.5	21.5	21.0					

Keys: Initial denotes the original interpretation without corrections; B.Y. and E. par. is the effect of corrections for boundary yield and updated elastic parameters, respectively; and final represent correction for both boundary yield and elastic parameters. All malfunctioning gauges have been removed and each measurement point includes the same set of strain gauges.

Table 5-12. Effect of corrections for boundary yield and elastic parameters on minimum horizontal stress, σ_h, at the single test scale.

		Correction					Correction					Correction		
Borehole	Initial	B.Y.	E. par.	Final	Borehole	Initial	B.Y.	E. par.	Final	Borehole	Initial	B.Y.	E. par.	Final
KA1045A	14.8	5.9	12.6	4.8	KA1626A	9.0	-	5.8	5.8	KA2510A	8.0	6.2	5.8	3.6
KA1045A	5.4	-	3.0	3.0	KA1626A	6.0	5.9	4.9	4.7	KA2870A	15.9	12.5	12.1	8.8
KA1045A	5.7	-	4.0	4.0	KA1626A	2.8	2.2	2.0	1.7	KA2870A	14.5	13.6	11.5	10.3
KA1045A	5.2	-	2.3	2.3	KA1899A	7.9	7.5	5.7	5.3	KA2870A	8.1	-	7.8	7.8
KA1054A	6.4	5.3	5.7	5.0	KA1899A	6.8	-	5.3	5.3	KA2870A	8.5	3.4	10.0	5.3
KA1054A	4.9	-	4.0	4.0	KA1899A	9.2	8.7	6.5	6.0	KA2870A	9.2	3.4	7.1	2.5
KA1054A	7.8	6.3	5.4	4.9	KA1899A	8.1	8.1	6.3	6.0	KA3068A	9.1	-	6.8	6.8
KA1192A	8.0	4.5	7.6	4.0	KA1899A	8.9	8.4	6.2	5.7	KA3068A	18.5	17.5	15.8	14.9
KA1192A	11.7	7.8	9.5	5.2	KA2198A	7.2	6.0	6.0	4.7	KA3068A	15.8	13.9	13.6	12.0
KA1192A	6.0	-	5.0	5.0	KA2198A	3.7	-	6.3	6.3	KA3068A	13.2	13.3	10.6	10.6
KA1623A	14.4	13.9	9.7	9.6	KA2198A	9.1	9.1	6.3	6.2	KZ0059B	7.5	7.1	4.7	4.2
KA1623A	10.4	9.6	7.4	6.6	KA2198A	8.4	7.8	6.8	6.2	KZ0059B	11.1	9.5	6.6	5.9
KA1623A	8.9	-	6.0	6.0	KA2510A	20.2	-	8.2	8.2	KZ0059B	5.1	-	4.2	4.2
KA1625A	6.7	-	4.9	4.9	KA2510A	12.8	14.3	8.3	8.1	KZ0059B	5.6	5.1	3.3	3.0
KA1625A	5.1	-	3.9	3.9	KA2510A	8.8	6.8	7.8	5.8	KZ0059B	10.5	9.1	6.1	5.5
KA1625A	5.5	-	4.1	4.1	KA2510A	8.6	7.2	7.8	6.2	KZ0059B	10.5	9.2	7.0	6.2
					KA2510A	10.4	9.3	8.6	7.3					

Keys: Initial denotes the original interpretation without corrections; B.Y. and E. par. is the effect of corrections for boundary yield and updated elastic parameters, respectively; and final represent correction for both boundary yield and elastic parameters. All malfunctioning gauges have been removed and each measurement point includes the same set of strain gauges.

Table 5-13. Effect of corrections for boundary yield and elastic parameters on maximum horizontal stress, σ_v, at the single test scale.

		Correction					Correction					Correction	
Borehole	Initial	B.Y.	E. par.	Final	Borehole	Initial	B.Y.	E. par.	Final	Borehole	Initial	B.Y.	E. par.	Final
KA1045A	7.6	4.9	6.5	4.5	KA1626A	7.6	-	5.1	5.1	KA2510A	7.7	8.5	7.7	7.4
KA1045A	2.7	-	2.3	2.3	KA1626A	5.7	6.8	5.7	5.4	KA2870A	20.7	19.7	17.4	16.6
KA1045A	2.7	-	2.3	2.3	KA1626A	3.8	3.4	3.1	2.9	KA2870A	22.6	22.3	20.4	20.2
KA1045A	1.5	-	1.1	1.1	KA1899A	6.6	6.1	4.6	4.2	KA2870A	12.8	-	13.3	13.3
KA1054A	6.0	3.6	4.1	3.4	KA1899A	6.1	-	4.7	4.7	KA2870A	12.6	11.2	13.4	12.4
KA1054A	1.3	-	3.5	3.5	KA1899A	8.6	8.0	6.0	5.6	KA2870A	12.9	10.4	11.1	9.8
KA1054A	4.7	2.9	2.7	2.2	KA1899A	7.5	7.5	5.9	5.7	KA3068A	7.8	-	6.8	6.8
KA1192A	4.5	4.7	4.9	4.4	KA1899A	8.2	7.8	5.8	5.5	KA3068A	10.6	10.5	9.5	8.8
KA1192A	9.4	8.4	7.9	7.3	KA2198A	7.5	7.0	6.5	6.2	KA3068A	10.8	10.6	10.6	9.3
KA1192A	9.0	-	8.3	8.3	KA2198A	4.2	-	7.2	7.2	KA3068A	9.9	9.2	7.2	7.2
KA1623A	12.3	12.0	9.3	9.3	KA2198A	10.6	10.5	9.0	9.0	KZ0059B	13.1	12.8	10.0	9.8
KA1623A	6.9	6.6	5.5	5.4	KA2198A	7.9	7.4	6.8	6.6	KZ0059B	17.7	16.7	12.2	11.5
KA1623A	6.7	-	5.4	5.4	KA2510A	17.7	-	10.8	10.8	KZ0059B	12.1	-	10.7	10.7
KA1625A	11.3	-	8.6	8.6	KA2510A	11.1	12.1	9.8	9.7	KZ0059B	13.6	12.6	10.0	9.8
KA1625A	6.8	-	5.5	5.5	KA2510A	12.1	11.8	11.3	11.0	KZ0059B	17.4	16.0	11.6	11.2
KA1625A	7.3	-	6.3	6.3	KA2510A	11.6	11.3	10.0	10.7	KZ0059B	17.0	15.8	12.5	11.9
					KA2510A	8.0	7.8	7.1	7.7					

Keys: Initial denotes the original interpretation without corrections; B.Y. and E. par. is the effect of corrections for boundary yield and updated elastic parameters, respectively; and final represent correction for both boundary yield and elastic parameters. All malfunctioning gauges have been removed and each measurement point includes the same set of strain gauges.

6 Stress calculations

6.1 General

In this chapter, results from stress calculations based on the least squares algorithm are presented. For this, an inversion program was developed that can handle all types of CSIRO HI cells used at the Äspö HRL. The program was also calibrated against the original data available at the Äspö HRL. The program calculates the full stress tensor in one point where the measured strains are related to the *in situ* stress field according to:

$$[e] = [A][B][\sigma] \tag{6-1}$$

where [e] is a matrix of strains; [A] is a matrix that contains the elastic parameters; [B] is a rotation matrix from the local to the geographical coordinate system (i.e. not the Äspö local system); and [σ] is the components of the stress tensor. The system of equations is described in detailed in eqs. 3-11 to 3-14, Ch. 3.3.2.

The results are based on viewing the overcoring data as individual measurement points (Chapter 6.2 to 6-13), borehole averages and site averages (Chapter 6-14). The results are also presented in Appendix 7. The re-analyzed strain data have been used and erroneous data have been excluded. Questionable data are excluded if they are proven to have a major impact on the calculated stresses. Gauges have also been rejected in accordance with the empirical Chauvenet's criterion (Holman, 1994). The original data is found in the following publications: Lee et al. (1993 and 1994), Litterbach et al. (1994), and Nilsson et al. (1997).

6.2 Borehole KA1045A

The stress analysis and comparison with original data in borehole KA1045 includes 4 measurement points (Figs. 6-1 to 6-5). The re-calculated principal and horizontal stresses are in average about 3.5 MPa lower compared to the original data (Lee et al., 1993). Both principal and horizontal stress magnitudes vary fairly linear versus borehole length, except for the shallowest measurement which indicates slightly larger stress magnitudes. This measurement point suffers from boundary yield and when corrected for, the principal stress orientations become well defined.

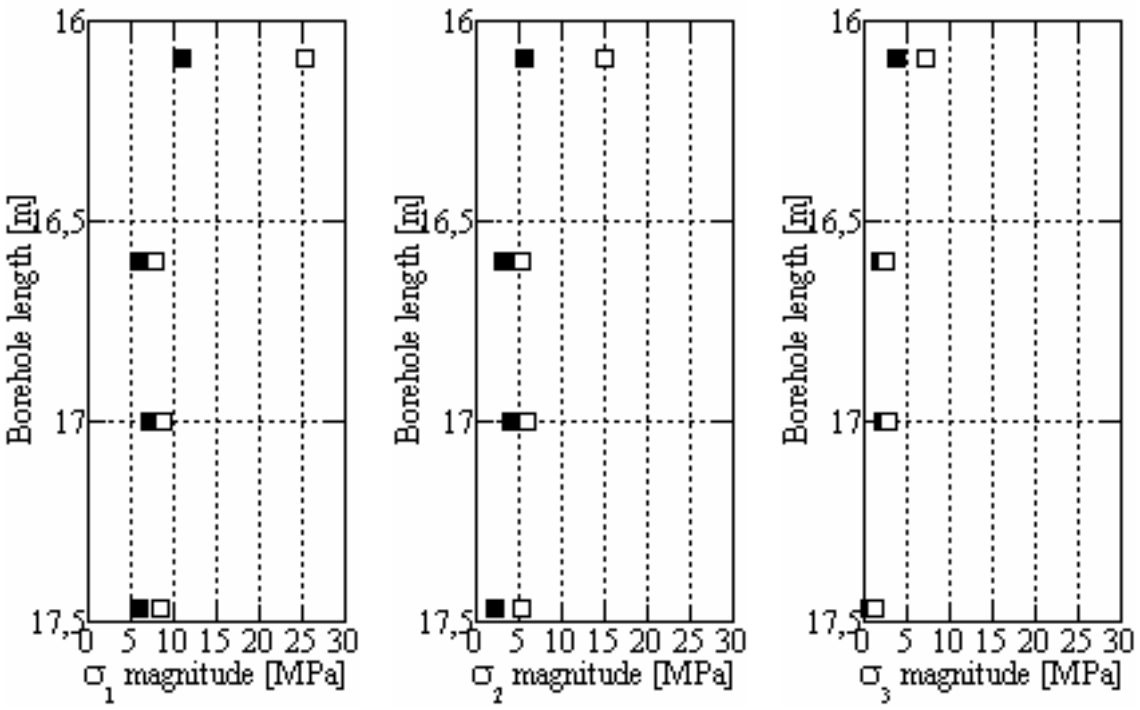

Figure 6-1. *Principal stress magnitudes in borehole KA1045A. The principal stresses are represented with filled and unfilled symbols for the re-analyzed and original data, respectively.*

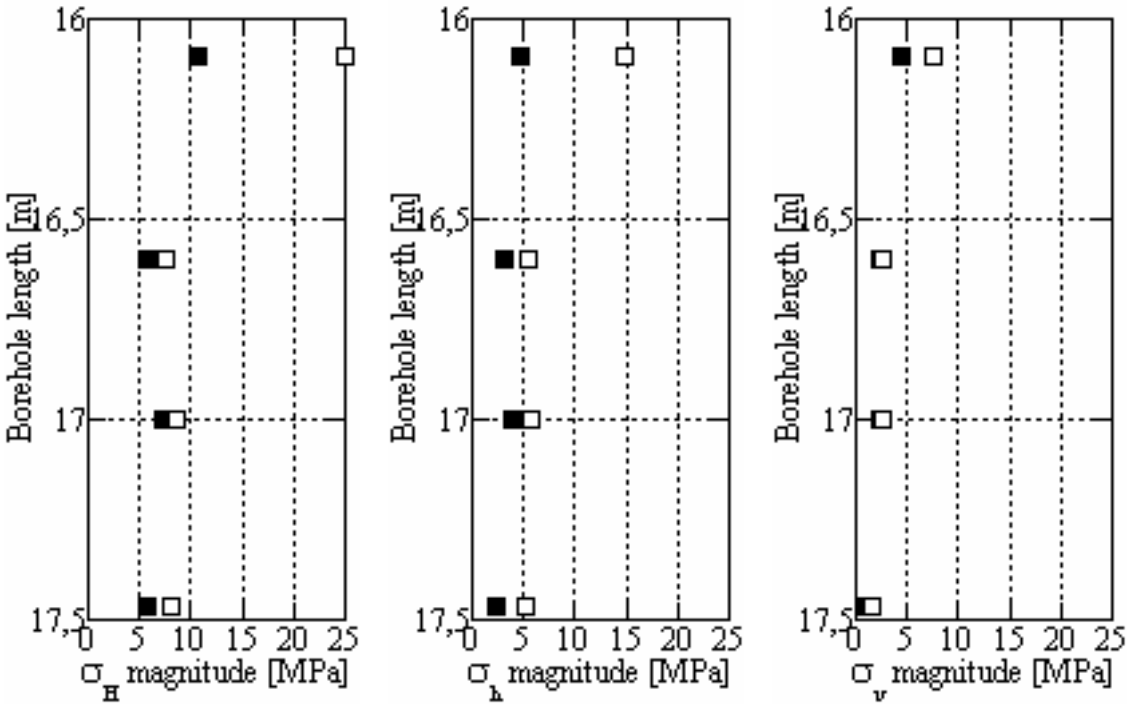

Figure 6-2. *Horizontal stress magnitudes in borehole KA1045A. The horizontal stresses are represented with filled and unfilled symbols for the re-analyzed and original data, respectively.*

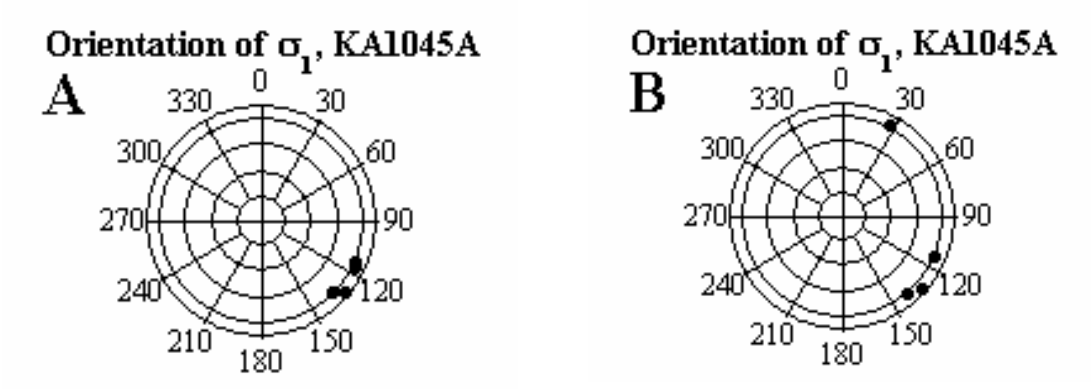

Figure 6-3. *Orientation of maximum principal stress in borehole KA1045A. A and B are the re-calculated stresses and the original data, respectively.*

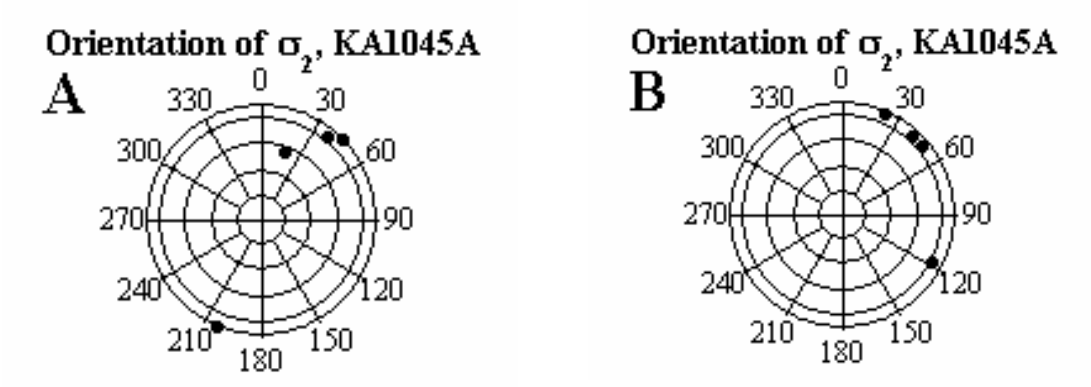

Figure 6-4. *Orientation of intermediate principal stress in borehole KA1045A. A and B are the re-calculated stresses and the original data, respectively.*

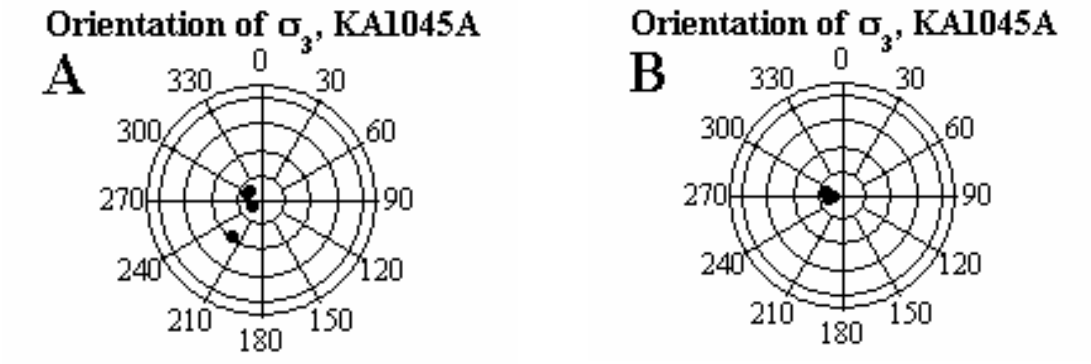

Figure 6-5. *Orientation of minimum principal stress in borehole KA1045A. A and B are the re-calculated stresses and the original data, respectively.*

6.3 Borehole KA1054A

The stress analysis and comparison with original data in borehole KA1054 includes 3 measurement points (Figs. 6-6 to 6-10). The re-calculated principal and horizontal stresses are in average about 2.5 MPa lower compared to the original data (Lee et al., 1993). Both principal and horizontal stress magnitudes vary fairly linear versus borehole length. The solutions using re-analyzed data are somewhat less scattered concerning the stress magnitudes.

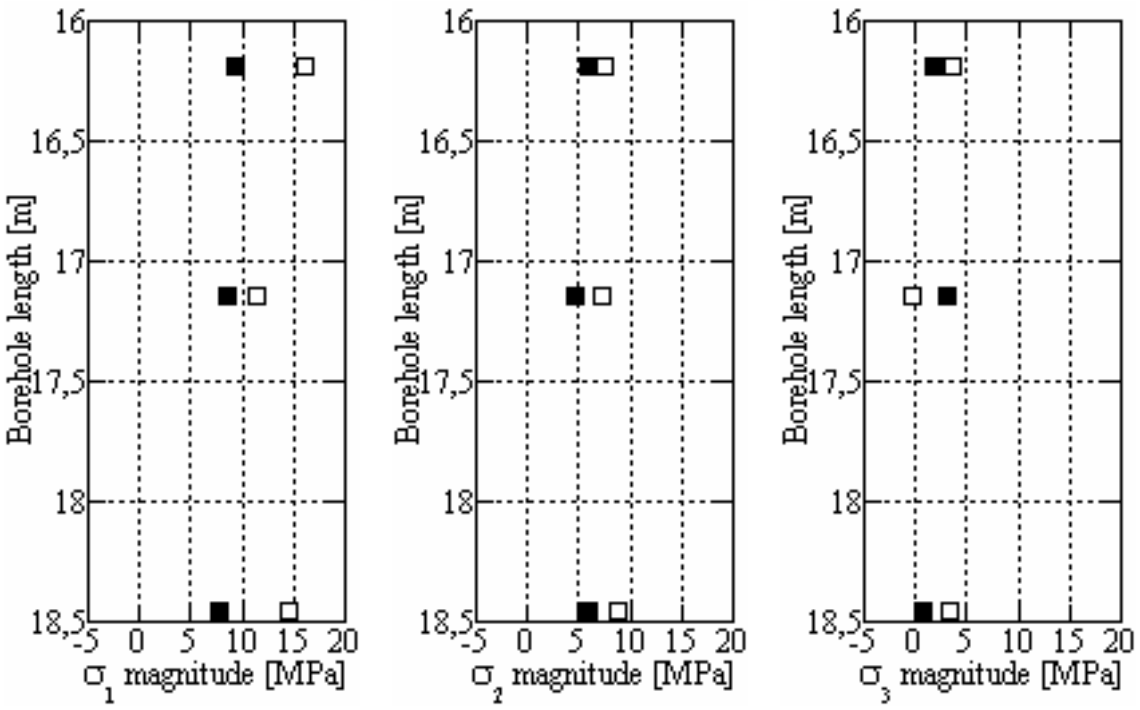

Figure 6-6. *Principal stress magnitudes in borehole KA1054A. The principal stresses are represented with filled and unfilled symbols for the re-analyzed and original data, respectively.*

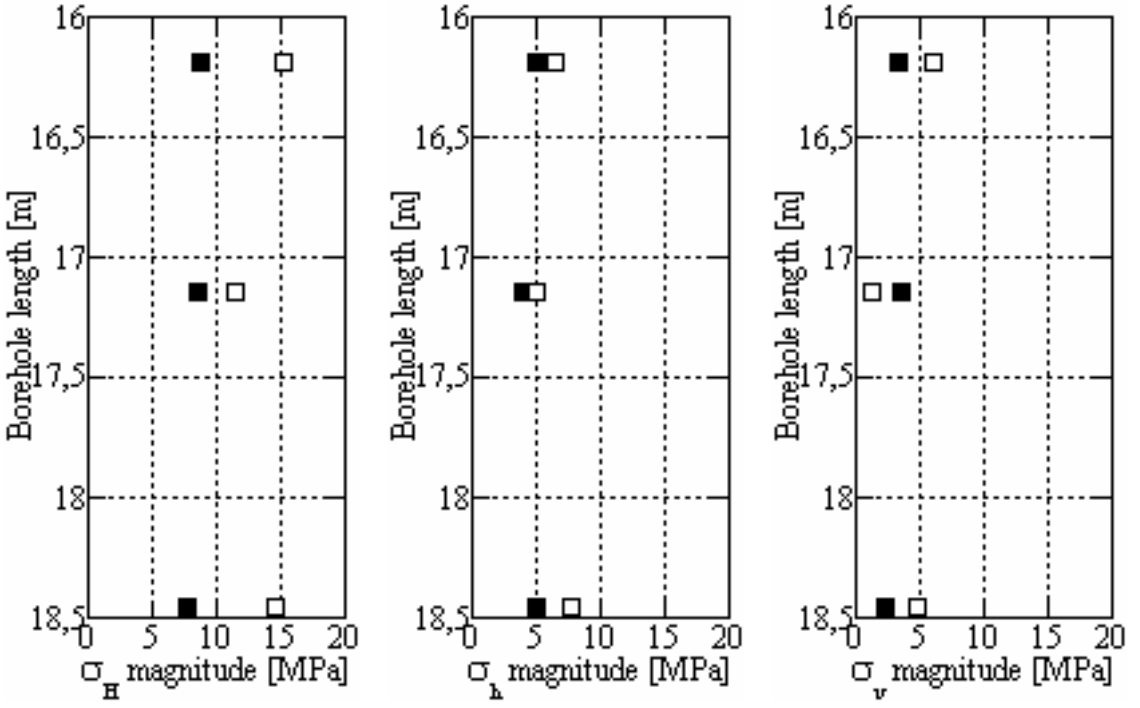

Figure 6-7. *Horizontal stress magnitudes in borehole KA1054A. The horizontal stresses are represented with filled and unfilled symbols for the re-analyzed and original data, respectively.*

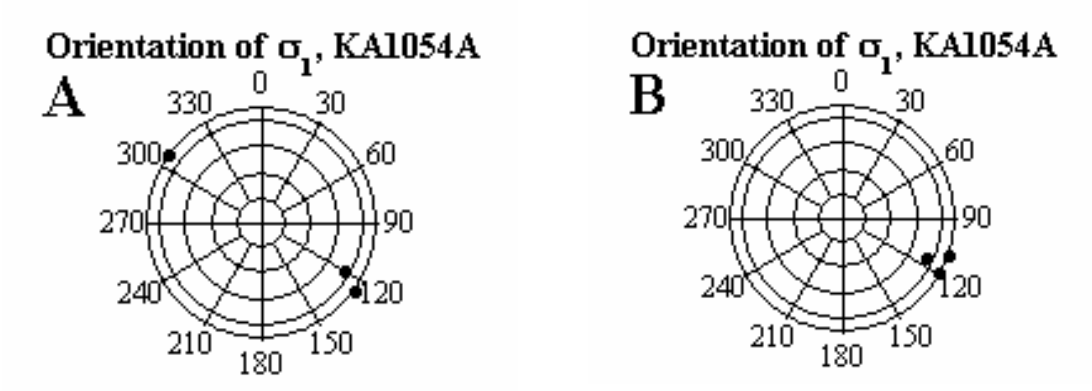

Figure 6-8. *Orientation of maximum principal stress in borehole KA1054A. A and B are the re-calculated stresses and the original data, respectively.*

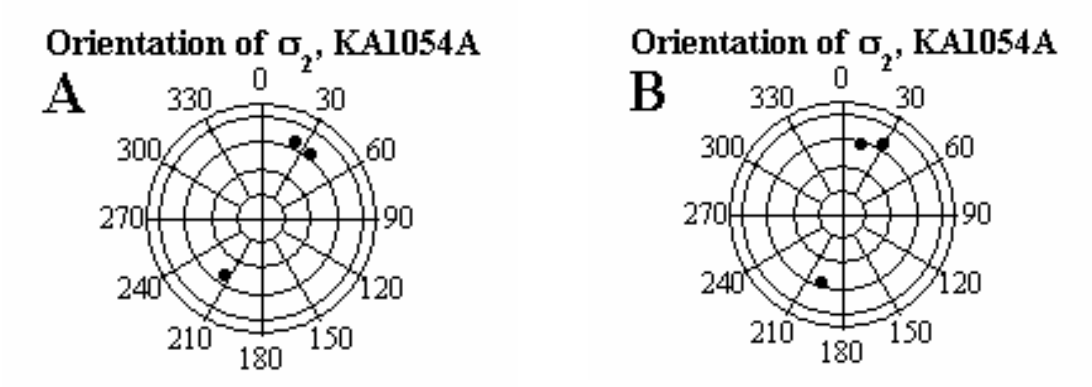

Figure 6-9. *Orientation of intermediate principal stress in borehole KA1054A. A and B are the re-calculated stresses and the original data, respectively.*

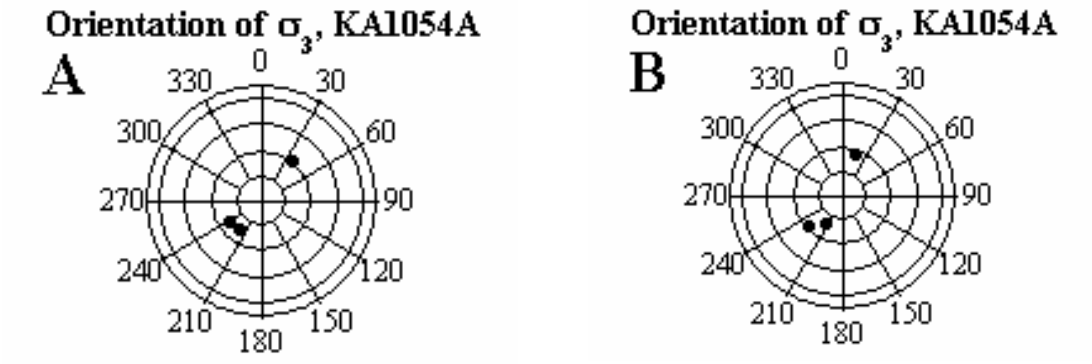

Figure 6-10. *Orientation of minimum principal stress in borehole KA1054A. A and B are the re-calculated stresses and the original data, respectively.*

6.4 Borehole KA1192A

The stress analysis and comparison with original data in borehole KA1192 includes 3 measurement points (Figs. 6-11 to 6-15). The re-calculated principal and horizontal stresses are in average about 2.5 MPa lower compared to the original data (Lee et al., 1993). Both principal and horizontal stress magnitudes indicate slight stress increase versus borehole length. The solutions using re-analyzed data are considerably less scattered compared to the original data.

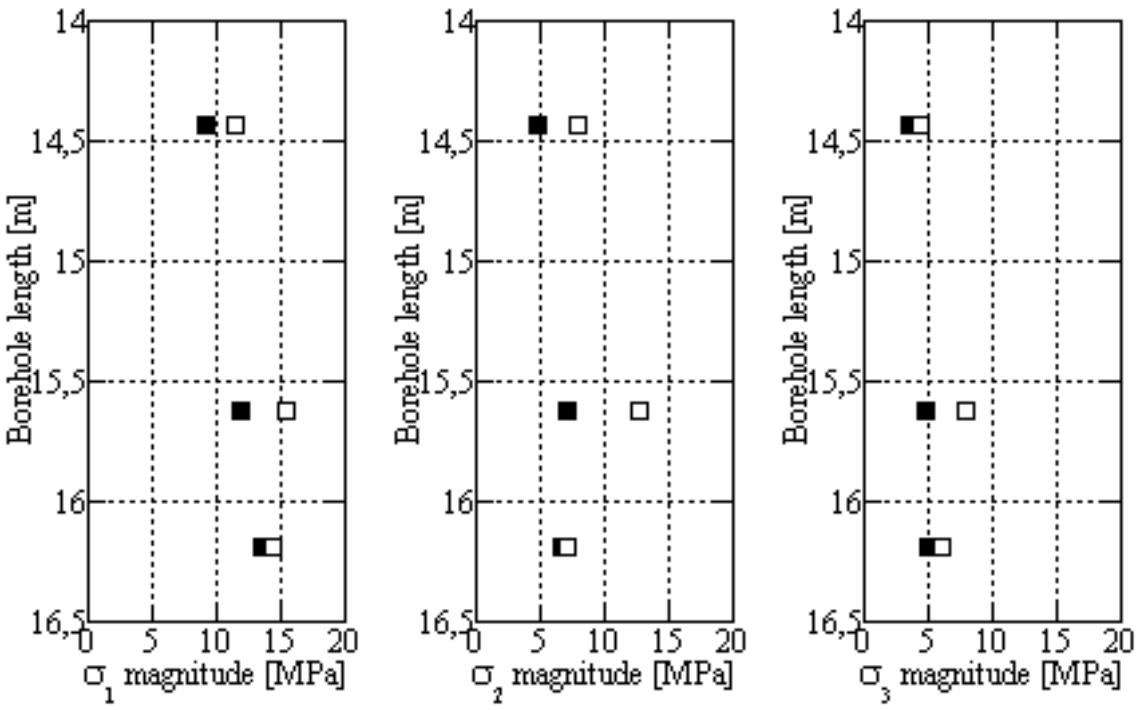

Figure 6-11. *Principal stress magnitudes in borehole KA1192A. The principal stresses are represented with filled and unfilled symbols for the re-analyzed and original data, respectively.*

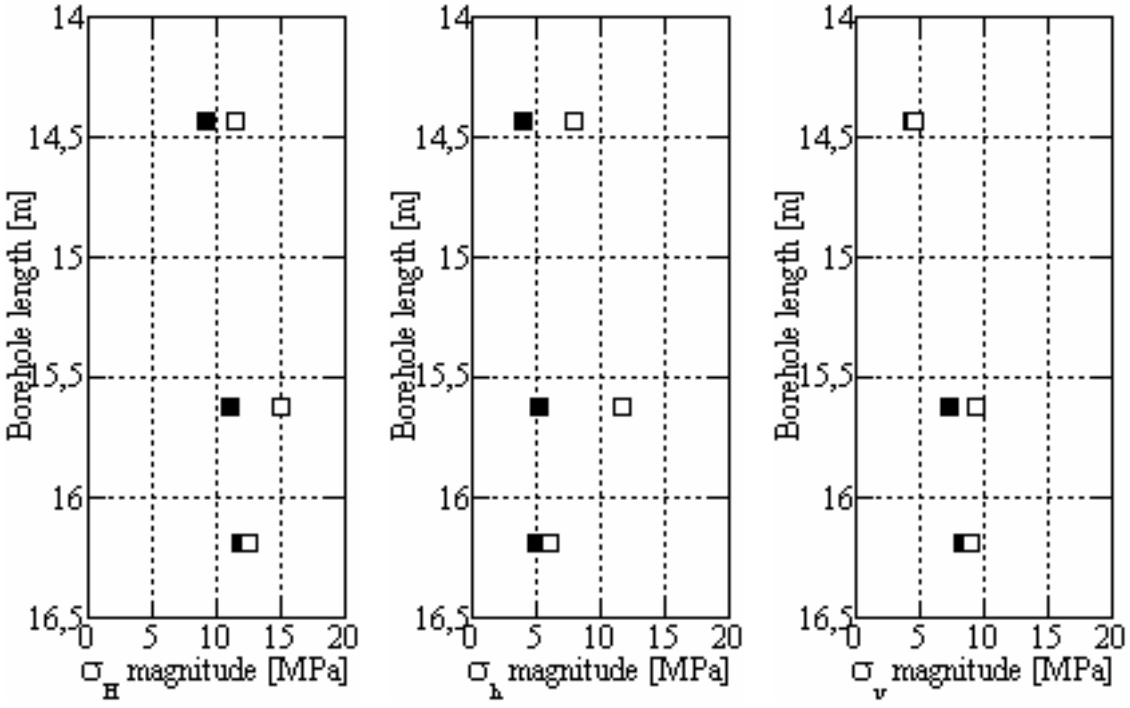

Figure 6-12. *Horizontal stress magnitudes in borehole KA1192A. The horizontal stresses are represented with filled and unfilled symbols for the re-analyzed and original data, respectively.*

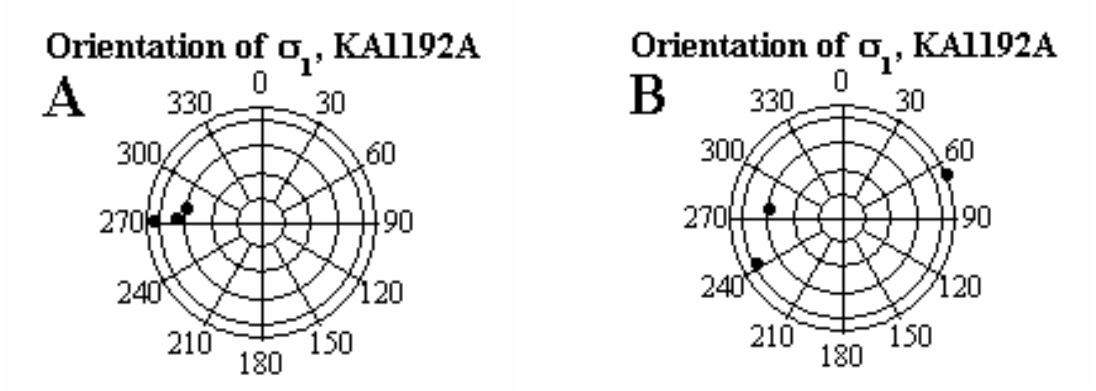

Figure 6-13. *Orientation of maximum principal stress in borehole KA1192A. A and B are the re-calculated stresses and the original data, respectively.*

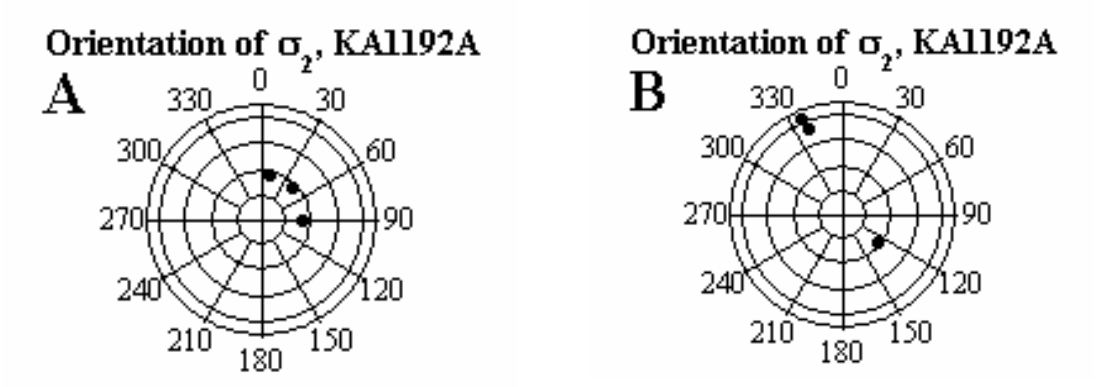

Figure 6-14. *Orientation of intermediate principal stress in borehole KA1192A. A and B are the re-calculated stresses and the original data, respectively.*

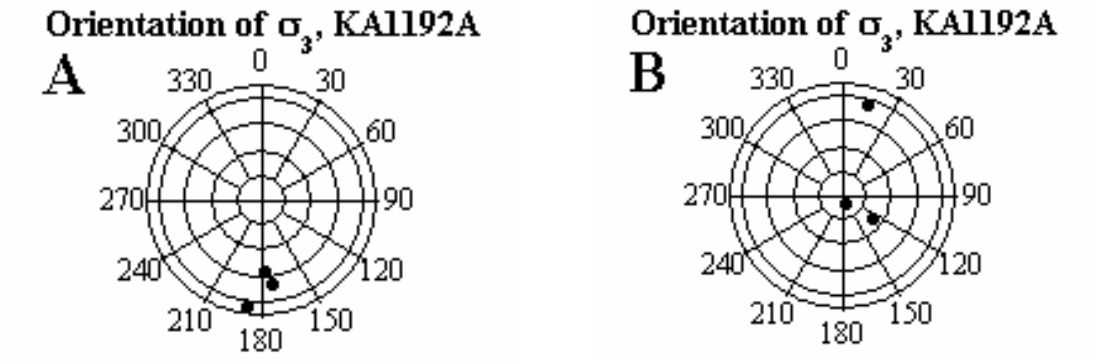

Figure 6-15. *Orientation of minimum principal stress in borehole KA1192A. A and B are the re-calculated stresses and the original data, respectively.*

6.5 Borehole KA1623A

The stress analysis and comparison with original data in borehole KA1623 includes 3 measurement points (Figs. 6-16 to 6-20). The re-calculated principal and horizontal stresses are in average about 3.5 MPa lower compared to the original data (Lee et al., 1994). The shallowest measurement point indicates somewhat larger stress magnitudes compared to the two deeper points. The solutions using re-analyzed data are slightly more scattered compared to the original data.

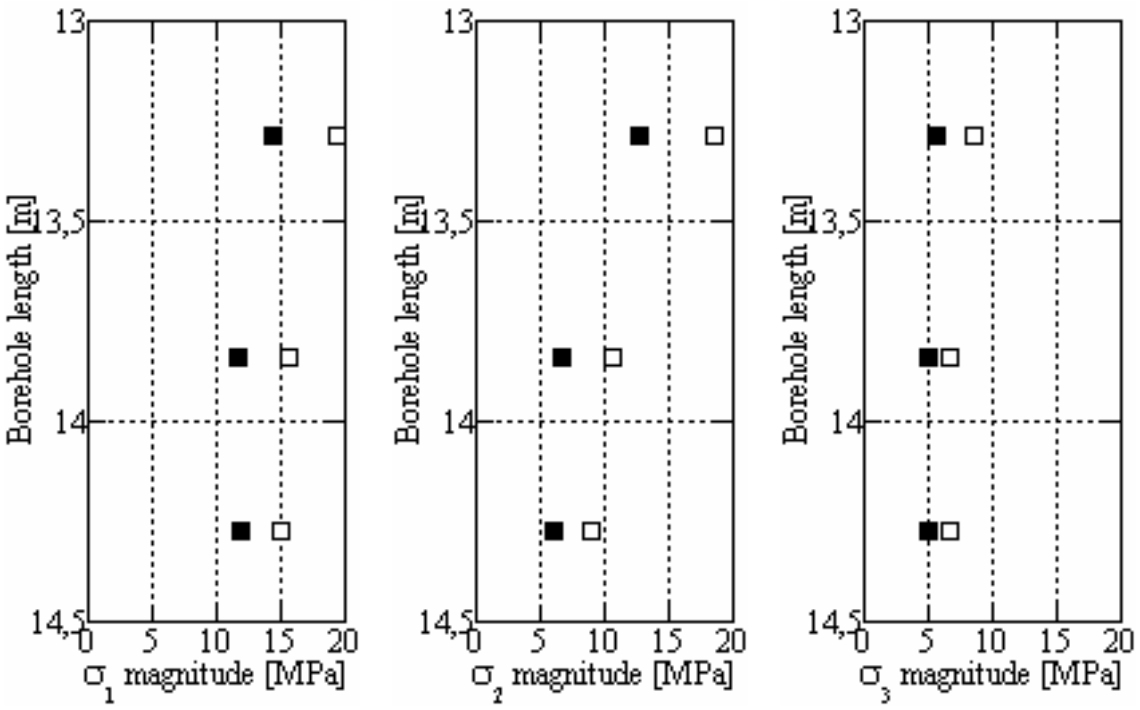

Figure 6-16. *Principal stress magnitudes in borehole KA1623A. The principal stresses are represented with filled and unfilled symbols for the re-analyzed and original data, respectively.*

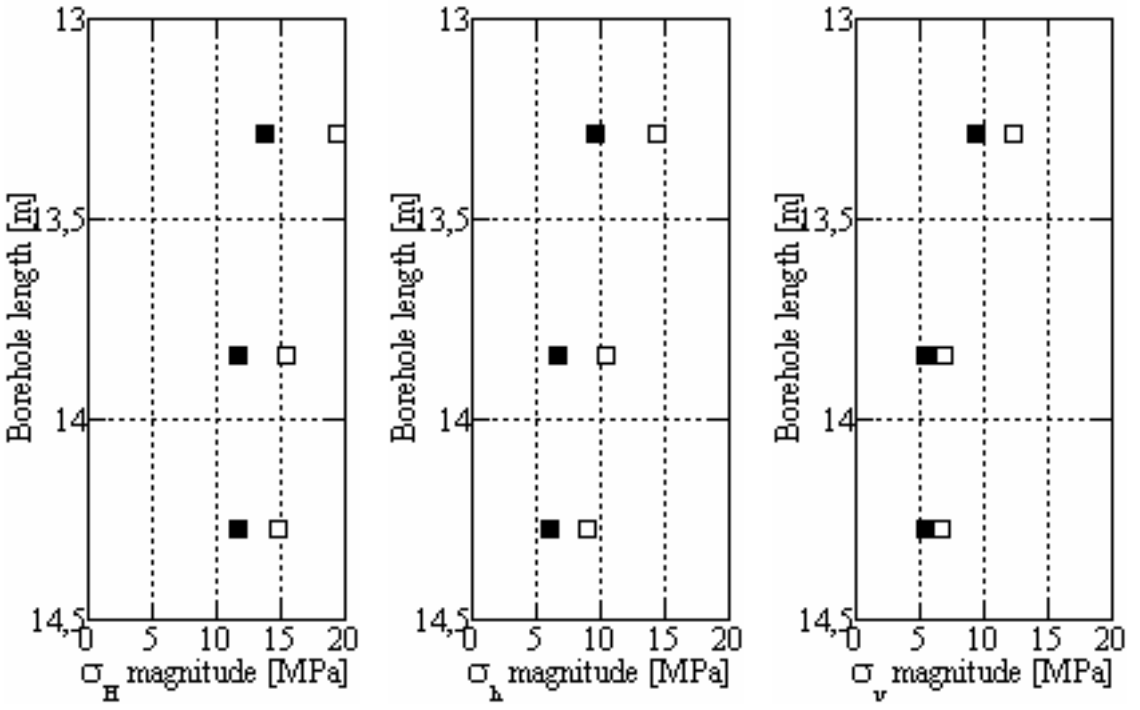

Figure 6-17. *Horizontal stress magnitudes in borehole KA1623A. The horizontal stresses are represented with filled and unfilled symbols for the re-analyzed and original data, respectively.*

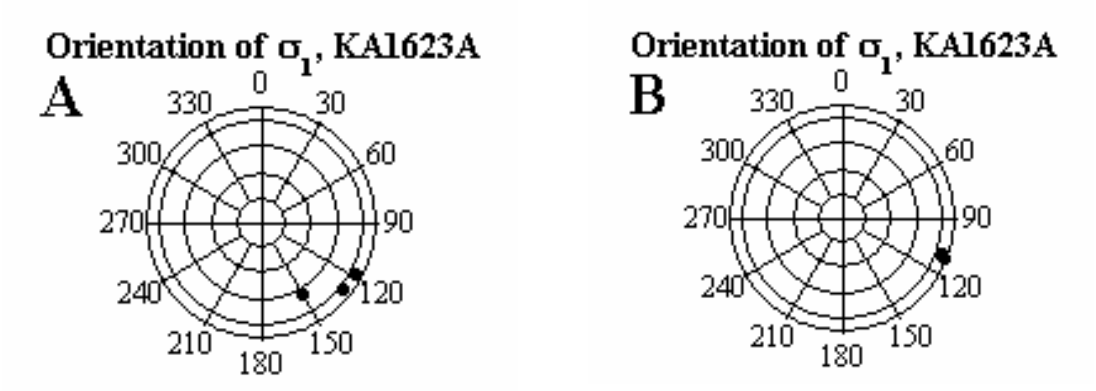

Figure 6-18. *Orientation of maximum principal stress in borehole KA1623A. A and B are the re-calculated stresses and the original data, respectively.*

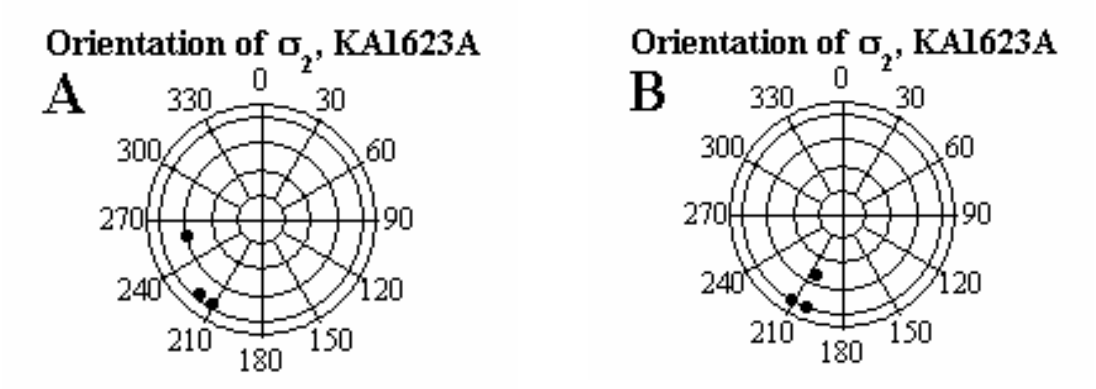

Figure 6-19. *Orientation of intermediate principal stress in borehole KA1623A. A and B are the re-calculated stresses and the original data, respectively.*

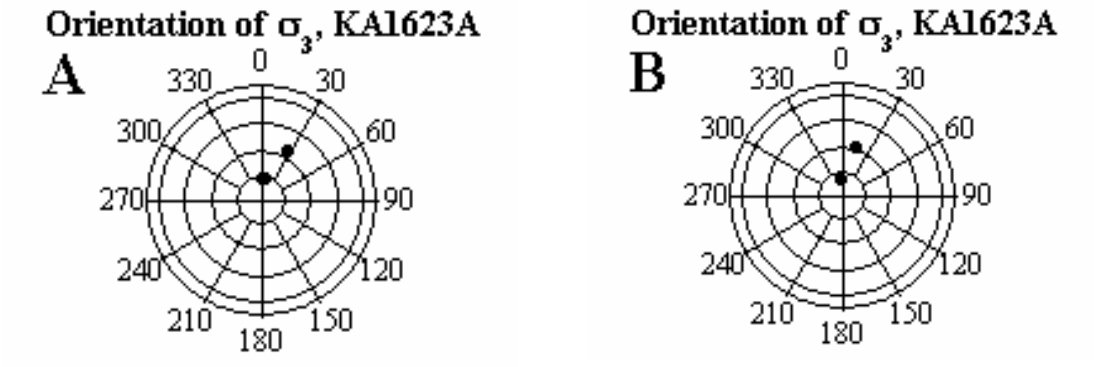

Figure 6-20. *Orientation of minimum principal stress in borehole KA1623A. A and B are the re-calculated stresses and the original data, respectively.*

6.6 Borehole KA1625A

The stress analysis and comparison with original data in borehole KA1625 includes 3 measurement points (Figs. 6-21 to 6-25). The re-calculated principal and horizontal stresses are in average about 2.0 MPa lower compared to the original data (Lee et al., 1994). The shallowest measurement point indicates somewhat larger stress magnitudes compared to the two deeper points. The principal stress orientations are very little changed after re-analysis (i.e. to the new elastic parameters and K-factors).

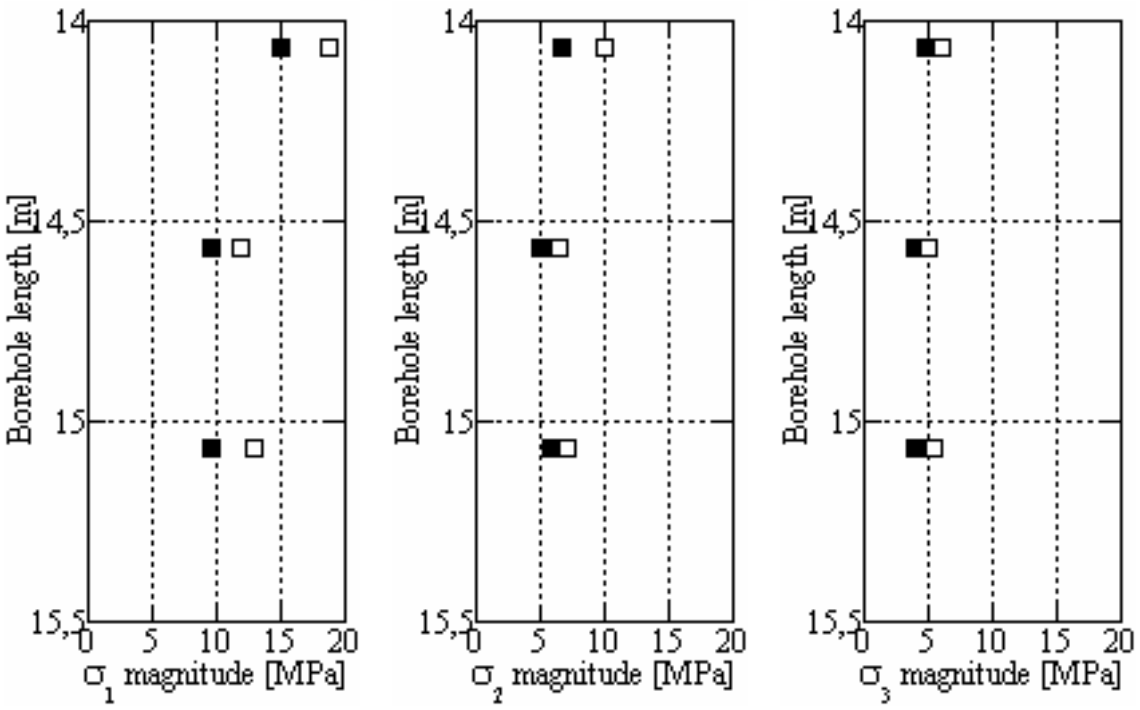

Figure 6-21. *Principal stress magnitudes in borehole KA1625A. The principal stresses are represented with filled and unfilled symbols for the re-analyzed and original data, respectively.*

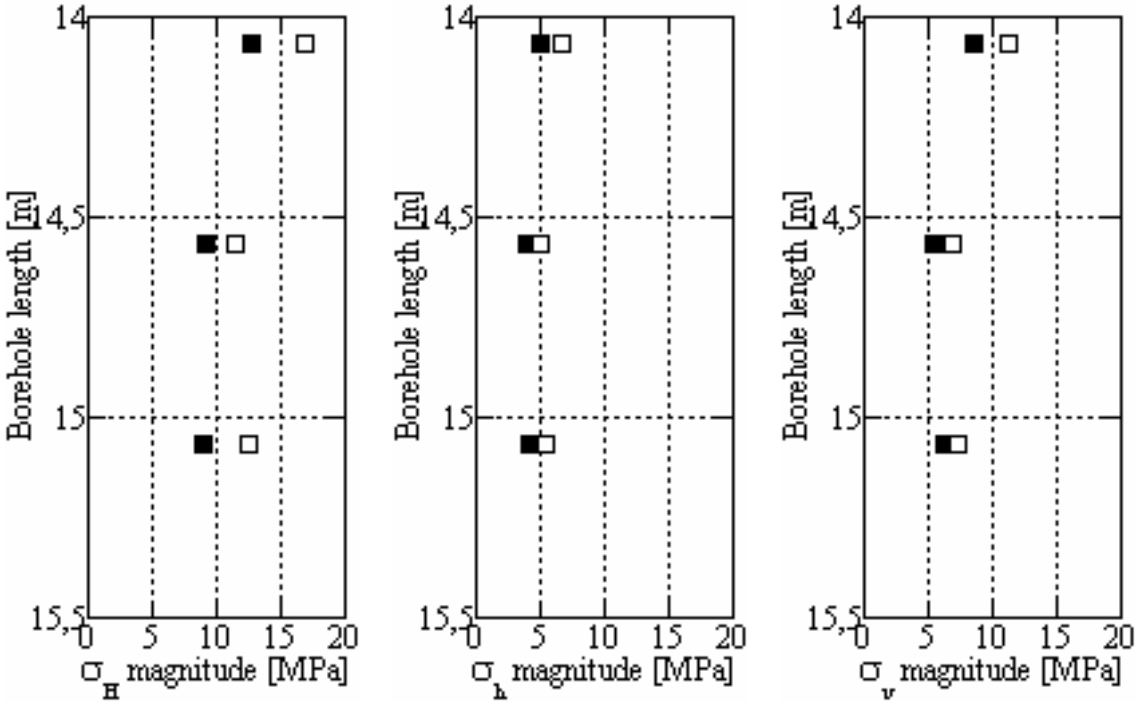

Figure 6-22. *Horizontal stress magnitudes in borehole KA1625A. The horizontal stresses are represented with filled and unfilled symbols for the re-analyzed and original data, respectively.*

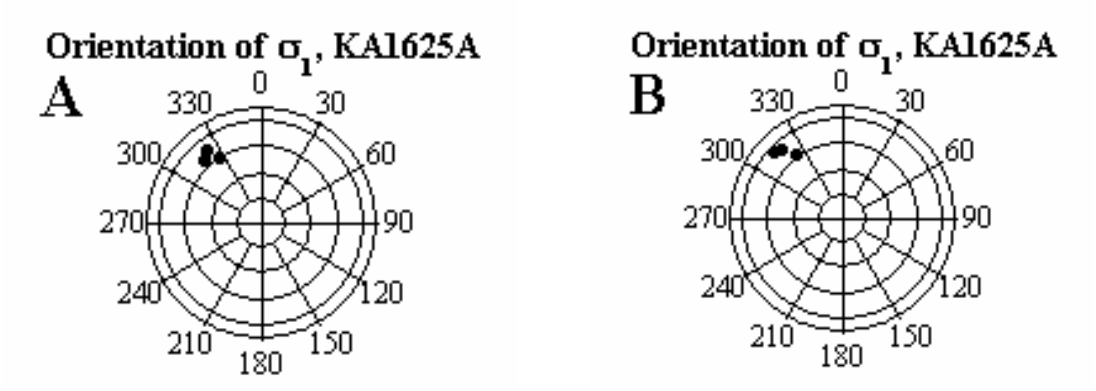

Figure 6-23. *Orientation of maximum principal stress in borehole KA1625A. A and B are the re-calculated stresses and the original data, respectively.*

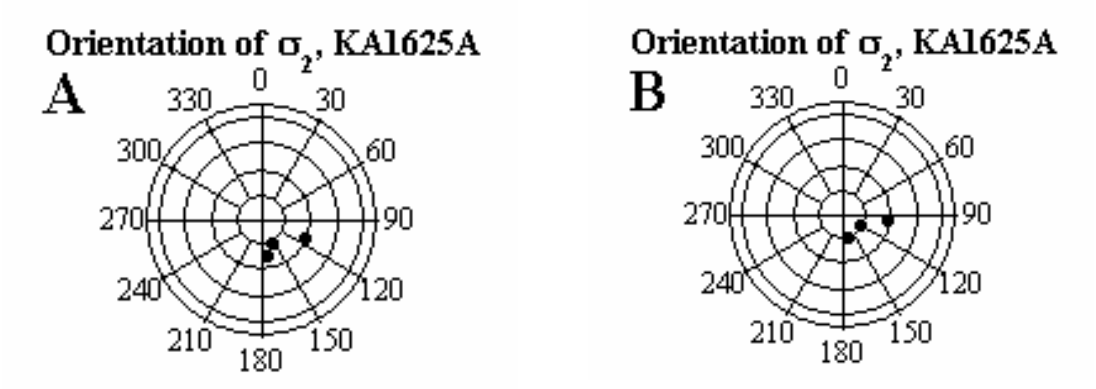

Figure 6-24. *Orientation of intermediate principal stress in borehole KA1625A. A and B are the re-calculated stresses and the original data, respectively.*

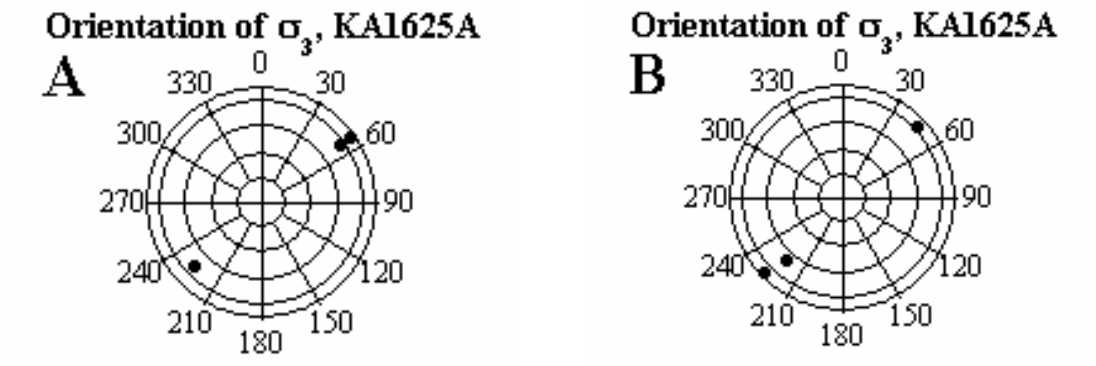

Figure 6-25. *Orientation of minimum principal stress in borehole KA1625A. A and B are the re-calculated stresses and the original data, respectively.*

6.7 Borehole KA1626A

The stress analysis and comparison with original data in borehole KA1626 includes 3 measurement points (Figs. 6-26 to 6-30). The re-calculated principal and horizontal stresses are in average about 2.0 MPa lower compared to the original data (Lee et al., 1994). The stress magnitudes are rather scattered versus borehole length. The principal stress orientations are little affected by the re-analysis (i.e. to the new elastic parameters and K-factors).

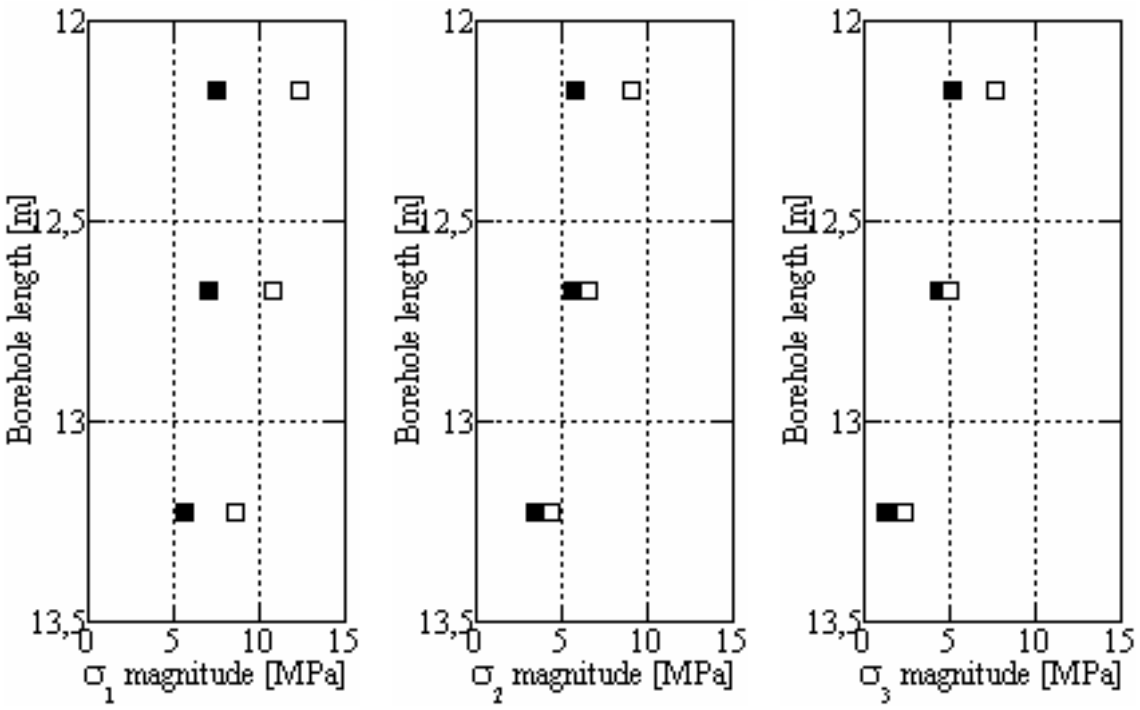

Figure 6-26 *Principal stress magnitudes in borehole KA1626A. The principal stresses are represented with filled and unfilled symbols for the re-analyzed and original data, respectively.*

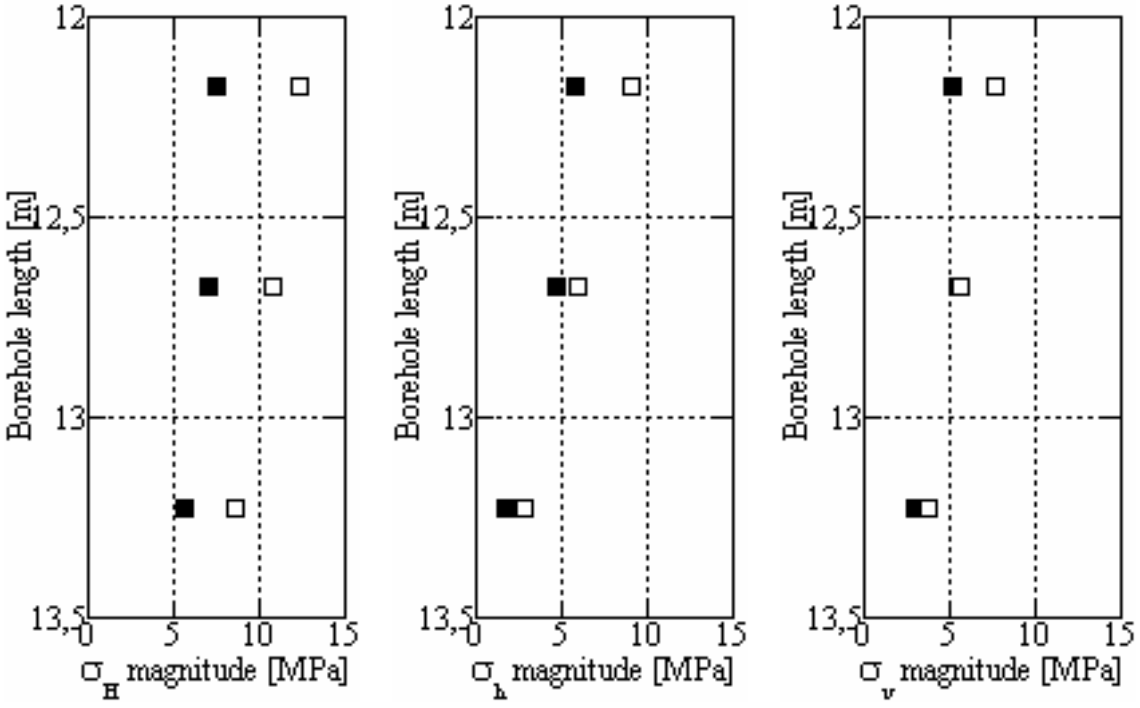

Figure 6-27. *Horizontal stress magnitudes in borehole KA1626A. The horizontal stresses are represented with filled and unfilled symbols for the re-analyzed and original data, respectively.*

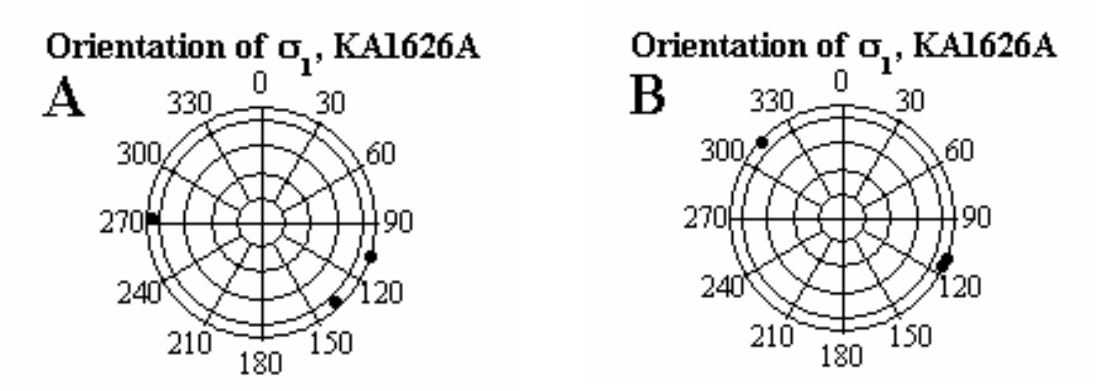

Figure 6-28. *Orientation of maximum principal stress in borehole KA1626A. A and B are the re-calculated stresses and the original data, respectively.*

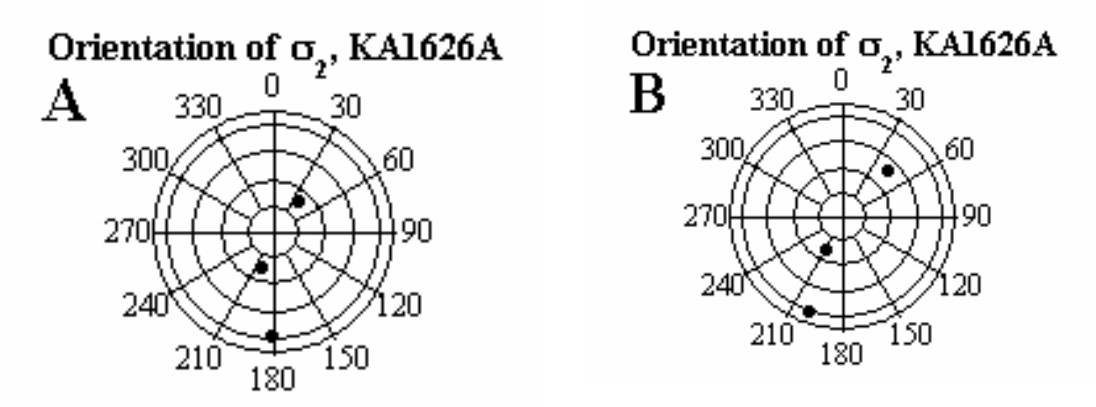

Figure 6-29. *Orientation of intermediate principal stress in borehole KA1626A. A and B are the re-calculated stresses and the original data, respectively.*

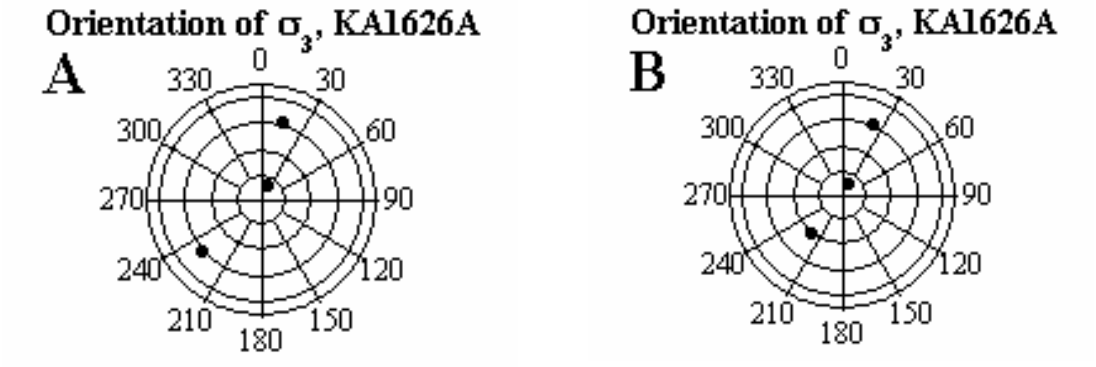

Figure 6-30. *Orientation of minimum principal stress in borehole KA1626A. A and B are the re-calculated stresses and the original data, respectively.*

6.8 Borehole KA1899A

The stress analysis and comparison with original data in borehole KA1899 includes 5 measurement points (Figs. 6-31 to 6-35). The re-calculated principal and horizontal stresses are in average about 3.5 MPa lower compared to the original data (Lee et al., 1994). The principal and horizontal stress magnitudes are fairly linear versus borehole length and the principal stress orientations are little affected by the re-analysis.

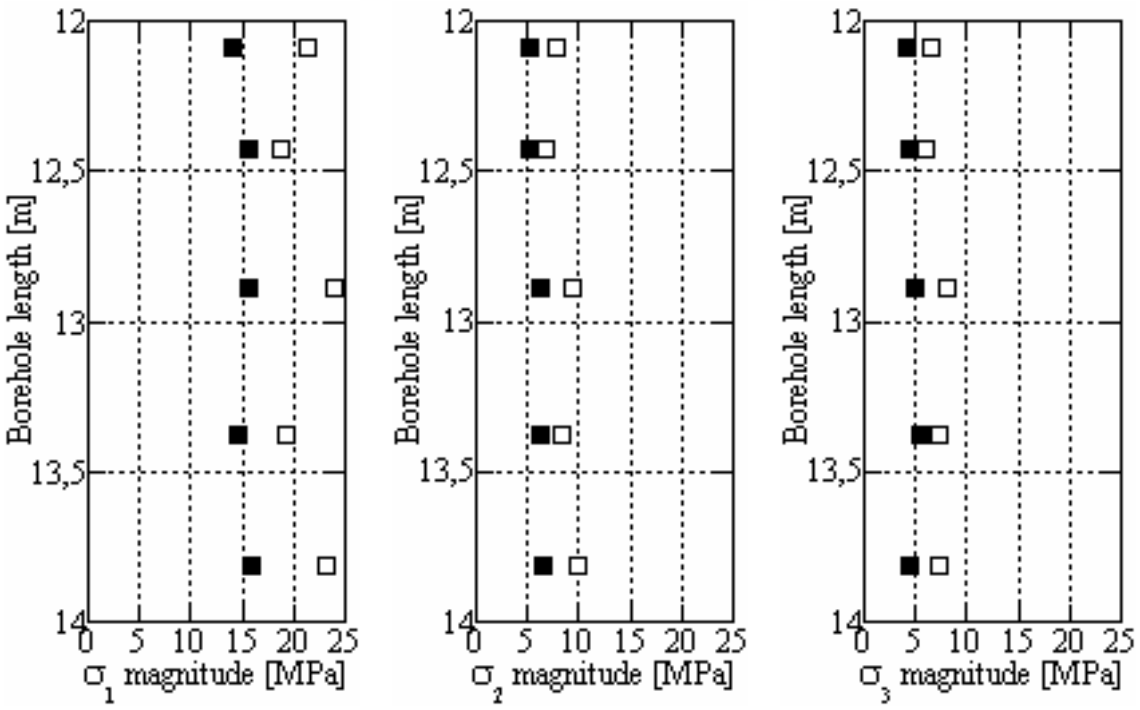

Figure 6-31. *Principal stress magnitudes in borehole KA1899A. The principal stresses are represented with filled and unfilled symbols for the re-analyzed and original data, respectively.*

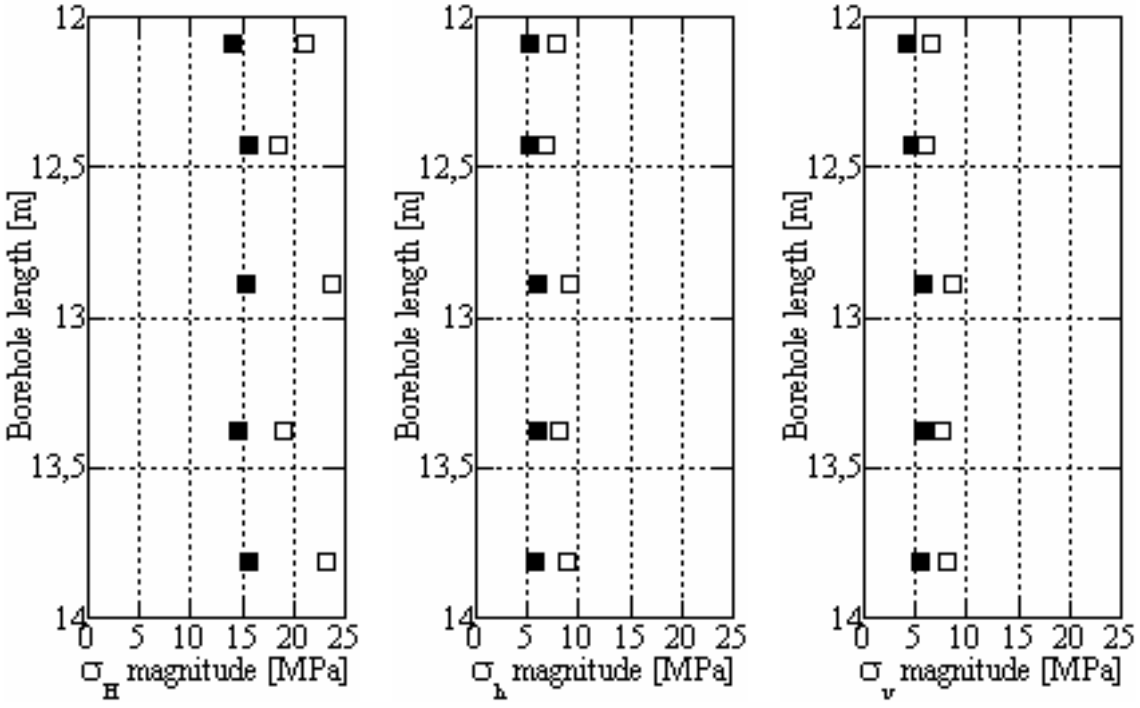

Figure 6-32. *Horizontal stress magnitudes in borehole KA1899A. The horizontal stresses are represented with filled and unfilled symbols for the re-analyzed and original data, respectively.*

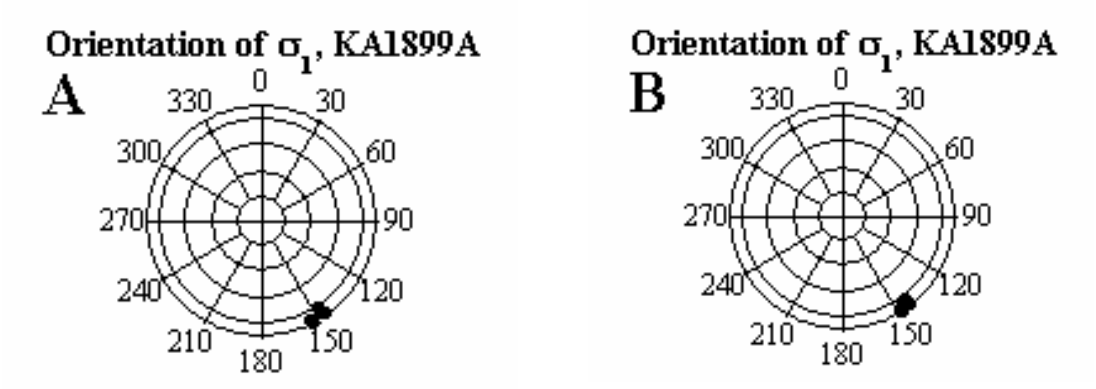

Figure 6-33. *Orientation of maximum principal stress in borehole KA1899A. A and B are the re-calculated stresses and the original data, respectively.*

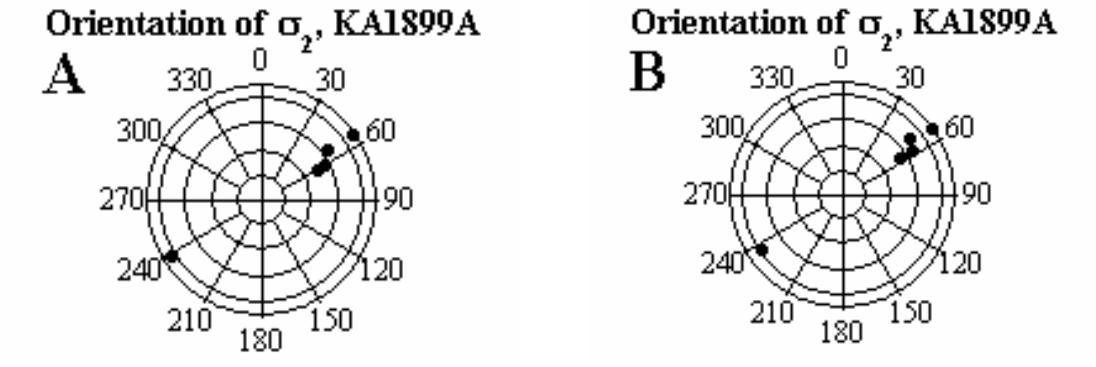

Figure 6-34. *Orientation of intermediate principal stress in borehole KA1899A. A and B are the re-calculated stresses and the original data, respectively.*

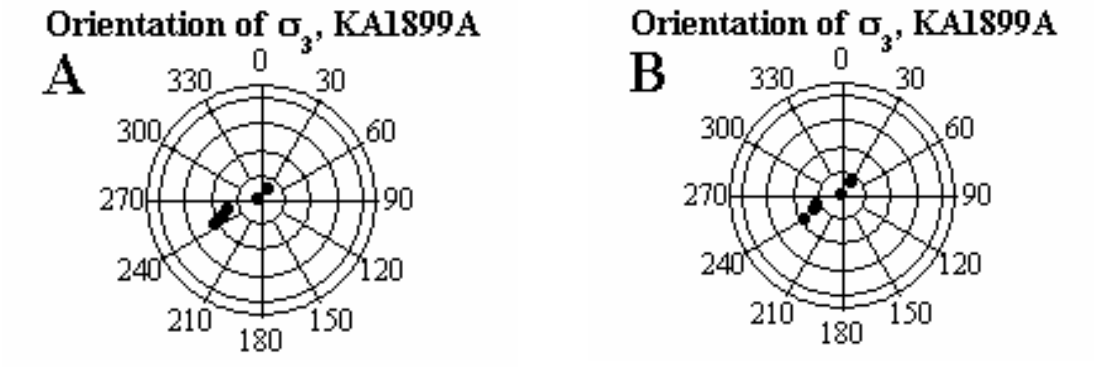

Figure 6-35. *Orientation of minimum principal stress in borehole KA1899A. A and B are the re-calculated stresses and the original data, respectively.*

6.9 Borehole KA2198A

The stress analysis and comparison with original data in borehole KA2198 includes 4 measurement points (Figs. 6-36 to 6-40). The re-calculated principal and horizontal stresses are in average about 0.5 MPa lower compared to the original data (Lee et al., 1994). The principal and horizontal stress magnitudes vary fairly linear versus borehole length. The solutions using re-analyzed data are slightly less scattered compared to the original data.

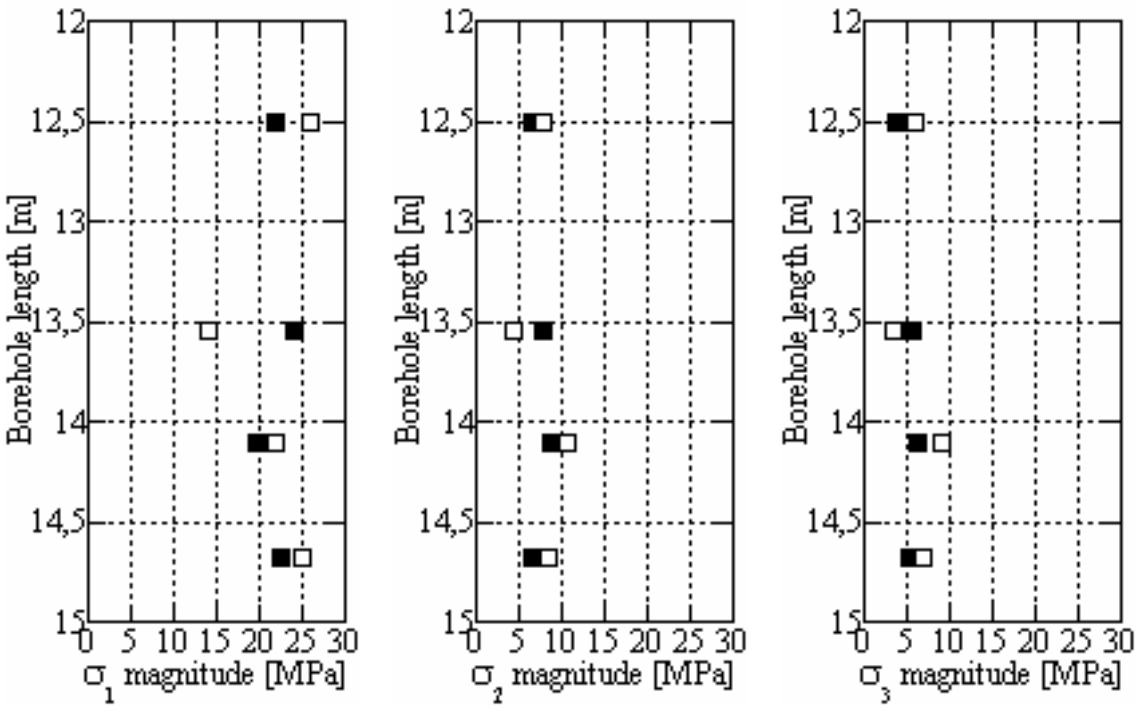

Figure 6-36. *Principal stress magnitudes in borehole KA2198A. The principal stresses are represented with filled and unfilled symbols for the re-analyzed and original data, respectively.*

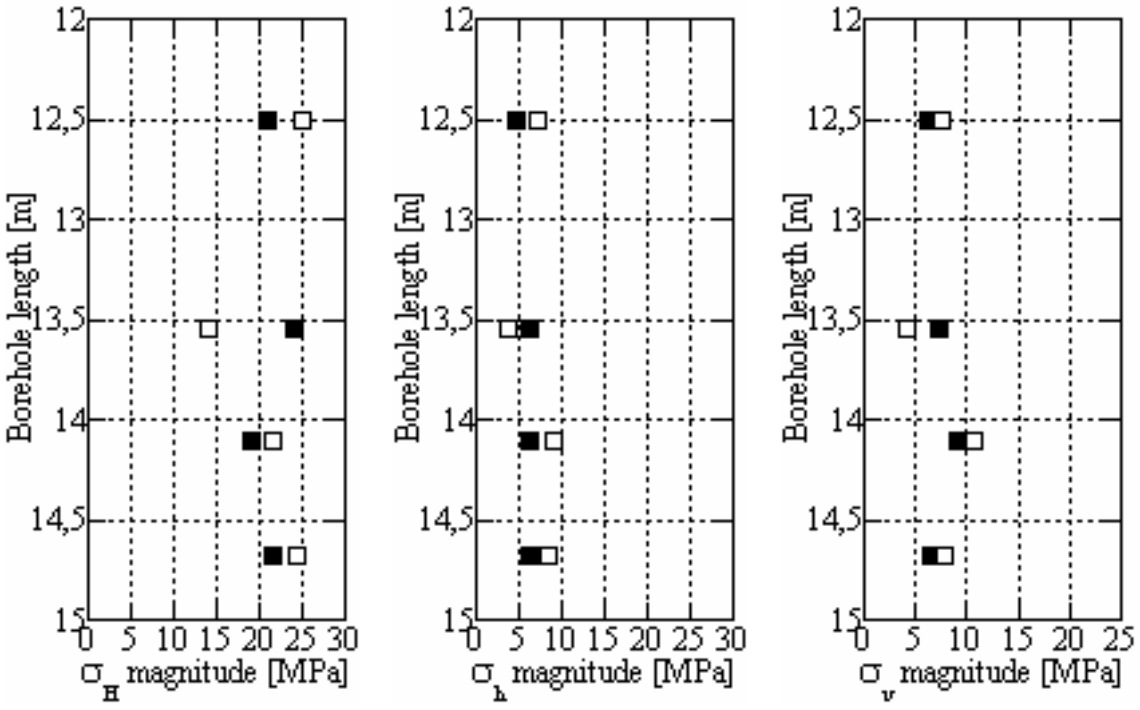

Figure 6-37. *Horizontal stress magnitudes in borehole KA2198A. The horizontal stresses are represented with filled and unfilled symbols for the re-analyzed and original data, respectively.*

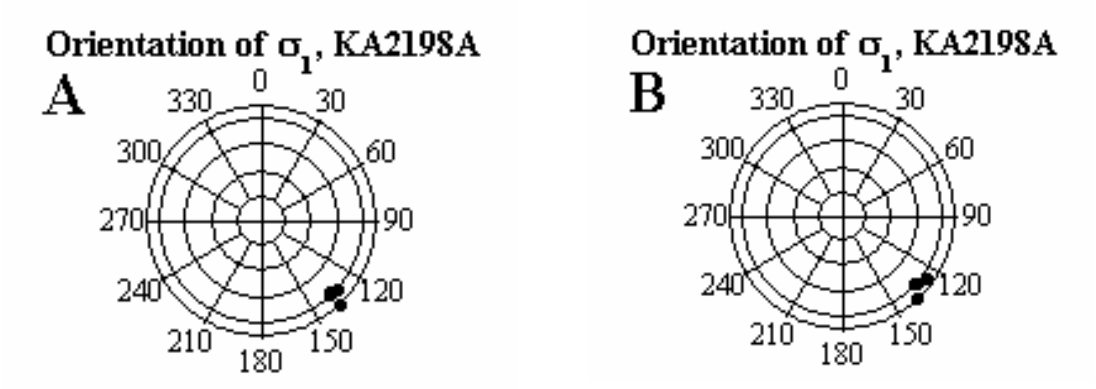

Figure 6-38. *Orientation of maximum principal stress in borehole KA2198A. A and B are the re-calculated stresses and the original data, respectively.*

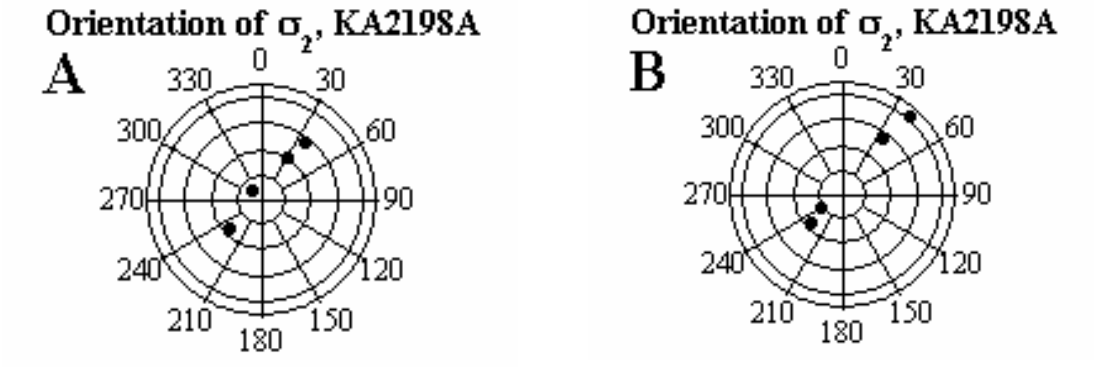

Figure 6-39. *Orientation of intermediate principal stress in borehole KA2198A. A and B are the re-calculated stresses and the original data, respectively.*

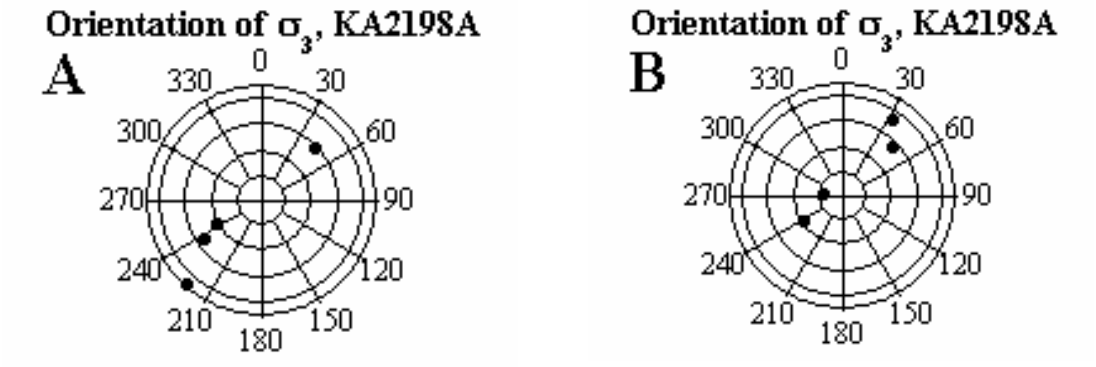

Figure 6-40. *Orientation of minimum principal stress in borehole KA2198A. A and B are the re-calculated stresses and the original data, respectively.*

6.10 Borehole KA2510A

The stress analysis and comparison with original data in borehole KA2510 includes 6 measurement points (Figs. 6-41 to 6-45). The re-calculated principal and horizontal stresses are in average about 3.5 MPa lower compared to the original data (Lee et al., 1994). The principal and horizontal stress magnitudes are decreasing slightly towards borehole length. The solutions using re-analyzed data are less scattered compared to the original data.

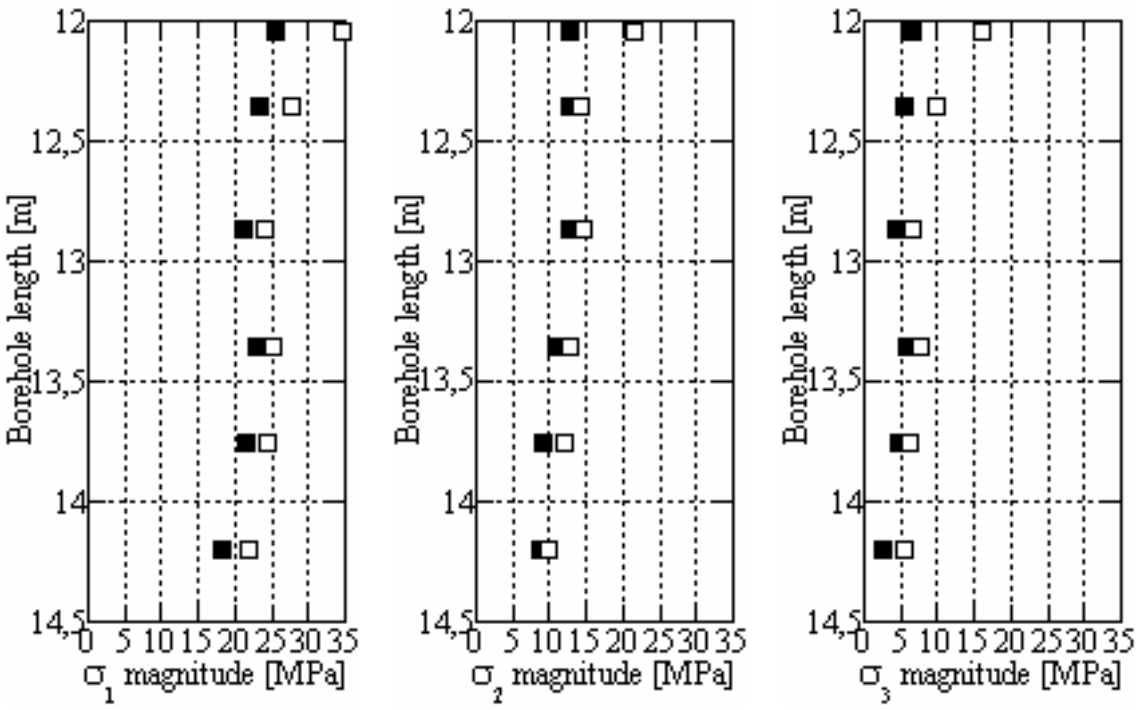

Figure 6-41. *Principal stress magnitudes in borehole KA2510A. The principal stresses are represented with filled and unfilled symbols for the re-analyzed and original data, respectively.*

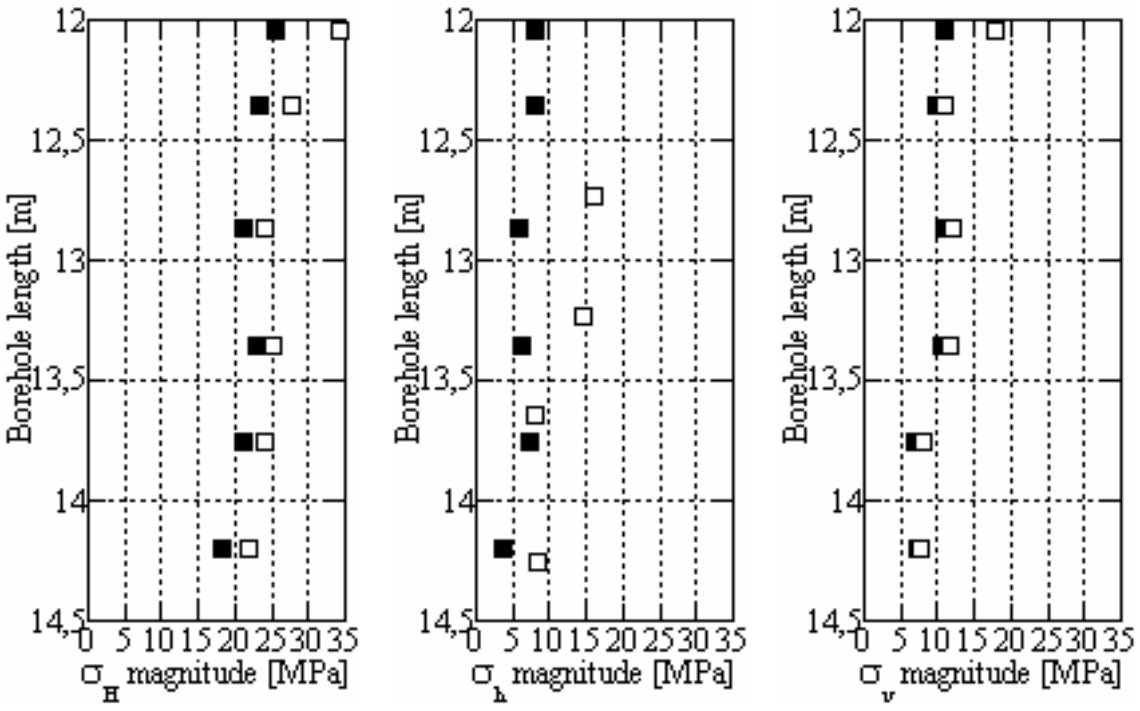

Figure 6-42. *Horizontal stress magnitudes in borehole KA2510A. The horizontal stresses are represented with filled and unfilled symbols for the re-analyzed and original data, respectively.*

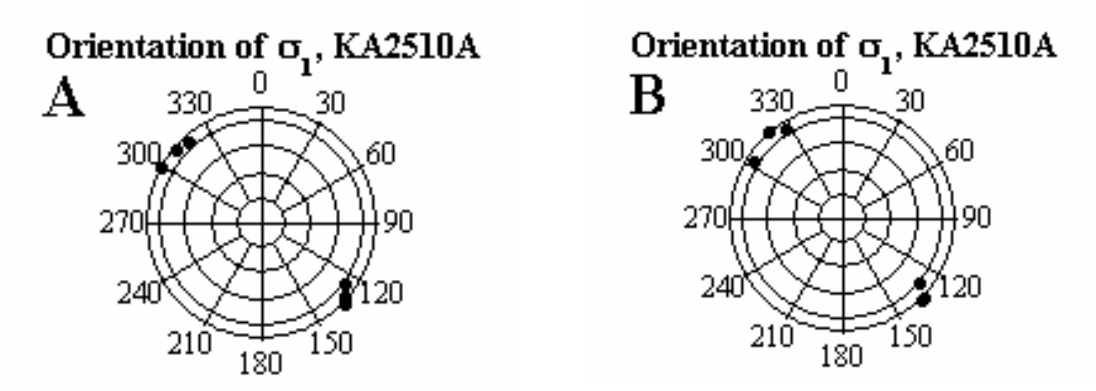

Figure 6-43. *Orientation of maximum principal stress in borehole KA2510A. A and B are the re-calculated stresses and the original data, respectively.*

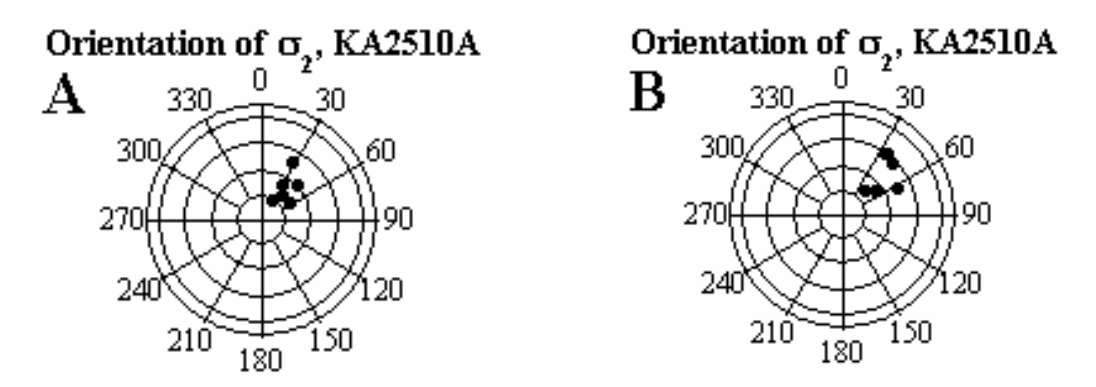

Figure 6-44. *Orientation of intermediate principal stress in borehole KA2510A. A and B are the re-calculated stresses and the original data, respectively.*

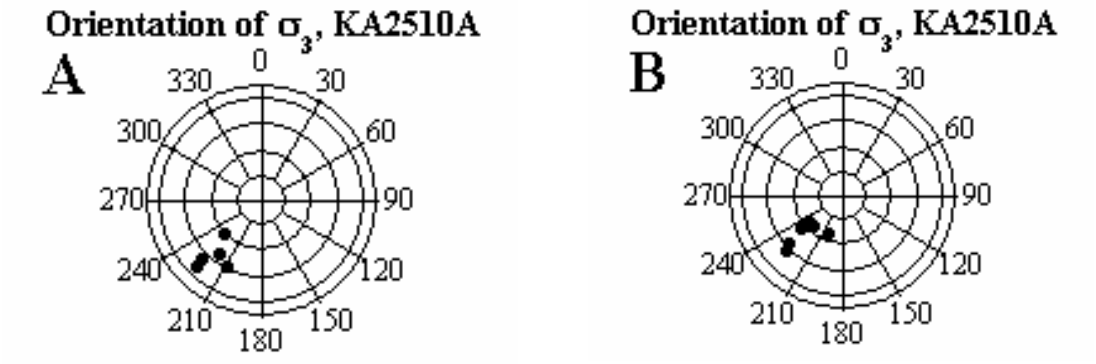

Figure 6-45. *Orientation of minimum principal stress in borehole KA2510A. A and B are the re-calculated stresses and the original data, respectively.*

6.11 Borehole KA2870A

The stress analysis and comparison with original data in borehole KA2870 includes 5 measurement points (Figs. 6-46 to 6-50). The re-calculated principal and horizontal stresses are in average about 4.0 MPa lower compared to the original data (Litterbach et al., 1994). The principal and horizontal stress magnitudes vary fairly linear versus borehole length and the principal stress orientations are little affected by the re-analysis.

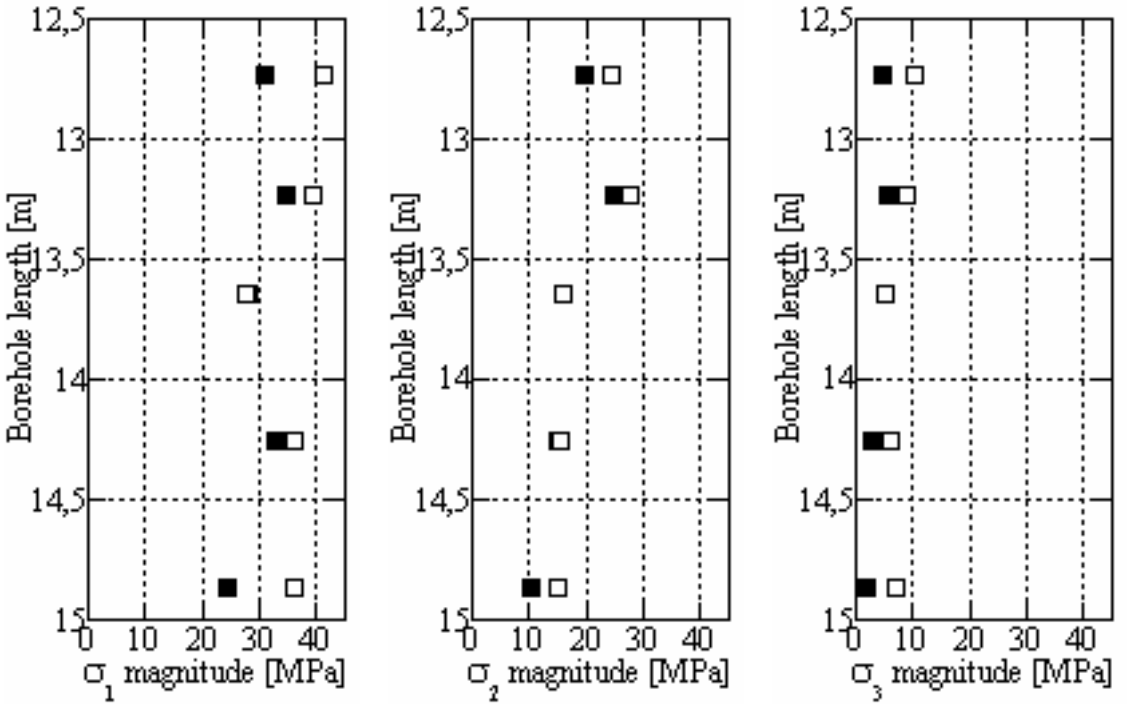

Figure 6-46. *Principal stress magnitudes in borehole KA2870A. The principal stresses are represented with filled and unfilled symbols for the re-analyzed and original data, respectively.*

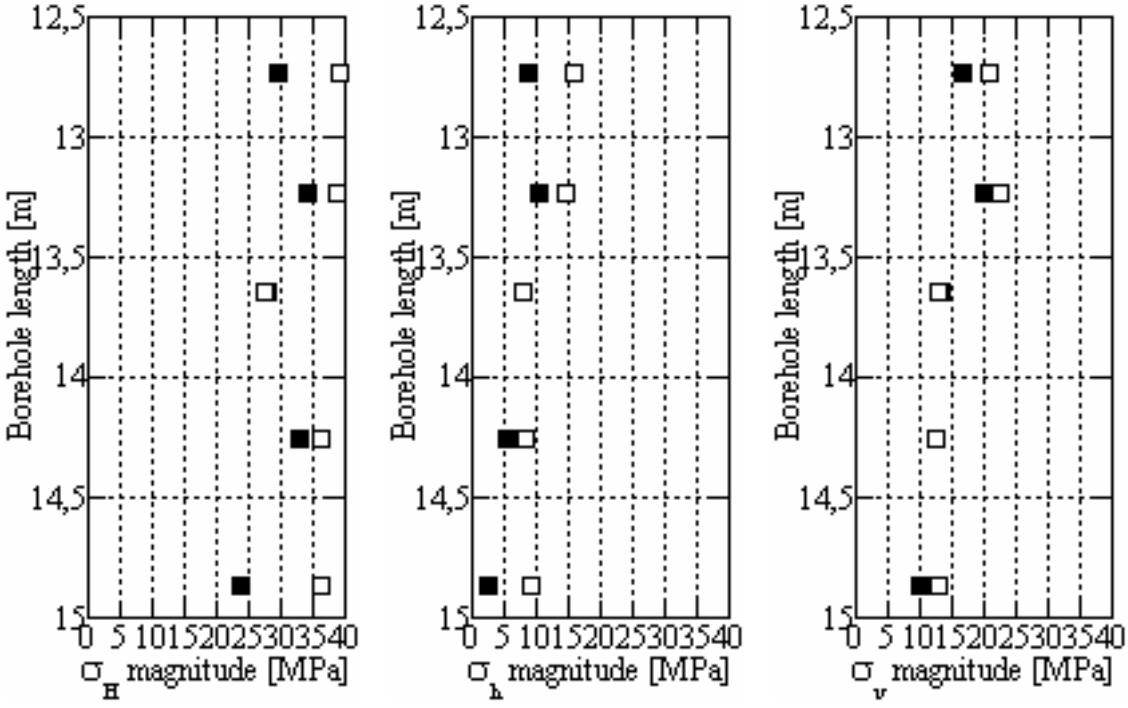

Figure 6-47. *Horizontal stress magnitudes in borehole KA2870A. The horizontal stresses are represented with filled and unfilled symbols for the re-analyzed and original data, respectively.*

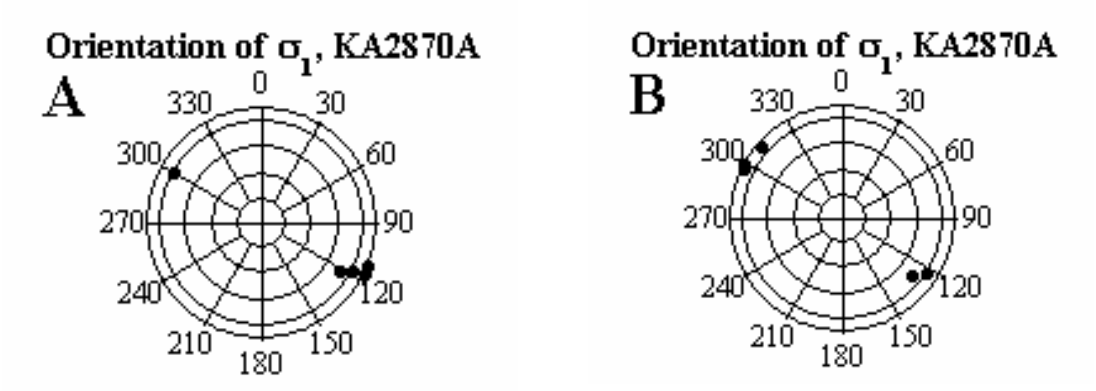

Figure 6-48. *Orientation of maximum principal stress in borehole KA2870A. A and B are the re-calculated stresses and the original data, respectively.*

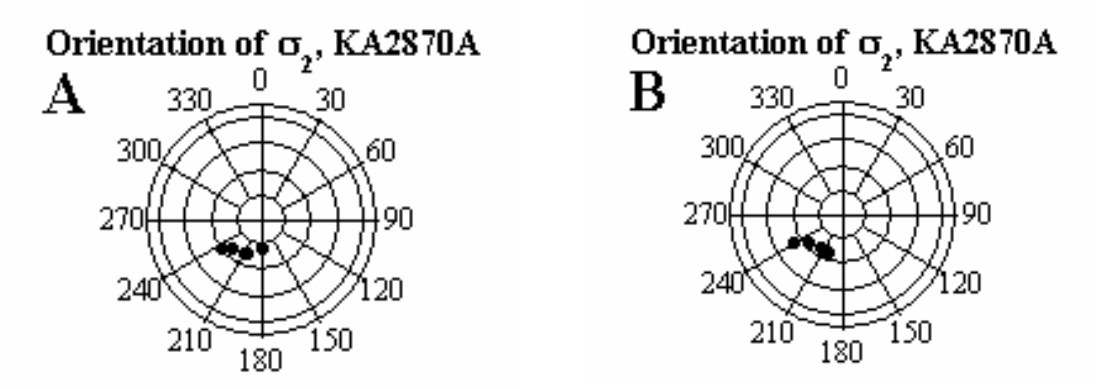

Figure 6-49. *Orientation of intermediate principal stress in borehole KA2870A. A and B are the re-calculated stresses and the original data, respectively.*

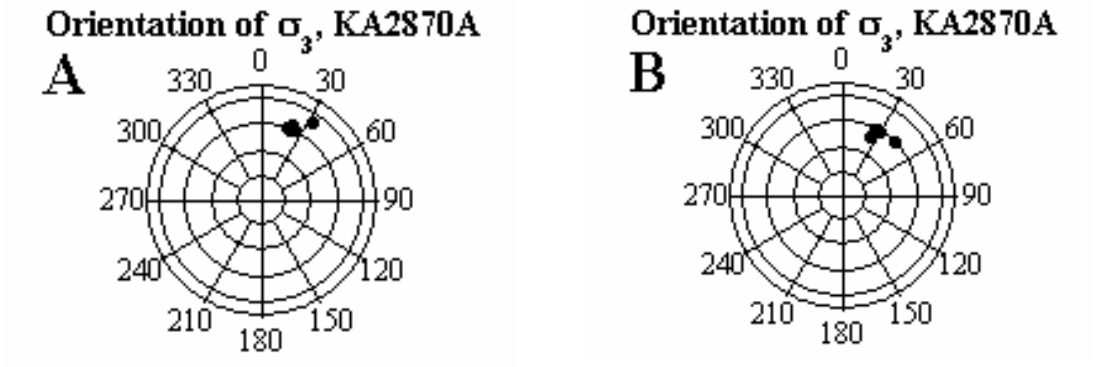

Figure 6-50. *Orientation of minimum principal stress in borehole KA2870A. A and B are the re-calculated stresses and the original data, respectively.*

6.12 Borehole KA3068A

The stress analysis and comparison with original data in borehole KA3068A includes 4 measurement points (Figs. 6-51 to 6-55). The re-calculated principal and horizontal stresses are in average about 4.5 MPa lower compared to the original data (Litterbach et al., 1994). The principal and horizontal stress magnitudes vary non-linearly versus borehole length.

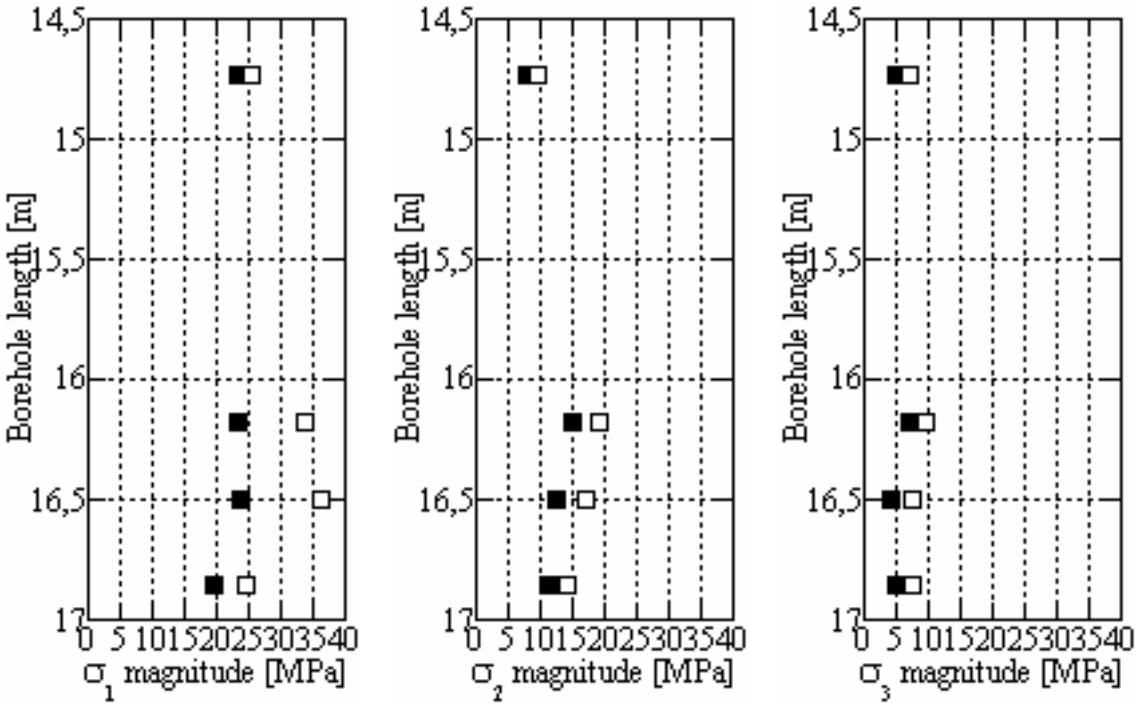

Figure 6-51. *Principal stress magnitudes in borehole KA3068A. The principal stresses are represented with filled and unfilled symbols for the re-analyzed and original data, respectively.*

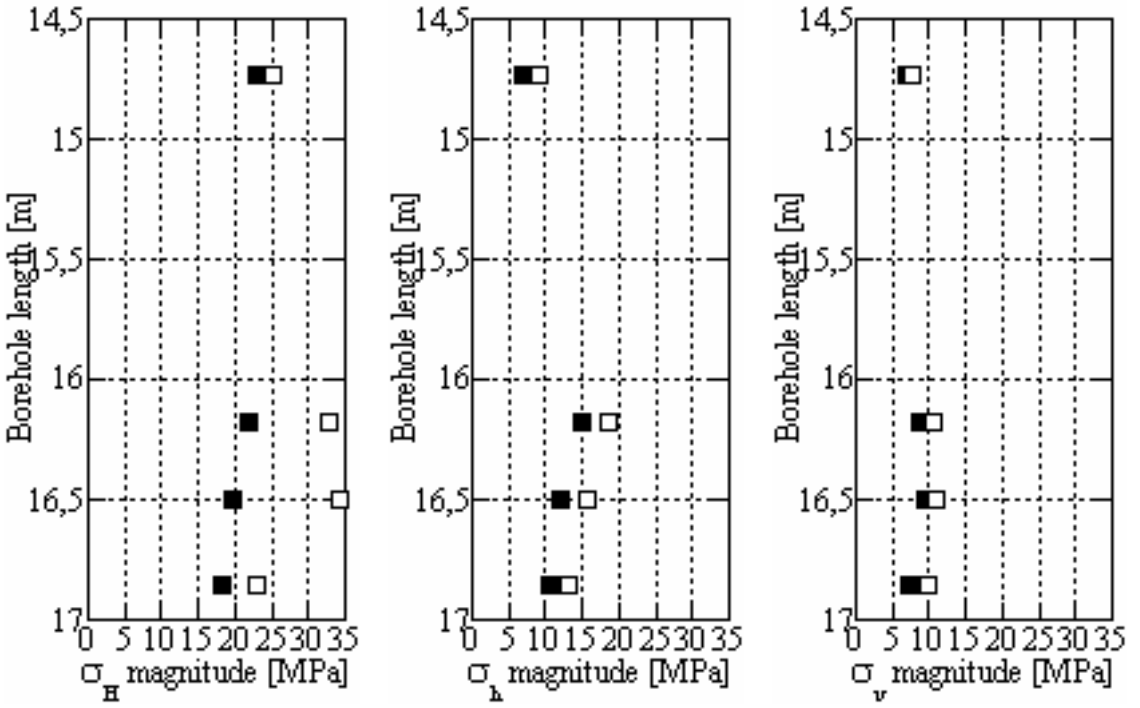

Figure 6-52. *Horizontal stress magnitudes in borehole KA3068A. The horizontal stresses are represented with filled and unfilled symbols for the re-analyzed and original data, respectively.*

The σ_1-orientation rotates 54° from NW to ESE-WSW versus borehole length together and with a 19° increase of the dip direction (i.e. towards a more inclined principal stress component). The σ_2-orientation rotates 53° from NE to SSE-NNW versus borehole length, whereas the dip of σ_2 and strike/dip of σ_3 are more difficult to identify.

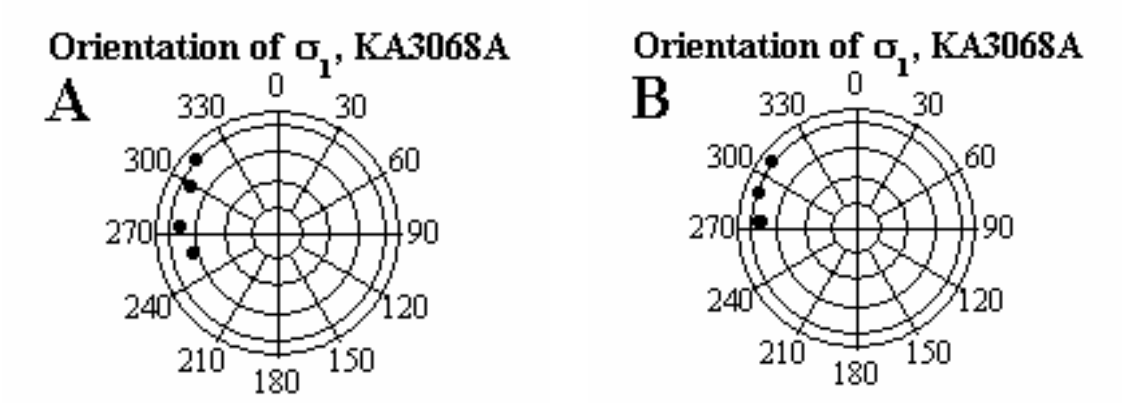

Figure 6-53. *Orientation of maximum principal stress in borehole KA3068A. A and B are the re-calculated stresses and the original data, respectively.*

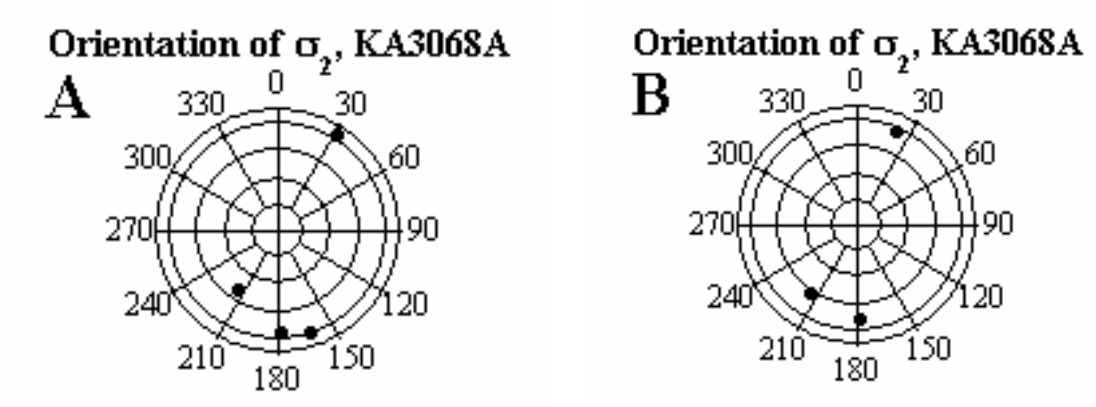

Figure 6-54. *Orientation of intermediate principal stress in borehole KA3068A. A and B are the re-calculated stresses and the original data, respectively.*

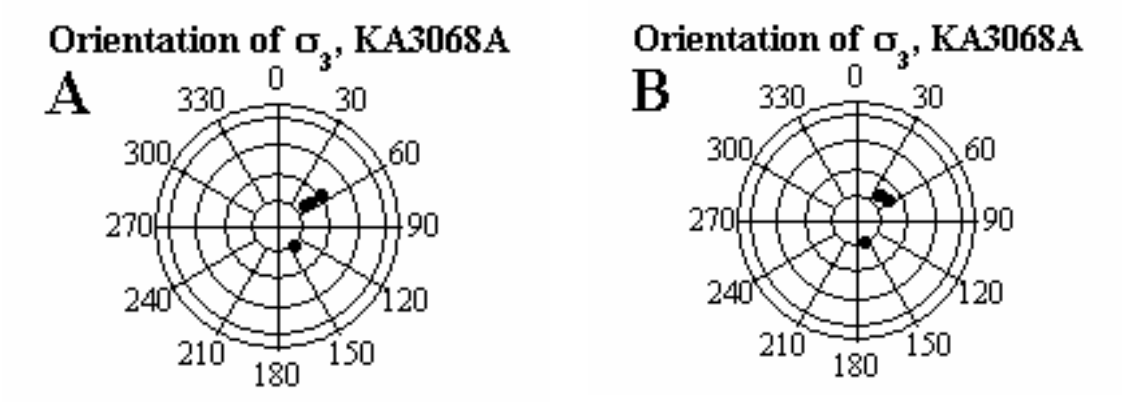

Figure 6-55. *Orientation of minimum principal stress in borehole KA3068A. A and B are the re-calculated stresses and the original data, respectively.*

6.13 Borehole KZ0059B

The stress analysis and comparison with original data in borehole KZ0059B includes 6 measurement points (Figs. 6-56 to 6-60). The re-calculated principal and horizontal stresses are in average about 6.0 MPa lower compared to the original data (Nilsson et al., 1997). The principal and horizontal stress magnitudes vary fairly linear versus borehole length. The solutions using re-analyzed data are slightly less scattered compared to the original data.

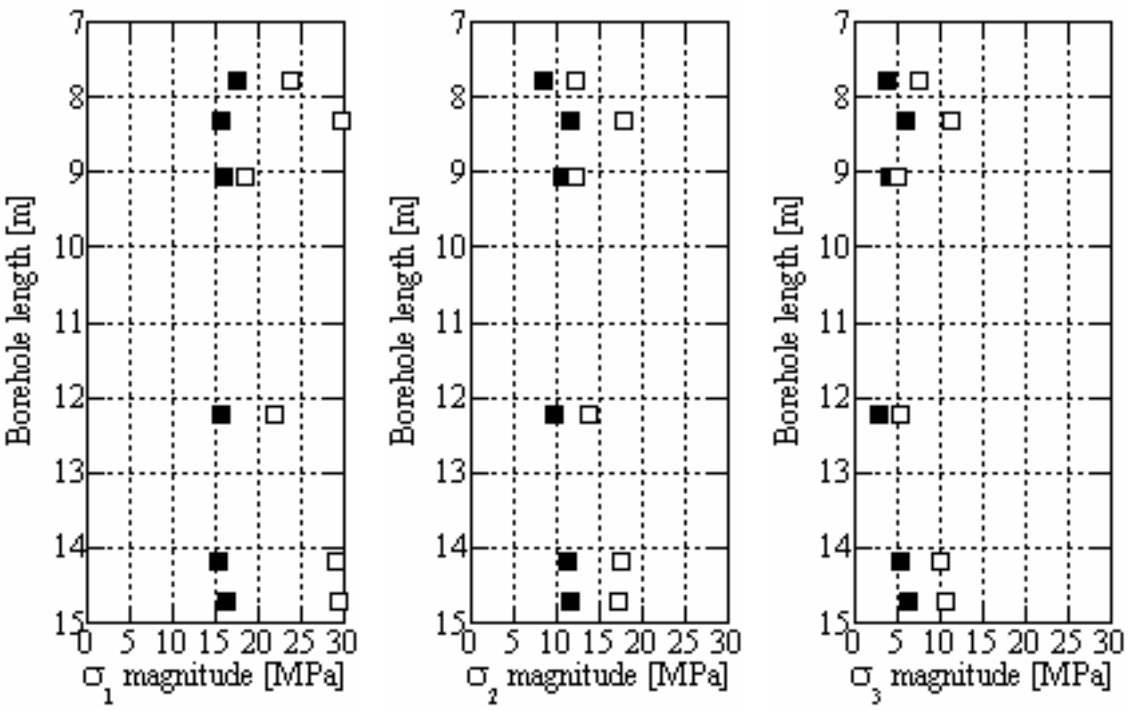

Figure 6-56. *Principal stress magnitudes in borehole KZ0059B. The principal stresses are represented with filled and unfilled symbols for the re-analyzed and original data, respectively.*

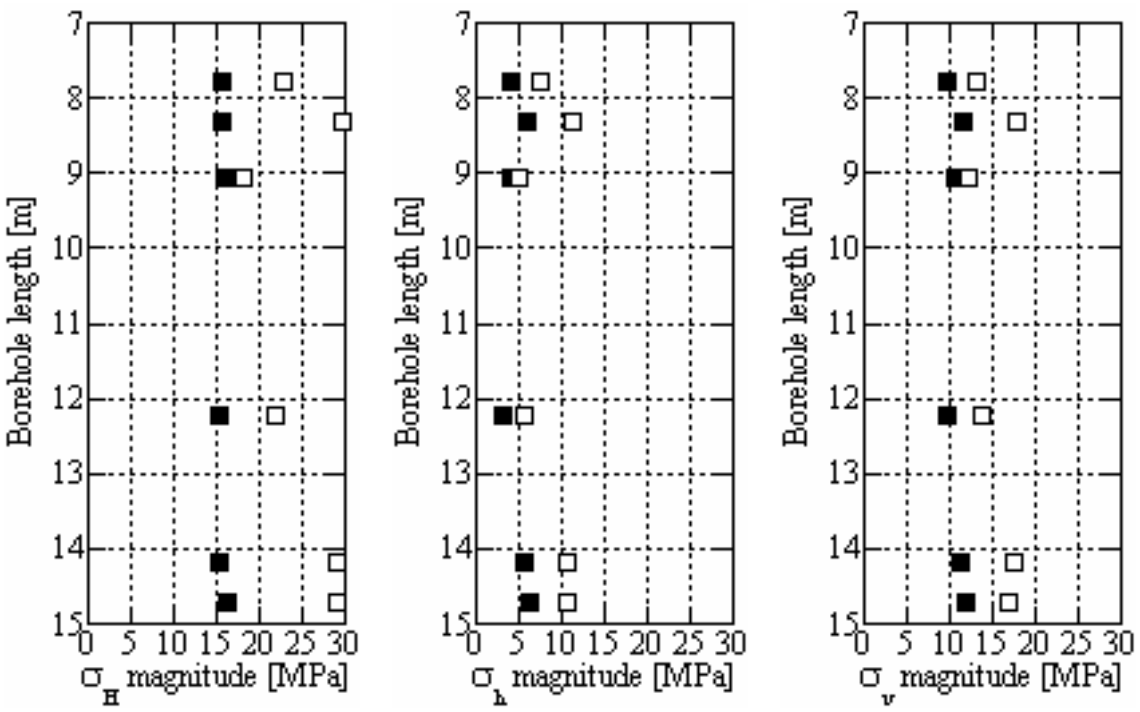

Figure 6-57. *Horizontal stress magnitudes in borehole KZ0059B. The horizontal stresses are represented with filled and unfilled symbols for the re-analyzed and original data, respectively.*

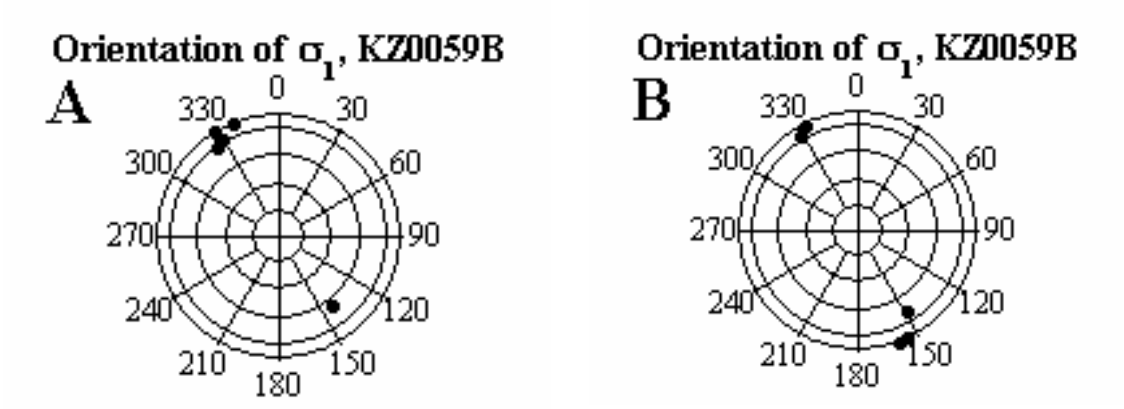

Figure 6-58. *Orientation of maximum principal stress in borehole KZ0059B. A and B are the re-calculated stresses and the original data, respectively.*

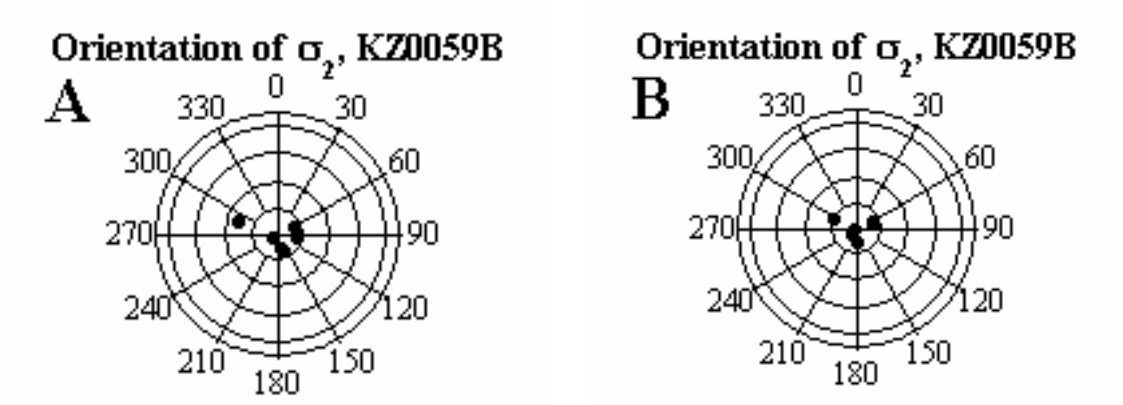

Figure 6-59. *Orientation of intermediate principal stress in borehole KZ0059B. A and B are the re-calculated stresses and the original data, respectively.*

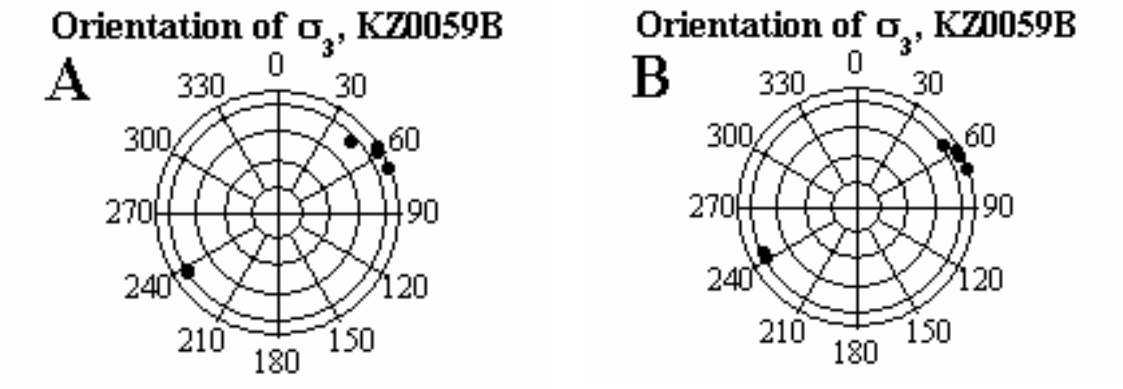

Figure 6-60. *Orientation of minimum principal stress in borehole KZ0059B. A and B are the re-calculated stresses and the original data, respectively.*

6.14 Results from stress calculation using the re-analyzed strain data

6.14.1 Summary of stress calculation results

The stress calculation using re-analyzed strain data indicates lower and less scattered principal and horizontal stress magnitudes (summarized in Figs. 6-61 to 6-63). In general, the re-interpretation has in average lowered the stress magnitudes by about 3 MPa, which may be explained by both boundary yield corrections and the new elastic parameters determined using unloading secant modulus. The stress orientations generally are unaffected by the applied re-analysis (summarized in Fig. 6-64) but the scatter have been slightly reduced compared to the original result. The horizontal and vertical stress magnitudes at the individual boreholes and site scales (1050 and 1620 m levels) for the CSIRO HI data at the Äspö HRL are displayed in Figs. 6-65 to 6-67 together with results using the Borre Probe (Ask et al., 2002; Ask, 2003) and hydraulic fracturing stress data (Bjarnasson et al., 1989; Klee and Rummel, 2002).

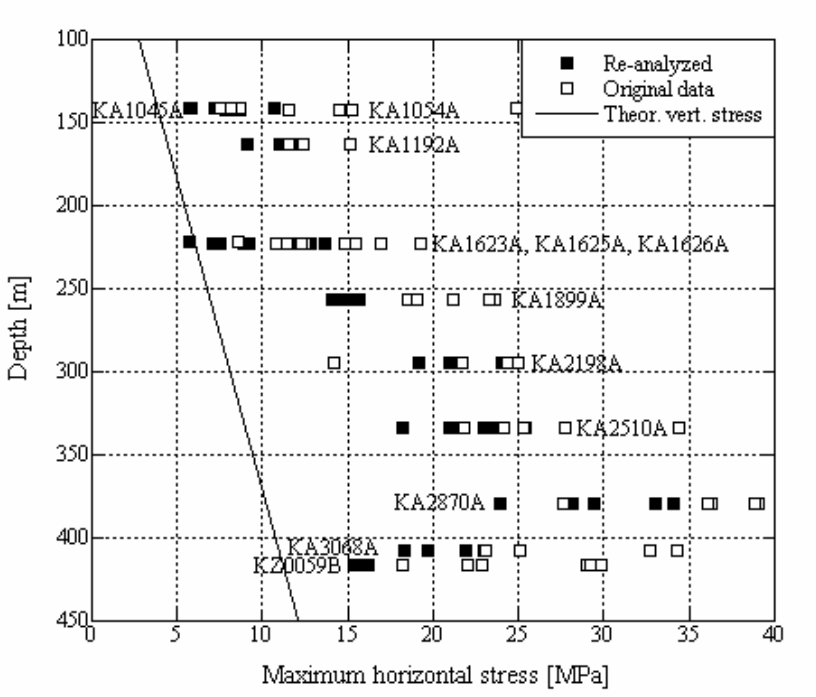

Figure 6-61. *Maximum horizontal stress using all CSIRO HI data and single measurement scale. Filled and unfilled symbols represent the re-analyzed and original data, respectively, and the solid line the theoretical vertical stress from weight of the overburden.*

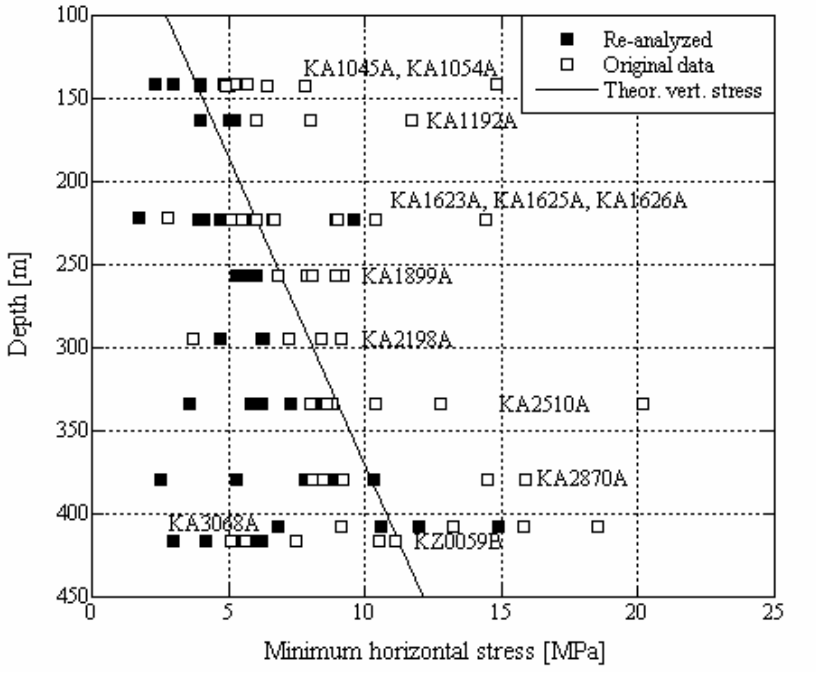

Figure 6-62. *Minimum horizontal stress using all CSIRO HI data and single measurement scale. Filled and unfilled symbols represent the re-analyzed and original data, respectively, and the solid line the theoretical vertical stress from weight of the overburden.*

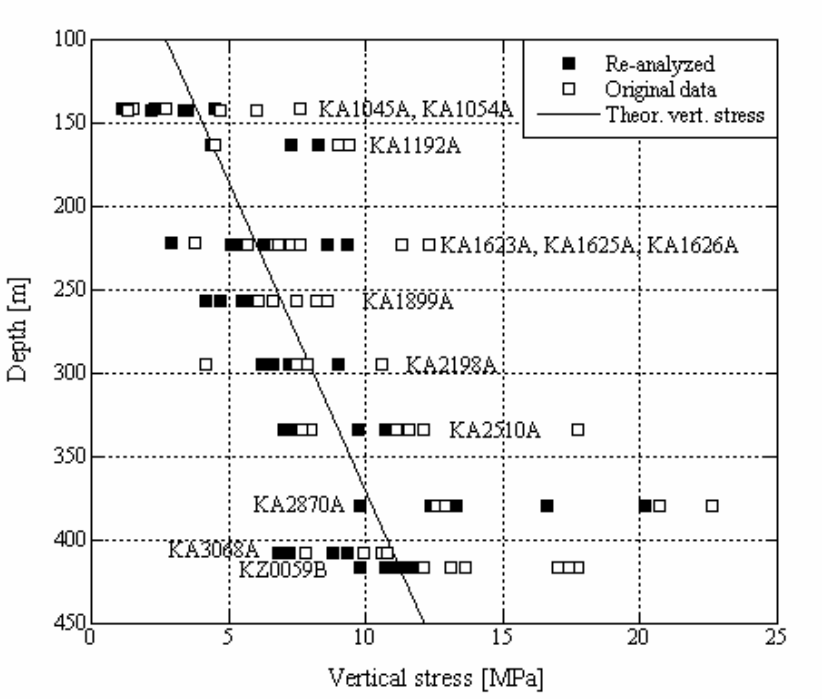

Figure 6-63. *Vertical stress using all CSIRO HI data and single measurement scale. Filled and unfilled symbols represent the re-analyzed and original data, respectively, and the solid line the theoretical vertical stress from weight of the overburden.*

The re-interpreted results generally agree well with results from inversion of both hydraulic fracturing stress data (Bjarnasson et al., 1989; Klee and Rummel, 2002; although the magnitude of σ_H have known uncertainties Ito et al., 1999; Rutqvist et al., 2000) and overcoring data in borehole KA3579G (Ask, 2001; Ask et al., 2001) using the ISDM-technique (Cornet, 1993a). The comparison with hydraulic fracturing stress data indicate that re-analyzed CSIRO HI and Borre Probe overcoring data are: (1) overestimating σ_H between 250-400 m (boreholes KA1899A, KA2198A, KA2510A and KA2870A); (2) underestimating σ_h in boreholes KXZSD8HL, KZ0059B, KF0093A01, and KK0045G01 (deeper level). The magnitude of σ_v versus depth is rather scattered around the trend of the theoretical vertical stress, with a standard deviation of ±2.4 MPa at the single test scale for all overcoring data.

The re-analysis have small impact on the orientation of σ_H (Fig. 6-64) and is similar to the average orientation of σ_H obtained from hydraulic fracturing data, 134±18°N (Bjarnasson et al., 1989; Klee and Rummel, 2002).

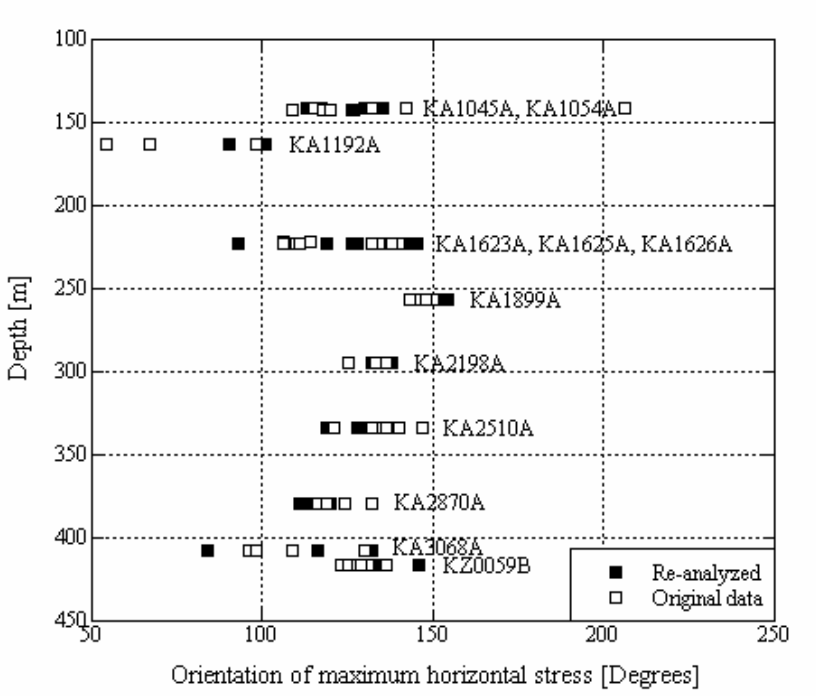

Figure 6-64. *Orientation of maximum horizontal stress using all CSIRO HI data and single measurement scale. Filled and unfilled symbols represent the re-analyzed and original data.*

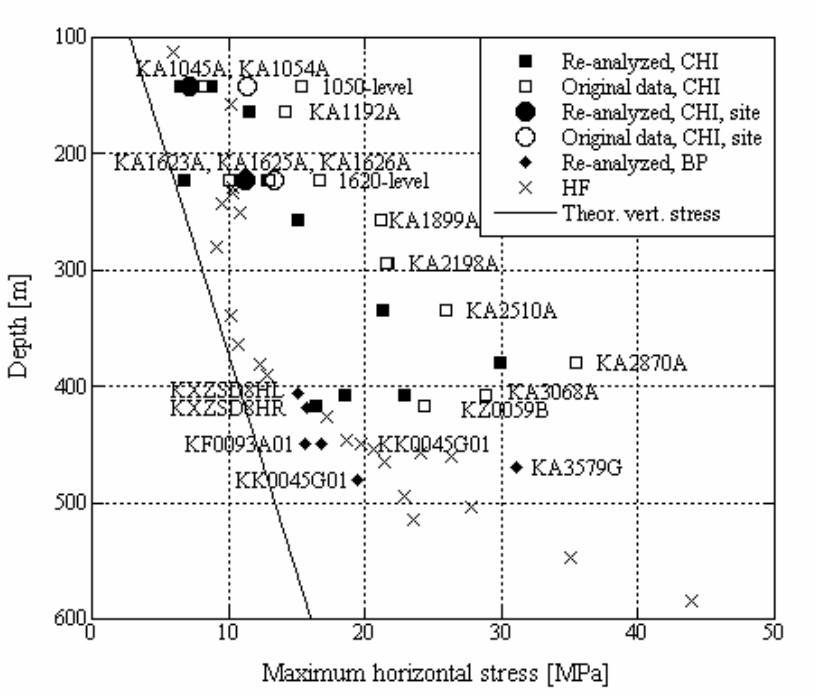

Figure 6-65. *Maximum horizontal stress using all CSIRO HI data at borehole and site average scale. Filled and unfilled symbols represent the re-analyzed and original data, respectively, and the solid line the theoretical vertical stress from weight of the overburden.*

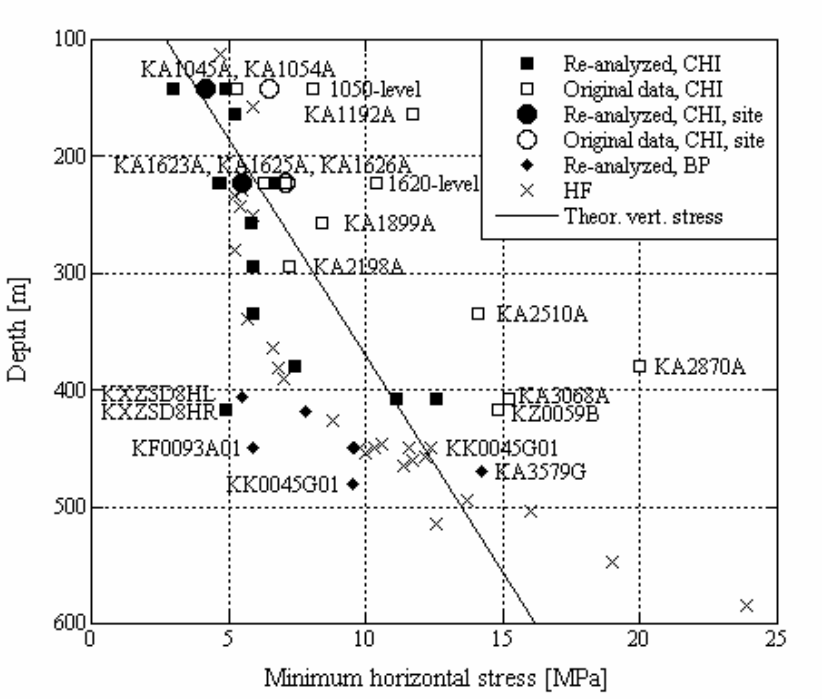

Figure 6-66. *Minimum horizontal stress using all CSIRO HI data at borehole and site average scale. Filled and unfilled symbols represent the re-analyzed and original data, respectively, and the solid line the theoretical vertical stress from weight of the overburden.*

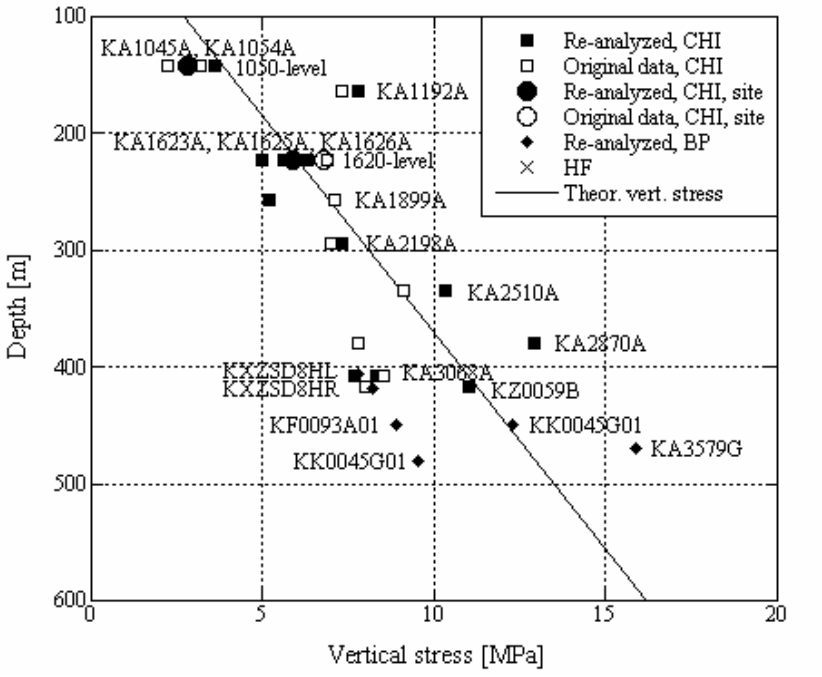

Figure 6-67. *Vertical stress using all CSIRO HI data at borehole and site average scale. Filled and unfilled symbols represent the re-analyzed and original data, respectively, and the solid line the theoretical vertical stress from weight of the overburden.*

Comparison of stress magnitudes (Fig. 6-68) indicates a thrust-prone regime down to about 150 m depth followed by a section with very similar σ_h and σ_v magnitudes (150-275 m depth). Between 275 and 400 m depth, a wrench-prone regime exists, which is again followed by a section with very similar σ_h and σ_v magnitudes (400-500 m depth). Hydraulic fracturing data (e.g. Bjarnasson et al., 1989) indicate a thrust-prone regime down to about 750 m depth. Below this depth (750-1000 m depth), the σ_h and σ_v magnitude are of equal size. Based on focal plane solutions in Fennoscandia (e.g. Slunga, 1990; Slunga and Nordgren, 1987), it is likely that from about 1000 m depth, wrench faulting conditions apply.

6.14.2 Influence of geological structures and tunnel excavation on stresses at Äspö HRL

The most interesting observation found when considering all available data at the Äspö HRL is the effect of the NE-2 zone. All data located close to and West of the NE-2 zone (Fig. 1-2), including overcoring data in borehole KA1623A, KA1625A, KA1626A, KA2510A, KF0093A01 and KA3579G and hydraulic fracturing data from borehole KF0093A01 and KA2599G01, are very well grouped concerning the orientation of σ_H (124±14°N at the single test scale). If the outlayers in boreholes KA1192A and KA3068A are disregarded, the average orientation of all data located East of the NE-2 zone becomes 139±16°N (at the single test scale using data from boreholes KA1045A, KA1054A, KA1899A, KZ0059B, KXZSD8HL, KXZSD8HR, KK0045G01, KAS02).

The overcoring data at Äspö HRL indicate influence of geological discontinuities at different scales; (1) major fracture zones (more than 5 m wide); (2), minor fracture zones (more than 10 cm but less than 5 m wide); and (3) individual fractures of fracture sets. The influence is expressed in the stress results with σ_H and σ_h oriented perpendicular and parallel to the zone, respectively. Minor zones influencing the results were found in boreholes 92A and 68A, see below. Furthermore, the dominant NW-oriented and water bearing fracture set influence the measurements at the Zedex Test Site including borehole KXZSD8HL, KXZSD8HR, KXZSD81HR, and KZ0059B (Ask et al., 2003). The same is valid for borehole KK0045G01, in the nearby Demonstration tunnel, although less obvious (see Ask et al., 2002). This agrees well with the distribution of water-bearing fractures being sub-horizontal above about 240 m depth and sub-vertical between 240-460 m depth (Talbot and Sirat, 2001).

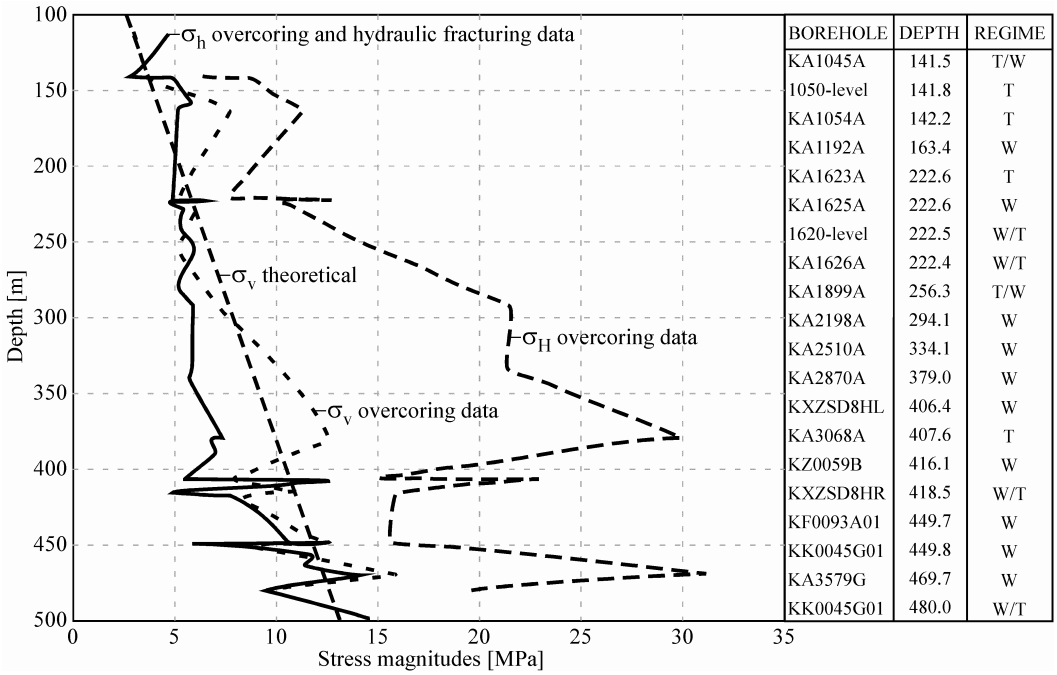

BOREHOLE	DEPTH	REGIME
KA1045A	141.5	T/W
1050-level	141.8	T
KA1054A	142.2	T
KA1192A	163.4	W
KA1623A	222.6	T
KA1625A	222.6	W
1620-level	222.5	W/T
KA1626A	222.4	W/T
KA1899A	256.3	T/W
KA2198A	294.1	W
KA2510A	334.1	W
KA2870A	379.0	W
KXZSD8HL	406.4	W
KA3068A	407.6	T
KZ0059B	416.1	W
KXZSD8HR	418.5	W/T
KF0093A01	449.7	W
KK0045G01	449.8	W
KA3579G	469.7	W
KK0045G01	480.0	W/T

Figure 6-68. *Horizontal and vertical stress magnitudes for all re-analyzed overcoring data. Note that also hydraulic fracturing data have been used the for minimum horizontal stress line.*

For most boreholes with CSIRO HI measurements, the stress field versus borehole length is almost linear. The only clear exceptions are boreholes KA1192A and KA3068A. The reason for the non-linear stress field versus depth in these boreholes is not fully understood. It has been suggested that data in borehole KA3068 may reflect: (1) influence of the excavation; (2) microcracking of the core; and (3) boundary yield between the cell and the rock (Hermansson et al., 1995).

The tunnel geometry at KA3068A would tend to lower major principal stress with about 5 % (Hermansson et al., 1995). This small effect of the tunnel excavation is valid for all CSIRO HI data at Äspö. Further, the measurements in both boreholes are located over a short section (about 2 m) which is unlikely enough to record an excavation-induced stress gradient, considering the accuracy of the method. The biaxial test results display slightly non-linear stress-strain relationship but not more than normal and the effect of microfractures in the core is judged as being small. The boundary yield effect has been tested, and the result still includes non-linear stresses and rotations of the principal stresses.

Thus, if all listed explanations are ruled out, the most plausible explanation is influence of water-bearing fractures. In both boreholes two tests were unsuccessful because the cell was pushed out of the borehole due to water pressure build up behind the cell. The fracture of fracture zone in borehole KA1192A, of unknown width and orientation, is located between test point number 1 and test points 3 and 4, at 0.5 to 1.3 m from the test points. In borehole KA3068A, the test points are located deeper in the borehole than the water bearing fracture and about 2-4 metres from the test points, i.e. the deeper measurement points should be less affected.

The stresses in borehole KA1192A (Fig. 6-69) indicate an E-W orientation of maximum horizontal stress with the minimum principal stress oriented approximately N-S. This corresponds well to an ESE-WNW oriented water bearing and minor fracture zone dipping 74° towards south (e.g. Fig. 4.19 in Rhén et al., 1997). Based on fracture frequency in the borehole, the centre of the zone intersects borehole KA1192A around 12 m borehole length and the fracture between the measurements points, at 14.9 m depth, is likely a branch of that zone. The measurements may also be influenced by the NE-1 zone, which is characterized by open, centimeter-wide fractures and cavities with a central 1 m wide clay-altered rock (Rhén et al., 1997).

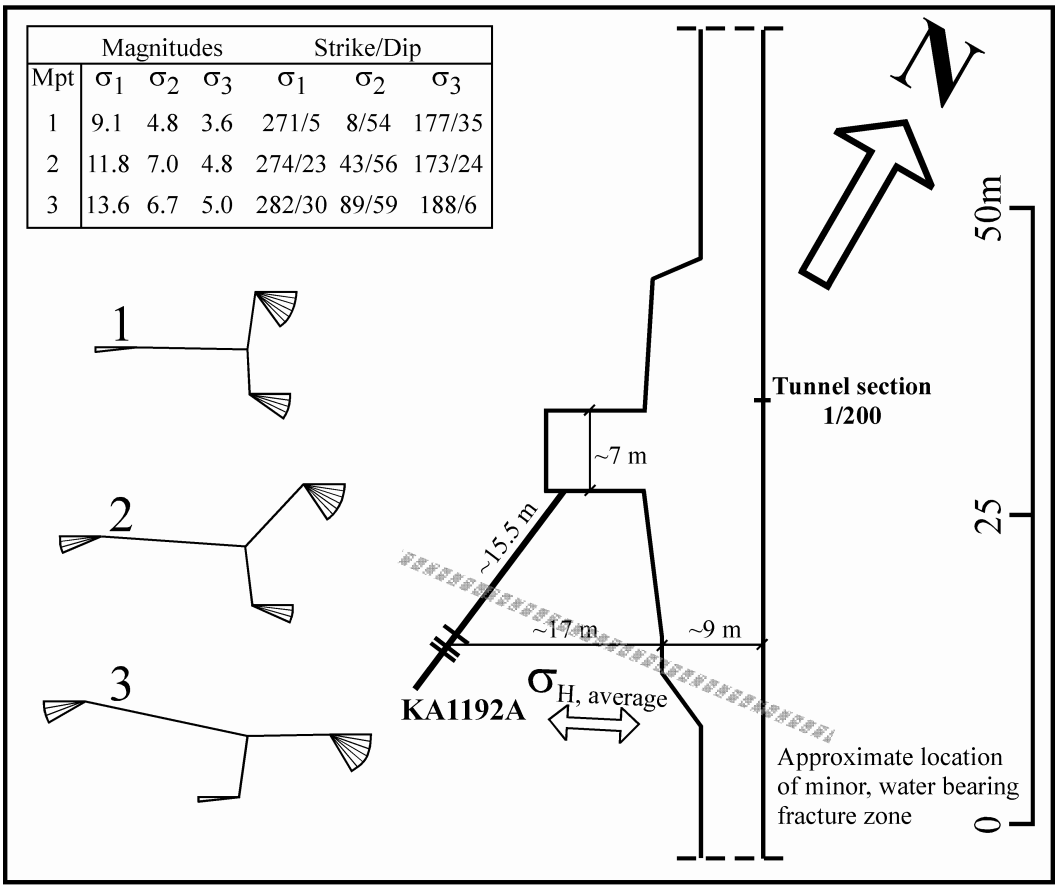

Figure 6-69. *Site geometry and principal stresses for the three measurements conducted in borehole KA1192A.*

For borehole KA3068A (Fig. 6-70), the stress data from the measurement points closest to the fracture indicate a rotation of major principal stress from NW-SE to E-W. The situation for the intermediate and minor principal stresses is less clear. Minor principal stress is generally oriented NE-SW, whereas the intermediate stress seems to rotate from NE-SW to N-S. The orientation of minimum horizontal stress and maximum horizontal stress for the two deeper measurement points may be explained by a water bearing minor fracture zone striking ENE-WSW with a 75° dip towards South (Fig. 2.6 in Stanfors et al., 1997). The shallower measurement points are likely to be influenced by the fracture or fracture zone intersecting the borehole between these measurement points. The dominating water-bearing fracture set at this depth strikes NW-SE and may thus explain the results observed.

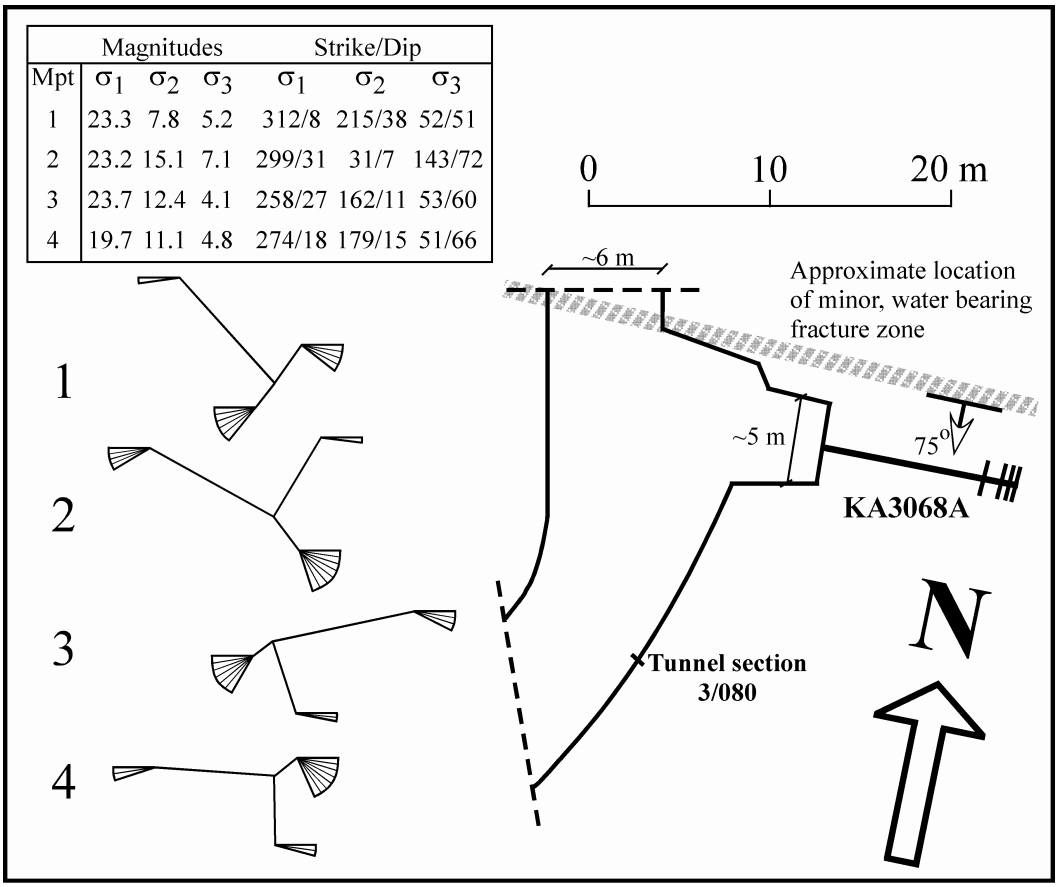

Figure 6-70. *Site geometry and principal stresses for the three measurements conducted in borehole KA3068A.*

A relatively large number of boreholes indicate that the shallowest measurement point or points, i.e. closest to the tunnel, deviate from the general trend of stress state in the borehole. The boreholes where this has been observed include KA1054A, KA1192A, KA1623A, KA1625A, KA2510A and KZ0059B, and the boreholes with the two shallowest measurement points deviating are KA1899A and KA2870A. In average, these measurements indicate a 23 % difference in the average principal stress magnitude and a 15° difference in the principal stress orientations compared to the remainder of the tests in each borehole. Thus, this could reflect influence by the tunnel excavation. Although it is doubtful that gradients can be observed, giving the short test intervals used in each borehole, attempts were made to identify possible excavation disturbances. The analysis, based on the relationship between the σ_H-orientation and the site geometry for each borehole, indicates that a majority of the measurements are affected by the tunnel excavation, but to a very small extent (less than 10%). Thus, the tunnel excavation disturbance for the CSIRO HI measurements at Äspö HRL is interpreted as small. The deviations mentioned above are thus judged to be the result of small scale geological discontinuities or uncertainties in the measurement method.

7 Recommendations for future overcoring stress measurements

Based on the re-analysis of the existing CSIRO HI stress data, a number of recommendations are made which may improve the results in future testing:

1. After each overcoring test, the core at the position of the strain rosettes should be investigated thoroughly. The quality of the gluing, position of the rosettes and geology (grain sizes, fractures) at the gauge should be documented. The position and orientation of the pilot hole (if decentralized and/or non-axial) should also be documented.

2. The frequency for data sampling is insufficient for a reliable analysis of both the overcoring and biaxial tests and should be improved.

3. During installation, the CSIRO HI cell has sometimes been pushed out of the borehole due to high water pressure. This may be overcome by including a drainage though the cell because even if a correct installation is accomplished, water pressure may build up during the test possibly influencing the result. On the other hand, measurements conducted close to such features may not be of interest as they are unlikely to sample the *in situ* stress field.

4. It is likely that the CSIRO HI measurements at the Äspö HRL suffer from yielding of the epoxy adhesive. The epoxy has a predetermined temperature interval where it's function is guaranteed. Careful monitoring of the temperature during the overcoring process with adjustment of the drilling if a strong temperature increase is observed may help to overcome this problem.

5. Potential boundary yield should be tested by plotting the average axial strain versus rotation of σ_H towards the borehole direction.

6. The biaxial testing of the CSIRO HI cores normally includes pressures up to 20 MPa, which evidently is too high. It is recommended that the maximum biaxial load is set to 10 MPa with current core dimensions.

7. The strain analysis should involve a detailed investigation of the strains response during overcoring and may be complemented by studying the results in each borehole (see Table 3-1).

8. The biaxial test analysis should be made attempting to use all available strain gauges, i.e. also the 45°- and 135°-inclined gauges. The stress-strain curves should be analyzed in detail, especially if high biaxial pressures have been applied (i.e. more than 10 MPa although not recommended) to reveal possible non-linearity as a result of core fracturing.

8 Acknowledgements

The research was made possible through financial support from the Swedish Nuclear Fuel and Waste Management Co. (SKB). I would like to acknowledge my supervisor Prof. Ove Stephansson for encouragement and comments throughout my PhD-work. MSc. Kristina Larsson is acknowledged for sharing the thermal expansion data for Äspö rocks and MSc. Max Lee is acknowledged for sending complementary raw material from the CSIRO HI measurements. Comments from Ass. Prof. Maria Ask, Mr. Lennart Ekman, Mr. Jan Malmtorp, and Mr. Rolf Christiansson are also greatly acknowledged.

References

Andersson, J. Statistisk analys av bergspänningsdata - En inledande studie av vertikalspänningars och töjningars djupberoende på Äspö. SKB Utveckling, Arbetsrapport U-96-33, Stockholm, 1996, 21 p.

Andersson, J. Statistiska ansatser för att studera skillnader mellan hydraulisk spräckning och överborrning. SKB Utveckling, Arbetsrapport U-97-04, Stockholm, 1997, 12 p.

Amadei, B. and Stephansson, O. *Rock Stress and Its Measurements*, Chapman and Hall Publ., London, 1997, 490 p.

Ask, D. Inversion and interpretation of hydraulic and overcoring stress measurements in the Äspö region. Licentiate Thesis, Royal Institute of Technology, Stockholm, 2001, 101 p.

Ask, D. Evaluation of measurement-related uncertainties in the analysis of overcoring rock stress data from Äspö HRL, Sweden: a case study. *Int. J. Rock Mech. Min. Sci.*, in press 2003.

Ask, D., Stephansson, O. and Cornet, F.H. Analysis of overcoring rock stress data in the Äspö region. *Proc. 38th U.S. Rock Mechanics Symposium,* Washington, USA. A.A. Balkema Publisher, 2001a, pp 1401-05.

Ask, D., Stephansson, O. and Cornet, F.H. Integrated stress analysis of hydraulic and overcoring rock stress data in the Äspö region. Analysis of hydraulic fracturing stress measurements and hydraulic tests in pre-existing fractures (HTPF) in boreholes KAS02, KAS03, and KLX02. SKB International Progress Report IPR-01-26, Stockholm, 2001b, 155 p.

Ask, D., Cornet, F.H. and Stephansson, O. Analysis of overcoring stress data at the Äspö HRL, Sweden. Analysis of overcoring rock stress measurements using the Borre Probe. SKB Report in press. 2002.

Ask, D., Cornet, F.H. and Stephansson, O. Integration of CSIR- and CSIRO-type of overcoring rock stress data at the Zedex Test Site, Äspö HRL, Sweden. Submitted to the *ISRM 10th Int. Congr. on Rock Mech.*, Johannesburg, 2003.

Blackwood, R.L. Diagnostic stress-relief curves in stress measurement by overcoring. *Int. J. Rock Mech. Min. Sci. & Geomech. Abstr.*, **15**, 1978, pp. 205-9.

Bjarnason, B., Klasson, H., Leijon, B., Strindell, L. and Öhman, T. Rock stress measurements in boreholes KAS02, KAS03 and KAS05 on Äspö. SKB Progress Report 25-89-17, Stockholm, 1989, 59 p.

Christiansson, R. Rock stress measurements by overcoring. Quality control of overcoring data from the Äspö HRL with special emphasis on the properties of intact rock and geological influence. SKB Technical Document TD-00-01, 2000, 2000, 19 p.

Christiansson, R. and Jansson, T. Test with three different stress measurement methods in two orthogonal boreholes. *Proc. 38th North American Rock Mechanics Symposium,* Toronto, Canada, 2002, pp. 1429-36.

Cornet, F.H. The HTPF and the integrated stress determination methods. *Comprehensive Rock Engineering*, Vol **3**. (J. Hudson, Ed.). Pergamon Press, Oxford, 1993a, pp. 413-432.

Cornet, F.H. Stresses in rock and rock masses. *Comprehensive Rock Engineering*, Vol **3**. (J. Hudson, Ed.). Pergamon Press, Oxford, 1993b, pp. 297-327.

Cornet, F.H. and Valette, B. In situ determination from hydraulic injection test data. *J. Geophys. Res.*, **89**, 1984, pp. 11527-37.

Duncan Fama, M.E. and Pender, M.J. Analysis of the hollow inclusion gauges with implications for stress monitoring. *Int. J. Rock Mech. Min. Sci& Geomech. Abstr.*, **17**, 1980, pp. 137-146.

***Ekman, D.** Rock stress, hydraulic conductivity and stiffness of fracture zones in the Laxemar borehole, Småland, Sweden. Master of Science Thesis, Royal Institute of Technology, Stockholm, Sweden, 1997, 52 pp.

***Ekman, D., Rutqvist, J. and Ljunggren, C.** Determination of hydromechanical parameters down to 1 340 m depth in borehole KLX02 in Laxemar, Sweden. Rock Mechanics Meeting in Stockholm March 12, 1997 (Ed. C. Bachman). Swedish Rock Engineering Research (SveBeFo), Stockholm, 1997a, pp. 39-61.

Ekman, L. Project deep drilling KLX02 - Phase 2. Mothods, scope of activities and results. Summary report. SKB Technical Report TR-01-11, Stockholm, 2001, 188 p.

Gray, W.M. and Toews, N.A. Optimization of the design and use of a triaxial strain cell for stress determination, in *Field Testing and Instrumentation of Rock*, ASTM STP 554, 1974, pp. 116-33.

Hakami, E., Hakami, H. and Cosgrove, J. Strategy for rock mechanics site descriptive model. Development and testing of an approach to modeling the state of stress. SKB Report R-02-03, Stockholm, 2002, 129 p.

Hansson, H., Stephansson, O. and Shen, B. Site-94, Far-field rock mechanics modelling for nuclear waste disposal. SKI Report 95:40, Stockholm, 1995, 83 p.

Hermansson, J., Leijon, B., Markström, I., Munier, R. and Stanfors, R. Geological interpretation of the Zedex rock volume. SKB Technical Note 25-95-06z, Stockholm, 1995, 46 p.

Heuze, F.E. High-temperature mechanical, physical and thermal properties of granitic rocks – A review. *Int. J. Rock Mech. Min. Sci& Geomech. Abstr.*, **20** (1), 1983, pp. 3-10.

Hirashima, K. and Koga, A. Determination of stress in anisotropic elastic medium unaffected by boreholes from measured strains or deformations. *Proc. Int. Symp. Field Meas. in Rock Mech.*, Zurich, A.A. Balkema Publ., Rotterdam, 1977, pp. 173-82.

*Ekman, D., now Ask, D.

Holman, J.P. *Experimental methods for engineers*, McGraw and Hill, Inc., New York, 1994.

Hudson, J.A. Strategy for rock mechanics site descriptive model. A test case based on data from the Äspö HRL. SKB Report R-02-04, Stockholm, 2002, 123 p.

Ito, T., Evans, K., Kawai, K. and Hayashi, K. Hydraulic fracturing reopening pressure and the estimation of maximum horizontal stress. *Int. J. Rock Mech. & Geomech. Abstr.*, **36**, 1999, 811-26.

Irvin, R.A., Garritty, P. and Farmer, I.W. The effect of boundary yield on the results of in-situ stress measurements using overcoring techniques. *Int. J. Rock Mech. Min. Sci. & Geomech. Abstr.*, **24**, 1987, pp. 87-93.

Klasson, H. and Andersson, S. 3D overcoring rock stress measurements in borehole KF0093A01 at the Äspö HRL. SKB Report in press, 2001.

Klasson, H., Persson, M., Ljunggren, C. and Bergsten, K-Å. SKB Report in press, 2001.

Klasson, H., Lindblad, K., Lindfors, U. and Andersson, S. Overcoring rock stress measurements in borehole KOV01, Oskarshamn. SKB Report in press, 2002.

Klee, G. and Rummel, F. Rock stress measurements at the Äspö HRL. Hydraulic fracturing in boreholes KA2599G01 and KF0093A01. SKB International Progress Report IPR-02-02, Stockholm, 2002, 33 p.

Lama, R.D. and Vutukuri, V.S. *Handbook on mechanical properties of rocks – Testing techniques and results, volume II*, Series on rock and soil mechanics (vol. 3), no 1. Trans. Tech Publ., Clasusthal, 1978.

Larsson, K. Determination of the coefficient of thermal expansion for two Äspö rocks, diorite and granite. MSc Thesis, Luleå University of Technology, Luleå, 2001, 35 p.

Lee, M. and Stillborg, B. Äspö virgin stress measurement results in sections 1050, 1190 and 1620 m of the access ramp. SKB Progress Report 25-93-02, Stockholm, 1993, 117 p.

Lee, M., Hewitt, T. and Stillborg, B. Äspö virgin stress measurement results. Measurements in boreholes KA1899A, KA2198A and KA2510A. In SKB Progress Report 25-94-02, Stockholm, 1994, 66 p.

Leeman, E.R. and Hayes, D.J. A technique for determining the complete state of stress in rock using a single borehole. In *Proc. Ist Cong. Int. Soc. Rock mech.* (ISRM), Lisbon, Lab Nac. De eng. Civil, Lisbon, vol 2, 1966, pp. 17-24.

Leijon, B. A. Summary of rock stress data from Äspö. SKB Progress Report 25-95-15, Stockholm, 1995, 12 p.

Leijon, B. A. Relevance of pointwise rock stress measurements – an analysis of overcoring data. *Int. J. Rock Mech. Min. Sci. & Geomech. Abstr.*, **26**, 1989, pp. 61-68.

Leijon, B. A. and Stillborg, B.L. A comparative study between two rock stress measurement techniques at Loussavaara mine. *Rock Mech. Rock Eng.*, **19**, 1986, pp. 143-63.

Litterbach, N., Lee, M. Struthers, M. and Stillborg, B. Virgin stress measurement results in boreholes KA2870A and KA3068A. SKB Progress Report 25-94-32, Stockholm, 1994, 26 p.

Ljunggren, C. and Persson, M. Beskrivning av databas – Bergspänningsmätningar i Sverige. SKB Djupförvar, Projektrapport PR D-95-017, Stockholm, 1995, 21p.

Ljunggren, C. and Klasson H. Rock stress measurements at Zedex test area, Äspö HRL. Äspö Hard Rock Laboratory, Technical Note TN-96-08z, Stockholm, 1996, 34 p.

Ljunggren, C. and Klasson, H. Deep hydraulic fracturing rock stress measurements in borehole KLX02, Laxemar, Drilling KLX02-Phase 2, Lilla Laxemar, Oskarshamn. SKB Utveckling, Project Report U-97-27, Stockholm, 1997, 33 p.

Ljunggren, C. and Bergsten, K-Å. Rock stress measurements in KA3579G, prototype repository. SKB Progress Report HRL-98-09, Stockholm, 1998, 25 p.

Ljunggren, C., Chang, Y. och Andersson, J. Bergspänningsmätningars representativitet - Mätnoggrannhet och naturliga variationer vid hydraulisk spräckning och överborrning. SveBeFo Rapport 37, Stockholm, 1998, 79 p.

Lundholm, B. Analysis of rock stress and rock stress measurements with application to Äspö HRL. Licentiate Thesis, Luleå University of Technology, Luleå, 2000a, 125 p.

Lundholm, B. Rock stress and rock stress measurements at Äspö HRL. SKB International Progress Report IPR-00-24, Stockholm, 2000b, 64 p.

Myrvang, A.M. Evaluation of in-situ rock stress measurements at the Zedex test area. SKB, Progress Report HRL-97-22, 1997, 14 p.

Merril, R.H. In situ determination of stress by relief techniques. *Proc. Int. Conf. State of stress in the Earth's crust*, Santa Monica, Elsevier, New York, 1964, pp 343-69.

Nilsson, G., Litterbach, N., Lee, M. and Stillborg, B. Virgin stress measurement results, borehole KZ0059B. Äspö Hard Rock Laboratory, Technical Note TN-97-25g, Stockholm, 1997, 3 p.

Nordlund, E., Li, C. and Larsson, B. Mechanical properties of the diorite in the Prototype Repository at Äspö HRL. SKB International Progress Report, IPR-99-25, Stockholm, 1999.

Price, N.J. and Cosgrove, J.W. *Analysis of geological structures*, Cambridge University Press, Cambridge, 1990, 502 p.

Rhén, I., Gustafson, G., Stanfors, R. and Wikberg, P. Äspö HRL – geoscientific evaluation 1997/5. Models based on site characterization 1986-1995. SKB Technical Report, TR-97-06, Stockholm, 1997, 440 p.

Rutqvist, J., Tsang, C.-F. and Stephansson, O. Uncertainty in the principal stress estimated from hydraulic fracturing measurements due to the presence of the induced fracture. *Int. J. Rock Mech. & Geomech. Abstr.*, **37**, 2000, 107-20.

Rummel, F., Klee, G. and Weber, U. Rock stress measurements in Oskarshamn. Hydraulic fracturing and core testing in boreholes KOV01. SKB International Progress Report IPR-02-01, Stockholm, 2002, 62 p.

Sandström, D. Utvärdering av genomförda bergspänningsmätningar i Kiirunavvaara. MSc Thesis, Luleå university of Technology, Luleå, 1999, 48 p.

Savin, G.N. *Stress concentrations around holes*, Pergamon Press, Oxford, 1961, pp. 241-96.

SKB. Numerical modelling, acoustic emission and velocity studies of the excavation disturbed zone at the hard rock laboratory. SKB Technical Note TN-97-02z, Stockholm, 1996, 118 p.

Slunga, R. The earthquakes of the Baltic shield. SKB Technical Report 90-30, Stockholm, 1990, 15 p.

Slunga, R. and Nordgren, L. Earthquake measurements in southern Sweden. SKB Technical Report 87-27, Stockholm, 1987, 60 p.

Stacey, T.R. A simple extension strain criterion for fracture of brittle rock. *Int. J. Rock Mech. Min. Sci. & Geomech. Abstr.*, 18, 1981, pp. 469-74.

Stanfors, R., Olsson, P. and Stille, H. Results from pre-investigation and detailed site characterization. Comparison of predictions and observations, geology and mechnical stability. SKB Technical Report 97-04, Stockholm, 1997, 115 p.

Staub, I., Fredriksson, A. and Outters, N. Strategy for rock mechanics site descriptive model. Development and testing of the theoretical approach. SKB Report R-02-02, Stockholm, 2002, 236 p.

Stephansson, O. The importance of rock stress measurement and it's interpretation for rock disposal of hazardous waste. *Proc. Int. Symp. on rock stress*, Kumamoto, Japan. A.A. Balkema Publisher, 1997, pp. 3-13.

Stillborg, B.L. and Leijon, B.A. A comparative study of rock stress measurements at Loussavaara mine. Report FB 8217, Swedish Mining Research Foundation, Kiruna, 1982.

Stille, H. and Olsson, P. First evaluation of rock mechanics. SKB Progress Report 25-89-07, Stockholm, 1989.

Talbot C. and Sirat, M. Stress control of hydraulic conductivity in fracture-saturated Swedish bedrock. *Eng. Geol.*, 61, 2001, pp. 145-53.

Timoshenko, S.P. and Goodier, J.N. *Theory of elasticity*, United Engineering trustees Inc. 1934, 567 p.

Walton, R.J. and Worotnicki, G. A comparison of three borehole instruments for monitoring the change of rock stress with time. *Proc. Int. Symp. on rock stress and rock stress measurements*, Stockholm, Centek Publ., Luleå, 1986, pp. 479-88.

Walton, R.J. and Worotnicki, G. Virgin rock stress measurements at the Warrego Mine. CSIRO Australia, Division of applied geomechanics, Technical report No 93, 1979.

Worotniki, G. and Walton, R.J. Triaxial hollow inclusion gauges for determination of rock stresses in situ. In *Investigation of stresses in rock; Advances in stress measurements* (A.J. Hargraves, Ed.), p. 8, Institute of Engineers, Sydney, 1976.

Worotnicki, G. CSIRO triaxial stress measurement cell. *Comprehensive Rock Engineering*, Vol **3**. (J. Hudson, Ed.). Pergamon Press, Oxford, 1993, pp. 329-94.

Appendix 1

Borehole coordinates

Borehole	Bearing [°]	Dip [°]	X	Y	Z	Measurement depth [m]
KA1045A	206.4	-5.3	6693.7	2135.3	143.00	16.09
						16.60
						17.00
						17.47
KA1054A	293.8	-5.1	6703.1	2132.8	143.7	16.19
						17.15
						18.46
KA1192A	197.0	2.0	6838.9	2108.5	164.0	14.43
						15.62
						16.19
KA1623A	260.0	2.0	7257.9	2004.3	223.1	13.29
						13.84
						14.27
KA1625A	300.0	2.0	7260.2	2004.3	223.1	14.07
						14.57
						15.07
KA1626A	305.0	3.0	7260.6	2009.3	223.0	12.17
						12.67
						13.23
KA1899A	317.0	1.5	7439.3	2207.9	256.6	12.06
						12.43
						12.89
						13.38
						13.81
KA2198A	100.5	1.4	7181.3	2315.4	294.5	12.50
						13.55
						14.11
						14.68
KA2510A	190.8	2.5	7209.7	2202.1	334.7	12.04
						12.36
						12.87
						13.36
						13.75
						14.20
KA2870A	338.7	1.2	7468.0	2225.2	379.3	12.73
						13.23
						13.64
						14.25
						14.865
KA3068A	101.8	2.8	7343.3	2392.6	408.4	14.73
						16.18
						16.50
						16.85
KZ0059B	340.2	2.0	7280.3	2256.3	416.5	7.77
						8.33
						9.05
						12.22
						14.20
						14.72

Dip positive downwards, depth positive downwards. *RT38-RH00 system, and the rest according to the Äspö local system

Appendix 2

Influence of the biaxial test on the rock core – A calculation example

This appendix is based on Sandström (1999).

A2.1 Calculation prerequisites

The calculation example is based on the following prerequisites:

σ_H = 23.0 MPa; σ_h = 10.0 MPa; σ_v = 36.0 MPa

E = 65.0 GPa; υ = 0.25

This corresponds to the average values for borehole KA3579G, Prototype Repository, Äspö HRL.

A2.1 Calculation of strains

The strains become

ε_{axial} = [(36.0-0.25*(23.0+10.0)]/65000 = 427 μstrain;

ε_H = [(23.0-0.25*(36.0+10.0)]/65000 = 177 μstrain;

ε_h = [10.0-0.25*(36.0+23.0)]/65000 = -73 μstrain;

A2.2 Stresses in the rock core

The thick pipe solution gives:

$$\sigma_r = p\frac{D^2}{D^2 - d^2}\left(1 - \frac{d^2}{r^2}\right) \quad \text{(A5-1)}$$

$$\sigma_\theta = p\frac{D^2}{D^2 - d^2}\left(1 + \frac{d^2}{r^2}\right) \quad \text{(A5-2)}$$

$$\sigma_{axial} = 0 \quad \text{(A5-3)}$$

where p is the applied biaxial pressure, D and d are the outer and inner diameter respectively, and r is the radius. The stresses at outer diameter becomes:

$$\sigma_r = p \quad \text{(A5-4)}$$

$$\sigma_\theta = p\frac{D^2 + d^2}{D^2 - d^2} \quad \text{(A5-5)}$$

$$\sigma_{axial} = 0 \quad \text{(A5-6)}$$

and at the inner diameter:

$$\sigma_r = 0 \quad \text{(A5-7)}$$

$$\sigma_\theta = 2p\frac{D^2}{D^2 - d^2} \quad \text{(A5-8)}$$

$$\sigma_{axial} = 0 \quad \text{(A5-9)}$$

The least strain (axial) becomes:

At the outer diameter

$$\varepsilon_{axial} = \frac{1}{E}\left[\sigma_{axial} - \upsilon\left(\sigma_r + \sigma_\theta\right)\right] = -\frac{2p\upsilon}{E}\frac{D^2}{D^2 - d^2} \quad \text{(A3-10)}$$

and at inner diameter

$$\varepsilon_{axial} = \frac{1}{E}\left[\sigma_{axial} - \upsilon\left(\sigma_r + \sigma_\theta\right)\right] = -\frac{2p\upsilon}{E}\frac{D^2}{D^2 - d^2} \quad \text{(A3-11)}$$

During biaxial testing, the Borre Probe has a maximum pressure of 10 MPa and the CSIRO HI 15 MPa. The approximate dimensions for the cells are D_{BP}=62 mm; d_{BP}=37 mm and D_{CHI}=72 mm; d_{CHI}=38 mm respectively. This gives (neglecting correction factors for the CSIRO HI cell):

At the outer and inner diameter:

Borre Probe $\varepsilon_{axial,\ 10\ MPa}$ = -119 μstrain

CSIRO HI $\varepsilon_{axial,\ 10\ MPa}$ = -107 μstrain

$\varepsilon_{axial,\ 15\ MPa}$ = -160 μstrain

$\varepsilon_{axial,\ 20\ MPa}$ = -213 μstrain

According to Stacey (1981), the tension crack initiation strain in granite is approximately 125 μstrain and macroscopic tensional cracks at approximately 250 μstrain. For the Äspö diorite, the crack initiation begins at approximately 60 MPa and that this level is only somewhat dependent on confining stress (SKB, 1997). Using the average in-situ Young's modulus of 60.9 GPa obtained from biaxial tests on Borre Probe cores, results in a crack initiation strain of about 100 μstrain for the Äspö diorite. Thus, this calculation indicates that the biaxial test may be exposed to a critical tensional strain and microcrack generation.

Appendix 3

Derivation of correction factors for the CSIRO HI cells

This appendix is a summary of information presented by Savin (1961), Worotniki and Walton (1976), Duncan Fama and Pender (1980) and Worotnicki (1993).

A3 Stress-strain solutions for CSIRO HI cells and computation of K factors

A3.1 Relief of transverse rock stresses σ_x^o, σ_y^o, and τ_{xy}^o

Savin (1961) derived the relationship between the circumferential strains and the rock stresses perpendicular to the borehole for isotropic rings welded into a circular hole in an infinite elastic and isotropic plate. In a uniaxial tension, p, the stresses and displacements at a point within the K_j:th ring, i.e. $R_j \le r \le R_{j+1}$, may be expressed as:

$$\sigma_r^{(j)} = \frac{p}{2}\left[\left(a_1^{(j)} - \frac{b_{-1}^{(j)}}{2}\frac{R^2}{r^2}\right) + \left(\frac{b_1^{(j)}}{2} - 2a_{-1}^{(j)}\frac{R^2}{r^2} - \frac{3}{2}b_{-3}^{(j)}\frac{R^4}{r^4}\right)\cos 2\theta\right] \tag{A3-1}$$

$$\sigma_\theta^{(j)} = \frac{p}{2}\left[\left(a_1^{(j)} + \frac{b_{-1}^{(j)}}{2}\frac{R^2}{r^2}\right) - \left(\frac{b_1^{(j)}}{2} - 6a_3^{(j)}\frac{r^2}{R^2} - \frac{3}{2}b_{-3}^{(j)}\frac{R^4}{r^4}\right)\cos 2\theta\right] \tag{A3-2}$$

$$\tau_{r\theta}^{(j)} = \frac{p}{2}\left[3a_3^{(j)}\frac{r^2}{R^2} - \frac{b_1^{(j)}}{2} - a_{-1}^{(j)}\frac{R^2}{r^2} - \frac{3}{2}b_{-3}^{(j)}\frac{R^4}{r^4}\right]\sin 2\theta \tag{A3-3}$$

$$u_r^{(j)} = \frac{pR}{8E_j}\left\{\begin{array}{l}\left[a_1^{(j)}(\chi_j - 1)\frac{r}{R} + b_{-1}^{(j)}\frac{R}{r}\right] + \\ \left[a_3^{(j)}(\chi_j - 3)\frac{r^3}{R^3} + b_1^{(j)}\frac{r}{R} + a_{-1}^{(j)}(\chi_j + 1)\frac{R}{r} + b_{-3}^{(j)}\frac{R^3}{r^3}\right]\cos 2\theta\end{array}\right\} \tag{A3-4}$$

$$u_\theta^{(j)} = \frac{pR}{8E_j}\left[a_3^{(j)}(\chi_j + 3)\frac{r^3}{R^3} - b_1^{(j)}\frac{r}{R} - a_{-1}^{(j)}(\chi_j - 1)\frac{R}{r} + b_{-3}^{(j)}\frac{R^3}{r^3}\right]\sin 2\theta \tag{A3-5}$$

where the coefficients a_i and b_i for a single ring are given by:

$$a_{-1} = \frac{2(1+\chi)}{D_1}\left[\left(\frac{E}{E_1} - 1\right) + n^4\left(1 + \chi_1\frac{E}{E_1}\right)\right] \tag{A3-6}$$

$$a_1 = \frac{n^2(1+\chi)}{2\left(\frac{E}{E_1} - 1\right) - n^2\left[\left(\frac{E}{E_1} - 1\right) - \left(1 + \chi_1\frac{E}{E_1}\right)\right]} \tag{A3-7}$$

$$a_3 = -\frac{2(1+\chi)}{D_1}n^4(n^2 - 1)\left(\frac{E}{E_1} - 1\right) \tag{A3-8}$$

$$b_{-3} = -\frac{2(1+\chi)}{D_1}\left[\left(\frac{E}{E_1} - 1\right) + n^4\left(1 + \chi_1\frac{E}{E_1}\right)\right] \tag{A3-9}$$

$$b_{-1} = \frac{2(1+\chi)}{2\left(\frac{E}{E_1} - 1\right) - n^2\left[\left(\frac{E}{E_1} - 1\right) - \left(1 + \chi_1\frac{E}{E_1}\right)\right]} \tag{A3-10}$$

$$b_1 = \frac{2(1+\chi)}{D_1}\left[\left(\frac{E}{E_1} - 1\right)(4 - 3n^2) + n^6\left(1 + \chi_1\frac{E}{E_1}\right)\right]n^2 \tag{A3-11}$$

$$\alpha_{-1} = 2 - \frac{2(1+\chi)}{D_1}\left[\left(\frac{E}{E_1}-1\right)\left(3n^6 - 6n^4 + 4n^2 - 1\right) + n^6\left(n^2-1\right)\left(1+\chi_1\frac{E}{E_1}\right)\right] \quad \text{(A3-12)}$$

$$\beta_{-1} = 2 - \frac{2\left(n^2-1\right)(1+\chi)}{2\left(\frac{E}{E_1}-1\right) - n^2\left[\left(\frac{E}{E_1}-1\right) - \left(1+\chi_1\frac{E}{E_1}\right)\right]} \quad \text{(A3-13)}$$

$$\beta_{-3} = -2 + \frac{2(1+\chi)}{D_1}\left[\left(\frac{E}{E_1}-1\right)\left(4n^6 - 7n^4 + 4n^2 - 1\right) + n^4\left(n^4-1\right)\left(1+\chi_1\frac{E}{E_1}\right)\right] \quad \text{(A3-14)}$$

and n is the ratio R_2/R_1 (R_2 being the outer and R_1 the inner radius), χ_i is the ratio $(3-\nu_i)/(1+\nu_i)$, E and E_1 is the Young's modulus of the plate and ring respectively, and D_1 is the following expression:

$$D_1 = \left(\chi + \frac{E}{E_1}\right)n^2\left[\left(\frac{E}{E_1}-1\right)\left(3n^4 - 6n^2 + 4\right) + n^6\left(1+\chi_1\frac{E}{E_1}\right)\right] + \\ + \left(\chi_1\frac{E}{E_1} - \chi\right)\left[\left(\frac{E}{E_1}-1\right) + n^6\left(1+\chi_1\frac{E}{E_1}\right)\right] \quad \text{(A3-15)}$$

Thus, the coefficients in Eqs. A3-6 to A3-14, are functions of (1) the dimensions of the ring; (2) the radial distance to the point; and (3) on the material properties of the plate and ring. Worotnicki (1993) simplified Eqs. A3-1 and A3-2 in a plate subjected to a uniaxial uniform stress field, σ_1^0, according to:

$$\sigma_r^{(j)} = \sigma_1^0\left[A - 2B\cos 2\theta\right] \quad \text{(A3-16)}$$

$$\sigma_\theta^{(j)} = \sigma_1^0\left[C + 2D\cos 2\theta\right] \quad \text{(A3-17)}$$

where θ is the angle between σ_1^0 and the radius to the point. Note that for the surface of an inclined borehole A = B = 0 and C = D = 1.

Assuming that the stress cell and the cement layer have the same mechanical properties, the rock core, the epoxy pipe and the cement layer are concentric cylinders bonded one to another, the general plane strain solution becomes (see also Appendix 2):

$$E_r\varepsilon_\theta = \left(1-\upsilon_r^2\right)\left\{\left(\sigma_x + \sigma_y\right)K_1^{plstrain} - 2K_2^{plstrain}\left[\left(\sigma_x - \sigma_y\right)\cos 2\theta + 2\tau_{xy}\sin 2\theta\right]\right\} \quad \text{(A3-18)}$$

where

$$K_1^{plstrain} = \frac{G_r}{G_p}\left(a\frac{1-\upsilon_p}{1-\upsilon_r} - c\frac{\upsilon_p}{1-\upsilon_r}\right) \quad \text{(A3-19)}$$

$$K_2^{plstrain} = \frac{G_r}{G_p}\left(b\frac{1-\upsilon_p}{1-\upsilon_r} + d\frac{\upsilon_p}{1-\upsilon_r}\right) \quad \text{(A3-20)}$$

where G_r, G_p, ν_r, and ν_p are the shear moduli and Poisson's ratio of the rock and plastic respectively. The thick pipe solution for analysis of elastic parameters in biaxial tests gives an independently an expression for $K_1^{plstrain}$:

$$K_1^{plstrain} = \frac{mn + 1 - 2\upsilon_p}{e(1-n) + n + 1 - 2\upsilon_p} \quad \text{(A3-21)}$$

where $m = R_p^2/R_{sg}^2$; $n = R_1^2/R_p^2$; R_p, R_{sg}, and R_1 are the radius of the pilot hole, the radius of the strain gauge position and the inner radius of the stress sensor pipe; and e is the ratio of the shear moduli of plastic and rock (G_p/G_r). This formula agrees well with Savin's solution (Worotnicki, 1993).

Note that the assumption of plane strain gives an additional "artificial stress" or restraint that must be resolved (see A1.3).

The corresponding expression for $K_2^{plstrain}$ may be expressed as (rearrangement of Duncan Fama and Pender (1980) and Savin (1961)):

$$K_2^{plstrain} = \frac{(1-e)d_2 + (\chi_p + e)d_3}{D} \tag{A3-22}$$

where

$$D = (1+\chi_r e)\left[\chi_p + e + (1-e)n(3-6n+4n^2)\right] + (\chi_p - e\chi_r)n\left[(1-e)n^3 + \chi_p + e\right] \tag{A3-23}$$

$$d_2 = 12\frac{n}{m}(1-n)(1-\upsilon_p) + n^2\left[n^2 m(3m-4\upsilon_p) + 4n - 3\right] \tag{A3-24}$$

$$d_3 = 1 - 4\upsilon_p mn + 3m^2 n^2 \tag{A3-25}$$

$$\chi_p = 3 - 4\upsilon_p \tag{A3-26}$$

$$\chi_r = 3 - 4\upsilon_r \tag{A3-27}$$

A3.2 Relief of axial-transverse shear stresses τ_{yz}° and τ_{zx}°

The general solution of for the K_3-factor has been derived by Savin (1961) and Duncan Fama and Pender (1980) and is only briefly presented here. The solution for the ±45° inclined gauges is (see also Appendix 2):

$$E_r \gamma_{\theta z} = 4(1+\upsilon_r)\left(\tau_{yz}^0 \cos\theta - \tau_{zx}^0 \sin\theta\right) \tag{A3-28}$$

with the general relationships

$$\gamma_{\theta z} = \frac{1}{r}\frac{\partial u_z}{\partial \theta} \tag{A3-29}$$

where

$$u_z = \frac{2d_6}{G_r}\left[r + \frac{R_1^2}{r}\right]\left[\tau_{xz}^0 \cos\theta + \tau_{yz}^0 \sin\theta\right] + \frac{z}{E_r}\left[\sigma_z^0 - \upsilon_r\left(\sigma_x^0 + \sigma_y^0\right)\right] \tag{A3-30}$$

and

$$d_6 = \frac{1}{1+m^2+e(1-m^2)} \tag{A3-31}$$

$$G_r = \frac{E_r}{2(1+\upsilon_r)} \tag{A3-32}$$

At $r = R_{sg}$, Eqs. A3-29 and As-30 becomes:

$$\gamma_{oz} = \frac{1}{R_{sg}} \frac{2\dfrac{1}{1+\left(\dfrac{R_1}{R_p}\right)^2 + e\left(1-\left(\dfrac{R_1}{R_p}\right)^2\right)}}{\dfrac{E_r}{2(1+\upsilon_r)}} \left[R_{sg} + \frac{R_1^2}{R_{sg}}\right]\left[-\tau_{xz}^0 \sin\theta + \tau_{yz}^0 \cos\theta\right] + 0 \qquad \text{(A3-33)}$$

or

$$E_r\gamma_{\theta z} = 4(1+\upsilon_r)\left[\tau_{yz}^0 \cos\theta - \tau_{xz}^0 \sin\theta\right] \frac{R_p^2\left(1+\dfrac{R_1^2}{R_{sg}^2}\right)}{R_p^2 + R_1^2 + e\left(R_p^2 - R_1^2\right)} \qquad \text{(A3-34)}$$

or

$$E_r\gamma_{\theta z} = 4(1+\upsilon_r)\left[\tau_{yz}^0 \cos\theta - \tau_{xz}^0 \sin\theta\right] K_3$$

Worotnicki (1993) later simplified K_3 according to:

$$K_3 = \frac{1+nm}{1+n+e(1-n)} \qquad \text{(A3-35)}$$

For most rocks an approximation may be made regarding the relationship $E_r:E_p>3$ giving (Worotniki and Walton (1976)):

$$K_3 \approx 1 + \frac{R_p - R_{sg}}{R_p} \qquad \text{(A3-36)}$$

A3.3 Relief of axial stress and axial restraint $\Delta\sigma z = -\nu(\sigma_x^o+\sigma_y^o)$

The relief of axial stress and axial restraint from the core (in addition to the changes in the axial strains in the rock and the HI cell) causes changes in the circumferential and inclined strain gauges, the axial expansion being accompanied by the circumferential contraction.

The axial strain in the plastic is the same as the rock except near the very ends of the glued-in section of the gauge shell. The axial stiffness of the gauge shell compared with the rock may be neglected giving:

$$E_r\varepsilon_z = \sigma_z^0 - \upsilon_r\left(\sigma_x^0 + \sigma_y^0\right) \qquad \text{(A3-37)}$$

When the cell is bonded to the rock and if the Poisson's ratio of the rock and the cell were equal, the circumferential contraction is given by:

$$E_r\varepsilon_\theta = \upsilon_r\left[\sigma_z^0 - \upsilon_r\left(\sigma_x^0 + \sigma_y^0\right)\right] \qquad \text{(A3-38)}$$

However, as their Poisson's ratios are normally different the plastic in the gauge shell tend to strain laterally different from the rock resulting in a small uniform radial stress developing between the rock and the plastic inclusion.

Matching of the axial and radial displacements at the interface core-shell and using the thick pipe solution of the theory of elasticity, an expression may be derived for circumferential strain in the HI shell associated with the axial stress and axial restraint:

$$E_r \varepsilon_\theta = -\upsilon_r \left[\sigma_z^0 - \upsilon_r \left(\sigma_x^0 + \sigma_y^0\right)\right] K_4 \tag{A3-39}$$

Where the correction factor K_4 is a function of the Poisson's ratio of the materials and the magnitude of $K_1^{plstrain}$:

$$K_4 = 1 - \left(K_1^{plstrain}\right)\left(\frac{\upsilon_p}{\upsilon_r} - 1\right) \tag{A3-40}$$

A3.4 Superposition of the partial solutions

Superposition of partial solutions gives the final expression for the correction factors:

$$K_1 = \left(1 - \upsilon_r^2\right) K_1^{plstrain} + \upsilon_r^2 K_4 = K_1^{plstrain}\left(1 - \upsilon_p \upsilon_r\right) + \upsilon_p \upsilon_r = \\ = \frac{\left(mn + 1 - 2\upsilon_p\right)\left(1 - \upsilon_p \upsilon_r\right)}{e\left(1 - n\right) + n + 1 - 2\upsilon_p} \tag{A3-41}$$

$$K_2 = K_2^{plstrain} = \frac{\left(1 - e\right) d_2 + \left(\chi_p + e\right) d_3}{D} \tag{A3-42}$$

$$K_3 = \frac{1 + nm}{1 + n + e\left(1 - n\right)} \tag{A3-43}$$

$$K_4 = 1 - \left(K_1 - 1\right)\frac{\upsilon_p - \upsilon_r}{\upsilon_r\left(1 - \upsilon_p \upsilon_r\right)} \tag{A3-44}$$

Appendix 4

Overcoring graphs

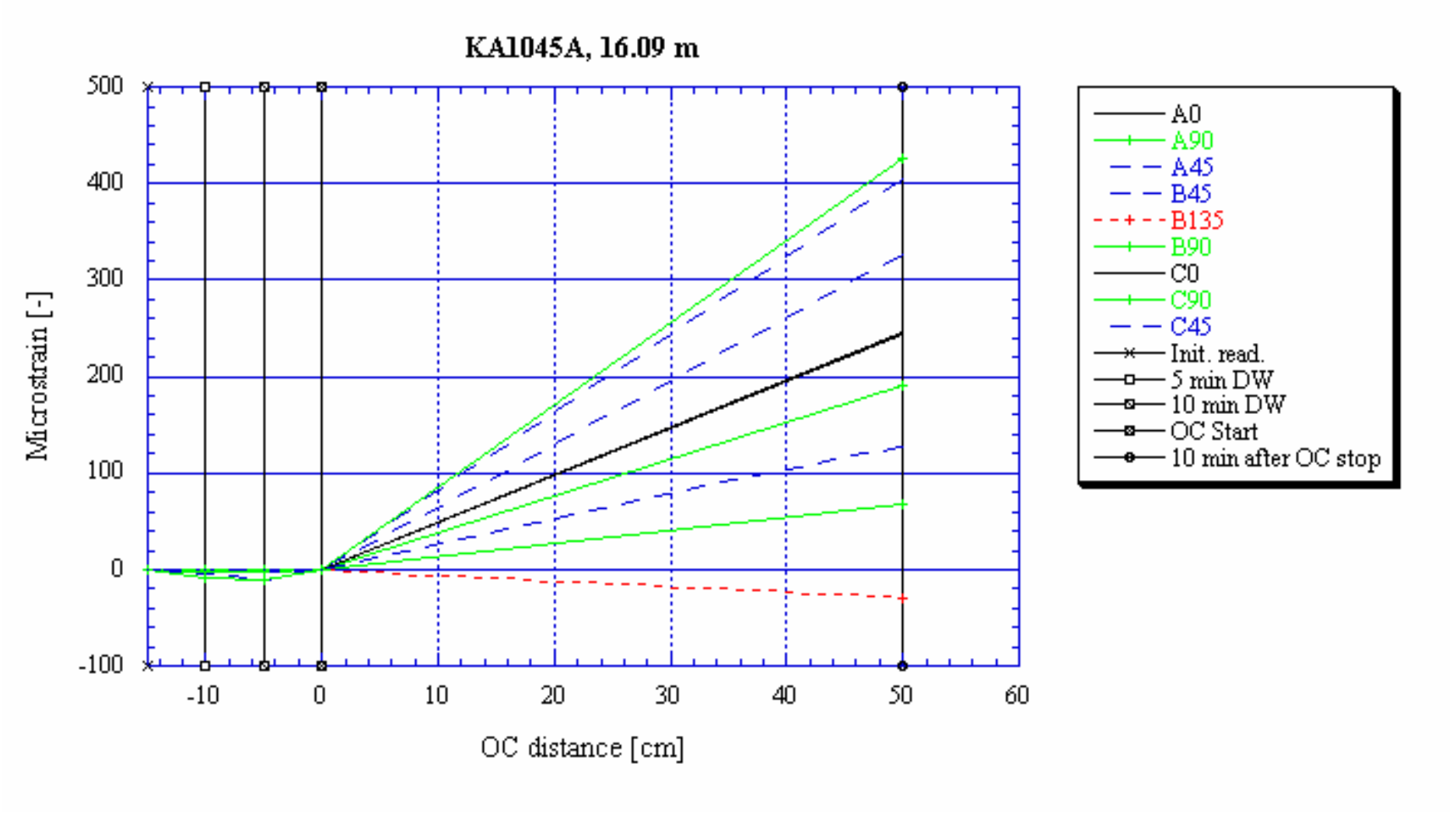

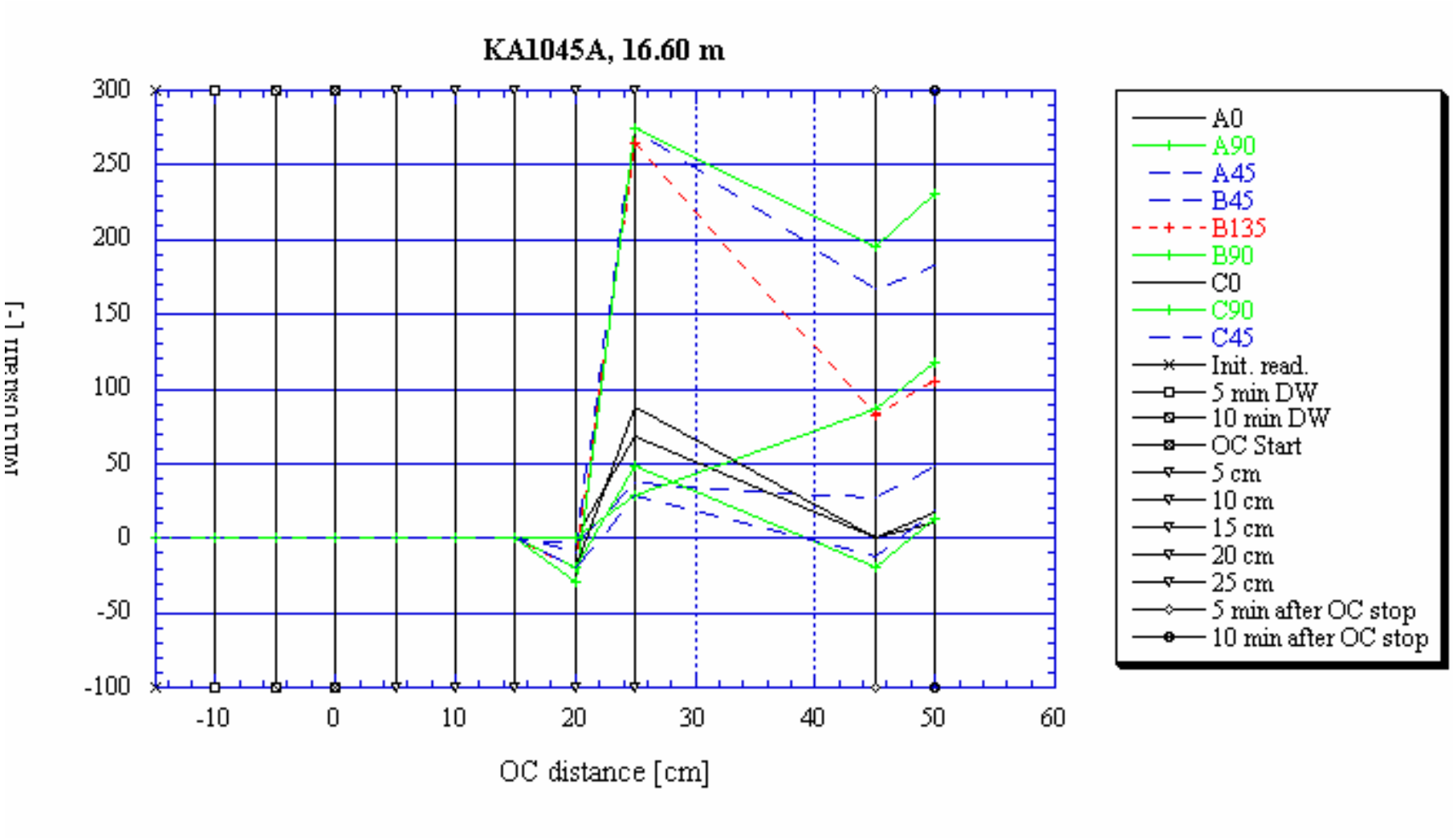
KA1045A, 16.60 m
Magnetic field [-]
300
250
200
150
100
50
0
-50
-100
-10
0
10
20
30
40
50
60
OC distance [cm]
A0
A90
A45
B45
B135
B90
C0
C90
C45
Init. read.
5 min DW
10 min DW
OC Start
5 cm
10 cm
15 cm
20 cm
25 cm
5 min after OC stop
10 min after OC stop

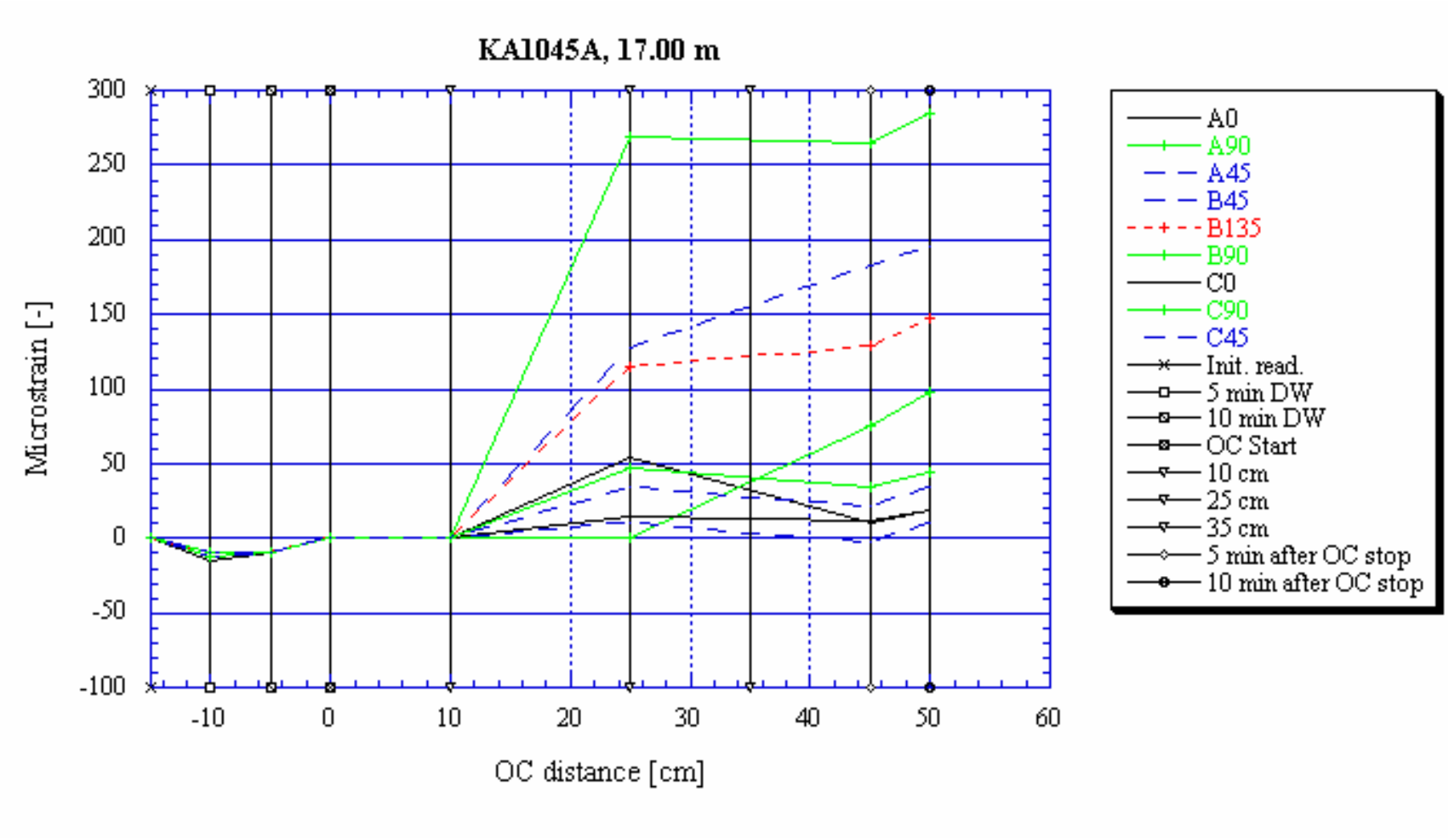
KA1045A, 17.00 m
Microstrain [-]
300
250
200
150
100
50
0
-50
-100
-10
0
10
20
30
40
50
60
OC distance [cm]
A0
A90
A45
B45
B135
B90
C0
C90
C45
Init. read.
5 min DW
10 min DW
OC Start
10 cm
25 cm
35 cm
5 min after OC stop
10 min after OC stop

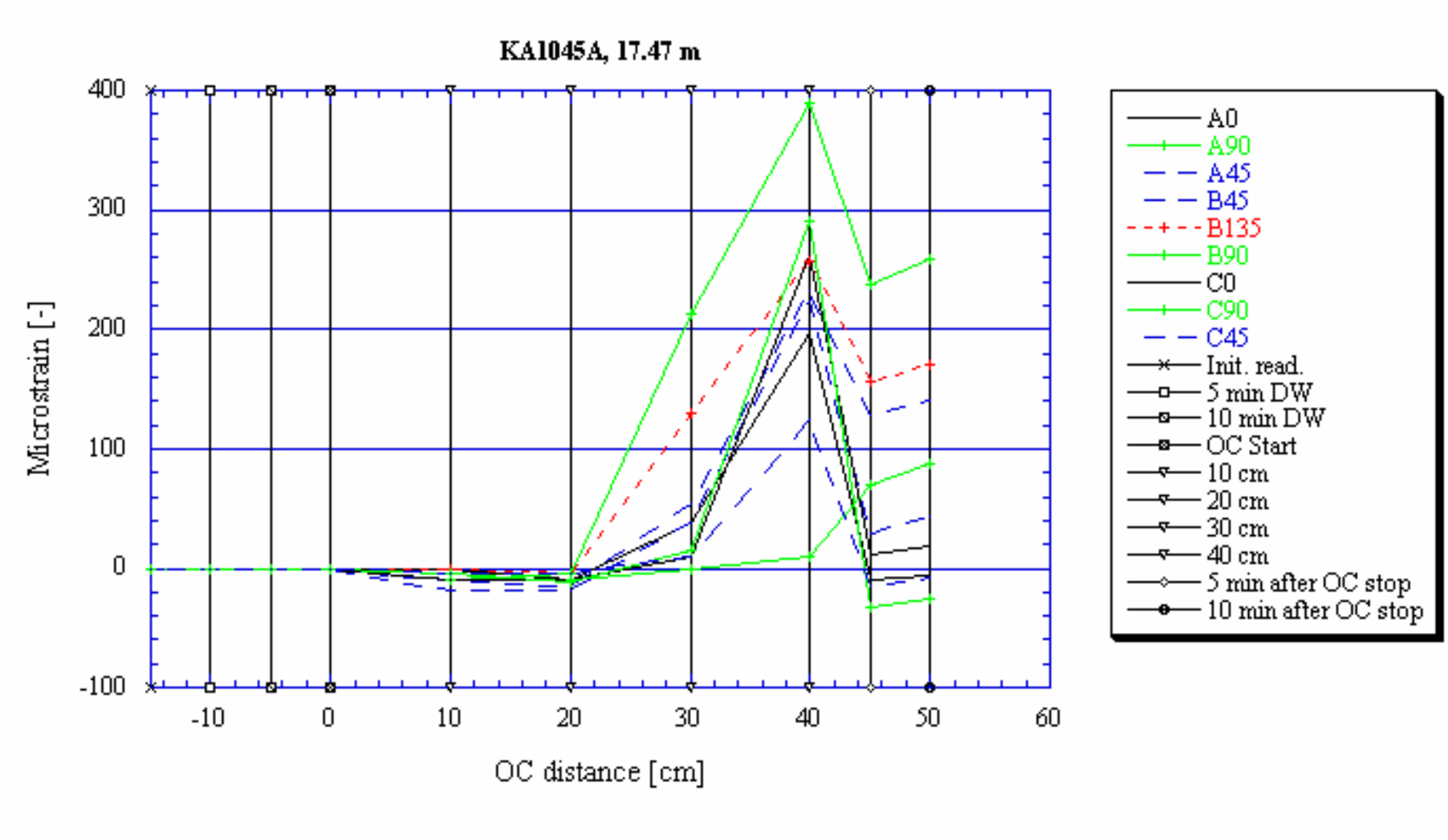
KA1045A, 17.47 m
Microstrain [-]
400
300
200
100
0
-100
-10
0
10
20
30
40
50
60
OC distance [cm]
A0
A90
A45
B45
B135
B90
C0
C90
C45
Init. read.
5 min DW
10 min DW
OC Start
10 cm
20 cm
30 cm
40 cm
5 min after OC stop
10 min after OC stop

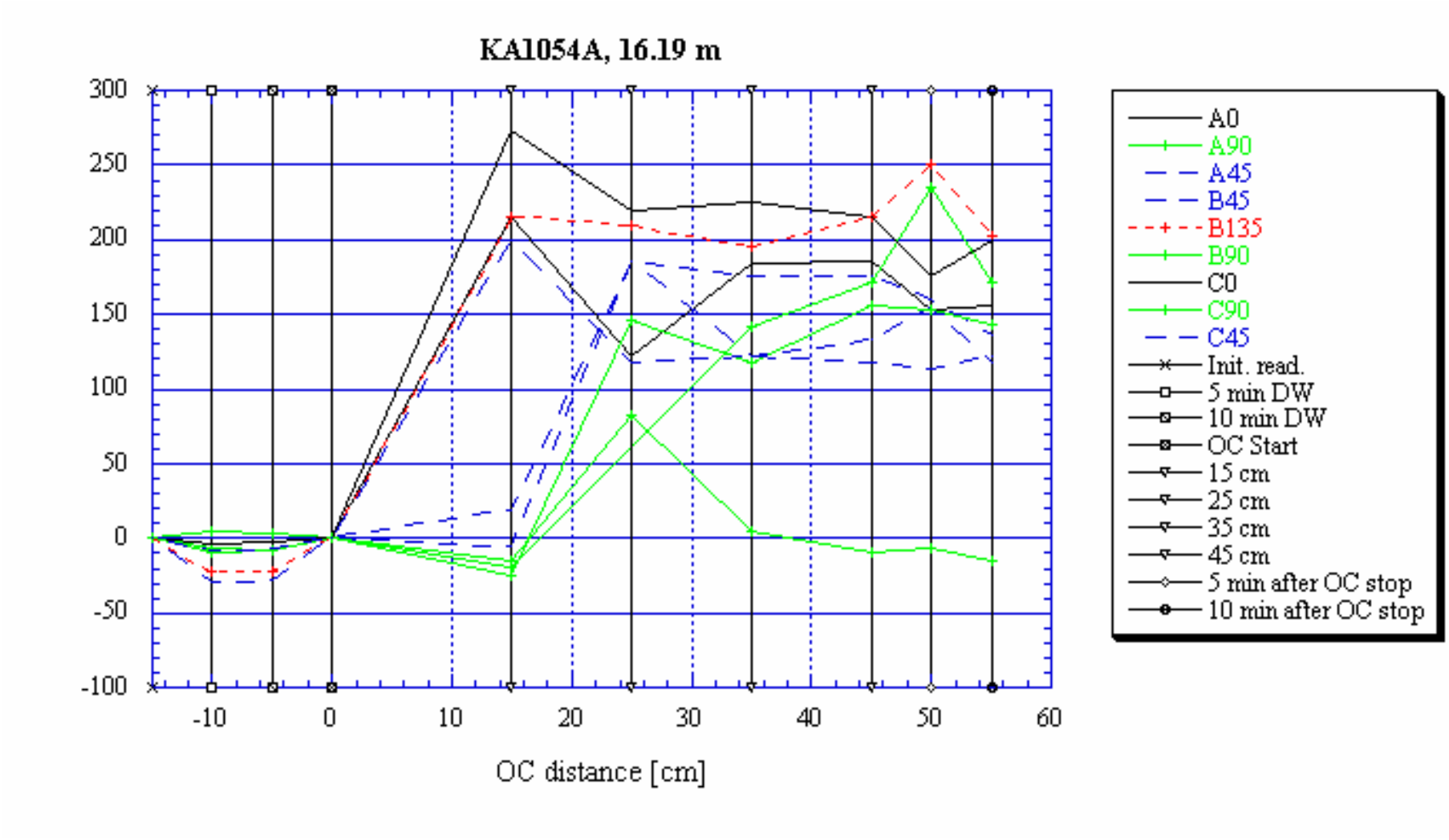
KA1054A, 16.19 m
300
250
200
150
100
50
0
-50
-100
-10
0
10
20
30
40
50
60
OC distance [cm]
A0
A90
A45
B45
B135
B90
C0
C90
C45
Init. read.
5 min DW
10 min DW
OC Start
15 cm
25 cm
35 cm
45 cm
5 min after OC stop
10 min after OC stop

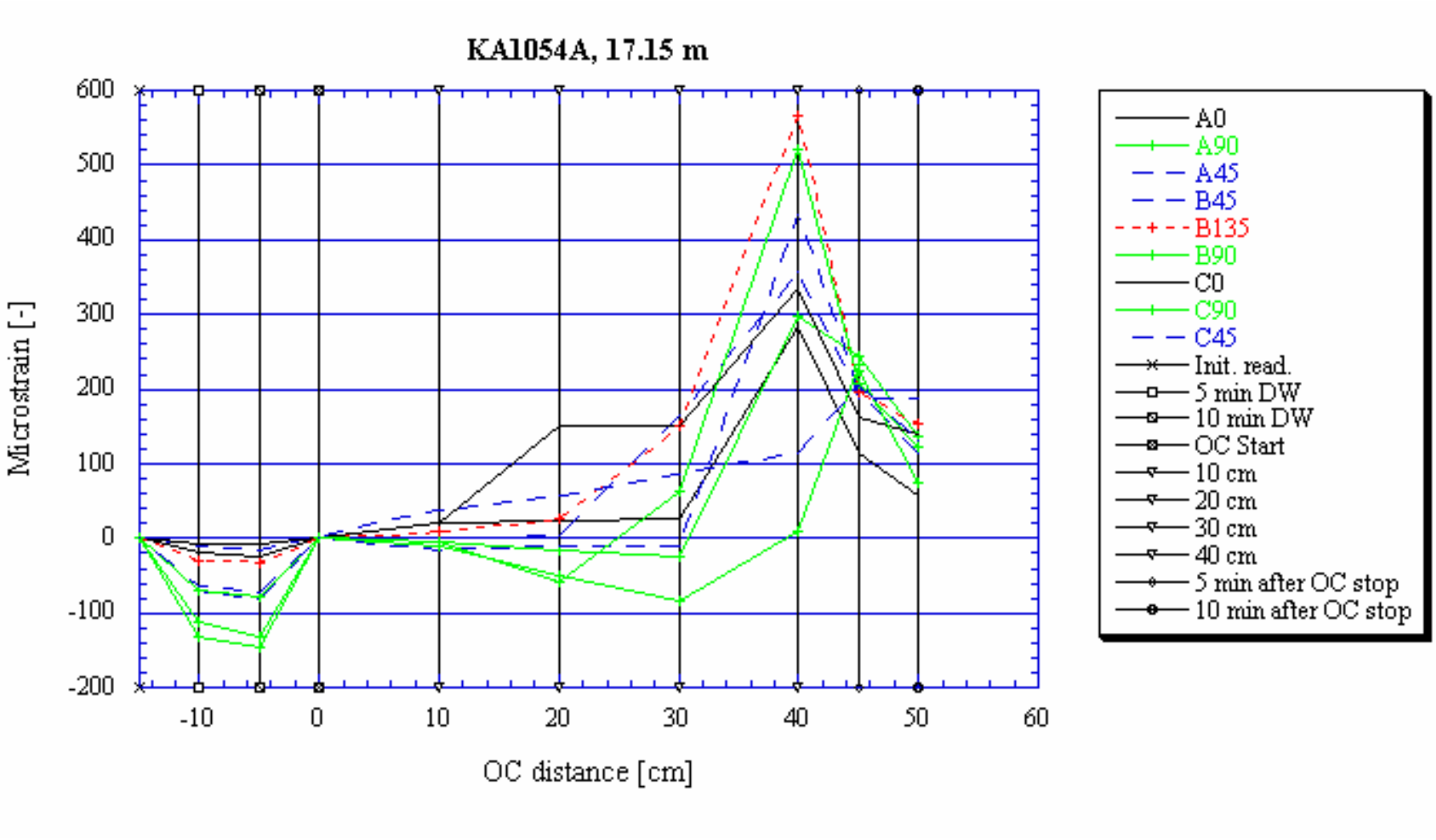
KA1054A, 17.15 m
Microstrain [-]
600
500
400
300
200
100
0
-100
-200
-10
0
10
20
30
40
50
60
OC distance [cm]
A0
A90
A45
B45
B135
B90
C0
C90
C45
Init. read.
5 min DW
10 min DW
OC Start
10 cm
20 cm
30 cm
40 cm
5 min after OC stop
10 min after OC stop

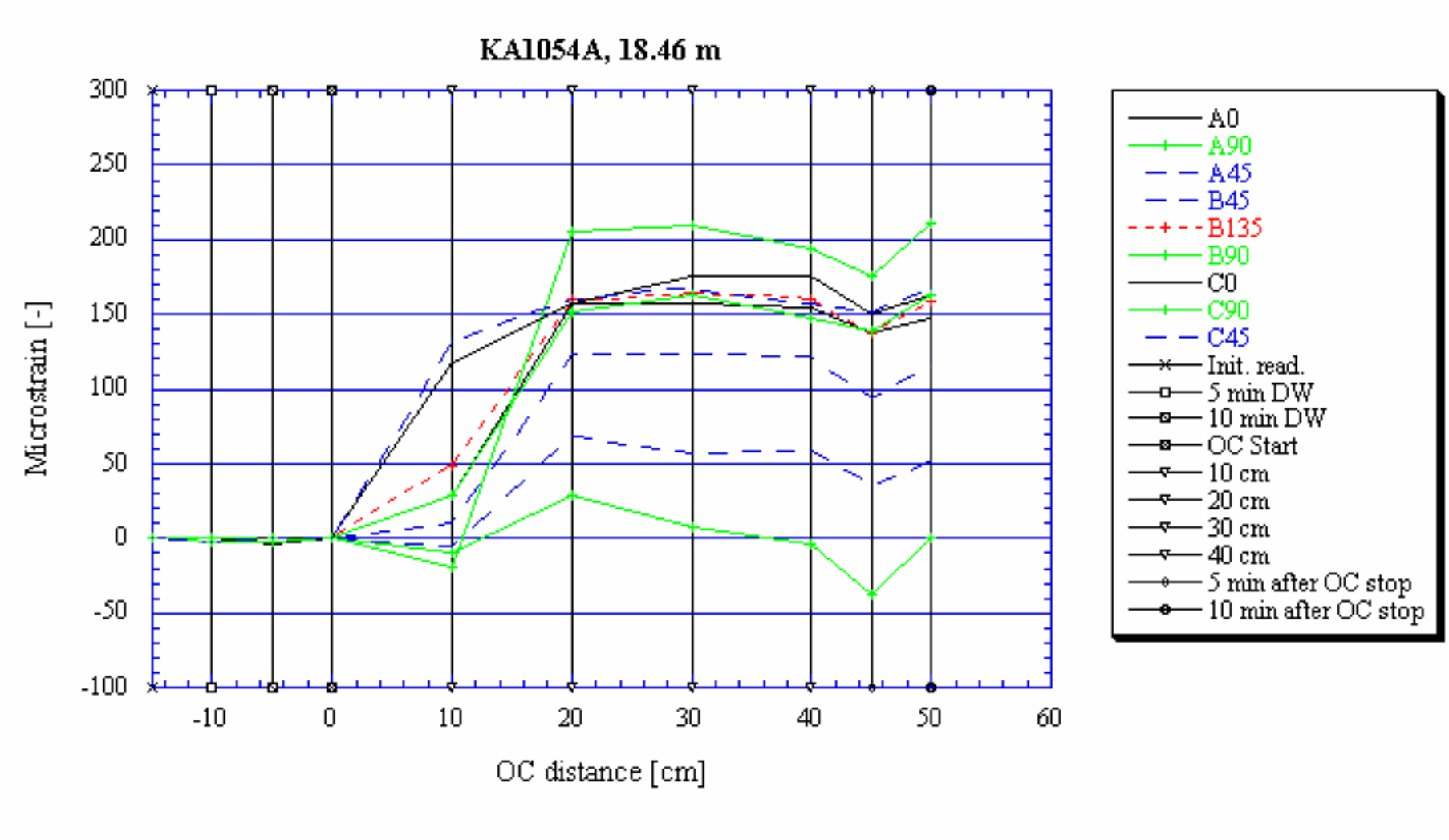
KA1054A, 18.46 m
Microstrain [-]
300
250
200
150
100
50
0
-50
-100
-10
0
10
20
30
40
50
60
OC distance [cm]
A0
A90
A45
B45
B135
B90
C0
C90
C45
Init. read.
5 min DW
10 min DW
OC Start
10 cm
20 cm
30 cm
40 cm
5 min after OC stop
10 min after OC stop

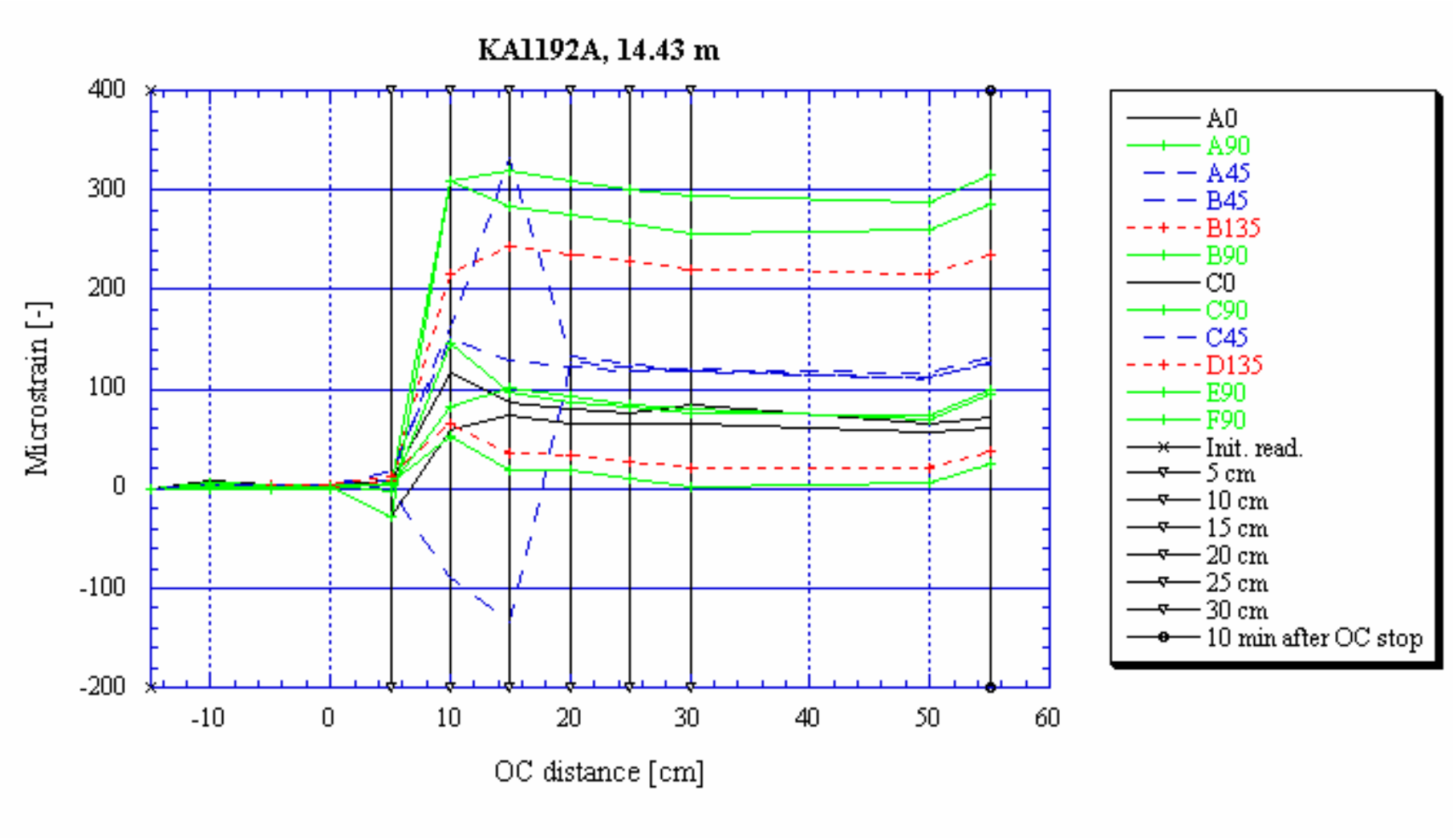
KA1192A, 14.43 m
Microstrain [-]
OC distance [cm]
400
300
200
100
0
-100
-200
-10
0
10
20
30
40
50
60
A0
A90
A45
B45
B135
B90
C0
C90
C45
D135
E90
F90
Init. read.
5 cm
10 cm
15 cm
20 cm
25 cm
30 cm
10 min after OC stop

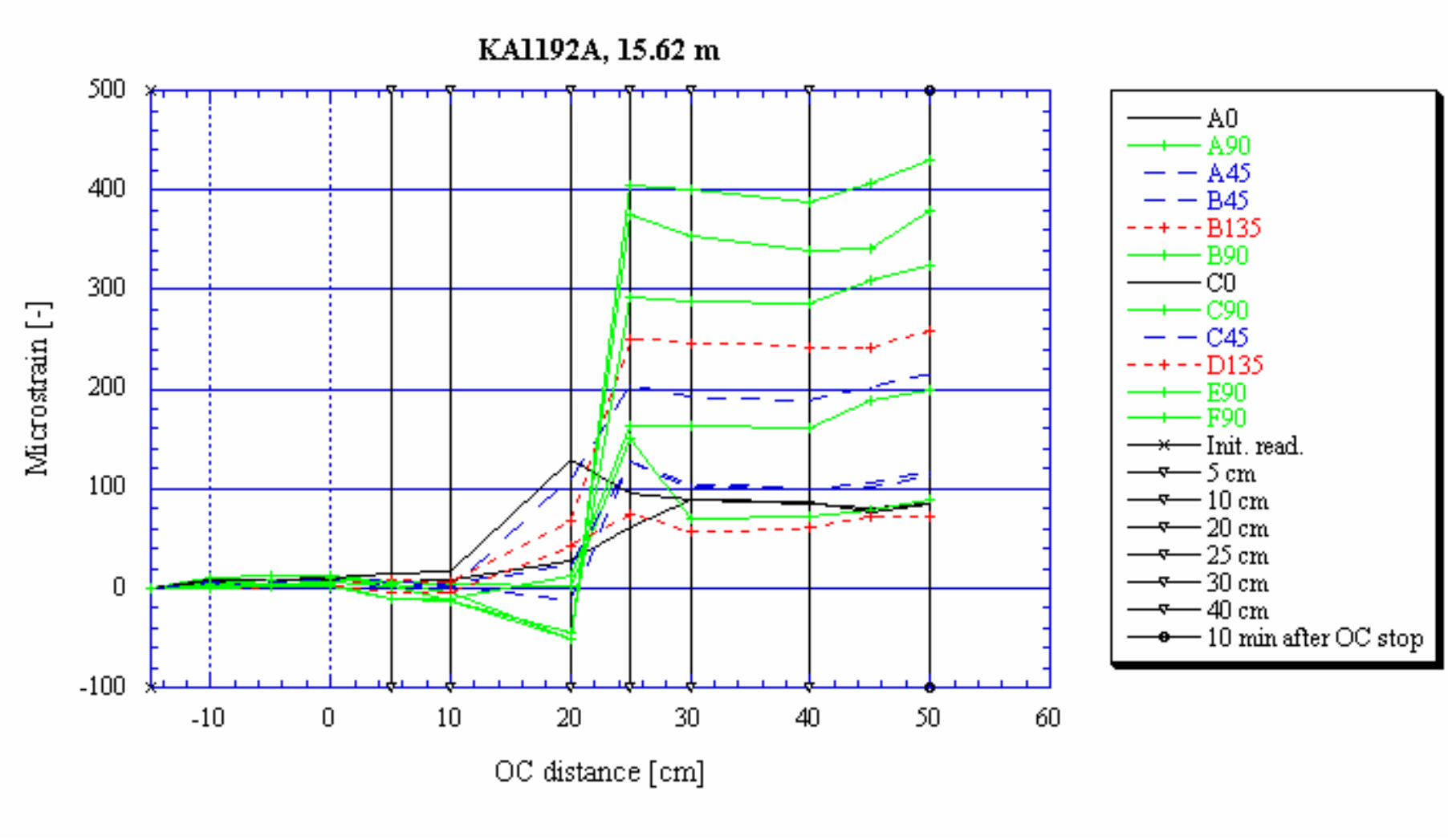
KA1192A, 15.62 m
Microstrain [-]
500
400
300
200
100
0
-100
-10
0
10
20
30
40
50
60
OC distance [cm]
A0
A90
A45
B45
B135
B90
C0
C90
C45
D135
E90
F90
Init. read.
5 cm
10 cm
20 cm
25 cm
30 cm
40 cm
10 min after OC stop

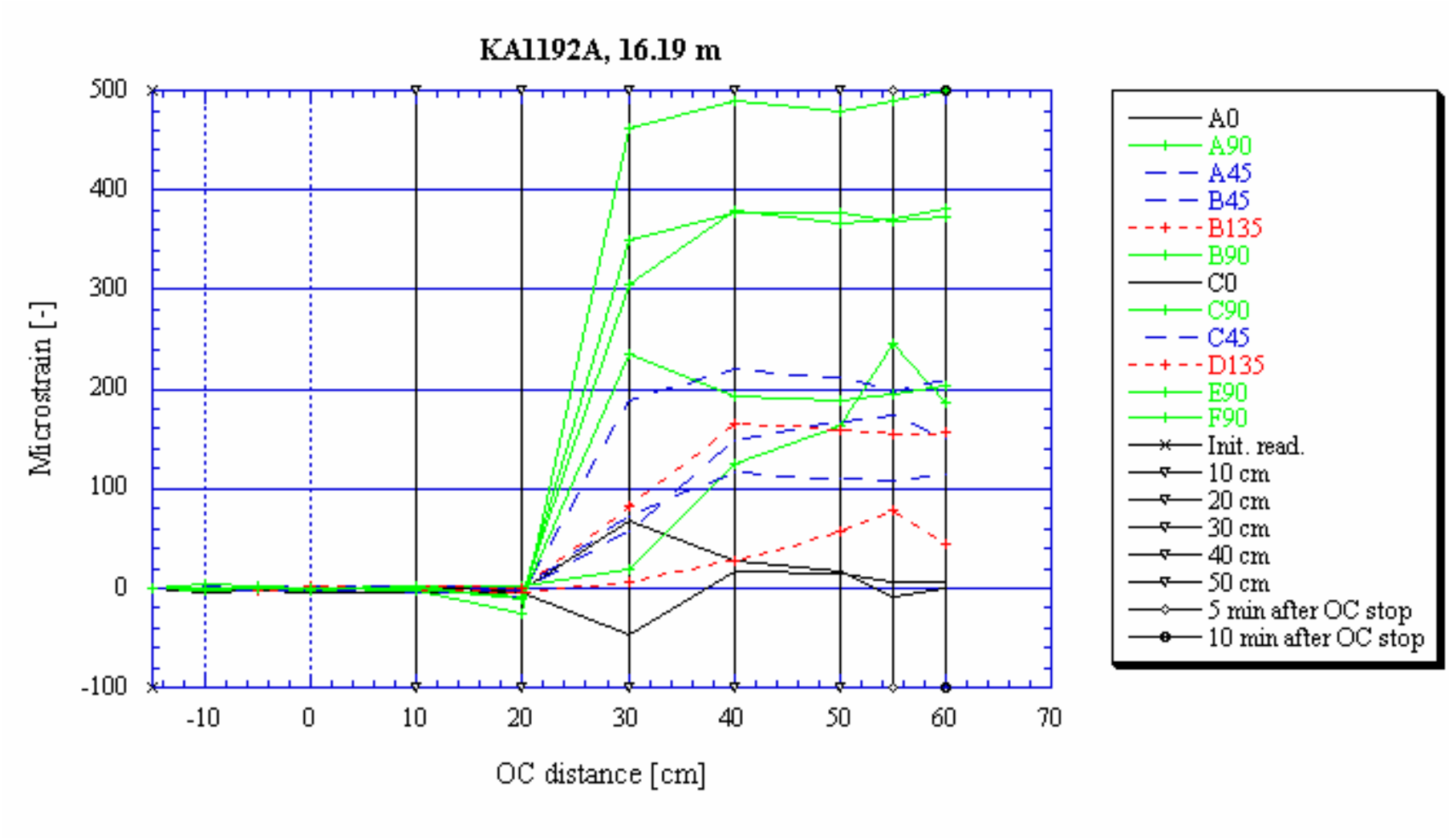
KA1192A, 16.19 m
Microstrain [-]
OC distance [cm]
500
400
300
200
100
0
-100
-10
0
10
20
30
40
50
60
70
A0
A90
A45
B45
B135
B90
C0
C90
C45
D135
E90
F90
Init. read.
10 cm
20 cm
30 cm
40 cm
50 cm
5 min after OC stop
10 min after OC stop

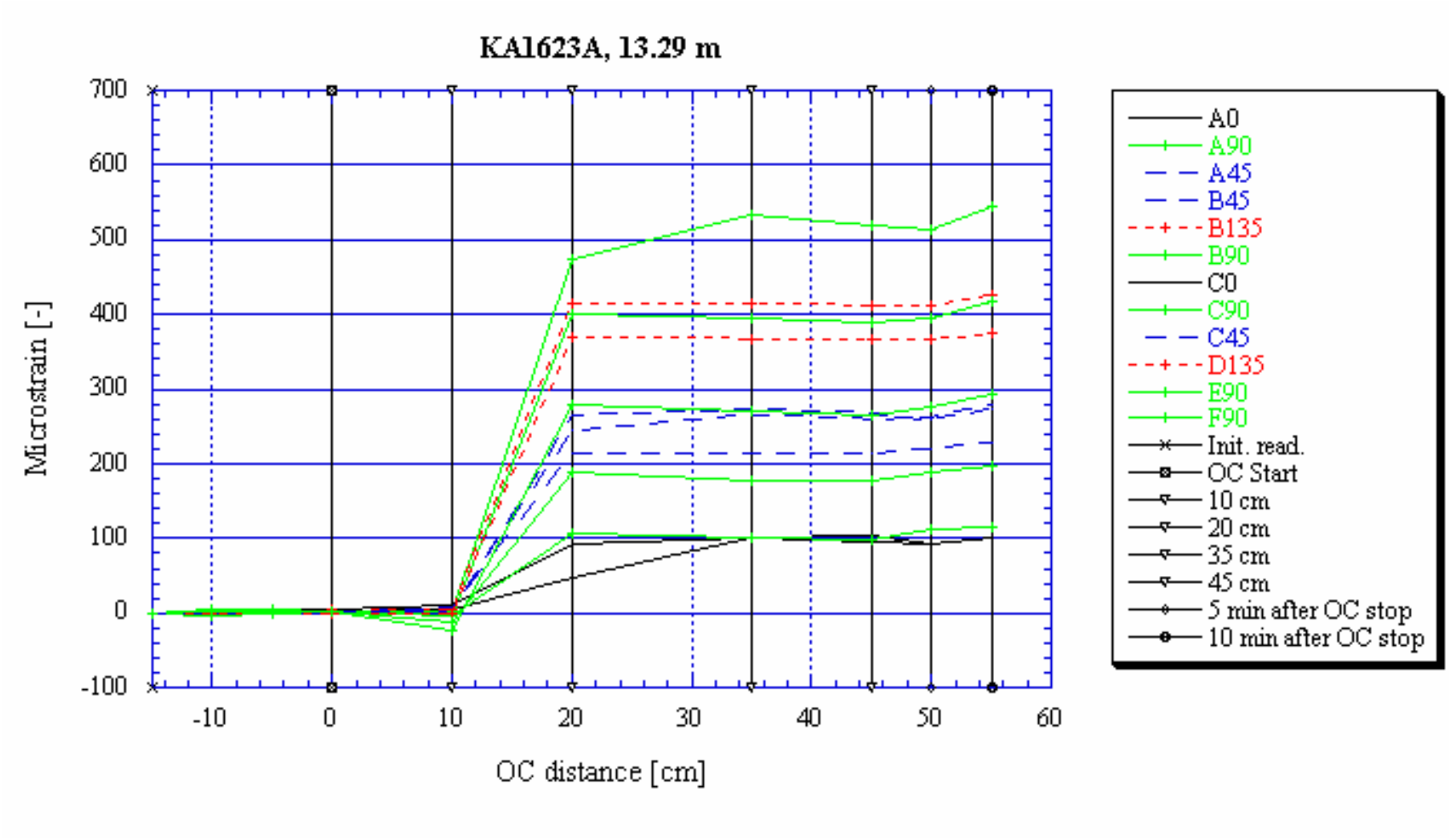
KA1623A, 13.29 m
Microstrain [-]
700
600
500
400
300
200
100
0
-100
-10
0
10
20
30
40
50
60
OC distance [cm]
A0
A90
A45
B45
B135
B90
C0
C90
C45
D135
E90
F90
Init. read.
OC Start
10 cm
20 cm
35 cm
45 cm
5 min after OC stop
10 min after OC stop

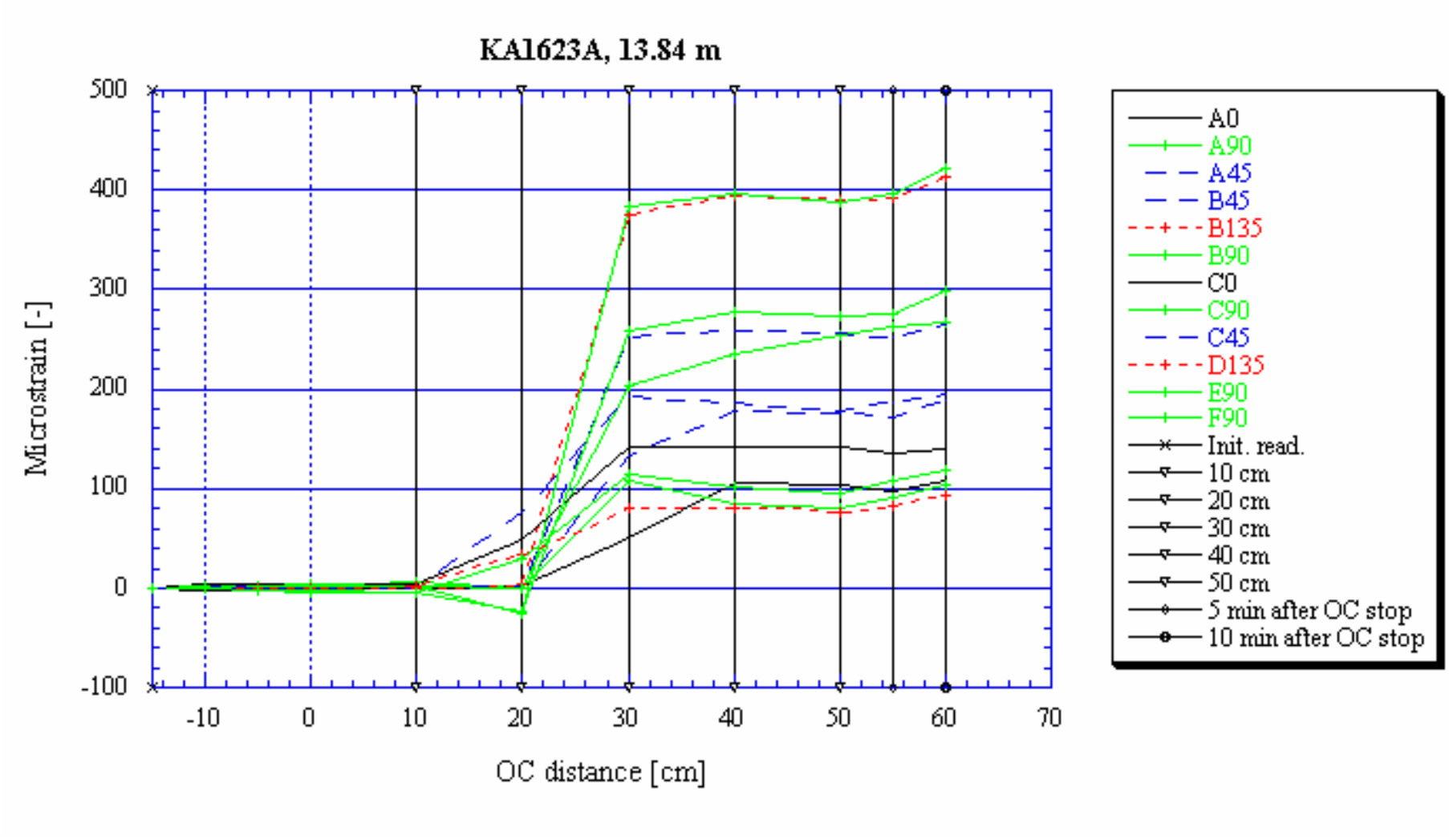
KA1623A, 13.84 m
Microstrain [-]
500
400
300
200
100
0
-100
-10
0
10
20
30
40
50
60
70
OC distance [cm]
A0
A90
A45
B45
B135
B90
C0
C90
C45
D135
E90
F90
Init. read.
10 cm
20 cm
30 cm
40 cm
50 cm
5 min after OC stop
10 min after OC stop

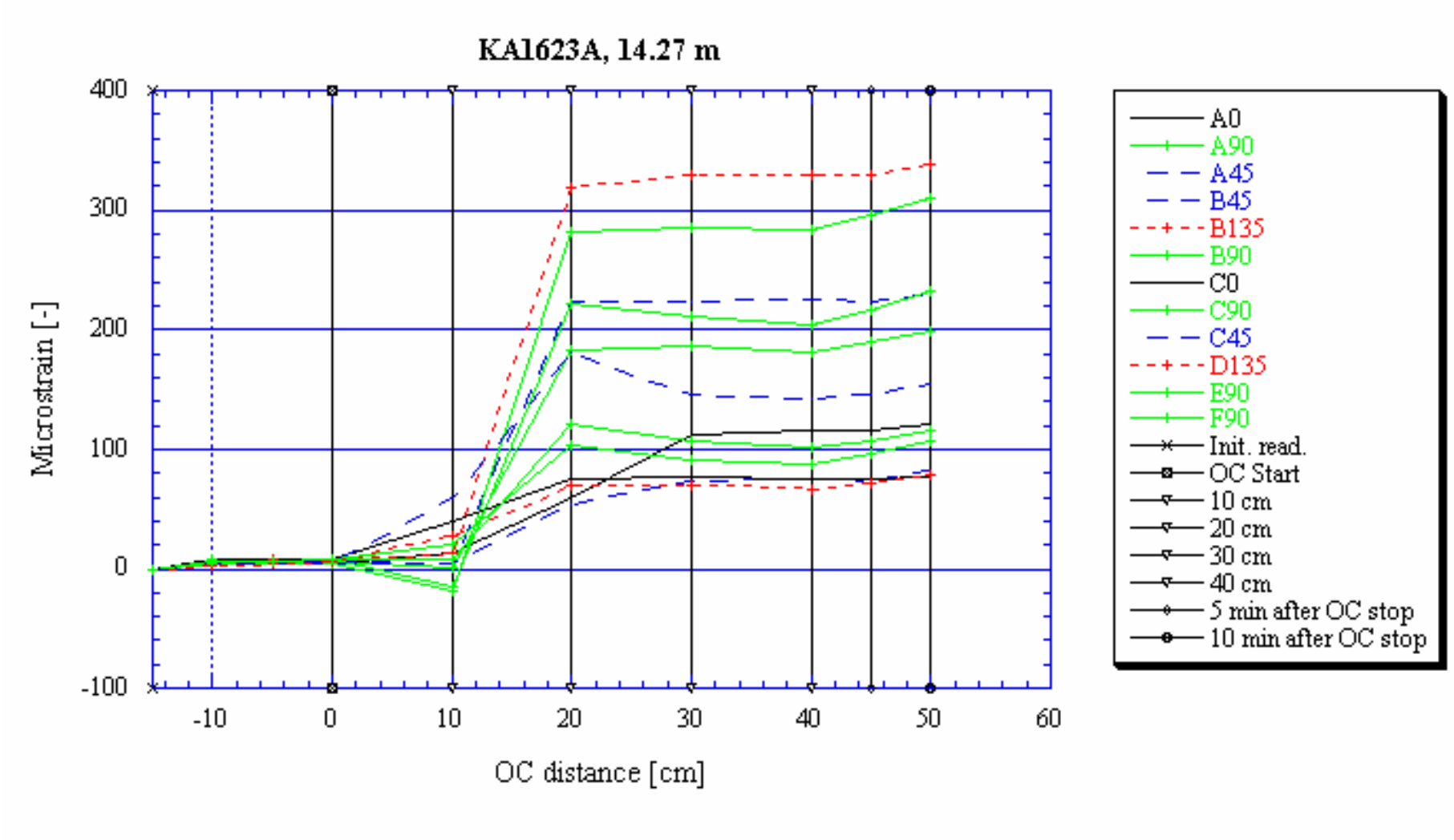
KA1623A, 14.27 m
Microstrain [-]
400
300
200
100
0
-100
-10
0
10
20
30
40
50
60
OC distance [cm]
A0
A90
A45
B45
B135
B90
C0
C90
C45
D135
E90
F90
Init. read.
OC Start
10 cm
20 cm
30 cm
40 cm
5 min after OC stop
10 min after OC stop

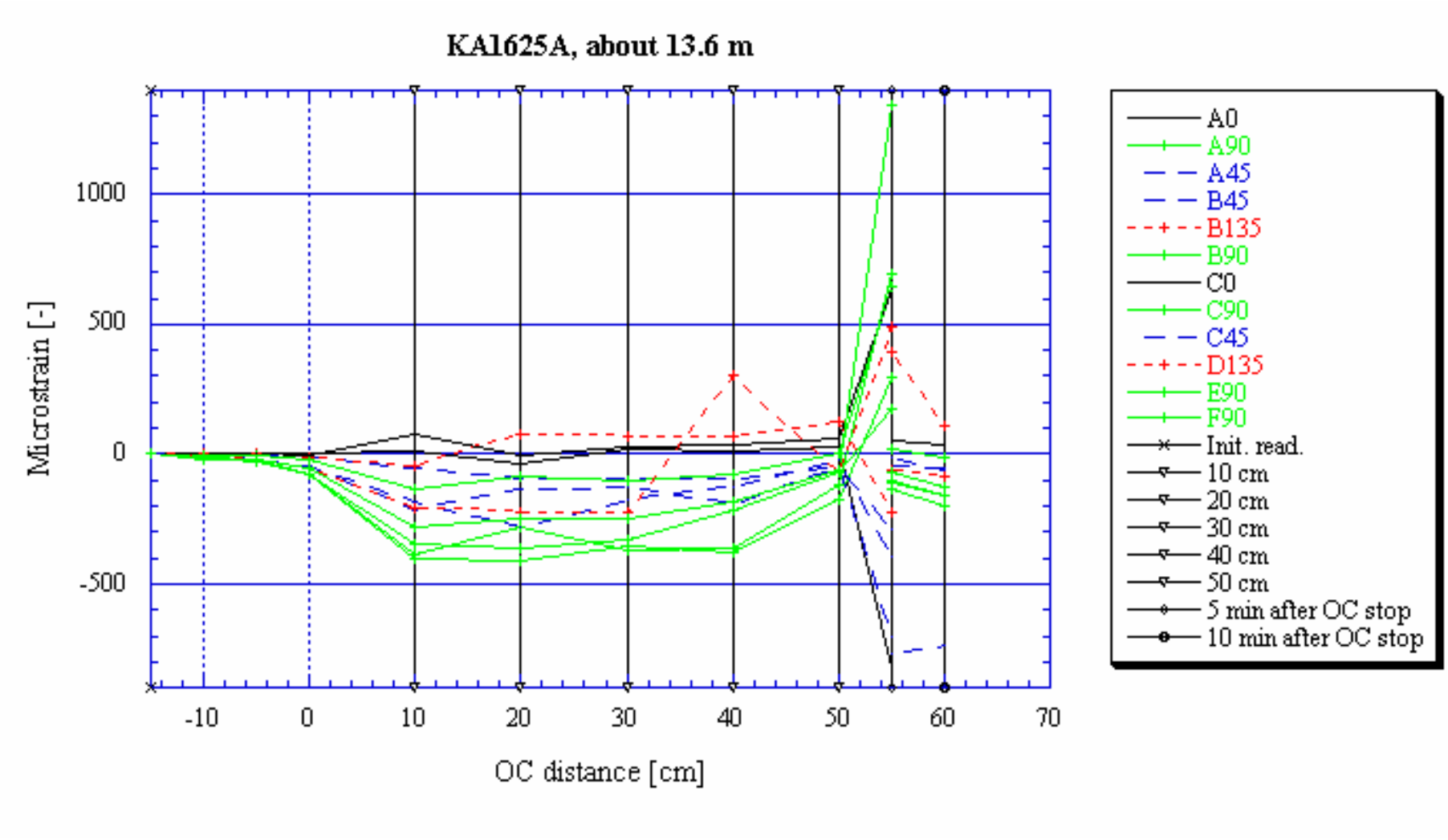
KA1625A, about 13.6 m
Microstrain [-]
1000
500
0
-500
-10
0
10
20
30
40
50
60
70
OC distance [cm]
A0
A90
A45
B45
B135
B90
C0
C90
C45
D135
E90
F90
Init. read.
10 cm
20 cm
30 cm
40 cm
50 cm
5 min after OC stop
10 min after OC stop

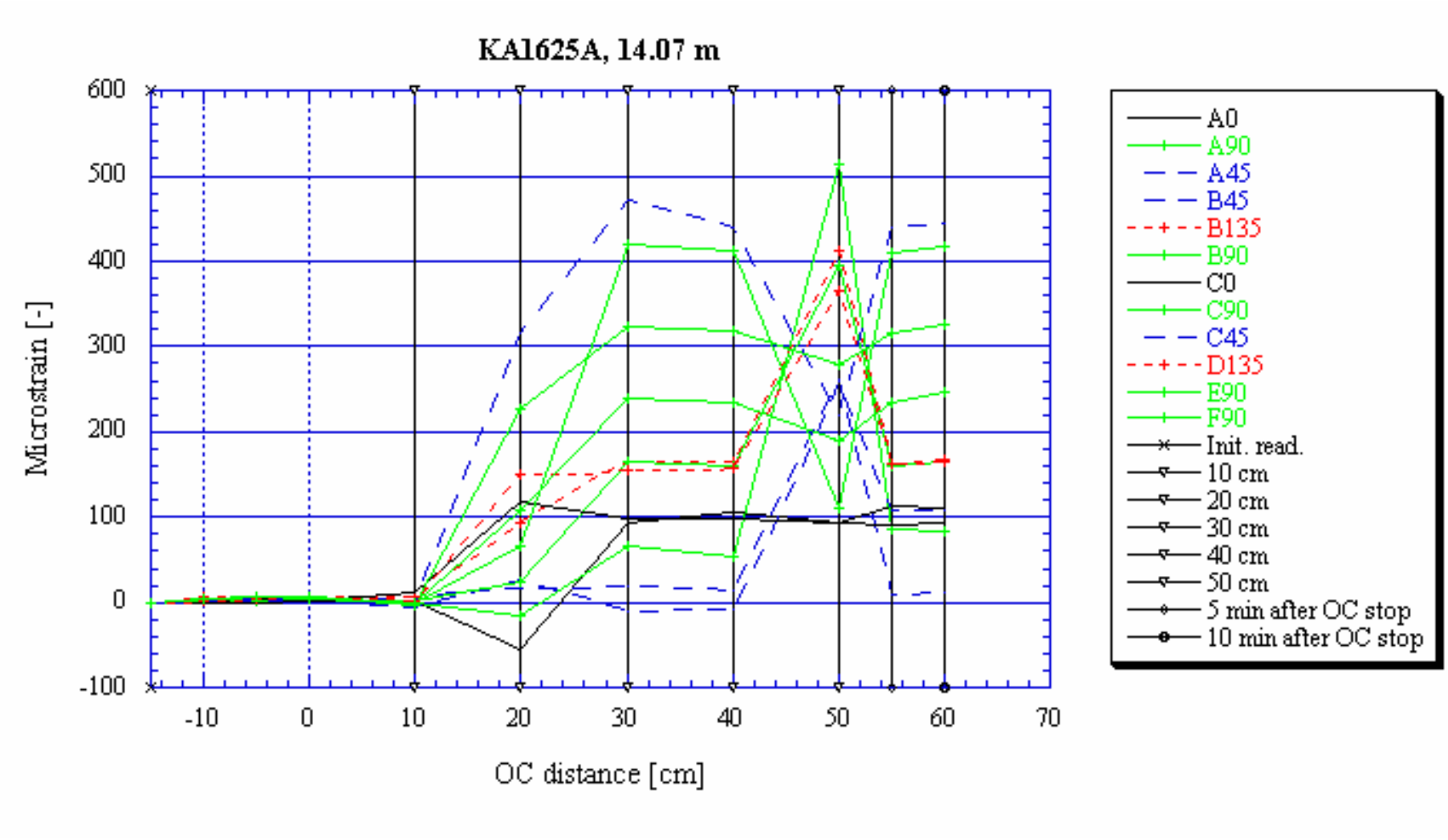
KA1625A, 14.07 m
Microstrain [-]
600
500
400
300
200
100
0
-100
-10
0
10
20
30
40
50
60
70
OC distance [cm]
A0
A90
A45
B45
B135
B90
C0
C90
C45
D135
E90
F90
Init. read.
10 cm
20 cm
30 cm
40 cm
50 cm
5 min after OC stop
10 min after OC stop

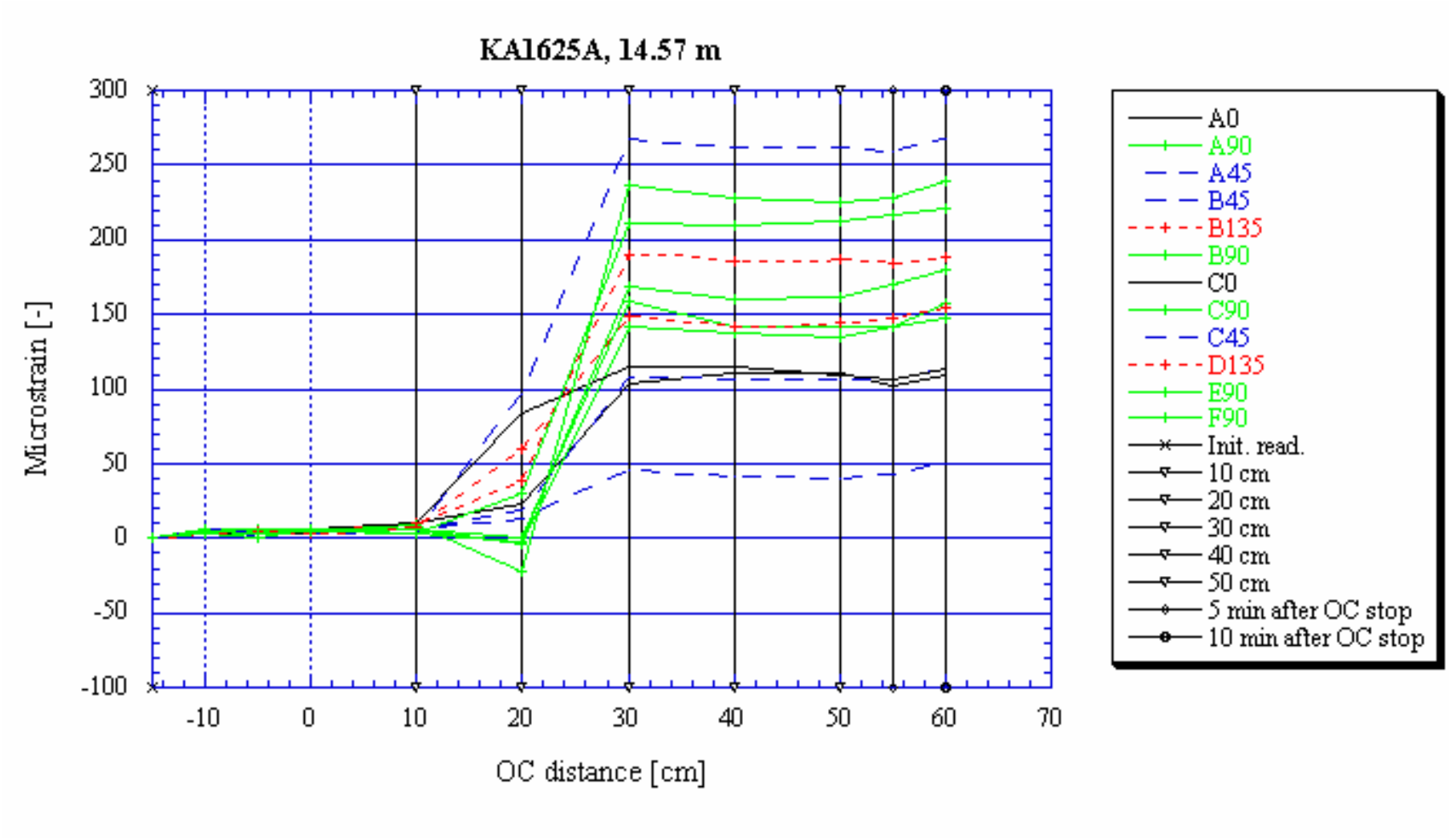
KA1625A, 14.57 m
Microstrain [-]
OC distance [cm]
300
250
200
150
100
50
0
-50
-100
-10
0
10
20
30
40
50
60
70
A0
A90
A45
B45
B135
B90
C0
C90
C45
D135
E90
F90
Init. read.
10 cm
20 cm
30 cm
40 cm
50 cm
5 min after OC stop
10 min after OC stop

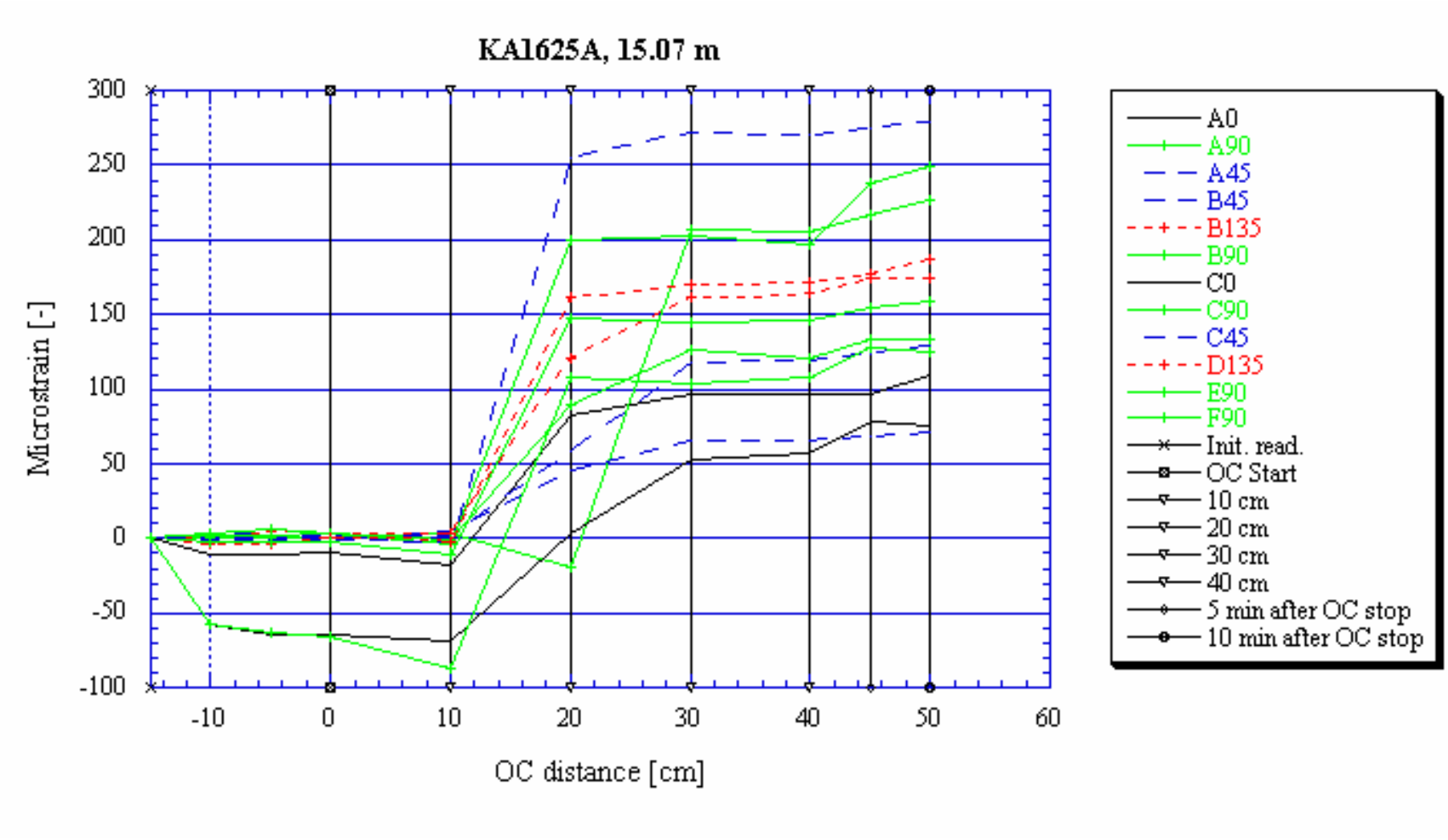
KA1625A, 15.07 m
Microstrain [-]
300
250
200
150
100
50
0
-50
-100
-10
0
10
20
30
40
50
60
OC distance [cm]
A0
A90
A45
B45
B135
B90
C0
C90
C45
D135
E90
F90
Init. read.
OC Start
10 cm
20 cm
30 cm
40 cm
5 min after OC stop
10 min after OC stop

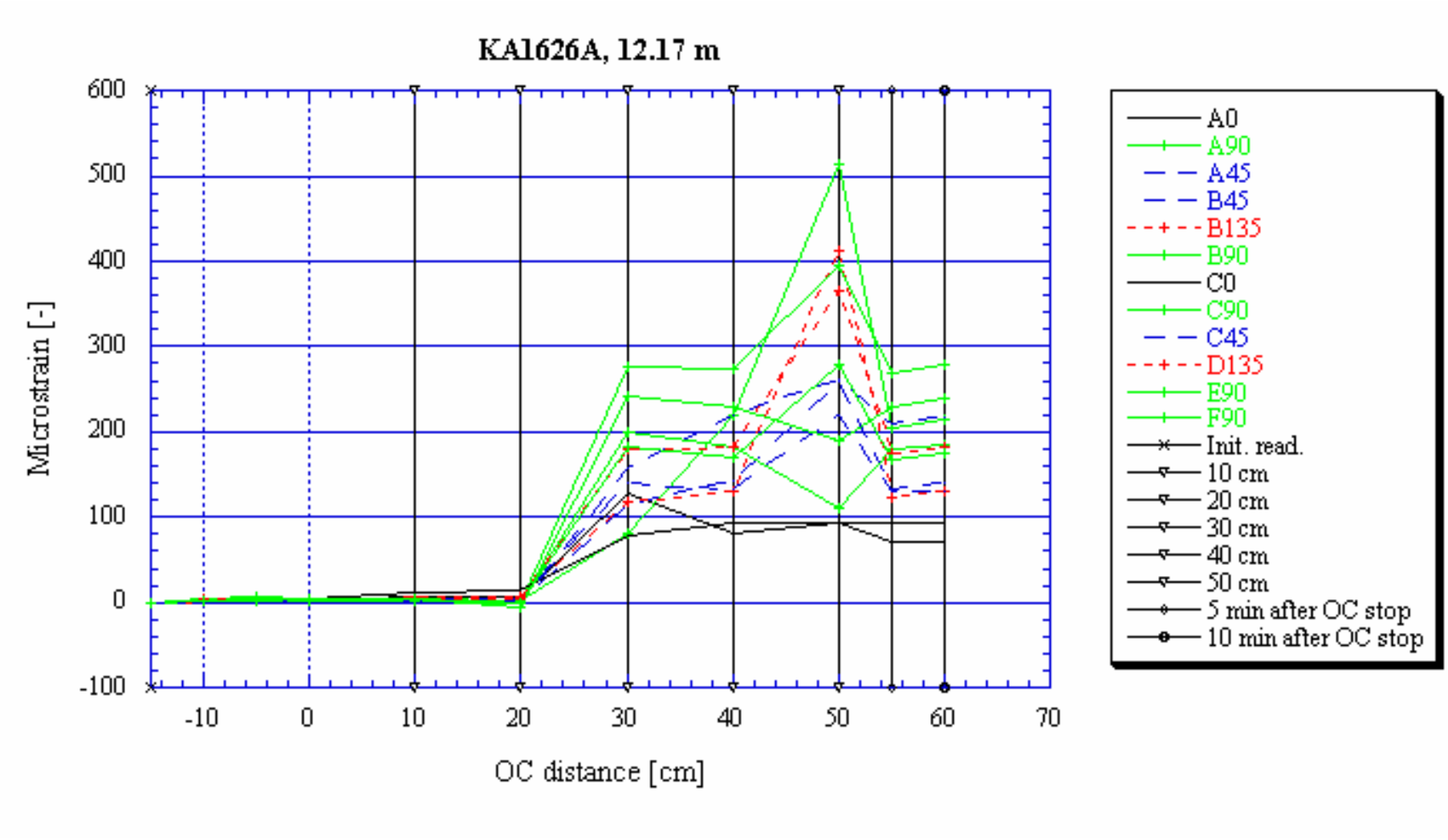
KA1626A, 12.17 m
Microstrain [-]
600
500
400
300
200
100
0
-100
-10
0
10
20
30
40
50
60
70
OC distance [cm]
A0
A90
A45
B45
B135
B90
C0
C90
C45
D135
E90
F90
Init. read.
10 cm
20 cm
30 cm
40 cm
50 cm
5 min after OC stop
10 min after OC stop

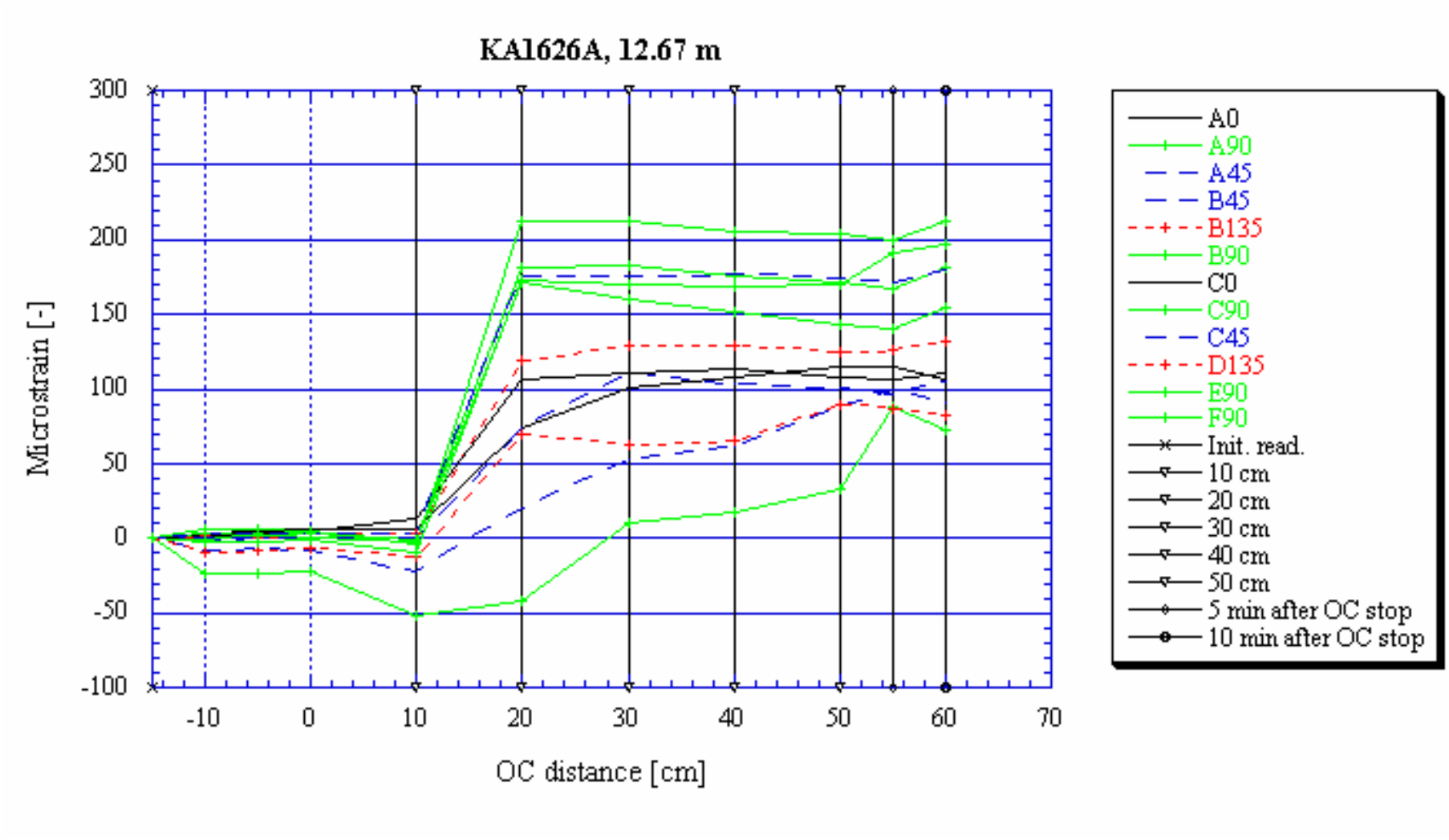
KA1626A, 12.67 m
Microstrain [-]
OC distance [cm]
300
250
200
150
100
50
0
-50
-100
-10
0
10
20
30
40
50
60
70
A0
A90
A45
B45
B135
B90
C0
C90
C45
D135
E90
F90
Init. read.
10 cm
20 cm
30 cm
40 cm
50 cm
5 min after OC stop
10 min after OC stop

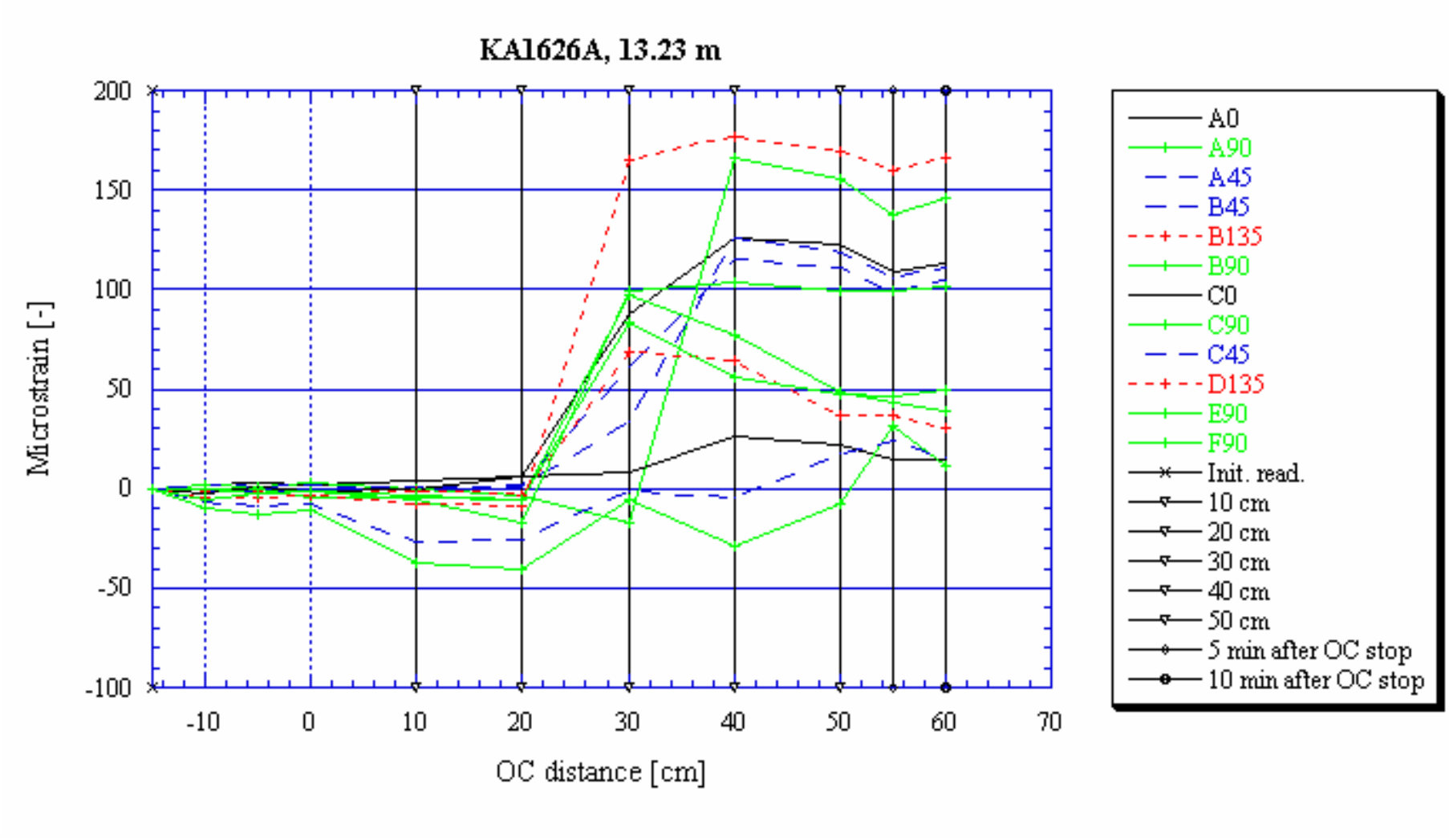
KA1626A, 13.23 m
Microstrain [-]
200
150
100
50
0
-50
-100
-10
0
10
20
30
40
50
60
70
OC distance [cm]
A0
A90
A45
B45
B135
B90
C0
C90
C45
D135
E90
F90
Init. read.
10 cm
20 cm
30 cm
40 cm
50 cm
5 min after OC stop
10 min after OC stop

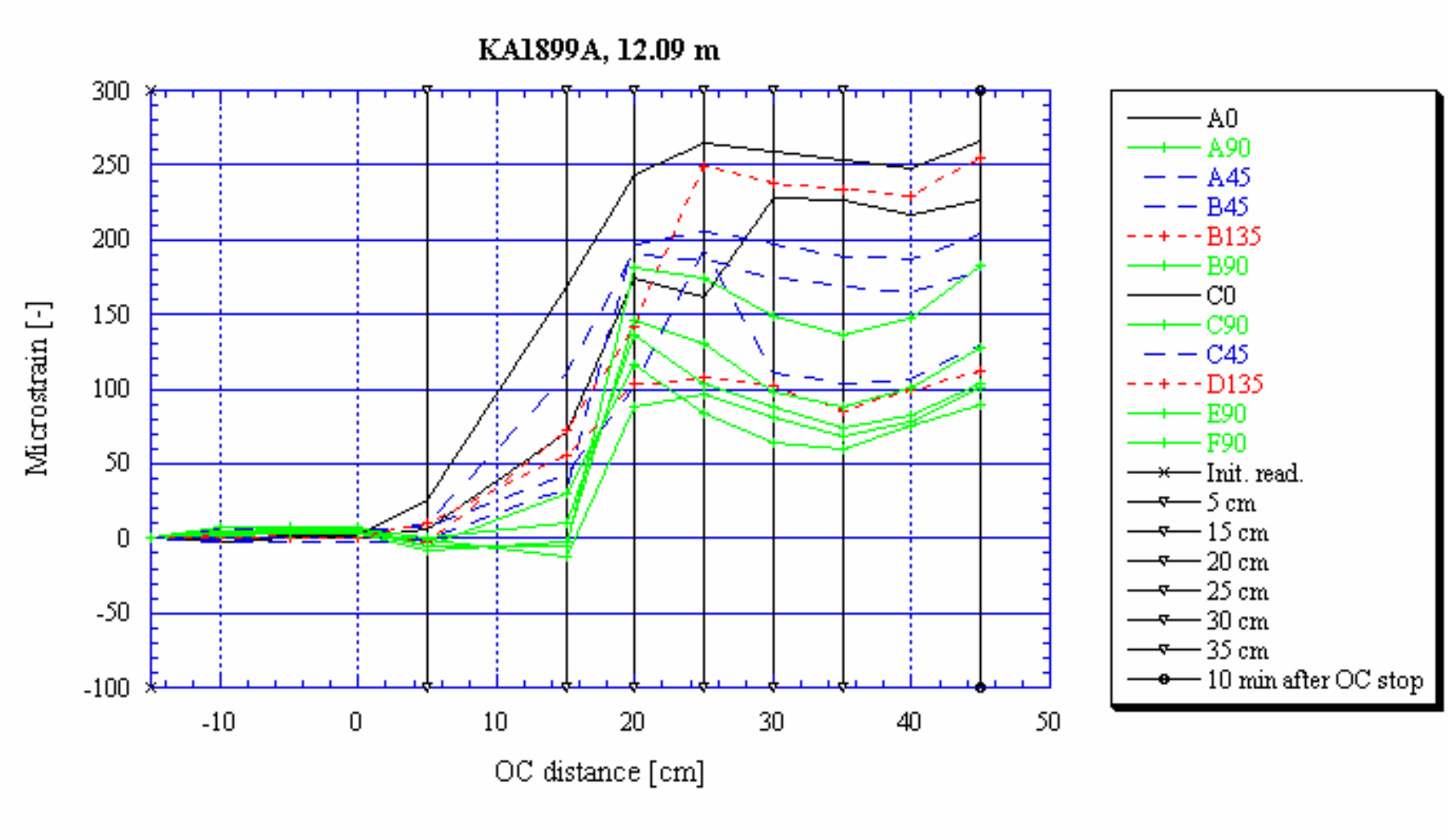
KA1899A, 12.09 m
Microstrain [-]
300
250
200
150
100
50
0
-50
-100
-10
0
10
20
30
40
50
OC distance [cm]
A0
A90
A45
B45
B135
B90
C0
C90
C45
D135
E90
F90
Init. read.
5 cm
15 cm
20 cm
25 cm
30 cm
35 cm
10 min after OC stop

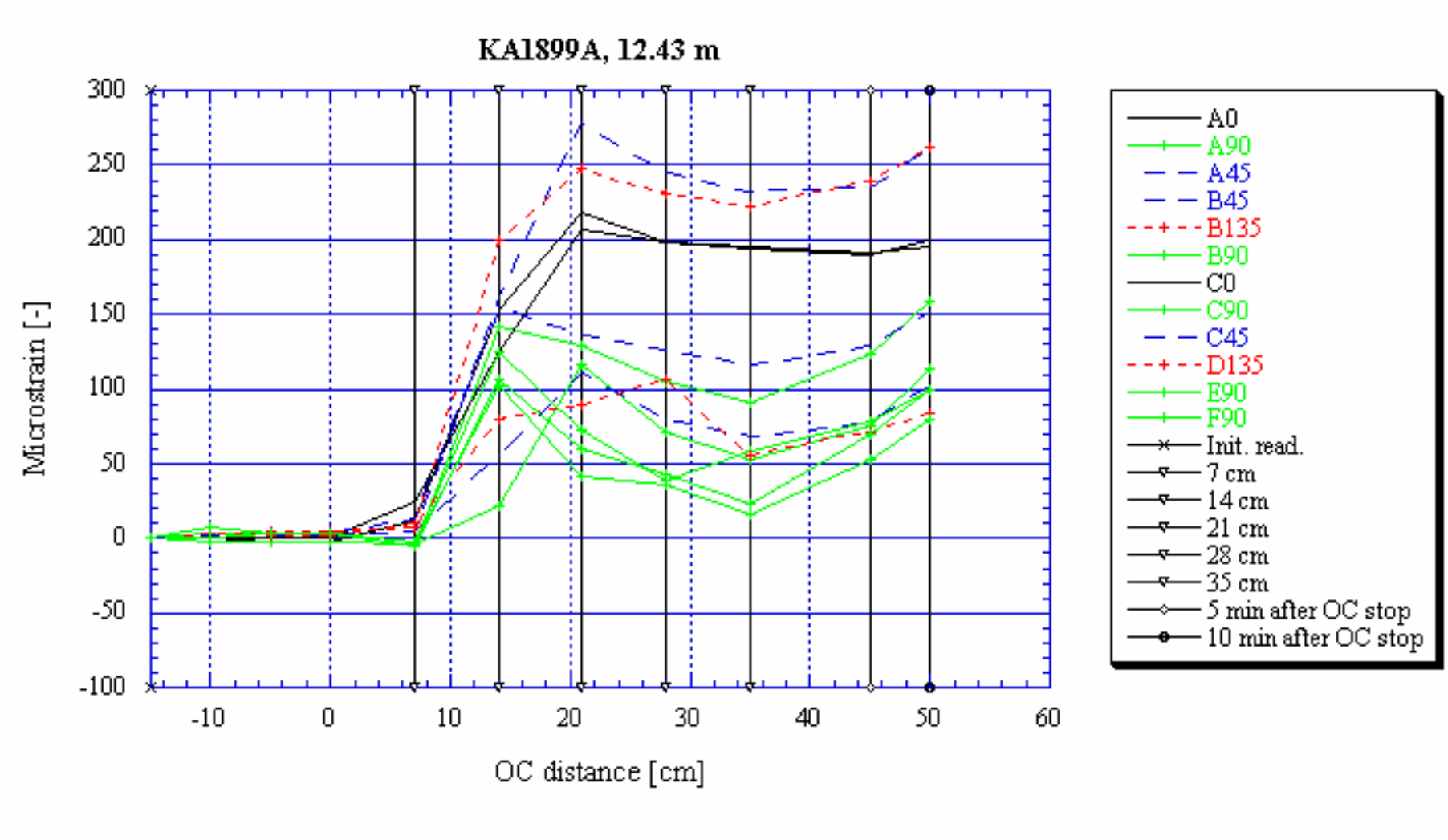
KA1899A, 12.43 m
Microstrain [-]
300
250
200
150
100
50
0
-50
-100
-10
0
10
20
30
40
50
60
OC distance [cm]
A0
A90
A45
B45
B135
B90
C0
C90
C45
D135
E90
F90
Init. read.
7 cm
14 cm
21 cm
28 cm
35 cm
5 min after OC stop
10 min after OC stop

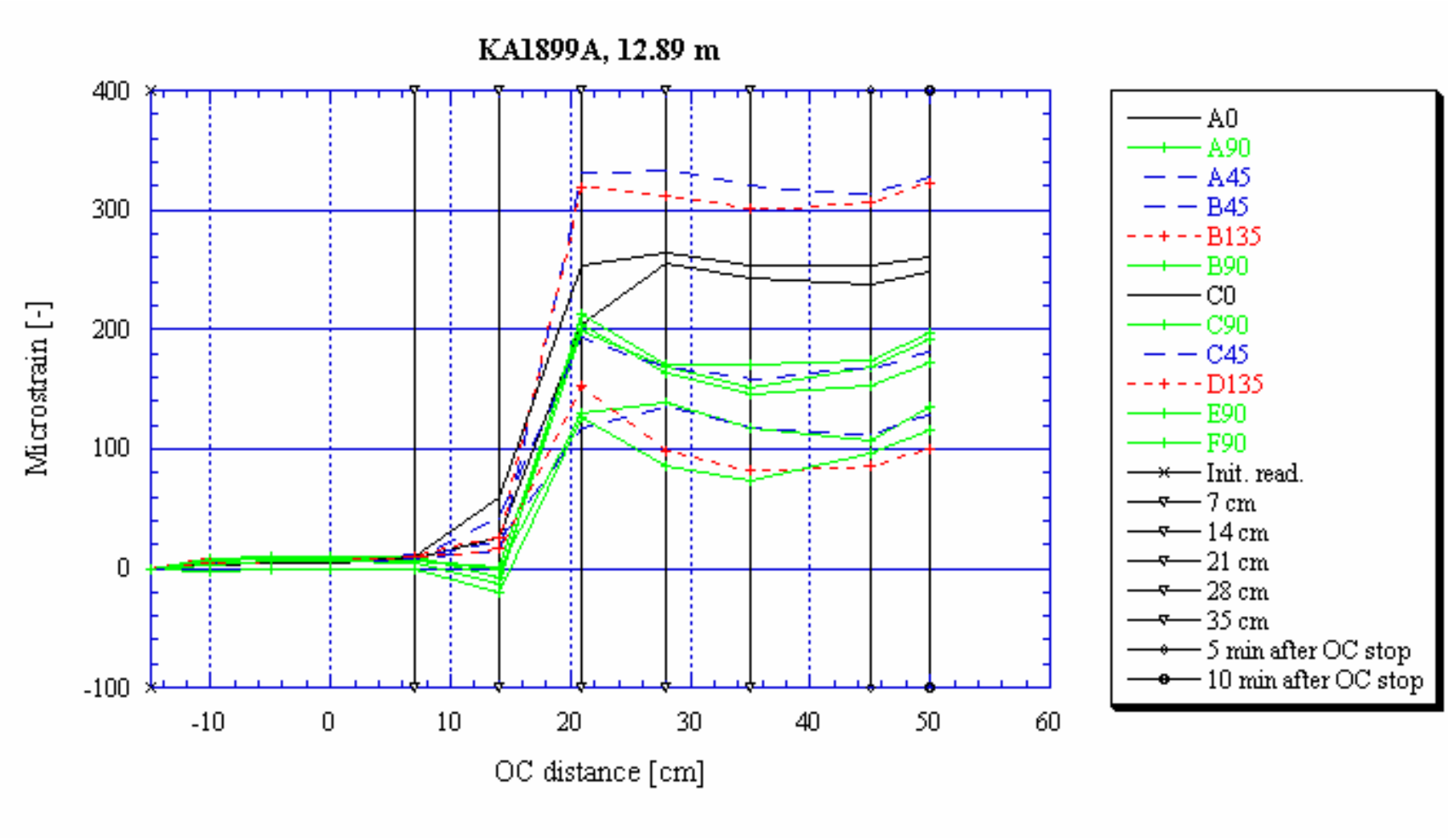
KA1899A, 12.89 m
Microstrain [-]
400
300
200
100
0
-100
-10
0
10
20
30
40
50
60
OC distance [cm]
A0
A90
A45
B45
B135
B90
C0
C90
C45
D135
E90
F90
Init. read.
7 cm
14 cm
21 cm
28 cm
35 cm
5 min after OC stop
10 min after OC stop

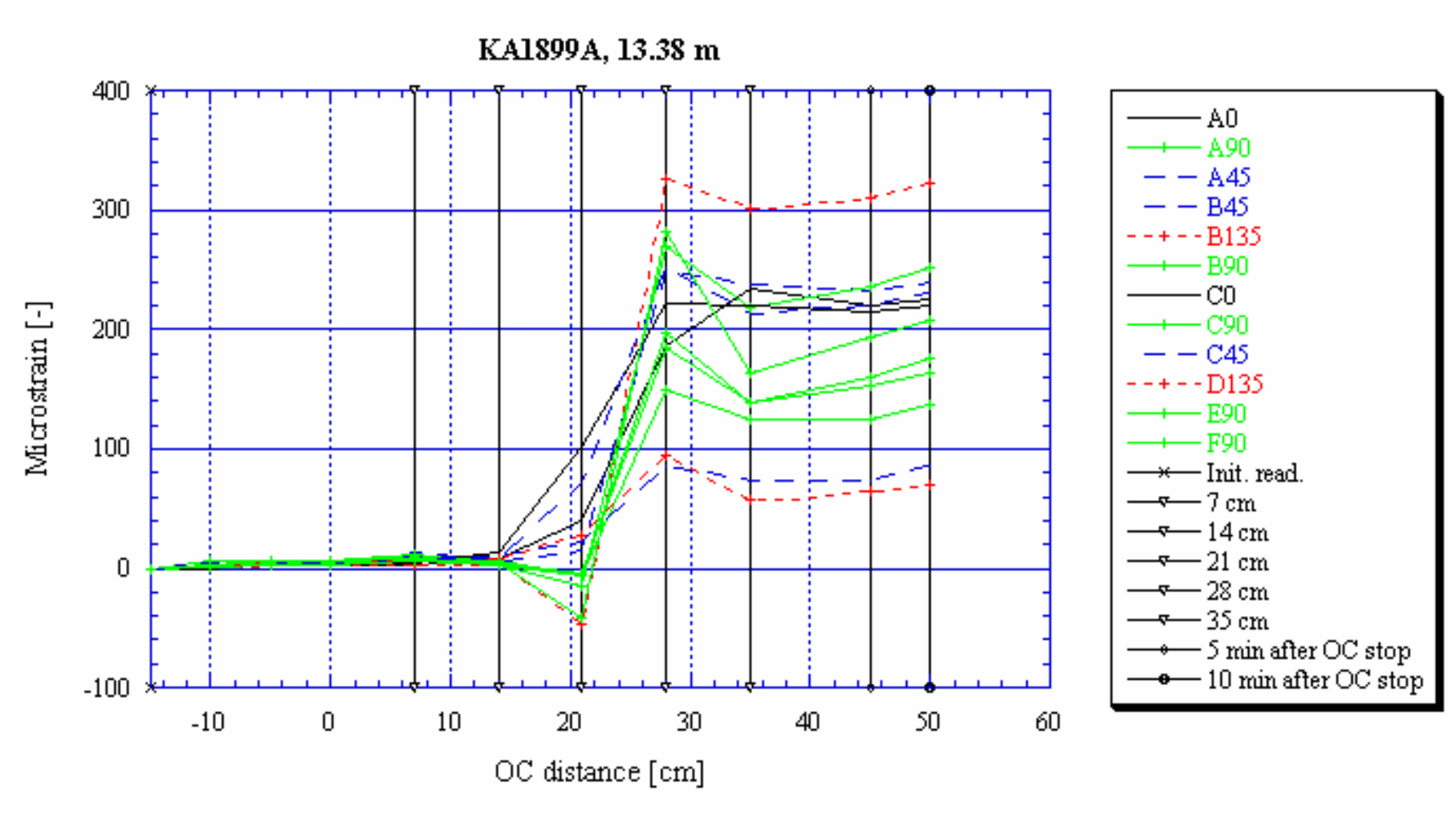
KA1899A, 13.38 m
Microstrain [-]
400
300
200
100
0
-100
-10
0
10
20
30
40
50
60
OC distance [cm]
A0
A90
A45
B45
B135
B90
C0
C90
C45
D135
E90
F90
Init. read.
7 cm
14 cm
21 cm
28 cm
35 cm
5 min after OC stop
10 min after OC stop

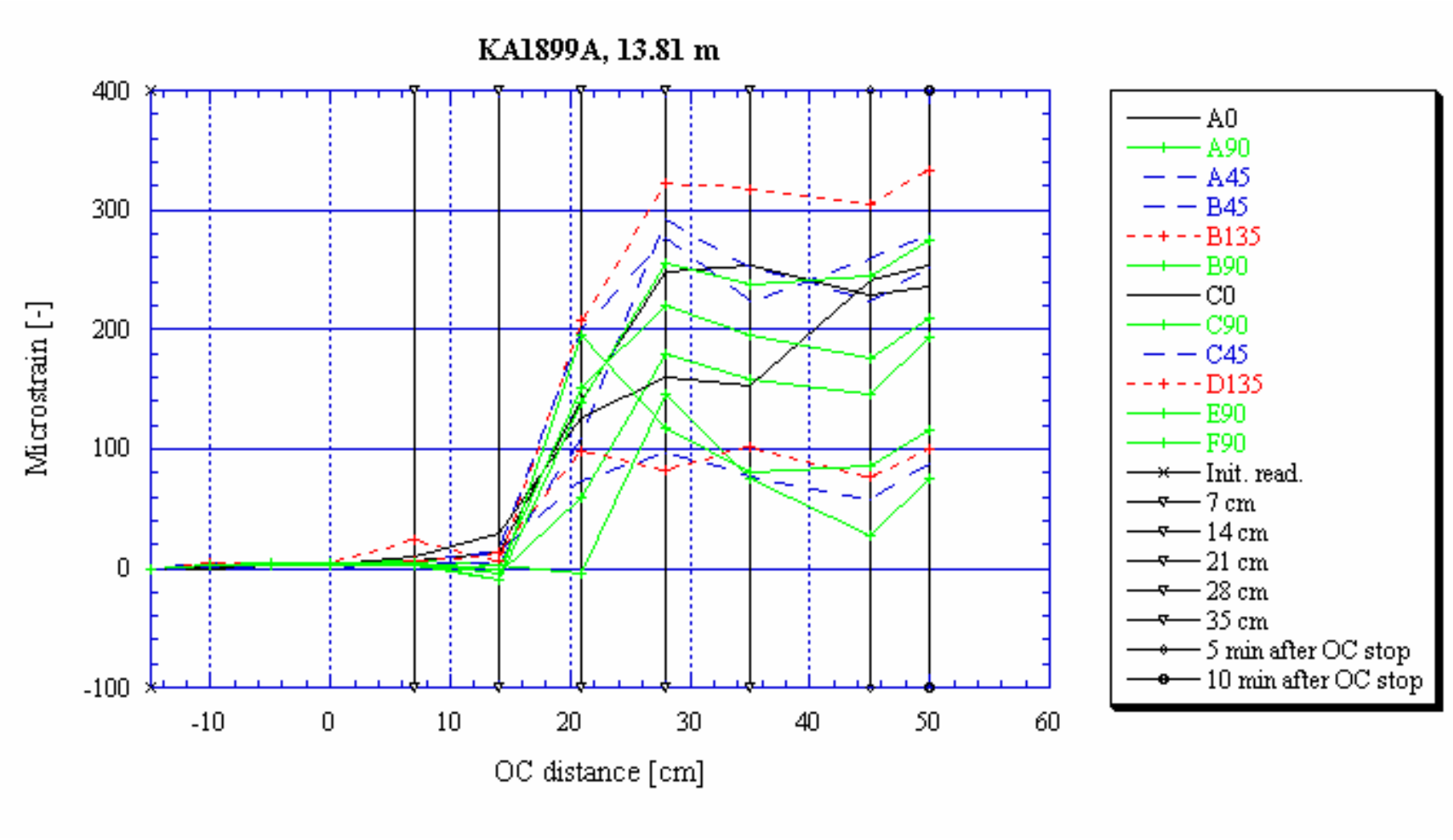
KA1899A, 13.81 m
Microstrain [-]
400
300
200
100
0
-100
-10
0
10
20
30
40
50
60
OC distance [cm]
A0
A90
A45
B45
B135
B90
C0
C90
C45
D135
E90
F90
Init. read.
7 cm
14 cm
21 cm
28 cm
35 cm
5 min after OC stop
10 min after OC stop

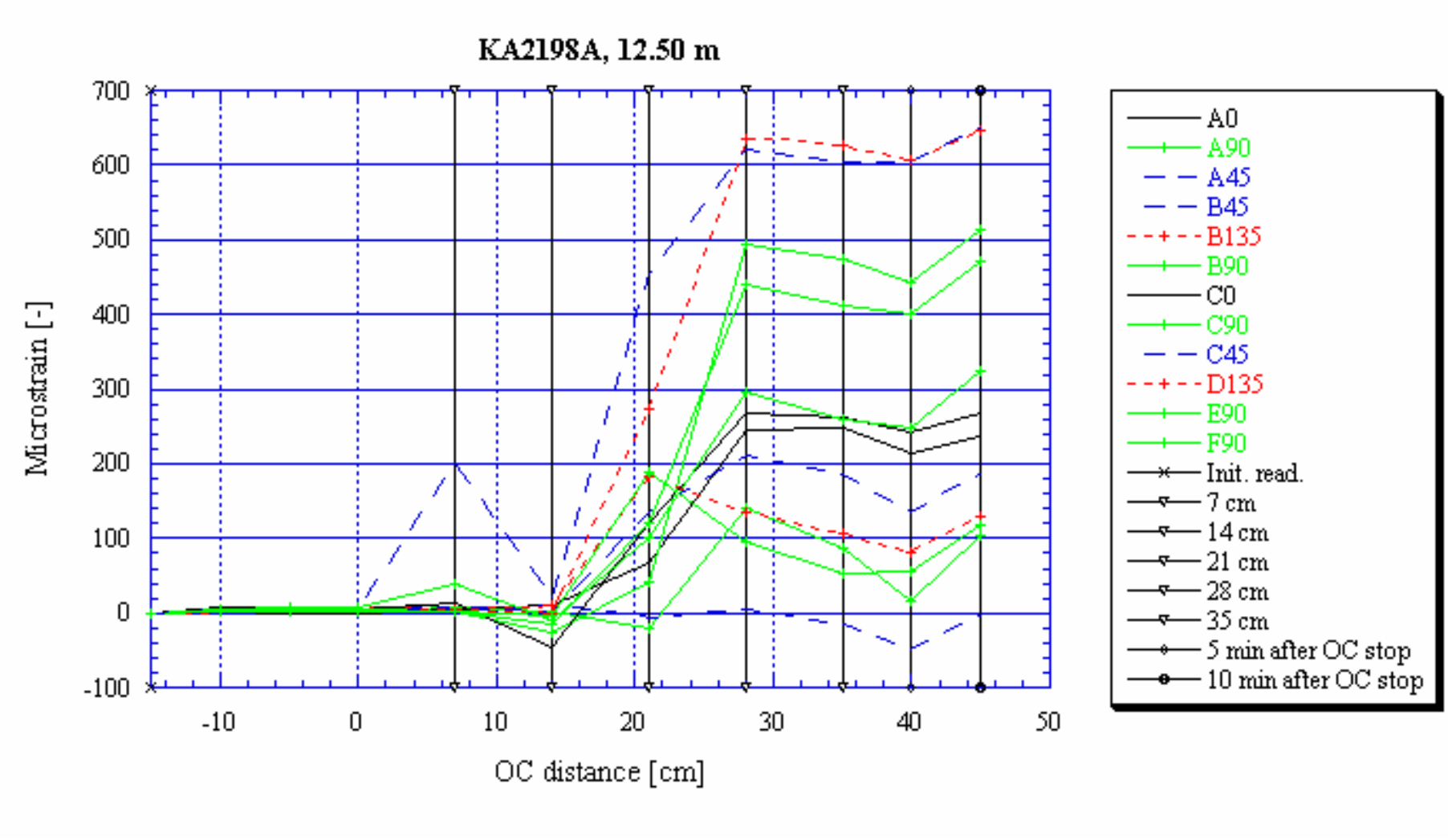
KA2198A, 12.50 m
Microstrain [-]
700
600
500
400
300
200
100
0
-100
-10
0
10
20
30
40
50
OC distance [cm]
A0
A90
A45
B45
B135
B90
C0
C90
C45
D135
E90
F90
Init. read.
7 cm
14 cm
21 cm
28 cm
35 cm
5 min after OC stop
10 min after OC stop

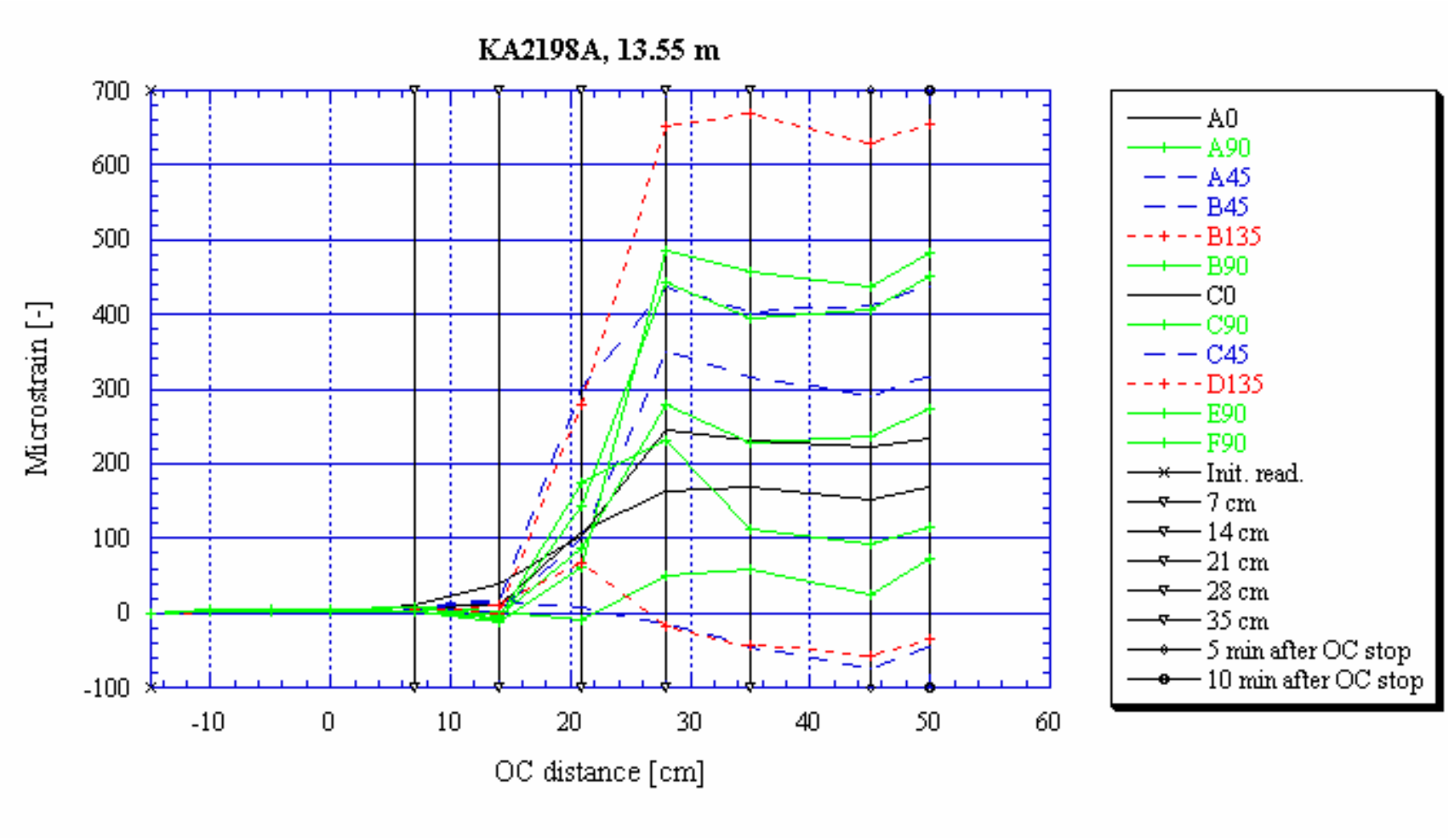
KA2198A, 13.55 m
Microstrain [-]
700
600
500
400
300
200
100
0
-100
-10
0
10
20
30
40
50
60
OC distance [cm]
A0
A90
A45
B45
B135
B90
C0
C90
C45
D135
E90
F90
Init. read.
7 cm
14 cm
21 cm
28 cm
35 cm
5 min after OC stop
10 min after OC stop

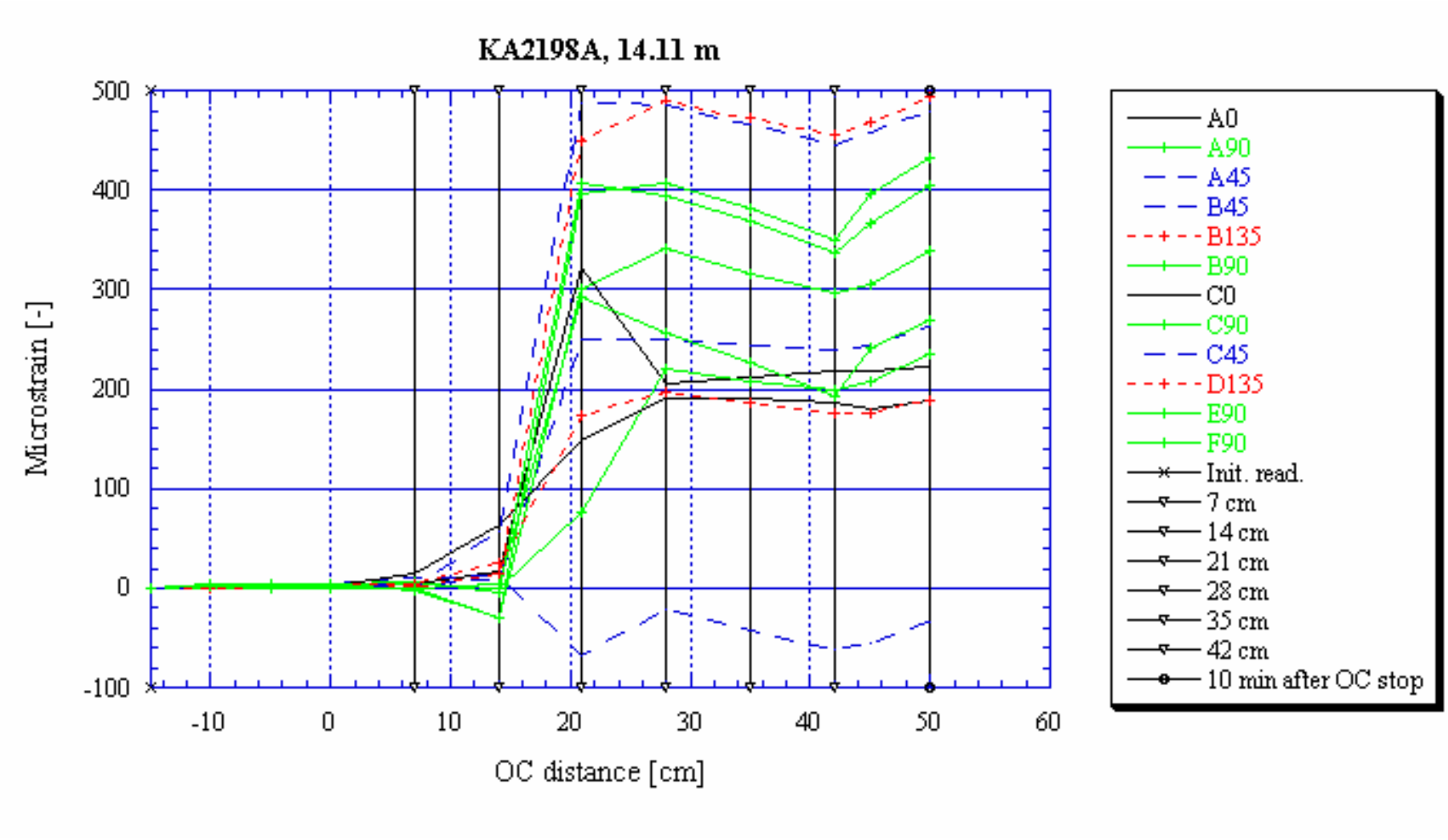
KA2198A, 14.11 m
Microstrain [-]
500
400
300
200
100
0
-100
-10
0
10
20
30
40
50
60
OC distance [cm]
A0
A90
A45
B45
B135
B90
C0
C90
C45
D135
E90
F90
Init. read.
7 cm
14 cm
21 cm
28 cm
35 cm
42 cm
10 min after OC stop

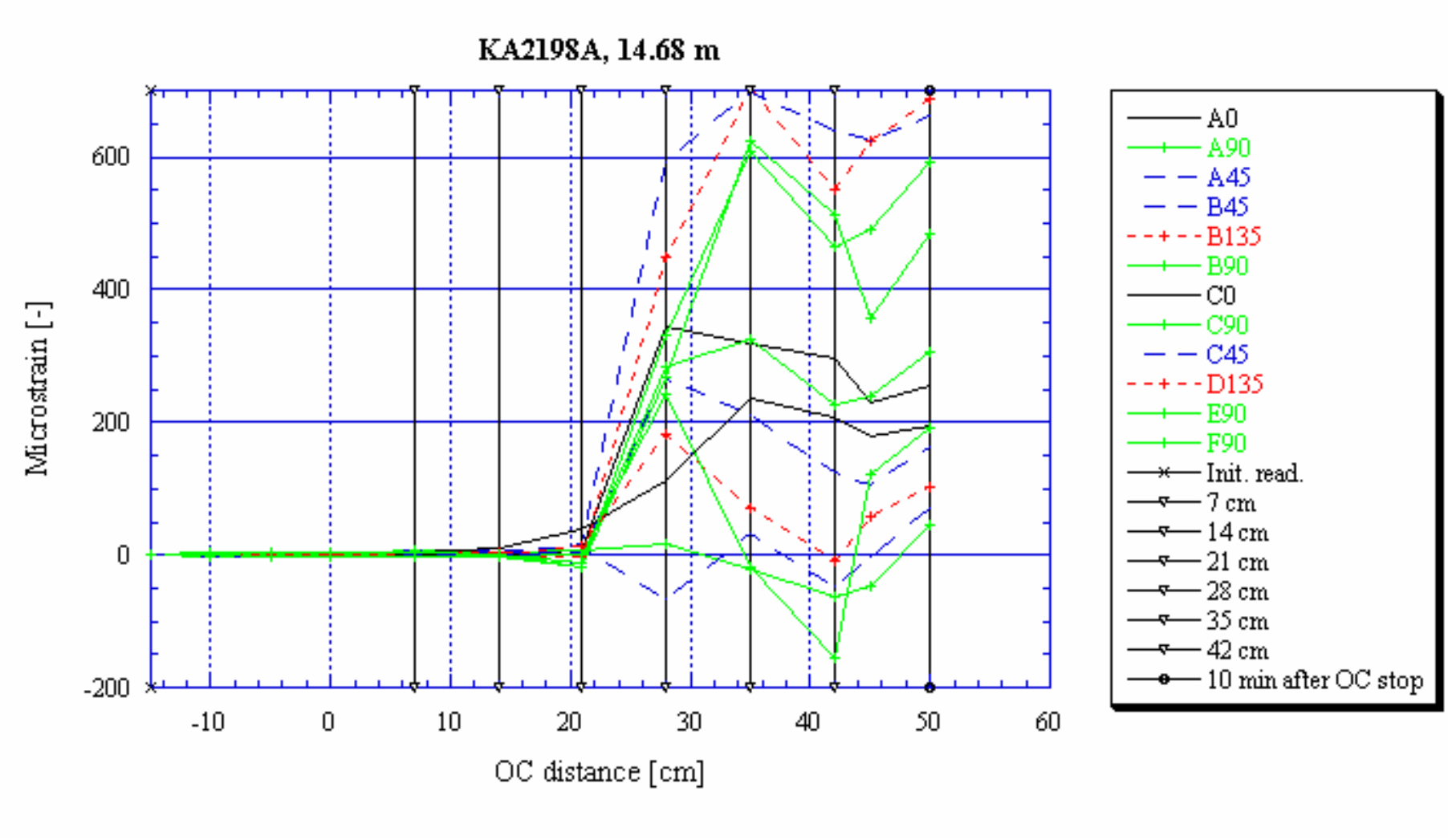
KA2198A, 14.68 m
Microstrain [-]
600
400
200
0
-200
-10
0
10
20
30
40
50
60
OC distance [cm]
A0
A90
A45
B45
B135
B90
C0
C90
C45
D135
E90
F90
Init. read.
7 cm
14 cm
21 cm
28 cm
35 cm
42 cm
10 min after OC stop

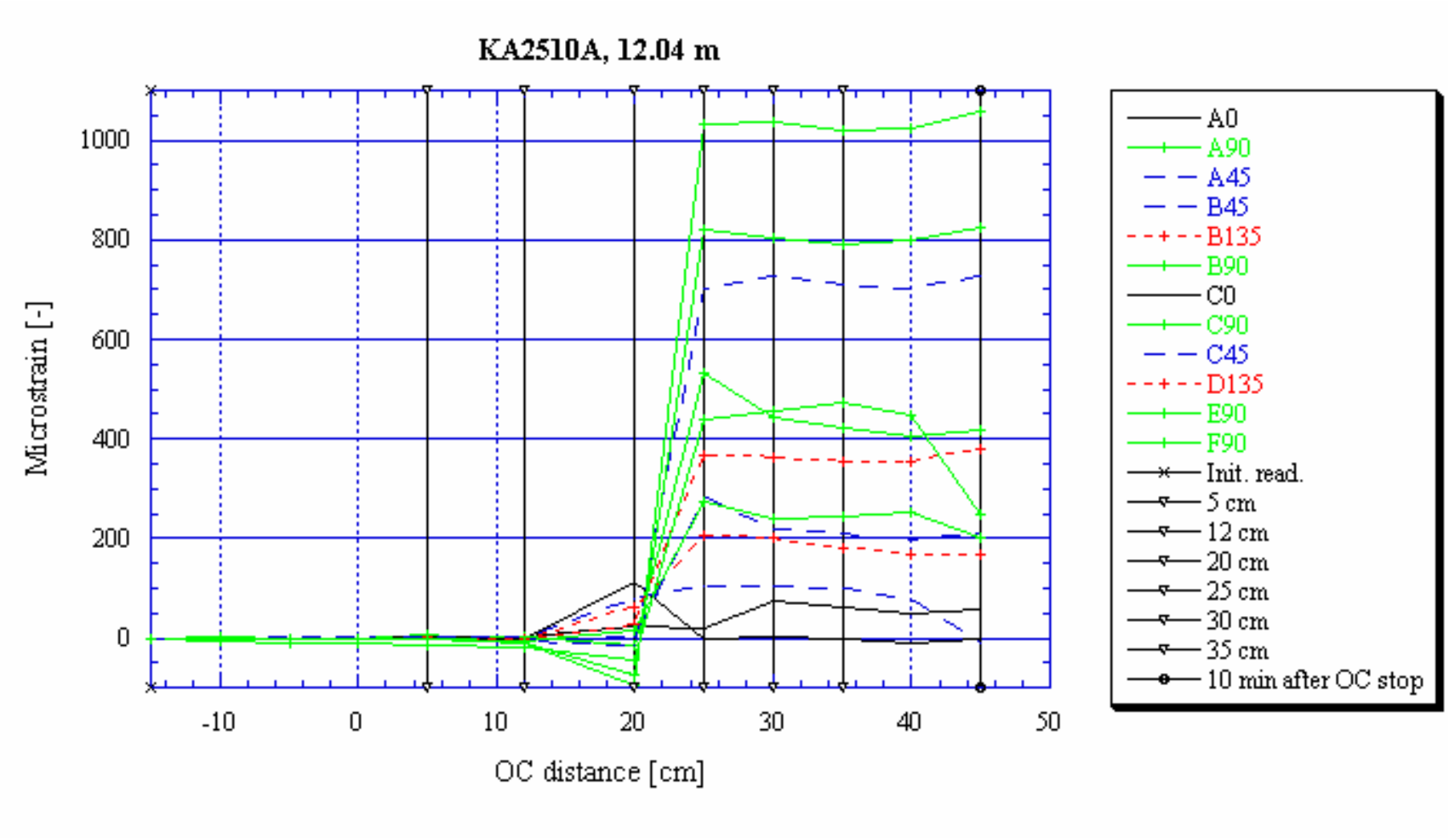
KA2510A, 12.04 m
Microstrain [-]
1000
800
600
400
200
0
-10
0
10
20
30
40
50
OC distance [cm]
A0
A90
A45
B45
B135
B90
C0
C90
C45
D135
E90
F90
Init. read.
5 cm
12 cm
20 cm
25 cm
30 cm
35 cm
10 min after OC stop

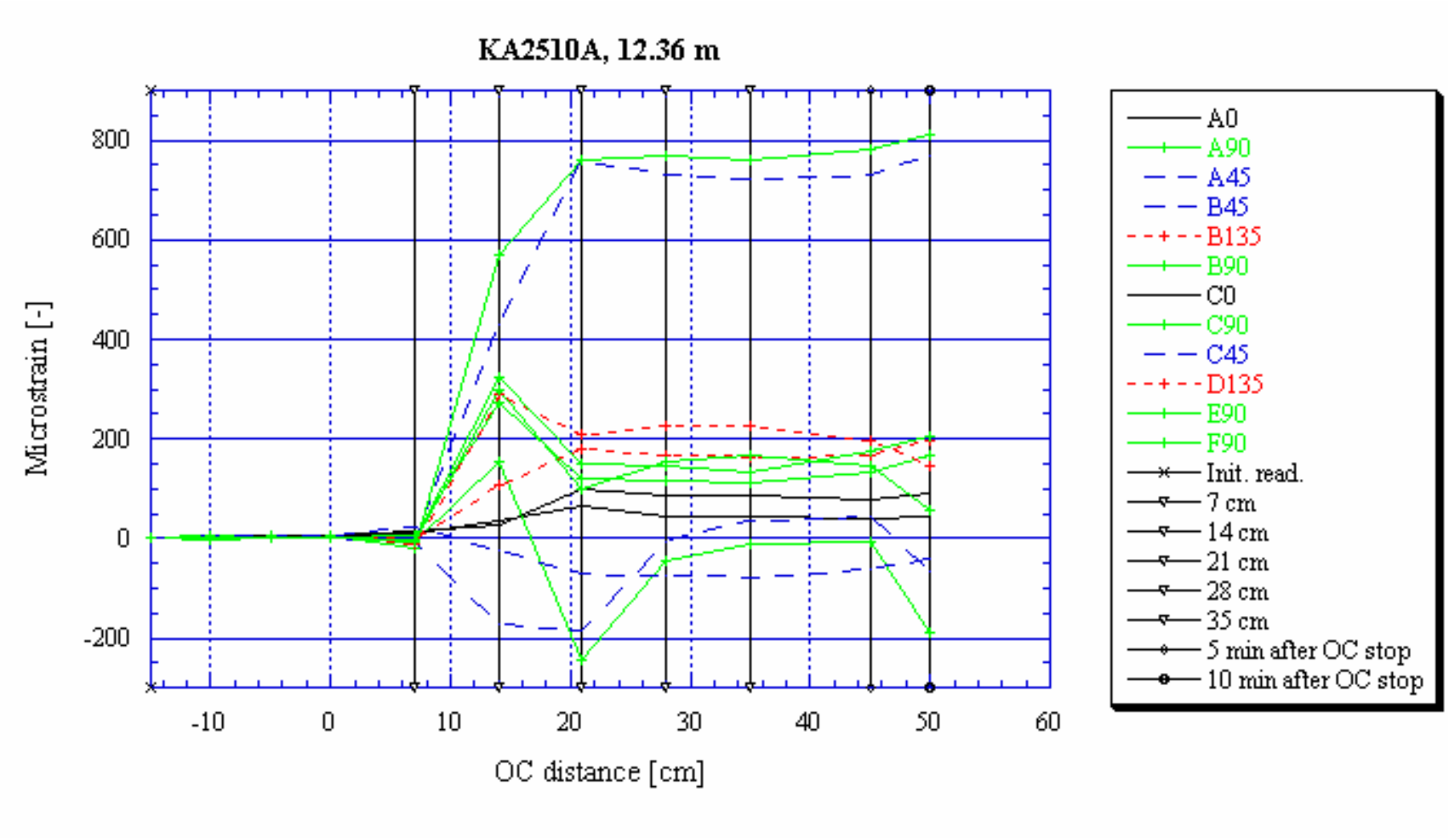
KA2510A, 12.36 m
Microstrain [-]
800
600
400
200
0
-200
-10
0
10
20
30
40
50
60
OC distance [cm]
A0
A90
A45
B45
B135
B90
C0
C90
C45
D135
E90
F90
Init. read.
7 cm
14 cm
21 cm
28 cm
35 cm
5 min after OC stop
10 min after OC stop

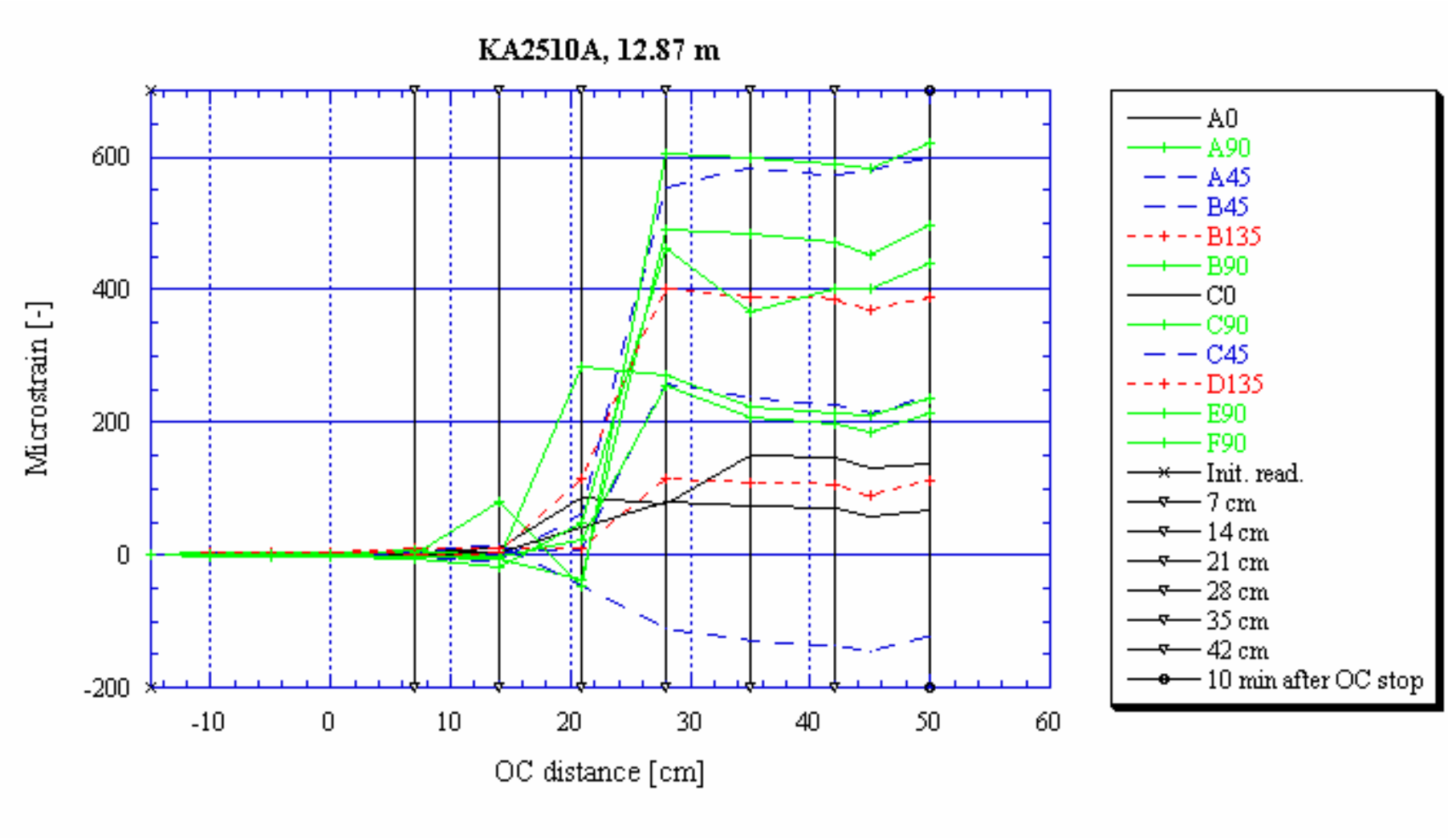
KA2510A, 12.87 m
Microstrain [-]
600
400
200
0
-200
-10
0
10
20
30
40
50
60
OC distance [cm]
A0
A90
A45
B45
B135
B90
C0
C90
C45
D135
E90
F90
Init. read.
7 cm
14 cm
21 cm
28 cm
35 cm
42 cm
10 min after OC stop

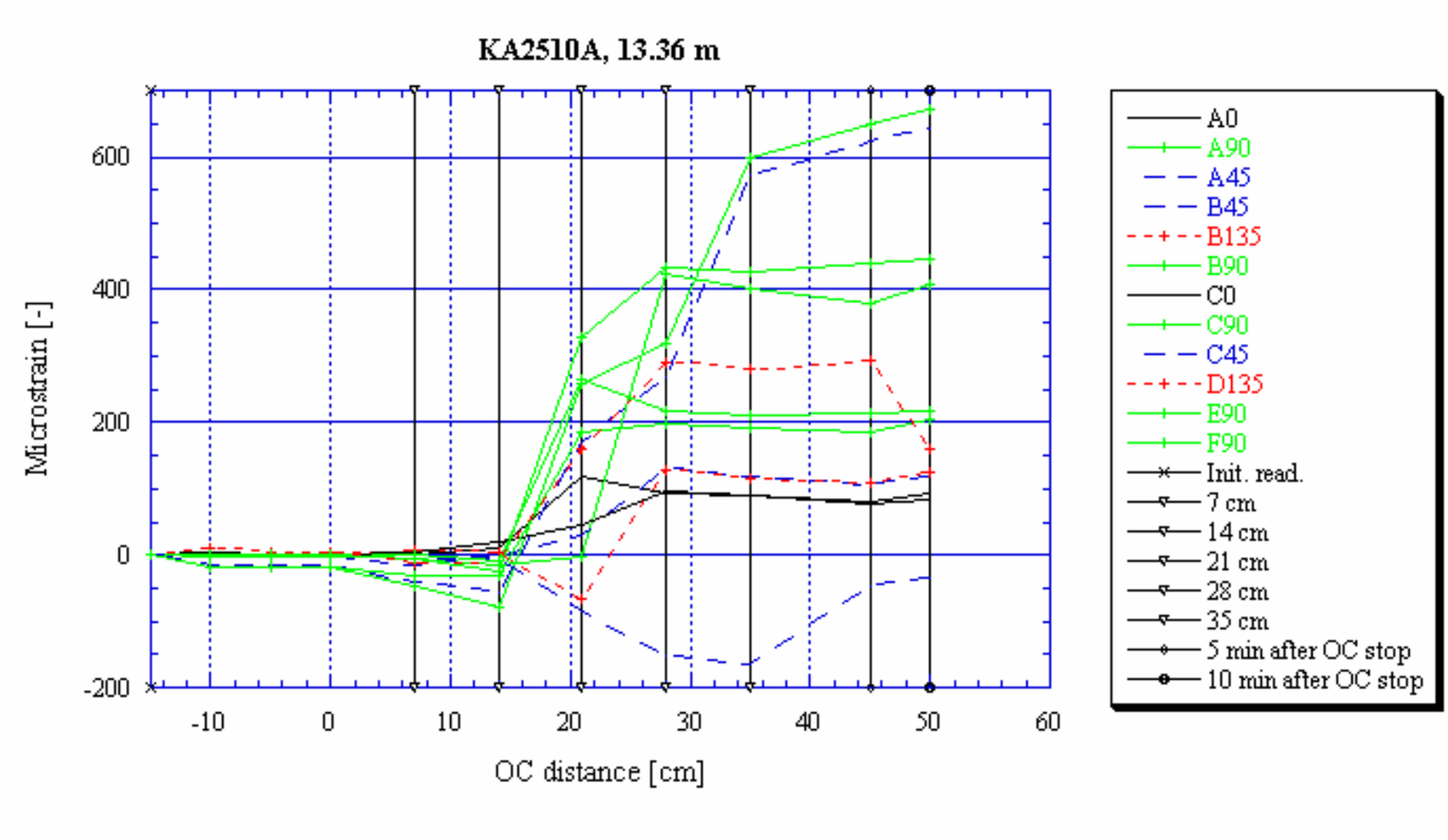
KA2510A, 13.36 m
Microstrain [-]
600
400
200
0
-200
-10
0
10
20
30
40
50
60
OC distance [cm]
A0
A90
A45
B45
B135
B90
C0
C90
C45
D135
E90
F90
Init. read.
7 cm
14 cm
21 cm
28 cm
35 cm
5 min after OC stop
10 min after OC stop

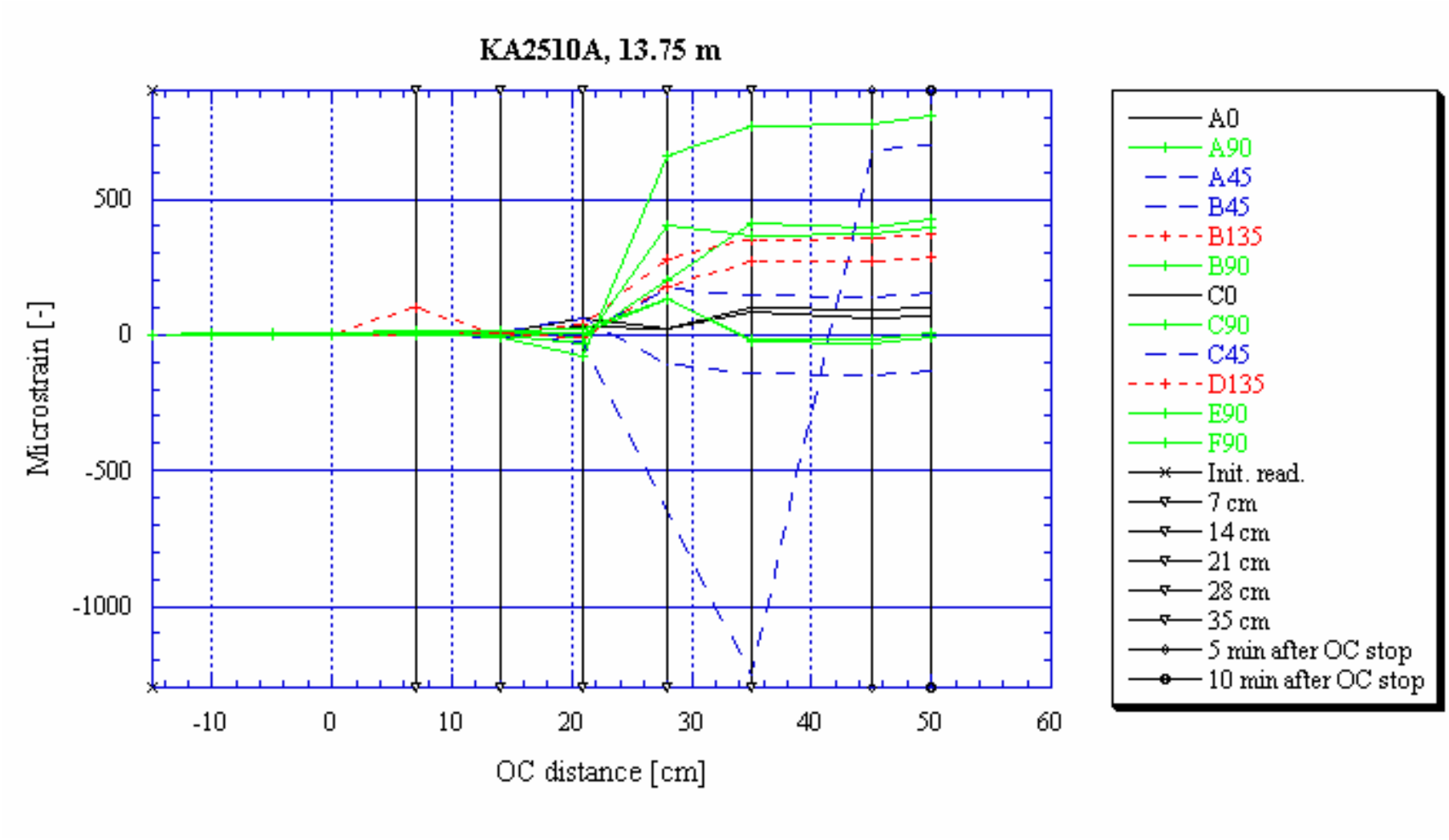
KA2510A, 13.75 m
Microstrain [-]
500
0
-500
-1000
-10
0
10
20
30
40
50
60
OC distance [cm]
A0
A90
A45
B45
B135
B90
C0
C90
C45
D135
E90
F90
Init. read.
7 cm
14 cm
21 cm
28 cm
35 cm
5 min after OC stop
10 min after OC stop

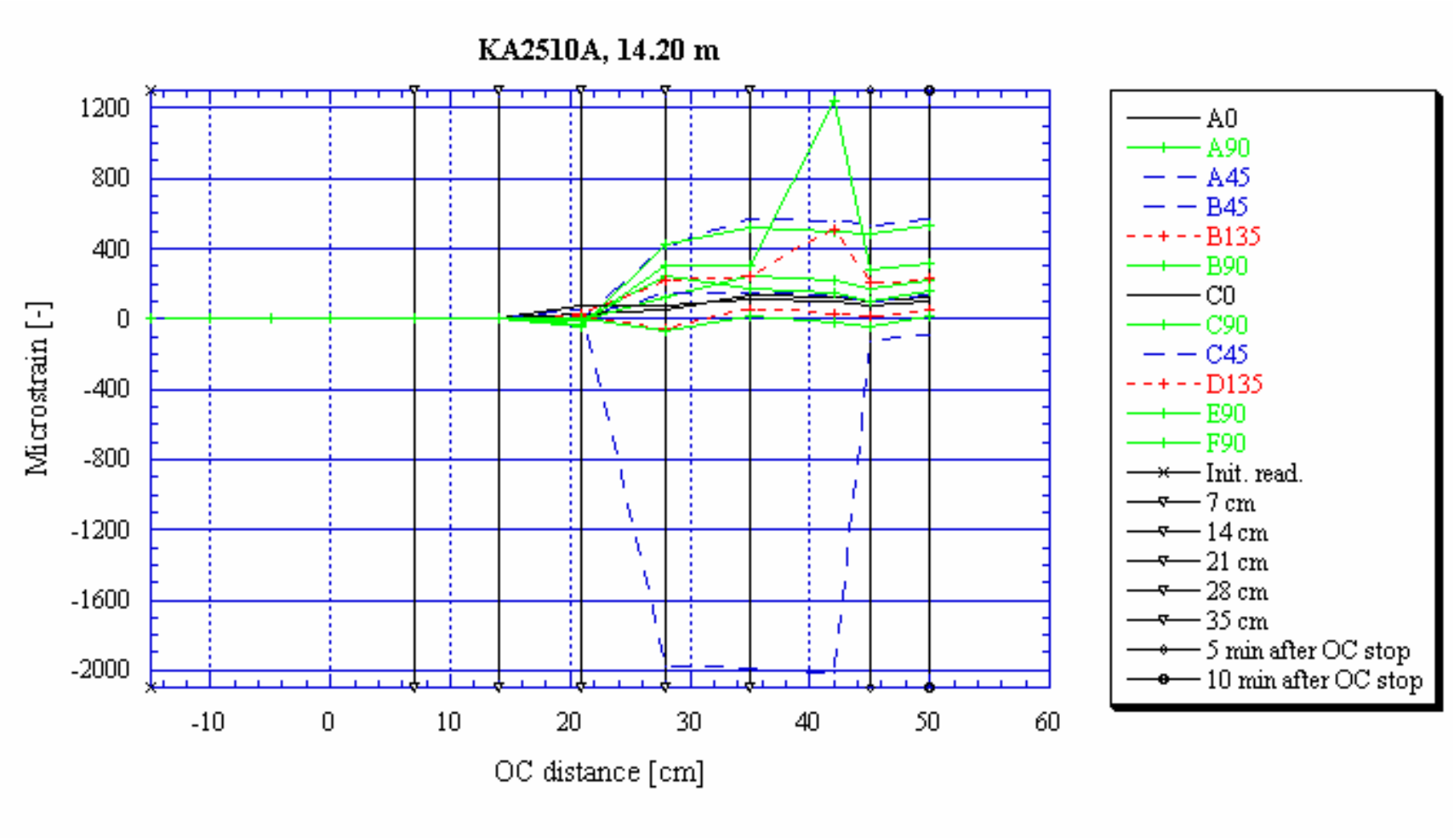
KA2510A, 14.20 m
Microstrain [-]
1200
800
400
0
-400
-800
-1200
-1600
-2000
-10
0
10
20
30
40
50
60
OC distance [cm]
A0
A90
A45
B45
B135
B90
C0
C90
C45
D135
E90
F90
Init. read.
7 cm
14 cm
21 cm
28 cm
35 cm
5 min after OC stop
10 min after OC stop

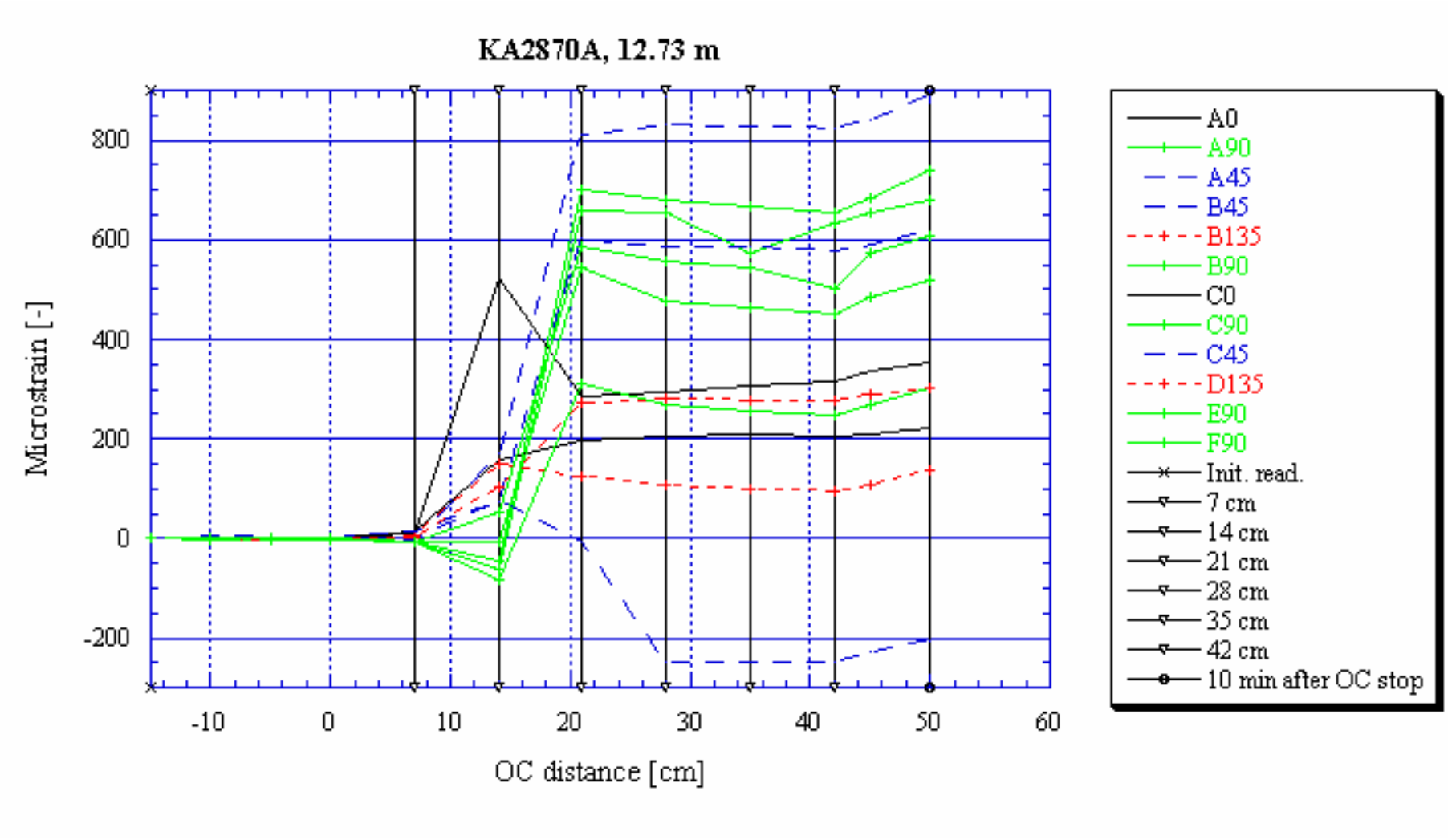
KA2870A, 12.73 m
Microstrain [-]
800
600
400
200
0
-200
-10
0
10
20
30
40
50
60
OC distance [cm]
A0
A90
A45
B45
B135
B90
C0
C90
C45
D135
E90
F90
Init. read.
7 cm
14 cm
21 cm
28 cm
35 cm
42 cm
10 min after OC stop

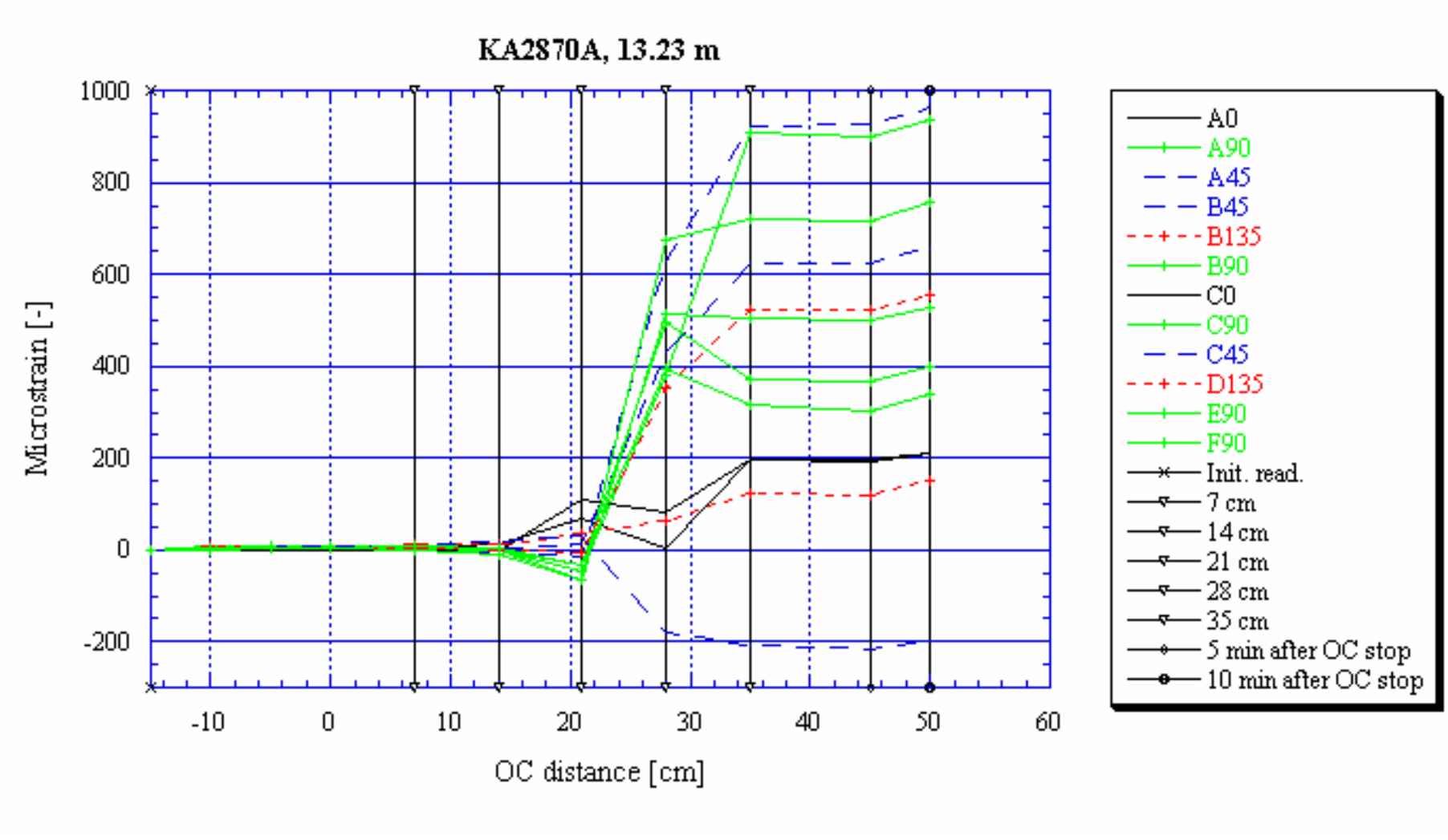
KA2870A, 13.23 m
Microstrain [-]
1000
800
600
400
200
0
-200
-10
0
10
20
30
40
50
60
OC distance [cm]
A0
A90
A45
B45
B135
B90
C0
C90
C45
D135
E90
F90
Init. read.
7 cm
14 cm
21 cm
28 cm
35 cm
5 min after OC stop
10 min after OC stop

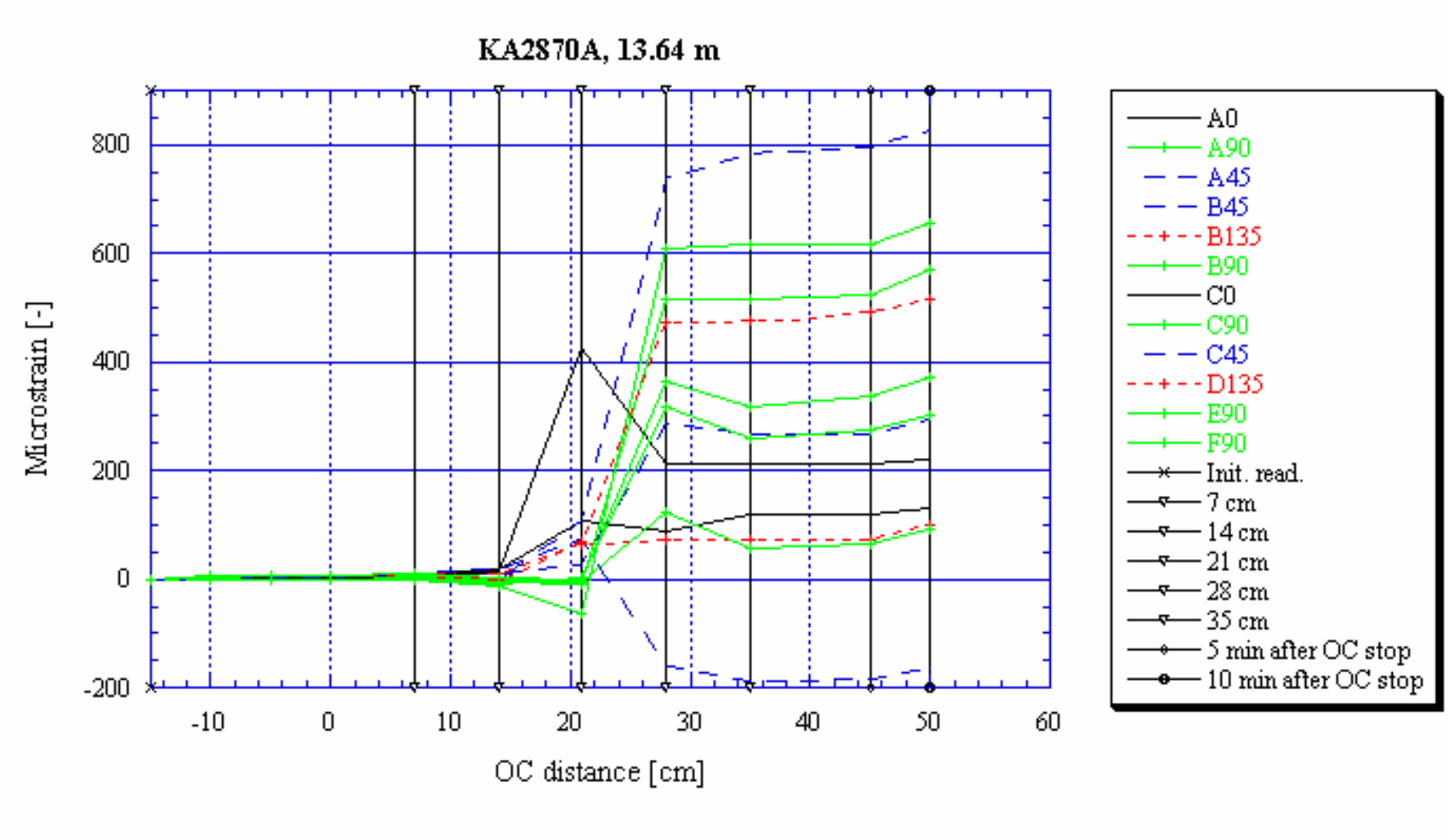
KA2870A, 13.64 m
Microstrain [-]
800
600
400
200
0
-200
-10
0
10
20
30
40
50
60
OC distance [cm]
A0
A90
A45
B45
B135
B90
C0
C90
C45
D135
E90
F90
Init. read.
7 cm
14 cm
21 cm
28 cm
35 cm
5 min after OC stop
10 min after OC stop

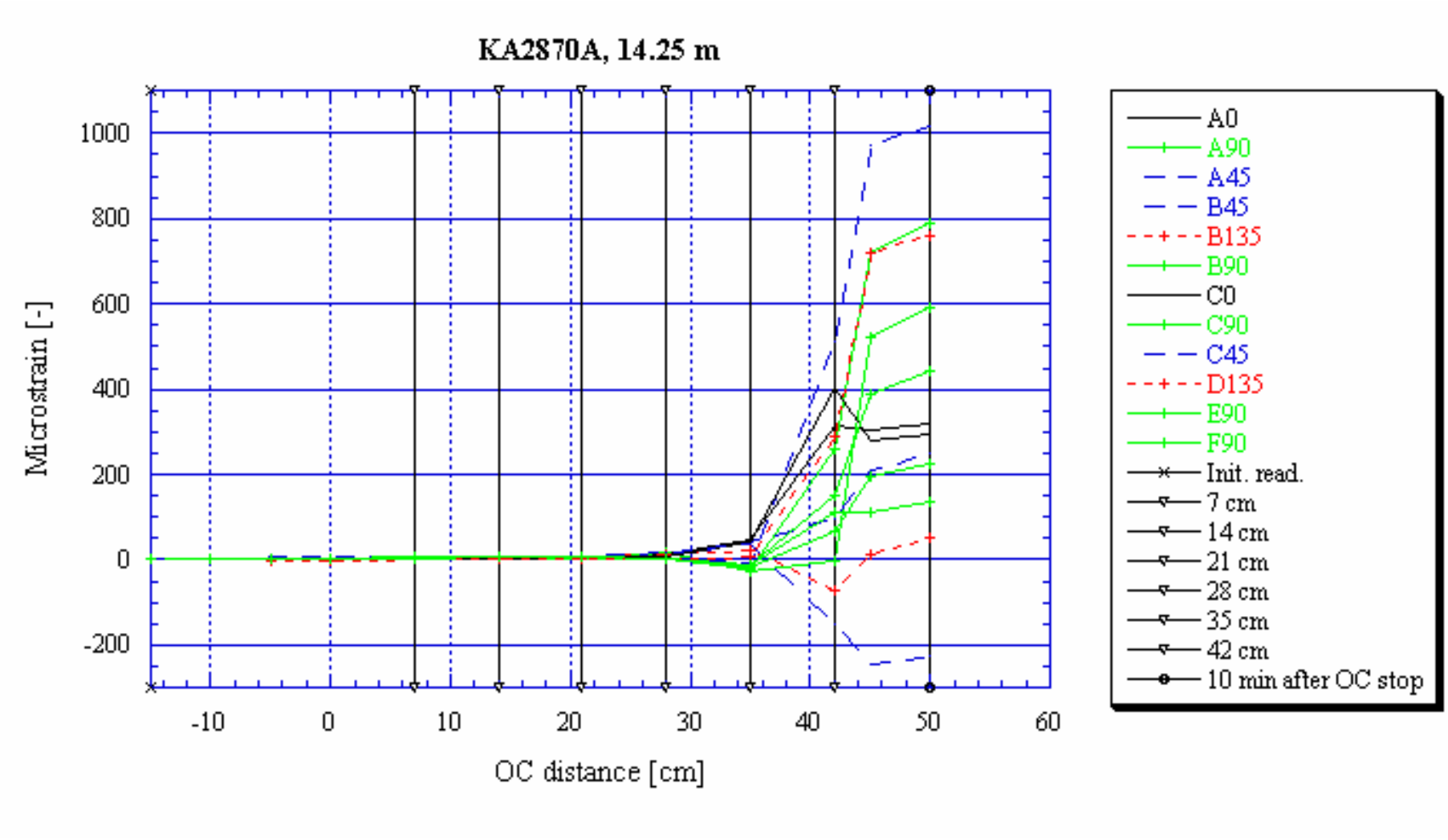
KA2870A, 14.25 m
Microstrain [-]
1000
800
600
400
200
0
-200
-10
0
10
20
30
40
50
60
OC distance [cm]
A0
A90
A45
B45
B135
B90
C0
C90
C45
D135
E90
F90
Init. read.
7 cm
14 cm
21 cm
28 cm
35 cm
42 cm
10 min after OC stop

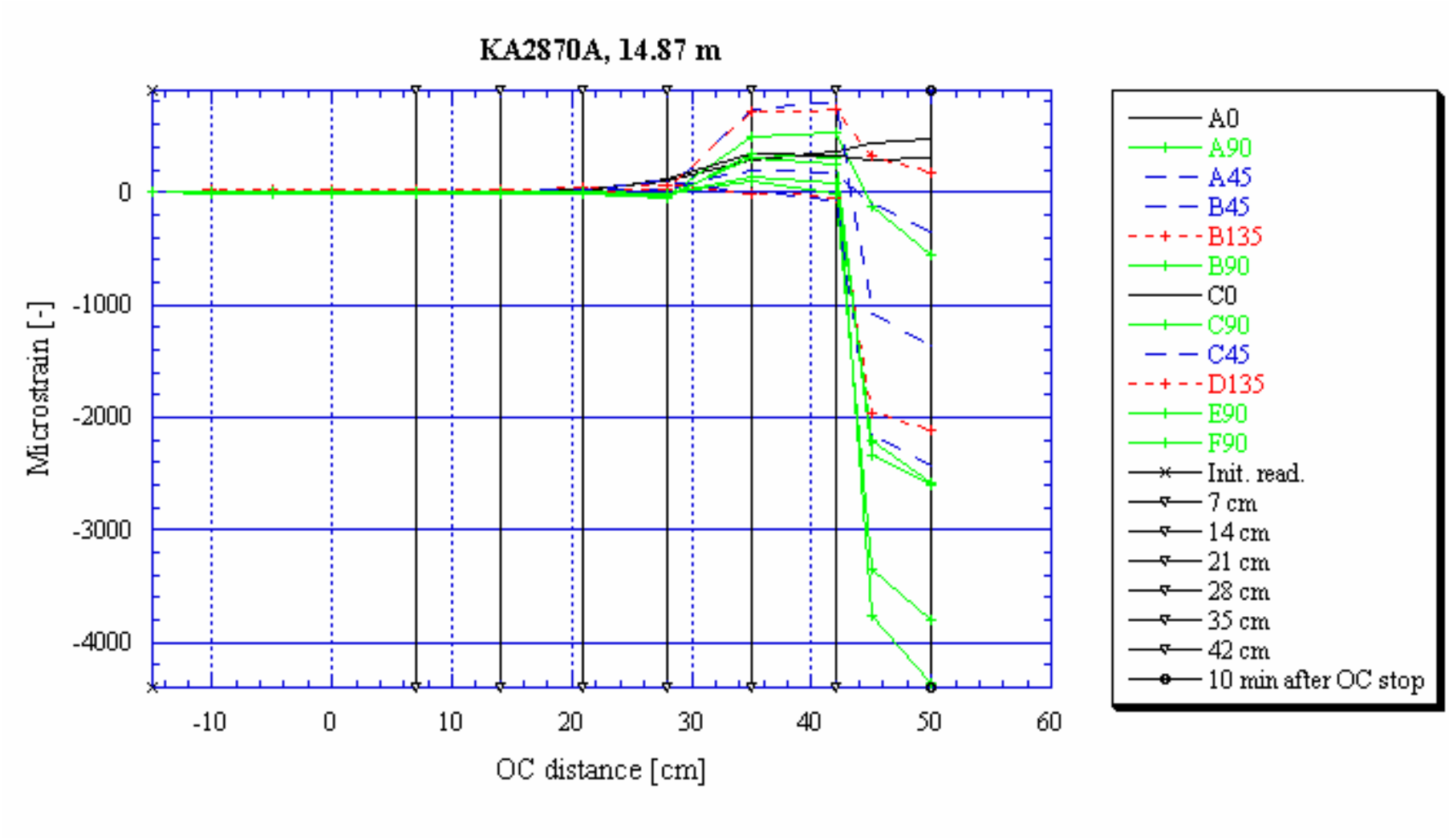
KA2870A, 14.87 m
Microstrain [-]
0
-1000
-2000
-3000
-4000
-10
0
10
20
30
40
50
60
OC distance [cm]
A0
A90
A45
B45
B135
B90
C0
C90
C45
D135
E90
F90
Init. read.
7 cm
14 cm
21 cm
28 cm
35 cm
42 cm
10 min after OC stop

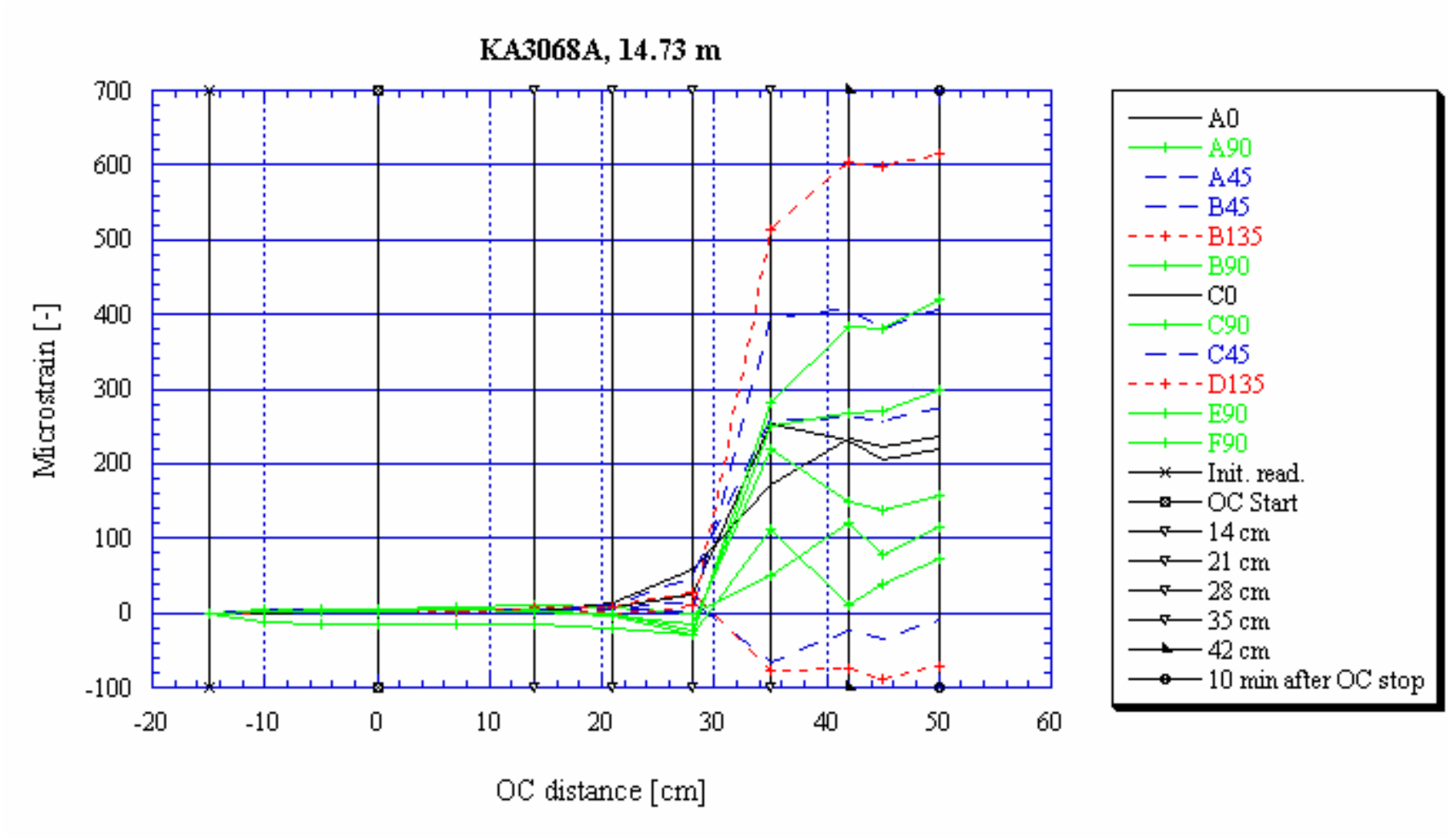
KA3068A, 14.73 m
Microstrain [-]
700
600
500
400
300
200
100
0
-100
-20
-10
0
10
20
30
40
50
60
OC distance [cm]
A0
A90
A45
B45
B135
B90
C0
C90
C45
D135
E90
F90
Init. read.
OC Start
14 cm
21 cm
28 cm
35 cm
42 cm
10 min after OC stop

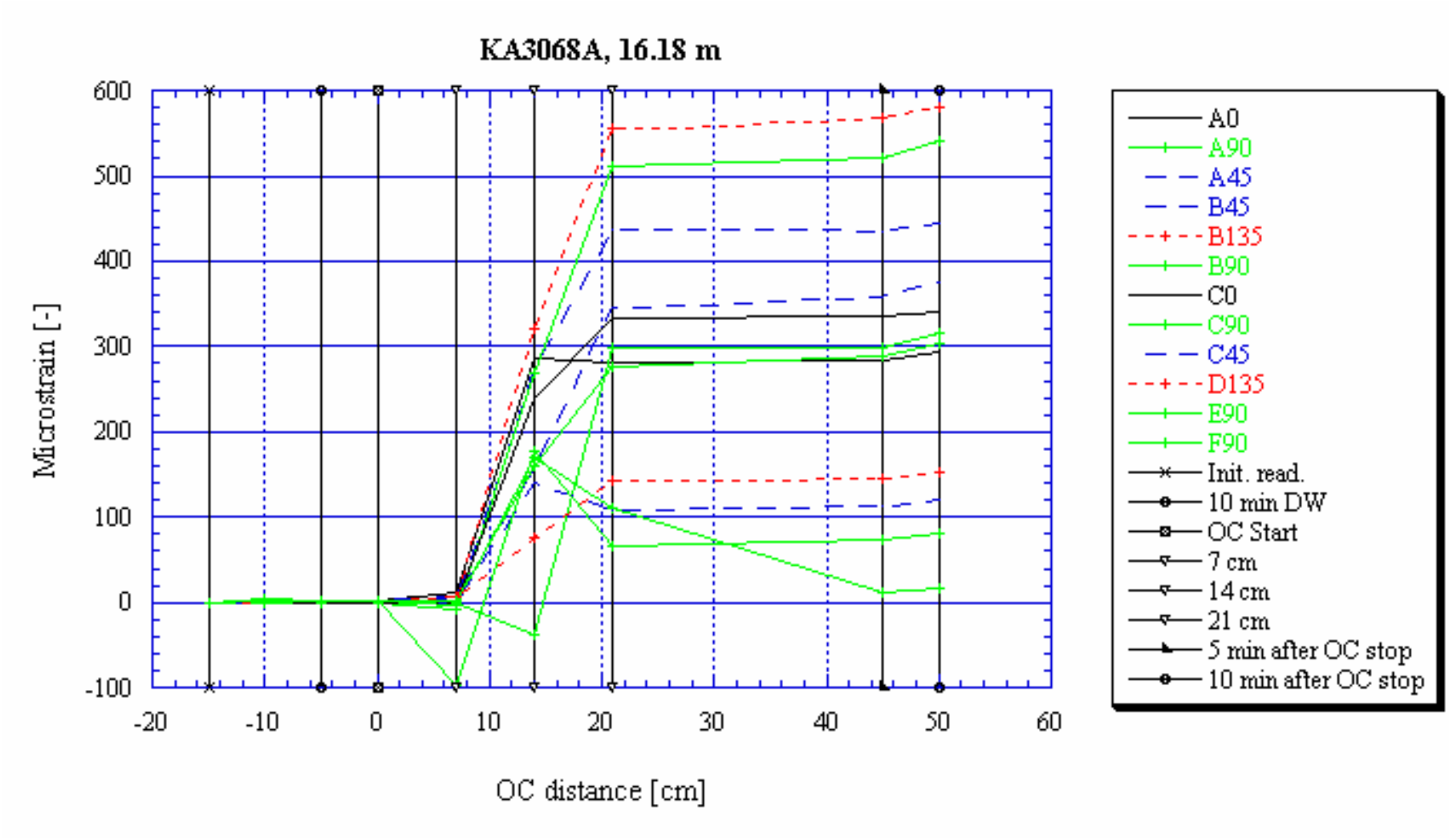
KA3068A, 16.18 m
Microstrain [-]
600
500
400
300
200
100
0
-100
-20
-10
0
10
20
30
40
50
60
OC distance [cm]
A0
A90
A45
B45
B135
B90
C0
C90
C45
D135
E90
F90
Init. read.
10 min DW
OC Start
7 cm
14 cm
21 cm
5 min after OC stop
10 min after OC stop

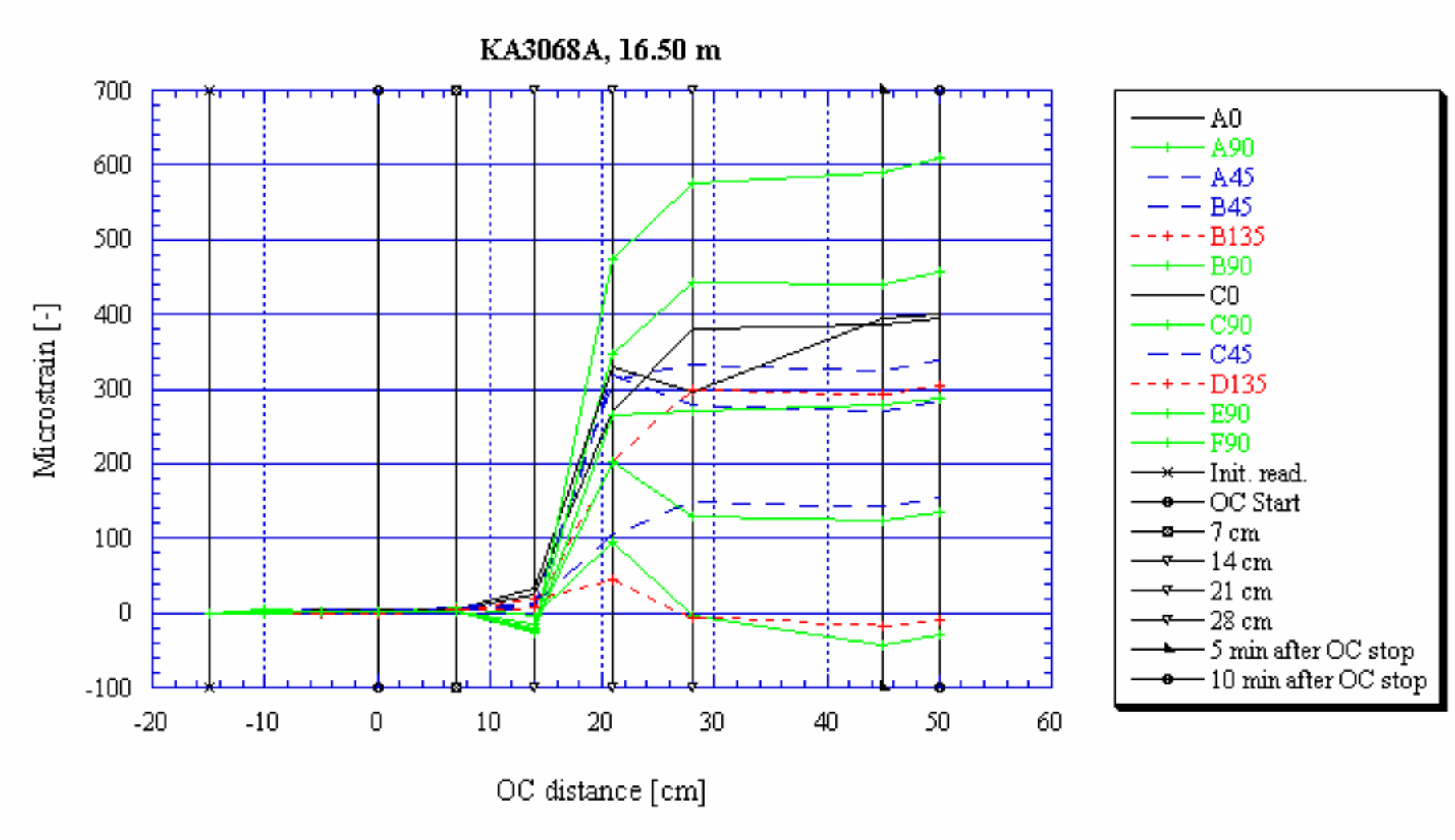
KA3068A, 16.50 m
Microstrain [-]
700
600
500
400
300
200
100
0
-100
-20
-10
0
10
20
30
40
50
60
OC distance [cm]
A0
A90
A45
B45
B135
B90
C0
C90
C45
D135
E90
F90
Init. read.
OC Start
7 cm
14 cm
21 cm
28 cm
5 min after OC stop
10 min after OC stop

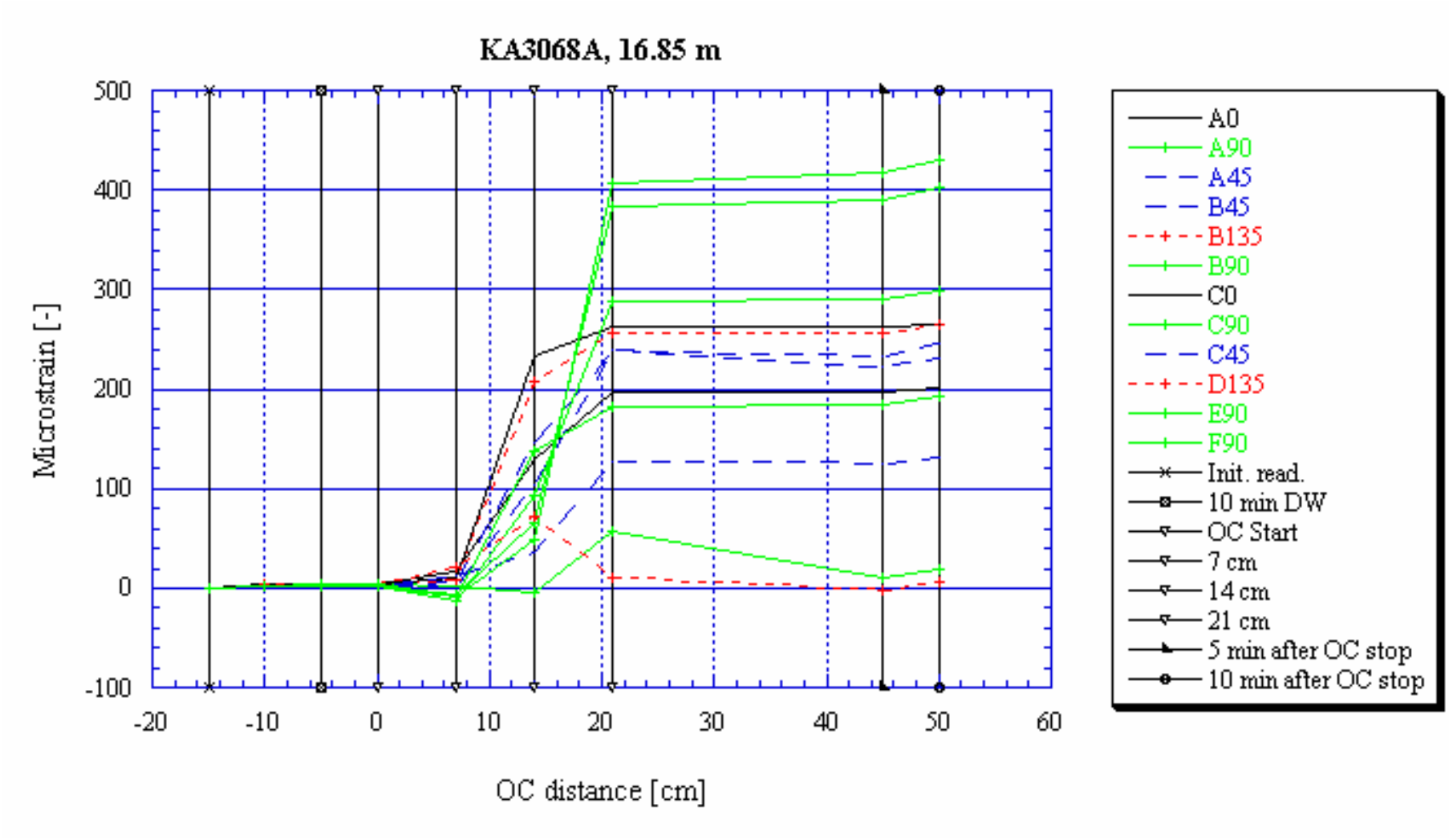
KA3068A, 16.85 m
Microstrain [-]
OC distance [cm]
500
400
300
200
100
0
-100
-20
-10
0
10
20
30
40
50
60
A0
A90
A45
B45
B135
B90
C0
C90
C45
D135
E90
F90
Init. read.
10 min DW
OC Start
7 cm
14 cm
21 cm
5 min after OC stop
10 min after OC stop

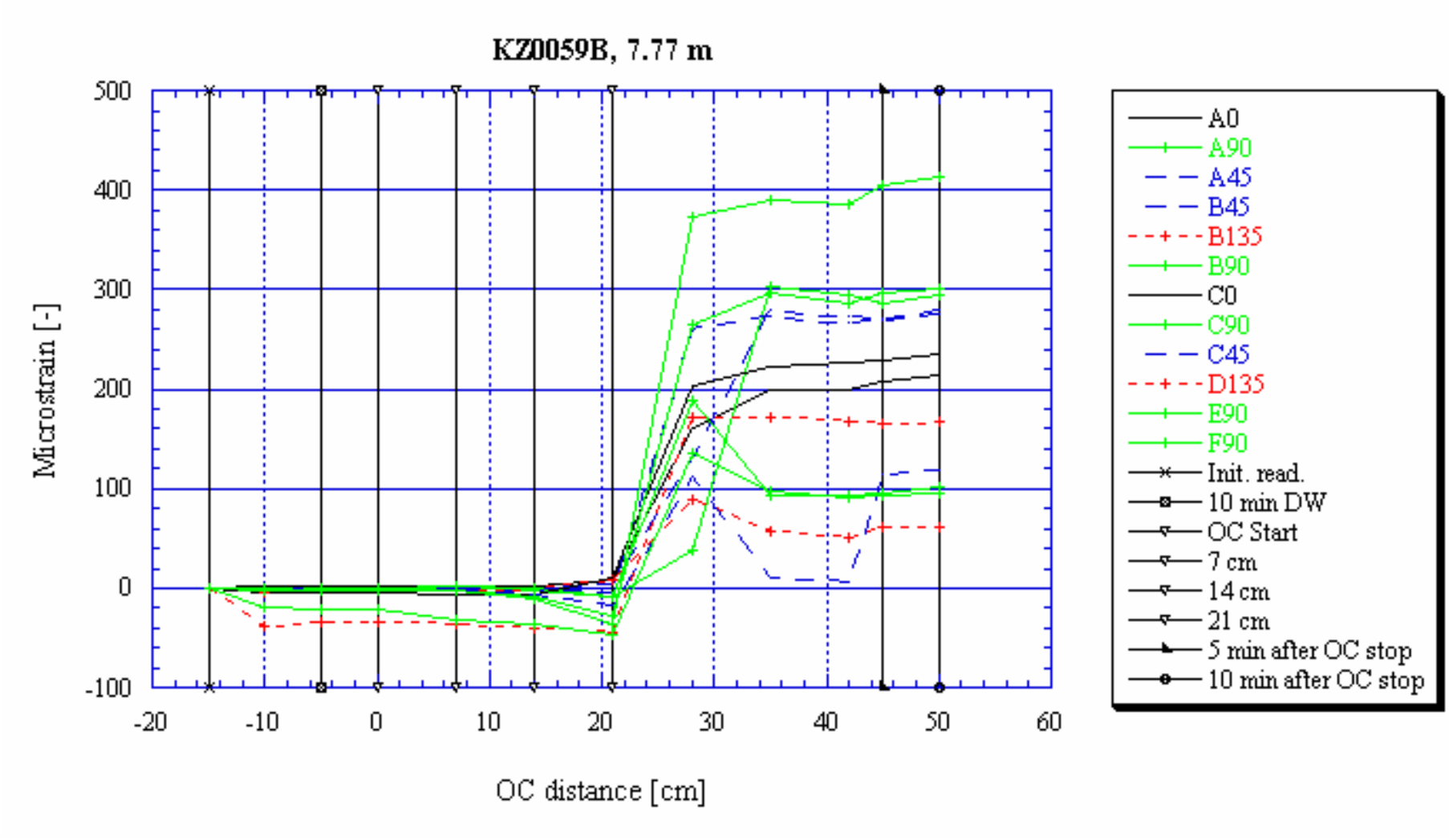
KZ0059B, 7.77 m
Microstrain [-]
500
400
300
200
100
0
-100
-20
-10
0
10
20
30
40
50
60
OC distance [cm]
A0
A90
A45
B45
B135
B90
C0
C90
C45
D135
E90
F90
Init. read.
10 min DW
OC Start
7 cm
14 cm
21 cm
5 min after OC stop
10 min after OC stop

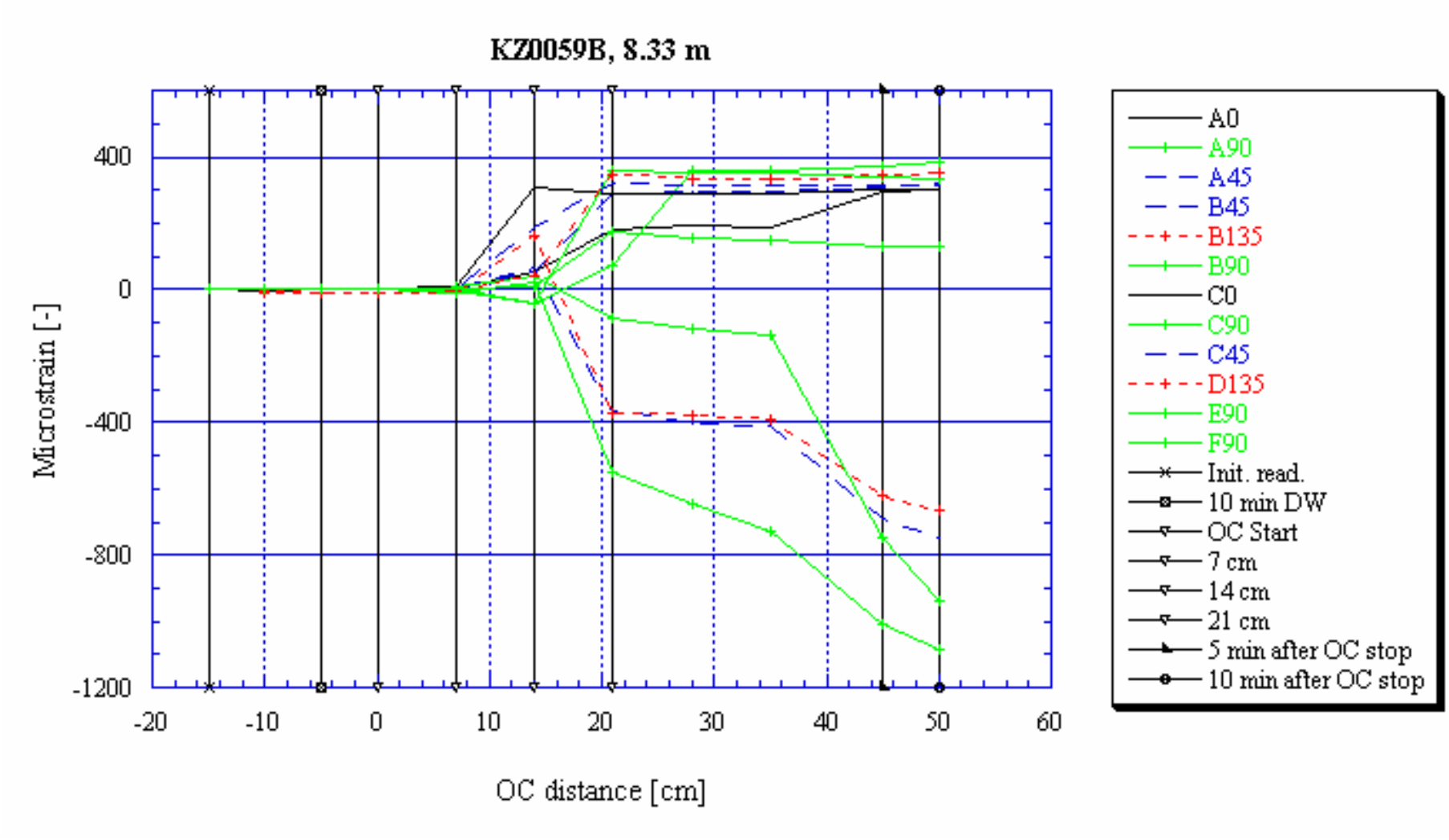
KZ0059B, 8.33 m
Microstrain [-]
400
0
-400
-800
-1200
-20
-10
0
10
20
30
40
50
60
OC distance [cm]
A0
A90
A45
B45
B135
B90
C0
C90
C45
D135
E90
F90
Init. read.
10 min DW
OC Start
7 cm
14 cm
21 cm
5 min after OC stop
10 min after OC stop

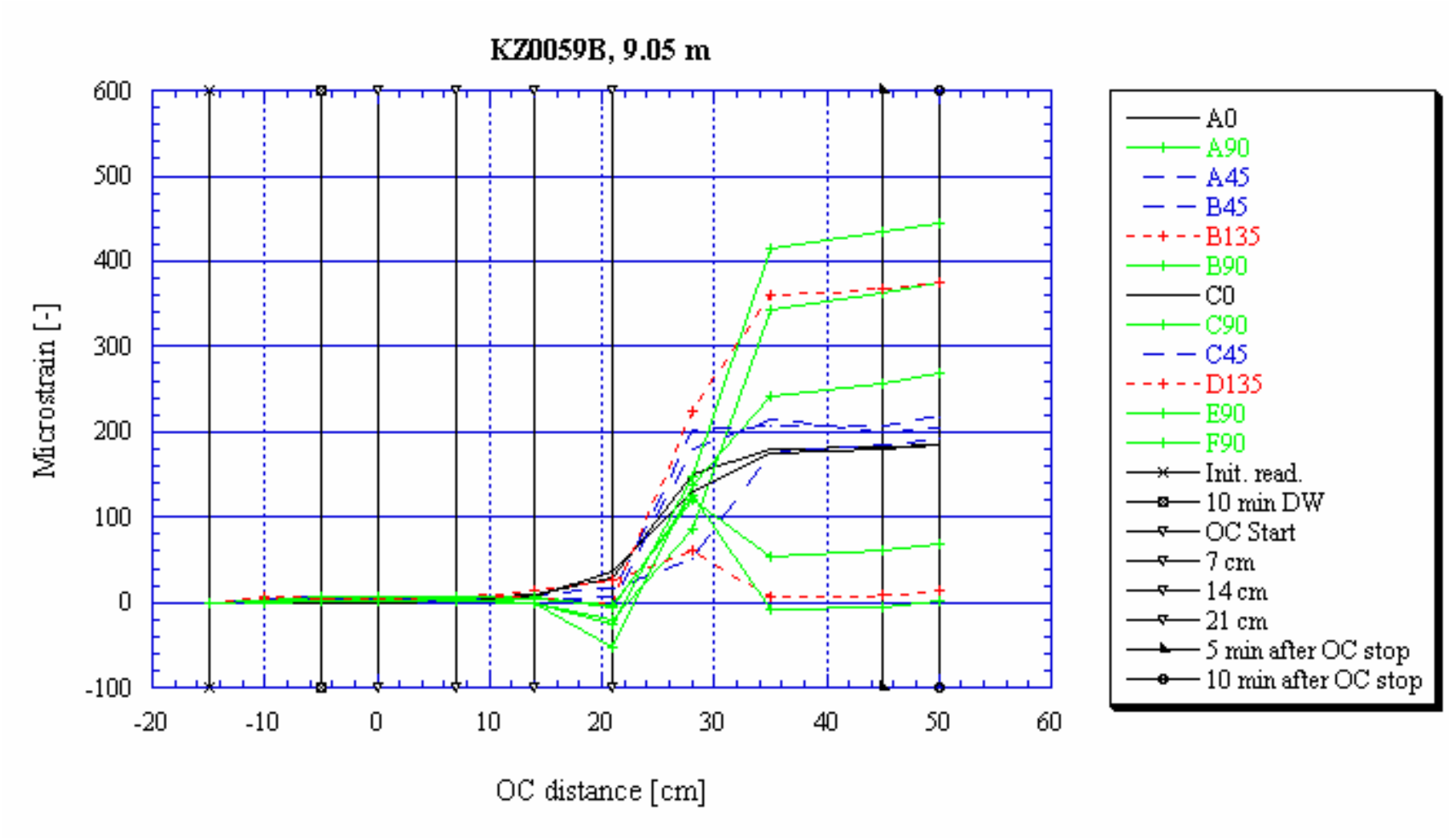
KZ0059B, 9.05 m
Microstrain [-]
600
500
400
300
200
100
0
-100
-20
-10
0
10
20
30
40
50
60
OC distance [cm]
A0
A90
A45
B45
B135
B90
C0
C90
C45
D135
E90
F90
Init. read.
10 min DW
OC Start
7 cm
14 cm
21 cm
5 min after OC stop
10 min after OC stop

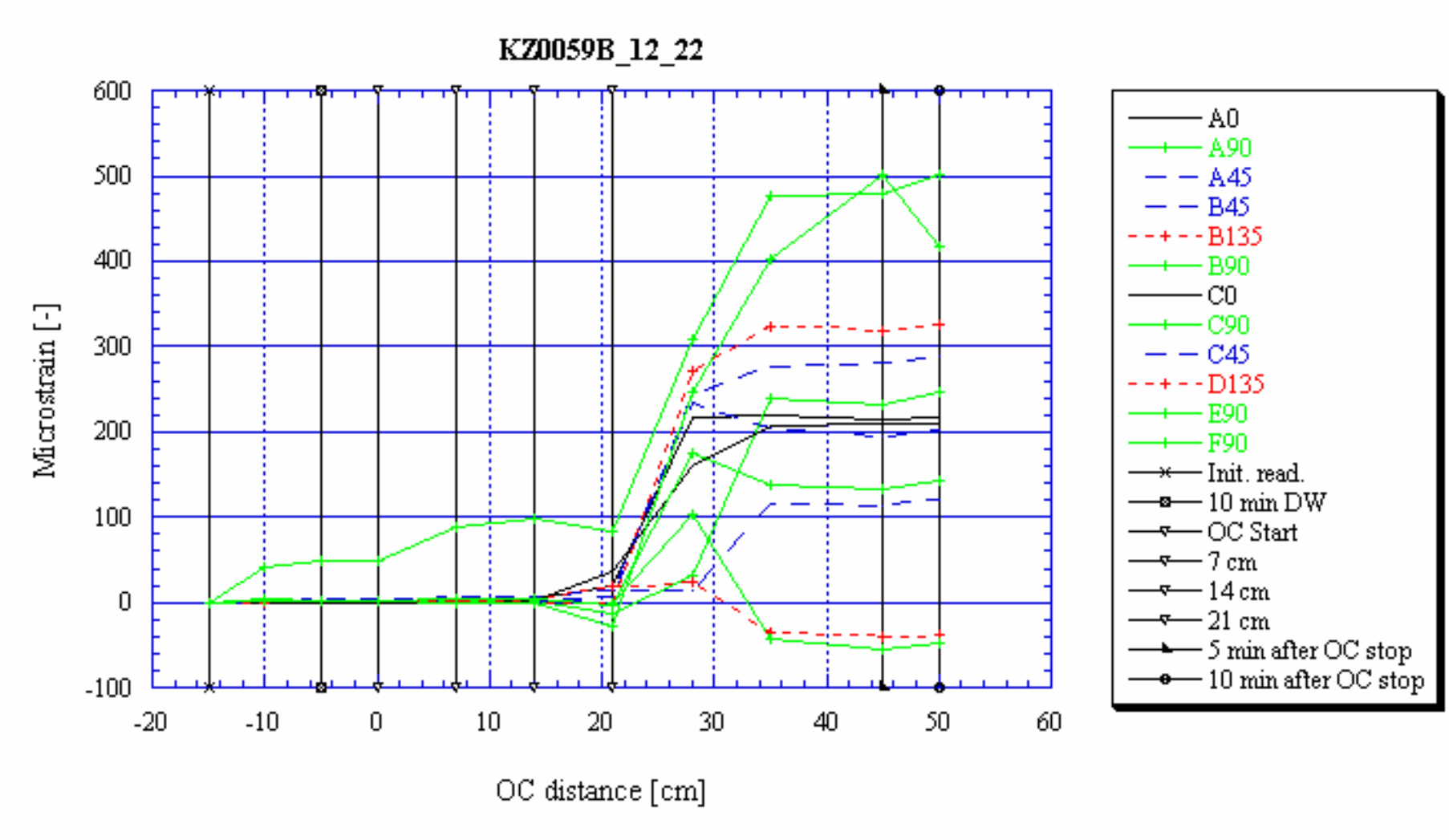
KZ0059B_12_22
Microstrain [-]
600
500
400
300
200
100
0
-100
-20
-10
0
10
20
30
40
50
60
OC distance [cm]
A0
A90
A45
B45
B135
B90
C0
C90
C45
D135
E90
F90
Init. read.
10 min DW
OC Start
7 cm
14 cm
21 cm
5 min after OC stop
10 min after OC stop

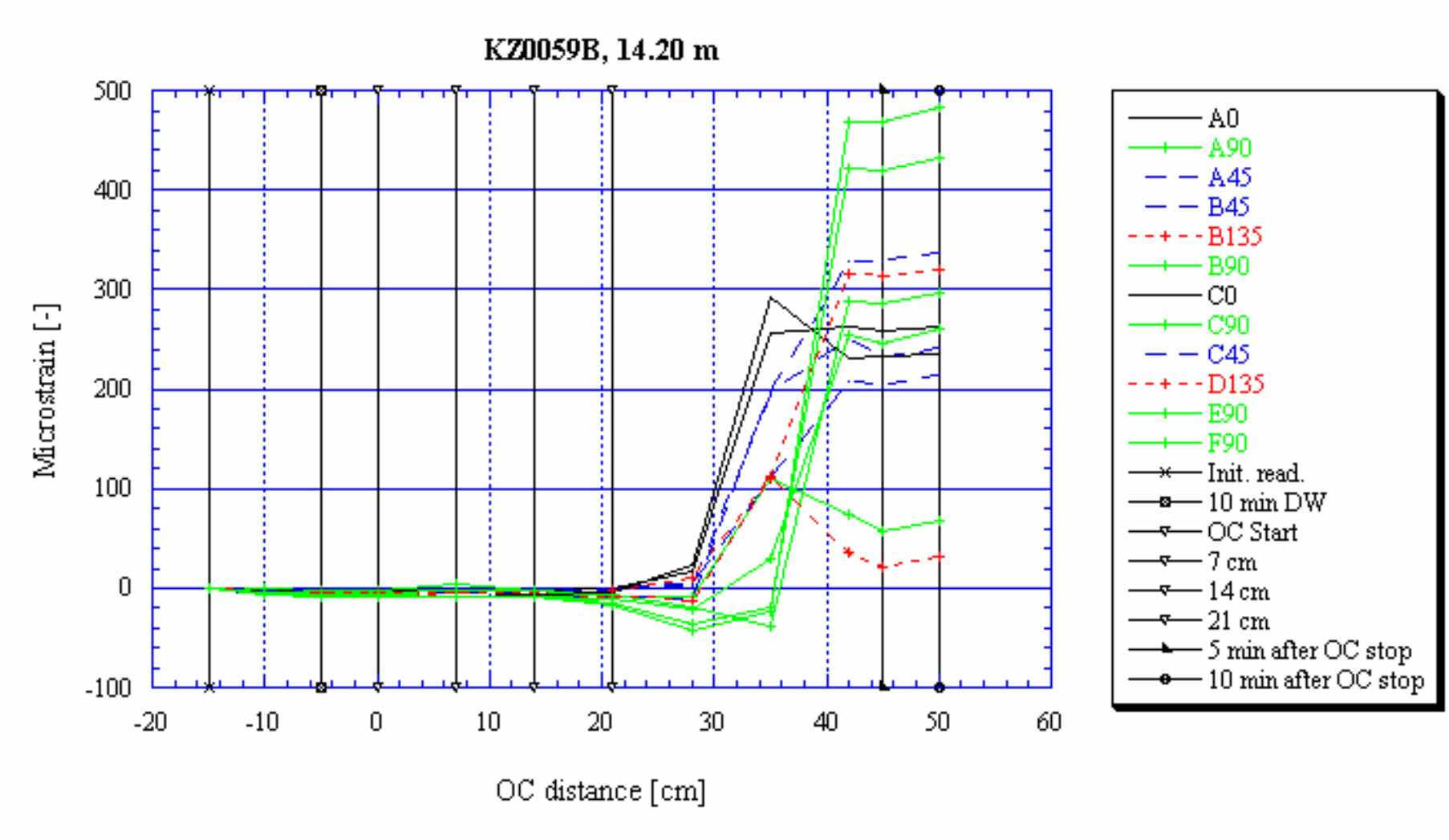
KZ0059B, 14.20 m
Microstrain [-]
500
400
300
200
100
0
-100
-20
-10
0
10
20
30
40
50
60
OC distance [cm]
A0
A90
A45
B45
B135
B90
C0
C90
C45
D135
E90
F90
Init. read.
10 min DW
OC Start
7 cm
14 cm
21 cm
5 min after OC stop
10 min after OC stop

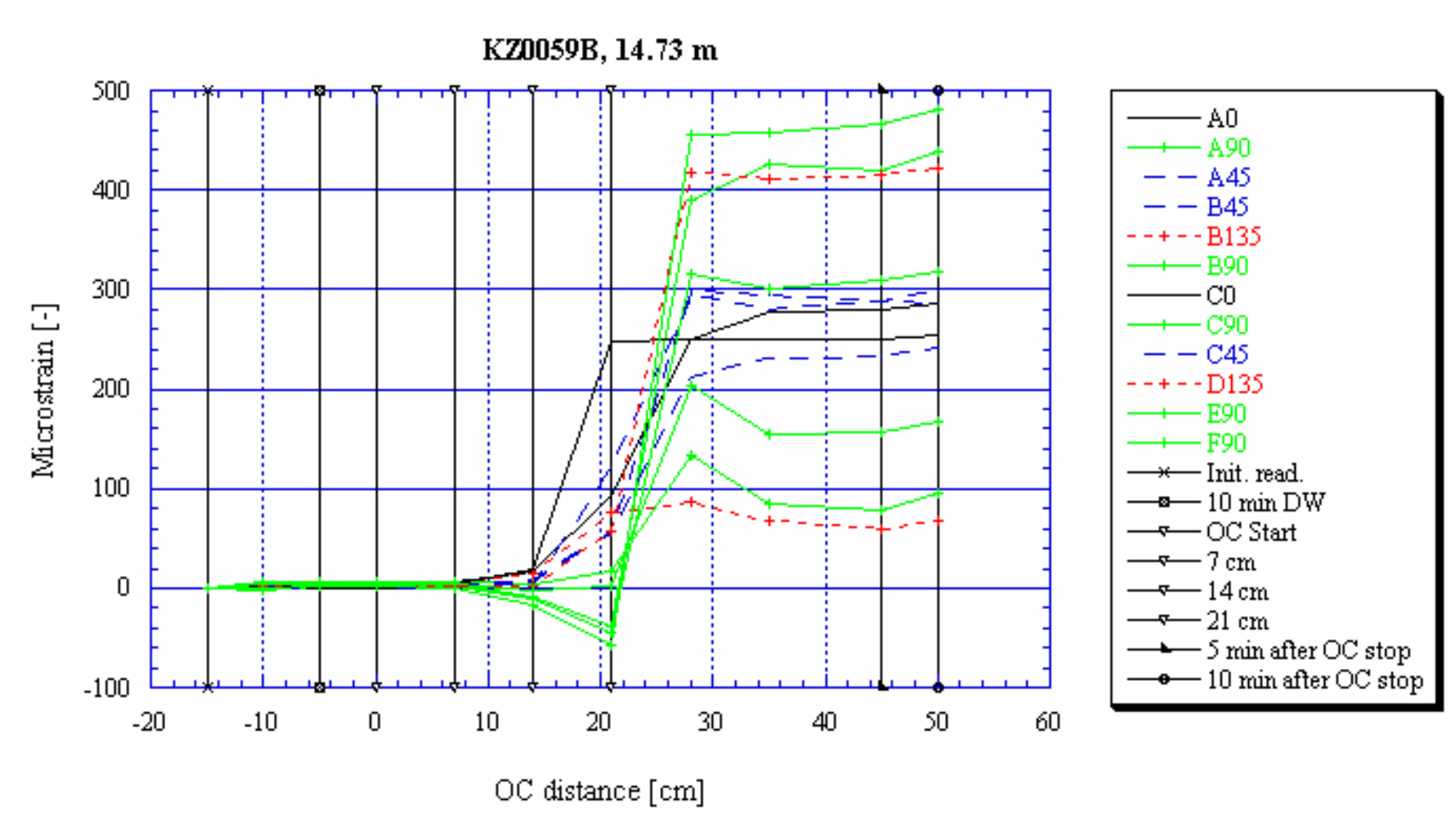
KZ0059B, 14.73 m
Microstrain [-]
500
400
300
200
100
0
-100
-20
-10
0
10
20
30
40
50
60
OC distance [cm]
A0
A90
A45
B45
B135
B90
C0
C90
C45
D135
E90
F90
Init. read.
10 min DW
OC Start
7 cm
14 cm
21 cm
5 min after OC stop
10 min after OC stop

Appendix 5

Biaxial graphs

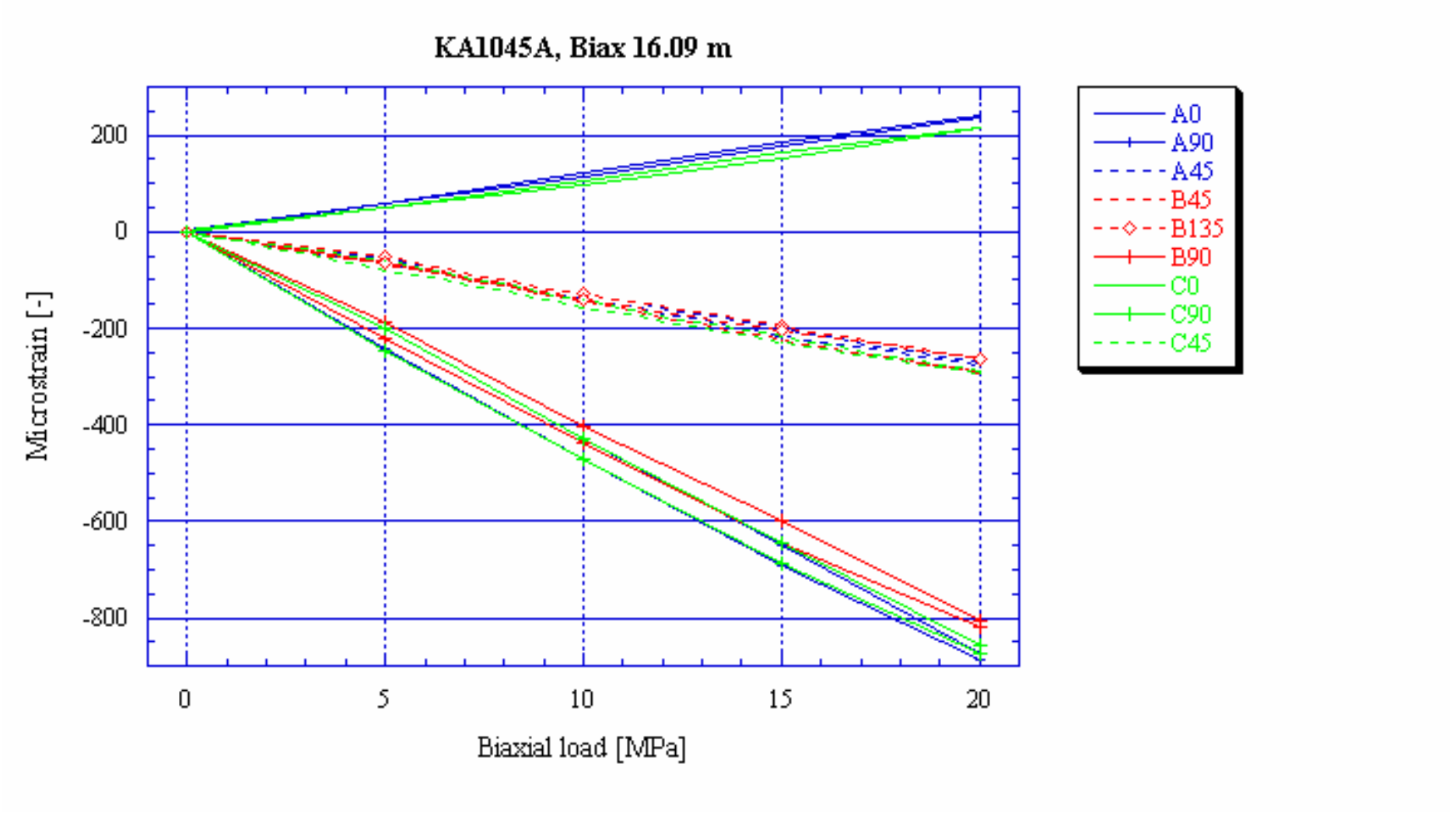

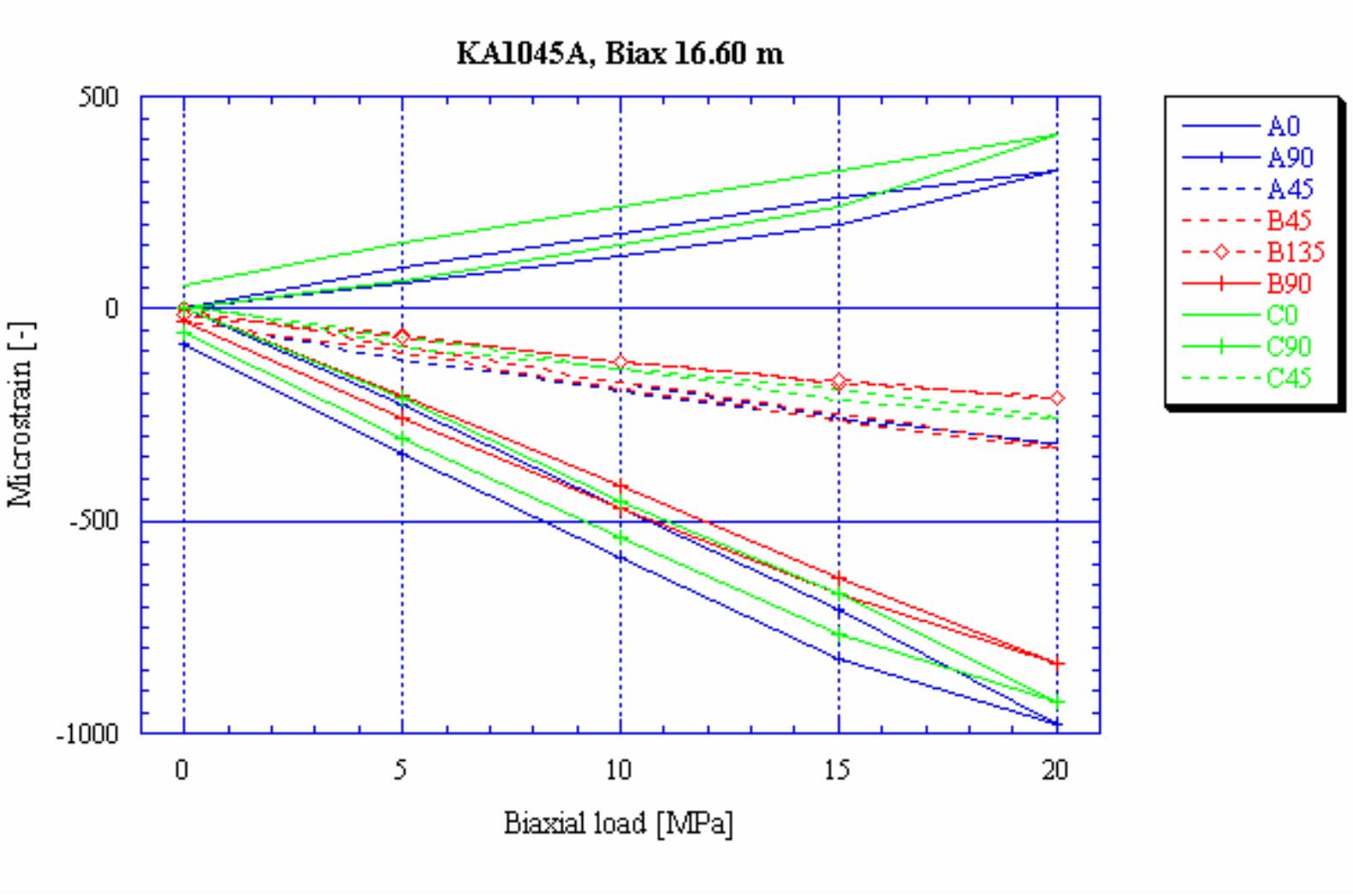
KA1045A, Biax 16.60 m
500
0
-500
-1000
Microstrain [-]
0
5
10
15
20
Biaxial load [MPa]
A0
A90
A45
B45
B135
B90
C0
C90
C45

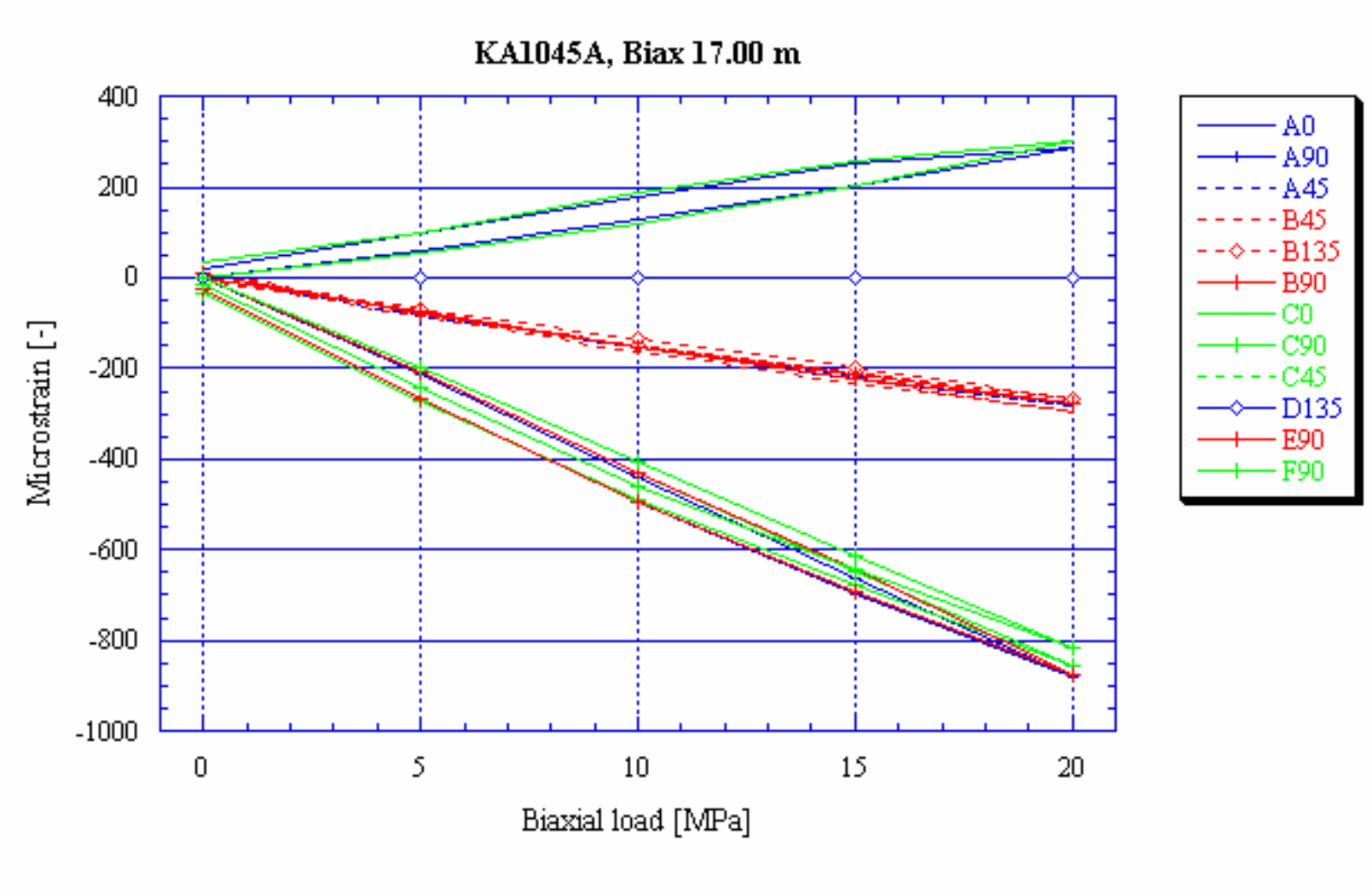
KA1045A, Biax 17.00 m
Microstrain [-]
400
200
0
-200
-400
-600
-800
-1000
0
5
10
15
20
Biaxial load [MPa]
A0
A90
A45
B45
B135
B90
C0
C90
C45
D135
E90
F90

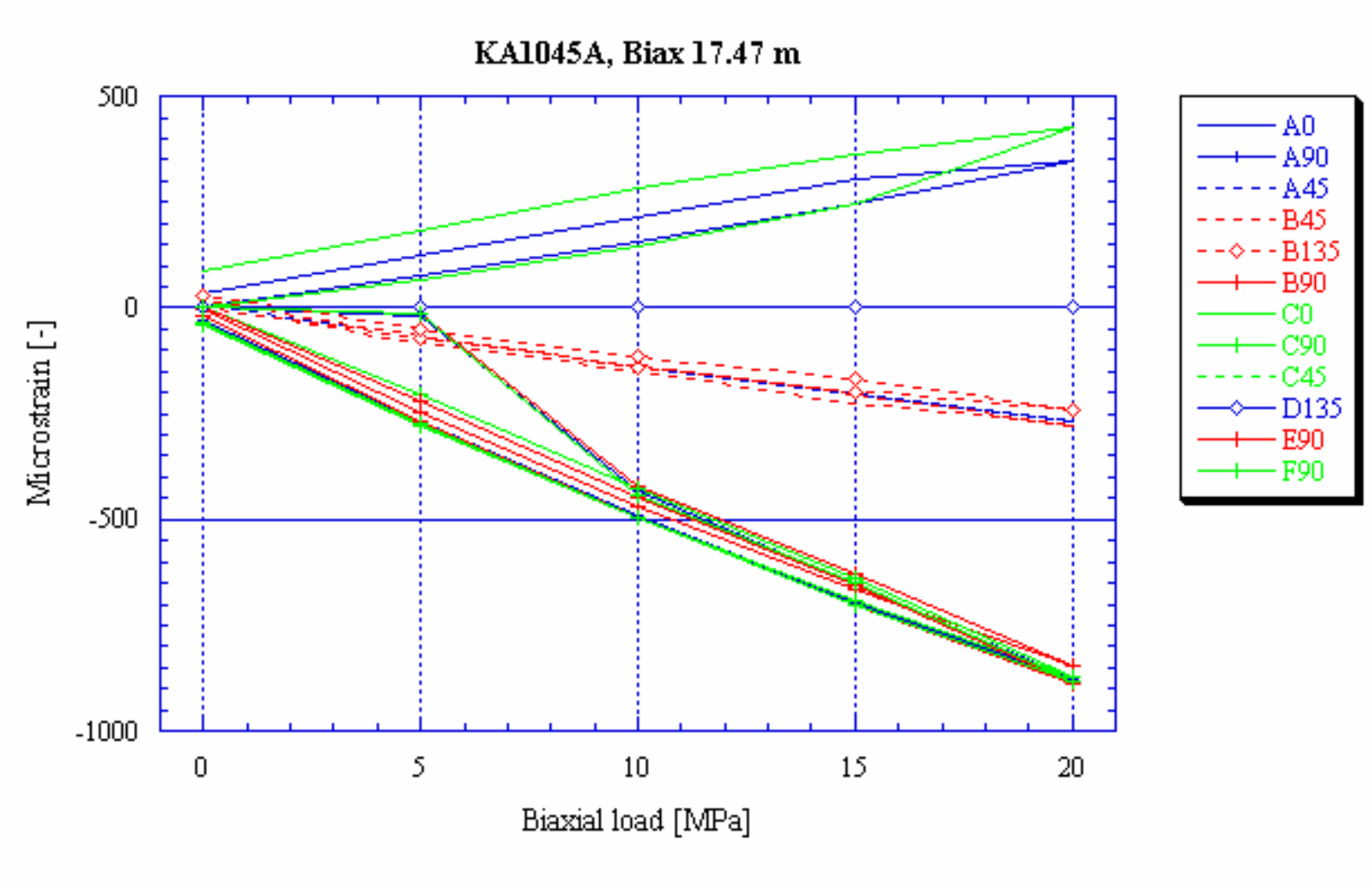
KA1045A, Biax 17.47 m
Microstrain [-]
500
0
-500
-1000
0
5
10
15
20
Biaxial load [MPa]
A0
A90
A45
B45
B135
B90
C0
C90
C45
D135
E90
F90

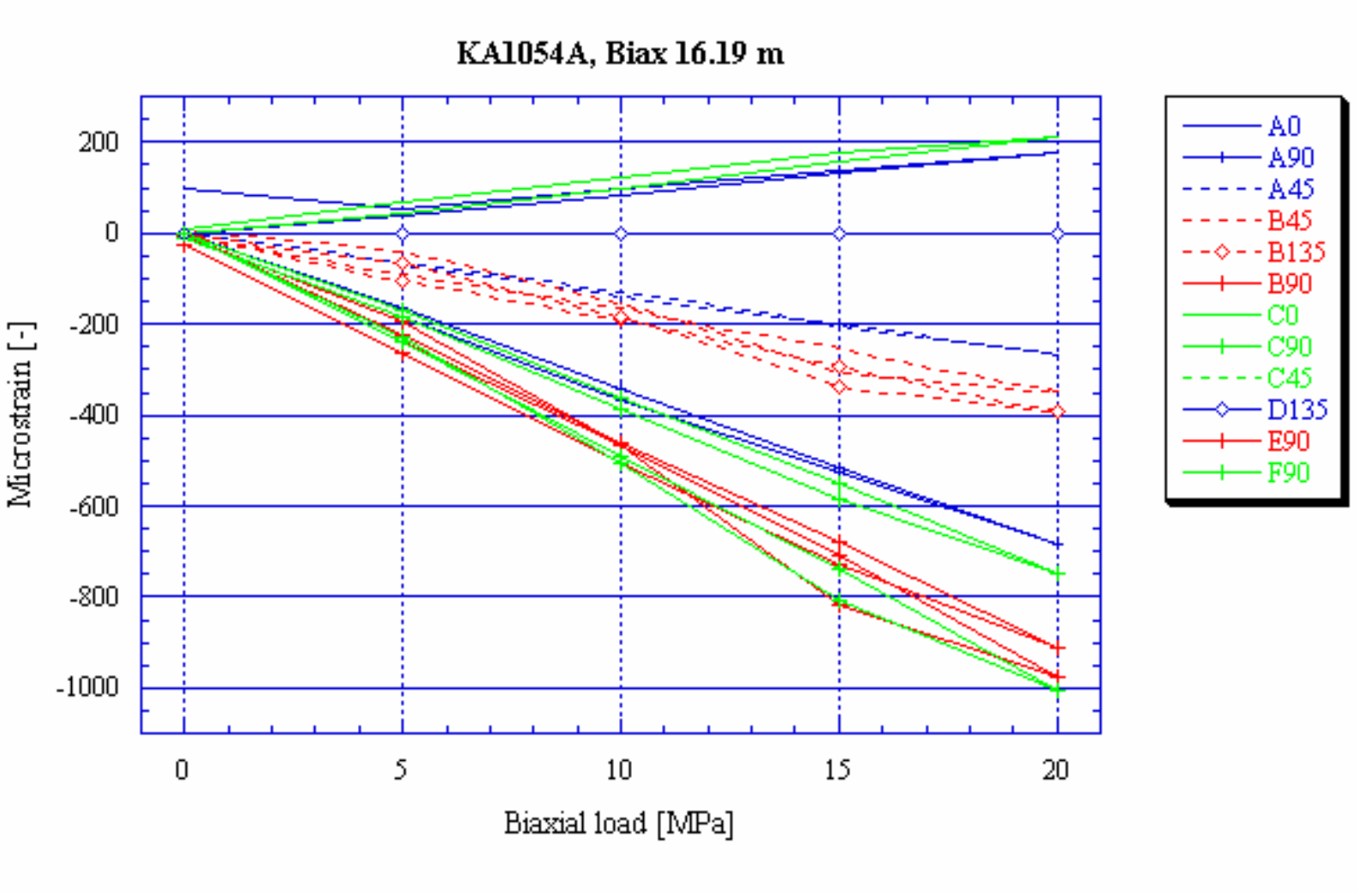
KA1054A, Biax 16.19 m
Microstrain [-]
200
0
-200
-400
-600
-800
-1000
0
5
10
15
20
Biaxial load [MPa]
A0
A90
A45
B45
B135
B90
C0
C90
C45
D135
E90
F90

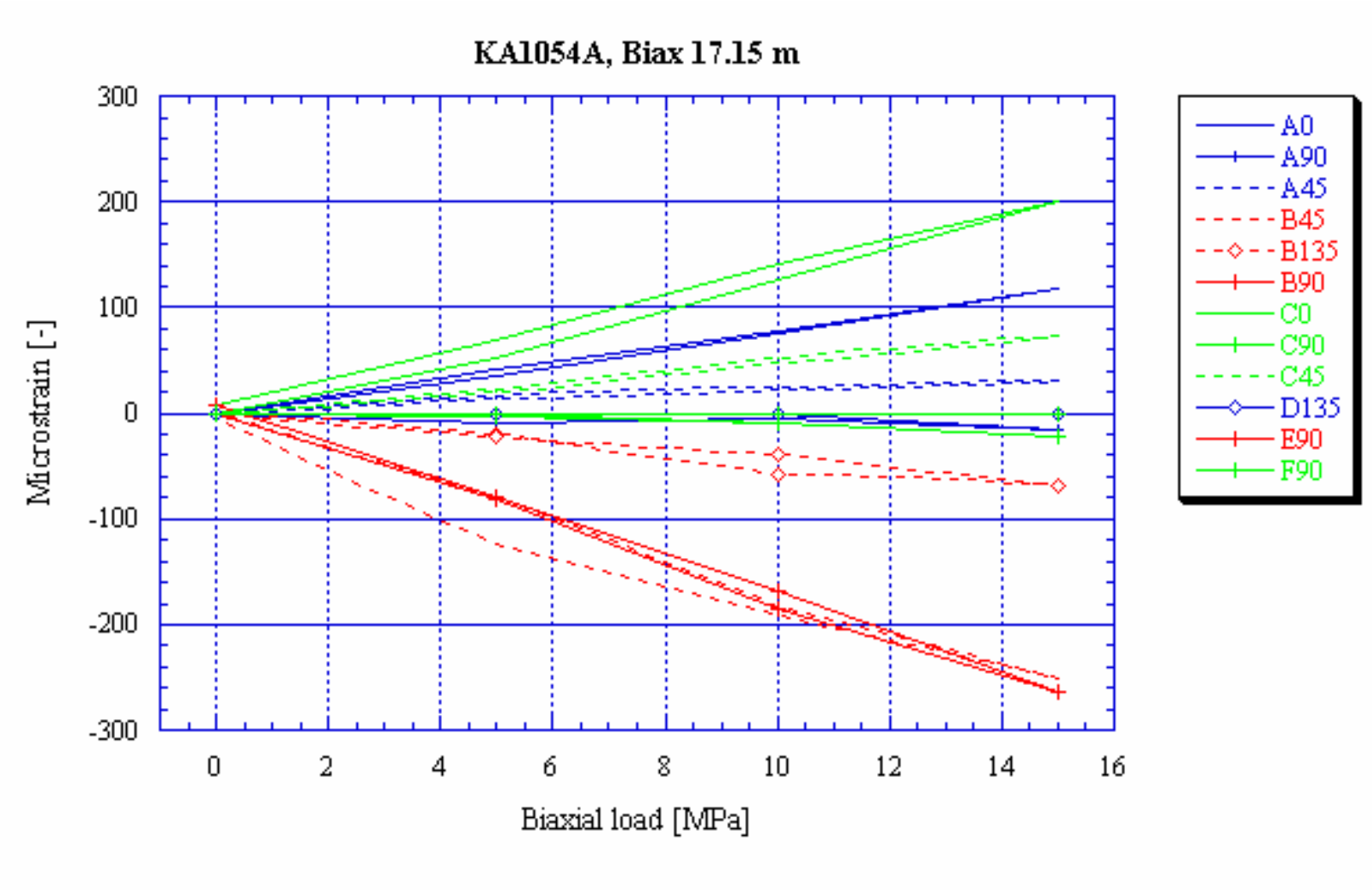
KA1054A, Biax 17.15 m
Microstrain [-]
300
200
100
0
-100
-200
-300
0
2
4
6
8
10
12
14
16
Biaxial load [MPa]
A0
A90
A45
B45
B135
B90
C0
C90
C45
D135
E90
F90

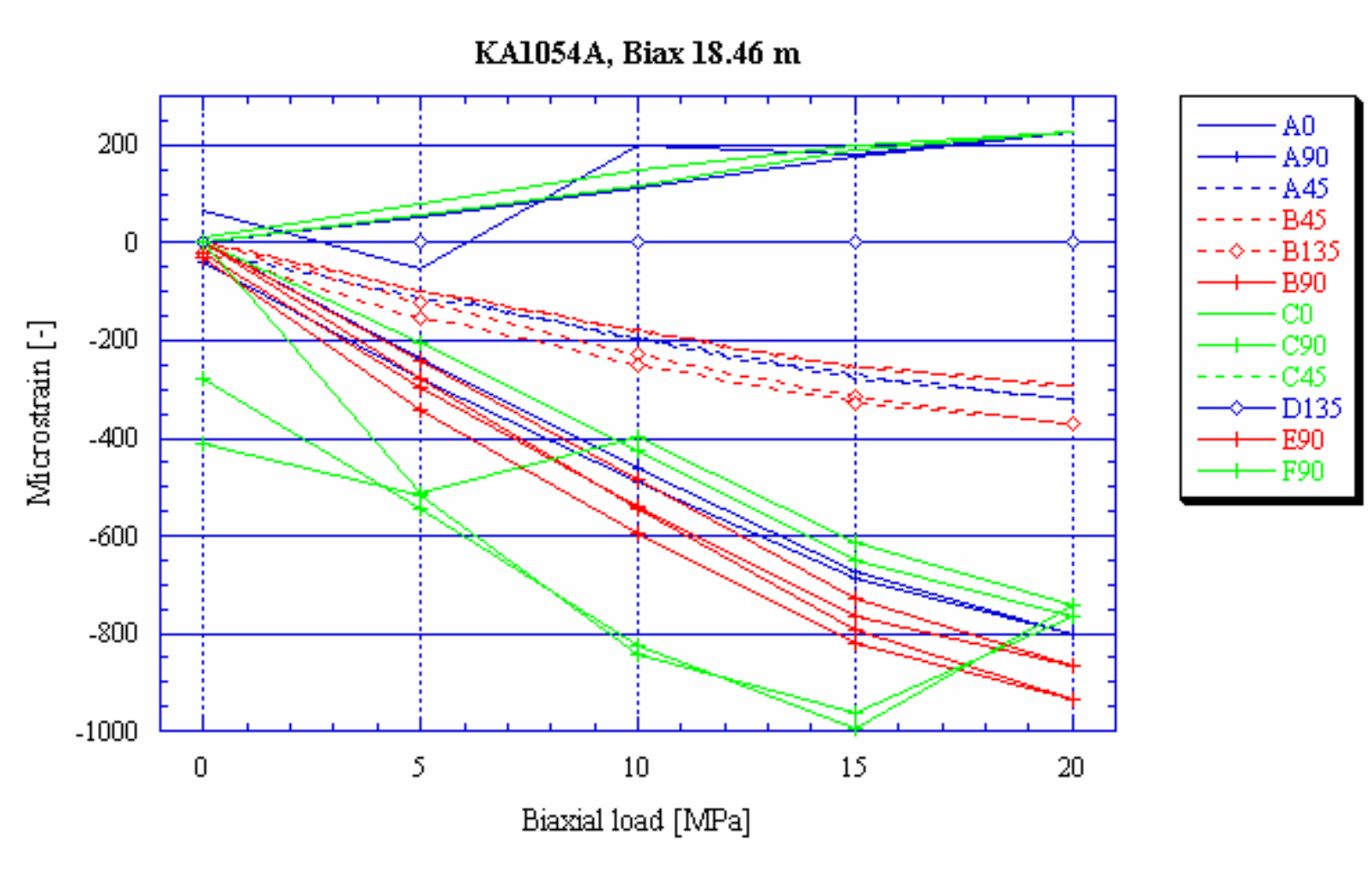
KA1054A, Biax 18.46 m
Microstrain [-]
200
0
-200
-400
-600
-800
-1000
0
5
10
15
20
Biaxial load [MPa]
A0
A90
A45
B45
B135
B90
C0
C90
C45
D135
E90
F90

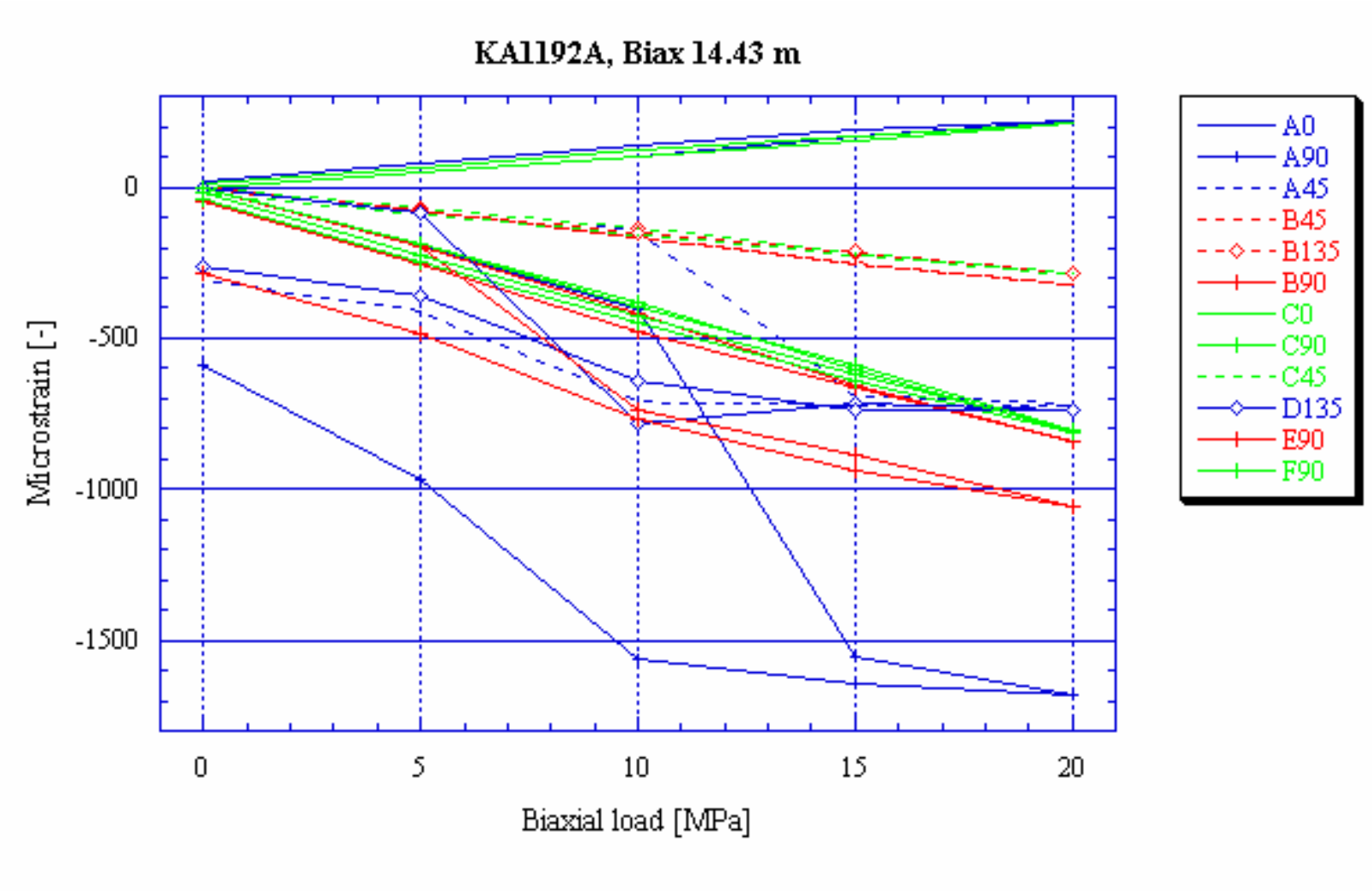
KA1192A, Biax 14.43 m
Microstrain [-]
0
-500
-1000
-1500
0
5
10
15
20
Biaxial load [MPa]
A0
A90
A45
B45
B135
B90
C0
C90
C45
D135
E90
F90

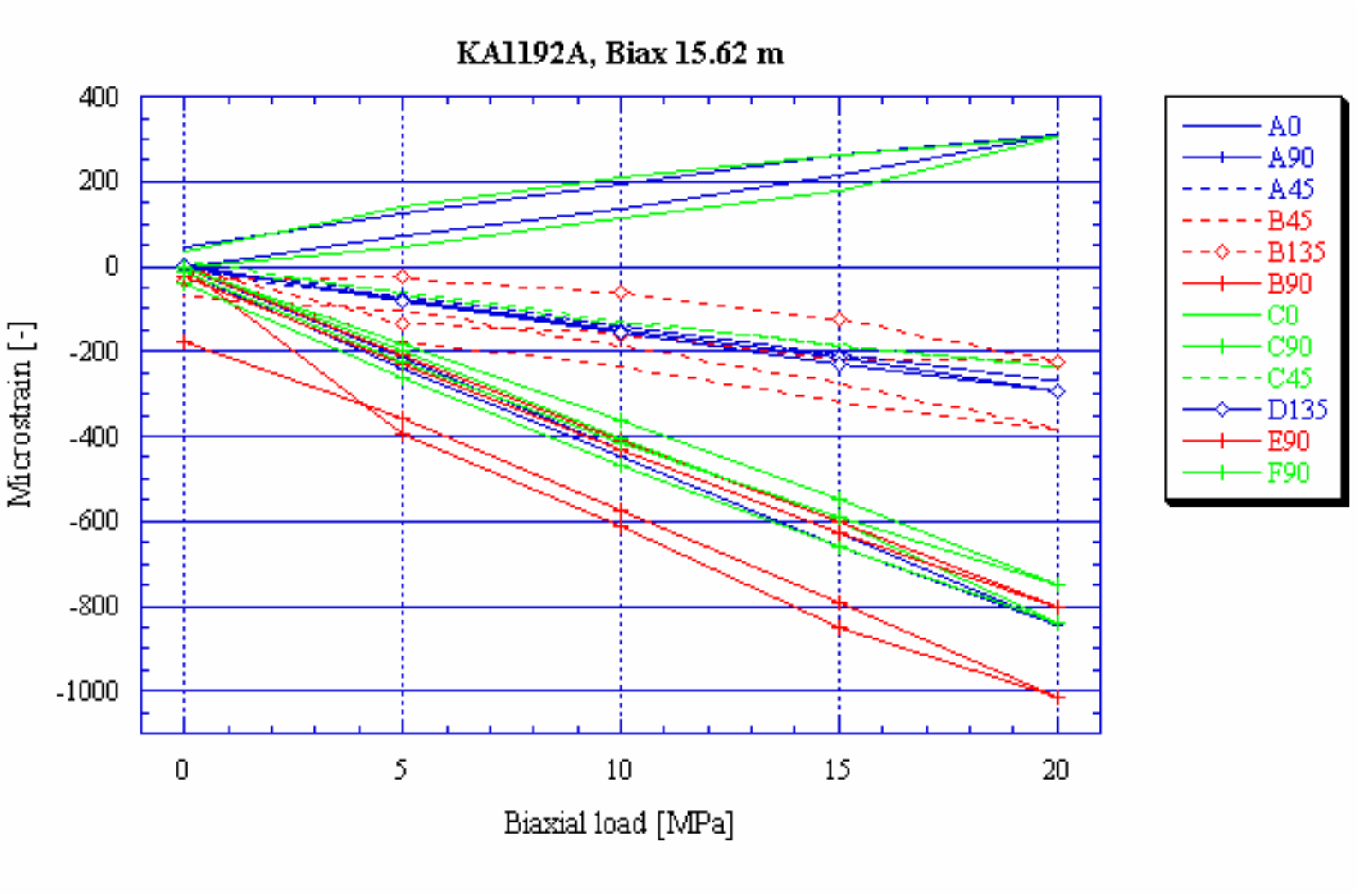
KA1192A, Biax 15.62 m
Microstrain [-]
400
200
0
-200
-400
-600
-800
-1000
0
5
10
15
20
Biaxial load [MPa]
A0
A90
A45
B45
B135
B90
C0
C90
C45
D135
E90
F90

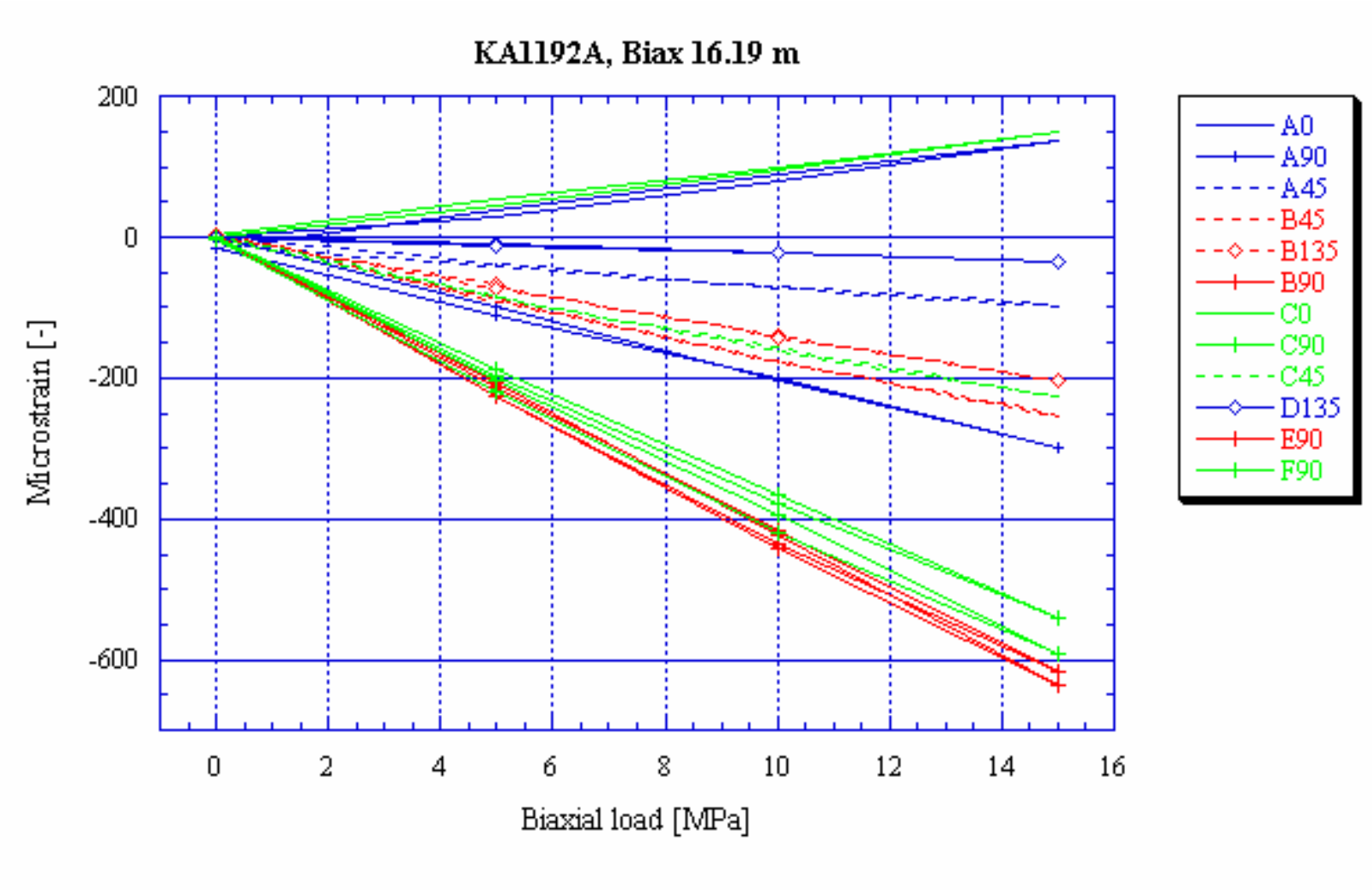
KA1192A, Biax 16.19 m
Microstrain [-]
200
0
-200
-400
-600
0
2
4
6
8
10
12
14
16
Biaxial load [MPa]
A0
A90
A45
B45
B135
B90
C0
C90
C45
D135
E90
F90

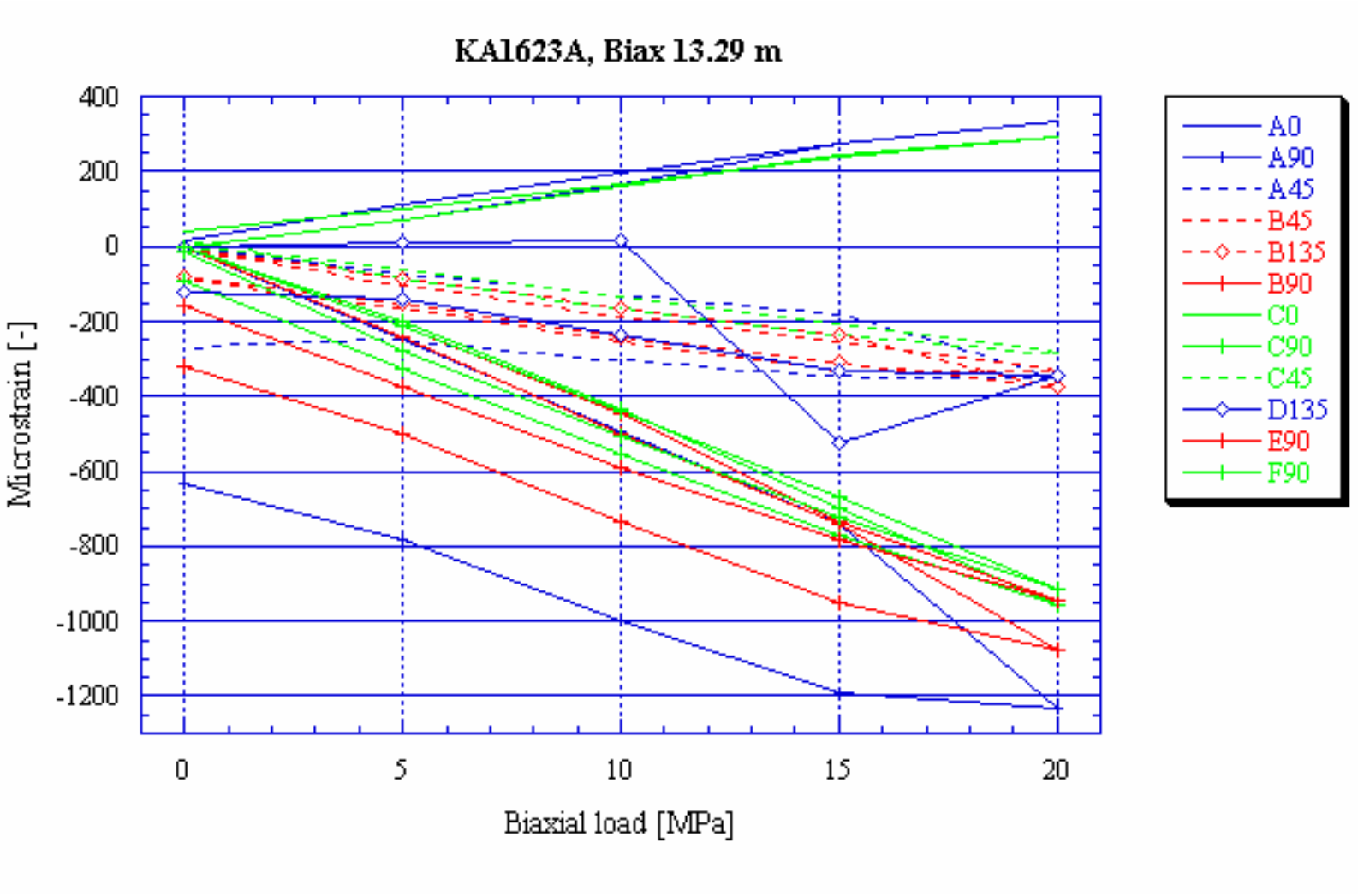
KA1623A, Biax 13.29 m
Microstrain [-]
400
200
0
-200
-400
-600
-800
-1000
-1200
0
5
10
15
20
Biaxial load [MPa]
A0
A90
A45
B45
B135
B90
C0
C90
C45
D135
E90
F90

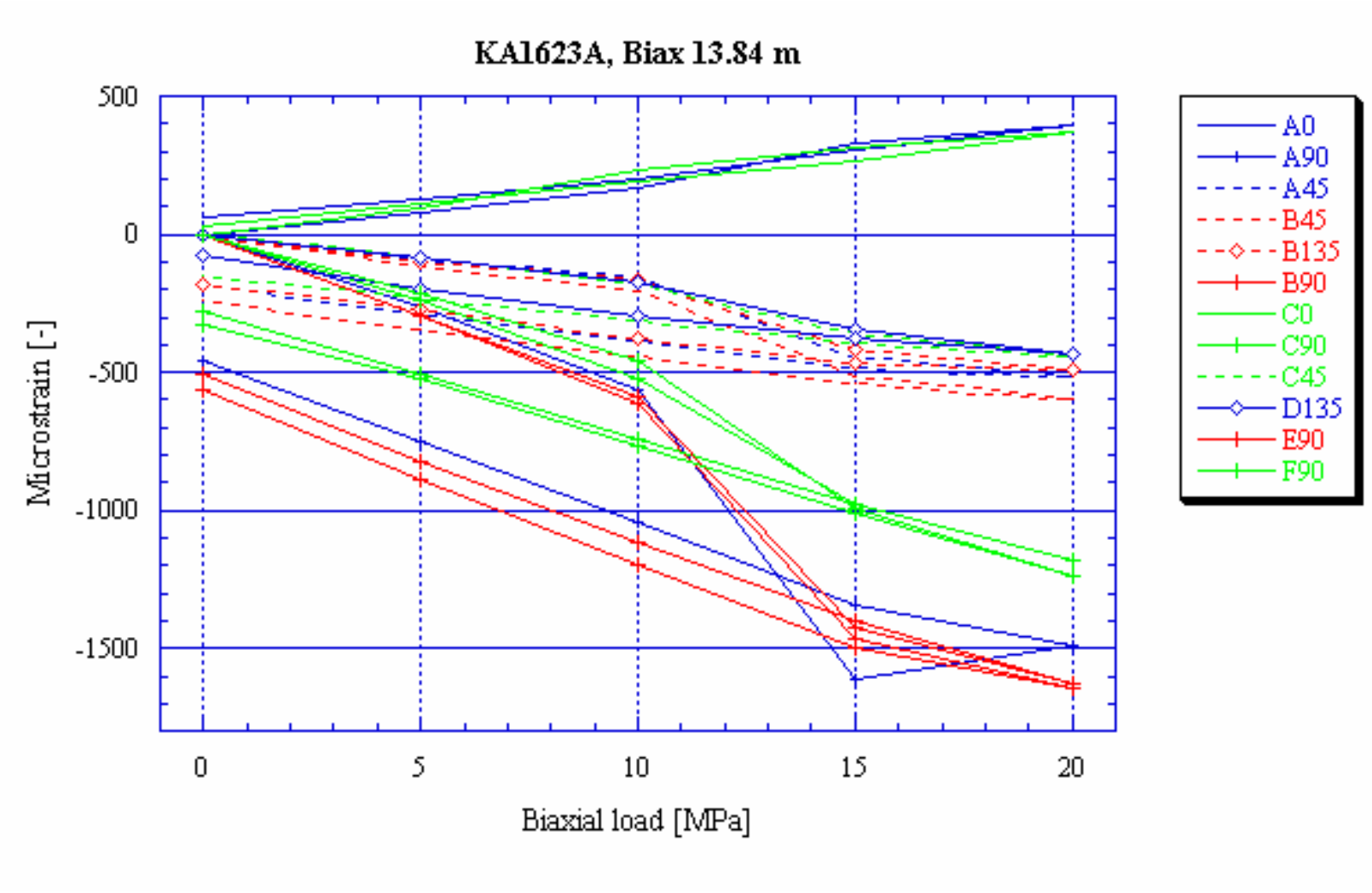
KA1623A, Biax 13.84 m
500
0
-500
-1000
-1500
Microstrain [-]
0
5
10
15
20
Biaxial load [MPa]
A0
A90
A45
B45
B135
B90
C0
C90
C45
D135
E90
F90

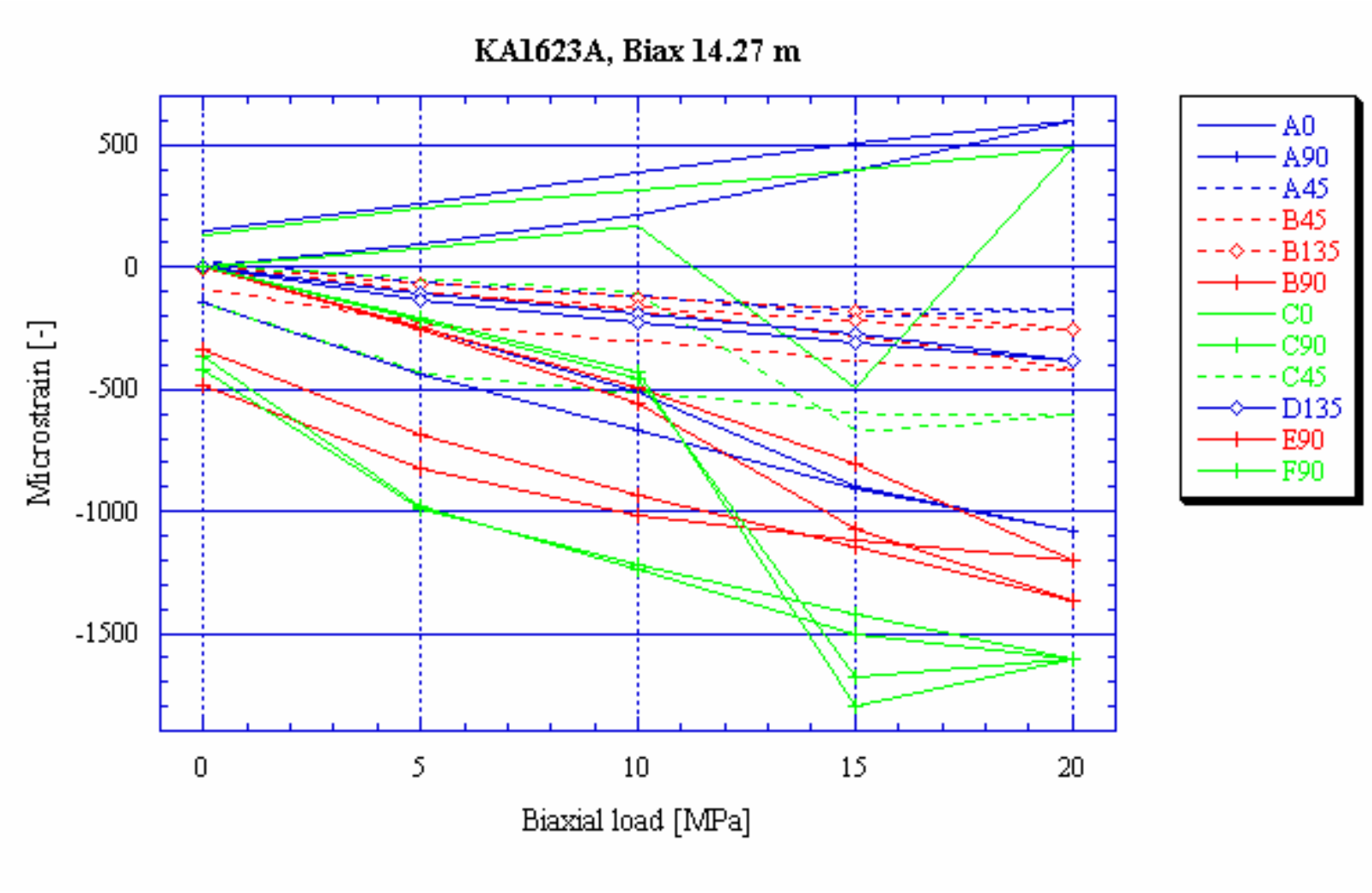
KA1623A, Biax 14.27 m
Microstrain [-]
500
0
-500
-1000
-1500
0
5
10
15
20
Biaxial load [MPa]
A0
A90
A45
B45
B135
B90
C0
C90
C45
D135
E90
F90

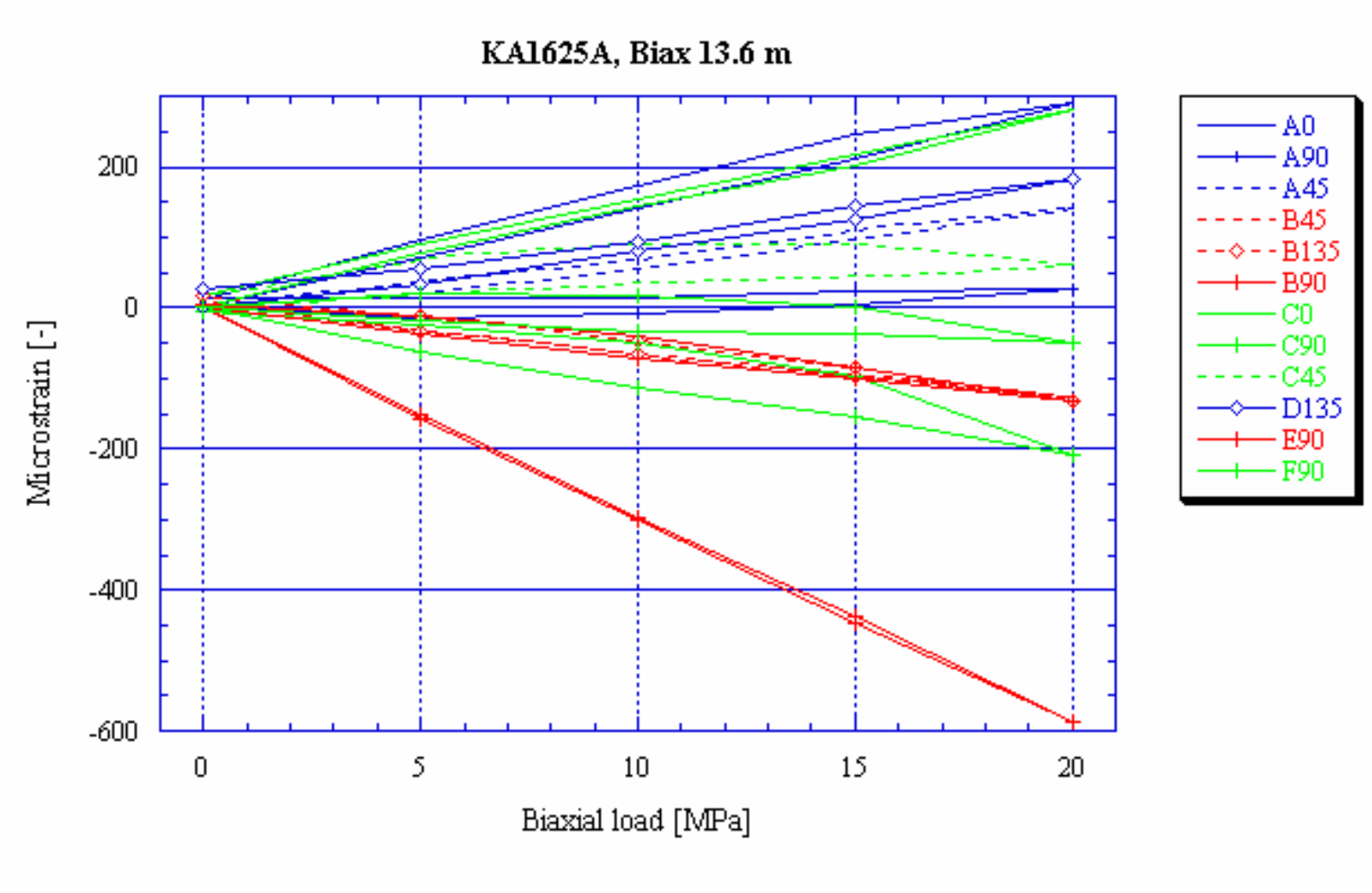
KA1625A, Biax 13.6 m
Microstrain [-]
200
0
-200
-400
-600
0
5
10
15
20
Biaxial load [MPa]
A0
A90
A45
B45
B135
B90
C0
C90
C45
D135
E90
F90

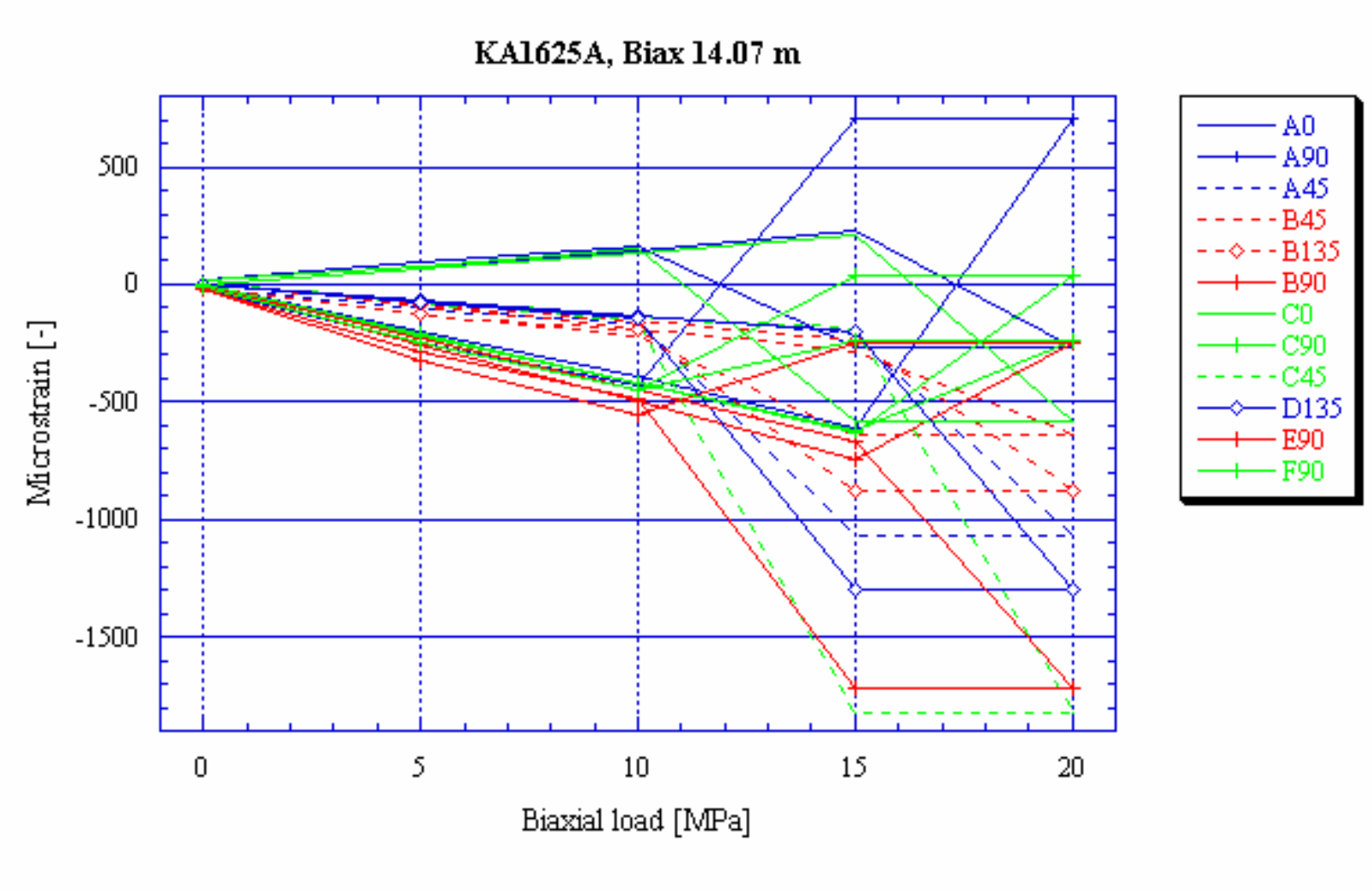
KA1625A, Biax 14.07 m
Microstrain [-]
500
0
-500
-1000
-1500
0
5
10
15
20
Biaxial load [MPa]
A0
A90
A45
B45
B135
B90
C0
C90
C45
D135
E90
F90

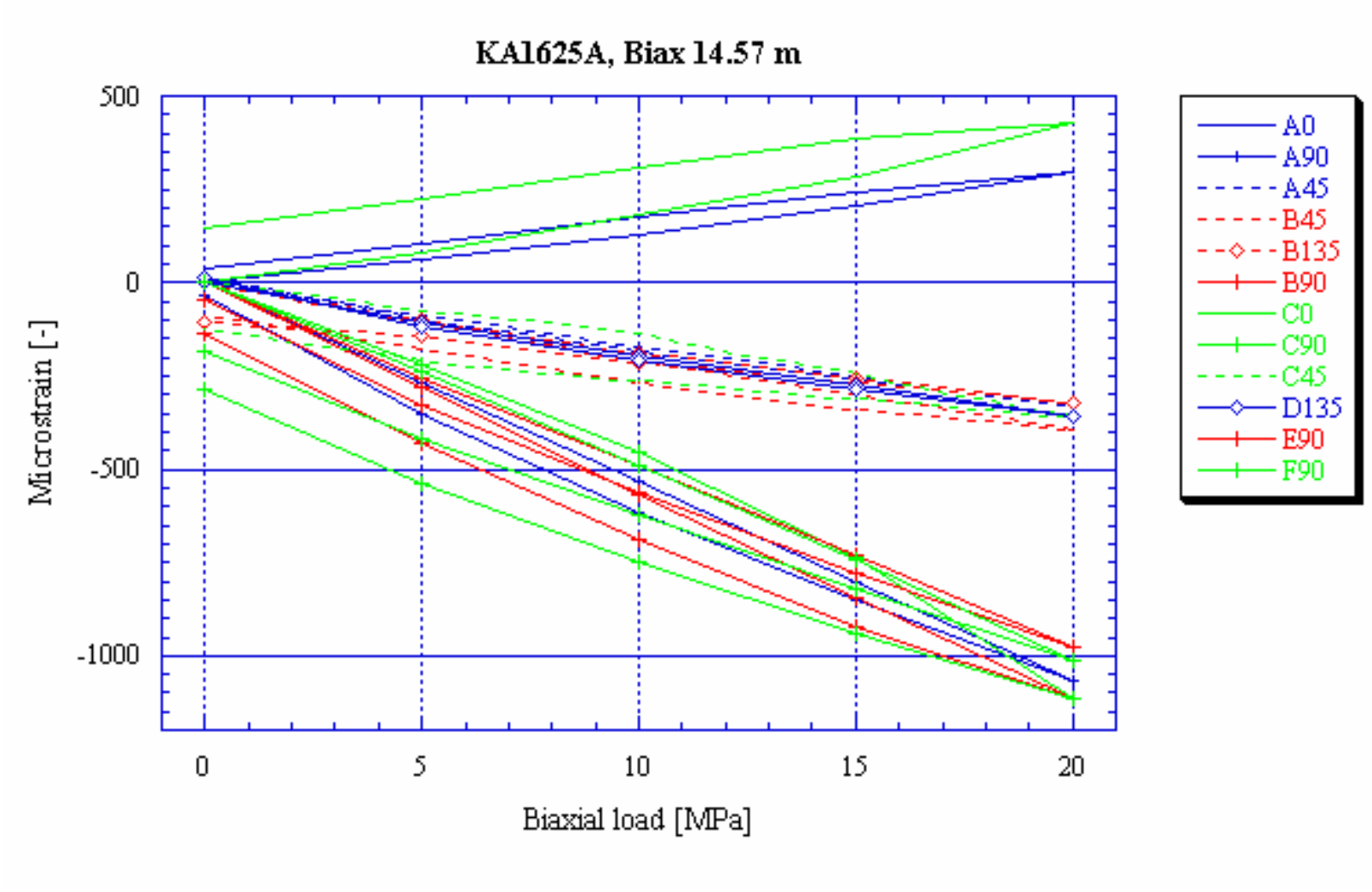
KA1625A, Biax 14.57 m
500
0
-500
-1000
Microstrain [-]
0
5
10
15
20
Biaxial load [MPa]
A0
A90
A45
B45
B135
B90
C0
C90
C45
D135
E90
F90

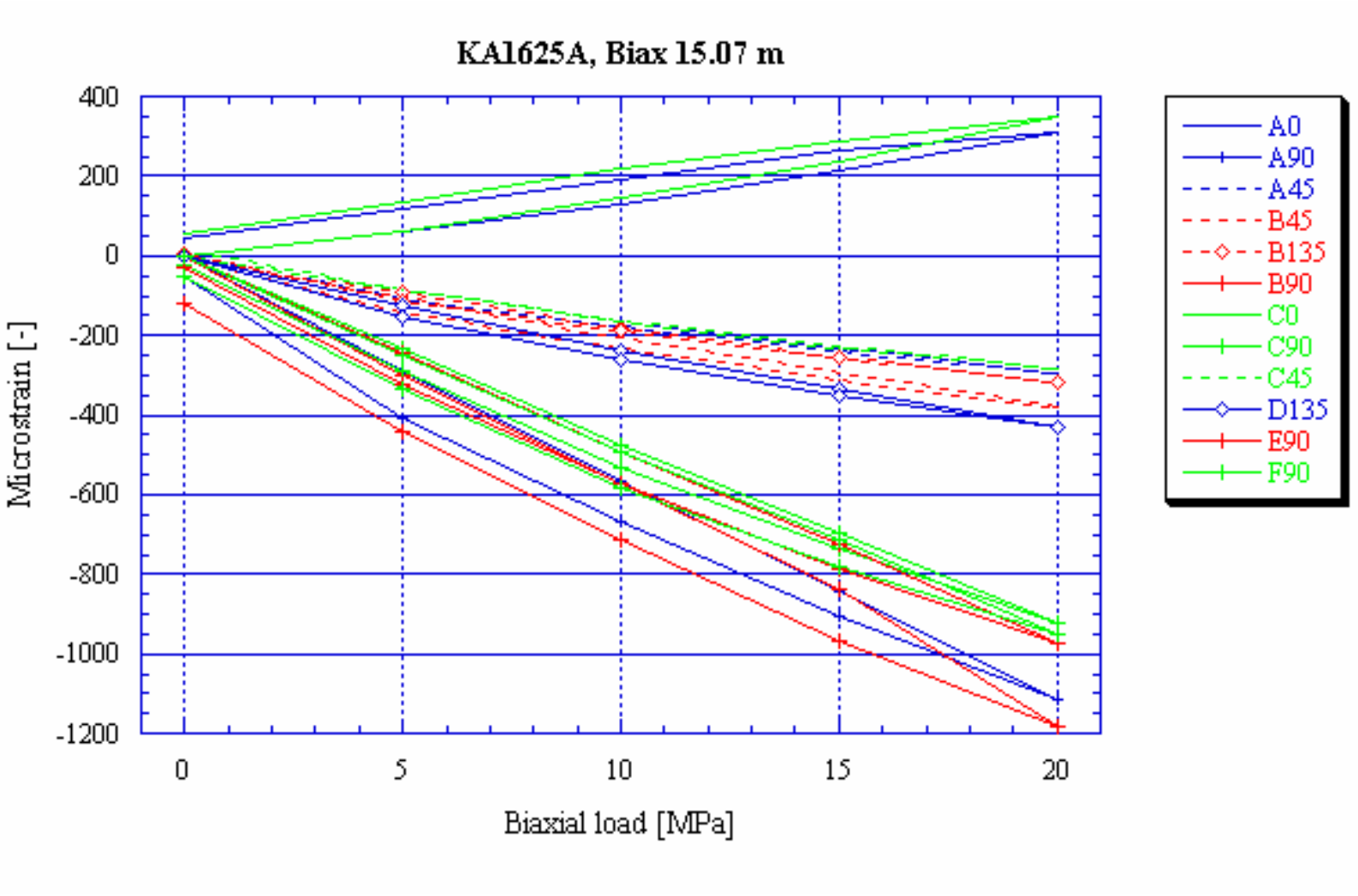
KA1625A, Biax 15.07 m
Microstrain [-]
400
200
0
-200
-400
-600
-800
-1000
-1200
0
5
10
15
20
Biaxial load [MPa]
A0
A90
A45
B45
B135
B90
C0
C90
C45
D135
E90
F90

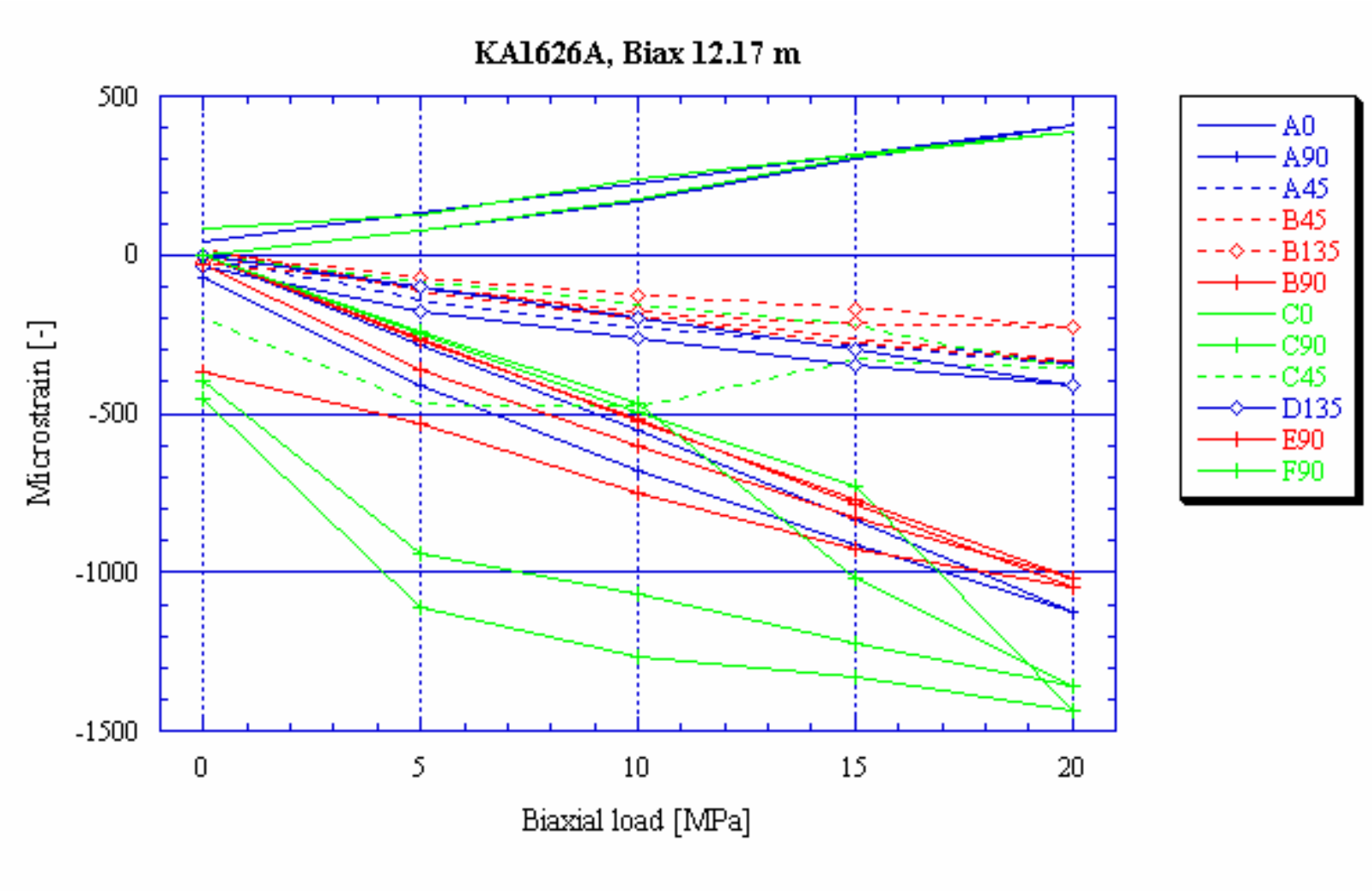
KA1626A, Biax 12.17 m
500
0
-500
-1000
-1500
Microstrain [-]
0
5
10
15
20
Biaxial load [MPa]
A0
A90
A45
B45
B135
B90
C0
C90
C45
D135
E90
F90

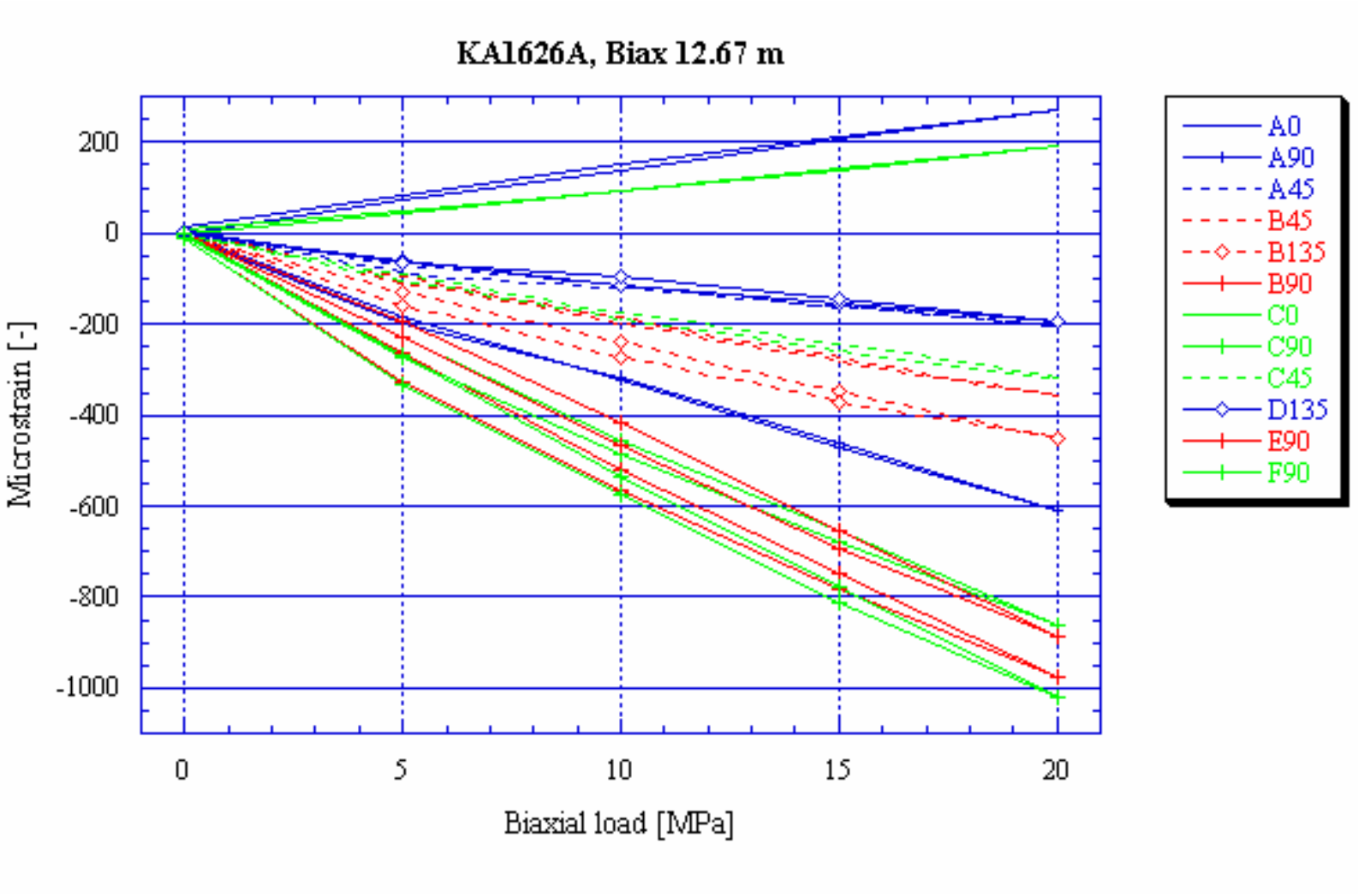
KA1626A, Biax 12.67 m
Microstrain [-]
200
0
-200
-400
-600
-800
-1000
0
5
10
15
20
Biaxial load [MPa]
A0
A90
A45
B45
B135
B90
C0
C90
C45
D135
E90
F90

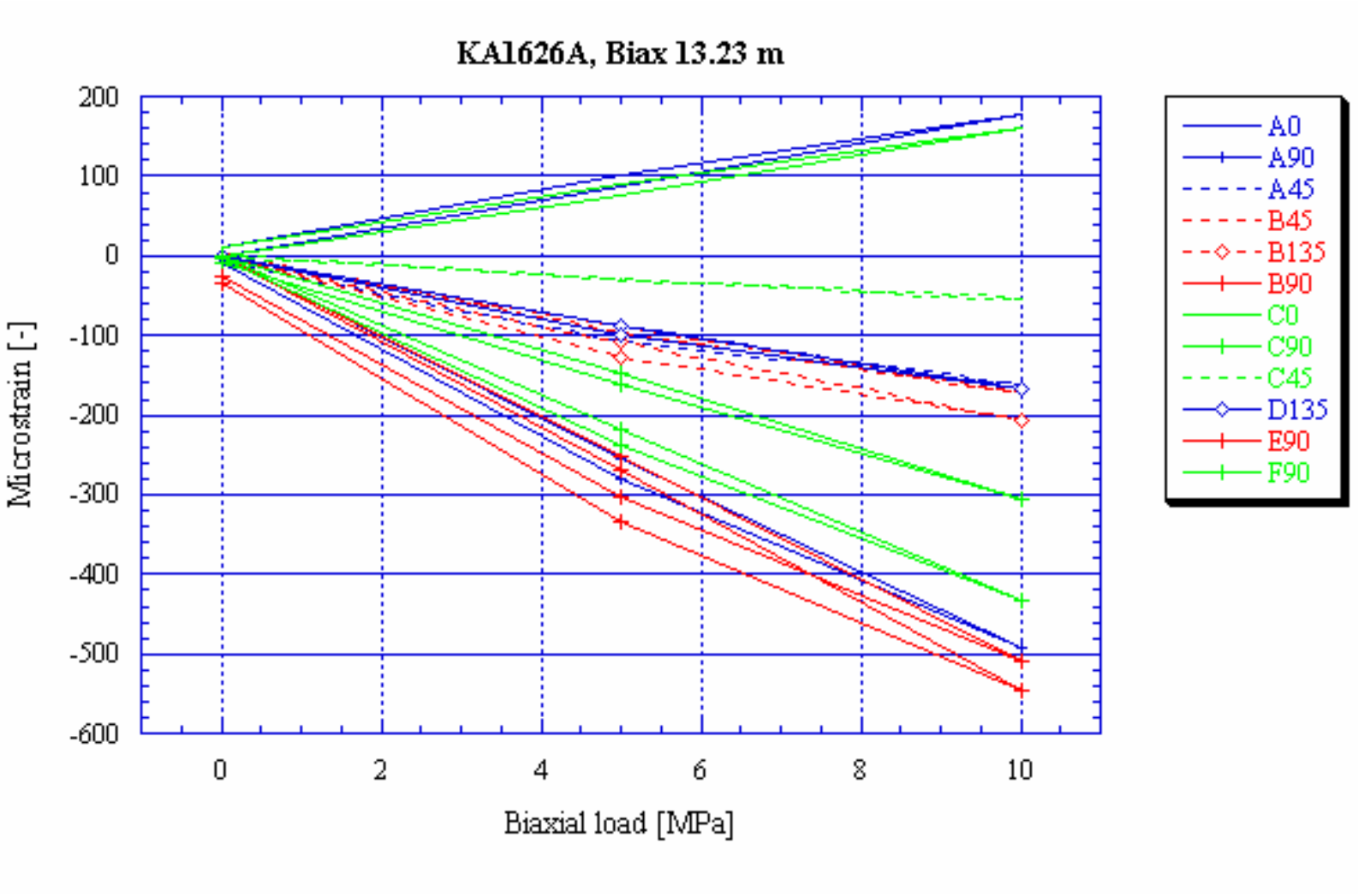
KA1626A, Biax 13.23 m
Microstrain [-]
200
100
0
-100
-200
-300
-400
-500
-600
0
2
4
6
8
10
Biaxial load [MPa]
A0
A90
A45
B45
B135
B90
C0
C90
C45
D135
E90
F90

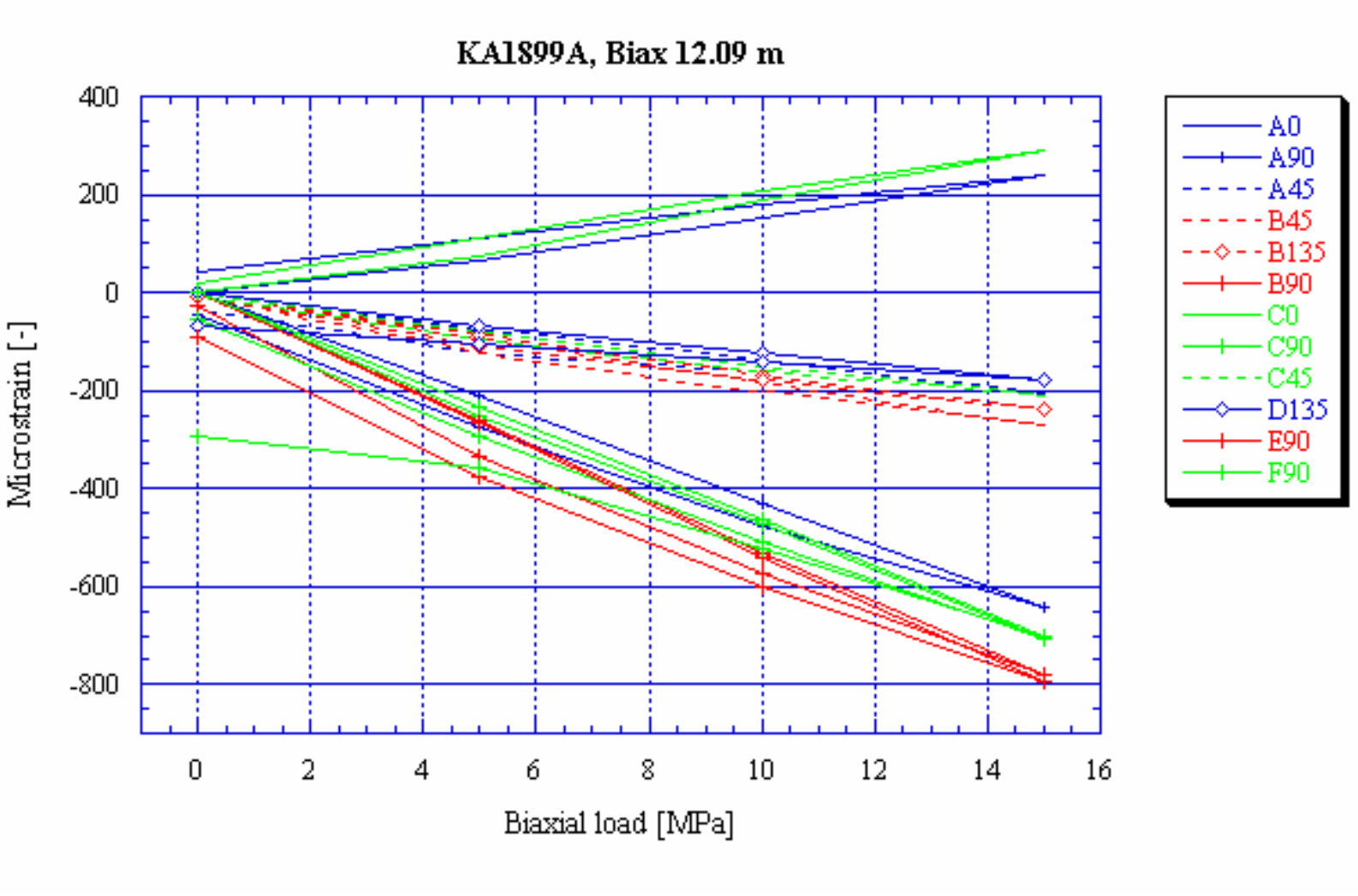
KA1899A, Biax 12.09 m
Microstrain [-]
400
200
0
-200
-400
-600
-800
0
2
4
6
8
10
12
14
16
Biaxial load [MPa]
A0
A90
A45
B45
B135
B90
C0
C90
C45
D135
E90
F90

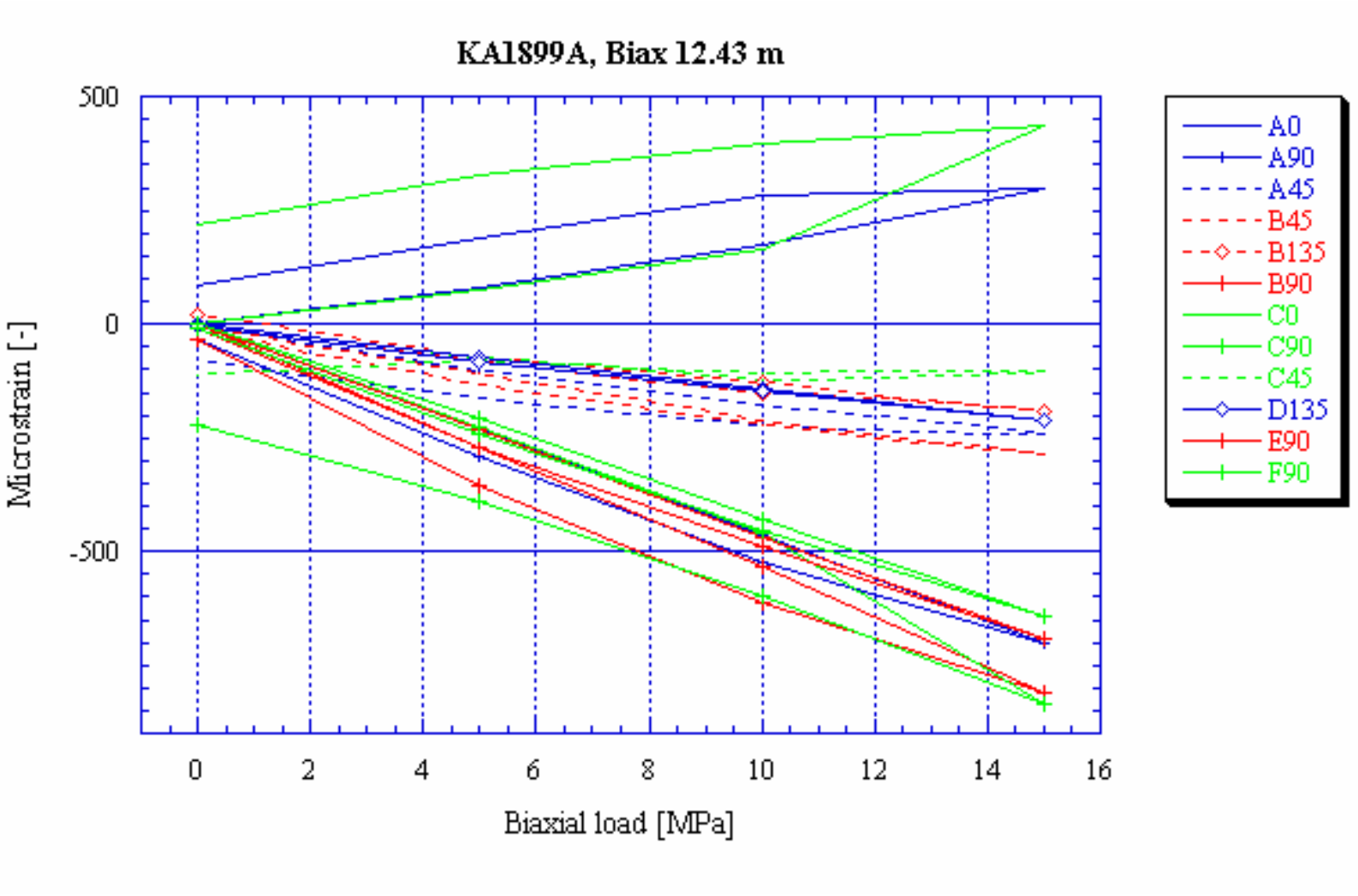
KA1899A, Biax 12.43 m
500
0
-500
Microstrain [-]
0
2
4
6
8
10
12
14
16
Biaxial load [MPa]
A0
A90
A45
B45
B135
B90
C0
C90
C45
D135
E90
F90

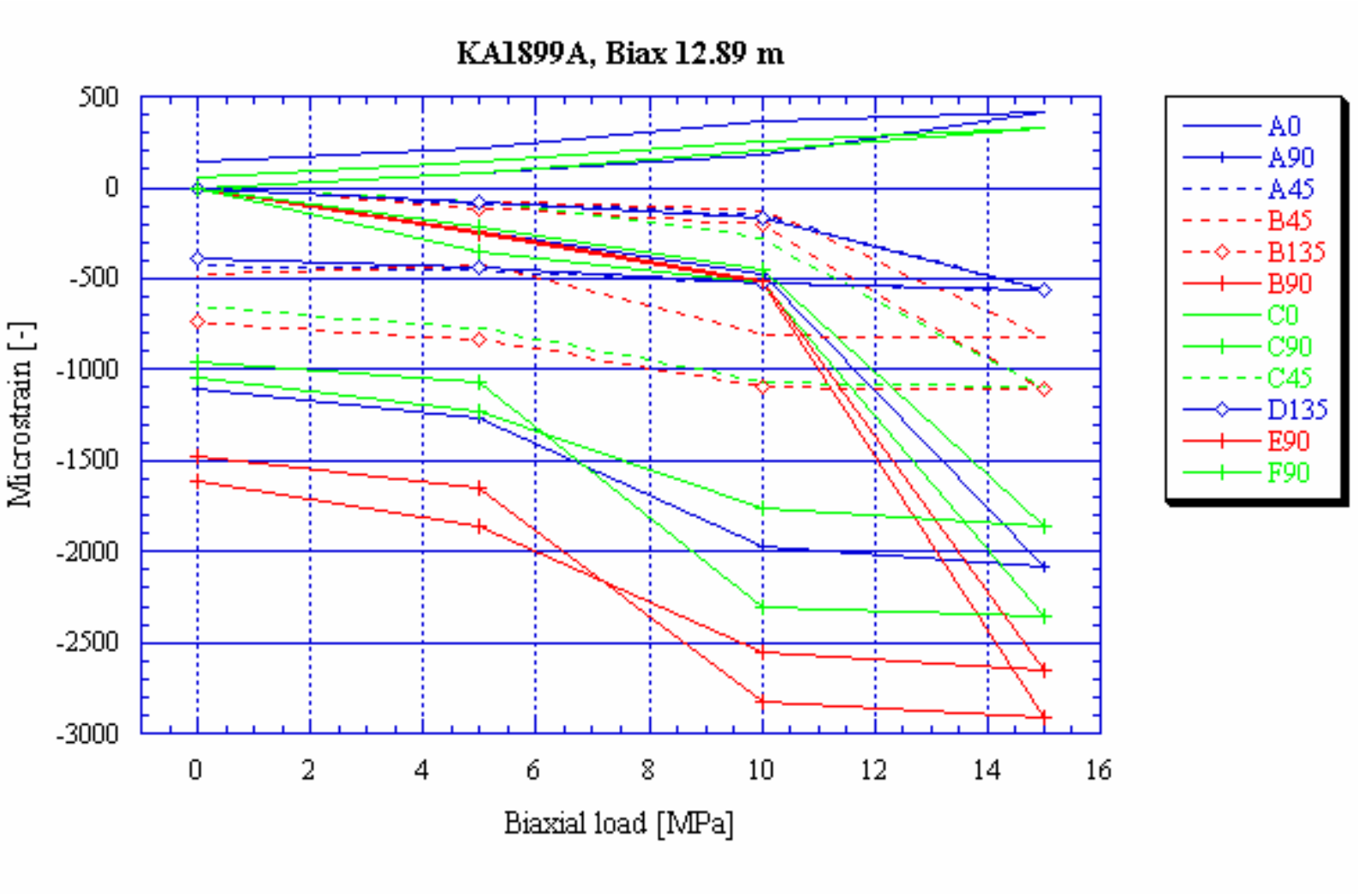
KA1899A, Biax 12.89 m
Microstrain [-]
500
0
-500
-1000
-1500
-2000
-2500
-3000
0
2
4
6
8
10
12
14
16
Biaxial load [MPa]
A0
A90
A45
B45
B135
B90
C0
C90
C45
D135
E90
F90

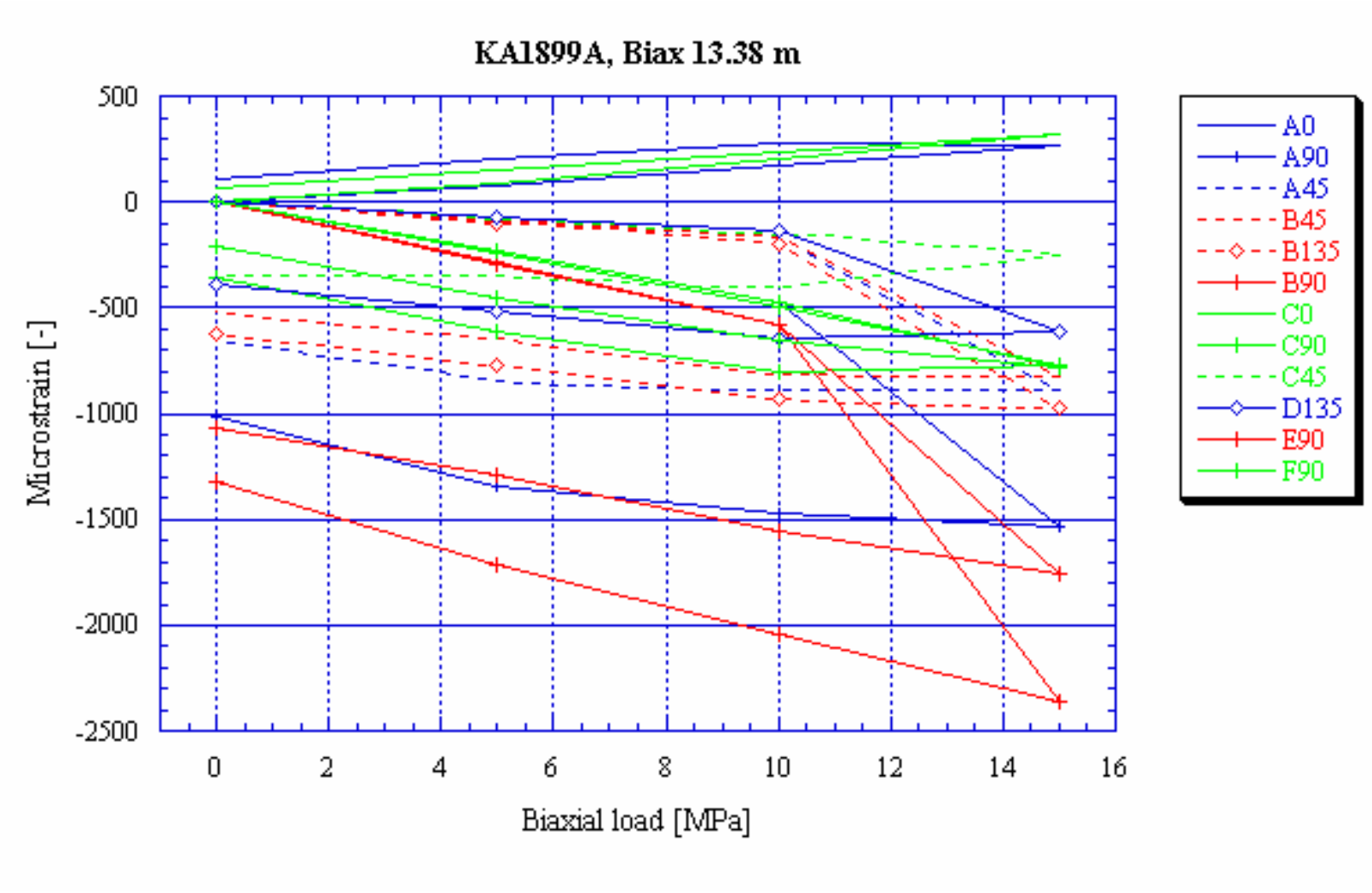
KA1899A, Biax 13.38 m
Microstrain [-]
500
0
-500
-1000
-1500
-2000
-2500
0
2
4
6
8
10
12
14
16
Biaxial load [MPa]
A0
A90
A45
B45
B135
B90
C0
C90
C45
D135
E90
F90

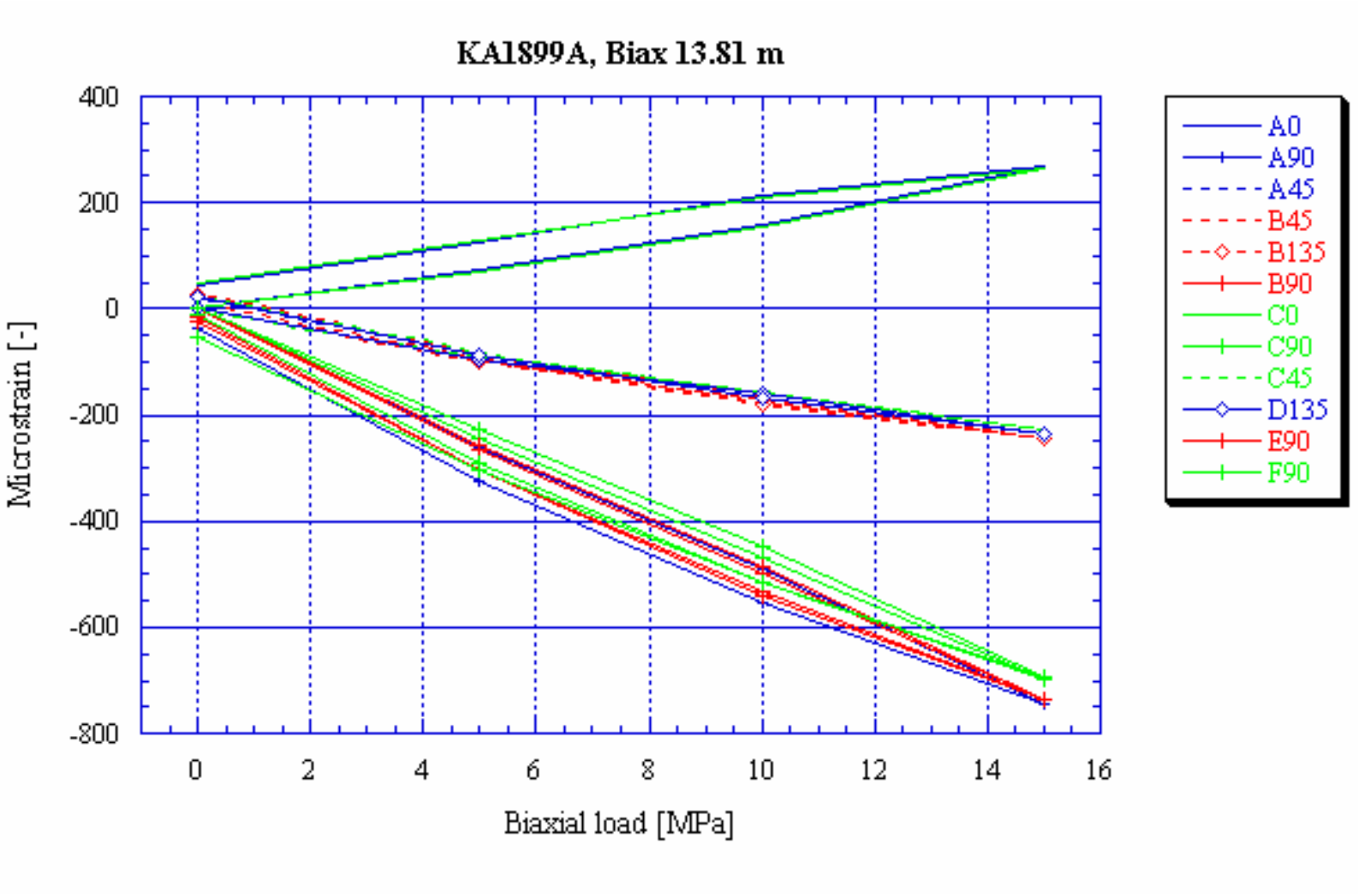
KA1899A, Biax 13.81 m
Microstrain [-]
400
200
0
-200
-400
-600
-800
0
2
4
6
8
10
12
14
16
Biaxial load [MPa]
A0
A90
A45
B45
B135
B90
C0
C90
C45
D135
E90
F90

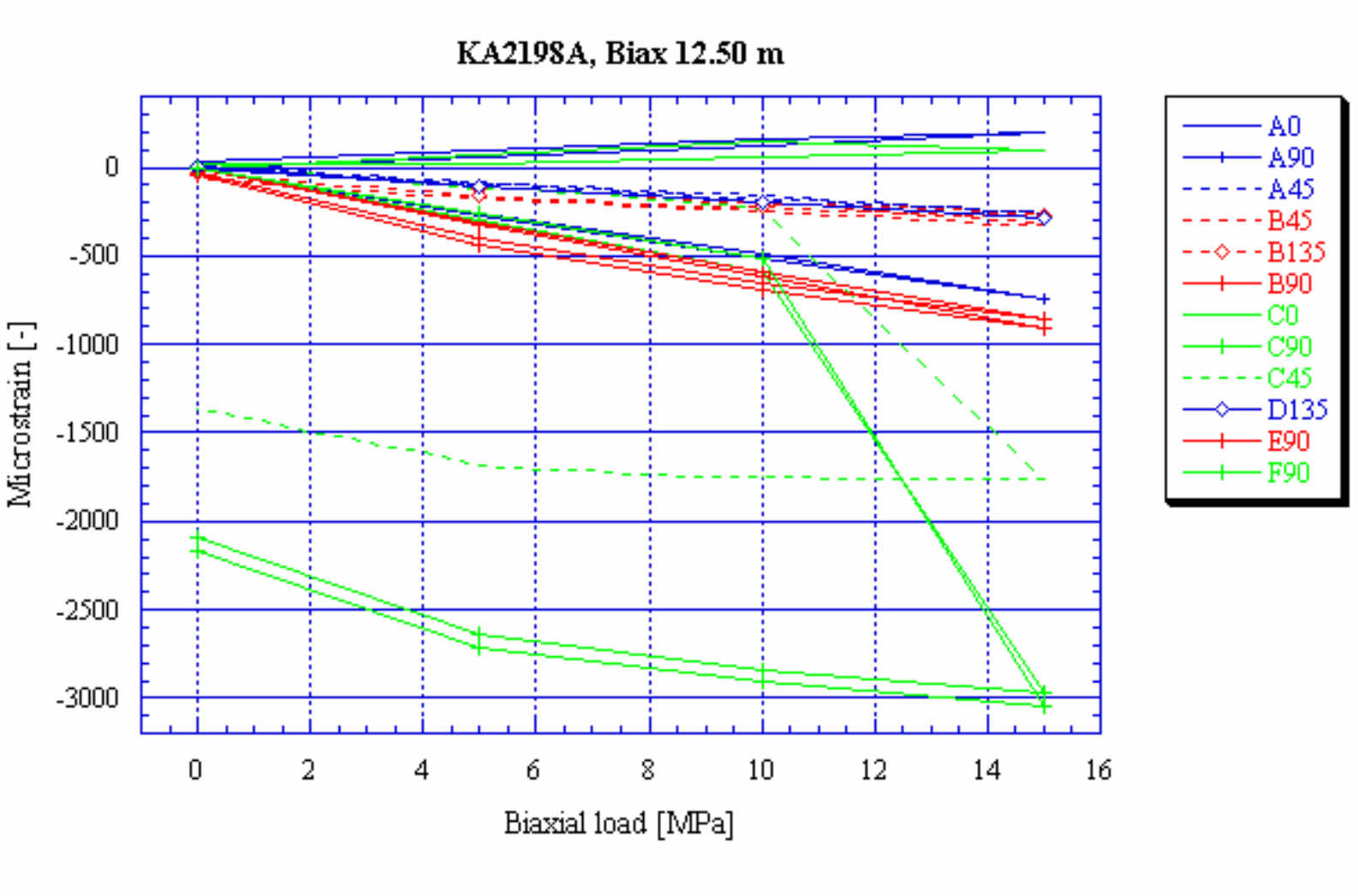
KA2198A, Biax 12.50 m
Microstrain [-]
0
-500
-1000
-1500
-2000
-2500
-3000
0
2
4
6
8
10
12
14
16
Biaxial load [MPa]
A0
A90
A45
B45
B135
B90
C0
C90
C45
D135
E90
F90

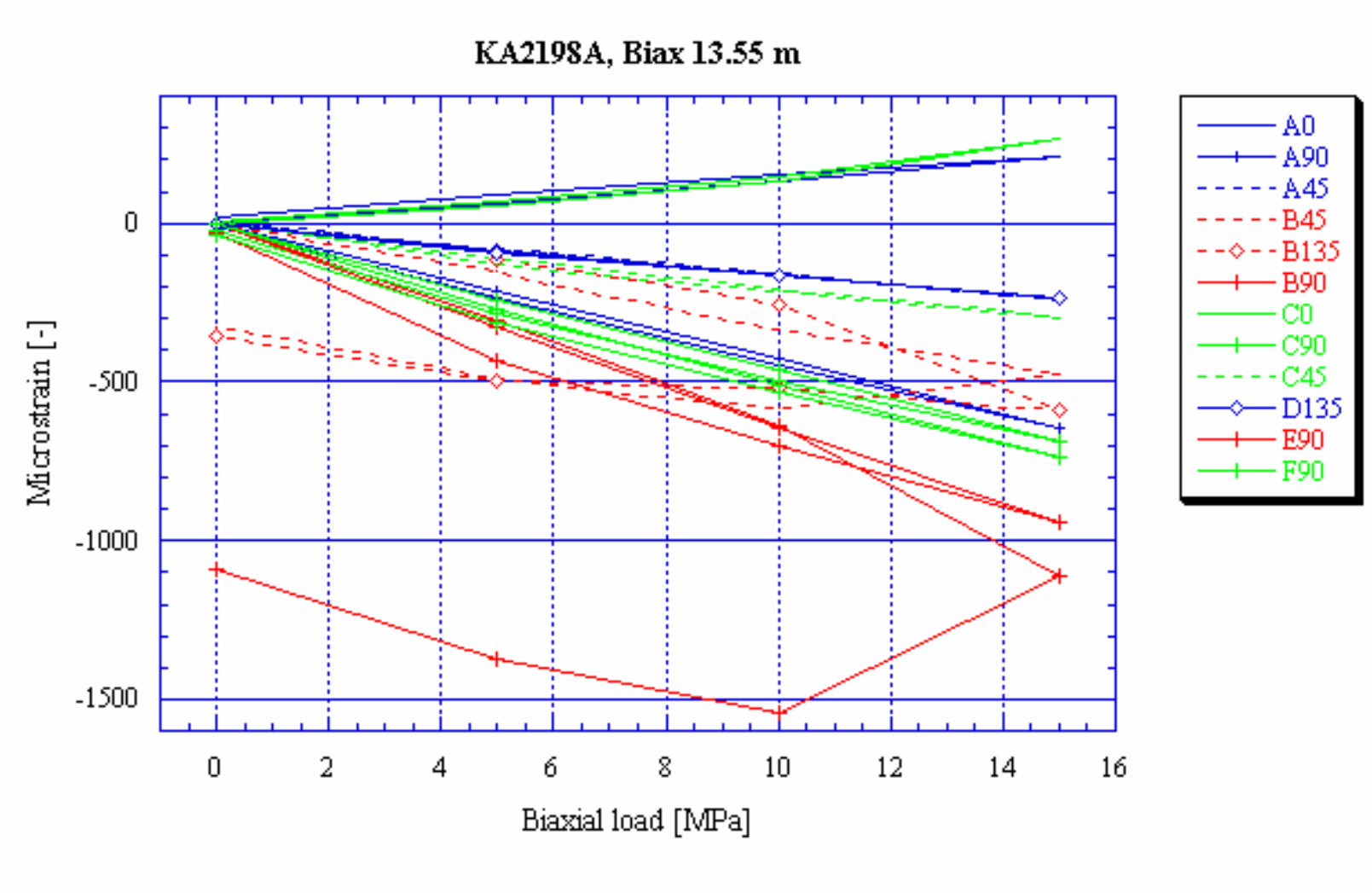
KA2198A, Biax 13.55 m
Microstrain [-]
0
-500
-1000
-1500
0
2
4
6
8
10
12
14
16
Biaxial load [MPa]
A0
A90
A45
B45
B135
B90
C0
C90
C45
D135
E90
F90

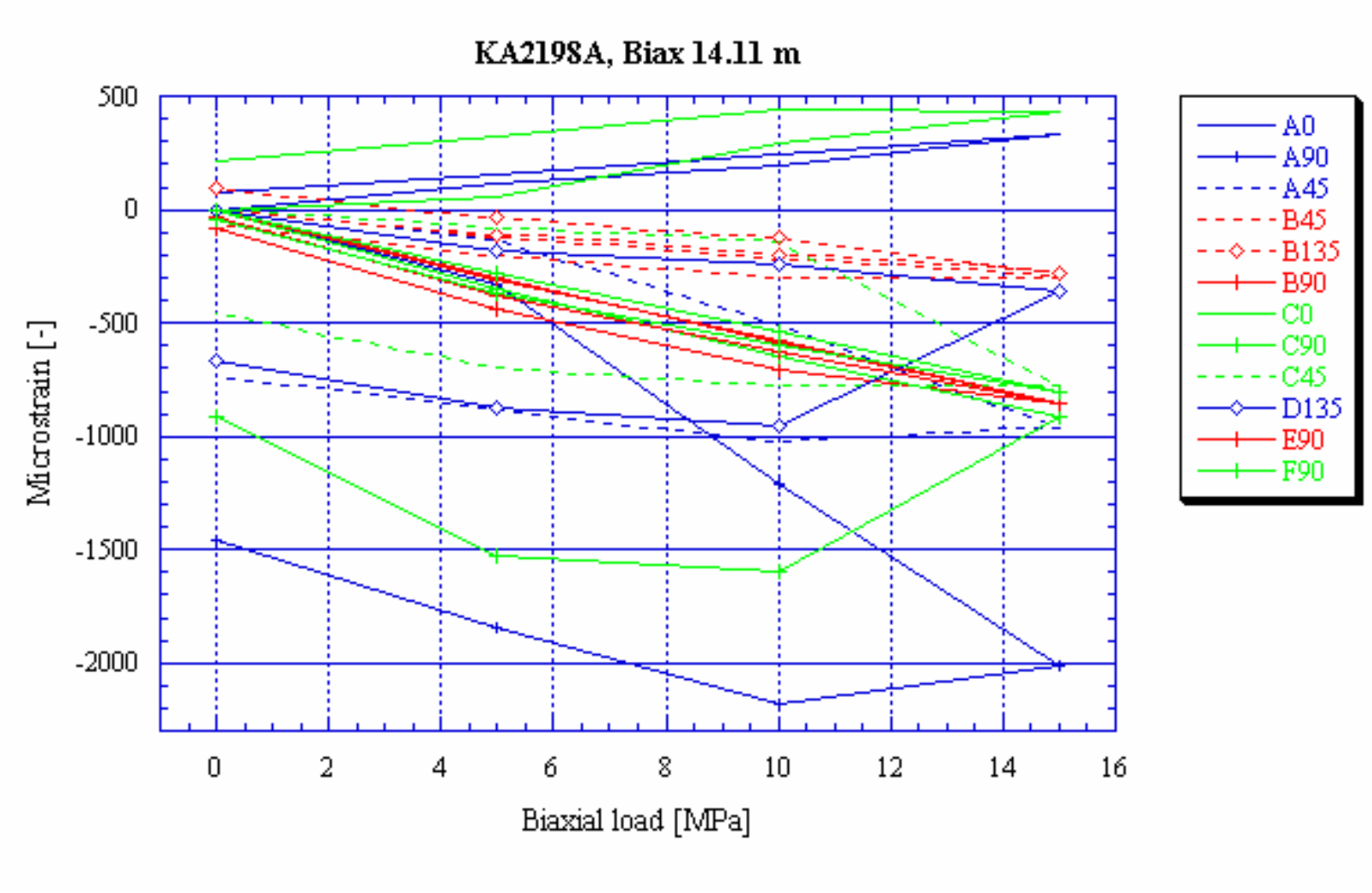
KA2198A, Biax 14.11 m
Microstrain [-]
500
0
-500
-1000
-1500
-2000
0
2
4
6
8
10
12
14
16
Biaxial load [MPa]
A0
A90
A45
B45
B135
B90
C0
C90
C45
D135
E90
F90

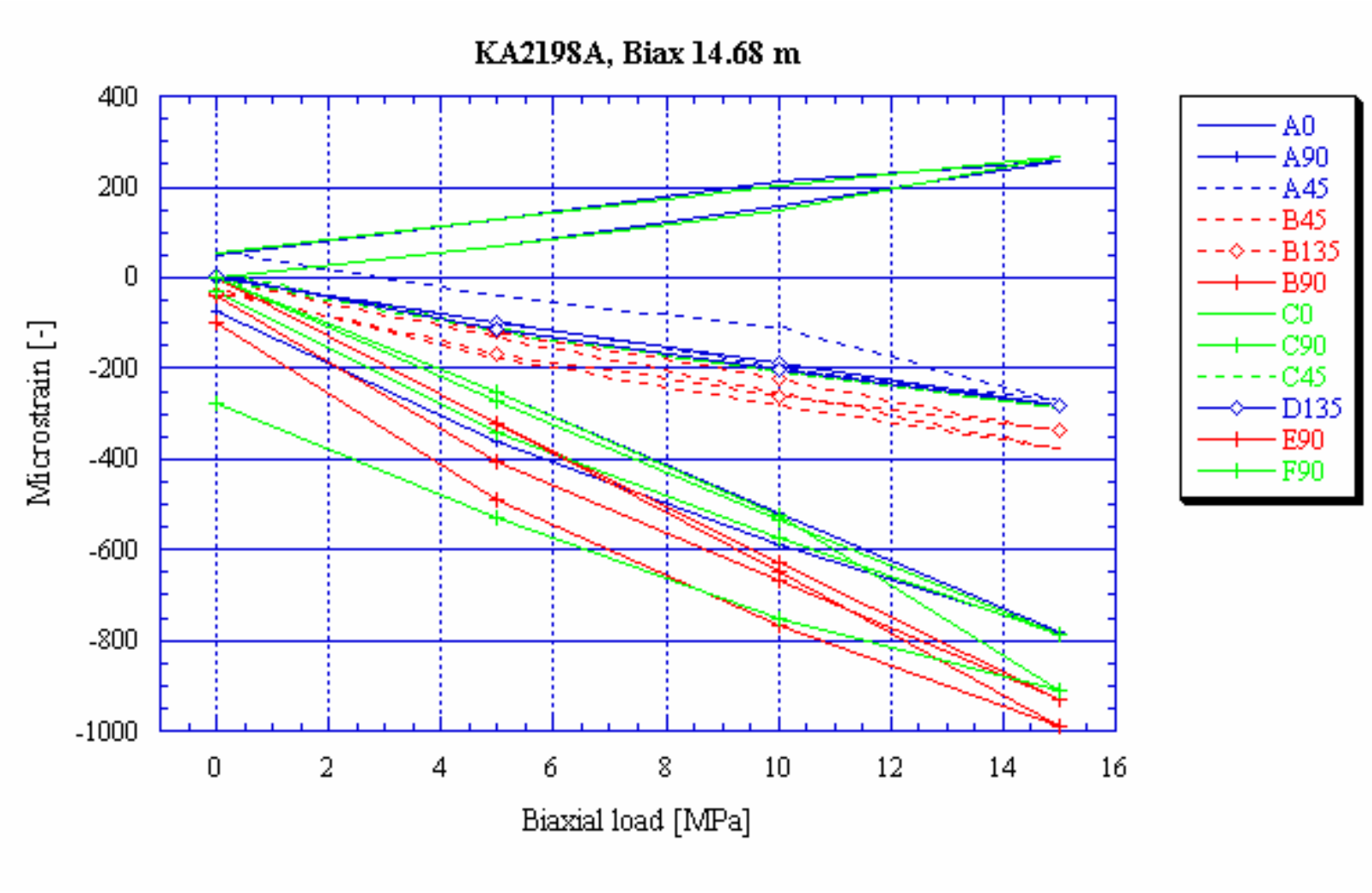
KA2198A, Biax 14.68 m
Microstrain [-]
400
200
0
-200
-400
-600
-800
-1000
0
2
4
6
8
10
12
14
16
Biaxial load [MPa]
A0
A90
A45
B45
B135
B90
C0
C90
C45
D135
E90
F90

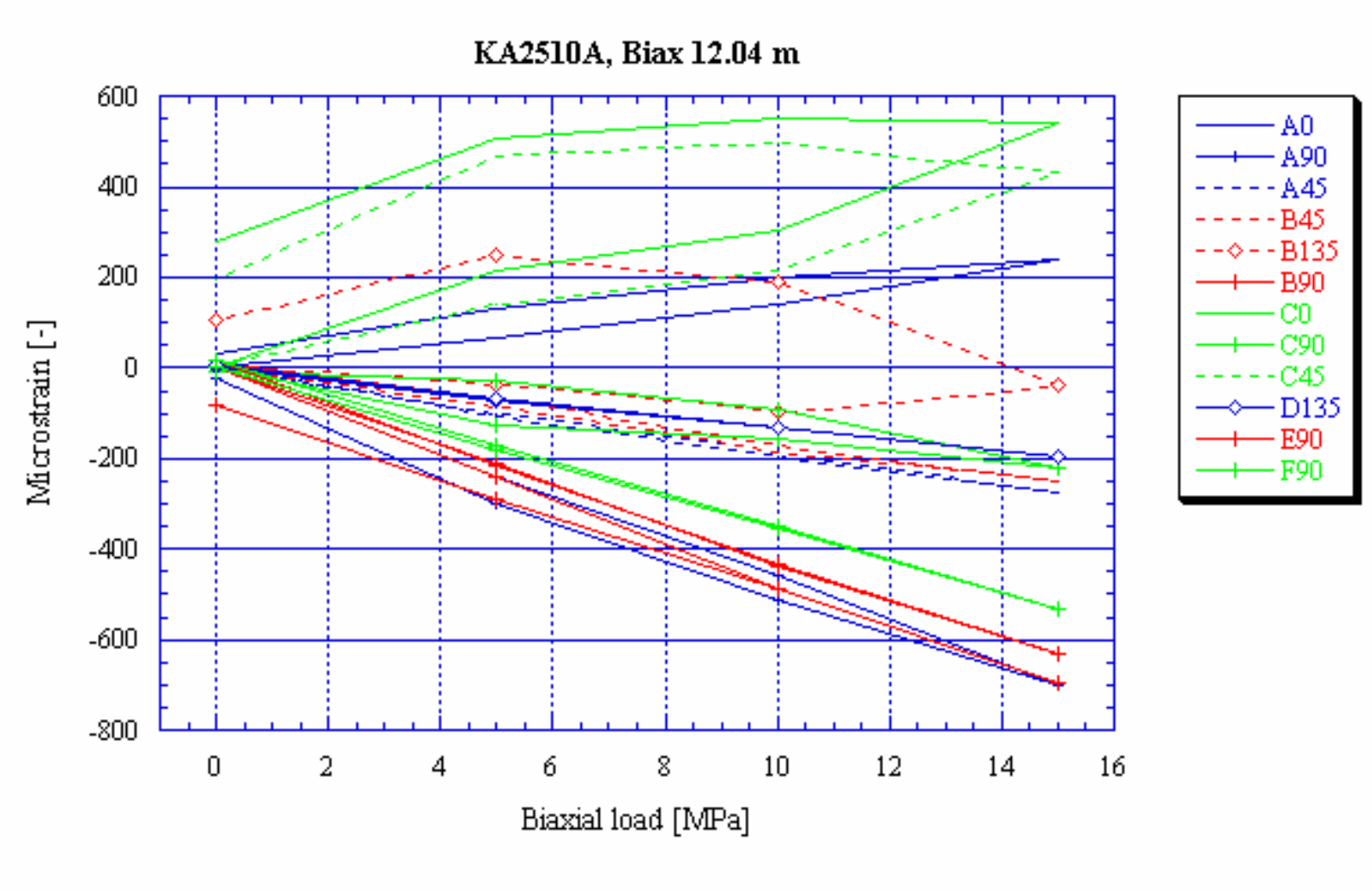
KA2510A, Biax 12.04 m
Microstrain [-]
600
400
200
0
-200
-400
-600
-800
0
2
4
6
8
10
12
14
16
Biaxial load [MPa]
A0
A90
A45
B45
B135
B90
C0
C90
C45
D135
E90
F90

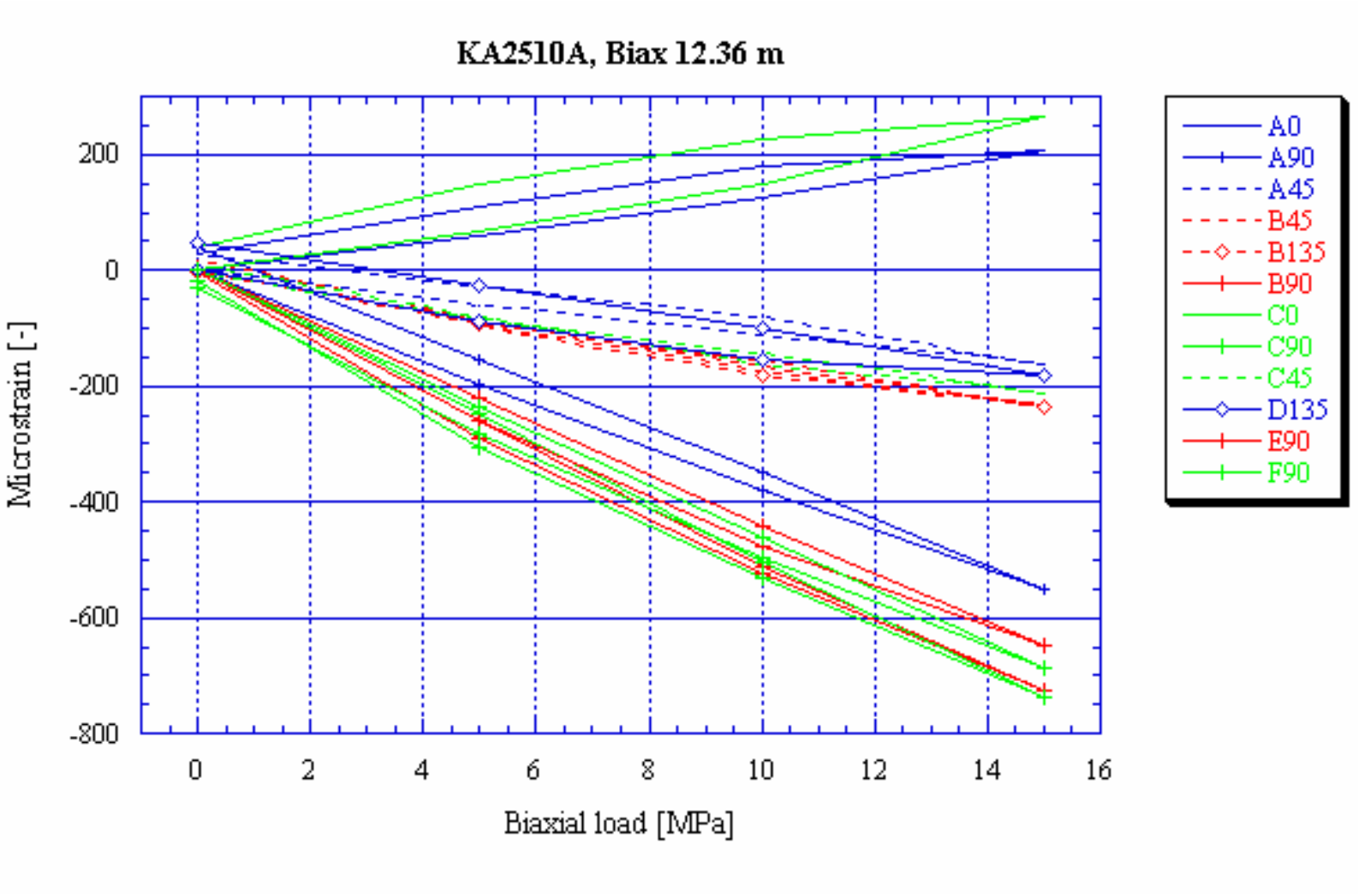
KA2510A, Biax 12.36 m
Microstrain [-]
200
0
-200
-400
-600
-800
0
2
4
6
8
10
12
14
16
Biaxial load [MPa]
A0
A90
A45
B45
B135
B90
C0
C90
C45
D135
E90
F90

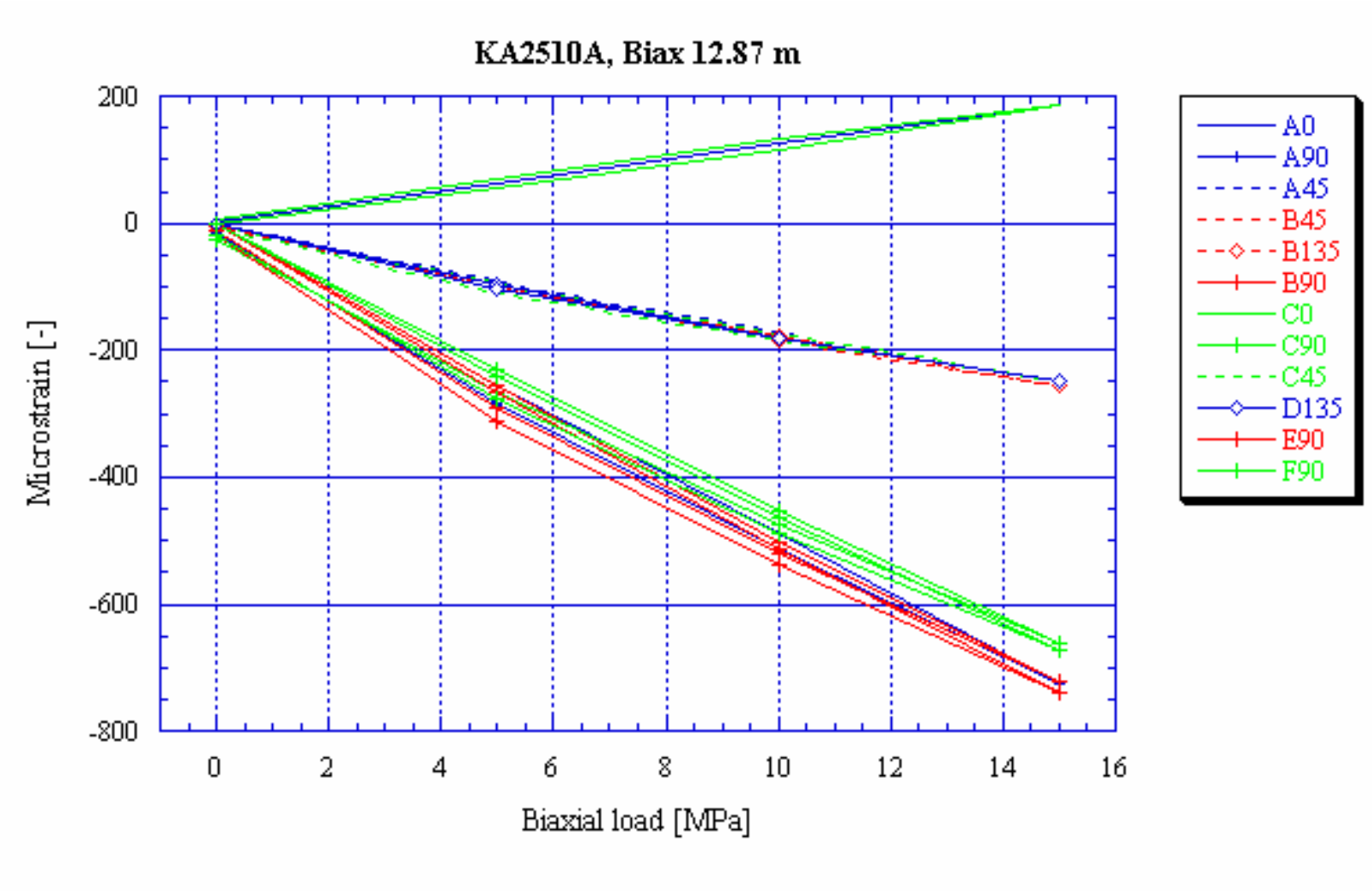
KA2510A, Biax 12.87 m
Microstrain [-]
200
0
-200
-400
-600
-800
0
2
4
6
8
10
12
14
16
Biaxial load [MPa]
A0
A90
A45
B45
B135
B90
C0
C90
C45
D135
E90
F90

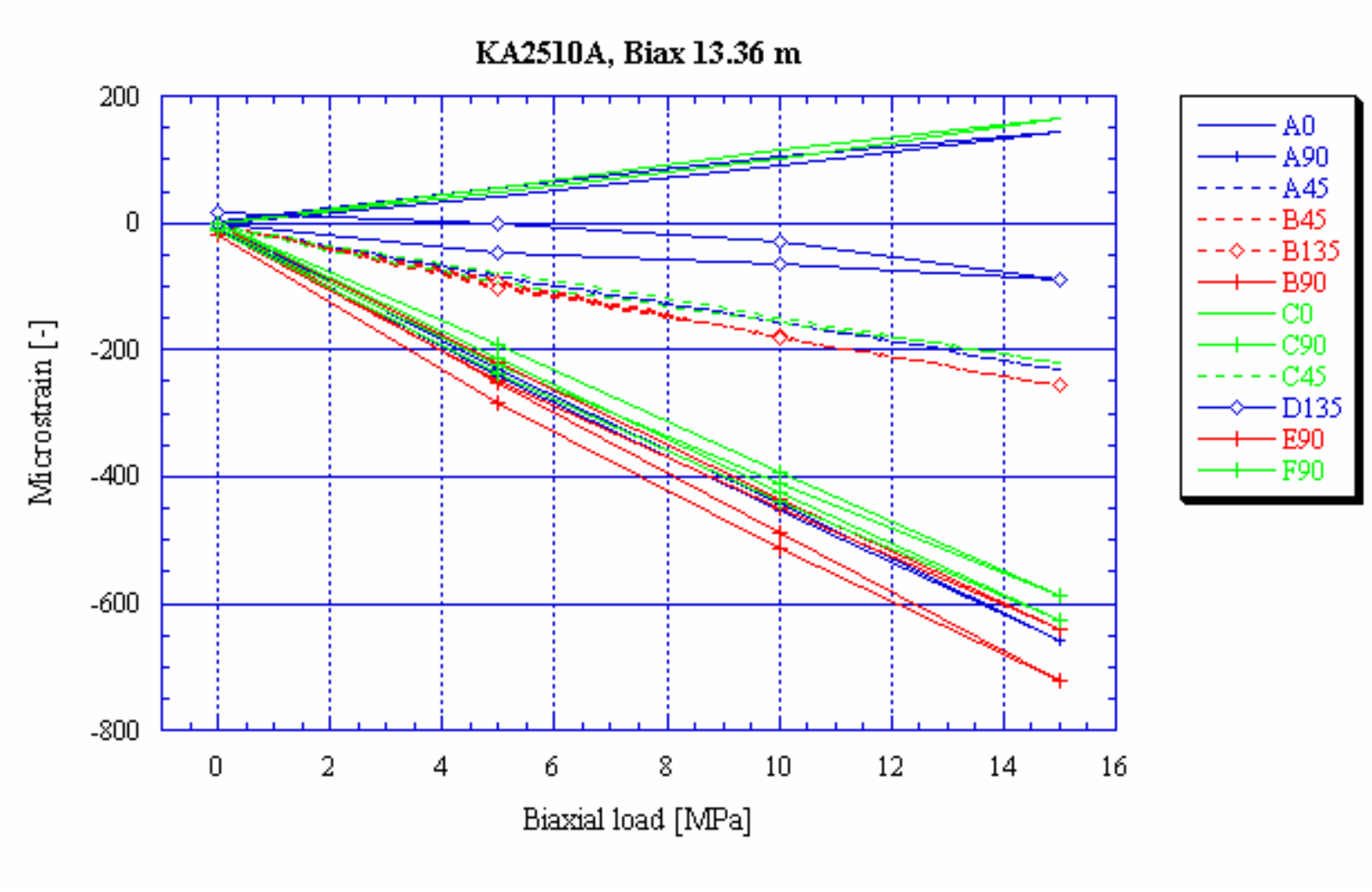
KA2510A, Biax 13.36 m
Microstrain [-]
200
0
-200
-400
-600
-800
0
2
4
6
8
10
12
14
16
Biaxial load [MPa]
A0
A90
A45
B45
B135
B90
C0
C90
C45
D135
E90
F90

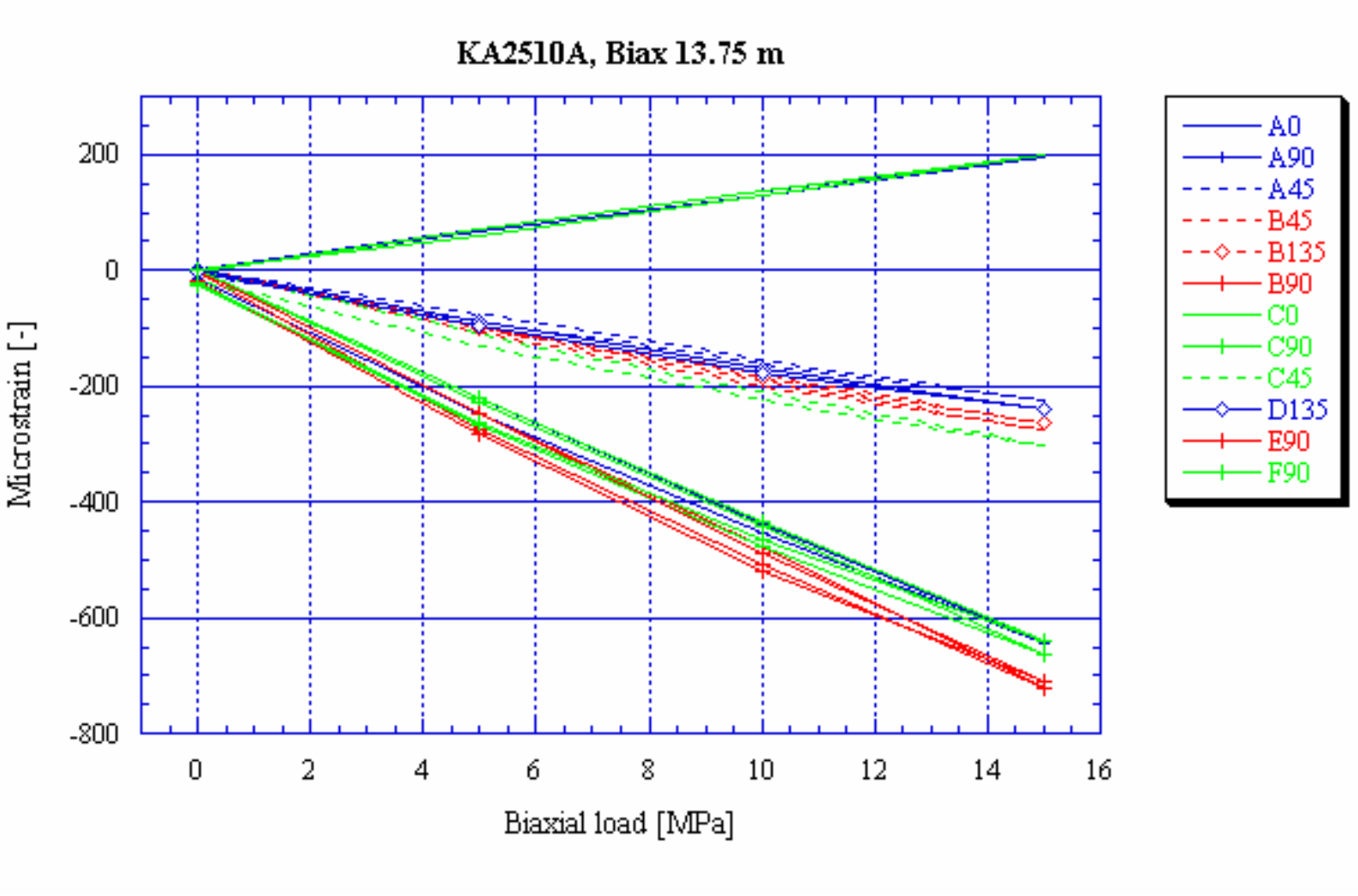
KA2510A, Biax 13.75 m
Microstrain [-]
200
0
-200
-400
-600
-800
0
2
4
6
8
10
12
14
16
Biaxial load [MPa]
A0
A90
A45
B45
B135
B90
C0
C90
C45
D135
E90
F90

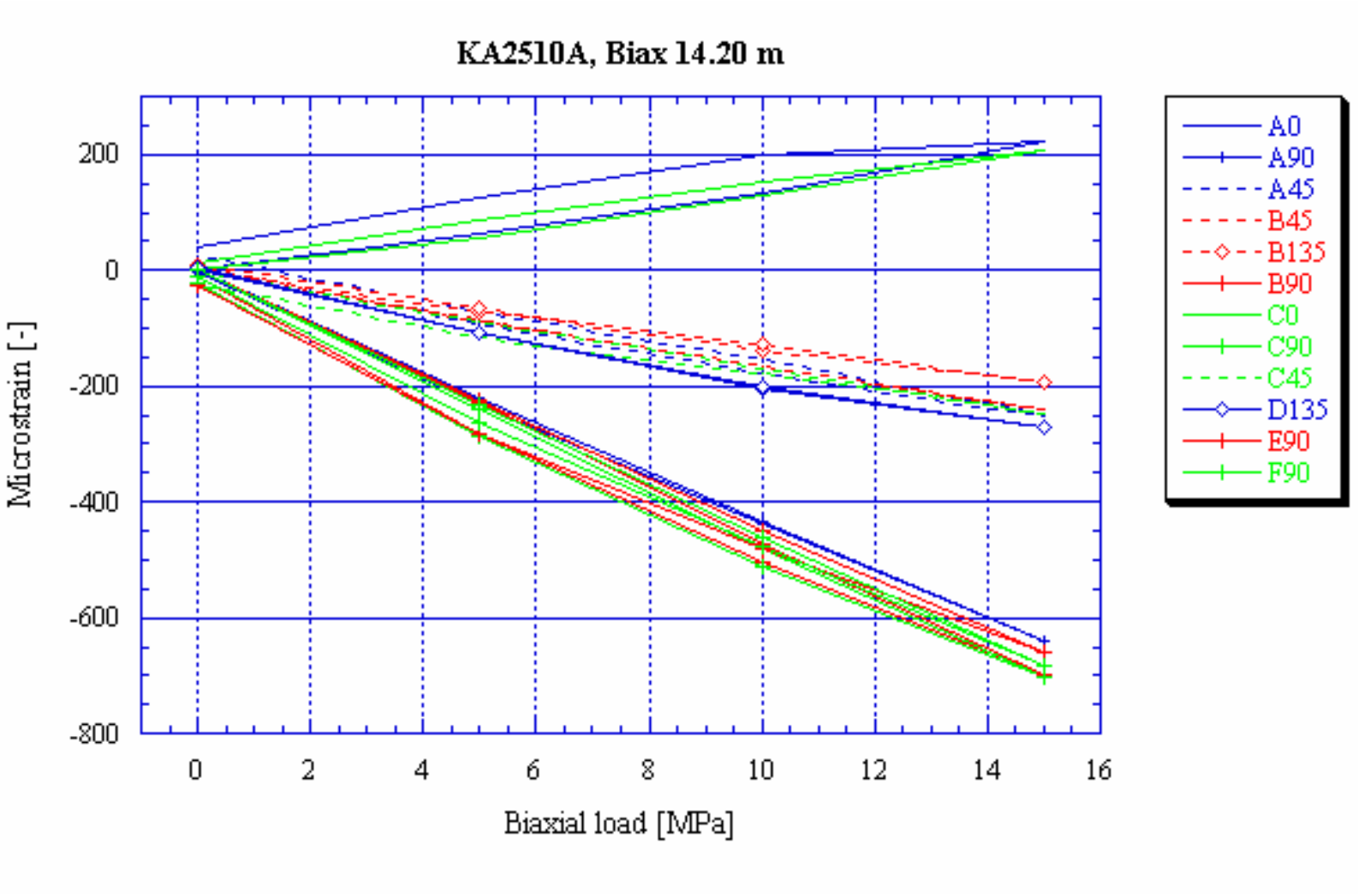
KA2510A, Biax 14.20 m
Microstrain [-]
200
0
-200
-400
-600
-800
0
2
4
6
8
10
12
14
16
Biaxial load [MPa]
A0
A90
A45
B45
B135
B90
C0
C90
C45
D135
E90
F90

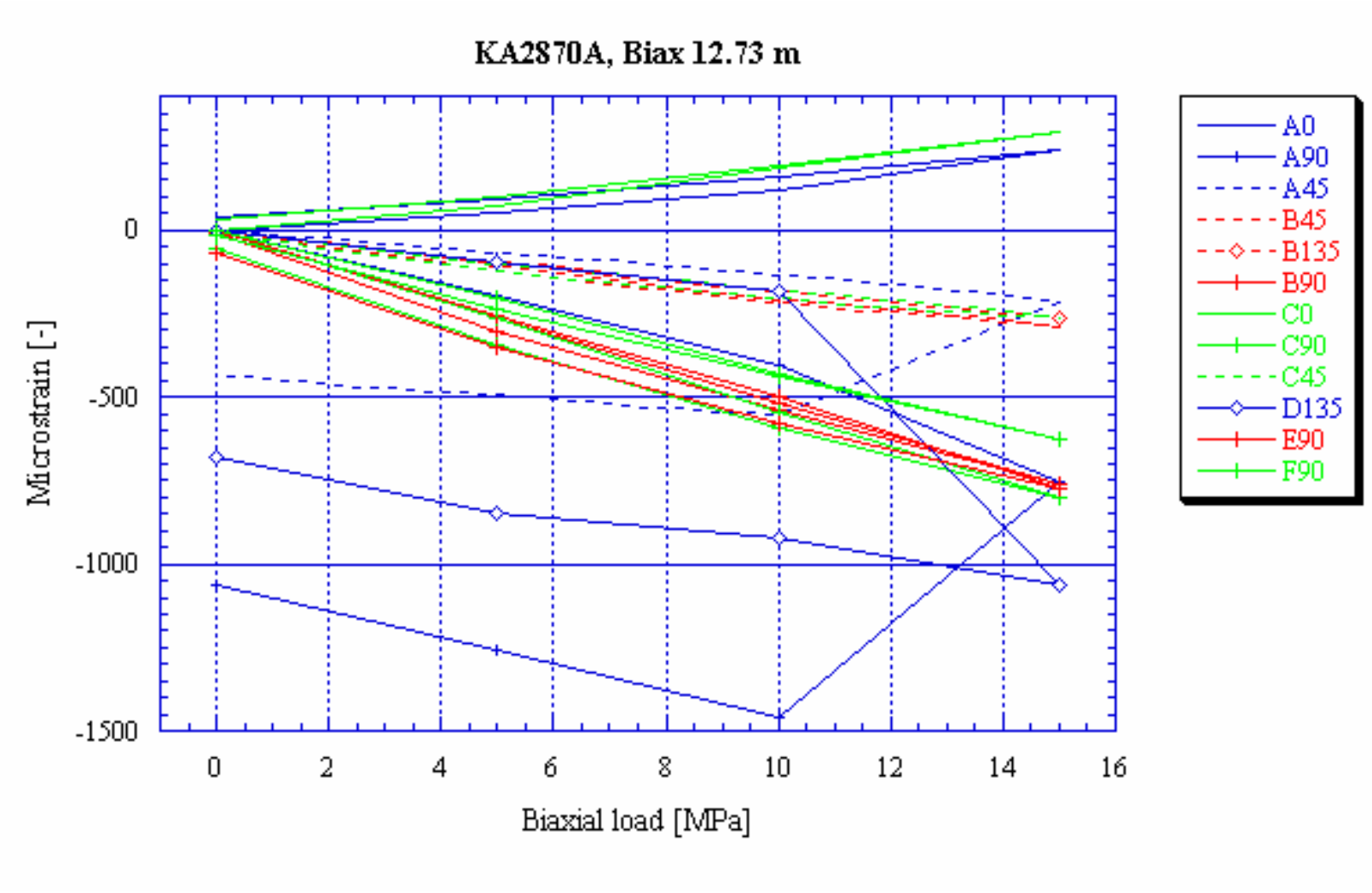
KA2870A, Biax 12.73 m
Microstrain [-]
0
-500
-1000
-1500
0
2
4
6
8
10
12
14
16
Biaxial load [MPa]
A0
A90
A45
B45
B135
B90
C0
C90
C45
D135
E90
F90

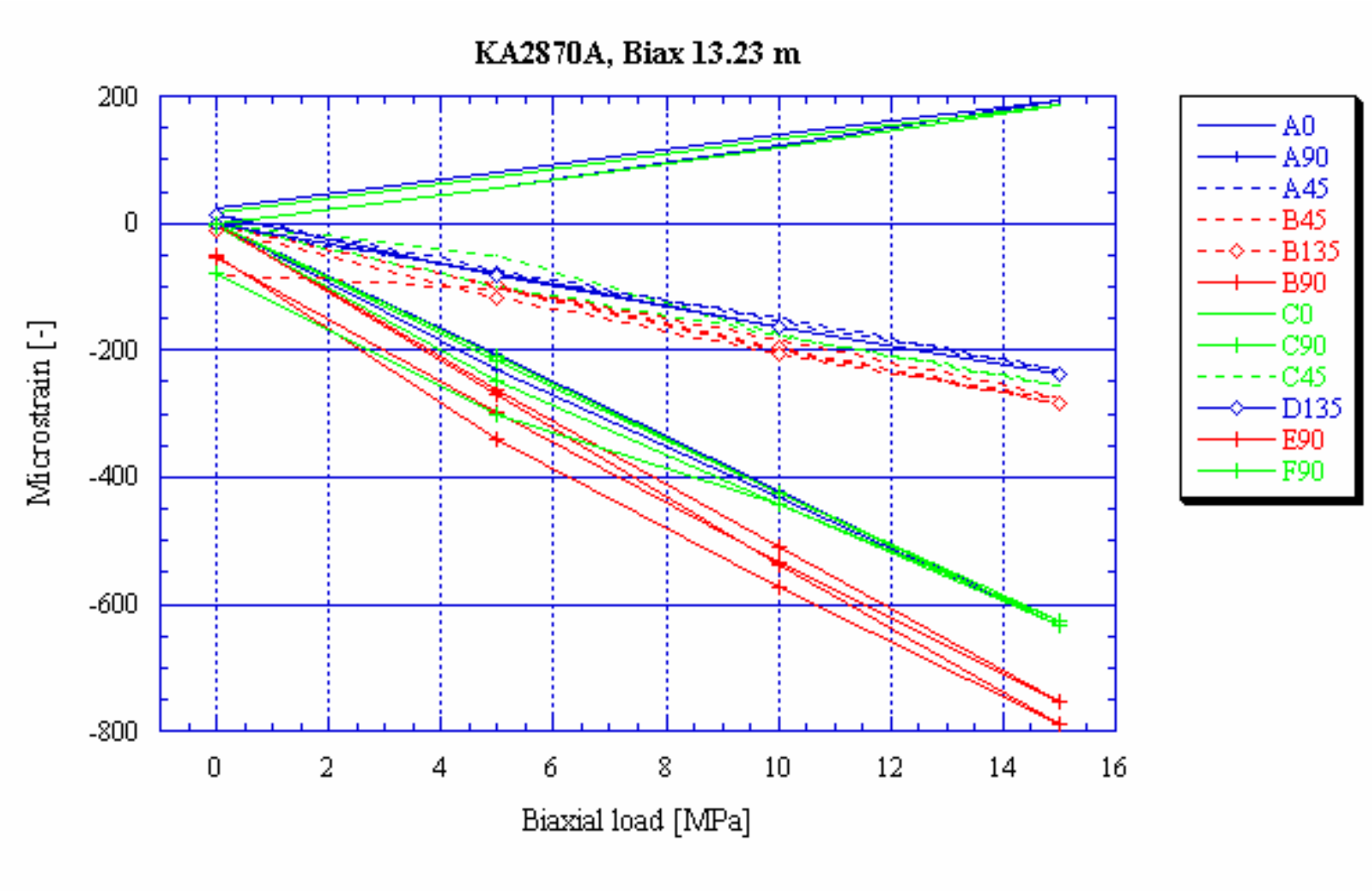
KA2870A, Biax 13.23 m
Microstrain [-]
200
0
-200
-400
-600
-800
0
2
4
6
8
10
12
14
16
Biaxial load [MPa]
A0
A90
A45
B45
B135
B90
C0
C90
C45
D135
E90
F90

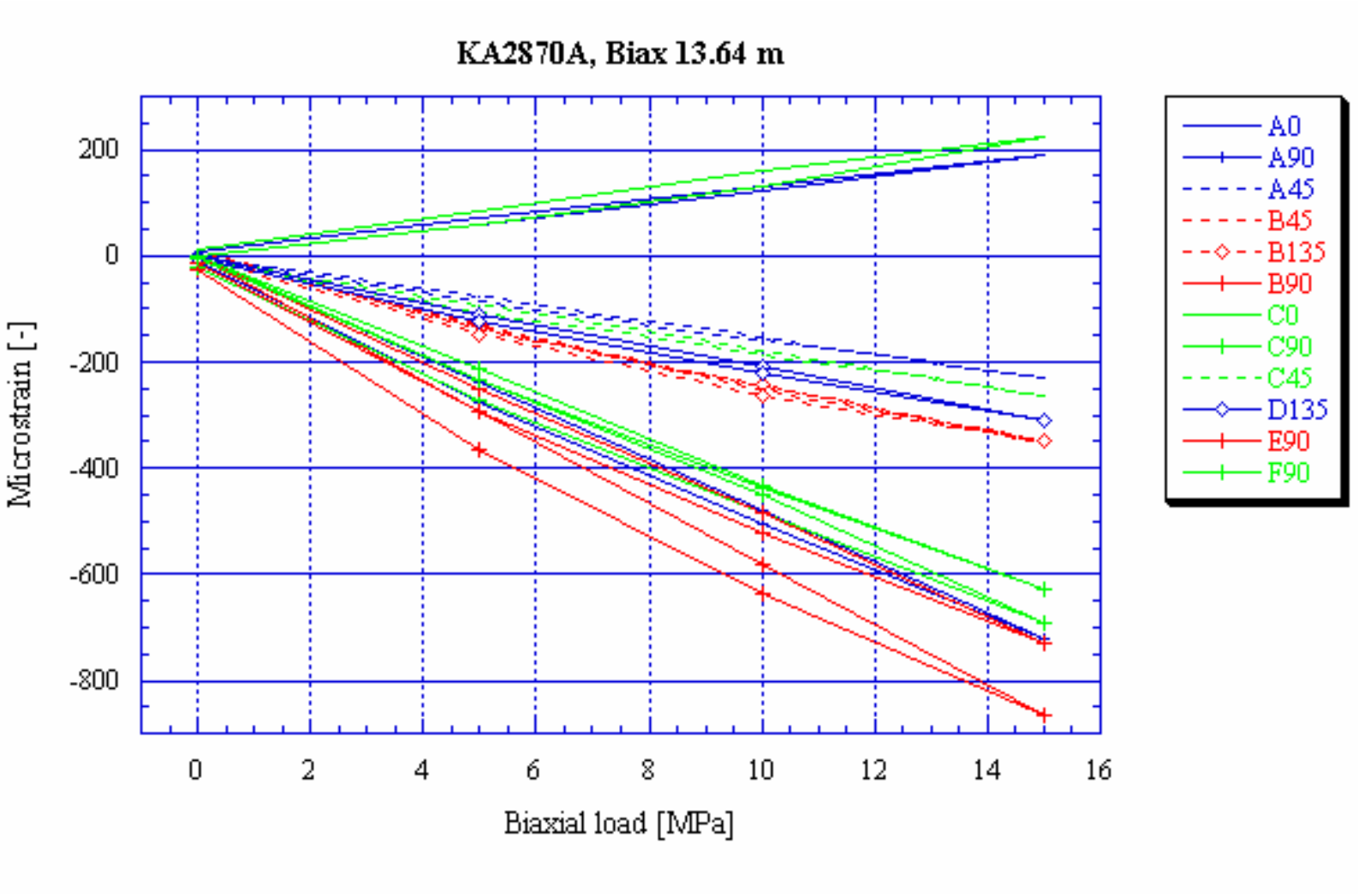
KA2870A, Biax 13.64 m
Microstrain [-]
200
0
-200
-400
-600
-800
0
2
4
6
8
10
12
14
16
Biaxial load [MPa]
A0
A90
A45
B45
B135
B90
C0
C90
C45
D135
E90
F90

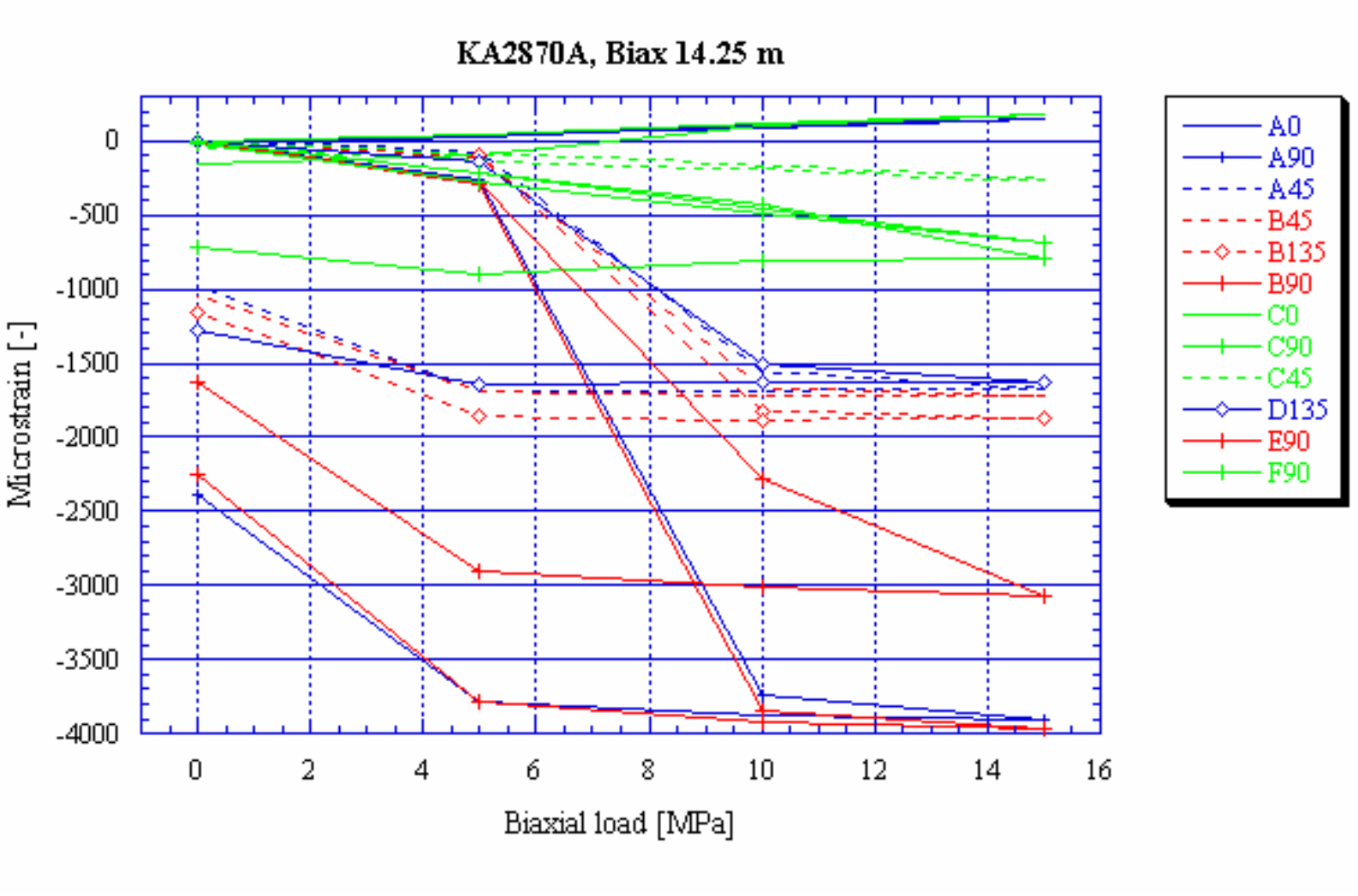
KA2870A, Biax 14.25 m
Microstrain [-]
0
-500
-1000
-1500
-2000
-2500
-3000
-3500
-4000
0
2
4
6
8
10
12
14
16
Biaxial load [MPa]
A0
A90
A45
B45
B135
B90
C0
C90
C45
D135
E90
F90

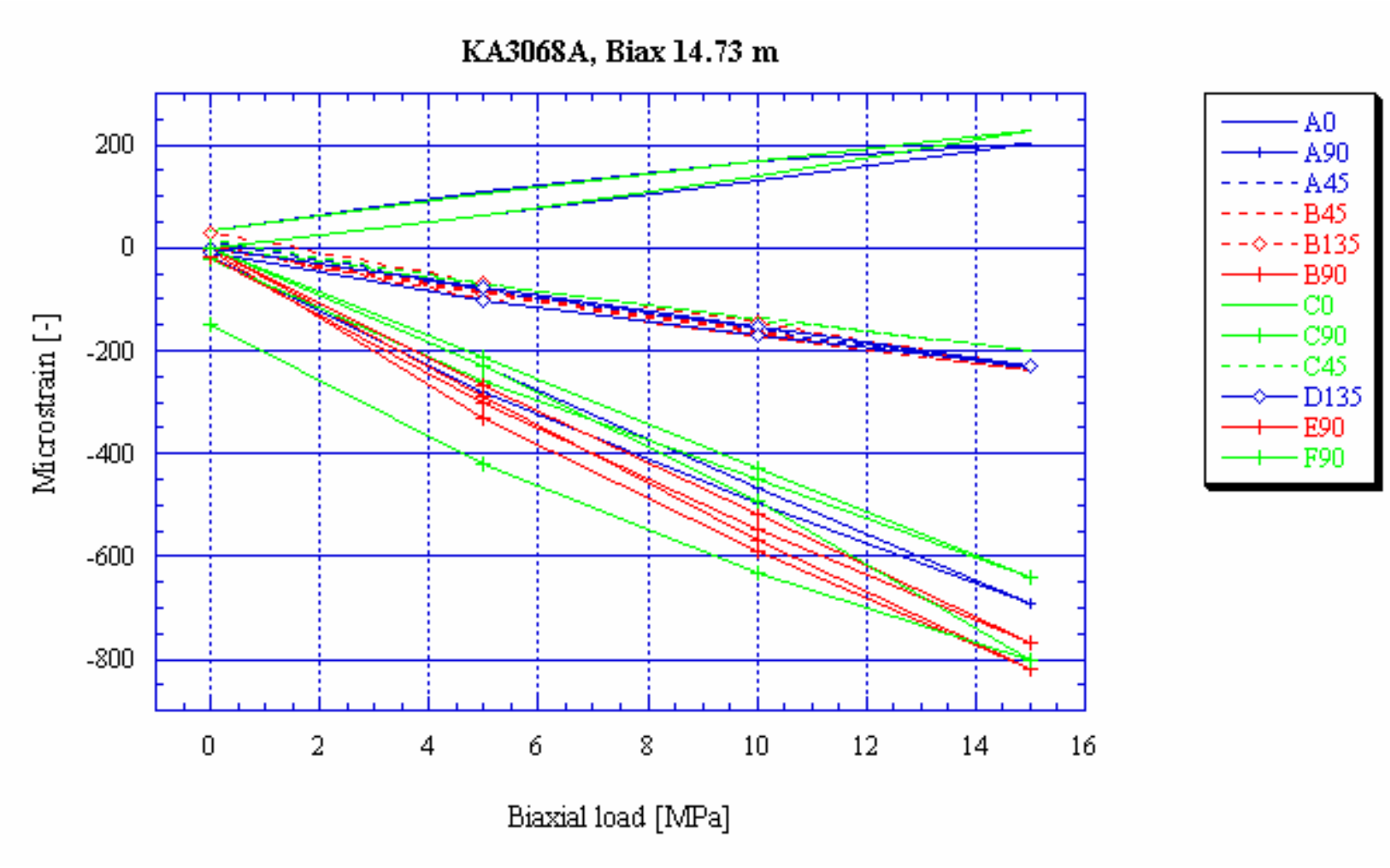
KA3068A, Biax 14.73 m
Microstrain [-]
200
0
-200
-400
-600
-800
0
2
4
6
8
10
12
14
16
Biaxial load [MPa]
A0
A90
A45
B45
B135
B90
C0
C90
C45
D135
E90
F90

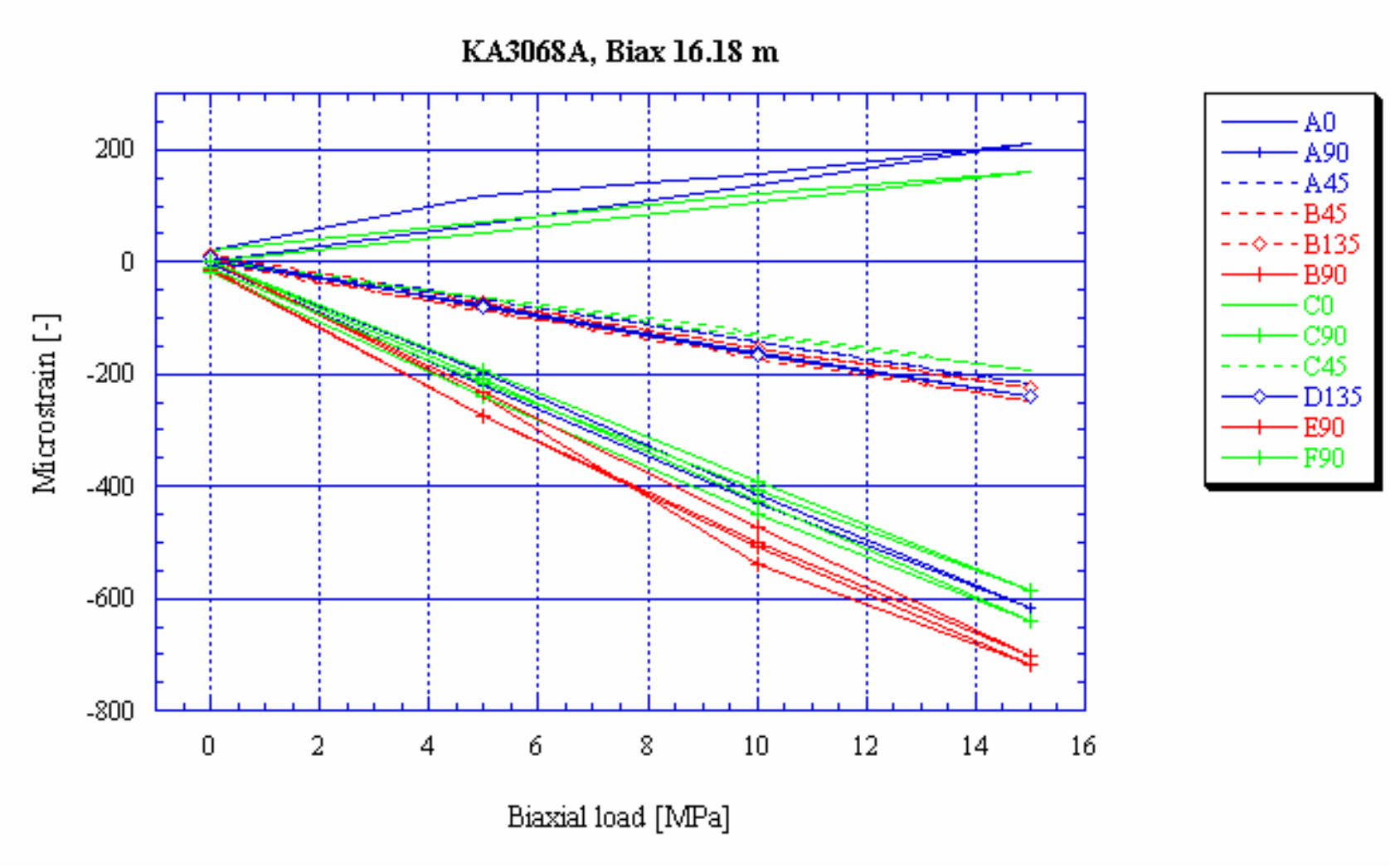
KA3068A, Biax 16.18 m
Microstrain [-]
200
0
-200
-400
-600
-800
0
2
4
6
8
10
12
14
16
Biaxial load [MPa]
A0
A90
A45
B45
B135
B90
C0
C90
C45
D135
E90
F90

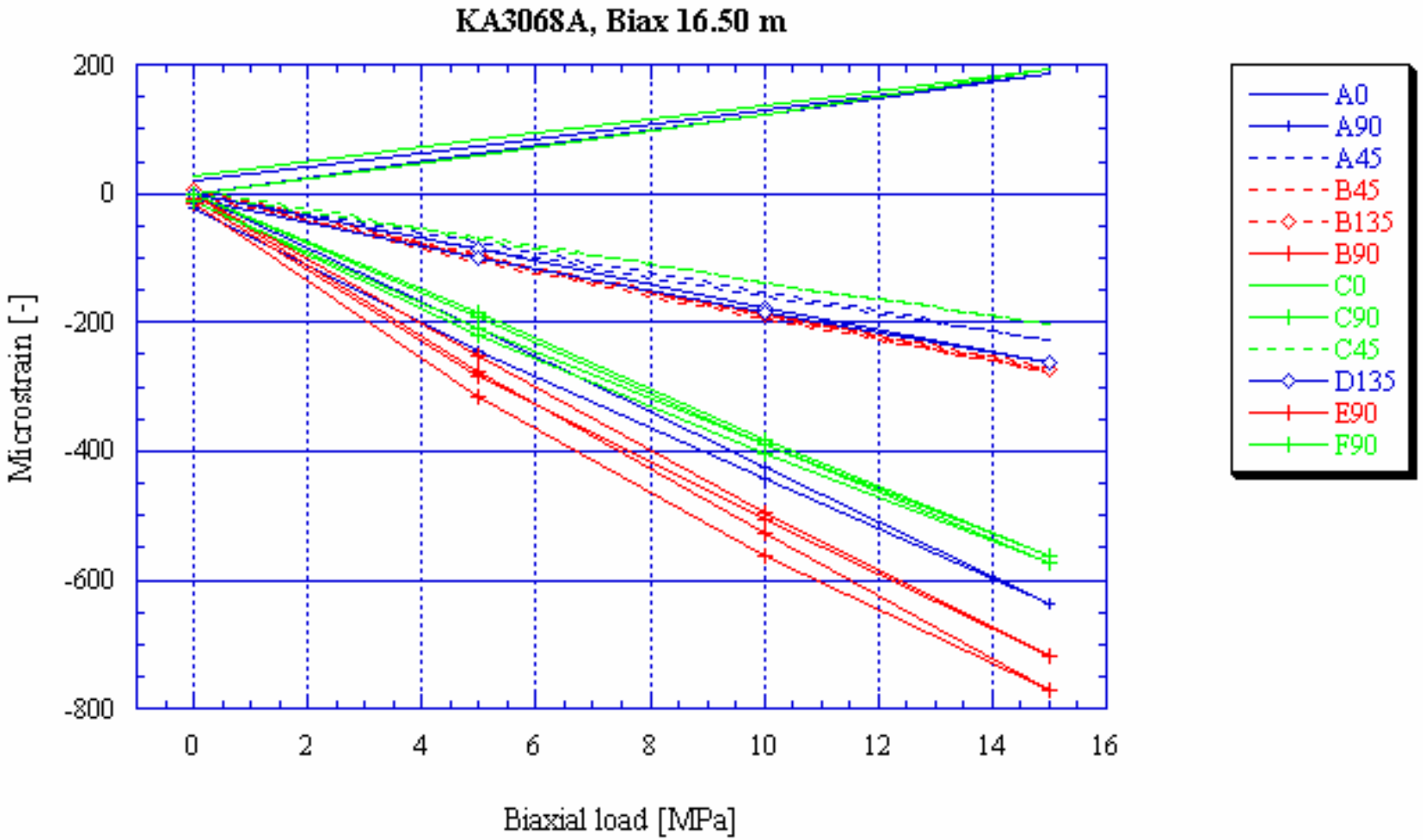
KA3068A, Biax 16.50 m
Microstrain [-]
200
0
-200
-400
-600
-800
0
2
4
6
8
10
12
14
16
Biaxial load [MPa]
A0
A90
A45
B45
B135
B90
C0
C90
C45
D135
E90
F90

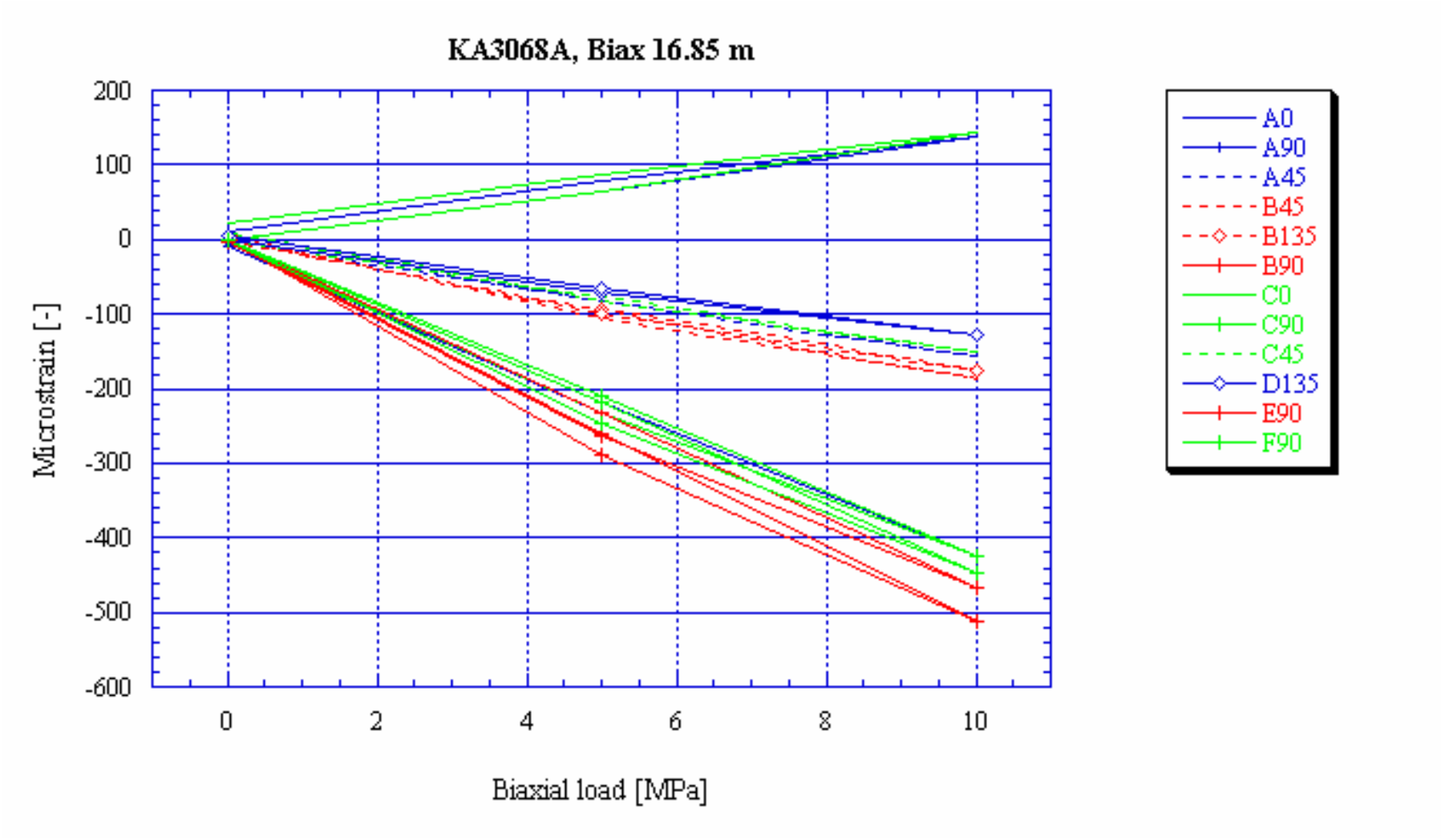
KA3068A, Biax 16.85 m
Microstrain [-]
200
100
0
-100
-200
-300
-400
-500
-600
0
2
4
6
8
10
Biaxial load [MPa]
A0
A90
A45
B45
B135
B90
C0
C90
C45
D135
E90
F90

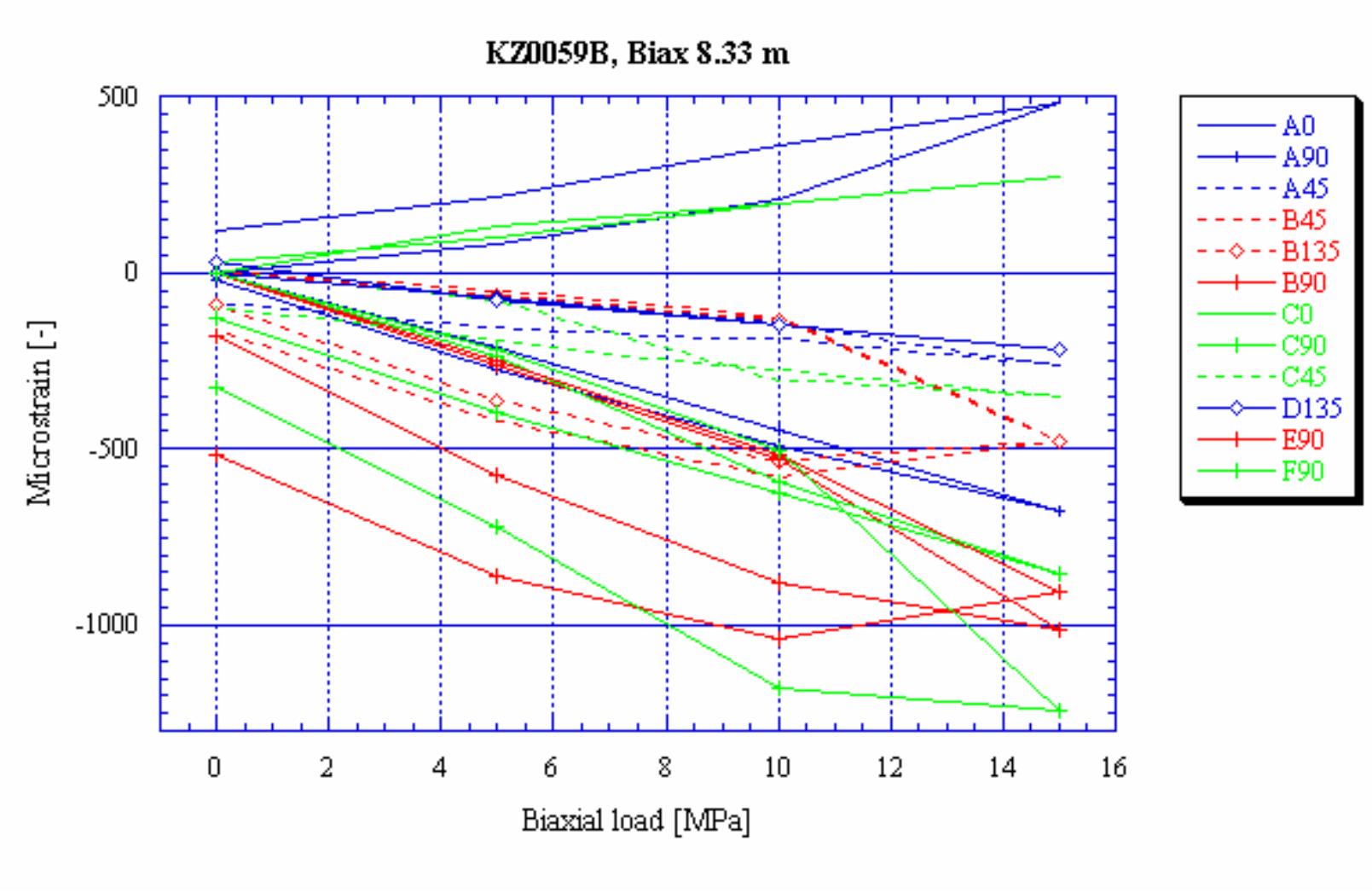
KZ0059B, Biax 8.33 m
500
0
-500
-1000
Microstrain [-]
0
2
4
6
8
10
12
14
16
Biaxial load [MPa]
A0
A90
A45
B45
B135
B90
C0
C90
C45
D135
E90
F90

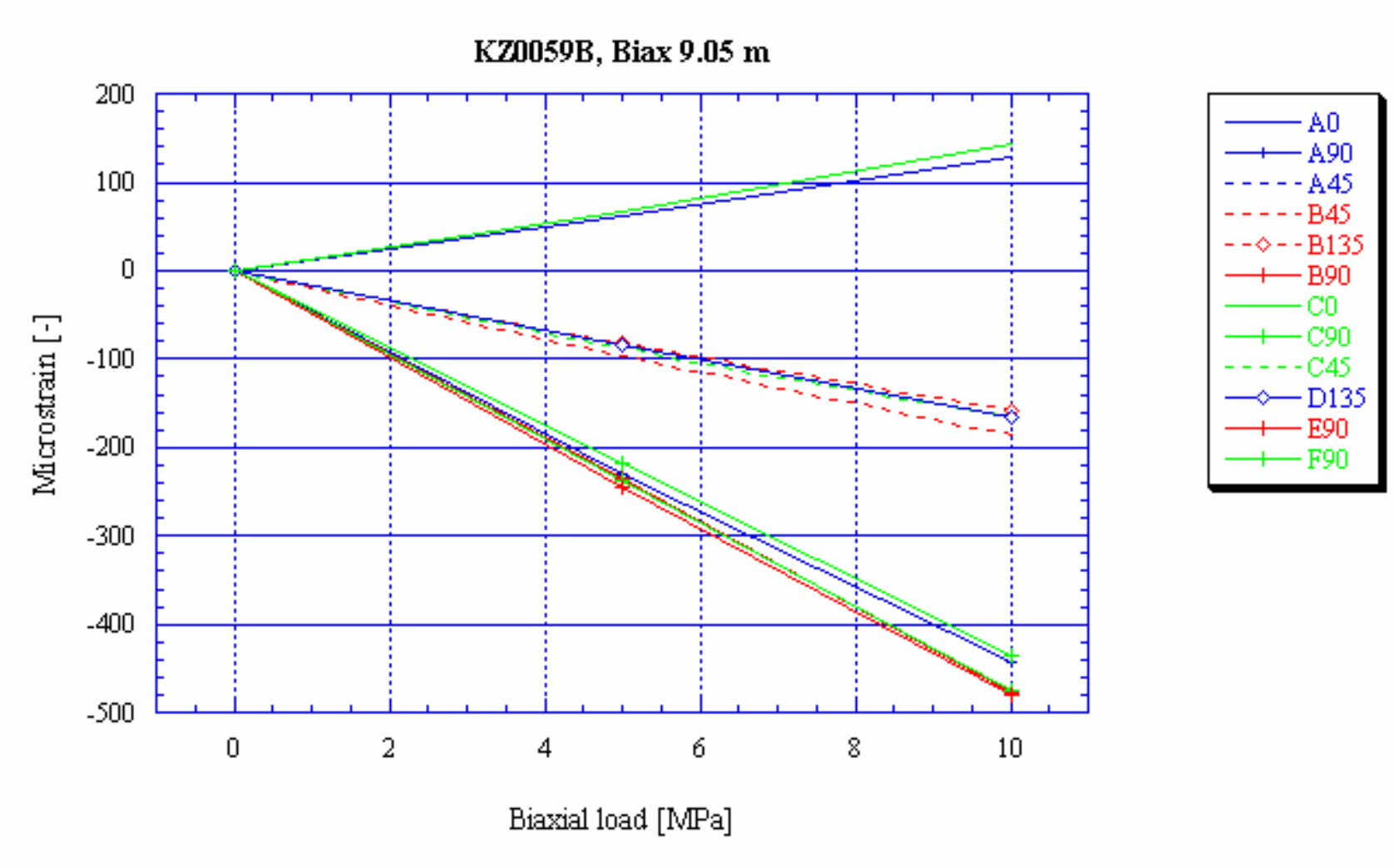
KZ0059B, Biax 9.05 m
Microstrain [-]
200
100
0
-100
-200
-300
-400
-500
0
2
4
6
8
10
Biaxial load [MPa]
A0
A90
A45
B45
B135
B90
C0
C90
C45
D135
E90
F90

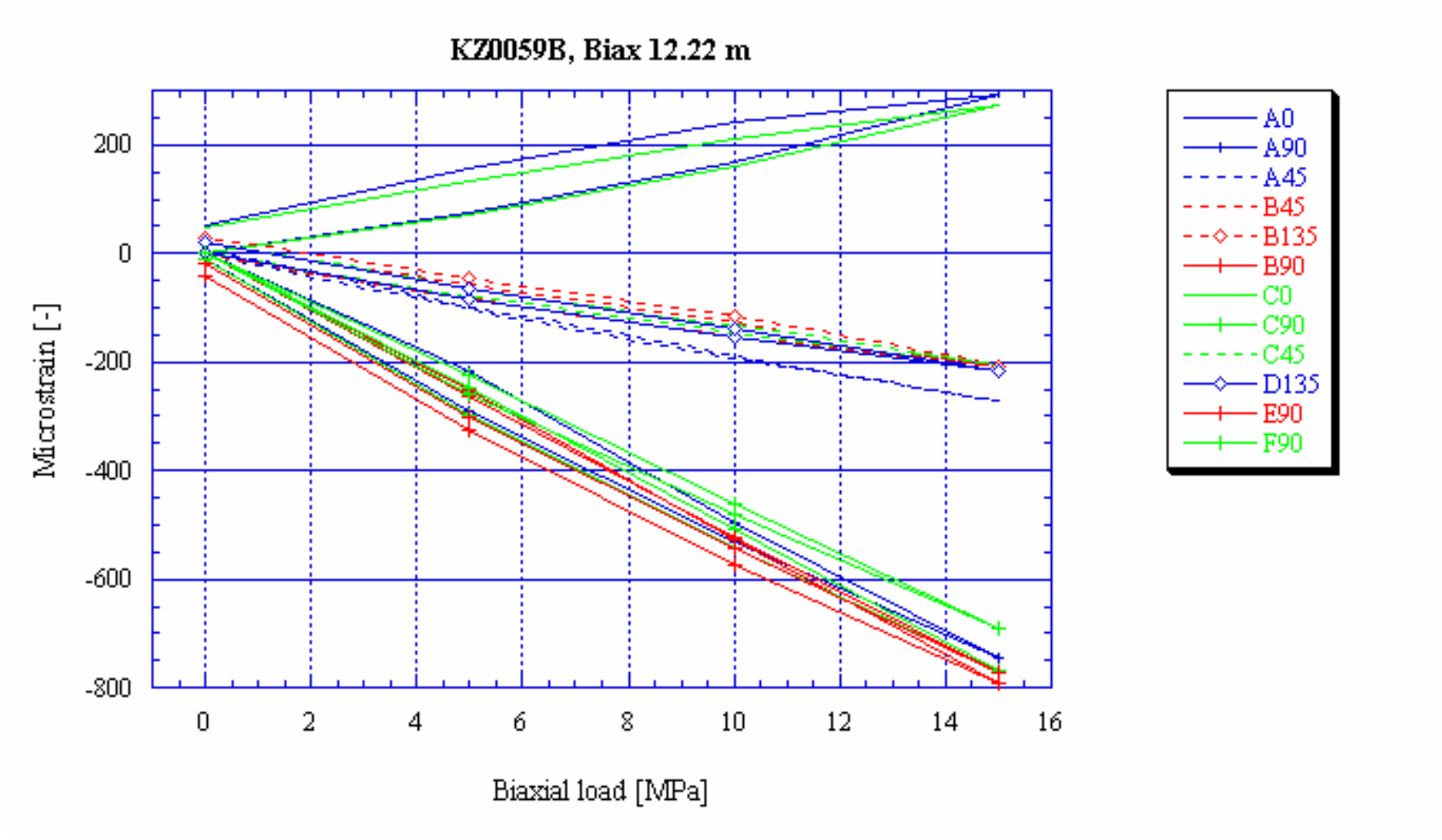
KZ0059B, Biax 12.22 m
Microstrain [-]
200
0
-200
-400
-600
-800
0
2
4
6
8
10
12
14
16
Biaxial load [MPa]
A0
A90
A45
B45
B135
B90
C0
C90
C45
D135
E90
F90

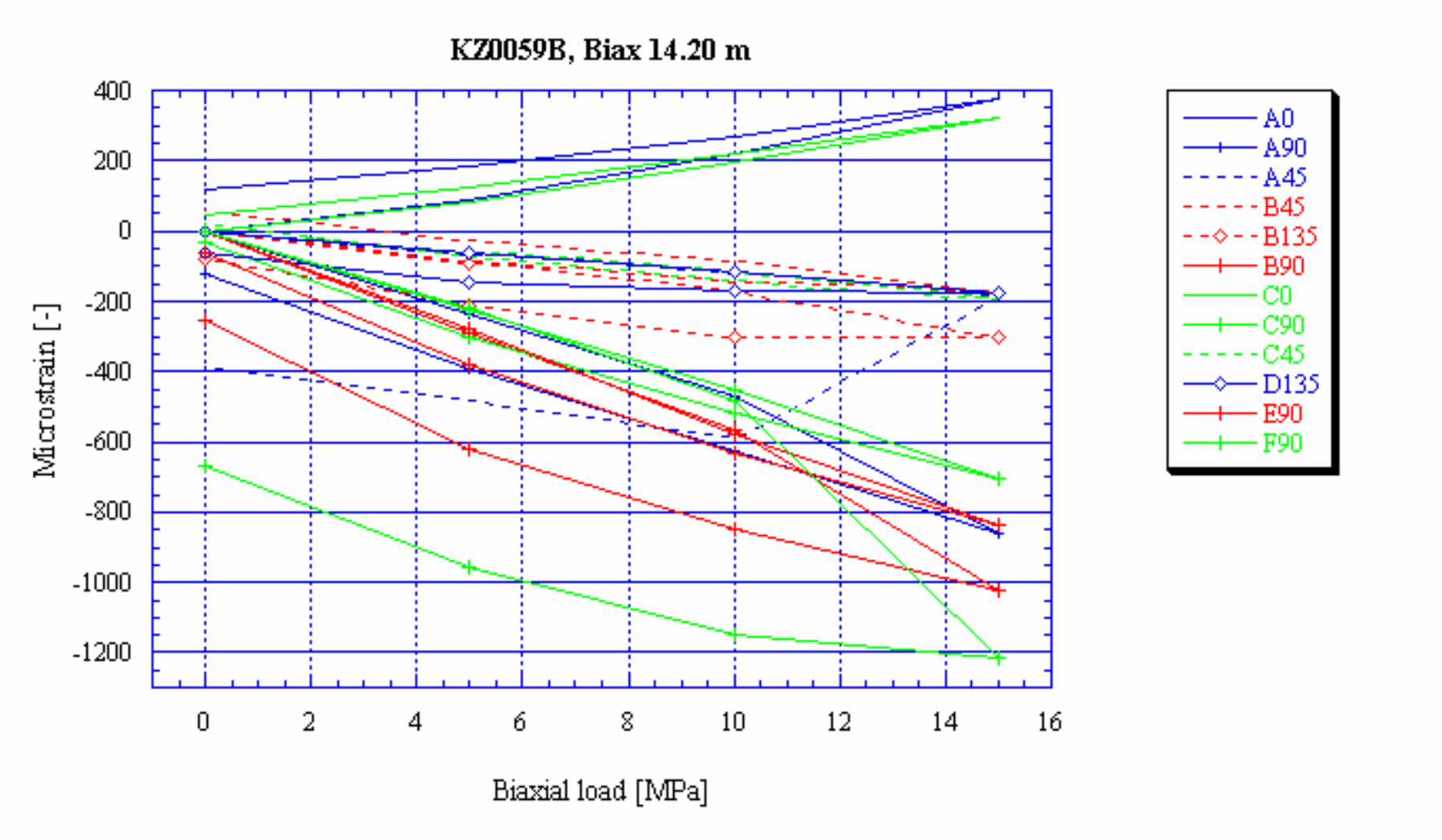
KZ0059B, Biax 14.20 m
Microstrain [-]
400
200
0
-200
-400
-600
-800
-1000
-1200
0
2
4
6
8
10
12
14
16
Biaxial load [MPa]
A0
A90
A45
B45
B135
B90
C0
C90
C45
D135
E90
F90

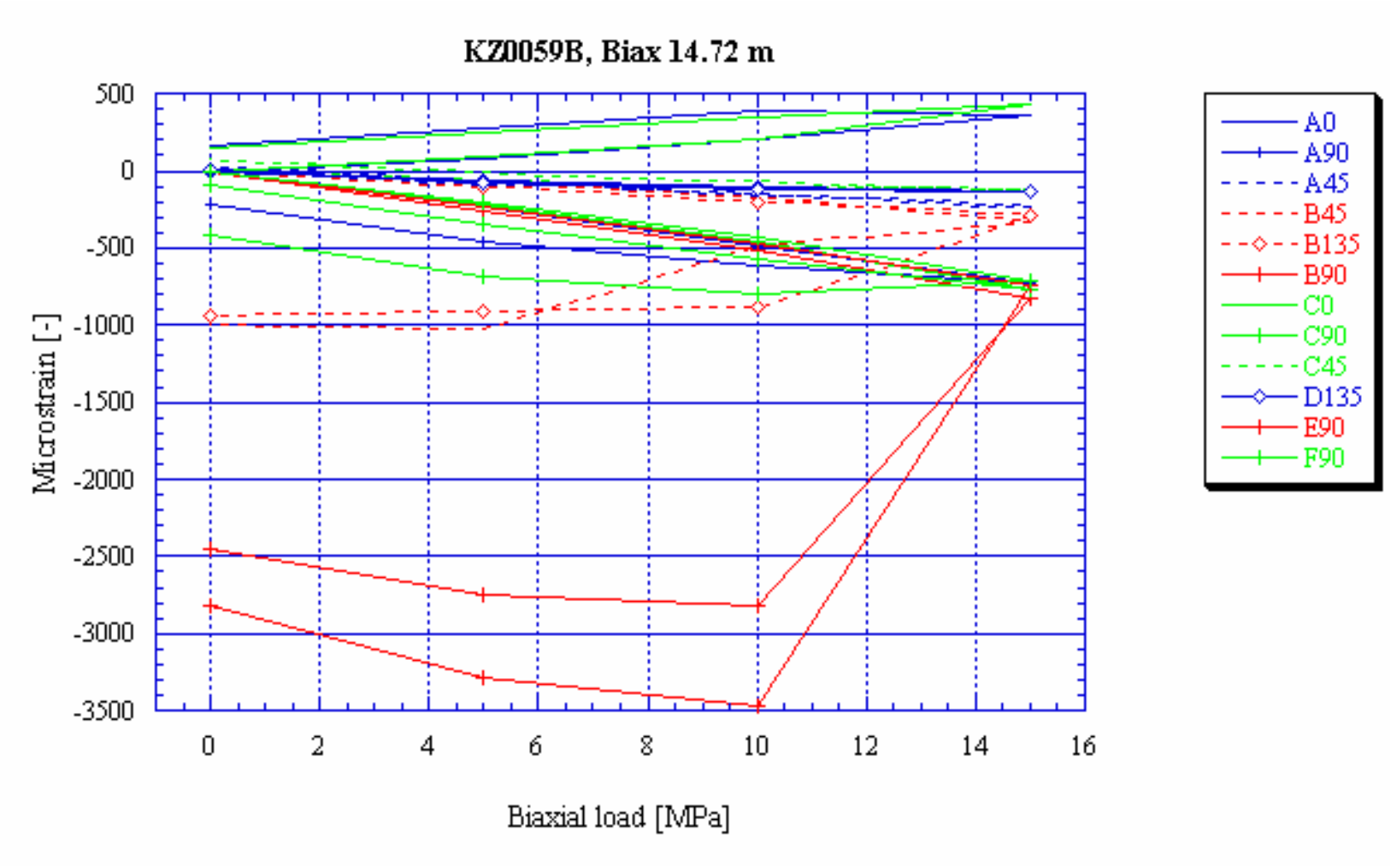
KZ0059B, Biax 14.72 m
Microstrain [-]
500
0
-500
-1000
-1500
-2000
-2500
-3000
-3500
0
2
4
6
8
10
12
14
16
Biaxial load [MPa]
A0
A90
A45
B45
B135
B90
C0
C90
C45
D135
E90
F90

Appendix 6

Evaluated strains and their standard deviation

A6.1 Overcoring data from the CSIRO HI cells

Note that SD^{ind} includes all data, i.e. also strain gauges that are likely to be erroneous or are questionable (marked with italic font). The original strain interpretations are given below the re-analyzed data and the re-analyzed data include corrections for boundary yield (axial and 45-/135-degree inclined gauges)

A6.1.1 Borehole KA1045A

Depth [m]	Microstrain [-]											
	A0	**A90**	**A45**	**B45**	**B135**	**B90**	**C0**	**C90**	**C45**	**D135**	**E90**	**F90**
16.09	12	190	*289*	211	*-146*	*425*	12	68	11	-	-	-
	250	190	*415*	335	*-30*	*425*	252	68	130			
16.60	10	118	49	183	105	231	18	14	20	-	-	-
	10	118	49	183	105	231	18	14	78			
17.00	20	*98*	34	196	147	284	*20*	44	10	-	-	-
	20	*98*	34	196	147	284	*20*	44	10			
17.47	-6	*87*	44	141	170	258	19	-25	-8	-	-	-
	-10	*72*	29	130	159	240	12	-33	-15			
	SD^{gauge}											
16.09	0	0	*0*	1	*0*	*1*	0	0	0	-	-	-
16.60	0	5	7	0	0	0	0	0	0	-	-	-
17.00	3	*2*	2	2	2	2	*2*	2	3	-	-	-
17.47	0	*0*	0	0	0	0	0	0	0	-	-	-
	$SD^{diff,ind}$											
16.09	0	9	*50*	21	*66*	*39*	0	29	35	-	-	-
16.60	4	2	2	3	1	2	1	0	2	-	-	-
17.00	1	*0*	3	3	6	4	*1*	2	2	-	-	-
17.47	5	*0*	3	3	5	3	3	2	2	-	-	-
	SD^{ind}											
16.09	0	9	*50*	22	*66*	*40*	0	29	35	-	-	-
16.60	4	7	9	3	1	2	1	0	2	-	-	-
17.00	4	*2*	5	5	8	6	*3*	4	5	-	-	-
17.47	5	*0*	3	3	5	3	3	2	2	-	-	-

A6.1.2 Borehole KA1054A

Depth [m]	Microstrain [-]											
	A0	**A90**	**A45**	**B45**	**B135**	**B90**	**C0**	**C90**	**C45**	**D135**	**E90**	**F90**
16.19	87	-15	98	78	163	171	112	143	83	-	-	-
	156	-15	166	117	202	171	200	143	122			
17.15	59	*137*	113	*186*	155	124	140	*74*	*131*	-	-	-
	59	*194*	141	*201*	171	147	147	*145*	*176*			
18.46	105	*0*	23	87	131	212	94	164	139	-	-	-
	161	*0*	51	115	159	212	147	164	167			
	SD^{gauge}											
16.19	1	1	5	0	4	1	2	1	1	-	-	-
17.15	4	*23*	14	*3*	6	13	1	*25*	*12*	-	-	-
18.46	1	*0*	0	0	0	0	0	0	0	-	-	-
	$SD^{diff,ind}$											
16.19	5	0	2	2	4	3	3	2	1	-	-	-
17.15	19	*5*	3	*10*	8	8	8	*1*	*2*	-	-	-
18.46	5	*3*	5	4	0	2	1	7	3	-	-	-
	SD^{ind}											
16.19	6	1	7	2	8	4	5	3	2	-	-	-
17.15	23	*28*	15	*13*	14	21	9	*26*	*14*	-	-	-
18.46	6	*3*	5	4	0	2	1	7	3	-	-	-

A6.1.3 Borehole KA1192A

Depth [m]	Microstrain [-]											
	A0	**A90**	**A45**	**B45**	**B135**	**B90**	**C0**	**C90**	**C45**	**D135**	**E90**	**F90**
14.43	7	94	96	94	204	314	7	*100*	101	9	286	*25*
	69	95	125	124	237	317	62	*99*	130	36	288	*25*
15.62	7	89	105	73	219	378	7	324	175	33	430	200
	78	79	110	108	256	374	77	326	211	71	429	200
16.19	*0*	*187*	*149*	114	157	382	7	372	207	*45*	500	202
				114	162	389	11	381	241		507	205
	SD^{gauge}											
14.43	1	1	1	0	0	1	0	*1*	1	1	0	*0*
15.62	1	2	2	1	1	2	2	1	1	0	1	1
16.19	*13*	*28*	*29*	20	29	66	11	66	39	*7*	87	41
	$SD^{diff,ind}$											
14.43	1	2	4	1	3	4	1	*6*	4	1	7	*1*
15.62	0	8	0	3	3	3	0	3	4	6	0	8
16.19	*2*	*9*	*19*	3	12	4	1	5	7	*0*	11	11
	SD^{ind}											
14.43	2	3	5	1	3	5	1	*7*	5	2	7	*1*
15.62	1	10	2	4	4	5	2	4	5	6	1	9
16.19	*15*	*37*	*47*	23	41	70	12	71	46	*7*	98	50

A6.1.4 Borehole KA1623A

Depth [m]	Microstrain [-]											
	A0	**A90**	**A45**	**B45**	**B135**	**B90**	**C0**	**C90**	**C45**	**D135**	**E90**	**F90**
13.29	99	*544*	272	279	427	418	99	116	227	*373*	197	*292*
	101	*543*	271	278	426	418	99	115	227	*374*	196	*291*
13.84	86	267	251	176	401	423	112	104	183	80	298	120
	111	268	263	191	413	423	137	101	197	93	301	121
14.27	121	200	230	83	338	310	77	116	154	78	232	108
	118	197	227	79	336	311	70	110	153	73	227	101
	SD^{gauge}											
13.29	0	*0*	1	1	1	1	1	0	1	*0*	0	*1*
13.84	0	1	1	0	1	0	1	1	0	0	1	0
14.27	1	1	1	1	1	1	1	1	1	1	1	1
	$SD^{diff,ind}$											
13.29	1	*1*	4	3	10	8	1	2	5	*3*	4	*0*
13.84	5	3	1	7	0	5	3	7	6	9	4	3
14.27	7	0	48	25	0	2	8	1	27	2	3	0
	SD^{ind}											
13.29	1	*1*	5	3	11	9	2	2	6	*3*	4	*1*
13.84	5	4	2	7	1	6	4	8	7	9	5	3
14.27	8	1	49	26	1	3	9	2	28	3	4	1

A6.1.5 Borehole KA1625A

Depth [m]	Microstrain [-]											
	A0	**A90**	**A45**	**B45**	**B135**	**B90**	**C0**	**C90**	**C45**	**D135**	**E90**	**F90**
14.07	110	83	*109*	11	167	165	92	*417*	*444*	164	246	326
	110	80	*110*	9	163	163	91	*417*	*448*	162	244	322
14.57	109	157	113	50	189	147	114	239	268	154	180	221
	105	154	109	48	186	144	112	238	269	152	177	218
15.07	109	227	130	71	174	134	*76*	249	279	188	159	*124*
	121	230	131	70	174	132	*143*	250	285	189	163	*193*
	SD^{gauge}											
14.07	1	1	*0*	1	1	1	1	*1*	*1*	1	1	1
14.57	1	1	1	1	1	1	1	1	1	1	1	1
15.07	2	0	0	1	1	1	*11*	1	0	1	0	*11*
	$SD^{diff,ind}$											
14.07	2	15	*9*	5	3	14	8	*7*	*6*	0	19	5
14.57	0	2	47	35	71	3	1	3	34	16	4	2
15.07	3	13	7	1	3	6	*8*	18	3	3	3	*27*
	SD^{ind}											
14.07	3	16	*9*	6	4	15	9	*8*	*7*	1	20	6
14.57	1	3	48	36	4	4	2	4	35	17	5	3
15.07	5	13	7	2	4	7	*19*	19	3	4	3	*38*

A6.1.6 Borehole KA1626A

Depth [m]	Microstrain [-]											
	A0	**A90**	**A45**	**B45**	**B135**	**B90**	**C0**	**C90**	**C45**	**D135**	**E90**	**F90**
12.17	71	*215*	141	*216*	131	278	92	184	130	183	238	175
	69	*217*	140	*219*	129	279	90	185	127	180	237	172
12.67	80	*73*	*78*	92	120	155	84	181	167	70	197	212
	102	*97*	*101*	107	132	157	107	180	180	91	200	210
13.23	82	146	96	90	*15*	*39*	*11*	*12*	*1*	151	*49*	102
	113	146	114	105	*32*	*44*	*16*	*23*	*24*	171	*51*	104
	SD^{gauge}											
12.17	1	*0*	1	*0*	1	1	1	1	1	1	1	1
12.67	1	*4*	*1*	0	1	1	1	1	1	2	1	1
13.23	1	1	0	0	*0*	*1*	*1*	*2*	*2*	1	*0*	1
	$SD^{diff,ind}$											
12.17	5	*0*	5	*1*	4	1	2	1	2	2	1	2
12.67	0	*9*	*4*	4	3	4	1	10	1	6	2	18
13.23	11	1	6	8	*3*	*4*	*12*	*4*	*4*	11	*14*	1
	SD^{ind}											
12.17	6	*0*	6	*1*	5	2	3	2	3	3	2	3
12.67	1	*13*	*5*	4	4	5	2	11	2	8	3	19
13.23	12	2	6	8	*3*	*5*	*13*	*6*	*6*	12	*14*	2

A6.1.7 Borehole KA1899A

Depth [m]	Microstrain [-]											
	A0	**A90**	**A45**	**B45**	**B135**	**B90**	**C0**	**C90**	**C45**	**D135**	**E90**	**F90**
12.09	182	101	179	*105*	232	183	214	104	155	88	127	89
	226	98	205	*123*	256	178	264	98	178	110	123	81
12.43	200	114	262	102	262	159	196	99	151	84	100	80
	202	116	259	100	260	155	196	95	148	79	96	76
12.89	193	135	301	101	294	191	203	173	154	73	197	115
	248	128	328	127	317	185	261	167	179	96	194	117
13.38	200	137	227	73	310	252	196	164	218	59	208	175
	227	133	239	101	294	251	203	163	230	66	208	172
13.81	191	75	229	64	310	193	205	210	256	77	275	115
	238	73	253	85	334	194	255	211	284	97	274	114
	SD^{gauge}											
12.09	1	1	0	*1*	0	1	1	1	0	1	1	1
12.43	0	0	1	0	0	1	0	1	1	1	1	1
12.89	1	2	1	1	2	2	1	2	1	1	1	0
13.38	0	1	1	1	1	1	1	1	1	1	1	1
13.81	44	1	1	1	1	1	1	1	0	1	1	1
	$SD^{diff,ind}$											
12.09	2	0	4	*2*	1	6	8	1	1	3	5	3
12.43	2	3	6	2	2	3	3	4	4	0	6	3
12.89	5	1	6	1	0	3	1	3	1	4	1	6
13.38	5	2	7	1	2	9	4	5	1	7	5	12
13.81	5	1	4	1	1	6	0	1	0	4	6	3
	SD^{ind}											
12.09	3	1	4	*3*	1	7	9	2	1	4	6	3
12.43	2	3	7	2	2	4	3	5	5	1	7	4
12.89	6	3	7	2	2	5	2	5	4	6	7	6
13.38	5	3	8	2	3	10	5	6	2	8	6	13
13.81	49	2	5	2	2	7	1	2	0	5	7	4

A6.1.8 Borehole KA2198A

Depth [m]	Microstrain [-]											
	A0	**A90**	**A45**	**B45**	**B135**	**B90**	**C0**	**C90**	**C45**	**D135**	**E90**	**F90**
12.50	187	104	158	-31	620	514	211	324	*623*	102	470	117
	238	101	181	-9	640	513	263	317	*645*	127	465	116
13.55	170	73	315	-46	656	484	233	274	436	-34	450	116
	166	68	310	-51	655	482	231	227	434	-36	445	115
14.11	215	232	258	-36	485	334	183	399	471	184	427	265
	221	230	256	-38	484	334	184	395	471	182	422	263
14.68	225	44	150	57	666	478	173	301	643	90	586	188
	252	43	161	69	678	481	192	300	656	100	583	189
	SD^{gauge}											
12.50	1	1	1	1	1	1	1	1	*1*	1	1	0
13.55	1	1	1	1	1	0	0	1	1	1	1	1
14.11	0	0	1	1	1	0	1	1	0	1	1	1
14.68	0	0	0	0	0	1	0	0	0	0	1	0
	$SD^{diff,ind}$											
12.50	1	1	5	0	0	7	7	5	*0*	6	10	2
13.55	11	7	3	4	4	4	10	1	0	3	6	9
14.11	8	4	3	12	2	2	3	5	11	13	6	8
14.68	3	11	7	19	17	14	14	19	2	10	9	24
	SD^{ind}											
12.50	2	2	6	1	1	8	8	6	*1*	7	11	2
13.55	12	8	4	5	5	4	10	2	1	4	7	10
14.11	8	4	4	13	3	2	4	6	11	14	7	9
14.68	3	11	7	19	17	15	14	19	2	10	10	24

A6.1.9 Borehole KA2510A

Depth [m]	Microstrain [-]											
	A0	**A90**	**A45**	**B45**	**B135**	**B90**	**C0**	**C90**	**C45**	**D135**	**E90**	**F90**
12.04	57	418	209	*726*	*379*	*1059*	-1	248	-9	*167*	*827*	200
	57	421	207	*725*	*379*	*1059*	0	484	93	*168*	*827*	276
12.36	38	*-189*	*-71*	*768*	192	*811*	82	165	-46	*143*	*58*	206
	42	*-23*	*59*	*751*	184	*804*	75	163	-44	*214*	*86*	206
12.87	80	495	216	576	89	620	40	214	-147	367	438	235
	135	494	233	596	106	617	68	214	-126	386	439	235
13.36	58	408	105	631	112	671	62	203	*-48*	*145*	446	216
	85	407	126	658	122	690	89	223	*-31*	*311*	446	218
13.75	47	427	145	*685*	*276*	*808*	73	*-9*	*-147*	*360*	396	*6*
	67	433	157	*707*	*291*	*818*	95	*-5*	*-142*	*376*	400	*1*
14.20	66	*225*	109	551	*28*	543	54	168	-120	212	326	*18*
	118	*225*	133	581	*51*	547	98	170	-98	234	331	*20*
	SD^{gauge}											
12.04	0	1	0	*0*	*0*	*0*	0	2	0	*0*	*0*	0
12.36	0	*1*	*0*	*0*	1	*1*	1	1	1	*1*	*1*	0
12.87	1	1	1	1	1	1	0	0	0	1	0	0
13.36	0	0	0	3	1	3	1	3	*1*	*2*	0	1
13.75	1	1	1	*0*	*0*	*2*	1	*1*	*1*	*0*	1	1
14.20	1	*1*	1	1	*1*	1	0	0	0	1	0	*0*
	$SD^{diff,ind}$											
12.04	10	1	7	*12*	*2*	*7*	9	24	8	*18*	*11*	22
12.36	23	*98*	*17*	*55*	44	*69*	8	27	9	*29*	*122*	94
12.87	10	4	2	17	4	2	3	1	10	15	12	8
13.36	6	13	17	15	2	4	7	9	*14*	*36*	8	13
13.75	4	2	3	*3*	*6*	*3*	4	*3*	*8*	*7*	2	0
14.20	1	*1*	8	1	*5*	5	5	14	5	2	12	*13*
	SD^{ind}											
12.04	10	2	7	*12*	*2*	*7*	9	26	8	*18*	*11*	22
12.36	23	*99*	*17*	*55*	45	*70*	9	28	10	*30*	*123*	94
12.87	11	5	3	18	5	3	3	1	10	16	12	8
13.36	6	13	17	18	3	7	8	12	*15*	*38*	8	14
13.75	5	3	4	*3*	*6*	*5*	5	4	*9*	*7*	*3*	1
14.20	2	*2*	9	2	*6*	6	5	14	5	3	12	*13*

A6.1.10 Borehole KA2870A

Depth [m]	Microstrain [-]											
	A0	**A90**	**A45**	**B45**	**B135**	**B90**	**C0**	**C90**	**C45**	**D135**	**E90**	**F90**
12.73	135	627	*553*	828	80	732	214	297	-259	*246*	514	*600*
	219	671	*607*	882	136	734	349	297	-205	*301*	513	*598*
13.23	175	*926*	*629*	932	131	746	174	394	-212	*531*	334	521
	203	*919*	*641*	945	139	740	207	386	-201	*545*	328	519
13.64	129	648	289	815	97	564	217	*90*	-164	508	368	298
	125	648	281	810	93	557	214	*85*	-167	503	362	292
14.25	183	583	182	942	-12	779	166	136	-285	685	436	223
	319	595	256	1013	64	798	293	145	-217	761	448	229
14.87	186	551	104	719	*-114*	*326*	163	*15*	-128	656	*103*	270
	383	605	228	864	*2*	*400*	338	*44*	28	773	*170*	292
	SD^{gauge}											
12.73	0	0	*1*	1	0	1	0	0	0	*0*	0	*0*
13.23	1	*2*	*1*	1	2	1	0	1	1	*1*	1	1
13.64	1	0	1	1	1	1	1	*1*	1	1	1	1
14.25	9	1	1	1	1	1	1	0	1	1	1	1
14.87	1	0	1	1	*3*	*1*	0	*0*	1	0	*3*	2
	$SD^{diff,ind}$											
12.73	10	8	*2*	6	16	12	16	35	17	*23*	5	*33*
13.23	5	*2*	*17*	4	11	9	6	22	12	*0*	20	24
13.64	14	9	1	2	1	17	15	*15*	3	2	25	1
14.25	8	5	2	30	2	5	2	1	22	34	13	4
14.87	7	1	0	15	*2*	*2*	1	*5*	11	16	*14*	2
	SD^{ind}											
12.73	10	8	*3*	7	16	13	16	35	17	*23*	5	*33*
13.23	6	*4*	*18*	5	13	10	7	23	13	*1*	21	25
13.64	15	9	2	3	2	18	16	*16*	4	3	26	2
14.25	17	6	3	31	3	6	3	1	23	35	14	5
14.87	8	1	1	16	*5*	*3*	1	*5*	12	16	*17*	4

A6.1.11 Borehole KA3068A

Depth [m]	Microstrain [-]											
	A0	**A90**	**A45**	**B45**	**B135**	**B90**	**C0**	**C90**	**C45**	**D135**	**E90**	**F90**
14.73	220	*116*	406	*-10*	606	421	236	157	*274*	*-72*	300	73
	218	*113*	404	*-13*	614	418	233	155	*272*	*-73*	298	88
16.18	211	315	401	330	536	541	245	*16*	74	109	303	80
	293	312	445	373	579	542	342	*13*	118	151	302	78
16.50	227	*-30*	197	254	218	458	229	288	69	-95	611	135
	392	*-32*	279	337	301	455	398	286	153	-11	608	133
16.85	198	*20*	230	243	263	404	258	299	130	5	429	192
	198	*16*	227	243	261	402	260	296	132	3	427	188
	SD^{gauge}											
14.73	1	*1*	1	*1*	1	1	1	1	*0*	*0*	1	3
16.18	0	0	1	0	0	0	0	*1*	0	1	1	1
16.50	1	*1*	1	0	1	1	1	0	0	0	1	1
16.85	1	*1*	1	1	1	0	1	1	0	1	1	1
	$SD^{diff,ind}$											
14.73	2	*4*	1	*3*	2	7	3	1	*4*	*6*	9	6
16.18	6	1	5	7	5	5	5	*8*	2	7	4	9
16.50	7	*3*	10	4	6	1	8	27	1	12	16	22
16.85	8	*11*	6	3	2	10	12	9	0	7	7	21
	SD^{ind}											
14.73	3	*5*	2	*4*	3	8	4	2	*4*	*6*	10	9
16.18	6	1	6	7	5	5	5	*9*	2	8	5	10
16.50	8	*4*	11	4	7	2	9	27	1	12	17	23
16.85	9	*12*	7	4	3	10	13	10	0	8	18	24

A6.1.12 Borehole KZ0059B

Depth [m]	Microstrain [-]											
	A0	**A90**	**A45**	**B45**	**B135**	**B90**	**C0**	**C90**	**C45**	**D135**	**E90**	**F90**
7.77	176	295	261	255	41	102	193	301	*99*	*146*	96	414
	197	294	274	268	52	94	231	286	*9*	*200*	112	389
8.33	184	386	261	-	-	-	185	337	258	295	128	-
	185	358	296				285	347	311	329	156	
9.05	185	376	193	216	13	2	184	*269*	204	375	68	*444*
	183	372	187	211	9	-1	184	*268*	202	369	63	*442*
12.22	188	245	*107*	188	-52	-48	181	*500*	274	312	143	417
	215	243	*116*	202	-38	-49	210	*452*	286	324	141	414
14.20	195	297	181	210	-1	68	174	433	306	288	261	483
	265	300	218	246	36	71	243	438	346	324	268	489
14.72	195	438	199	257	25	95	174	319	243	379	167	481
	283	437	240	298	66	89	253	316	284	419	163	475
	SD^{gauge}											
7.77	0	0	0	0	1	0	1	0	*0*	*7*	4	1
8.33	1	0	0	-	-	-	1	1	0	1	1	-
9.05	1	1	1	1	1	1	0	*0*	0	1	1	*1*
12.22	0	1	*1*	0	0	0	0	*9*	1	0	0	1
14.20	1	1	1	1	1	1	2	1	2	1	1	1
14.72	1	0	0	0	1	1	0	1	0	1	1	0
	$SD^{diff,ind}$											
7.77	1	2	6	10	2	11	5	0	*9*	*19*	17	12
8.33	1	1	1	-	-	-	1	0	0	1	0	-
9.05	2	1	1	5	1	1	1	*3*	3	4	3	*2*
12.22	0	4	*3*	1	6	0	2	*21*	4	3	13	15
14.20	4	2	3	0	7	1	3	8	5	5	4	2
14.72	8	6	2	6	7	2	1	7	1	3	7	1
	SD^{ind}											
7.77	1	2	6	10	3	11	6	0	*9*	*26*	21	13
8.33	2	1	1	-	-	-	2	1	0	2	1	-
9.05	3	2	2	6	2	2	1	*3*	3	5	4	*3*
12.22	0	5	*4*	1	6	0	2	*30*	5	3	13	16
14.20	5	3	4	1	8	2	5	9	7	6	5	3
14.72	9	6	2	6	8	3	1	8	1	4	8	1

Appendix 7

Results from calculation of stresses using standard least squares method

A7.1 Overcoring data from the CSIRO HI cells

The results from the stress calculation are based on viewing the data as individual measurement points, borehole averages, and site averages.

A7.1.1 Borehole KA1045A

Table A7-1. Results from stress calculation using re-analyzed strain data in borehole KA1045A. The published results are presented in brackets.

Borehole depth [m]	Principal stress magnitudes [MPa]			orientations [°N/°]			Elastic parameters [GPa]	[-]
	σ_1	σ_2	σ_3	σ_1	σ_2	σ_3	E	υ
16.09	10.9 (25.3)	5.5 (15.0)	3.6 (7.2)	116/10 (27/8)	18/35 (118/10)	220/53 (257/77)	67.0 (72.3)	0.28 (0.32)
16.60	5.9 (7.7)	3.0 (5.4)	1.9 (2.6)	135/13 (140/12)	45/1 (49/8)	309/77 (287/76)	60.9 (65.8)	0.26 (0.44)
17.00	7.2 (8.8)	4.1 (5.8)	2.2 (2.7)	130/5 (132/5)	39/8 (41/6)	250/81 (263/82)	63.8 (69.5)	0.285 (0.38)
17.47	6.0 (8.3)	2.3 (5.2)	0.7 (1.4)	113/12 (114/11)	203/0 (23/3)	295/78 (279/78)	63.1 (68.7)	0.26 (0.46)
Average 16.79	6.8 (8.1)	3.0 (5.3)	2.3 (2.2)	128/15 (126/8)	220/4 (35/6)	326/74 (270/80)	63.5 (69.2)	0.26 (0.41)

Borehole depth [m]	Horizontal stress magnitudes [MPa]			orientations [°N]
	σ_H	σ_h	σ_v	σ_H
16.09	10.7 (24.9)	4.8 (14.8)	4.5 (7.6)	117 (206)
16.60	5.7 (7.5)	3.0 (5.4)	2.3 (2.7)	135 (142)
17.00	7.2 (8.7)	4.0 (5.7)	2.3 (2.7)	130 (132)
17.47	5.8 (8.1)	2.3 (5.2)	1.1 (1.5)	113 (115)
Average 16.79	6.5 (8.1)	3.0 (5.3)	2.8 (2.2)	128 (127)

A7.1.2 Borehole KA1054A

Table A7-2. Results from stress calculation using re-analyzed strain data in borehole KA1054A. The published results are presented in brackets.

Borehole depth [m]	Principal stress magnitudes [MPa]			orientations [°N/°]			Elastic parameters [GPa]	[-]
	σ_1	σ_2	σ_3	σ_1	σ_2	σ_3	E	υ
16.19	9.2 (16.2)	5.9 (7.6)	1.8 (3.5)	120/16 (115/17)	22/24 (14/31)	239/60 (230/54)	67.1 (70.1)	0.25 (0.25)
17.15	8.5 (11.5)	4.6 (7.2)	3.0 (-0.4)	306/1 (109/0)	214/38 (199/34)	38/51 (18/56)	62.2 (72.7)	0.26 (0.27)
18.46	7.8 (14.5)	6.0 (8.8)	0.8 (3.3)	126/1 (119/2)	36/27 (28/25)	219/63 (214/65)	59.6 (74.7)	0.255 (0.28)
Average 17.27	8.9 (15.3)	5.8 (8.1)	2.1 (3.2)	120/13 (114/10)	23/28 (20/25)	232/74 (225/63)	64.2 (72.7)	0.255 (0.27)
Average 1050-lev.	7.1 (11.4)	4.6 (6.5)	2.3 (2.8)	136/2 (118/10)	45/25 (25/17)	230/65 (236/71)	63.8 (70.3)	0.27 (0.36)

Borehole depth [m]	Horizontal stress magnitudes [MPa]			orientations [°N]
	σ_H	σ_h	σ_v	σ_H
16.19	8.7 (15.2)	5.0 (6.4)	3.4 (6.0)	126 (118)
17.15	8.5 (11.5)	4.0 (4.9)	3.5 (1.3)	126 (109)
18.46	7.8 (14.5)	4.9 (7.8)	2.2 (4.7)	127 (120)
Average 17.27	8.7 (15.3)	4.9 (8.1)	3.6 (3.2)	126 (117)
Average 1050-lev.	7.1 (11.4)	4.2 (6.5)	2.8 (2.8)	136 (120)

A7.1.3 Borehole KA1192A

Table A7-3. Results from stress calculation using re-analyzed strain data in borehole KA1192A. The published results are presented in brackets.

Borehole depth [m]	Principal stress magnitudes [MPa]			orientations [°N/°]			Elastic parameters [GPa]	[-]
	σ_1	σ_2	σ_3	σ_1	σ_2	σ_3	E	υ
14.43	9.1 (11.5)	4.8 (8.0)	3.6 (4.4)	271/5 (67/0)	8/54 (337/7)	177/35 (159/83)	69.7 (75.3)	0.285 (0.30)
15.62	11.8 (15.4)	7.0 (12.8)	4.8 (7.9)	274/23 (243/14)	43/56 (339/16)	173/24 (126/60)	67.5 (72.3)	0.29 (0.38)
16.19	13.6 (14.3)	6.7 (7.0)	5.0 (6.0)	282/30 (277/30)	89/59 (128/56)	188/6 (15/15)	74.5 (74.8)	0.24 (0.27)
Average 15.41	12.5 (14.2)	7.2 (11.7)	4.9 (7.3)	276/25 (274/27)	51/56 (16/21)	175/21 (138/55)	71.0 (74.6)	0.26 (0.32)

Borehole depth [m]	Horizontal stress magnitudes [MPa]			orientations [°N]
	σ_H	σ_h	σ_v	σ_H
14.43	9.1 (11.5)	4.0 (8.0)	4.4 (4.5)	90 (67)
15.62	11.0 (15.1)	5.2 (11.7)	7.3 (9.4)	90 (54)
16.19	11.9 (12.4)	5.0 (6.0)	8.3 (9.0)	101 (98)
Average 15.41	11.5 (14.2)	5.2 (11.7)	7.8 (7.3)	93 (76)

A7.1.4 Borehole KA1623A

Table A7-4. Results from stress calculation using re-analyzed strain data in borehole KA1623A. The published results are presented in brackets.

Borehole depth [m]	Principal stress magnitudes [MPa]			orientations [°N/°]			Elastic parameters [GPa]	[-]
	σ_1	σ_2	σ_3	σ_1	σ_2	σ_3	E	υ
13.29	14.3 (19.3)	12.7 (18.5)	5.6 (8.6)	150/27 (111/5)	258/31 (205/39)	27/47 (15/50)	58.1 (63.8)	0.255 (0.40)
13.84	11.7 (15.6)	6.7 (10.6)	5.0 (6.7)	129/9 (111/7)	221/15 (202/12)	8/72 (353/76)	52.5 (53.3)	0.24 (0.40)
14.27	11.9 (15.0)	6.1 (9.0)	5.1 (6.6)	119/8 (110/7)	211/15 (212/12)	3/73 (353/12)	60.2 (61.9)	0.26 (0.44)
Average 13.80	13.0 (16.7)	7.0 (10.4)	5.2 (6.9)	125/8 (113/6)	219/24 (205/17)	19/65 (4/72)	58.0 (61.8)	0.265 (0.41)

Borehole depth [m]	Horizontal stress magnitudes [MPa]			orientations [°N]
	σ_H	σ_h	σ_v	σ_H
13.29	13.7 (19.3)	9.6 (14.4)	9.3 (12.3)	126 (106)
13.84	11.6 (15.5)	6.6 (10.4)	5.4 (6.9)	128 (110)
14.27	11.7 (14.8)	6.0 (8.9)	5.4 (6.7)	119 (110)
Average 13.80	12.8 (16.7)	6.7 (10.4)	5.6 (6.9)	124 (112)

A7.1.5 Borehole KA1625A

Table A7-5. Results from stress calculation using re-analyzed strain data in borehole KA1625A. The published results are presented in brackets.

Borehole depth [m]	Principal stress magnitudes [MPa]			orientations [°N/°]			Elastic parameters [GPa]	[-]
	σ_1	σ_2	σ_3	σ_1	σ_2	σ_3	E	υ
14.07	14.9 (18.7)	6.7 (10.1)	4.7 (6.0)	327/30 (324/26)	112/55 (97/54)	227/17 (222/23)	67.3 (71.7)	0.28 (0.38)
14.57	9.6 (11.8)	5.0 (6.4)	3.9 (5.1)	322/19 (318/16)	154/71 (123/74)	53/4 (227/4)	53.7 (58.7)	0.24 (0.35)
15.07	9.6 (12.9)	5.8 (7.0)	4.0 (5.5)	318/24 (314/15)	171/62 (166/72)	54/14 (46/9)	53.6 (59.5)	0.235 (0.33)
Average 14.57	10.8 (13.0)	5.8 (7.1)	4.6 (5.8)	320/20 (318/17)	163/69 (140/73)	53/8 (48/1)	59.7 (63.4)	0.255 (0.35)

Borehole depth [m]	Horizontal stress magnitudes [MPa]			orientations [°N]
	σ_H	σ_h	σ_v	σ_H
14.07	12.8 (16.9)	4.9 (6.7)	8.6 (11.3)	145 (140)
14.57	9.2 (11.4)	3.9 (5.1)	5.5 (6.8)	142 (138)
15.07	8.9 (12.5)	4.1 (5.5)	6.3 (7.3)	140 (134)
Average 14.57	10.2 (13.0)	4.6 (7.1)	6.3 (5.8)	140 (138)

A7.1.6 Borehole KA1626A

Table A7-6. Results from stress calculation using re-analyzed strain data in borehole KA1626A. The published results are presented in brackets.

Borehole depth [m]	Principal stress magnitudes [MPa]			orientations [°N/°]			Elastic parameters [GPa]	[-]
	σ_1	σ_2	σ_3	σ_1	σ_2	σ_3	E	υ
12.17	7.5 (12.3)	5.8 (9.1)	5.1 (7.6)	273/3 (111/1)	182/13 (201/11)	18/77 (17/79)	47.7 (58.8)	0.26 (0.43)
12.67	7.1 (10.8)	5.6 (6.6)	4.4 (5.0)	137/6 (313/2)	37/61 (44/38)	230/28 (220/52)	57.3 (66.0)	0.24 (0.32)
13.23	5.7 (8.6)	3.4 (4.4)	1.3 (2.3)	107/2 (115/3)	201/63 (210/61)	15/27 (23/29)	59.7 (58.6)	0.24 (0.36)
Average 12.69	6.7 (10.0)	5.2 (6.3)	4.4 (6.0)	316/1 (117/4)	47/54 (17/69)	225/36 (208/20)	54.1 (61.6)	0.24 (0.37)
Average 1620-lev.	11.3 (13.3)	5.9 (7.1)	5.3 (6.8)	125/9 (124/4)	23/53 (13/78)	222/35 (215/11)	57.7 (61.6)	0.26 (0.38)

Borehole depth [m]	Horizontal stress magnitudes [MPa]			orientations [°N]
	σ_H	σ_h	σ_v	σ_H
12.17	7.5 (12.3)	5.8 (9.0)	5.2 (7.6)	93 (111)
12.67	7.1 (10.8)	4.7 (6.0)	5.4 (5.7)	138 (132)
13.23	5.7 (8.6)	1.7 (2.8)	2.9 (3.8)	106 (114)
Average 12.69	6.7 (10.0)	4.7 (6.3)	5.0 (6.0)	135 (117)
Average 1620-lev.	11.2 (13.3)	5.5 (7.1)	5.9 (6.8)	126 (124)

A7.1.7 Borehole KA1899A

Table A7-7. Results from stress calculation using re-analyzed strain data in borehole KA1899A. The published results are presented in brackets.

Borehole depth [m]	Principal stress magnitudes [MPa]			orientations [°N/°]			Elastic parameters [GPa]	[-]
	σ_1	σ_2	σ_3	σ_1	σ_2	σ_3	E	υ
12.09	14.1 (21.3)	5.3 (7.9)	4.2 (6.6)	145/4 (143/3)	55/3 (53/1)	289/85 (305/87)	59.5 (63.8)	0.265 (0.41)
12.43	15.7 (18.7)	5.3 (6.9)	4.5 (5.9)	147/7 (146/7)	238/8 (237/12)	16/79 (27/76)	60.6 (65.0)	0.28 (0.38)
12.89	15.7 (23.9)	6.3 (9.4)	5.0 (8.1)	147/11 (143/8)	52/25 (50/21)	259/62 (252/68)	57.8 (62.0)	0.265 (0.42)
13.38	14.6 (19.2)	6.3 (8.4)	5.4 (7.2)	154/5 (149/4)	61/34 (58/25)	250/56 (247/65)	56.5 (59.7)	0.275 (0.40)
13.81	15.8 (23.3)	6.6 (9.8)	4.5 (7.2)	153/2 (148/2)	61/41 (56/36)	245/49 (240/54)	58.0 (64.3)	0.26 (0.40)
Average 12.92	15.2 (21.2)	6.0 (8.4)	4.9 (7.1)	148/7 (146/5)	55/25 (54/20)	253/64 (248/69)	59.0 (63.0)	0.275 (0.38)

Borehole depth [m]	Horizontal stress magnitudes [MPa]			orientations [°N]
	σ_H	σ_h	σ_v	σ_H
12.09	14.1 (21.2)	5.3 (7.9)	4.2 (6.6)	145 (143)
12.43	15.5 (18.5)	5.3 (6.8)	4.7 (6.1)	147 (145)
12.89	15.3 (23.6)	6.0 (9.2)	5.6 (8.6)	147 (143)
13.38	14.6 (19.1)	6.0 (8.1)	5.7 (7.5)	154 (150)
13.81	15.7 (23.3)	5.7 (8.9)	5.5 (8.2)	153 (148)
Average 12.92	15.1 (21.2)	5.8 (8.4)	5.2 (7.1)	149 (146)

A7.1.8 Borehole KA2198A

Table A7-8. Results from stress calculation using re-analyzed strain data in borehole KA2198A. The published results are presented in brackets.

Borehole depth [m]	Principal stress magnitudes [MPa]			orientations [°N/°]			Elastic parameters [GPa]	[-]
	σ_1	σ_2	σ_3	σ_1	σ_2	σ_3	E	υ
12.50	21.9 (25.8)	6.5 (7.9)	3.7 (6.0)	137/13 (133/12)	31/51 (34/35)	237/36 (238/53)	53.5 (56.5)	0.255 (0.30)
13.55	24.1 (14.2)	7.8 (4.4)	5.7 (3.5)	137/2 (137/3)	230/57 (230/56)	45/33 (45/34)	62.2 (36.5)	0.27 (0.29)
14.11	19.6 (21.9)	8.7 (10.5)	6.2 (9.0)	132/11 (126/8)	320/79 (241/71)	222/2 (33/17)	56.4 (51.7)	0.25 (0.42)
14.68	22.5 (25.1)	6.7 (8.5)	5.4 (7.0)	136/13 (132/12)	36/35 (41/8)	243/51 (278/75)	52.5 (53.1)	0.265 (0.33)
Average 13.71	22.2 (21.6)	7.0 (7.2)	5.9 (7.0)	136/10 (132/10)	14/71 (37/26)	229/16 (241/62)	56.7 (49.5)	0.26 (0.34)

Borehole depth [m]	Horizontal stress magnitudes [MPa]			orientations [°N]
	σ_H	σ_h	σ_v	σ_H
12.50	21.0 (25.0)	4.7 (7.2)	6.2 (7.5)	138 (133)
13.55	24.0 (14.2)	6.3 (3.7)	7.2 (4.2)	136 (136)
14.11	19.2 (21.7)	6.2 (9.1)	9.0 (10.6)	132 (125)
14.68	21.6 (24.3)	6.2 (8.4)	6.6 (7.9)	136 (133)
Average 13.71	21.7 (21.6)	5.9 (7.2)	7.3 (7.0)	136 (133)

A7.1.9 Borehole KA2510A

Table A7-9. Results from stress calculation using re-analyzed strain data in borehole KA2510A. The published results are presented in brackets.

Borehole depth [m]	Principal stress magnitudes [MPa]			orientations [°N/°]			Elastic parameters [GPa]	[-]
	σ_1	σ_2	σ_3	σ_1	σ_2	σ_3	E	υ
12.04	25.4 (34.6)	12.7 (21.6)	6.4 (16.1)	299/0 (302/6)	29/58 (36/30)	209/32 (203/59)	62.0 (71.8)	0.24 (0.39)
12.36	23.5 (27.7)	12.6 (14.3)	5.4 (9.8)	311/3 (134/0)	46/52 (44/34)	219/38 (224/56)	60.9 (66.7)	0.27 (0.40)
12.87	21.2 (24.0)	12.6 (14.5)	4.3 (6.6)	134/1 (320/0)	41/65 (51/58)	225/25 (229/32)	62.3 (66.1)	0.28 (0.30)
13.36	23.0 (25.3)	11.1 (12.8)	5.7 (7.6)	132/4 (136/1)	29/72 (43/63)	224/18 (226/27)	69.1 (72.1)	0.25 (0.27)
13.75	21.5 (24.5)	9.1 (12.1)	4.6 (6.1)	126/11 (130/10)	28/38 (34/32)	229/50 (234/57)	63.2 (68.8)	0.26 (0.30)
14.20	18.3 (21.9)	8.7 (10.0)	2.4 (5.6)	318/5 (328/6)	57/64 (63/41)	226/26 (231/48)	65.3 (68.9)	0.25 (0.34)
Average 13.10	21.4 (25.9)	11.3 (14.1)	4.9 (9.1)	133/3 (135/0)	35/67 (45/44)	224/23 (225/46)	64.1 (68.9)	0.26 (0.33)

Borehole depth [m]	Horizontal stress magnitudes [MPa]			orientations [°N]
	σ_H	σ_h	σ_v	σ_H
12.04	25.4 (34.4)	8.2 (20.2)	10.8 (17.7)	119 (121)
12.36	23.4 (27.7)	8.1 (12.8)	9.7 (11.1)	131 (134)
12.87	21.1 (24.0)	5.8 (8.8)	11.0 (12.1)	134 (140)
13.36	23.0 (25.3)	6.2 (8.6)	10.7 (11.6)	133 (136)
13.75	21.0 (24.1)	7.3 (10.4)	7.0 (8.0)	128 (132)
14.20	18.2 (21.8)	3.6 (8.0)	7.4 (7.7)	137 (147)
Average 13.10	21.3 (25.9)	5.9 (14.1)	10.3 (9.1)	134 (135)

A7.1.10 Borehole KA2870A

Table A7-10. Results from stress calculation using re-analyzed strain data in borehole KA2870A. The published results are presented in brackets. ^{T} indicates that the strain data have been temperature corrected.

Borehole depth [m]	Principal stress magnitudes [MPa]			orientations [°N/°]			Elastic parameters [GPa]	[-]
	σ_1	σ_2	σ_3	σ_1	σ_2	σ_3	E	υ
12.73	30.8 (41.4)	19.8 (24.2)	4.6 (10.2)	121/19 (130/19)	237/52 (241/46)	19/31 (24/38)	57.8 (64.7)	0.27 (0.33)
13.23	34.6 (39.3)	24.9 (27.8)	5.5 (9.0)	118/11 (123/11)	227/58 (230/55)	22/30 (26/32)	65.2 (68.2)	0.24 (0.30)
13.64	28.1 (27.6)	16.0 (15.8)	5.2 (5.3)	116/1 (296/2)	207/61 (203/59)	25/29 (27/31)	64.1 (63.9)	0.25 (0.27)
14.25	33.0 (36.3)	15.2 (15.3)	2.8 (6.0)	112/1 (299/1)	204/63 (208/59)	21/27 (29/31)	66.7 (62.5)	0.255 (0.21)
14.87^{T}	24.5 (36.3)	10.1 (15.1)	1.7 (7.0)	299/11 (311/5)	178/69 (213/59)	33/18 (44/31)	63.1 (64.8)	0.25 (0.28)
Average 13.74	29.9 (35.5)	15.7 (20.0)	4.8 (7.8)	113/1 (123/5)	205/61 (220/57)	22/29 (30/33)	63.1 (64.8)	0.25 (0.28)

Borehole depth [m]	Horizontal stress magnitudes [MPa]			orientations [°N]
	σ_H	σ_h	σ_v	σ_H
12.73	29.4 (39.1)	8.8 (15.9)	16.6 (20.7)	114 (124)
13.23	34.1 (38.8)	10.3 (14.5)	20.2 (22.6)	114 (119)
13.64	28.1 (27.6)	7.8 (8.1)	13.3 (12.8)	116 (116)
14.25	33.0 (36.3)	5.3 (8.5)	12.4 (12.6)	111 (119)
14.87^{T}	23.9 (36.1)	2.5 (9.2)	9.8 (12.9)	120 (132)
Average 13.74	29.9 (35.5)	7.4 (20.0)	12.9 (7.8)	112 (122)

A7.1.11 Borehole KA3068A

Table A7-11. Results from stress calculation using re-analyzed strain data in borehole KA3068A. The published results are presented in brackets. * indicates that the average stress in the original interpretation includes all four test points.

Borehole depth [m]	Principal stress magnitudes [MPa]			orientations [°N/°]			Elastic parameters [GPa]	[-]
	σ_1	σ_2	σ_3	σ_1	σ_2	σ_3	E	υ
14.73	23.3 (25.4)	7.8 (9.7)	5.2 (6.9)	312/8 (309/8)	215/38 (215/27)	52/51 (54/62)	63.2 (63.9)	0.285 (0.37)
16.18	23.2 (33.6)	15.1 (19.0)	7.1 (9.5)	299/31 (291/11)	31/7 (23/13)	143/72 (161/73)	69.1 (72.1)	0.25 (0.34)
16.50	23.7 (36.1)	12.4 (16.9)	4.1 (7.4)	258/27 (274/15)	162/11 (178/19)	53/60 (40/65)	68.3 (71.6)	0.24 (0.31)
16.85	19.7 (24.4)	11.1 (14.0)	4.8 (7.5)	274/18 (274/17)	179/15 (178/19)	51/66 (43/64)	64.4 (70.6)	0.24 (0.34)
Average 15.46*	23.8 (28.9)	12.6 (15.2)	7.1 (8.5)	302/13 (287/13)	211/3 (195/11)	110/76 (64/73)	66.2 (69.5)	0.268 (0.34)
Average 16.68*	20.1 (28.9)	11.4 (15.2)	5.2 (8.5)	269/20 (287/13)	175/12 (195/11)	55/67 (64/73)	66.4 (69.5)	0.24 (0.34)

Borehole depth [m]	Horizontal stress magnitudes [MPa]			orientations [°N]
	σ_H	σ_h	σ_v	σ_H
14.73	23.0 (25.1)	6.8 (9.1)	6.8 (7.8)	132 (130)
16.18	21.9 (32.7)	14.9 (18.5)	8.8 (10.6)	116 (109)
16.50	19.7 (34.3)	12.0 (15.8)	9.3 (10.8)	84 (96)
16.85	18.3 (23.1)	10.6 (13.2)	7.2 (9.9)	98 (98)
Average 15.46	22.9 (28.9)	12.6 (15.2)	8.3 (8.5)	122 (108)
Average 16.68	18.5	11.1	7.7	93

A7.1.12 Borehole KZ0059B

Table A7-12. Results from stress calculation using re-analyzed strain data in borehole KZ0059B. The published results are presented in brackets.

Borehole depth [m]	Principal stress magnitudes [MPa]			orientations [°N/°]			Elastic parameters [GPa]	[-]
	σ_1	σ_2	σ_3	σ_1	σ_2	σ_3	E	υ
7.77	17.5 (23.9)	8.5 (12.3)	3.9 (7.4)	143/26 (148/18)	289/59 (295/70)	45/15 (54/10)	63.1 (64.2)	0.24 (0.43)
8.33	15.7 (29.8)	11.5 (17.7)	5.8 (11.1)	338/1 (160/0)	229/86 (253/88)	68/3 (70/2)	63.3 (65.3)	0.24 (0.49)
9.05	16.0 (18.3)	10.6 (12.1)	4.2 (5.1)	328/9 (329/8)	172/80 (181/81)	58/4 (60/5)	63.5 (67.4)	0.245 (0.32)
12.22	15.5 (22.0)	9.8 (13.8)	2.8 (5.3)	329/9 (332/3)	98/76 (75/78)	237/11 (242/12)	63.2 (62.1)	0.235 (0.43)
14.20	15.3 (29.0)	11.4 (17.6)	5.3 (10.1)	328/1 (155/1)	62/77 (62/77)	238/12 (245/13)	58.3 (61.3)	0.25 (0.48)
14.73	16.4 (29.3)	11.7 (17.1)	6.2 (10.5)	325/12 (333/3)	159/77 (216/84)	56/3 (63/5)	61.4 (64.9)	0.26 (0.44)
Average 11.05	16.5 (24.3)	11.0 (14.8)	4.9 (8.0)	329/5 (334/1)	118/85 (83/87)	239/3 (244/3)	63.1 (64.2)	0.25 (0.43)

Borehole depth [m]	Horizontal stress magnitudes [MPa]			orientations [°N]
	σ_H	σ_h	σ_v	σ_H
7.77	15.7 (22.9)	4.2 (7.5)	9.8 (13.1)	128 (123)
8.33	15.7 (29.8)	5.9 (11.1)	11.5 (17.7)	146 (136)
9.05	15.9 (18.2)	4.2 (5.1)	10.7 (12.1)	136 (125)
12.22	15.4 (22.0)	3.0 (5.6)	9.8 (13.6)	136 (128)
14.20	15.3 (29.0)	5.5 (10.5)	11.2 (17.4)	136 (131)
14.73	16.2 (29.2)	6.2 (10.5)	11.9 (17.0)	134 (129)
Average 11.05	16.4 (24.3)	4.9 (14.8)	11.0 (8.0)	137 (142)